# Max-Planck-Institut für extraterrestrische Physik

# RESEARCH 2002 – 2004

## A Book of Highlights

**Observations - Measurements**

**Theory - Simulations**

**Experiments - Projects - Detector Developments**

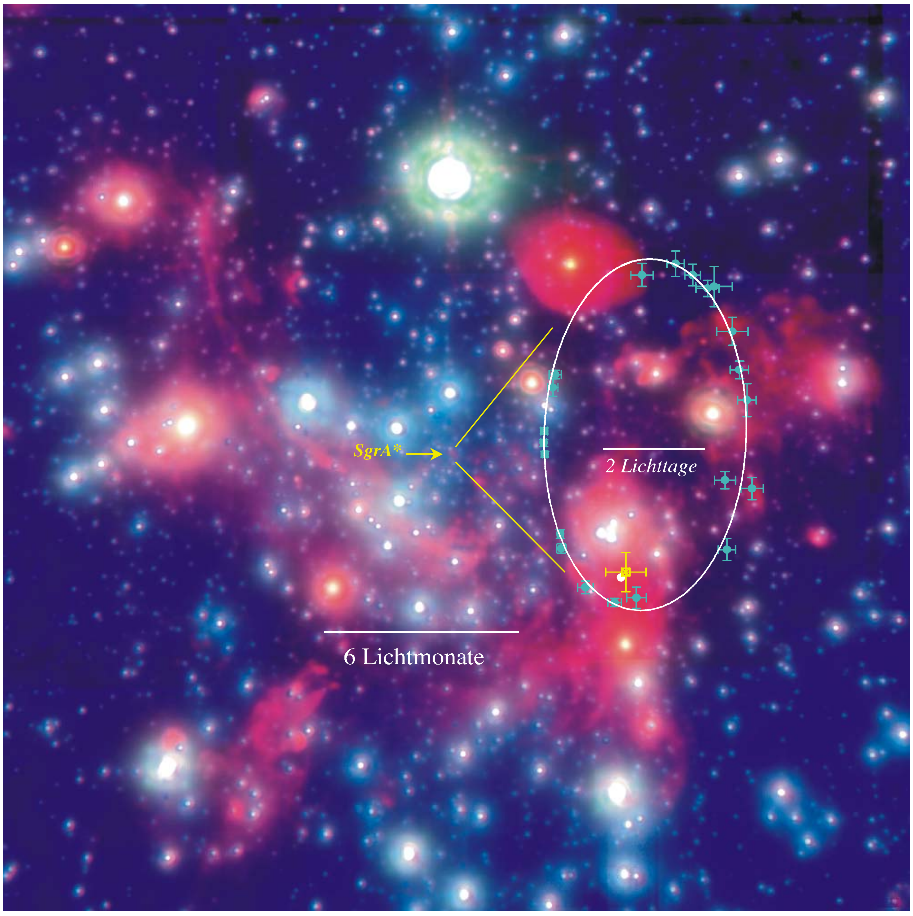


*October 2004*

# Book of MPE Research Highlights

This book of MPE research highlights from the years 2002 to 2004 was produced for the MPE Fachbeirat Meeting of November 29 to December 1, 2004. Its goal is to provide a comprehensive overview as well as detailed information on science results, data analysis activities, ongoing experimental projects and detector developments in a fashion that is supplementary to the Annual Reports of these years. The authors of individual posters are clearly identified and are solely responsible for their contents. No attempt was made to balance the contributions from the different MPE groups, or to achieve any kind of completeness.

Our most important scientific highlights are given at the beginning of the relevant sections. They are marked in the table of contents by **bold** letters, and their abstracts are framed by a red box.

*R. Genzel, W. Collmar*

# Table of Contents

# Solar System Physics

# Diffuse Upstream Ions at the Earth`s Foreshock

Cluster provides for the first time simultaneous measurements of energetic ions upstream of Earth`s quasi-parallel bow shock with several spacecraft. We have analyzed a 10 hour period at large separation distance. From the difference of partial densities between spacecraft 1 and 3 we determine the spatial gradient along the magnetic field and the e-folding distance.

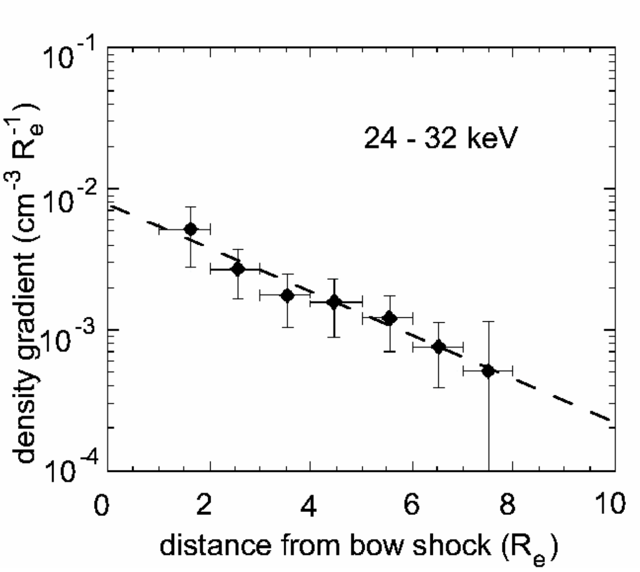


*Fig 1: Average partial ion density gradient in the 24-32 keV energy range versus distance from the bow shock.*

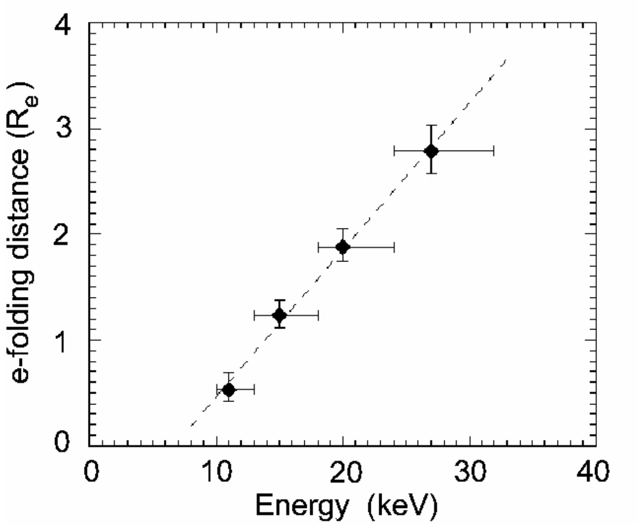


*Fig 2: The e-folding distance obtained by fitting an exponential to the partial density gradient in 4 energy channels.*

It has been demonstrated in the past that there is a one-to–one correlation between the presence of diffuse upstream ions and the occurrence of hydromagnetic waves in the foreshock region: the waves are excited by the particle streaming and the particles are pitch angle scattered by the waves. This leads to a diffusive particle transport Using a bow shock model we determined the distance of spacecraft 1 and spacecraft 3 to the shock along the magnetic field. Using the differences of the partial energetic ion densities at various distances from the bow shock we determined the spatial ion density gradient. The gradient decreases in the energy range 10-32 keV exponentially with distance from the shock with an e-folding distance from 0.5 Re to 2.8 Re, the e-folding distance depending approximately linearly on ion energy. Figure 2 shows the e-folding distance obtained between 10 and 32 keV. This demonstrates that ion transport in the upstream region is diffusive.


Kis, A., M. Scholer, B. Klecker, E. Moebius, E. A. Lucek, H. Reme, J. M. Bosqued, L. M. Kistler, and H. Kucharek, Geophysical Research Letters, 31, L20801, doi:10.1029/2004GL020759, 2004.



*A. Kis, M. Scholer, B. Klecker*

# Auroral Acceleration in thin Electric Layers

Extremely high-resolution observations of the space-time variation of the electron and ion energy fluxes in the auroral upward current (inverted-V) region prove that layers of field-aligned electric fields of altitudinal extension ~20 km or less are responsible for the field-aligned acceleration of electrons and ions.

The Figure shows a 3-s sequence of high-space-time resolution measurements of upward ion and electron as well as downward electron energy flux measurements of the FAST spacecraft when in the low altitude auroral magnetosphere during active auroral times. The fluxes are essentially at constant average energy similar for both particle components but exhibiting nearly sinusoidal well expressed oscillations in energy. The striking fact is the anti-correlation between ion and electron energies which suggests that the spacecraft is quasi-periodically crossing a narrow in altitude (presumably parallel electrostatic field) layer which accelerates hot auroral electrons downward along the magnetic field while accelerating cold auroral ionospheric ions

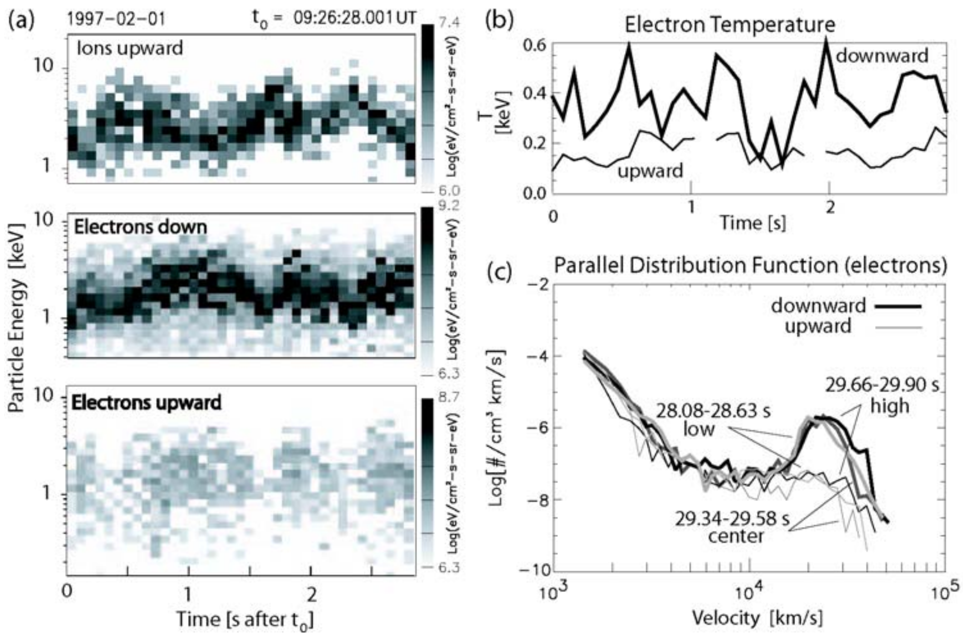


upward along the field. The energy gain in both components is comparable ~3-4 keV yielding a potential drop of ~3-4 kV alternatively experienced by the particle components belonging to an upward directed parallel electric field. From the spacecraft velocity and the undulation period one estimates that the field-aligned extension of the layer is the order of < 20 km, in excellent agreement with theoretical predictions of small-scale double layers in the auroral plasma. Moreover the presence of weak upward electron fluxes (lowest panel left) correlated with the downward electrons points on the backscatter of some downward flowing electrons with magnetic mirror points close to the position of the layer. The full distribution in the high electron energy regions is thus of ring distribution family. The panels on the right show the oscillation of the electron temperature as function of time for the downward and upward electrons (top panel) with the backscattered electrons having relatively low and constant temperature. The parallel distribution function of electrons at three energy positions is shown in the lower right panel expressing the variation in the width of the auroral electron beam.


Pottelette, R., R.A.Treumann,and E.Georgescu, Nonlin. Proc.Geophys. 11, 197-204 (2004).



*R. A. Treumann and E. Georgescu in collaboration with R. Pottelette*

# Magnetopause Current Determination

**A unique capability of the Cluster mission is the ability to infer local electric current densities through a direct application of Ampére's law. The technique, known as the curlometer, has been used to infer the structure of the current within the Earth's magnetopause.**

Figure 1 shows an example of a Cluster magnetopause crossing when the four spacecraft were only ~ 100 km apart. The top panel shows time series of the dominant magnetic field component, as recorded by the magnetometers on the four spacecraft. It changes from a stable value in the magnetosphere (on the left) to a different stable value in the magnetosheasth (on the right). The transitions between the two levels mark the passage of the magnetopause current layer over the four spacecraft. From the differences between the magnetic fields measured at the four spacecraft locations, together with the known specraft separation vectors, one can estimate $\Delta \times B$ , which according to Ampére's law yields the current densities. The middle panel shows the three components of the electric current vector, calculated with this technique, known as the curlometer.

It is evident from the three traces in the middle panel that the current within the magnetopause is not constant but highly structured. This fact is better illustrated by the two hodograms shown at the bottom. These hodograms are obtained by drawing all currents measured during the magnetopause traversal as vectors from the origin and connecting the arrowheads by line segments. As they occupy three dimensions, the current vectors have been projected into two orthogonal planes, one (left) being the plane of the magnetopause, the other (right) a plane orthogonal to the magnetopause. From inspection of the hodograms it is evident that the current changes not only in magnitude but also in direction, rotating by almost 180 °. The determination of spatial structure of the current sheds new light on the different large-scale current systems closing within the magnetgopause.

From the hodogram, one can also infer the magnetopause orientation. Then, by integrating Ampére's law across the magnetopause current layer, one also obtains the motion of the magnetopause relative to the spacecraft.

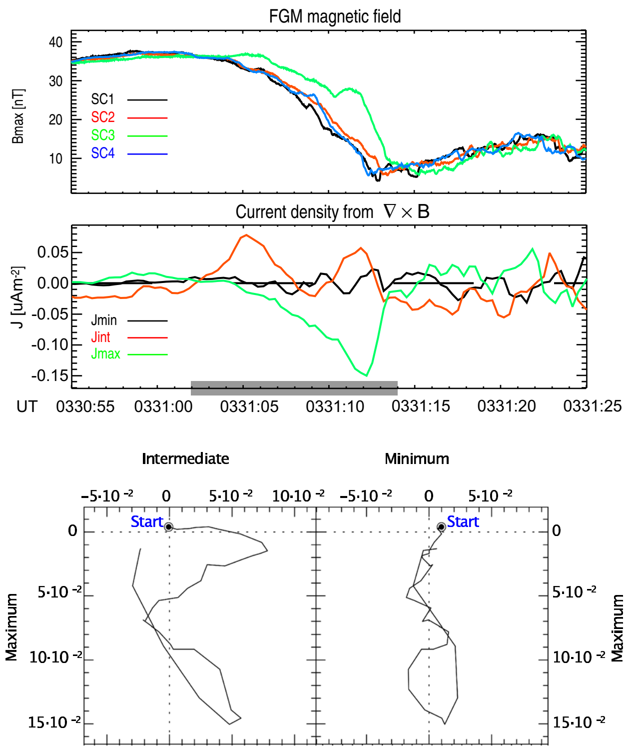


*Fig 1. Top panel: Main component of the magnetic field as measured by the four Cluster spacecraft during a magnetopause crossing on 2 March 2002. Bottom panel : the three components, of the current density vector, determined from the differences between the magnetic field vectors at the four spacecraft.*

Since the crossing duration is known (indicated by the shaded bar in the middle panel of Figure 1), the magnetopause current sheet thickness can then be calculated. For this case, we found a velocity of $\simeq$35 km/s, and a thickness of 160 km, corresponding to 2-3 ion gyro radii.

*S. Haaland, B. Sonnerup, E. Georgescu, G. Paschmann, B. Klecker*

# Characteristics of the Dawn side Magnetopause

**The Cluster mission is providing the first ever four-spacecraft measurements of the Earth's plasma environment. Here we utilize Cluster's multispacecraft capabilities to study the thickness, speed and current densities of Earth's magnetopause. We find a large range of thicknesses, from less than 200 km to thousands of km, uncorrelated with any properties of the solar wind or the interplanetary magnetic field.**

The magnetopause is a thin sheet of electric current that separates the solar wind from the Earth's magnetic field. When this boundary moves over a spacecraft, its instruments will record abrupt changes in magnetic field and plasma properties, but as the speed of the boundary motion is unknown a-priori, one cannot determine its thickness.

With Cluster, one can use the timing of the crossings recorded by the four spacecraft to directly determine the orientation and velocity of the magnetopause, and from this calculate its thickness. Together with the known changes in the magnetic field across the current layer one can also compute the net electric current flowing within the magnetopause. Figure 1 shows the results for 96 crossings of the dawnside magnetopause. in terms of the number of cases that fell within specified ranges of thickness, speed, and current.

Particularly striking is the large range of thicknesses, from less than 200 km to thousands of km. In simple models the magnetopause thickness should scale as the ion gyro-radius, because the gyro radius determines how deep the incident solar wind ions should penetrate the Earth's magnetic field. But the gyro radius was measured to be only about 50 km for the cases studied. Thus the magnetopause is usually much thicker than simple theory prediicts. Curiously, we find the variations in thickness uncorrelated with any properties of the solar wind or the interplanetary magnetic field.

The middle panel demonstrates the large range in magnetopause speeds, from less than 10 to several hundred km/s. This illustrates that one cannot infer the magnetopause thickness simply from the duration of the crossings. The bottom panel, finally, indicates that the current denities are typically 0.1 $\mu A\,m^{-2}$.

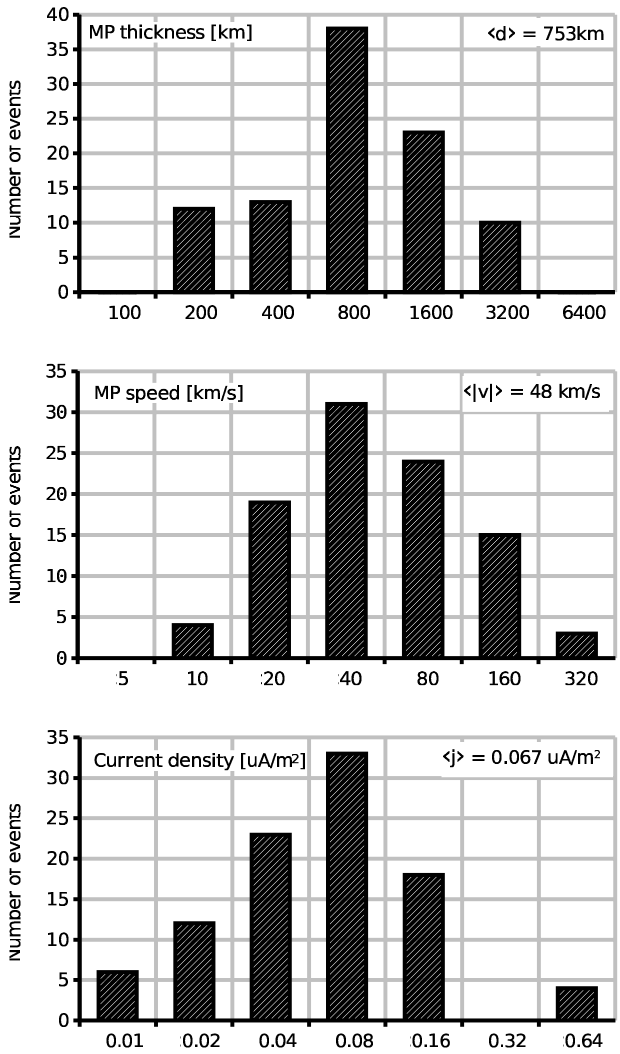


*Fig 1. Histograms of magnetopause speed, thickness and current density for 24 dawn flank magnetopause crossings by all four Cluster spacecraft on 5 July, 2001, resulting in a total of 96 individual crossings. Note that the bins are logarithmically spaced.*

*G. Paschmann, S. Haaland, B. Sonnerup, E. Georgescu, B. Klecker*

# Oxygen Outflow in the Cusp and Polar Cap Regions

Beams of singly ionized oxygen with narrow energy distributions originating in the dayside cusp region are observed frequently in the cusp and polar cap regions of the Earth. A statistical study using Cluster data shows that the source region is located near the equator-ward edge of the cusp/cleft, with a latitudinal range of ~1.5°. Cluster observations inside the source region, at ~ 4.5 - 6 $R_e$ show high transverse heating of the $O^+$ population by BBELF waves.

The instrumentation onboard CLUSTER enables us to investigate the acceleration mechanism, and the location and size of the source region in great detail. Figure 1 shows an example of such an $O^+$ outflow event, as observed on Cluster-4. The top two panels display energy-time spectrograms of $H^+$ and $O^+$ ions, respectively. The energy-time dispersion of protons (a) is typical for the cusp, and can be attributed to different travel times of ions with different energies from a reconnection site at the dayside magnetopause to the point of observation. Oxygen (panel b) shows a narrow, beam-like, energy distribution. The third panel (c) presents parallel velocities of $H^+$ (green) and $O^+$ (black). Oxygen outflow starts at 12:46 UT. Subsequently there is a strong increase of the parallel velocity. During this time interval the S/C crossed a narrow acceleration region. The dashed line in Fig. 1 marks the equator-ward boundary of this region. After 12:49 UT the satellite leaves the acceleration region, indicated by the gradually decreasing parallel velocity of $O^+$ ions. The increase in energy of $O^+$ ions is correlated with a strong increase in the electric wave power in the frequency range 1-180 Hz, as measured with the EFW (panel d) and STAFF (panel e) experiments onboard Cluster.

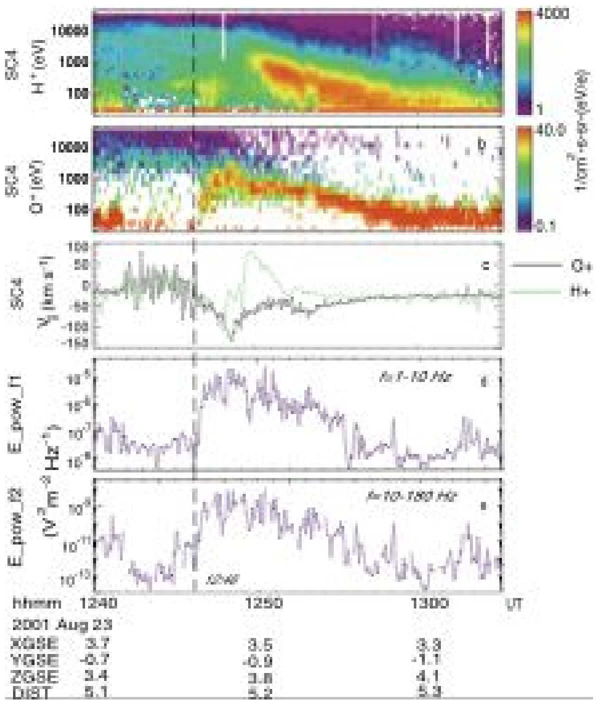


Fig. 1 *CIS, EFW and STAFF data from Cluster-4: $O^+$energization event.*

This correlation suggests perpendicular energization of $O^+$ ions by the broad-band low-frequency wave field at altitudes of ~4-6 $R_E$. The velocity distribution of ions shows indeed strong perpendicular heating at the time of the maximum energy of the $O^+$ ions, whereas 8 minutes later, when the satellite already left the acceleration region, the velocity distribution shows a narrow, field-aligned beam.

To estimate the latitudinal and longitudinal size of the source region we used the Tsyganenko-96 magnetic field model and traced the boundaries of the acceleration region to the ionosphere level (100 km). Using data from 3 Cluster spacecraft for 10 events we find that the source is located near the equator-ward boundary of the cusp, and has an extension of ~1.5° in latitude and ~14° in longitude.

Bogdanova, Y.V., B. Klecker, G. Paschmann, et al., Adv Space Res., doi:10.1016/j.asr.2004.02.014 , 2004, in press.

*Y.V. Bogdanova, B. Klecker, G. Paschmann*

# Spatio -Temporal Coherence of $O^+$ Outflows

Ion data aboard three Cluster satellites are used for the first time to assess the coherence in space and time of dayside ion outflows. The most remarkable finding is that, although dayside outflows are a permanent feature, steady-state conditions are surprisingly never achieved. A significant variability is particularly found for local outflow intensities on small time scales.

It is well known from earlier satellite missions that the Earth‘s ionosphere competes with the solar wind to supply plasma into the magnetosphere [Yau and Andre, 1997]. The outflow composition is mainly $O^+$ and $H^+$ ions, with the largest fluxes originating from the dayside cusp. Data from the Cluster multi-satellite system allow for the first time to access the spatial and temporal coherence of dayside outflows.

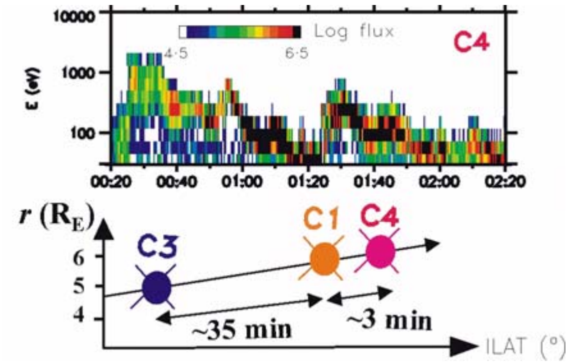


*Fig. 1: From top to bottom; time-energy spectra of $O^+$ ions measured onboard Cluster satellite C4; drawing of the satellite configuration along its polar orbit .*

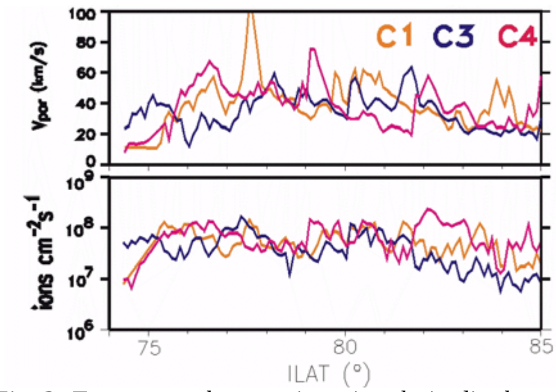


*Fig. 2: From top to bottom; invariant latitudinal series of $O^+$ upward mean velocity and integral flux from satellites C4 (pink), C1 (orange) and C3 (blue).*

Figure 1 shows an example of an $O^+$ outflow event observed on 3 of the Cluster satellites, when moving poleward in the high-altitude polar cap. The $O^+$ outflow detected in the time-energy spectra (left) is the result of multi stage processes. First, ionospheric processes raise the scale height of $O^+$ ions so that wave/particle interactions higher up in thin latitudinal regions lead to ion escape from gravity. Then, ions move up via the mirror force and drift in latitude due to the magnetospheric convection. This latter stage leads ions from a narrow source to spread out at Cluster altitudes.

To investigate whether $O^+$ features are spatial or temporal, one can compare them on the same field line. In Figure 2, plots of $O^+$ upward velocity and flux as a function of invariant latitude (ILAT) show significant variations at the same ILAT between satellites. This is the first direct evidence of $O^+$ variations being temporal, demonstrating the importance of non-steady processes in the development of the outflow.

A statistical study with 18 similar events [Bouhram et al., 2004] confirmed the presence of significant variability. Such results associated with small scale processes may have some implications in the large scale transport of mass and energy through the magnetospheric system.

Yau, A., and M. André, Space Sci. Rev., 80, 1-25, 1997.
Bouhram, M., B. Klecker, G. Paschmann, et al., Ann. Geophys., 22 (7), 2507-2514, 2004.

*M. Bouhram, B. Klecker, G. Paschmann, and A. Blagau*

# Plasma Convection across the Polar Cap

We present measurements of convection velocities obtained with the Electron Drift Instrument on Cluster, using 20 passes that are close to the noon-midnight meridional plane. Taking the single spacecraft measurements the convection velocities show the expected trend as a function of IMF $B_z$. The unique contribution by Cluster is the ability to provide multi-point measurements, thus allowing the inference of spatial scales. Correlation studies of the convection velocities show that the characteristic length scales are larger for southward IMF than for northward IMF.

Magnetospheric convection is driven primarily by magnetic reconnection. For southward interplanetary magnetic field (IMF) reconnection occurs along an X-line on the dayside magnetopause. Once interconnected, open magnetic flux tubes are carried by the solar wind over the poles downstream, resulting in anti-sunward convection of magnetic flux over the polar caps. For northward IMF, reconnection can occur poleward of the cusps, between interplanetary field lines and open tail-lobe field lines. The result is a circulation pattern, often described as tail lobe stirring, with sunward convection over part of the polar cap.

In Fig. 1 we show 10-min averaged convection velocities as a function of IMF $B_z$. To remove the height dependence of the velocities which is caused by the magnetic flux tube expansion with altitude, the velocities are scaled to an ionospheric altitude of 100 km. To evaluate the sense of convection we used the velocity component along the direction given by $\mathbf{B} \times \hat{\mathbf{y}}_{\mathbf{GSE}}$. This direction always maps to sunward convection in the ionosphere. Fig. 1 shows the expected trend, in spite of large scatter: for large negative IMF $B_z$ essentially all velocities are directed anti-sunward ($\tilde{V}_s < 0$), and the bulk of the velocities become smaller with increasing IMF $B_z$. The majority of the averaged velocities are negative even for an IMF $B_z$ as large as +5 nT. The main reason for this is that for northward IMF the convection is not expected to be uniformly sunward over the entire polar cap, but contains also regions with anti-sunward convection, the detailed distribution depending on IMF $B_y$.

From correlations of the convection velocities from three spacecraft it appears that the scales, when mapped down to ionospheric altitudes, are always larger than 1 km and sometimes, but not always larger than a few hundred km (cf. Fig. 2a). Splitting the data into cases of pure northward and southward IMF (Fig. 2b,c) shows that the large scales of a few hundred km exist only for southward IMF, whereas for northward IMF poor correlation occurs already at separation distances of only a few tens of km. These results are in qualitative agreement with models and observations reported in previous publications. While it seems hardly surprising that scales are larger than 1 km, poor correlation at only a few tens of km separation over the polar cap is surprising and is below the resolution achieved by the SuperDARN radars in their standard scan mode.

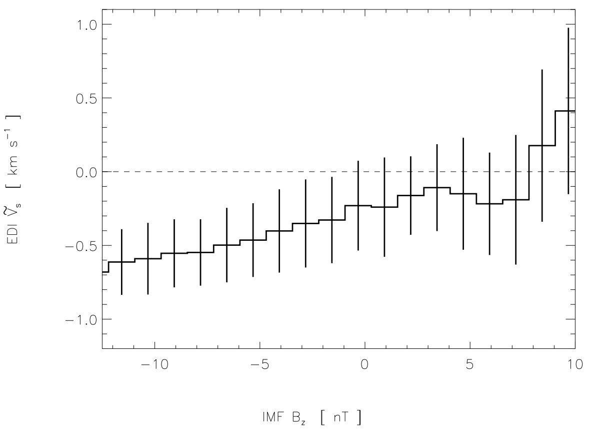


*Fig 1: Histogram of scaled 10-min averaged convection velocities vs. IMF $B_z$. Standard deviations are shown as vertical bars.*

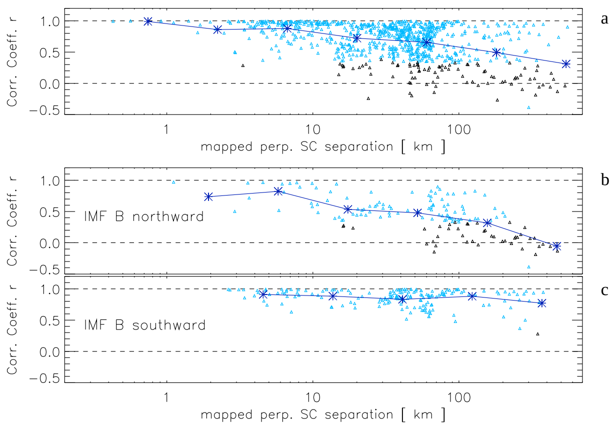


*Fig 2: Correlation coefficients of 1-h intervals of convection velocities vs. mapped spacecraft separation distances; correlation coefficients below the significance threshold are colored black.*

*H. Vaith, G. Paschmann, M. Förster, E. Georgescu, S.E. Haaland, B. Klecker*

# Magnetosphere - Ionosphere Coupling: Substorms

The classical paradigm of the substorm current wedge as diversion of the neutral sheet current closing through the ionosphere from dawn to dusk is probed with the four-point Cluster measurements in a new-fashioned way. We examine the current structures within the high-altitude (at $\sim 4.3\ R_E$) inner–magnetosphere intermediate region between the equatorial plasma sheet and the ionospheric Harang discontinuity or substorm current wedge (SCW) sector for one particular interval during a series of substorm pseudo-onsets. The traditional single–spacecraft methods for current estimations are applied to deduce both the field-aligned (FAC) and field-perpendicular currents. They are supplemented by various methods for the estimation of the current sheet normal and motion to determine the complex current structure in that region. These single–spacecraft methods are then contrasted with the new opportunities of the full vector current estimation with the Cluster tetrahedron by use of the reciprocal vector (RV) method (mathematically identical to the curlometer technique). The four-point methods allow the full vector spatial determination of the current structures with characteristic scale lengths of the satellite's volumetric tensor or larger and enable to differentiate between spatial and temporal variations in the same scales. Single-spacecraft methods allow, on the other hand, a much better resolution of fine structures, although their interpretation is often equivocal. The combination of both proves to be a valuable tool for the unambiguous description of such phenomena. The magnetometer-based current estimations are then compared with measurements of the particle and wave instruments of Cluster to deduce a more complete picture of the phenomenon and to come to conclusions about the intricate substorm-related plasma processes.

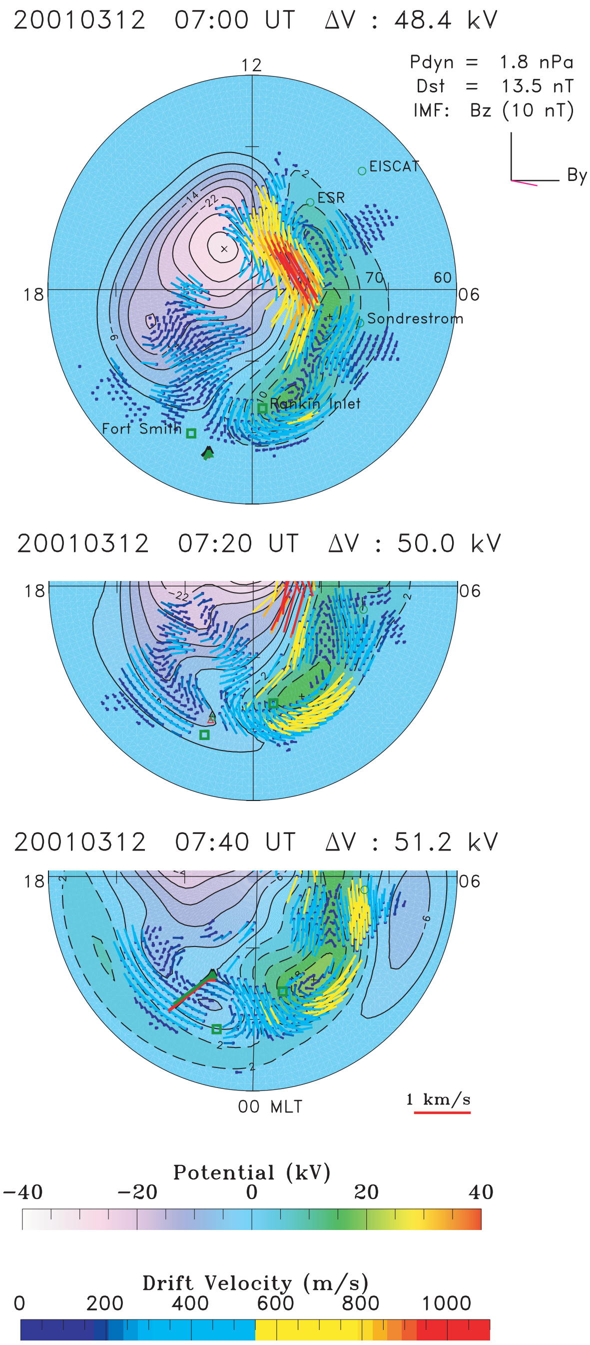


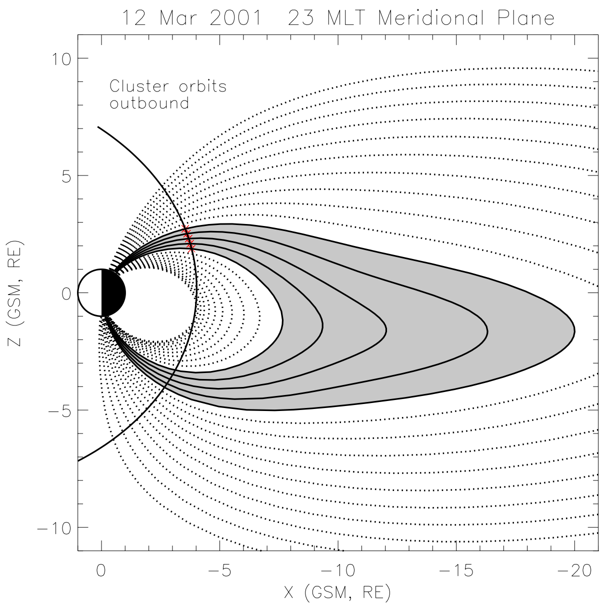


SuperDARN measurements of polar cap convection in MLT versus magnetic latitude ($60° - 90°$) coordinates for three characteristic two–minute intervals around the event under study of March 12, 2001, in comparison with EDI drift measurements mapped into the ionosphere (shown as triangles near 23 MLT with the corresponding vector arrows). Solar wind conditions are indicated in the upper right corner as well as the cross–polar cap potential for each subinterval.

*M. Förster, G. Paschmann, H. Vaith, E. Georgescu, J. Baker, R. Greenwald*

# Auroral Arc Electrodynamics from Satellite Data

The ALADYN (AuroraL Arc electroDYNamics) method provides a realistic description of an auroral arc (Marghitu, 2003; Marghitu et al., 2004). The method is based on a parametric arc model, that allows the derivation of the parameters by numerical fit to the experimental data. In order to obtain consistent results one has to take into account, as a minimum, the ionospheric polarization, the contribution of the Hall current to the meridional closure of the field-aligned current (FAC), and the coupling between the FAC and the electrojet (EJ) flowing along the arc.

ALADYN is illustrated with a wide, stable, winter evening arc, as seen in the 'Data' panels. The ionospheric electric field (IEF), potential, and current obtained by ALADYN are presented in the 'Results' panels. The IEF and potential are given for two arc models: YPYH, where only the polarization and Hall terms are considered, and YPYHX, where the FAC–EJ coupling is added. Outside of the ion beams the potential drops at FAST and ionospheric level match each other (as expected, because the magnetic field line is equipotential) for model YPYHX (panel *d),* which is not the case for model YPYH (panel *c*). This is a key feature, pointing to the importance of the variations along the arc. The negative excursions of $E_x$ at the arc boundaries indicate polarization charge double layers, as sketched in panel *f*. Once the IEF is derived, one can also find the ionospheric current. In our case the Pedersen and Hall components of $J_x$ compensate each other, and the ionospheric connection between the downward and upward FACs is vanishingly small (panel *e*). This quite atypical configuration is caused by the close vicinity of the FAC and convection reversal.

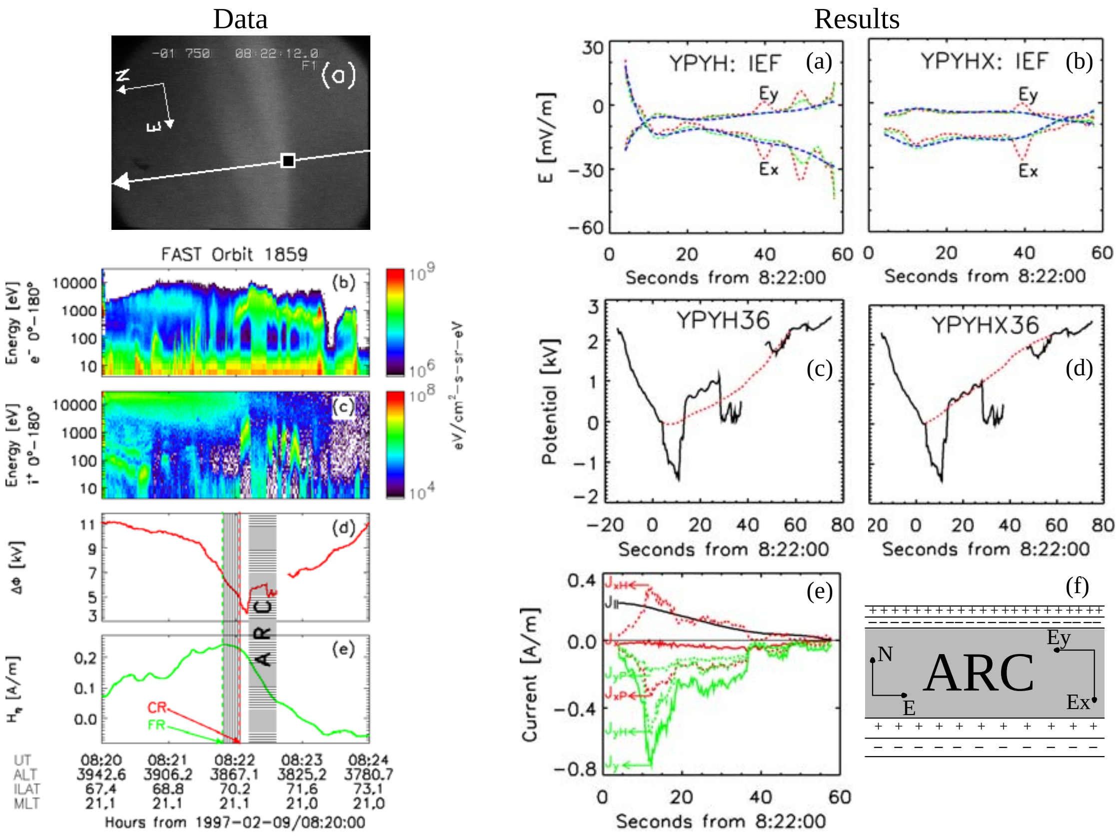


*Left* (*a*) Ground optical data. (b–e) FAST data: electron and ion energy spectrograms, high altitude electric potential, perturbation magnetic field. FR and CR indicate the FAC and convection reversal, respectively.

*Right:* Results obtained by ALADYN: (*a*, *b*) IEF for polarization length scales of 4km (red), 8km (green), and 20km (blue); (*c*, *d*) potential drop at FAST (black) and ionospheric level (red); (*e*) field-aligned (black) and ionospheric current ($J_x$ red, $J_y$ green, together with their respective Pedersen and Hall components); (f) schematic view of the arc.


Marghitu, O., Ph.D. Thesis, TU Braunschweig, MPE Report 284, 2003.
Marghitu, O., et al., J. Geophys. Res., in press, 2004.



*O. Marghitu, B. Klecker, G. Haerendel,* *in collaboration with J.P. McFadden*

# Wave Spectra in Auroral Acceleration Layers

Full waveform and electrostatic wave spectra obtained in crossings of auroral acceleration layers identify these layers as being the result of narrow wave structures in the ion acoustic and electron hole modes which can exist in collisionless plasmas under very exotic conditions only and contain strong potential drops along the magnetic field which accelerate charged particles.

The observation of thin auroral acceleration layers is particularly interesting from the point of view of the structure of wave spectra in these layers as these contain information about the dynamical processes inside the layer and in addition about the origin of such layers. This is a non-trivial problem as normally in collisionless plasmas no field-aligned electric fields should exist except when strong density gradients can be kept stable for long enough time without being depleted by electron motion. Such gradient electric fields are however very weak due to the large gradient scales. In comparison the observed structures are of only few km in width and therefore contain very strong electric fields of the order of up to ~1 V/m. The FAST spacecraft has been successful in traversing such acceleration layers. These have been recognized from the anticorrelation in electron and ion acceleration. Figure 1 shows, for such a transition, the full waveform of the electric field and the power spectrum of this waveform.

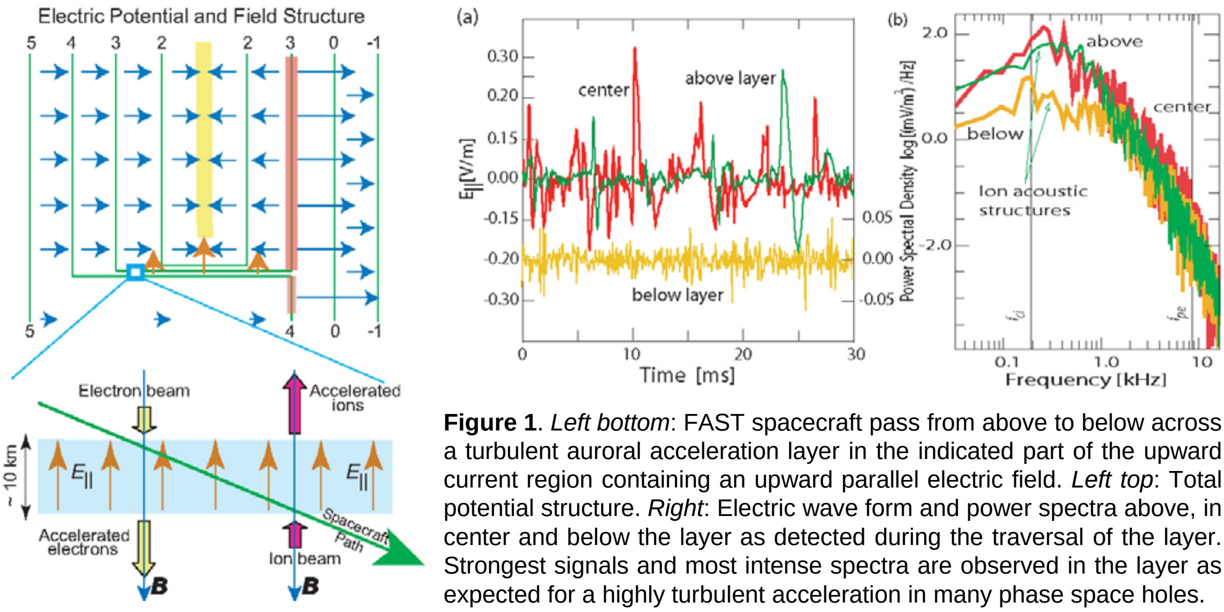


**Figure 1**. *Left bottom*: FAST spacecraft pass from above to below across a turbulent auroral acceleration layer in the indicated part of the upward current region containing an upward parallel electric field. *Left top*: Total potential structure. *Right*: Electric wave form and power spectra above, in center and below the layer as detected during the traversal of the layer. Strongest signals and most intense spectra are observed in the layer as expected for a highly turbulent acceleration in many phase space holes.

A global sketch of the potential distribution in the upward current region is shown on the left corresponding to converging (left) and diverging (right) perpendicular fields (or shear flows). Two charge layers are indicated causing the potential to form a trough. The tiny indicated region is expanded below showing the electric field pointing upward and its effect on electrons and ions as seen by the passing FAST spacecraft. The right part of the figure shows the three waveforms above, below and in the center of the sheet. Highest and spiky wave activity is observed in the center of the layer yielding also the most intense power spectrum with power law tail and a maximum in the ion acoustic wave band. Hence ion acoustic localized structures (phase space holes) accumulate in the very center of the layer, with the electric fields being concentrated in them but, as seen from the waveform, being asymmetric and thus generate the finite mesoscale potential drop and field aligned electric fields shown on the left which cause the acceleration of the auroral particle population. It is highly suggestive that similar processes will evolve elsewhere in the universe whenever shear flows are generated in low-$\beta$ plasmas.

Pottelette, R., R.A.Treumann and E.Georgescu , *Nonlin. Proc. Geophys*. **11**, 197-204 (2004).

*R. A. Treumann, E. Georgescu,* *in cooperation with R. Pottelette*

# Localized Electric Auroral Wave Fields

One-dimensional particle simulations are used to investigate the excitation of localized large amplitude electrostatic low-frequency structures in the active auroral inverted-V region. Excellent agreement is obtained between the observation of such structures and the simulation showing that the structures are ion-acoustic and Langmuir in nature and contribute to particle acceleration.

The original set-up of the simulation (top left of Figure) is a cold ion/warm electron background plus the hot fast auroral electron beam. At simulation end the distribution (below) shows backscattered electrons, top-flat electron backgrounds, a plateau (ring) in the beam and accelerated fast electrons. The electron phase space (lower left) sees initial electron-acoustic hole evolution becoming depleted at long time. The dispersion diagram (intensity in frequency-wavenumber space, upper right) shows Langmuir waves, wave coupling, ion acoustic waves and

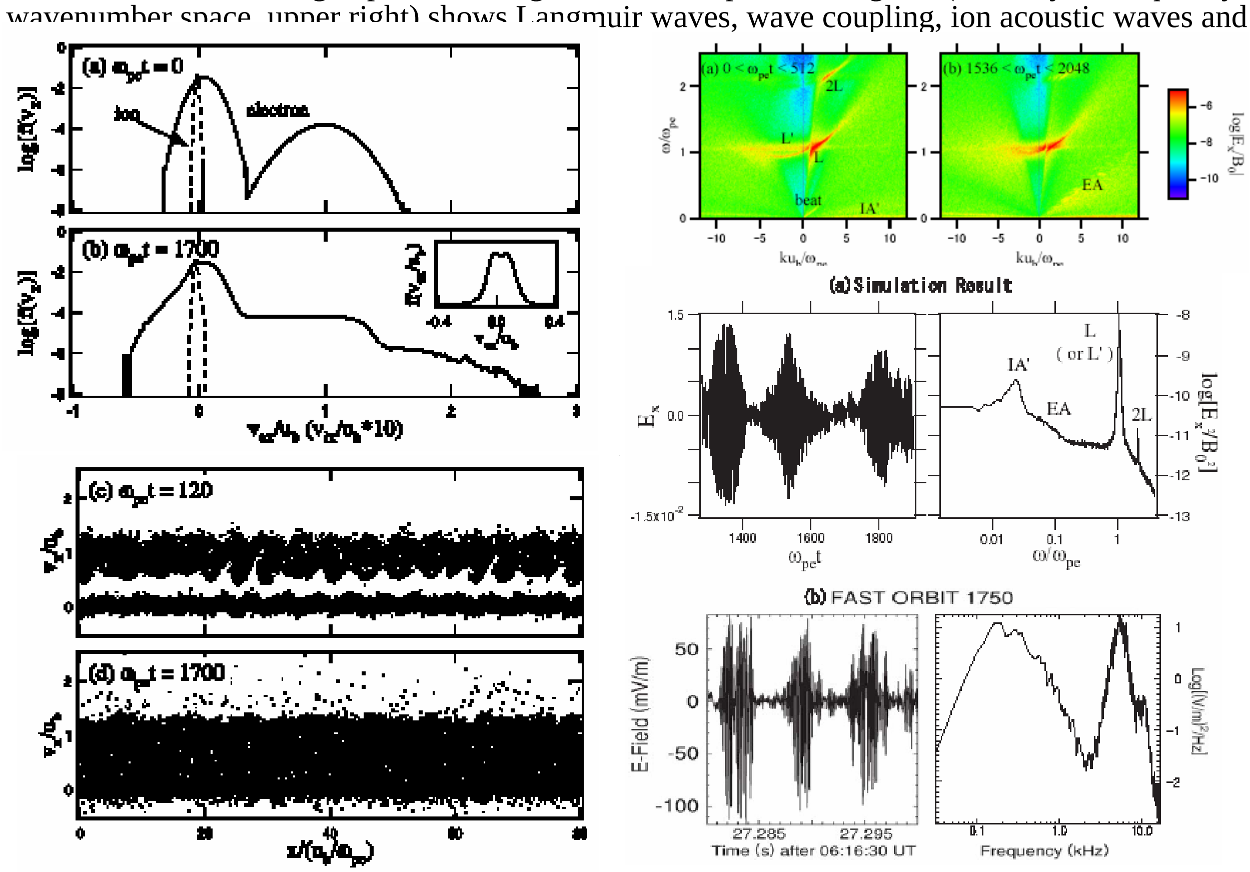


harmonic Langmuir waves developing initially with in the final state nonlinear electron acoustic waves arising. The time evolution of the electric waveforms of the simulation (right panel left center) and FAST auroral observations (right panel, left bottom) are strikingly similar exhibiting formation of bursty wave packets which indicate the localized self-modulated nature of wave generation and wave-particle interaction. The final simulated spectrum (right panel, right center) is qualitatively similar to the observed spectrum (right panel, right bottom). It shows ion-acoustic (IA), late electron acoustic (EA), Langmuir (L) and Langmuir harmonic (2L) emissions though of different relative strengths which is due to the one-dimensional simulation restriction in contrast to the three-dimensional observations. Obviously the ion acoustic waves are decisive for structure formation while ion acoustic and Langmuir waves are important in the accelration of particles and deformation of their distribution functions in the aurora. Waves of these intensities should substantially contribute to generation of radiation also in astrophysical systems.


Matsukiyo, S., R.A.Treumann and M.Scholer, J.Geophys. Res. 109,A06212,doi:10.1029/2004JA010477(2004).



*R. A. Treumann and M. Scholer in collaboration with S. Matsukiyo*

# General Linear Mirror Mode Theory

A fully kinetic theory of the magnetic mirror instability in high-β plasma has been developed accounting for the effect of electrons respectively the effect of arbitrary ion-Larmor radii. Taking into account electrons we find that two entirely new modes can develop which we call slow ion and kinetic slow modes. On the other hand, accounting for finite Larmor radii, we find that at scales the order of the ion-Larmor radius the ordinary ion-mode instability growth rate and threshold are substantially modified because the effective elasticity of the magnetic field lines increases. In addition the magnetic field develops a non-coplanar component which is otherwise not included in the theory of the mirror mode.

The magnetic mirror mode is one of the most interesting extremely low-frequency modes developing in anisotropic temperature high-β plasmas typical for space plasmas. In the last few years we have worked intensely at its understanding in spite of the now 50 years between their discovery and today. The reason is that they are frequently observed in near-Earth space as one of the fundamental low-frequency modes which dominate magnetic turbulence in contrast to what is usually believed that magnetic turbulence is mainly determined by Alfvén modes. The latter might be true for low-β plasmas but does not generally apply in the high-β case. We treat

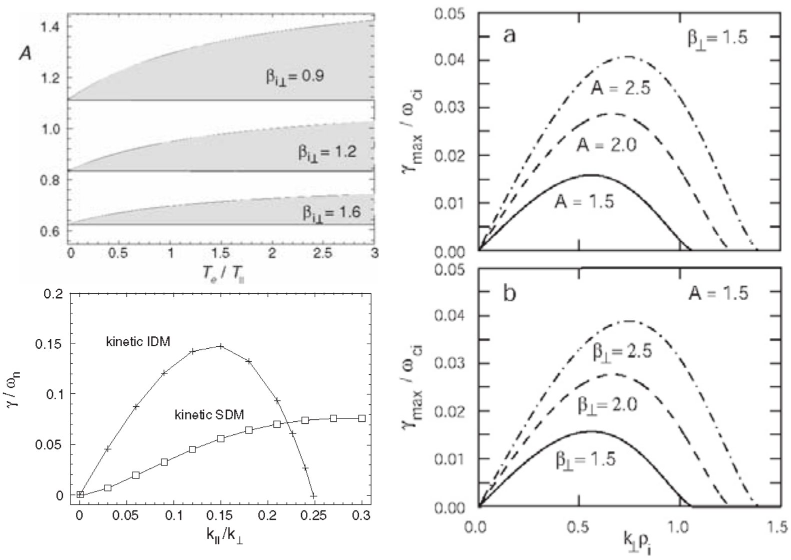


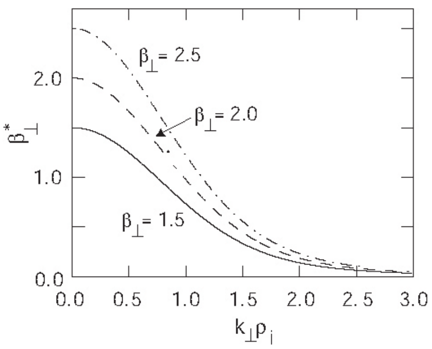


*Left*:The β-ranges and growth rates of the two new electron-modified mirror modes. *Center*: Growth rate Larmor-radius dependence. *Right*: Effective β for the kinetic mirror mode.

the mirror mode in two versions. First we investigate its dependence on the presence of a hot kinetic electron background. In this case we find that in addition to the ordinary ion-mirror mode the mirror mode develops two new branches, a slow-ion branch and a kinetic slow branch. The domains of existence of these branches are shown in the Figure (top left); the normalized growth rates are given below (bottom left) showing that the ion branch is restricted to small parallel wave numbers having large growth rate while the kinetic slow branch extends to larger parallel wave numbers. Both are oblique with the latter being more parallel. Another new mode appearing here is still under investigation. The center and right panels of the figure show the other case of the ordinary ion mode but for finite (kinetic) Larmor radius included. This causes the mode to have higher threshold for onset as seen in the right part of the effective β entering the threshold condition, and to have maximum growth rate at wavelength comparable to the ion Larmor radius and decaying both for shorter and longer wavelengths. This is an important finding since it tells that injection of turbulent energy by mirror instability at the lowest frequencies will take place at about the Larmor radius which is in approximate agreement with observation.

Pokhotelov, O.A. et al., Mirror instability at finite ion-Larmor radius wavelengths, J.Geophys.Res. **109**, 10.1029/2004JA010568(2004)

*R. A. Treumann, C. H. Jaroschek, in collaboration with O. A. Pokhotelov*

# Structure of Quasi-Perpendicular Shocks

The structure of quasi-perpendicular shocks is investigated by full particle simulations. An important parameter in such simulations is the ion to electron mass ratio, r. Because of computer limitations this ratio is usually artificially small. We have compared simulations with different values of r. While almost-perpendicular shocks periodically reform, the physical mechanism is different, depending on the mass ratio used.

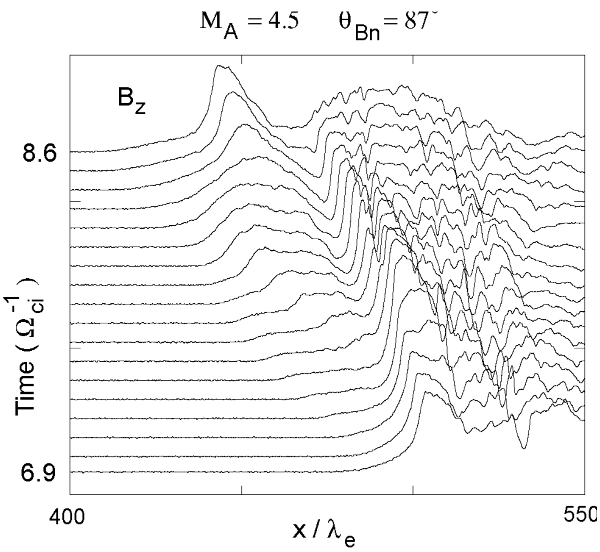


Fig. 1: Magnetic field profiles as a function of distance and time.

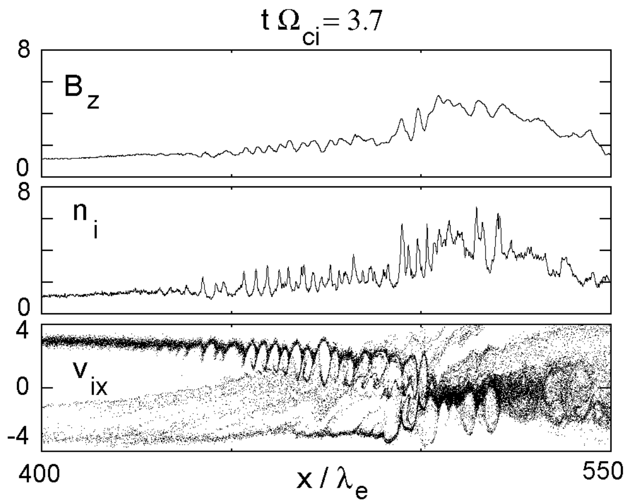


Fig. 2: $B_z$, $n_i$, and $V_{ix}$ as a function of distance.

We have performed 3 one-dimensional full particle electromagnetic simulations of a quasi-perpendicular shock with the same Alfven Mach number (4.5), shock normal - magnetic field angle 87 degrees, and ion and electron beta (particle to magnetic field pressure) of 0.05, but with different ion to electron mass ratios (r = 80, 400, 1840). It is known that at high ion beta the shock is steady. At low ion beta, as in the present simulations, the shock periodically reforms itself on the time scale of the inverse ion gyrofrequency. At unrealistically low mass ratios the reformation is due to accumulation of specularly reflected particles at the upstream edge of the foot. Figure 1 shows for a mass ratio 400 run stacked magnetic field profiles. The simulation is done in the downstream rest frame; thus the shock front moves to the left. One can see a growing upstream hump which develops into a new shock. The hump is due to specularly reflected ions accumulation at the upstream edge. At the realistic mass ratio the modified two-stream instability between the incoming solar wind ions and solar wind electrons is excited and leads to ion phase mixing and thermalization over the whole foot region. The reformation process is thereby considerably modified. Figure 2 shows at one particular time the magnetic field, the ion density, and ion phase space. The instability leads to vortices in incoming ion phase space and, by phase mixing, to thermalization. Eventually a new ramp appears at the upstream edge of the foot. At the lowest mass ratio the Buneman instability between the solar wind electrons and the reflected ions is excited, which is stabilized at higher mass ratios. Thus the occurrence of the Buneman instability in this parameter regime is purely artificial.


Scholer, M., I. Shinohara, I., and S. Matsukiyo, J. Geophys. Res., 108, 1014, doi:10:10.1029/2002JA009515, 2003
Scholer, M., and S. Matsukiyo, Annales Geophysicae, 22, 2345, 2004



*M. Scholer and S. Matsukiyo*

# Ionic Charge States in Impulsive SEP Events

New measurements of the mean ionic charge ($Q_m$) of Fe in impulsive solar energetic particle (SEP) events with our experiments onboard SOHO and ACE show a systematic increase of $Q_m$ with energy between ~0.01 and 0.6 MeV/nuc. This increase demonstrates that in these events stripping during acceleration in a dense plasma in the low corona is important and provides an upper limit of ~2 $R_s$ for the altitude of the acceleration region.

Solar energetic particle events are thought to have two basic classes, usually referred to as “impulsive” and “gradual”. Gradual events are related to CMEs (Coronal Mass Ejections) and interplanetary shocks, whereas impulsive events are related to flares. Our first direct charge state measurements for SEPs with ISEE-3 about 20 years ago showed that one of the characteristic differences between these 2 types of events are the ionic charge states of heavy ions. Whereas in gradual events the mean ionic charge of elements in the range O – Fe is mostly compatible with solar wind charge states, the heavy ion charge states in impulsive events at ~0.5-1.0 MeV/nuc had been found to be significantly larger (e.g. $Q_m$~20 for Fe, Klecker et al., 1984).

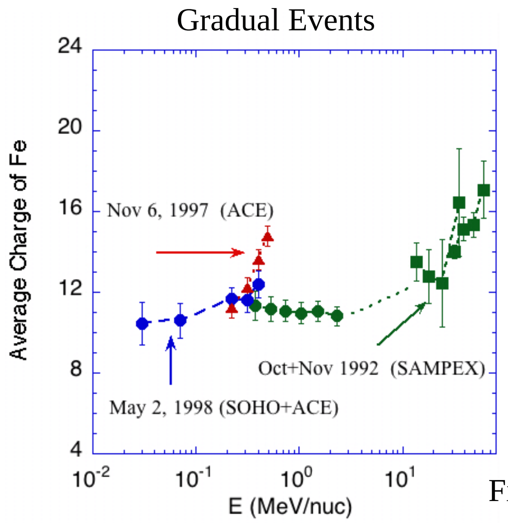

Fig. 1

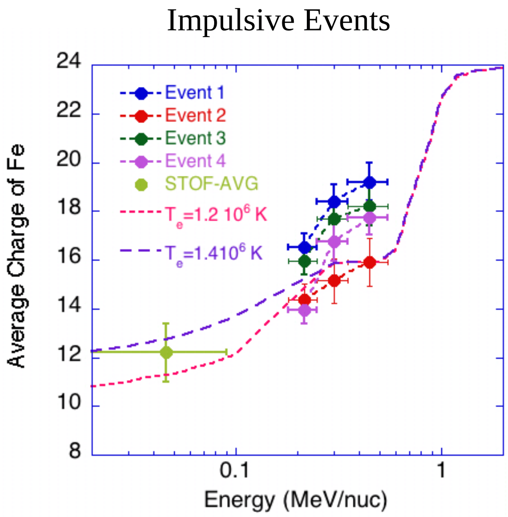

Fig. 2

Combining measurements of the experiments STOF onboard SOHO and SEPICA onboard ACE we are now able to extend the energy range to ~0.01 – 0.6 MeV/nuc. Fig. 1 and Fig. 2 show the mean ionic charge of Fe for typical gradual and impulsive events, respectively. Whereas the gradual events exhibit a large variability of the mean ionic charge of Fe from $Q_m$ (E) ~ const to increases by several charge states in the energy range 0.1 - 40 Mev/nuc, the impulsive events consistently show a large increase (ΔQ ~4-8) with energy at E < 1 MeV/nuc (Möbius et al., 2003), combined with low charge states of $Q_m$~ 11-13 at E < 0.1 MeV/nuc (Klecker et al., 2004). The substantial increase at energies of ~ 0.1 - 0.6 MeV/nuc is consistent with the prediction of models that combine acceleration in a high-density plasma environment with stripping during the acceleration (e.g. Kocharov et al., 2000). The relatively low charge states at low energies, compatible with $T_e$ ~1.5 $10^6$K, show that high ionic charge states in impulsive events are not caused by high temperatures, as previously thought, but by stripping in a dense environment in the low solar corona at R < 2 $R_s$.

Klecker B., D. Hovestadt, M. Scholer, et al., ApJ, 281, 458, 1984
Klecker,B., E. Möbius, M.A. Popecki. et al., Adv Space Res, 2004, submitted
Kocharov, L., G.A. Kovaltsov, and J. Torsti, A&A, 357, 716, 2000
Möbius, E., Y. Cao, M.A. Popecki, et al., 28th ICRC, 6, 3273, 2003

*B. Klecker, in collaboration with E. Möbius, M.A. Popecki*

# Solar Flare γ-rays observed with *INTEGRAL*/SPI

The very powerful X-class solar flare on 2003 Oct. 28 was detected by several instruments on board *INTEGRAL* as an intense flash of about 15 minutes in the hard-X and γ-ray bands. Despite the non-standard incidence of the solar γ-rays, time-resolved spectra including several nuclear γ-ray lines and a continuum at high energy were obtained with SPI. For the first time, in addition to the 2.2 MeV $^{1}H$ neutron capture line, the 4.4 MeV $^{12}C^*$ and 6.1 MeV $^{16}O^*$ nuclear interaction lines and the 6.9 and 7.1 MeV lines from $^{16}O^*$ are clearly resolved. Flux evolutions on sub-minute-scale show significant differences between lines and continuum. Several spectra have been extracted during the flare.

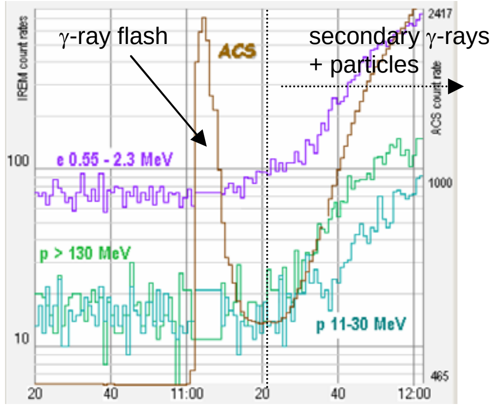


ACS and IREM count rates during γ-ray flare from 10:20 to 12:00 UT. The solar origin of the γ-ray flash was revealed by the strong anisotropy of the ACS counting rates

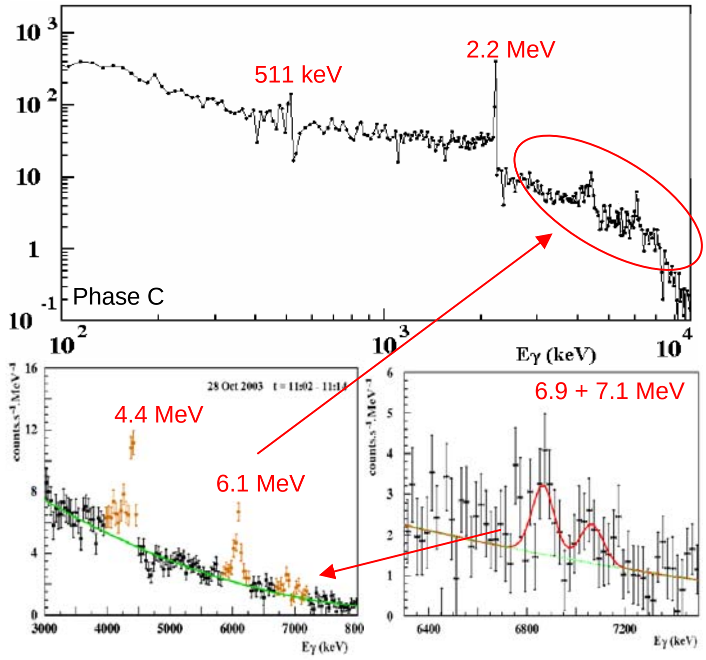


Background-subtracted spectra of SPI, recorded during the γ-ray flare. Precise line profiles on low background are obtained for the 4.4 MeV and 6.1 MeV lines. The 511 keV annihilation line is unfortunately instrument dominated. The two weaker lines emitted by $^{16}O^*$ at 6.9 and 7.1 MeV were resolved for the first time.

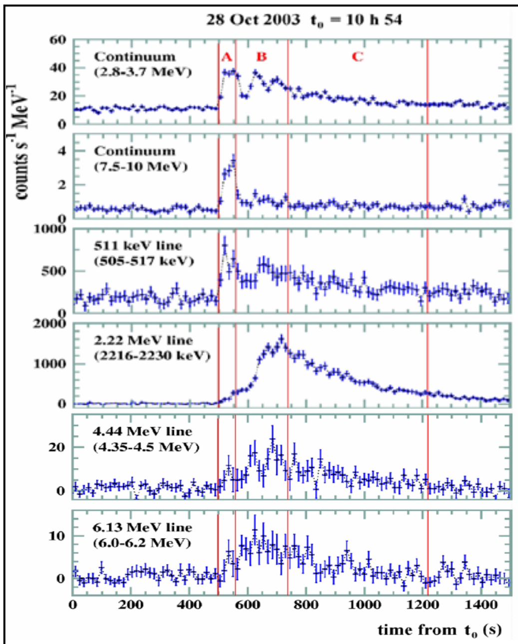


Time profiles observed during the flare.

It was possible to obtain the redshift of the 4.4 and 6.1 MeV line which is of the order of 0.6%. This is comparable with the SMM and RHESSI results. Detailed analysis of these lines could provide a new insight into the processes of ion acceleration and transport in a solar flare (figure on the right) favoured is the narrowed downward-directed distribution of accelerated particles.

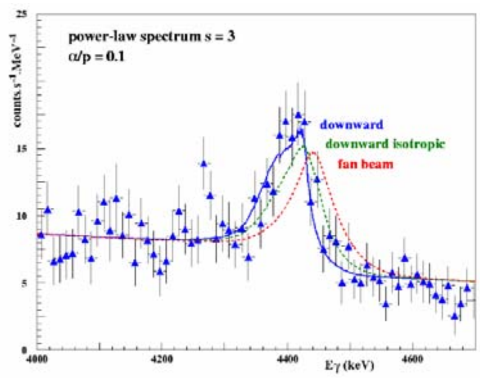


Line shapes for the 4.4 MeV line for three different proton flow models.

**References:**
• Gros, M., et al. 2004, Proc. 5th INTEGRAL Workshop

*A. v. Kienlin, R. Diehl in collaboration with M. Gros, V. Tatischeff, J. Kiener, B. Cordier, C. Chapuis, G. Weidenspointer, G. Vedrenne, A Bykov, M. Mendez*

# Discovery of X–rays from Mars with Chandra

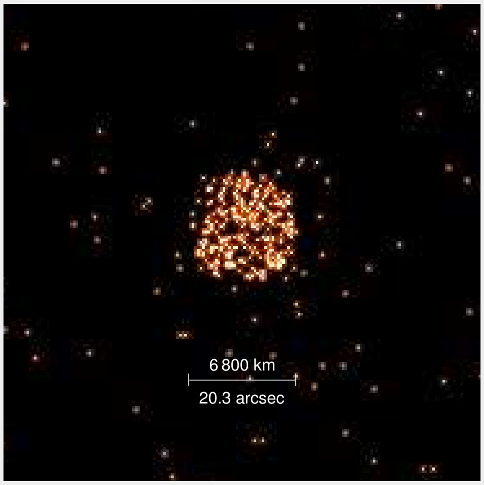


**Fig. 1.** *First X–ray image of Mars, obtained with Chandra ACIS–I (Dennerl 2002).*

X–rays from Mars were detected for the first time with Chandra. Mars is clearly resolved as an almost fully illuminated disk (Fig. 1), with an indication of limb brightening at the sunward side, accompanied by some fading on the opposite side. The morphology and the X–ray luminosity of $\sim 4$ MW are fully consistent with fluorescent scattering of solar X–rays in the upper Mars atmosphere. The X–ray spectrum is dominated by a single narrow emission line, which is most likely caused by O–$K_\alpha$ fluorescence. In addition to the X–ray fluorescence, there is evidence for an additional source of X–ray emission, indicated by a faint X–ray halo which can be traced to about three Mars radii, and by an additional component in the X–ray spectrum of Mars, which has a similar spectral shape as the halo. Within the available limited statistics, the spectrum of this component can be characterized by 0.2 keV thermal bremsstrahlung emission. This is indicative of charge exchange interactions between highly charged heavy ions in the solar wind and exospheric hydrogen and oxygen around Mars.

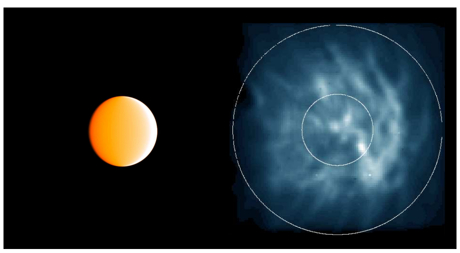

**Fig. 2.** *Simulated X–ray images due to $K_\alpha$ fluorescent scattering of solar X–rays (left, Dennerl 2002) and due to solar wind charge exchange (right, Gunell et al. 2004).*

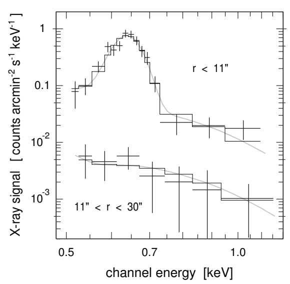


**Fig. 3.** *X–ray spectra from the disk of Mars (top) and its halo (bottom; Dennerl 2002).*

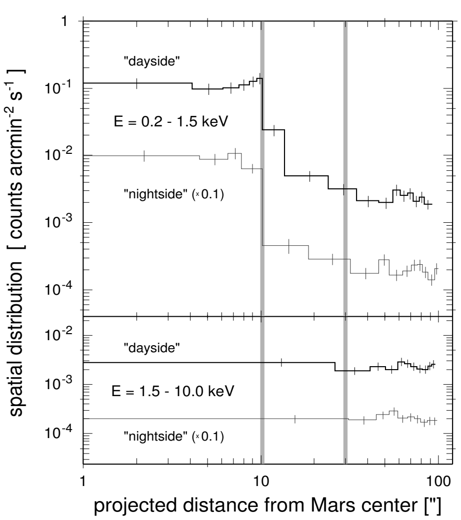


**Fig. 4.** *X–ray surface brightness for soft (top) and hard (bottom) energies, displayed separately for the "dayside" and the "nightside". For better clarity the nightside histograms were shifted by one decade downward. The two vertical lines mark the radius of Mars and 3 Mars radii. Note the gradual drop of the soft X–ray flux between these radii (Dennerl 2002).*

The detection of a faint X–ray halo around Mars (Figs. 2 - 4) is particularly exciting. This halo is most likely caused by charge exchange interactions between highly ionized heavy solar wind atoms and exospheric gas. Recent detailed simulations of this process by Gunell et al. (2004) agree well with the observation.

The first direct detection of such a mechanism in a planetary exosphere strongly suggests that a similar process occurs also in the geocorona. This result has important consequences for the interpretation of many soft X–ray observations from satellites orbiting the Earth, as these satellites are looking through a faint X–ray glow, which imposes characteristic spectral emission lines onto the diffuse X–ray background.

Mars is an ideal object to investigate this effect: it is sufficiently far away to get the whole halo into the field of view, but still sufficiently close for spatially separating the halo emission from the brighter, fluorescence dominated radiation of its atmosphere.

**References:** Dennerl, K., *"Discovery of X–rays from Mars with Chandra"*, 2002, A&A 394, 1119 – 1128

Gunell, H., Holmström, M., Kallio, E., Janhunen, P. and Dennerl, K., *"X–rays from solar wind charge exchange at Mars: a comparison of simulations and observations"*, 2004, submitted to GRL

*K. Dennerl*

# X–ray emission from Saturn

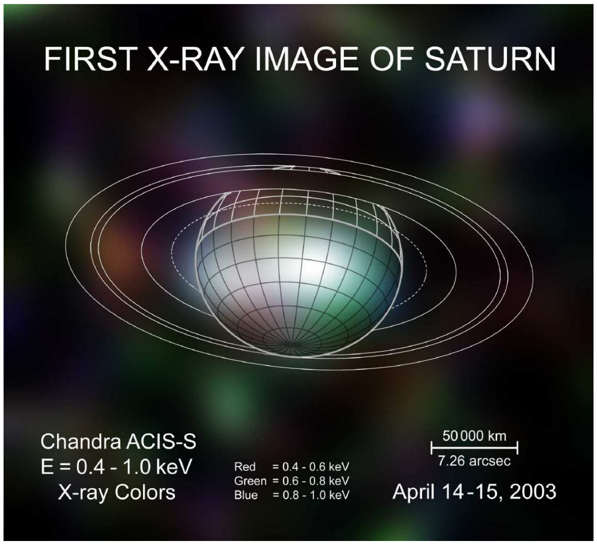


**Fig. 1.** *The first X–ray image of Saturn, obtained on April 14-15, 2003, with Chandra ACIS–S3. The distribution of the photons was smoothed using a Gaussian with a FWHM of 5 arcsec, and the information about the energy of the X-ray photons was transformed into colors. A drawing of Saturn and its rings at the time of the observation was overlaid for clarity (Ness et al. 2004).*

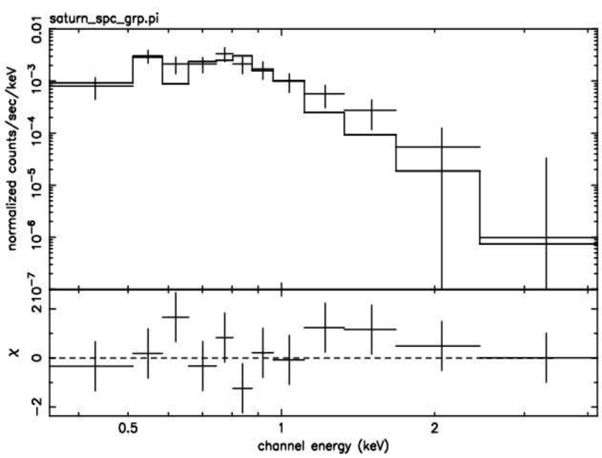


**Fig. 2.** *Observed ACIS–S3 spectrum of Saturn, modelled with thermal emission of a hot plasma (MEKAL, $kT = 0.39 \pm 0.08$ keV and solar abundances) and a single emission line at 0.527 keV, only instrumentally broadened (Ness et al. 2004).*

X-rays from Saturn were unambiguously detected for the first time with Chandra. The X-ray photons were found to come almost exclusively from the southern hemisphere, which is curently tilted toward us. No X-ray photons were detected from the regions which are covered by the rings (Fig. 1). This is an indication that the rings of Saturn are optically thick to X-rays and have a low X-ray albedo. Saturn was found to be a very faint X-ray source: during 18 hours of observing time, Chandra ACIS S3 detected 106 photons from Saturn. This corresponds to an average of only one photon every 10 minutes. The X-ray flux derived from the best fit spectral model is $\sim 6.8 \cdot 10^{-15}$ erg cm$^{-2}$ s$^{-1}$ in the energy range 0.1–2.0 keV, which corresponds to an X-ray luminosity of $\sim 87$ MW.

Despite the low number of photons, it is difficult to find a simple spectral model which reproduces the measured energy distribution. The only formally acceptable single component model, a 0.18 keV blackbody, is physically not plausible. A 0.39 keV thermal spectrum, with an oxygen fluorescence emission line superimposed, however, provides an acceptable and physically motivated fit (Fig. 2). The oxygen line accounts for one quarter of the energy emitted in the 0.3–2.0 keV band. This suggests that the X-rays from Saturn are due to solar X-rays, scattered in its upper atmosphere, by a superposition of elastic scattering, mainly on hydrogen, and fluorescent scattering, mainly on oxygen. The intensity of the oxygen fluorescence line is comparable to that observed from Mars, if the different size of both planets and their different distance from Sun and Earth are taken into account.

The X-ray intensity of Saturn, however, exceeds the intensity which is expected for scattering of solar X-rays, suggesting the presence of an additional emission mechanism. There are similarities between the X-ray emission of Saturn and the equatorial X-ray emission of Jupiter. However, while the X-ray intensity of Jupiter increases towards the magnetic poles, it decreases towards Saturn's south pole.

With this observation, all planets from Venus to Saturn have now been revealed to be X-ray sources, with MPE being involved in more than half of the original discoveries.

**Reference:** Ness, J.-U., Schmitt, J.H.M.M., Wolk, S.J., Dennerl, K., Burwitz, V., *"X–ray emission from Saturn"*, 2004, A&A 418, 337–345

# The Asteroid Preparatory Programme

**The goal of the ASTEROID PREPARATORY PROGRAMME is to establish a set of about 50 asteroids as far-IR/submm/mm calibrators for HERSCHEL, ASTRO-F and ALMA. The selected asteroids will fill the flux gap between Mars, Uranus and Neptune and the mid-IR calibration stars. ISO used 10 of these asteroids successfully for far-IR calibration, SPITZER integrated the fainter ones in the MIPS calibration scheme and several groundbased observatories established observing programmes either in support for the space projects or for own calibrators purposes.**

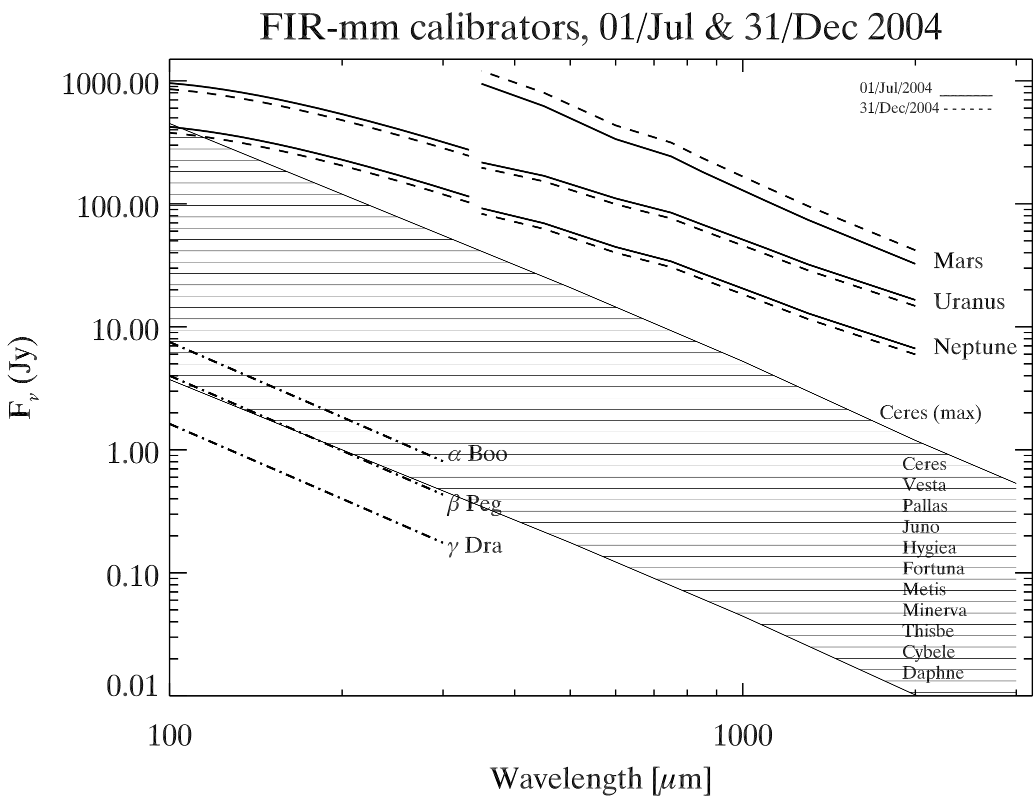


Celestial standards play a major role in astronomy. They are needed to characterise the performance of instruments and they are an important prerequisite for accurate photometry. With the access to the far-IR, submm and mm wavelength range through satellites, airborne and groundbased instruments, it became necessary to establish new calibrators for these wavelengths. The traditional far-IR/submm/mm calibrators, the outer planets, are too bright or cause nonlinearity problems for instruments on upcoming sensitive space missions like HERSCHEL or ASTRO-F. Stellar standards are quite faint in this range and pose problems of their own. The large flux gap between these two types of calibrators can be filled by a set of asteroids (Müller & Lagerros, A&A 1998, 2002, 2003). The "Asteroid Preparatory Programme" is currently conducted together with the HERSCHEL and ASTRO-F calibration teams. We investigate the physical and thermal properties of about 50 asteroids. All of them are large, almost spherical and belong the the main-belt. They cover the flux range between about 1 and several hundred Jansky at 100 $\mu$m and at 1 mm they still reach up to 10 Jy. Thermophysical model predictions (light curves, SEDs or monochromatic fluxes) are accurate on the 5-20 % level, depending on the object, the observing and the illumination geometry.

*T.G. Mueller & HERSCHEL CalSG & ASTRO-F calibration team*

# Stellar Evolution and the Interstellar Medium

# Interstellar emission in hard X-rays / soft γ-rays

**Images and spectra of hard X-ray/soft γ-ray emission from the inner Galaxy have been obtained using the first year and a half of data from INTEGRAL/SPI. Diffuse emission has been clearly separated from sources. The images are the first ever made of diffuse emission at these energies.**

The Galactic ridge is an intense emitter of hard X-rays and soft γ–rays, but their origin is as yet unclear. The study of this emission is a major goal of INTEGRAL, whose unique combination of angular and spectral resolution and sensitivity give it great advantages over previous missions.

The IBIS instrument on INTEGRAL has successfully separated sources from diffuse emission in the 20 – 40 keV band (Lebrun et al. 2004). Now with SPI we are able to extend the analysis to 1 MeV. Data from the Core Program of the first 1.5 years of the mission have been used. The spectrum is derived by model fitting to components tracing Galactic structure: HI, CO and a model for the positronium continuum around the Galactic centre. In addition, at low energies the 91 sources detected by IBIS are included; IBIS positions are used and the source fluxes are determined from the SPI data. The instrumental background is represented by a template which is scaled by a time-dependent factor .

Diffuse emission is ~10% of the total emission integrated over the inner radian of the Galaxy at low energies, and the fraction increases with energy to at least 50%.

The spectrum of diffuse emission is consistent with previous work (RXTE, OSSE, COMPTEL), but is more robust because of the explicit inclusion of many sources and the imaging properties of SPI. The positronium continuum is clearly detected as the excess between 300 keV and the 511 keV line. *In situ* acceleration of suprathemal electrons has been proposed as the origin of the remaining non-thermal component (Dogiel et al. 2002).

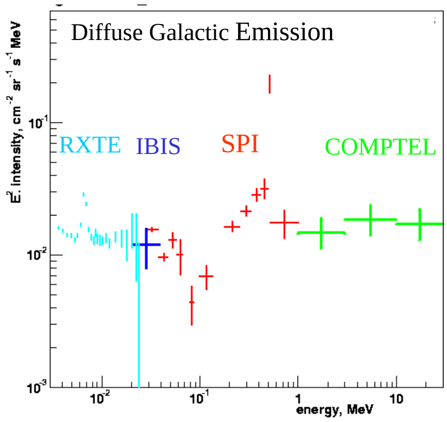


Images have been made using the maximum-entropy method, the first ever made at these energies. These show the sources dominating at low energies while the diffuse emission is visible from the Galactic ridge at higher energies. The band 393-518 keV shows a concentration to the Galactic centre and an elliptical form consistent with positronium emission.

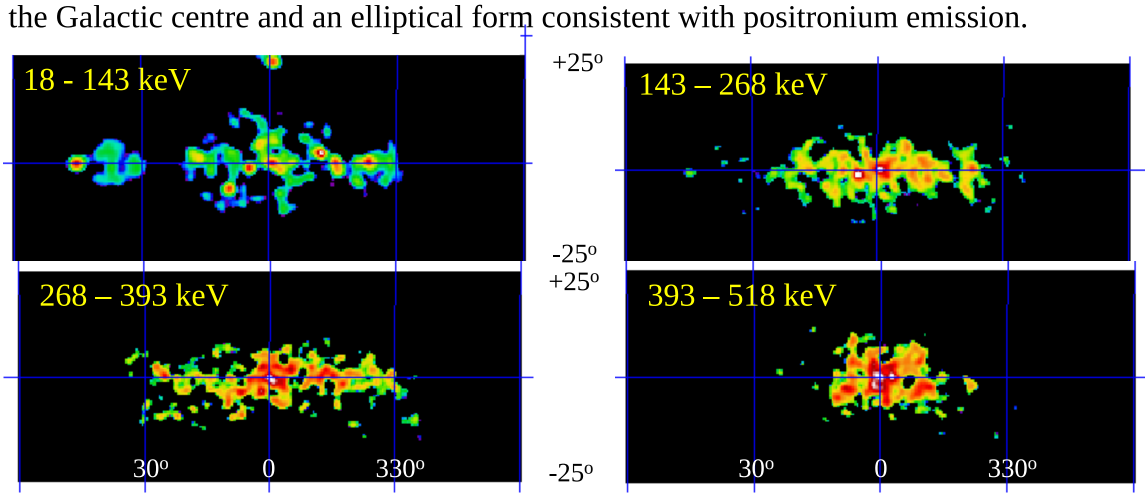


•**References:**
•Dogiel, V.A., Inoue H., Masai, K., Schönfelder, V., Strong, A.W. (2002) ApJ, 581, 1061
•Lebrun, F. et al. (2004) Nature, 428, 293
• Strong, A.W. , et al. (2003) A&A 411, L127 ; 411 L447; (2004) ESA SP-552, astro-ph/0405023

*A.W. Strong*

# Early stages of massive star formation

**In a search for young proto-stars, we selected 47 of the 67 FIR-brightest IRAS sources in the outer Galaxy (excluding well known regions like Orion and W3) and mapped relatively large regions around them in the millimetre continuum. We present these maps together with near, mid-infrared, and radio data collected from the 2MASS, MSX, and NVSS catalogs. Further data from the literature on detections of high-density tracers, outflows, and masers are added. The multi-wavelength data is used to characterize each observed region. The compiled database is a valuable tool for further detailed investigations of selected massive star-forming regions as well a useful collection of general properties of these regions. Despite their importance, these results are only by-products of our original goal: The search for the youngest stages of star formation. We can present eleven massive pre-stellar core candidates.**

We are going to publish the millimetre continuum maps together with an NIR image and the MSX and NVSS catalog data. The data will be presented like the figure to the right. The millimetre map is overlaid on the 2MASS image. The crosses denote MIR sources and the triangles denote radio sources from MSX and NVSS data respectively. The diamond with the ellipse mark the location of the IRAS source.

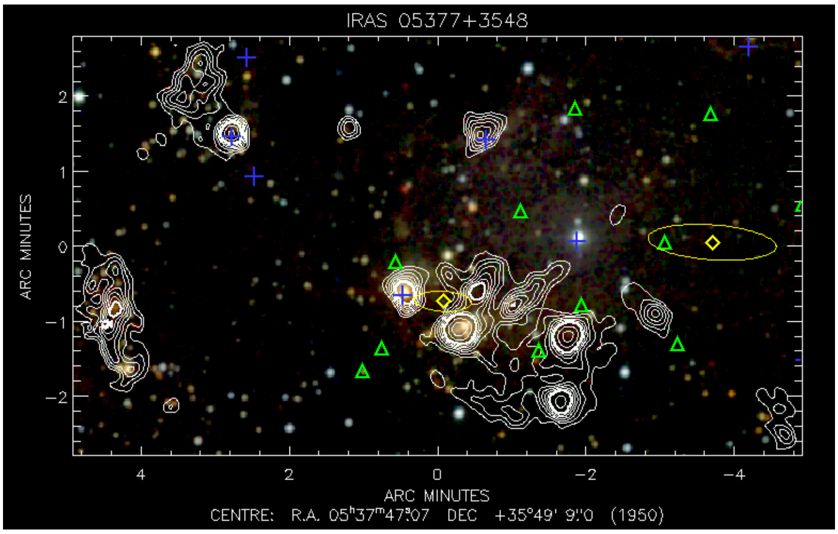


**IRAS 05377+3548:**
This region is the most fragmented region in our survey. It features a lot of separated prominent cores and various elongated structures. The western area is populated with NVSS radio sources (green triangles) coming from a large emission nebula. MSX sources (blue crosses) are associated to two cores and to the star BD+35 1201, an O9.5V star. The two cores in the center show K-band counterparts. The associations at different wavelength indicate different evolutionary stages. The two cores west of the centre are similar in mass (50-60$M_o$) and shape to the two in the centre, but lack NIR and MIR emission. This suggest that these cores are younger and less evolved and may be intermediate-mass pre-stellar cores.

**Massive Pre-stellar Core Candidates:**
Little is known about massive pre-stellar cores and the initial conditions for massive star formation. We identified 11 massive pre-stellar core candidates in five regions in our survey for further study with millimetre interferometers and FIR mission like Spitzer, SOFIA, or Herschel:

- IRAS 03064+5638 #1a: Quiescent part of a double-peaked cloud core.
- IRAS 04073+5102 #2, #4, #6, #7: A ring of cloud cores around a star cluster.
- IRAS 06058+2138 #1: A single peaked cloud core, but the MSX and IRAS sources are offset by 20”.
- IRAS 06073+1249 #2: A relatively small cloud core compared to the main component, but still massive.
- IRAS 06105+1756 #1a, #1b, #2, #3: The main component (1a) has and IRAS and and MSX source only on its flanks.

We regard cloud cores as candidates for massive pre-stellar cores if they have no association at any other wavelength within 10” of the peak and have a mass higher than 100$M_o$.

*R. Klein, B. Posselt, K. Schreyer, J. Forbrich, Th. Henning*

# IMF of the Massive Star-forming regions

One of the major unsolved problems in the understanding of starformation is the question, if the Initial Mass Function (IMF) varies with the physical conditions in the starforming region. In particular we want to test the hypothesis that starbursts form proportionally fewer low-mass stars than typically observed in more quiescent regions. We have thus started a program to measure the IMF in a sample of the most massive starforming regions in our Galaxy. Here we present the results for NGC 3603. Our adaptive optics observations at the VLT allow us for the first time to measure the IMF down to approx. 0.1 Msun. The measured IMF is significantly flatter than for the field stars. Our results thus support the hypothesis that the starformation in starbursts is biased towards higher mass stars.

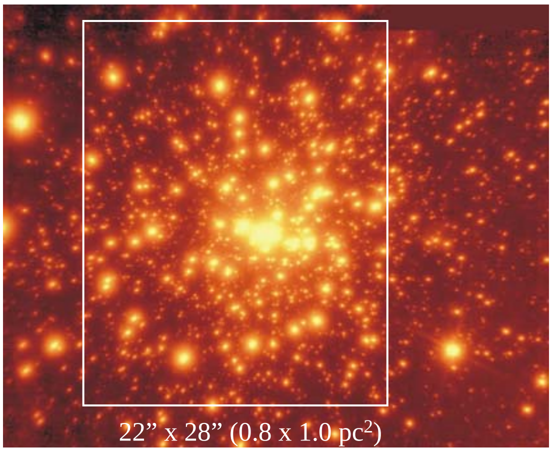


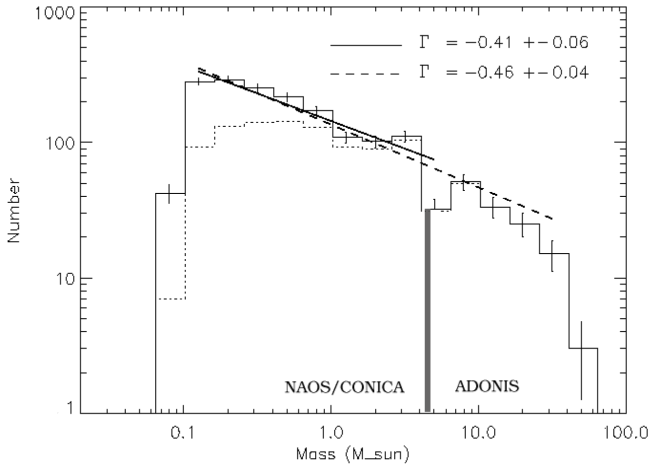


The left figure shows the K-band image of the central star-forming cluster HD 97950 in NGC 3603. The total observing time on source is approx.13 minutes. The faintest stars seen in the observations have a magnitude of approx. 20 mag, corresponding to stars with masses around the Hydrogen burning limit. The white box indicates the region for which we have analysed the IMF. A similar observing time has been spent on J- and H-band imaging of the same region. From the distribution of the stars in the color-color and color-magnitude diagrams we derive a cluster age of approx. 1-3 Myr. We have then calculated the IMF by applying various theoretical models for the pre-main sequence evolution of high, intermediate, and low mass stars. The right figure shows the resulting IMF (Harayama & Eisenhauer, 2005 ). The power law index is ~-0.4 in the mass range from 0.1 Msun up to 6 Msun. There is no truncation towards low stellar masses, confirming that NGC 3603 indeed forms a significant number of stars with masses close to the Hydrogen burning limit (Eisenhauer et al. 1998, Brandl et al. 1999). However, the measured IMF is significantly flatter than for the field stars (Salpeter IMF has a slope of -1.35), indicating that the starformation in NGC 3603 is biased towards higher mass stars. Our finding thus adds major evidence to the hypothesis of a “top-heavy” IMF in starbursts and a non-universal IMF.

**Reference:** Brandl et al. 1999, A&A, 352, L69
Eisenhauer et al. 1998, AJ, 498, 278
Harayama & Eisenhauer 2005, “IMF@50” Conf., in preparation

*Y. Harayama, F. Eisenhauer*

# Outflows from Super Star Clusters in Starbursts

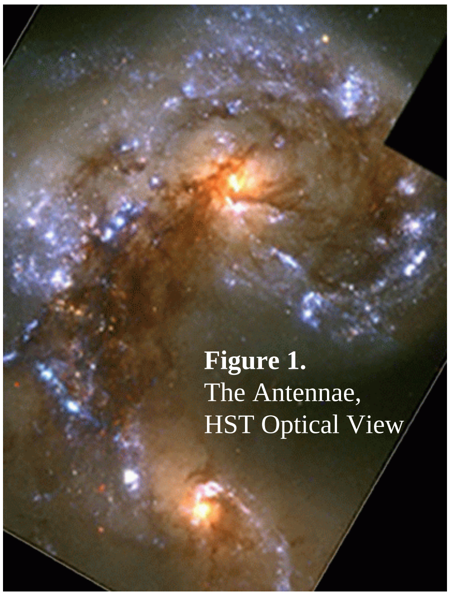

**Figure 1.**
The Antennae,
HST Optical View

### Superwind Engines in Starbursts

Intense star formation produces super star clusters (SSCs), which may be progenitors of globular clusters (GCs). SSCs are so called because they are as massive ($10^5$-$10^6$ $M_\odot$) and compact (radii of a few pc) as GCs, but much brighter since they are young. High-resolution near-IR spectroscopy of the youngest SSCs in the nearest starburst merger, the Antennae Galaxy (Fig. 1), reveals that these clusters drive mass-loaded supersonic outflows powered by stellar winds and supernovae. The combined outflows of many SSCs heat and clear away surrounding cool gas, ultimately producing a galactic-scale superwind if conditions are favorable (e.g. cluster density, total mass-loss rate, and relative galactic potential well depth).

### Energetics of SSC Outflows

The broad Br$\gamma$ line profiles of the youngest SSCs are not Gaussian; their high-velocity wings and pointy peaks are well fit by a $\beta$-law profile, assuming a constant mass-loss rate (dM/dt) and a power-law velocity flow that approaches a terminal value. Inferred values of dM/dt are 0.01-1 $M_\odot$ /yr, comparable to current star-formation rates but up to 25 times greater than expected due to stellar mass loss. SSC outflows are strongly mass-loaded. Observed momentum fluxes in the Br$\gamma$-emitting gas agree fairly well with predicted values, suggesting that the outflows are momentum driven (Fig 2). The kinetic energies and mechanical luminosities of the flows are not well-probed by $10^4$ K gas, however, indicating that the bulk of energy is in another phase. Thermal energies of recombining and X-ray-emitting hot gas also make small contributions to the total energy; most of the outflow mechanical energy is efficiently thermalized in the kinetic energy of hot gas. These are properties shared with galactic scale superwinds, which may be the ultimate evolutionary state of the Antennae starburst.

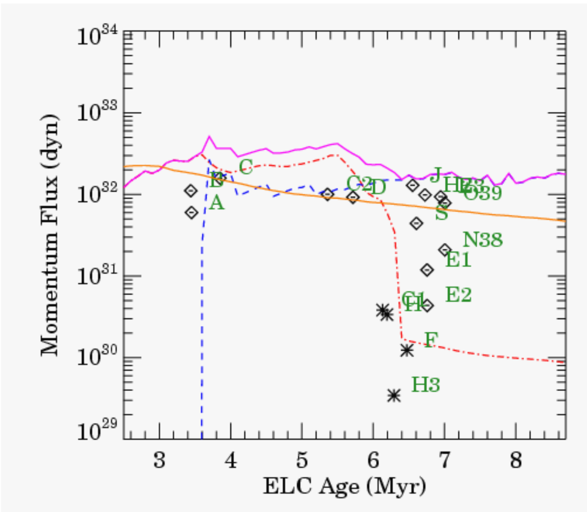


**Figure 2.** SSC outflow energetics quantities normalized to a $10^6$ $M_{sun}$ cluster (Kroupa IMF 0.1-100 $M_{sun}$, points), compared with Starburst99 predictions for stellar inputs (purple line) including contributions from stellar winds (red) and SNe (blue). The orange line represents the SSC's available radiative momentum flux.


**References:**
- Gilbert, A.M. 2002 PhD Thesis, UC Berkeley
- Gilbert, A.M., & Graham, J.R. 2004
- Kudritzki, R.P. & Puls, J. 2000 ARAA 38, 613
- Lehnert, M.D. & Heckman, T.M., 1996 ApJ 462, 651
- Leitherer, C., et al. 1999 ApJS 123, 3
- Metz, J.M., et al. 2004 ApJ 605, 725
- Whitmore, B.C., et al. 1999 AJ 118, 1551



*A.M. Gilbert*

We have constructed the full set of solutions for hydrostatic protoplanets with fully radiative envelopes around a solid core. The envelopes have solar abundances with dust of interstellar composition added and detailed, non-ideal equations of state for H-He mixtures. The results give an overview of all possible protoplanetary equilibria in the core accretion model.

The results of our calculations are a few $10^5$ protoplanetary models that allow a statistical analysis. The figures show the envelope masses of all solutions displayed as a function of core mass and inside pressure.
Great height and red colour of the surface correspond to a large envelope mass for the given combination of core mass and pressure. All axes are in logarithmic scale and SI units, 30 orders of magnitude are covered in this diagram in both mass and pressure. The left figure shows the results for an ideal gas with constant core temperature. The right side shows the same graph for a H-He mixture with an effective core temperature of a black body radiating with a fixed specific luminosity.

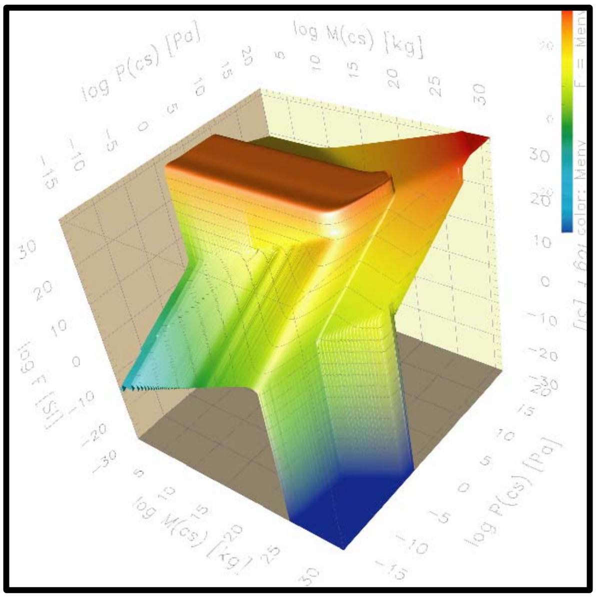


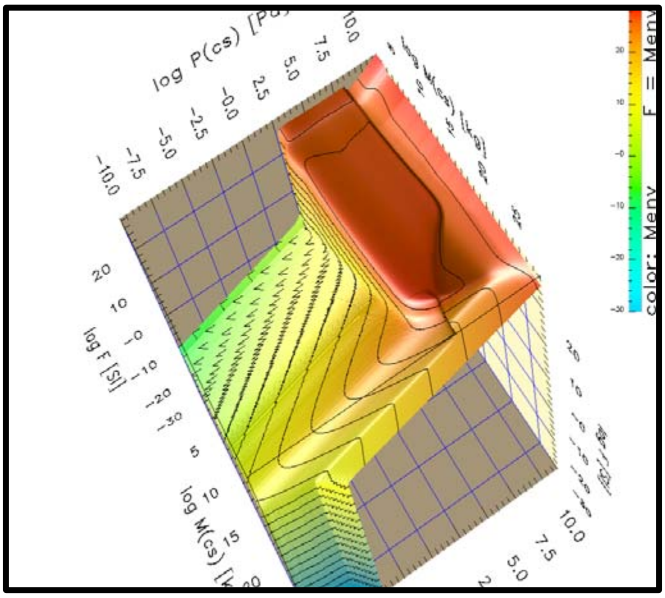


In the relatively flat surface in the middle (red, referred to as „island“), reside protoplanets with jovian masses. They are huge fluffy objects more than a hundred times larger than mature planets of the same mass and connect smoothly to the nebula. In contrast, the pressure of mature planets like Jupiter, drops to virtually zero on the surface, a static solution embedded inside a protoplanetary nebula does not exist. These objects sit in the top right corner of the figures, behind the „island“.
The front edge of the „island“ corresponds to the so-called critical core mass: for higher core masses no static solutions exist embedded inside a nebula. The outside pressure drops to very small values.

Our results clearly show that there is statistical evidence for a characteristic planetary mass as a consequence of fundamental principles and the properties of hydrogen and helium.

*C. Broeg, B. Pečnik, G. Wuchterl*

# Formation-Theory across the Substellar Limit

We calculated the formation and early evolution of stars, brown dwarfs and planets. Properties and observables for objects with masses ranging from Jupiter to the Sun are evaluated from zero age to million years, directly from the respective formation theories. Thus we provide theoretical properties of very young astrophysical objects for all masses that are within reach of present instruments. While shedding light on the formation process itself, these models are also of key importance for the observational identification of young extrasolar planets by direct imaging and their characterization in terms of mass, age and type. They allow to observationally separate planets from brown dwarfs and provide quantitative links to the respective formation process.

Our fluid dynamical models with radiation, self-gravity and time-dependent convection account for detailed non-ideal equations of state, opacities and D-burning. The time-dependent convection model is calibrated to the solar radius and tested by properties of the solar convection zone. The equation system is supplemented by boundary conditions and source-terms that account for the respective formation scenarios: the collapse of gas spheres for stars and brown-dwarfs, core-accretion and envelope-capture for planets.

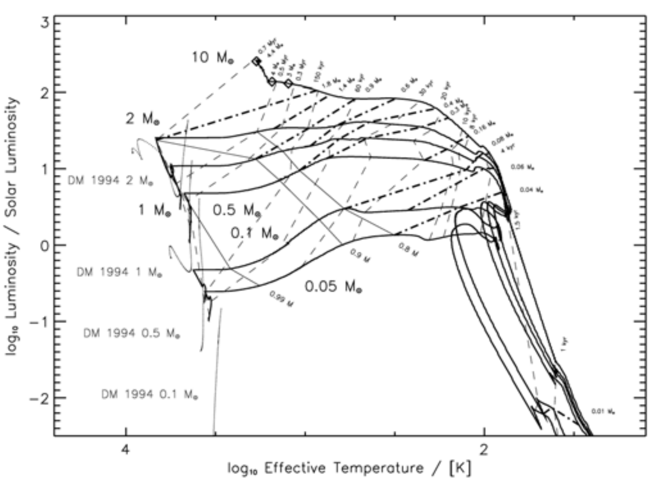


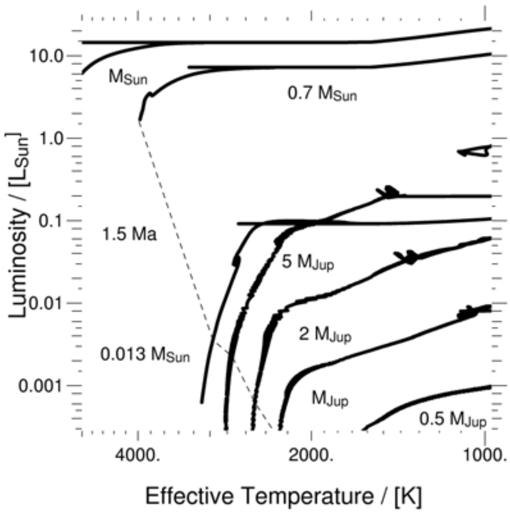


The left Fig. shows a large HRD for the collapse of Bonnor-Ebert spheres that reaches from quasi-isothermal collapsing cloud cores to pre-main sequence ages. The cloud masses range from 10 to 0.05 solar masses. Thick lines are *evolutionary tracks*, dashed lines are *isochrones*, dash-dotted lines are *isopleths*, i.e. lines of constant central object-mass. Thin lines show the *fraction of total cloud mass* that has been accreted with the remainder still in the envelope. Note the substantial corrections in pre-main sequence properties when compared to classical evolutionary tracks that start from an assumed initial state and ignore the formation process. D'Antona and Mazzitelli (1994), tracks, that are also calibrated to the Sun, are plotted for reference.

The right Fig. Shows an extension that reaches further into the substellar domain, down to half a Jupiter mass. The diagram shows that it is possible to separate planets (labelled in Jupiter-masses) from brown dwarfs by identifying regions in the HRD that are forbidden for objects above a given mass.


**References:**

- Wuchterl and Tscharnuter, 2003, A&A, 398, 1081-1090
- Wuchterl 2004, Rev. Mod. Astronomy, 17, 129-168



*G. Wuchterl*

# Planet-Formation Theory

We have developed the first classification scheme for protoplanets, in hope of gaining a fundamental understanding of the planetary phenomenon in general. A dynamical stability analysis has been performed to determine physically significant states in the evolution of a planet.

The scheme provided us with the mapping of all possible protoplanetary hydrostatic equilibria (A&A, accepted). Our model predicts two types of envelope equilibria: `uniform', with density of envelope gas dropping weakly with increase in radial distance, and `compact', having a small, but very dense gas layer wrapped around the core, and very low gas density further out. Each of those types can be self-gravitating.

A hydrodynamical code has been built to distinguish the stable protoplanetary equilibria from the unstable ones, and to study possible dynamic transitions between any pair of hydrostatic equilibria.

Stability analysis of the hydrostatic equilibria is done for both subsonic and supersonic perturbations.

The envelope-gas-dynamics of about fifty characteristic protoplanetary models, selected from the hydrostatic solution-set, was integrated over one hundred sound crossing times.

The initial analysis shows that some equilibria are very stable, some are unstable both for subsonic and supersonic perturbations. There are also states of "intermediate-stability" dynamical behavior.

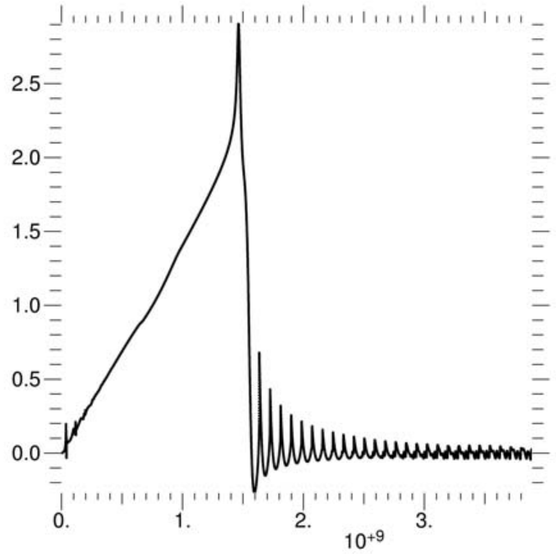


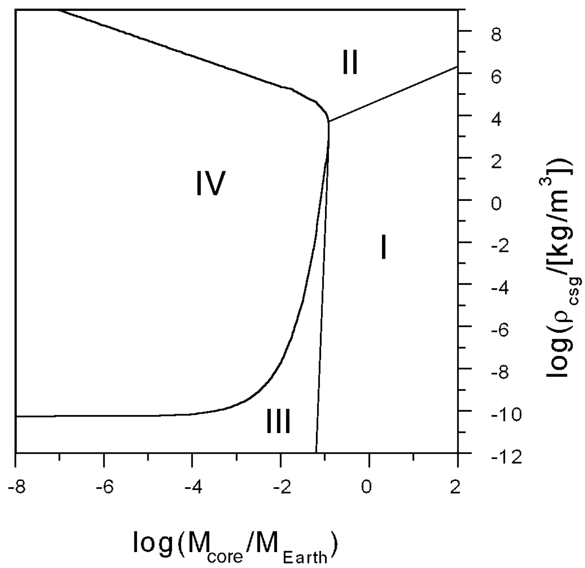


**Left:** Time evolution of the gas Mach number at the outer envelope boundary for the unstable model (Class IV)

**Right:** Classification of the hydrostatic protoplanetary models, according to the initial parameters

In summary we find protoplanets of Class I, II and III to be unconditionally stable, while the nonlinear growth of the unstable Class IV depends on the initial perturbation (cf. Pečnik and Wuchterl, A&A 2004).

Further investigation of the quasi-stable region (models on the border of Class III & IV) might provide important insight into the evolution of the planetary bodies.

*B. Pečnik, G. Wuchterl*

# Dynamical mass of a binary L-dwarf

Using the Hubble Space telescope, the Very Large telescope, the Keck Observatory, and the Gemini Observatory, we have been able to perform astrometric measurements of the relative motion of a binary L-dwarf. Our seven measurements cover 60% of the 10.5 years period. It was the first time that a dynamical mass of an object belonging to the recently discovered L spectral class was measured.

We present the results of astrometric and photometric observations leading to the determination of the dynamical masses of the binary L dwarf 2MASSW J0746425+2000321. High angular resolution observations spread over 4 years and obtained with the Hubble Space Telescope, the ESO Very Large Telescope, the W. M. Keck Observatory and the Gemini Observatory cover 60% of the orbit. We find an orbital period of 3850.9 days. The total mass is 0.146 $M_{Sun}$ with uncertainties depending on the distance. Spatially resolved low resolution optical (550-1025 nm) spectra have been obtained with HST/STIS, allowing us to measure the spectral types of the two components (L0$\pm$0.5 for the primary and L1.5$\pm$0.5 for the secondary). We also present precise photometry of the individual components measured on the high angular resolution images obtained with HST/ACS and WFPC2 (visible), VLT/NACO (J, H and K bands) and Keck I (K band). These spectral and photometric measurements enable us to estimate their effective temperatures and mass ratio, and to place the object accurately in a H-R diagram. The binary system is most likely formed by a primary with a mass of 0.085$\pm$0.010 $M_{Sun}$ and a secondary with a mass of 0.066$\pm$0.006 $M_{Sun}$, thus clearly substellar, for an age of approximately 0.5 1 Gyr. H$\alpha$ variability indicates chromospheric and/or magnetic activity.

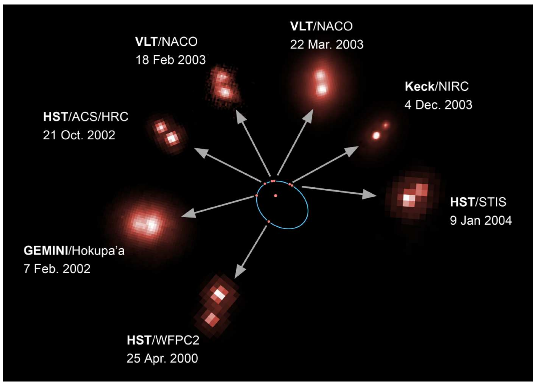


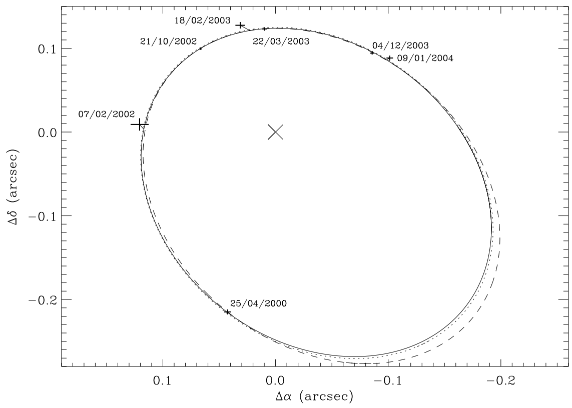


With spectral properties between those of giant planets and late-type stars, brown dwarfs have opened a new chapter in the study of atmospheric physics. One of the ultimate goals of a theory of sub-stellar objects is an accurate determination of the mass based on spectroscopic characteristics and luminosity. The degeneracy in the mass-luminosity relation makes it difficult to pin down their physical properties. Luminosities and effective temperatures of ultra-cool dwarfs are function of both age and mass so that an older, slightly more massive ultra-cool dwarf can exhibit the same effective temperature as a younger, less massive one. Dynamical masses, which are model-independent, are highly required in order to calibrate the mass-luminosity relation. Only very few observational constraints on the masses of this class of objects are available nowadays, and we present here the first measurement for field L-dwarfs, at the stellar/sub-stellar transition. Although the age of 2MASSW J0746425+2000321 is not known indenpendently from any models yet, these observations give promising results as a first step toward the calibration of the models.

*H. Bouy, G. Duchêne, R. Köhler, W. Brandner*

**XMM-Newton observations revealed broad absorption lines in the X-ray spectra of at least three radio-quiet isolated neutron stars. If interpreted as proton cyclotron resonance absorption the line center energies indicate magnetic field strengths in the range of $10^{13\text{-}14}$ G.**

Presently seven thermally emitting isolated neutron stars are known. Their X-ray spectra are characterized by soft blackbody-like emission (kT ~ 45 – 120 eV) without indication for harder, non-thermal components. These stars apparently show no radio emission and no association with supernova remnants. Four of them exhibit pulsations in their X-ray flux with periods in the range of 3.45 s to 11.37 s. XMM-Newton observations revealed broad absorption lines in the X-ray spectra of at least three of the stars. From the two pulsars RX J0720.4–3125 and RBS1223 variations of the depth of the line with pulse phase are observed.

The XMM-Newton spectra of RBS1223, RX J0720.4–3125 and RX J1605.3+3249 show deviations from a Planckian energy distribution which can be modeled by a broad Gaussian-shaped absorption line. The first two neutron stars are pulsars with 10.31 s and 8.39 s spin period and show spectral variations with pulse phase (Figure 1).

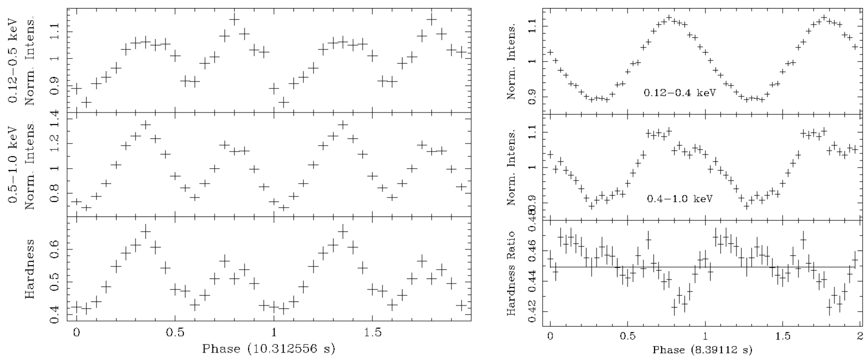


*Fig. 1 Folded light curves in soft and hard energy bands together with hardness ratio (the ratio of count rates in the hard and soft band) of the pulsars RBS1223 (left) and RX J0720.4–3125 (right).*

Pulse-phase spectroscopy for RX J0720.4–3125 shows that a large fraction of the spectral variations can be attributed to changes in the equivalent width of the absorption line (Figure 2). The observed dependence of temperature and equivalent width on pulse phase may be due to the change in the viewing geometry of the inclined magnetic rotator.

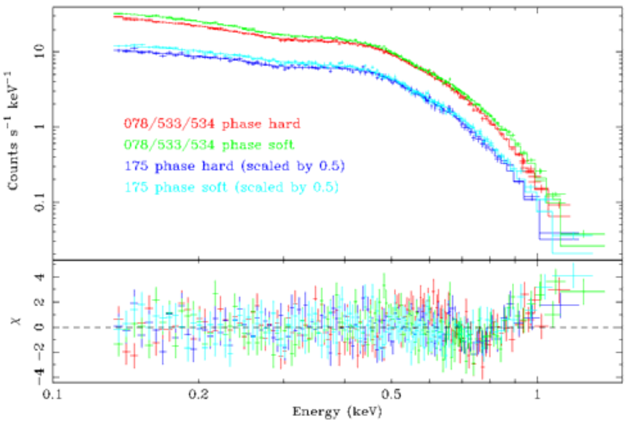


*Fig. 2 Phase-resolved EPIC-pn spectra of RX J0720.4–3125 from phases of high and low hardness ratios. The upper pair of spectra shows the combined data from 3 thin filter observations, the lower pair corresponds to the medium filter observation. The upper and lower spectra in each pair are extracted from the phases of low and high hardness ratio. The spectra demonstrate that spectral variations mainly originate below 0.5 keV where they can be described by changes in the depth of the absorption line (by a factor of ~2). In contrast temperature variations, determined by the spectrum above 0.5 keV are small (2 – 3 eV).*

**References:**

- Haberl, F., Schwope, A.D., Hambaryan, V., Hasinger, G., Motch, C. 2003, A&A 403, L19
- Haberl, F., Zavlin, V.E., Trümper, J., Burwitz, V. 2004, A&A 419, 1077
- Haberl, F., Motch, C., Zavlin, V.E., et al. 2004, A&A in press


*F. Haberl, V. Burwitz, J. Trümper, V.E. Zavlin, et al.*

# Searching for X-ray dim Isolated Neutron Stars

**This search correlates highly accurate X-ray observations with a deep optical sky survey. The small number of candidates found is in contradiction to the expectations.**

Searches for members of the exciting class of X-ray dim isolated neutron stars (XDINSs) so far suffered mainly from large X-ray positional uncertainties and there was no avaiable deep optical survey. The ROSAT pointings or XMM observations and the ongoing Sloan Digital Sky Survey (Sloan DSS) promise a significant improvement for a new search.

## Selection Criteria:

***Soft sources***

The hardness ratios should be similar to those of the known XDINSs. For the ROSAT High Resolution Imager pointings the hardness ratios have to be defined for the first time.

***No or very unlikely optical objects within the X-ray positional uncertainty***

Sloan DSS (only northern sky) reaches r=23.5 mag, USNO B1 goes down to R=21 mag. Everything else than XDINSs or AGNs can be ruled out as possible counterparts by taking into account the X-ray to optical flux ratio.

***No known catalogued source, especially no RADIO source***

XDINSs are radio-quiet. Using SIMBAD/NED ensures that there is e.g. no NVSS radio source.

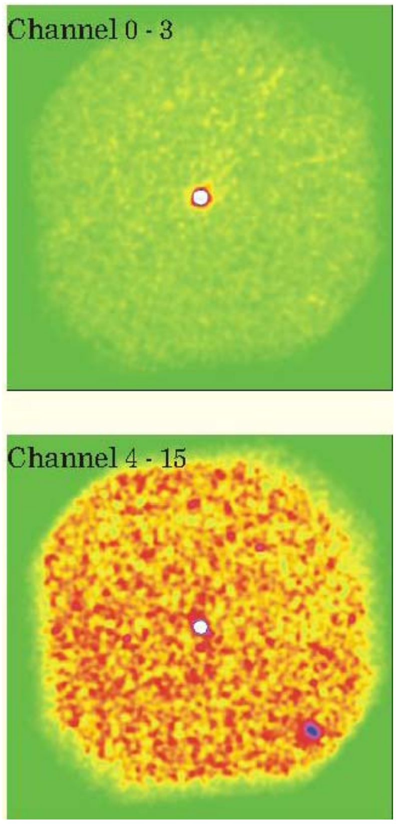


RXJ 1856.5-3754 – HRI observations
A hardness ratio based on these two bands can be successfully used to find soft sources.

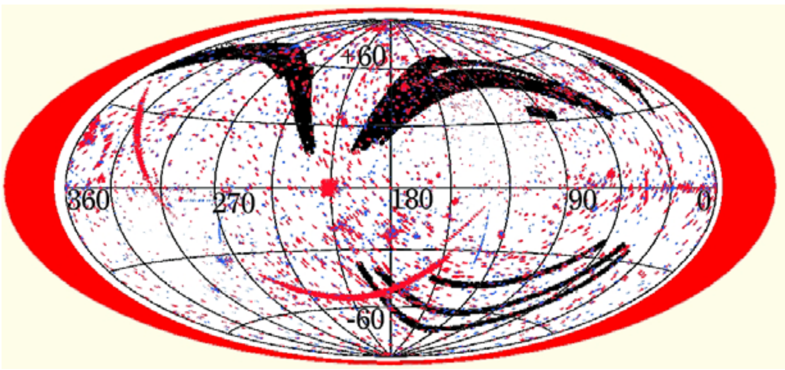


Sky coverage in galactical coordinates: The black area corresponds to the current Sloan data release 2. ROSAT PSPC (red dots) and HRI (blue dots) pointings are indicated.

## Preliminary Results:

A handful of XDINS candidates results from the ROSAT pointings together with the Sloan DSS and also with the USNO B1. No XDINSs were found using the first XMM catalogue. This is a significant deviation from the expectations.

A statistical analysis for the influence of the sky coverage of the ROSAT pointings and of the Sloan DSS is ongoing to clarify if there is a deviation for the XDINSs from the known pulsar distribution within our galaxy.

*B. Posselt, F. Haberl, R. Neuhaeuser, G. Hasinger, W. Voges*

# Optical polarization measurements of the Crab

We observed the Crab nebula and pulsar in the visual band for about 3 hours in January 2002 with the high-speed photo-polarimeter OPTIMA at the Calar Alto 3.5m telescope. The Crab pulsar and its net optical polarization are measured at all phases of rotation with unprecedented statistical accuracy. Recent theories indicate that the measured optical polarization of Crab is most compatible with a ‘two-pole caustic slot gap’ model. Radiation in this model is generated as beamed synchrotron light along the magnetic field lines throughout the open magnetosphere and the light curve peaks arise from caustic superposition. Emission from both poles is visible.

The OPTIMA instrument

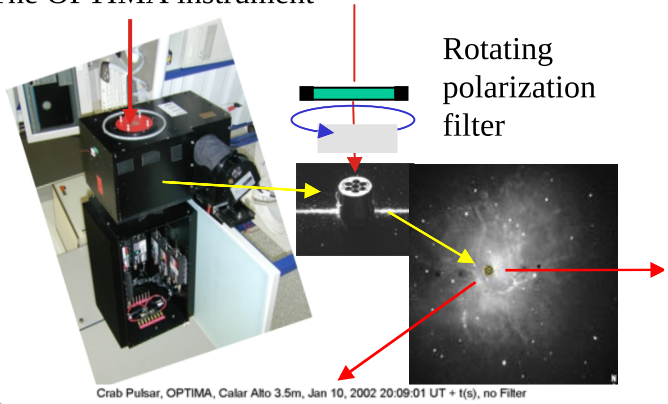


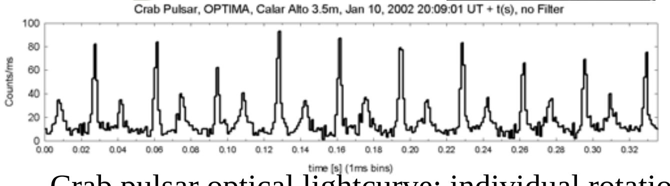


Crab pulsar optical lightcurve: individual rotations

Polarization of the inner Crab Nebula

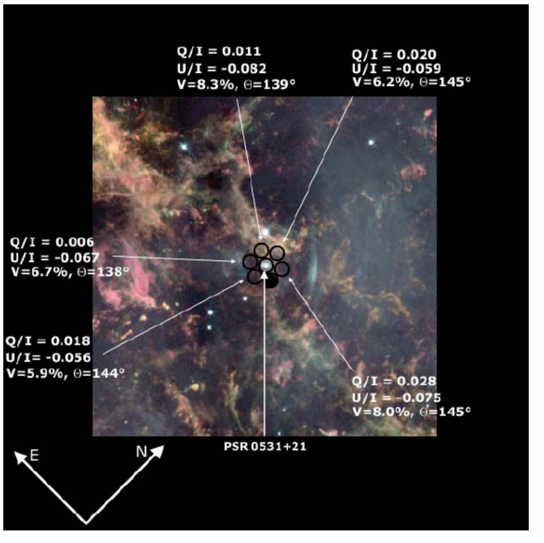


The Crab was imaged onto a hexagonal bundle of optical fibers which are coupled to single photon APD counters. Events are logged with GPS time tags. A rotating polaroid filter allows to measure the phase dependent linear polarization of the pulsar and the surrounding nebula.

OPTIMA Data (preliminary)

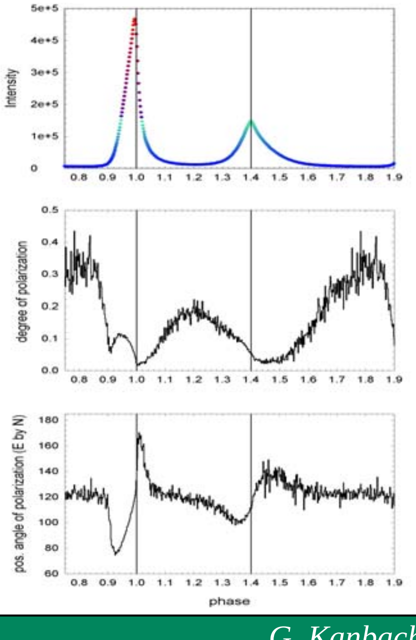


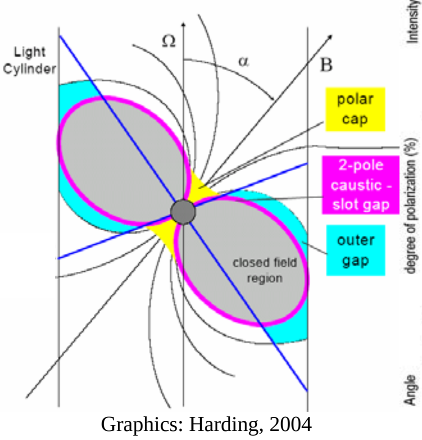


Graphics: Harding, 2004

Model: Dyks et al., 2004, ApJ, **606**, 1125, 2004

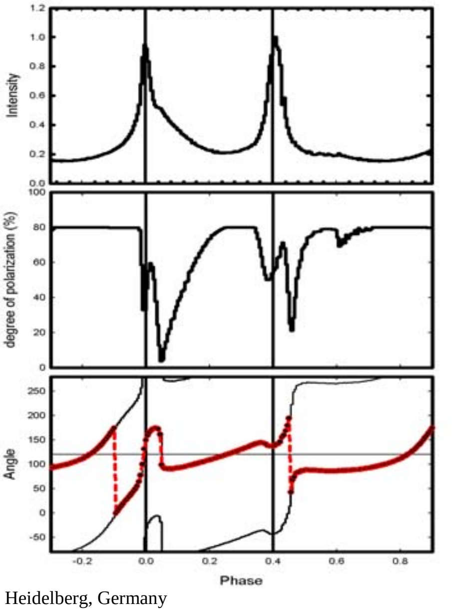


* now at NCAC, Torun, Poland, ** now at MPIA, Heidelberg, Germany

*G. Kanbach, A. Słowikowska* , S. Kellner**, H. Steinle*

# Revealing the X-ray emission processes of old rotation-powered pulsars: XMM-Newton observations of PSR B0950+08, B0823+26 and J2043+27

## The X-ray emission of old rotation-powered pulsars is largely dominated by non-thermal processes

We have completed part of a program to study the X-ray emission properties of old rotation-powered pulsars with XMM-Newton in order to probe and identify the origin of their X-radiation. Only XMM-Newton has enough sensitivity to allow to study these old and relatively faint pulsars. As it turns out, their X-ray emission is largely dominated by non-thermal processes. Although thermal polar caps were expected, none of the observed spectra required adding a thermal component consisting of either a hot polar cap or surface cooling emission to model the data.

The X-ray spectrum of PSR B0950+08 is best described by a single power law of photon-index $\alpha = 1.93^{+0.14}_{-0.12}$. Taking optical data from the VLT FORS1 into account, a broken power law model with the break point $E_{break} = 0.67^{+0.18}_{-0.41}$ keV and the photon-index $\alpha_1 = 1.27^{+0.02}_{-0.01}$ and $\alpha_2 = 1.88^{+0.14}_{-0.11}$ for $E < E_{break}$ and $E > E_{break}$, respectively, is found to describe the pulsar's broadband spectrum from the optical to the X-ray band.

We also find that the X-ray emission from PSR B0950+08 is pulsed with two peaks per rotation period. The phase separation between the two X-ray peaks is ~144° (maximum to maximum) which is similar to the pulse peak separation observed in the radio band at 1.4 GHz. The main radio peak and the trailing X-ray peak are almost phase aligned. The fraction of X-ray pulsed photons is ~30%. A phase-resolved spectral analysis confirms the non-thermal nature of the pulsed emission and finds no spectral variations as a function of pulse phase.

The spectral emission properties observed for PSR B0823+26 and PSR J2043+27 are similar to those of PSR B0950+08 (Becker et al., 2004, ApJ, in press).

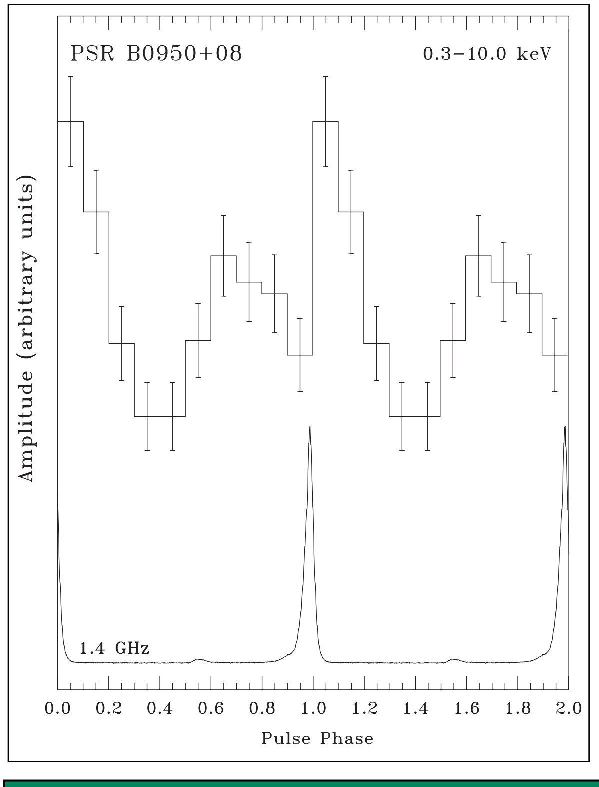


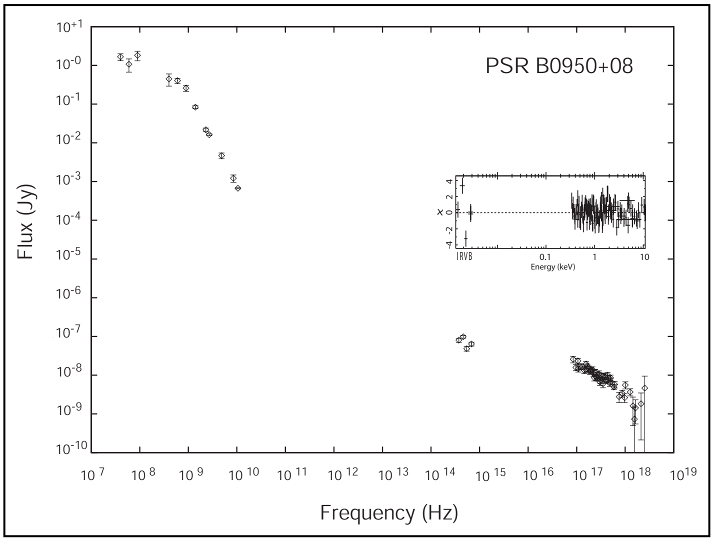


***Left:*** Integrated pulse profiles of PSR B0950+08 as observed with the EPIC-PN aboard XMM-Newton (top) and at 1.4 GHz with the Effelsberg radio telescope (bottom). ***Right:*** Combined radio, optical and X-ray spectral data of PSR B0950+08.The inset shows the contribution to the $\chi^2$ fit statistic for a broken power law model fitted to the optical and X-ray data.

*W. Becker, in collab. with* M.C.Weisskopf , A.F.Tennant, A.Jessner, J.Dyks, A.K.Harding, S.N.Zhang

# A multi-wavelength search for a counterpart of the brightest unidentified γ-ray source 3EG J2020+4017

## Deep X-ray and radio observations with Chandra and the Green Bank Radio Telescope leave Gamma-Cygni still unidentified

The final EGRET catalog of gamma-ray sources lists 271 objects (Hartman et al. 1999) of which about 170 are unidentified. 3EG J2020+4017 is among the brightest persistent sources in the EGRET sky. Originally listed as a COS-B source (2CG078+01) it is still unidentified. Its gamma-ray flux is consistent with constant flux and the spectrum is hard and best described by a power-law with photon-index of 1.9

In search of the counterpart we observed the Gamma-Cygni field with the *Chandra* X-ray Observatory and with the Green Bank Telescope (GBT). To complete the analysis we reanalyzed archival ROSAT data. With *Chandra* it became possible for the first time to measure the position of the putative gamma-ray counterpart RX J2020.2+4026 with sub-arcsecond accuracy and to deduce its X-ray spectral characteristics. These observations demonstrate that RX J2020.2+4026 is associated with a K- field star and therefore is unlikely to be the counterpart of the bright gamma-ray source in the SNR G78.2+2.1 as had been previously suggested by Brazier et al. (1996). In addition to RX J2020.2+4026, the *Chandra* observation detected 37 X-ray sources which were correlated with catalogs of optical and infrared data. Subsequent GBT radio observations covered the complete 99% EGRET likelihood contour of 3EG J2020+4017 with a sensitivity limit of $L_{820} \sim 0.1$ mJy kpc$^2$ which is lower than most of the recent deep radio search limits (Becker et al. 2004, ApJ, in press).

If there is a pulsar operating in 3EG J2020+4017, this sensitivity limit suggests that the pulsar either does not produce significant amounts of radio emission or that its geometry is such that the radio beam does not intersect with the line of sight. Finally, reanalysis of archival ROSAT data leads to a flux upper limit of $f_x$ (0.1-2.4 keV) $< 1.8 \times 10^{-13}$ erg s$^{-1}$cm$^{-2}$ for a putative point-like X-ray source located within the 68% confidence contour of 3EG J2020+4017. Adopting the SNR age of 5400 yrs and assuming a spin-down to X-ray energy conversion factor of $10^{-4}$ this upper limit constrains the parameters of a putative neutron star as a counterpart for 3EG J2020+401 to be $P \lesssim 160\,(d/1.5\,\mathrm{kpc})^{-1}$ ms, $\dot{P} \lesssim 5 \times 10^{-13}$ s s$^{-1}$, $B_\perp \lesssim 9 \times 10^{12}\,(d/1.5\,\mathrm{kpc})^{-1}$ G.

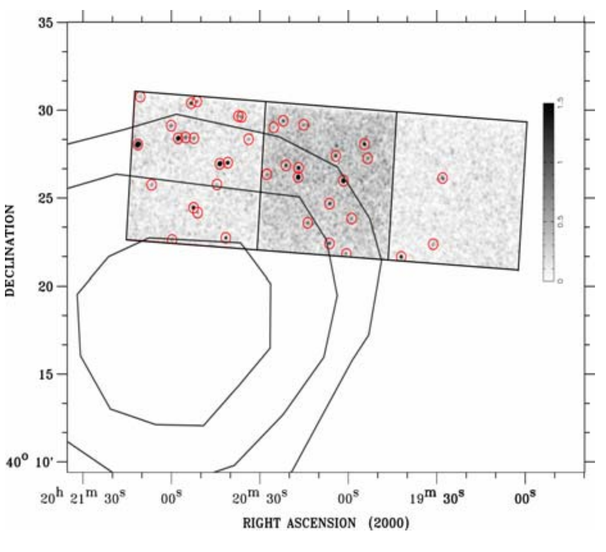


*Chandra* ACIS field of 3EG J2020+4017. The 68%, 95% and 99% contour lines from the 3EG EGRET likelihood map are shown.

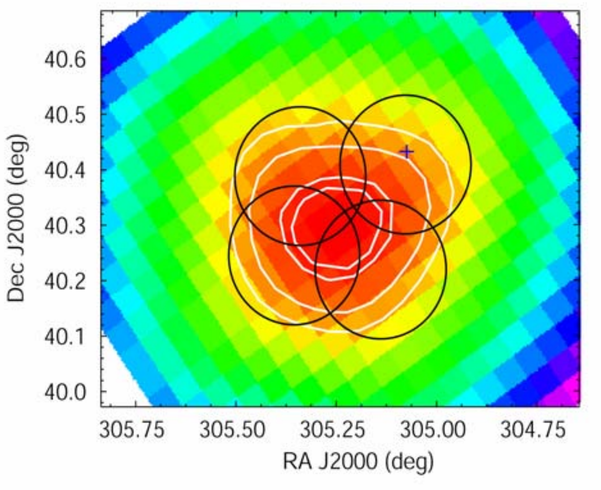


The fields covered by the GBT radio observations are indicated by black circles. The cross indicates the position of the putative ROSAT counterpart RX J2020+4026.


*W.Becker, G.Kanbach in collaboration with M.C. Weisskopf, O. Reimer, et al.*

# A new view of Vela X-1

*INTEGRAL* observations of Vela X-1 have shown flares of previously unknown strength with luminosity increases up to a factor of ~10, but small changes in the high-energy spectra. Other observations during a calm phase have led to the the first actual measurement of the width of the cyclotron line feature at ~53 keV due to the high energy resolution of the *INTEGRAL* spectrometer *SPI*.

The wind-accreting X-ray binary pulsar Vela X-1 has been observed extensively during *INTEGRAL* Core Program observations of the Vela region in June-July and November-December 2003. While in summer the source was mostly calm, the winter observations showed several large flares, possibly the largest ever observed. Unfortunately, due to the observation strategy not centered on Vela X-1, the *INTEGRAL* monitors did not cover the source during the flares. Dito for the *RXTE-ASM*.

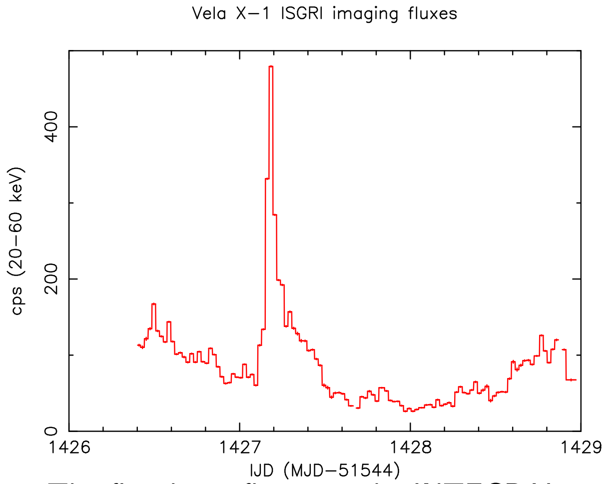


*The first huge flare seen by INTEGRAL.*

Spectral analysis of *ISGRI* and *SPI* spectra rom before and during the flare shown in Fig. 1 yields a flux increase by a factor of about 10 and a softening of the high energy spectra. Using a typical power law with exponential cutoff model, the parameter "folding energy", which can be seen as a measure of temperature, decreases by 1–1.5 keV during the flare. Otherwise the spectra are very similar, indicating only minor changes in the emission region geometry.

In long-term averaged spectra for the summer observations from *SPI* and *JEM-X* the known cyclotron line feature above 50 keV is evident in the fit residuals for *SPI*. It can be fitted by including a cyclotron scattering feature at $E \approx 54$ keV with $\sigma \approx 7$ keV. Since the SPI energy resolution at these energies is ~1.6 keV, the line shape can actually be resolved in spite of low statistical quality at the higher end. The line width is consistent with that expected from thermal broadening; the lack of substructure supports the interpretation as harmonic. The calibration uncertainties do not allow to determine the indicated line feature at ~25 keV.

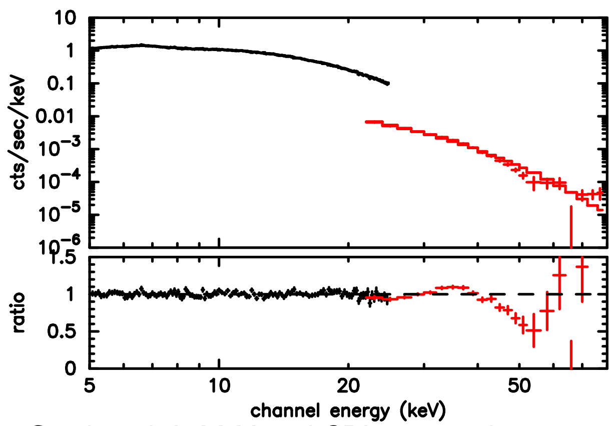


*Combined JEM-X and SPI averaged spectra*

| Parameter | *JEM-X + SPI* |
|---|---|
| photon index | $0.51^{+0.10}_{-0.20}$ |
| folding energy | $11.3^{+0.7}_{-1.3}$ keV |
| line center | $53.6^{+3.4}_{-1.8}$ keV |
| line $\sigma$ | $7.3^{+1.8}_{-1.3}$ keV |
| line depth | $0.63^{+0.13}_{-0.08}$ |
| $\chi^2_{\text{red}}$ with line | 1.19 |
| $\chi^2_{\text{red}}$ w/o line | 1.85 |

*P. Kretschmar, K. Pottschmidt, A. v. Kienlin*

# NGC 253 X-17: The first eclipsing X-ray binary outside the Local Group

**We have discovered the first eclipsing X-ray binary outside the Local Group of galaxies. We used data from the XMM-Newton, Chandra, ROSAT and Einstein satellites to determine candidate orbital periods, time variability and X-ray spectrum.**

Before the advent of the X-ray observatories XMM-Newton and *Chandra* the most distant eclipsing X-ray binary (XRB) known was source X-7 in the Local Group galaxy M 33 (distance 795 kpc) with an orbital period of 3.45 days (see Dubus et al. 1999, Pietsch et al. 2004). Already Fabbiano & Trinchieri (1984) detected with the *Einstein* observatory a source in the starburst galaxy NGC 253 in the Sculptor Group (distance 2.58 Mpc) that was found to be time variable during ROSAT observations (source X-17 in Vogler & Pietsch 1999). Twice, during an XMM-Newton EPIC observation in December 2000 (Figs. 1 and 2) and also during a *Chandra* observation one year earlier, this source, RX J004717.4-251811, was found to undergo changes from a low to a high state. The transitions are interpreted as egresses from eclipses of a compact

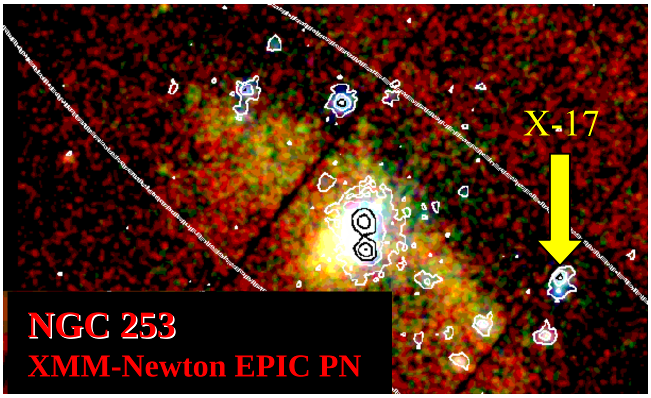


***Fig. 1:** EPIC PN image of NGC 253. The eclipsing X-ray binary X-17 is the brighter source in the pair marked by an arrow.*

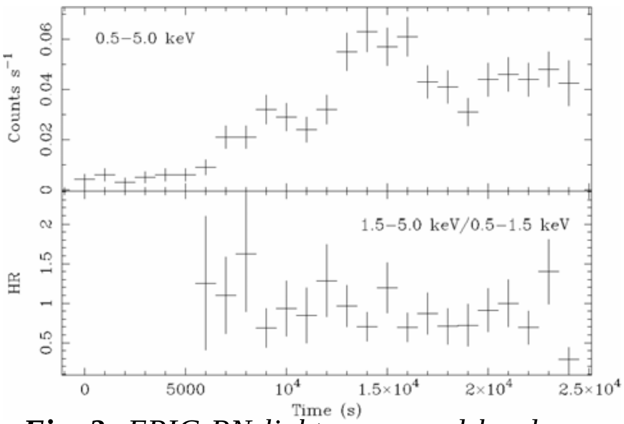


***Fig. 2:** EPIC PN light curve and hardness ratio of X-17 on Dec 13/14, 2000, showing a transition from low to high state.*

object in a high mass XRB system. The binary period is determined to $P = (352.870 \pm 0.012)\mathrm{d}/n$ by the time difference between the two egresses and number $n$ of periods in-between. Allowed periods can be further constrained by additional XMM-Newton, *Chandra*, ROSAT, and *Einstein* observations resulting in only seven acceptable periods with 1.47024 d and 3.20793 d most promising. No significant regular pulsations of the source in the range 0.3-1000 s were found. Fluctuations on time scales of 1000 s were observed together with extended intervals of low intensity. The energy spectrum during the bright state can be described by an absorbed flat power law ($N_H$=1.9 $10^{21}$ cm$^{-2}$, $\Gamma = 1.7$). In the bright state, the source luminosity is 4 $10^{38}$ erg s$^{-1}$ in the (0.5-5) keV band, just compatible with the Eddington luminosity of a 1.4 $M_{sun}$ neutron star.

**References:**
- Dubus, G., Charles, P.A., Long, K.S., et al. 1999, MNRAS, 302, 731
- Fabbiano, G., Trinchieri, G. 1984, ApJ, 286, 491
- Pietsch, W., Roberts, T.P., Sako, M., et al. 2001, A&A, 365, L174
- Pietsch, W., Haberl, F., Vogler, A. 2003, A&A, 402, 457
- Pietsch, W., Mochejska, B.J., Misanovic, Z., et al. 2004, A&A, 413, 879
- Vogler, A., Pietsch, W. 1999, A&A, 342, 101

*W. Pietsch, F. Haberl, A. Vogler*

# The black hole Cygnus X-1 as seen by *INTEGRAL*

Cyg X-1, the prototype X-ray binary containing a stellar mass black hole, was observed for 1.3 months during *INTEGRAL's* performance verification phase. We presented the first *INTEGRAL* broad band spectrum, as well as one of only a few multi-mission spectra in the early mission by organizing quasi-simultaneous *RXTE* observations. Parameters for several current Comptonization models were derived and refined with progressing calibration. We also presented the first power spectrum measured with *ISGRI*, again evaluated against contemporary *RXTE* data.

## Broad band energy spectra

During 2002 Nov. and Dec. the persistent black hole binary Cyg X-1 was found in its Comptonization dominated hard state. Summing the data by *INTEGRAL* orbit ($\sim$3 d) has proven to be a good choice to take spectral variability into account. Thermal Comptonization models like `compTT` or `eqpair` principally describe the data and give comparable results. We note residuals above 300 keV, where the non-thermal "hard tail" reported by *CGRO* should become visible. Typical physical parameters (2002 Nov. 16) are: $\tau = 0.71^{+0.05}_{-0.07}$, $kT = 82^{+16}_{-5}$ keV, $\Omega/2\pi = 0.11^{+0.01}_{-0.01}$, $\chi^2_{\mathrm{red}} = 1.58$, where $\tau$ is the electron optical depth, $kT$ is the electron temperature, and $\Omega/2\pi$ is the reflection fraction. A further refined calibration will enable us to distinguish between current models.

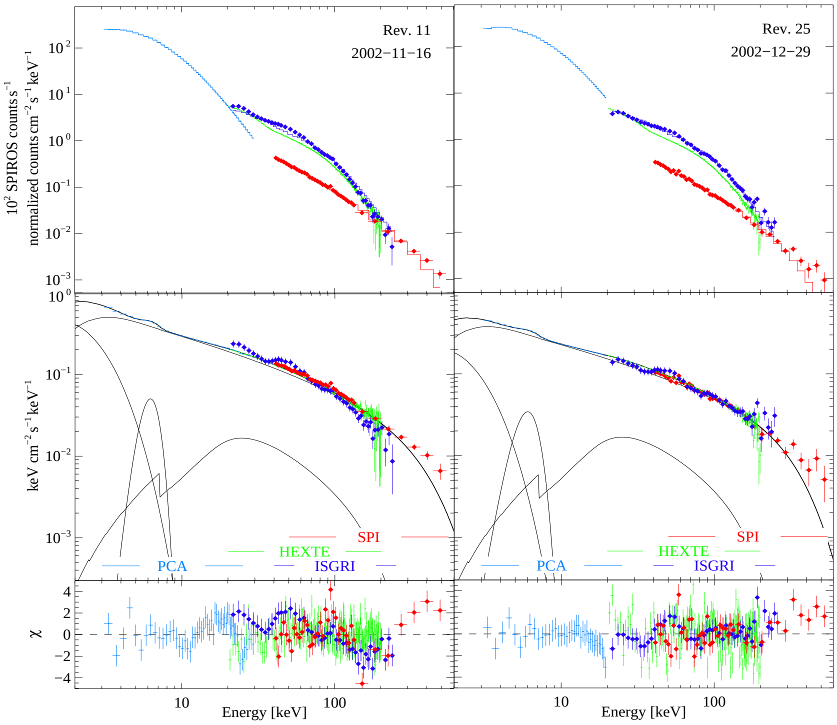


*INTEGRAL/RXTE* energy spectra and best fits of Cygnus X-1. Model: `const`$\times$`phabs`$\times$`[diskbb+gauss+compTT+reflect(compTT)]`.

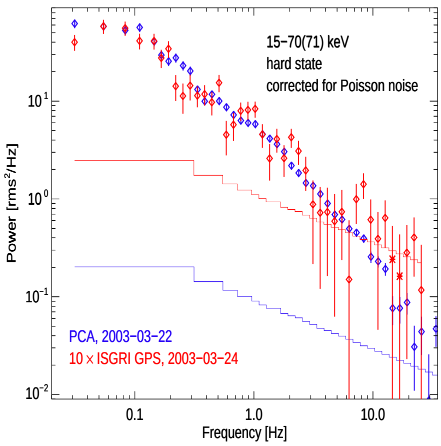


Noise corrected power spectra of Cygnus X-1. Lines: detection limit.

## High resolution timing

After subtraction of the Poisson noise level *RXTE* and *ISGRI* qualitatively measure the same 3-20 Hz source variability, i.e., the 15–70 keV power spectra show the same shape. Note, that the figure shows one of the few short Galactic Plane Scan observations of Cyg X-1 (analysis in collaboration with A.A. Zdziarski). The rms variability measured with *ISGRI* lies about an order of magnitude too low due to the high background. We are working on a correction and plan to analyse the less well studied power spectrum at energies >70 keV (*INTEGRAL/XMM/RXTE* campaign in 2004 Nov.) .

Pottschmidt, K., Wilms, J., Chernyakova, M., et al., 2003, A&A, 411, L383
Pottschmidt, K., Wilms, J., Nowak, M., et al., 2004, ESA SP-552, in press
Pottschmidt, K., Wilms, J., Nowak, M., et al., 2005, ASR, in prep.
Wilms, J., Pottschmidt, K., Nowak, M., et al., 2004, AIP Conf. 714, 116

*K. Pottschmidt, P. Kretschmar, V. Schönfelder, et al.*

# M 33 X-7: An eclipsing black hole XRB?

**We determined an improved period and ephemeris of the eclipsing X-ray binary (XRB) M33 X-7. We identified the optical counterpart by its ellipsoidal heating light curve. The data indicate that the source may be the first eclipsing high mass black hole (BH) XRB.**

The *Einstein* source X-7 in the Local Group galaxy M 33 was identified as an eclipsing XRB in ROSAT observations (see Dubus et al. 1999 and references therein). Before the detection of eclipses in the XRB X-17 in the starburst galaxy NGC 253 in the Sculptor group of galaxies (Pietsch et al. 2003) it was the most distant eclipsing XRB known (795 kpc).
M 33 X-7 was detected in the field of view during several observations of our XMM-Newton M 33 survey (Pietsch et al. 2004b) and in the archival *Chandra* observation 1730 which cover a large part of the 3.45 d orbital period. We detected emission of M33 X-7 during eclipse and a soft X-ray spectrum of the source out of eclipse that was best described by bremsstrahlung or disk black body models. No significant regular pulsations of the source in the range 0.25-1000 s were found. The average source luminosity out of eclipse was 5 $10^{37}$ erg $s^{-1}$ in the (0.5-4.5) keV band. In a special analysis of DIRECT observations we identified as optical counterpart a B0I to O7I star of 19.89 mag in V which showed the ellipsoidal heating light curve of a high mass XRB with the M 33 X-7 binary period (see Figs., Pietsch et al. 2004a).
The location of the X-ray eclipse and the optical minima allowed us to determine an improved binary period and ephemeris of mid eclipse. The mass of the compact object derived from orbital parameters and the optical companion mass, the lack of pulsations, and the X-ray spectrum of M 33 X-7 may indicate that the compact object in the system is a BH. M 33 X-7 would be the first detected eclipsing high mass BH XRB.

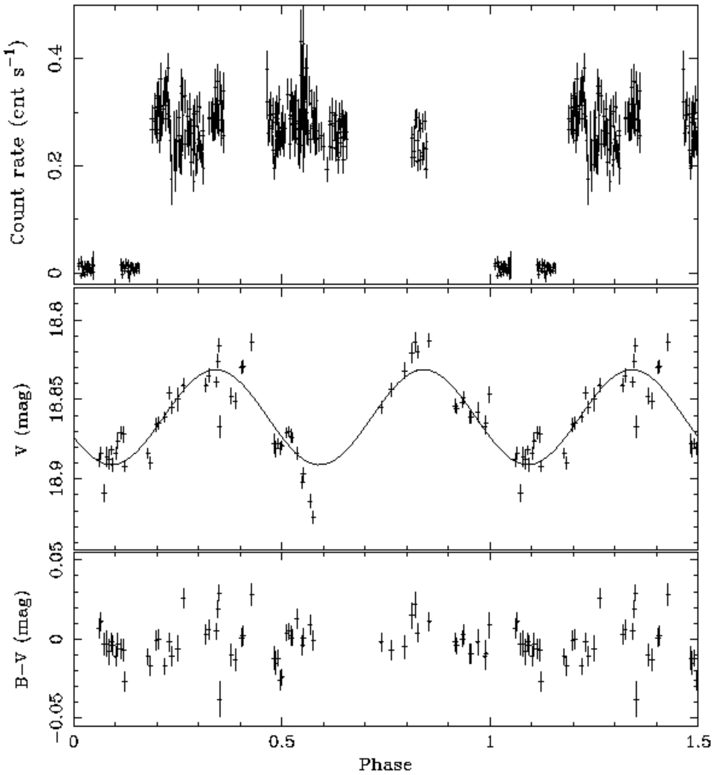


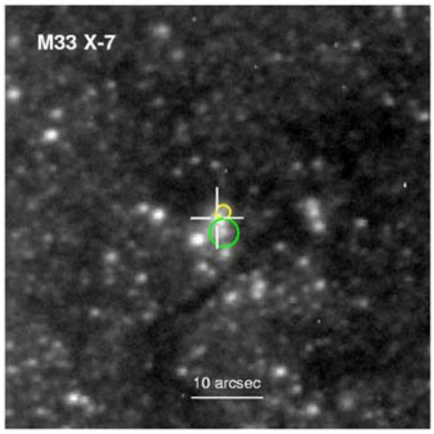


***Above:*** *ROSAT (green) and Chandra (yellow) position of M 33 X-7 on a V image of the DIRECT survey. The optical identification, i.e. the star showing the 3.4 d variability, is marked by the cross hair.*

***Left:*** *Light curve of M 33 X-7 in the 0.5-3 keV band and in optical V and B-V folded over the 3.45 d orbital period using ephemeris of D99. Added is a double-sinusoidal approximation to the V data.*

**References:**
• Dubus, G., Charles, P.A., Long, K.S., et al. 1999, MNRAS, 302, 731 (D99)
• Pietsch, W., Haberl, F., Vogler, A. 2003, A&A, 402, 457
• Pietsch, W., Mochejska, B.J., Misanovic, Z., et al. 2004a, A&A, 413, 879
• Pietsch, W., Misanovic, Z., Haberl, F., et al. 2004b, A&A, 426, 11

*W. Pietsch, F. Haberl, Z. Misanovic*

# Following the evolution of IGR J17464-3213

Serendipitous *INTEGRAL* observations of IGR J17464-3213 (H1743–322) over the duration of an extended outburst have determined its true position and allowed to study the physical properties of the outburst evolution of this transient BHC.

IGR J17464-3213 was detected as a new source in March 2003 during a Galactic Center Deep Exposure of *INTEGRAL*. Soon after, Markwardt & Swank (2003) identified it with the transient H1743–322 for which the wrong of two possible positions was recorded in the HEAO-1 catalog.

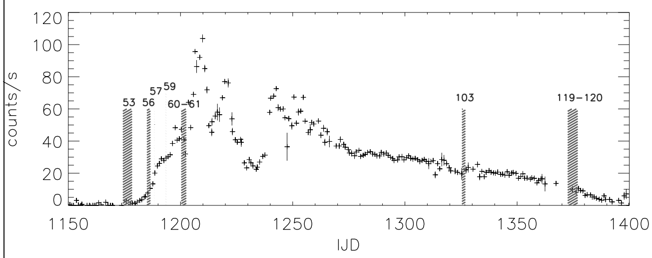


*Long term lightcurve of IGR J17464-3213 with indicated revolution numbers.*

When IGR J17464-3213 was first observed by *INTEGRAL*, it was in a low/hard state and only visible at higher energies with *ISGRI* and *SPI*; the spectrum well described by a comptonization model ($kT_e$~20keV, $\tau_p$~3) and no discernable disk emission.

About 10 days later the luminosity had increased by a factor of 30; with no change to $kT_e$ but reduced optical thickness ($\tau_p$~1.5). Again ~10 days later, the brightening source was in a soft/intermediate state, visible in all instruments with a strong disk blackbody component $T_{\rm in}$~1.5keV in addition to the hotter comptonized spectrum ($kT_e$~40keV, $\tau_p$~0.4).

A few months after the main outburst, when the region was observed again, the source was in a soft state, mainly visible in *JEM-X* as disk blackbody of $T_{\rm in}$~1keV. A very weak compton tail is visible again in the latest observations.

The outburst evolution is typical for a Black Hole Candidate, underlining the identification of IGR J17464-3213. It was followed serendipitously by a large collaboration in survey data without targeted observations (Capitanio et al. 2004).

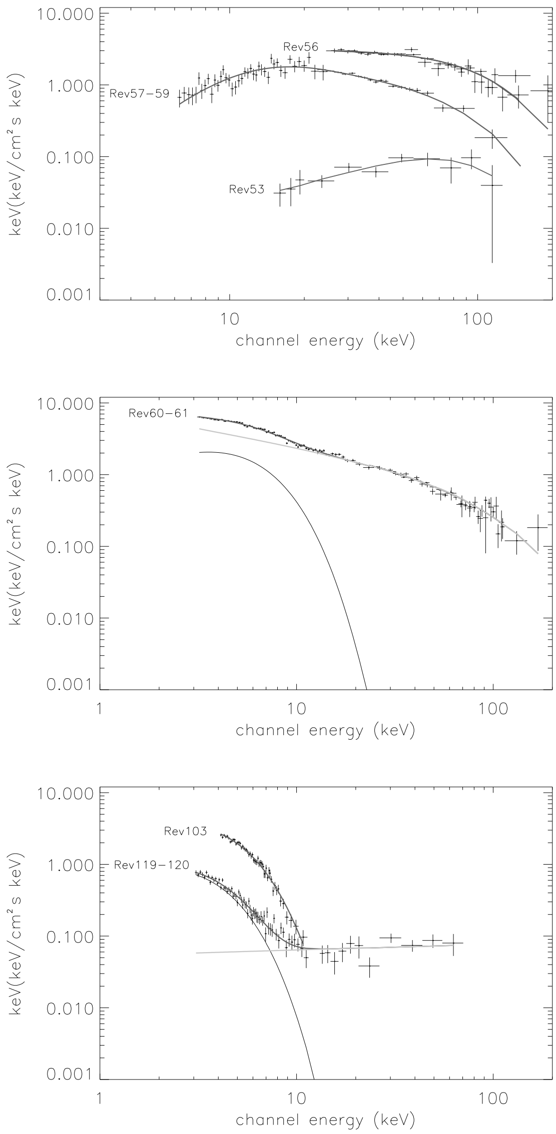


*Spectra in different phases of the outburst*

**References**


Markwardt C. B., Swank J. H., 2003, ATel, 133

Capitanio F., et al., 2004, ApJ, *submitted*



*P. Kretschmar*

# GRB 030329: Jets and Supernova connection

GRB 030329 had the brightest optical/IR afterglow of all localized GRBs so far, and allowed very detailed ground-based observations, e.g. using the VLT: Optical spectroscopy proved GRBs to originate from massive stars experiencing a supernova, and polarimetry provided unequivocal evidence for the jet-like emission geometry.

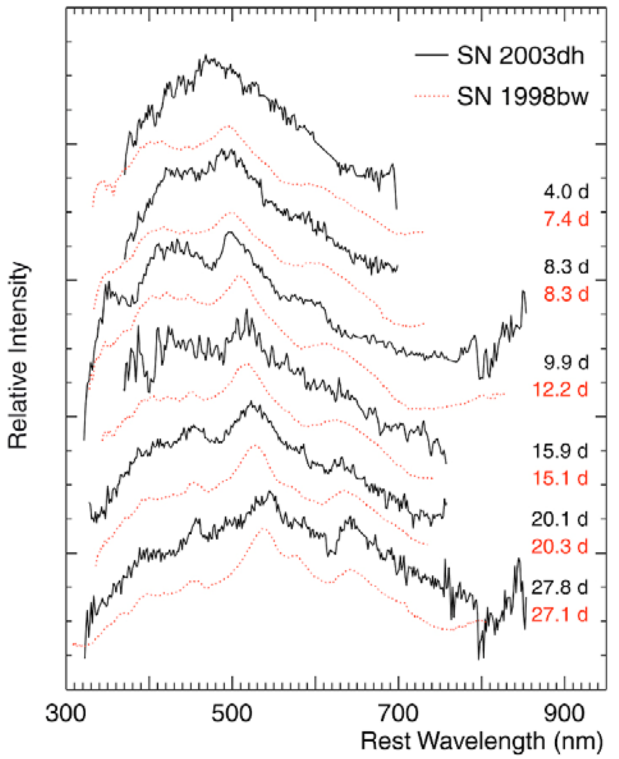


With a redshift of 0.168, GRB 030329 was among the GRBs with the smallest distance ever measured. It was brighter than *R*=20 mag for about 20 days, thus offering unique observing possibilities.

A sequence of FORS/VLT spectra revealed the signatures of a supernova Ic (Hjorth et al. 2003), named SN 2003dh, very similar to SN 1998bw connected to GRB 980425 (left figure). From the SiII λ6335 line the expansion velocity on day 10 was estimated to be 36000 km/s, considerably larger than any previously known SN.

Since type Ic SN light curves are powered by radioactive decay, the data indicate the synthesis of several tenths of a solar mass of $^{56}$Ni. This is the most direct evidence so far that long-duration GRBs result from the death of massive stars.

The lack of hydrogen lines is consistent with model expectations that the star lost its hydrogen envelope to become a WR star before exploding.

An extensive series of R-band polarimetry with FORS/VLT allowed to establish for the first time a polarization light curve, i.e. the variation of polarization degree and angle θ with time (right figure; Greiner et al. 2003). GRB 030329 is so far the only case where the polarization evolution supports the break as being due to the jet nature. The jet opening angle is determined to be 3 deg. The late-time (3-10 days) polarization variation is not the result of small number of coherent magnetic field cells with random orientation, but instead θ must be associated with some global geometry. This suggests an entangled magnetic field in the jet.

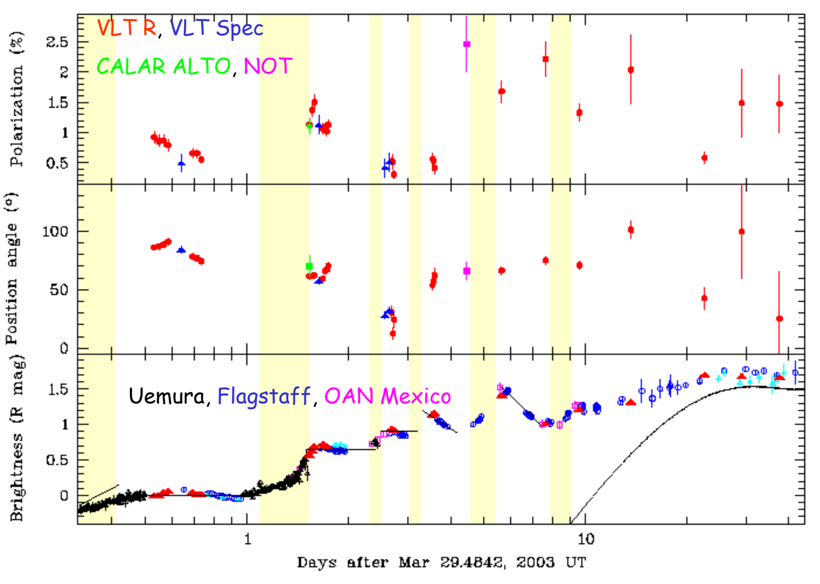



**References:**

- Greiner J., Klose S., Reinsch K. et al 2003, Nature 426, 157
- Hjorth J., Sollermann J., Moller P. et al. 2003, Nature 423, 847



*J. Greiner, A. Rau & the GRACE collaboration*

# Discovery of the near-IR Afterglow of GRB 030528

The rapid dissemination of an arcmin-sized *HETE-2* localization of the long-duration X-ray flash GRB 030528 led to the discovery of the near-IR afterglow and the detection of the underlying host galaxy in the optical and near-IR bands. The afterglow was not detected in the optical band. Our *K*-band photometry suggests that the lack of optical detection was simply due to the lack of rapid and deep follow-up observations and a high foreground extinction. The properties of the host are consistent with the idea that GRB hosts are star-forming blue galaxies.

**GRB 030528:**
The error box of the long-duration *HETE-2* X-ray flash was measured with a variety of ground based near-IR facilities. Following the detection of four *Chandra* X-ray sources inside the error box five days post-burst, one source was found fading in our NTT SofI $K_s$-band images taken 0.6 and 3.6 days after the burst by ~1 mag (Rau et al. 2004). This fading was confirmed later by the detection of a fading X-ray source in a second *Chandra* observation. No optical afterglow was found. Thus, the burst is classified as optically dark.

Compilation of K-band afterglow magnitudes (incl. GRB 030528; black squares)

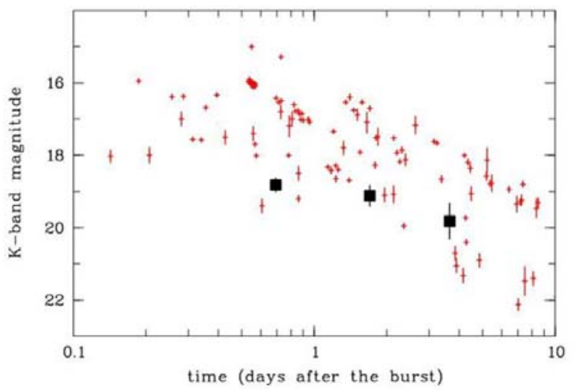


**The Near-IR Afterglow:**
The fading near-IR afterglow was only detected in the $K_s$-band, and is among the faintest *K*-band afterglows detected so far (upper right figure). No variability is observed in J-band observations between 0.6 and 120 days post-burst. The temporal ($\alpha$=0.7-2) and spectral ($\beta$>0.4) slopes are typical for GRBs.

The afterglow observation suffered from high Galactic forground extinction ($A_V$=2). A lower limit ($A_V$>2 ) on the intrinsic extinction can be derived from the near-IR afterglow photometry, consistent with X-ray results. An interpolation of the *K*-band afterglow into the optical regime shows that the early searches were not sensitive enough for a detection.

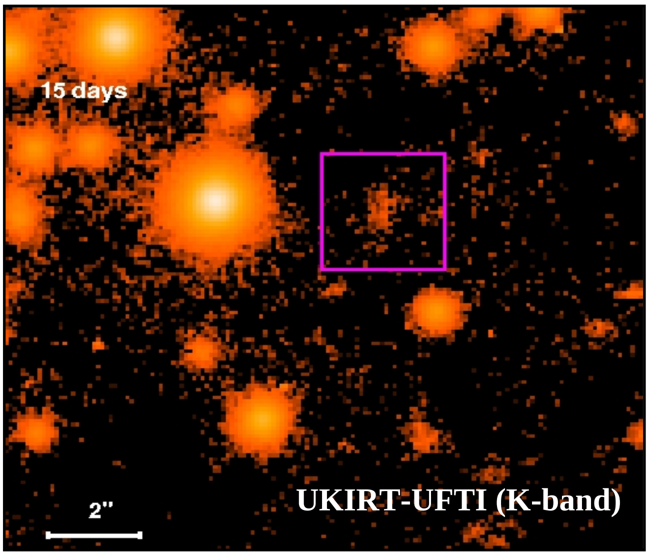


**The Host Galaxy:**
Late time imaging in *K* and $J_s$ revealed the underlying host galaxy (left) at *K*=19.9±0.7. This places it among the brightest hosts found. Our *VRIJHK* photometry is best fitted by a late type star-forming galaxy (similar to other known GRB hosts; le Floc'h et al. 2003) at z<4, using the photometric redshift method of Bender et al. (2001).
If the host galaxy has an absolute brightness comparable to that of the known sample of hosts (8% of $L_*$ in a Schechter distribution function), a redshift of z~0.4-0.6 is suggested. This is consistent with the value estimated from the prompt emission properties using the pseudo redshift indicator of Atteia (2003).

*A. Rau, J.Greiner, M. Salvato, A. Küpcü Yoldas et al.*

# GRBs observed in the FoV of *INTEGRAL*

Since the launch of ESA's gamma-ray mission *INTEGRAL* in October 2002, 16 gamma-ray bursts (GRBs) were detected in the field of view (FoV) of both main instruments, the imager IBIS and the spectrometer SPI by Sept. 15, 2004. In all cases the primary location was obtained by IBIS and an alert was distributed to the scientific community by the *INTEGRAL* burst alert system for rapid follow-up observations. The localizations, peak fluxes, fluences and spectral shapes obtained with SPI confirmed the IBIS results. One of the last GRBs, the X-ray rich GRB040812, was for the first time also detected in the FoV of *INTEGRAL*'s X-ray monitor JEM-X. In 6 cases an X-ray and/or optical/radio afterglow was detected by ground-based telescopes or X-ray satellites.

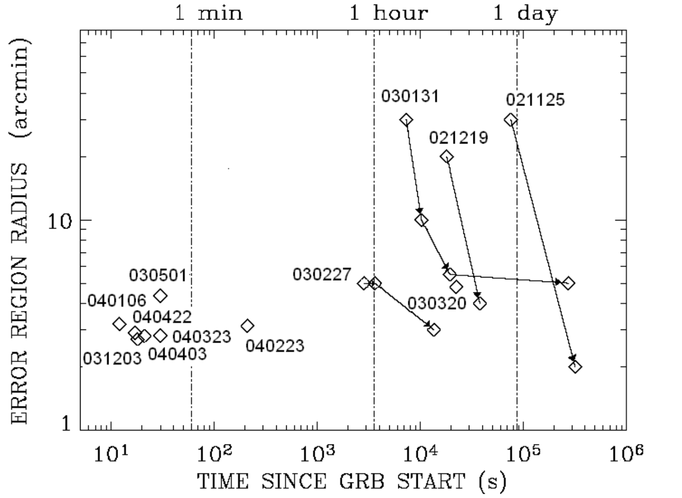


Accuracy versus time delay for the first 12 GRBs localized by IBAS. The arrows indicate the improvement of the burst location with time for the first four GRBs.

IBAS is able to provide error regions with radii as small as 3 arcminutes (90% c.l.) within a few tens of seconds of the GRB start. With this capability it is possible to catch the afterglow like for GRB 031203, which turned out to be a GRB with unusually low luminosity. This discovery suggests that an entire population of sub-energetic gamma-ray bursts, intermediate between normal gamma-ray bursts and supernovae, has so far gone unnoticed. GRB 031203 was also the first GRB for which a time-dependent dust-scattered X-ray halo was observed with XMM.

In most cases it was possible to deduce spectra and lightcurves with both main instruments as shown for GRB 030227 and GRB 030320 in the Figures on the right side. Both GRBs show evidence for a hard-to-soft spectral evolution.

**References:**


- von Kienlin. A., et al. 2003, A&A, 411, L299
- von Kienlin. A., et al. 2003, A&A, 411, L321
- Mereghetti, S., et al. 2003, ApJ590, L73
- Mereghetti, S., et al. 2004, Proc. 5th *INTEGRAL* Workshop
- Sazonov, S. Yu, et al. 2004, Nature, 430, 646
- Vaughan, S., et al. 2004, ApJ, 603, L5


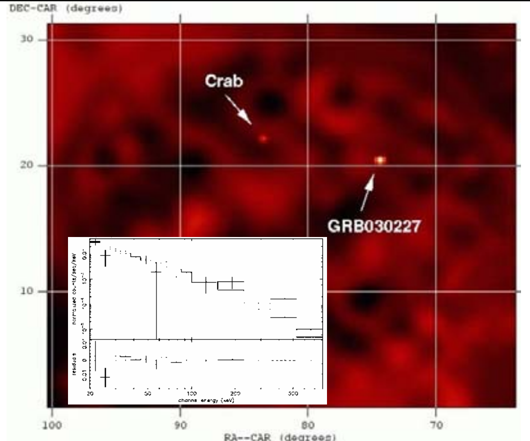


SPI analysis results of GRB 030227: Sky map and spectrum

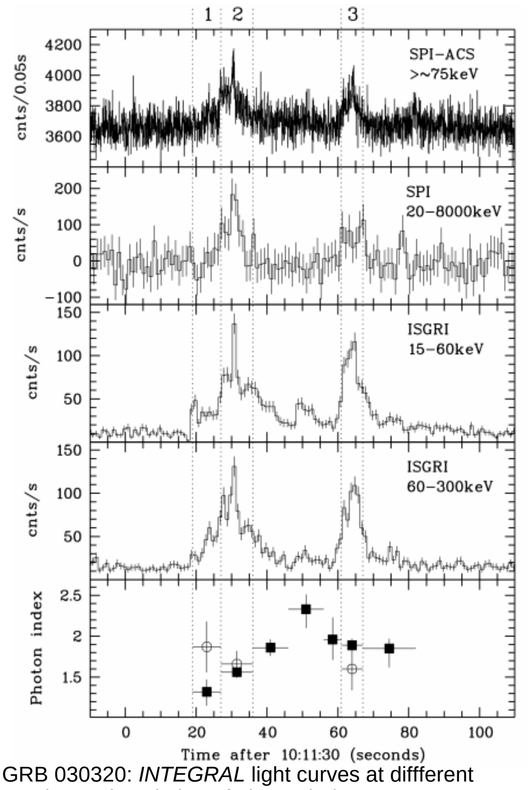


GRB 030320: *INTEGRAL* light curves at diffferent enrgies and evolution of photon index


*A. v. Kienlin, A. Rau, G. Lichti et al.*

# Gamma-Ray Bursts detected by SPI-ACS

The anticoincidence shield (ACS) of the spectrometer onboard INTEGRAL (SPI) is operated as a quasi omnidirectional gamma-ray burst (GRB) detector above ~75 keV. Since the start of the mission in October 2002 more than 300 GRB candidates have been detected. 50% of these could be confirmed and partly localized by the γ-ray instruments included in the 3rd Interplanetary Network. The previously known bimodality of durations is detected in the sample. A prominent population of short burst candidates (<200 ms) is found, which however is contaminated by events from cosmic-ray nuclei interactions in the detectors.

**SPI-ACS as GRB detector:**

The SPI-ACS consists of 91 BGO crystals and can detect GRBs nearly omnidirectional above ~75 keV. The upper end of the energy range is somewhat uncertain, but >10 MeV. The overall detector count rate is recorded in 50 ms time bins. Software was developed to search for excesses in the time profile and to alert the interested community. SPI-ACS measurements do not provide spatial information but help to localize bursts via triangulation, being an important member of the 3rd Interplanetary Network (IPN).

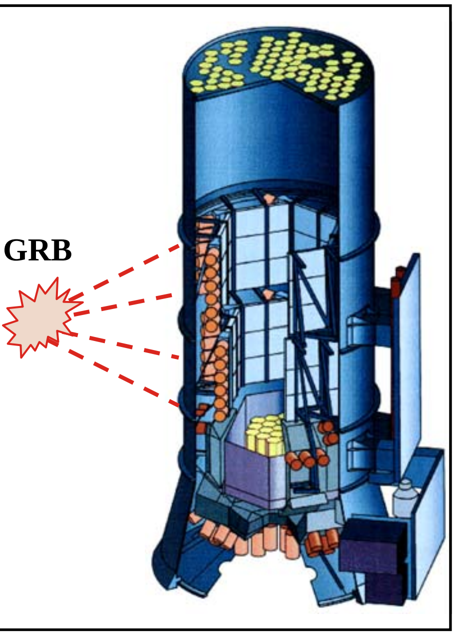


**GRB sample:**

Until August 2004 more than 300 GRB candidates have been detected (see bottom for examples). Nearly 50% of these candidates were also observed and confirmed by other IPN instruments. The sample exhibits the previously found bimodality in durations (peaks at 0.3s ~30s) but shows an unusually prominent population of short (<0.2 s) GRBs.

**Origin of the short event population:**

A significant fraction of the short events (e.g. event from March 3 2003) is accompanied by simultaneous saturation of one or several SPI detectors. Therefore, they are probably caused by a very energetic cosmic-ray particle, which hits the BGO. This causes a so-called afterglow of several milliseconds in the crystal and leads to a repetitive event trigger. The particle is stopped in the SPI Ge-detectors and deposits enough energy to saturate the detectors (Rau et al. 2004).

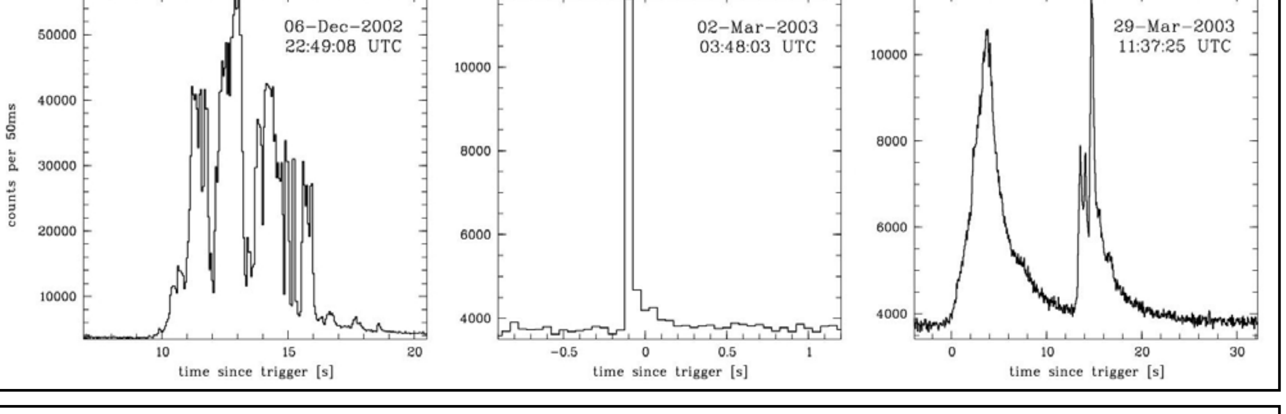


**Reference:** Rau A., von Kienlin A., Hurley K.& Lichti G.G. 2004, in Proc. of the 5th Integral Workshop, Munich

*A. Rau, A. von Kienlin & G.G. Lichti*

# Spectroscopy of $^{26}$Al in the Galaxy

**$^{26}$Al is an excellent tracer of recent nucleosynthesis activity in the Galaxy, with its decay time of 1.04 My. Through fine spectroscopy, we may be able to (a) measure Doppler shifts from Galactic rotation, thus disentagling source ambiguities along the line of sight, and (b) diagnose the level of turbulence in the ISM surrounding the $^{26}$Al sources in different locations of the Galaxy.**

The COMPTEL sky survey of gamma-rays from radioactive $^{26}$Al had indicated extended emission along the plane of the Galaxy, with some structure reflecting peculiar and active regions such as the Cygnus region. Massive stars were found to dominate $^{26}$Al production.

With fine spectroscopy as provided by INTEGRAL's spectrometer SPI, further diagnostics become possible: The narrow line width observed from the inner Galaxy may not hold for the Cygnus region, with its rich population of young massive stars.

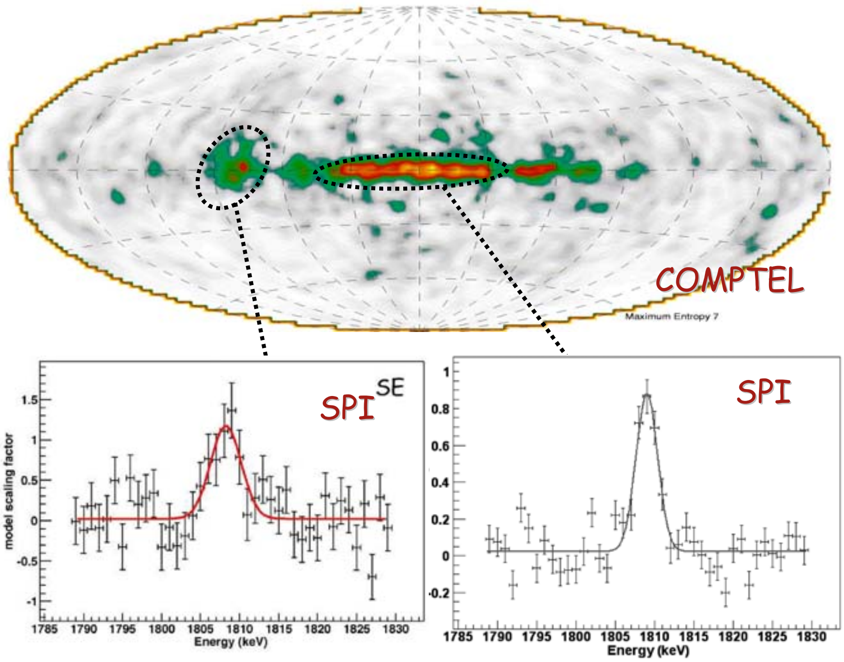



Since $^{26}$Al is ejected into the circumstellar environment of the source regions, its long decay time helps us diagnose how it spreads in the interstellar medium. We expect the interstellar medium morphology to differ significantly from average, in the vicinity of groups of young and massive stars.

An earlier measurement (GRIS) had reported a significantly-broadened line, corresponding to Doppler velocities of ~540 km $s^{-1}$; this would imply ISM cavities of kpc size. This appears to not hold up after the new Ge detector measurements. The Cygnus region may be an intermediate case.

When we use what we know about Galactic rotation, likely distribution of nucleosynthesis sources in the Galaxy, and $^{26}$Al source ejection characteristics, we can calculate expectations for the line profile. The characteristics of the $^{26}$Al line (centroid energy, width) would vary along the plane of the Galaxy in its inner region (see accompanying poster by Kretschmer et al.).. Comparing eastern with western regions, the expected line centroid difference would be 0.25 keV. This appears within reach of the SPI Spectrometer capabilities for the multi-year survey planned with INTEGRAL.

**References:**
- Diehl R., Knödlseder J., Lichti G.G., A&A 411, L451 (2003), and Diehl R., ESA-SP552, in press (2004)
- Knödlseder J., Valsesia M., Allain M., et al., ESA-SP552 (in press) (2004)
- Kretschmer K., Diehl R., Hartmann D. H. : A&A 412, 47 (2004), and corresponding Fachbeirat Poster

*R. Diehl, K. Kretschmer, D. Rodriguez, A.W. Strong, V. Schönfelder, et al.*

# Gamma rays from $^{26}$Al in the Galaxy

**The detailed appearance of the 1.8 MeV gamma-ray line from the radioactive isotope $^{26}$Al is determined by its kinematics when it decays after its ejection into the interstellar medium. We model the line shape as expected from Galactic rotation and expanding supernova ejecta, and predict a value below 1 keV (FWHM) with plausible assumptions about $^{26}$Al initial velocities and expansion history. Our results suggest that standard $^{26}$Al ejection models produce a line on the narrow side of what is observed by RHESSI and SPI on INTEGRAL. Improved SPI and RHESSI spatially-resolved line width measurements should help to disentangle the effects of Galactic rotation and of ISM trajectories of $^{26}$Al on the line shape.**

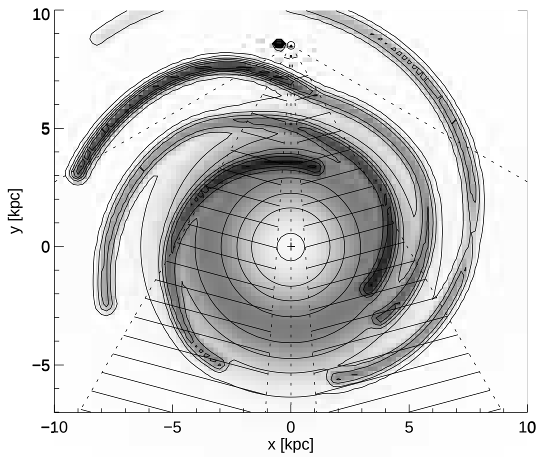


Our model is composed of a Monte Carlo sample of individual $^{26}$Al sources taken from a source density function we assume to be proportional to the density of free electrons. The figure shows a section through this function taken in the plane of the Galaxy. The shaded areas denote the east and west parts of the inner radian, where the largest Doppler shifts occur.

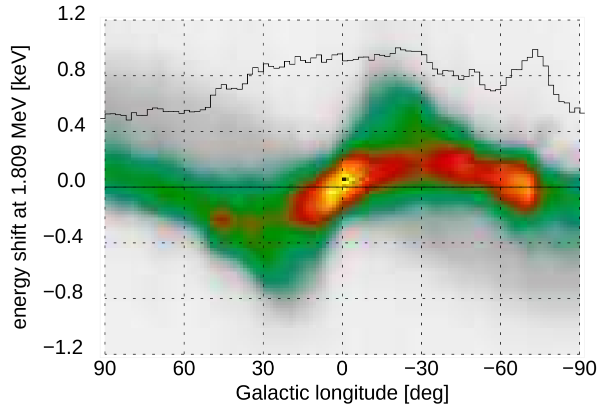


The colour-coded map shows the modelled $^{26}$Al intensity as a function of galactic longitude (horizontal axis, in 2° wide bins) and Doppler energy shift (vertical axis). The superimposed solid line shows the longitude profile of the energy-integrated intensity for comparison.

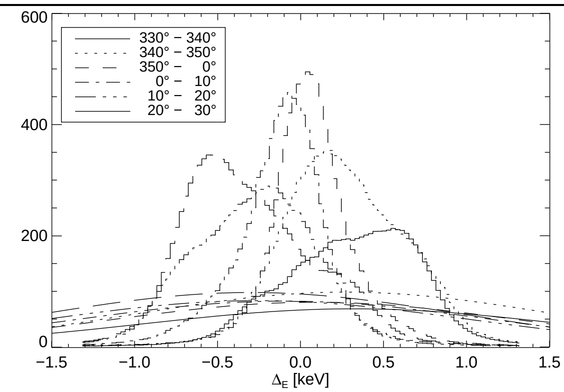


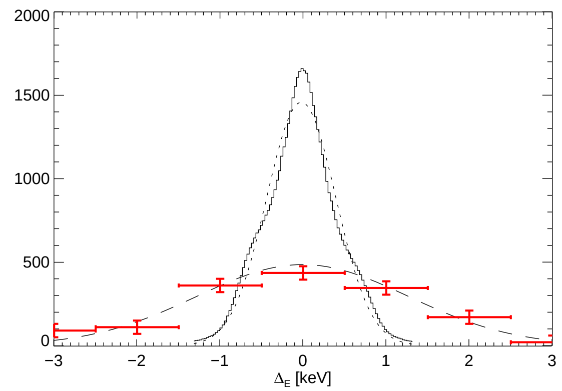


Model spectra for the inner Galaxy compared to first year data from SPI in adjacent $10°$ wide galactic longitude intervals (top, $l \in [-30°, 30°]$). The variation of the mean energy for the six regions shown is about $\pm 0.3$ keV. Integrating a measurement over this longitude range, we ideally expect a $\approx$ $1\,\mathrm{keV}$ wide line (histogram in bottom figure). SPI's instrumental resolution broadens this (dashed line).

**References:** K. Kretschmer, R. Diehl & D. H. Hartmann 2003, A&A, 412, L47-L51 (`astro-ph/0311218`)
R. Diehl et al. 2004, ESA SP-552, in press

*K. Kretschmer, R. Diehl, D. H. Hartmann*

# $^{44}$Ti and Rate of Supernovae in the Galaxy

**Core collapse supernovae have been demonstrated to produce $^{44}$Ti radioactivity gamma-rays, for the case of Cas A. Considering the Galactic supernova rate and the radioactive lifetime of $^{44}$Ti of 89 years, it is striking that only one such event has been seen in $^{44}$Ti, at 3.4 kpc distance and an age of 340 years. Possibly, deviations from spherical symmetry are decisive for $^{44}$Ti ejection (or not) in core collapse supernovae, as $^{44}$Ti production is deep inside near the mass cut between ejecta and neutron star remnant.**

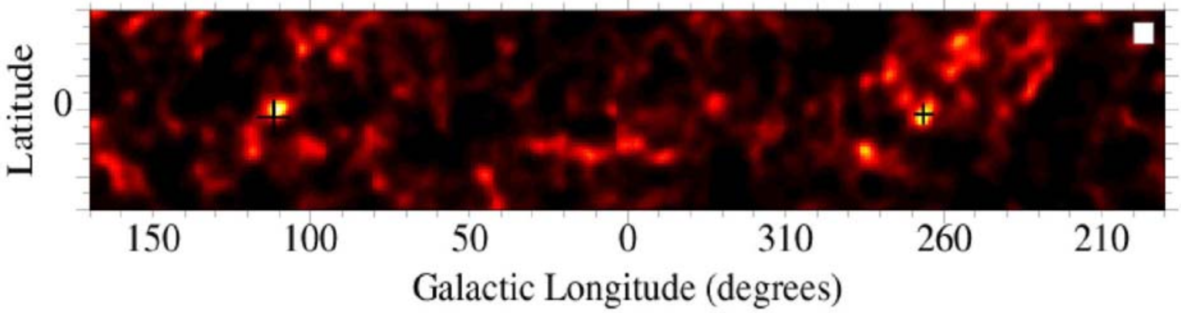


The COMPTEL survey of the plane of the Galaxy for young supernovae in gamma-ray line emission from $^{44}$Ti decay has shown one source very clearly: The Cas A SNR al l=112°. Possibly another source may have been seen in the Vela region.

The expected positions of these sources in the Galaxy are the regions where massive stars have been formed recently, i.e. the inner Galaxy and the molecular ring, out to longitudes of 35-40°.

Simulations show that statistical effects, combined with the sensitivity threshold of such a gamma-ray telescope, can lead to detections of less than a handful of sources, for a supernova rate of ~1/30 years, as is plausible for the Galaxy.

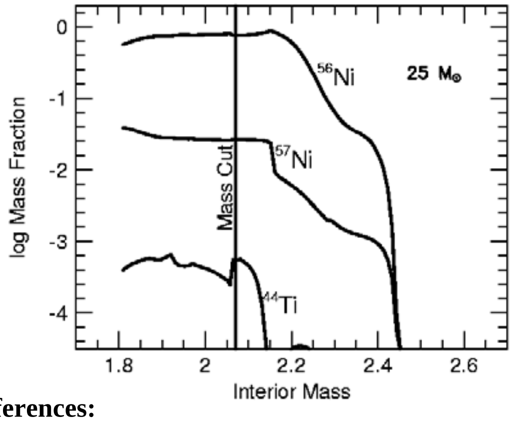


4 typical cases from model simulations

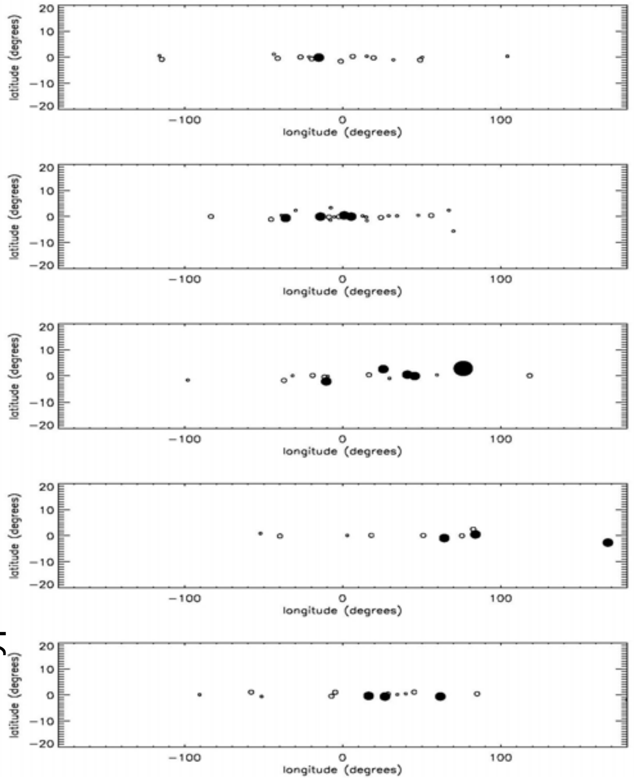


Nevertheless, the low number of candidate excesses seen by COMPTEL in the inner Galaxy is surprising, when estimated from standard models. This suggests that not every core collapse supernova may eject radioactive $^{44}$Ti - a conclusion that appears also plausible, given that $^{44}$Ti is produced very near the mass cut, hence is very sensitive to 3D effects/deviations from spherical symmetry. The $^{44}$Ti source Cas A is known to be asymmetric, even containing a jet.

**References:**
• The L., Diehl R., Hartmann D., et al.: AIP 510, 64 (2000)
• The L.-S., Clayton D.D., Diehl R., et al.: (*in preparation*)
• Iyudin A.F., et al.: Astroph.Lett.Comm. 38, 383 (2000)

*R. Diehl, D. Hartmann, A. Iyudin, V. Schönfelder, A.W. Strong et al.*

# Search for $^{44}$Ti emission from GRO J0852-4642

The gamma-ray source GRO J0852-4642, discovered by COMPTEL, is a possible counterpart of the supernova remnant RX J0852-4622. Detection of radioactive decay from $^{44}$Ti nuclei would prove it to be the youngest and nearest supernova remnant known so far. During the first year of the *INTEGRAL* core program, the Vela region was observed twice in all for more than 2000 ks. Among other nucleosynthesis studies, one of the most important scientific goals of this observation is the detection of $^{44}$Ti gamma-ray lines expected at 68 keV, 78 keV and 1157 keV. For this purpose the *INTEGRAL* Spectrometer (SPI), with its very high energy resolution is the key instrument, permitting a precise determination of gamma-ray line intensities and profiles. The upper limit for the 78.4 keV $^{44}$Ti gamma-ray line emission derived from the first analysis is $1.1 \times 10^{-4}\ \gamma\ cm^{-2}s^{-1}$. This value is mainly dominated by systematic uncertainties in the treatment of the instrumental background. By accumulating more observation time in the next years of the mission and by improving the background understanding, a reliable $^{44}$Ti flux for GRO J0852-4642 or an upper limit which constrains the COMPTEL flux can be expected.

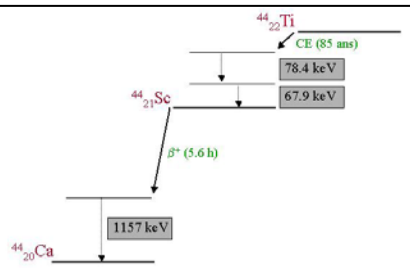


$^{44}$Ti → $^{44}$Sc→ $^{44}$Ca decay scheme

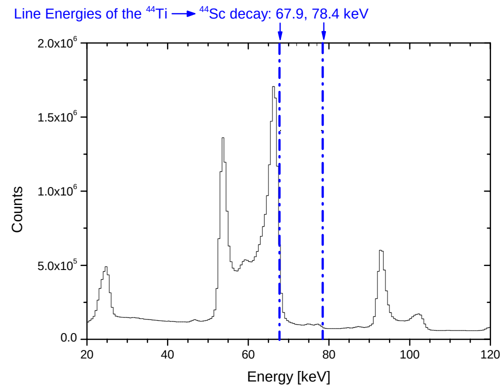


Low-energy part of a typical spectrum of SPI's germanium detectors. SPI's sensitivity at 67.9 keV is worsened due to a strong background line complex. At high energies (1.157 MeV) it is expected that the sensitivity is deteriorated by strong Doppler line broadening. The most promising results can be expected for the line at 78.4 keV.

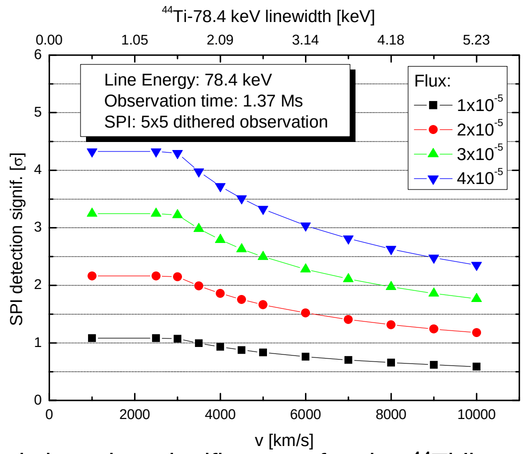


Expected detection significances for the $^{44}$Ti-line at 78.4 keV for source fluxes ranging from 1 to $4 \times 10^{-5}\ \gamma\ cm^{-2}\ s^{-1}$.

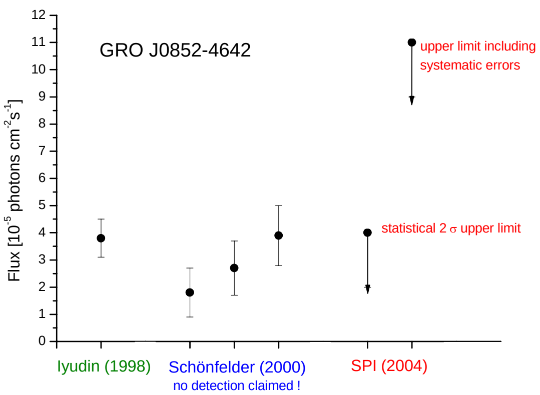


In this Figure the upper limits derived from the current analysis of the SPI Vela observation are compared with flux values quoted for GROJ0852-4642 in the literature. Without improving the systematic uncertainties the SPI result will not confirm the COMPTEL measurements.


**References:**
- Aschenbach, B., et al. 1998, Nature, 396, 141
- Iyudin, A., et al. 1998, Nature, 396, 142
- von Kienlin, A., et al. 2004, Proc. 5th INTEGRAL Workshop
- Schönfelder, V., et al. 2000, AIP, 510 54



*A. v. Kienlin, R. Diehl, G. Lichti, V. Schönfelder, A. Strong, et al.*

# $e^+$ Annihilation in the Galaxy

**Positrons are ejected into interstellar space from sources of nucleosynthesis, but also from compact sources such as pulsars and microquasars. Through imaging, INTEGRAL/SPI is able to map the Galaxy in annihilation emission, and thus help clarify its origin. The annihilation of positrons in the interstellar medium occurs under unknown conditions of temperature and density; these conditions characteristically shape the gamma-ray emission spectum. INTEGRAL/SPI can resolve spectral detail, to study the $e^+$ transport from its sources and the conditions of their annihilation.**

With INTEGRAL/SPI, first detailed mapping of annihilation emission is already possible. The coded-mask imaging suppresses strong instrumental-line background. First images of the inner Galaxy result from Maximum-Entropy deconvolution of ~4Ms of SPI data: The top Figure shows the general continuum emission of the Galaxy at an energy around 300(±50) keV, for reference. The $e^+$ emission (bottom image) clearly is more circular in appearance, and not dominated by the disk of the Galaxy - consistent with model fitting analyses. It has been suggested that such spherically-symmetric morphology may be the signature of dark-matter annihilation in the Galaxy's gravitational well.

After ejection from their sources, positrons preferentially annihilate only after they have been slowed down and thermalized, colliding with electrons either bound in atoms, or on grain surfaces, or free within the ISM. These different momentum transfers within the final annihilation process shape the 511 keV line.

The 511 keV line has now been measured with great spectral precision, even from the first year of observing (the mission will last >6 years). The line is clearly broadened beyond the instrumental resolution. Its shape does not represent any known or obvious profile, in particular it is not a simple Gaussian. Expected shapes of the annihilation lines have been determined from simulations. None of the single processes can produce the line shape as observed, hence ISM conditions are still uncertain. However, dust grains apparently play a significant role.

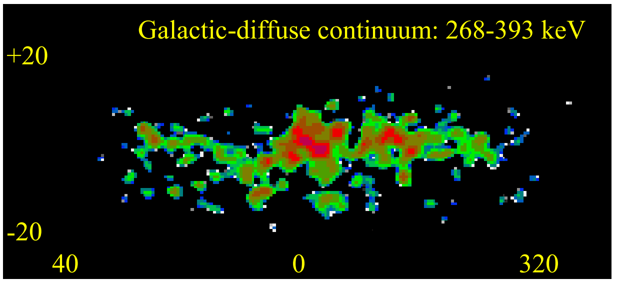


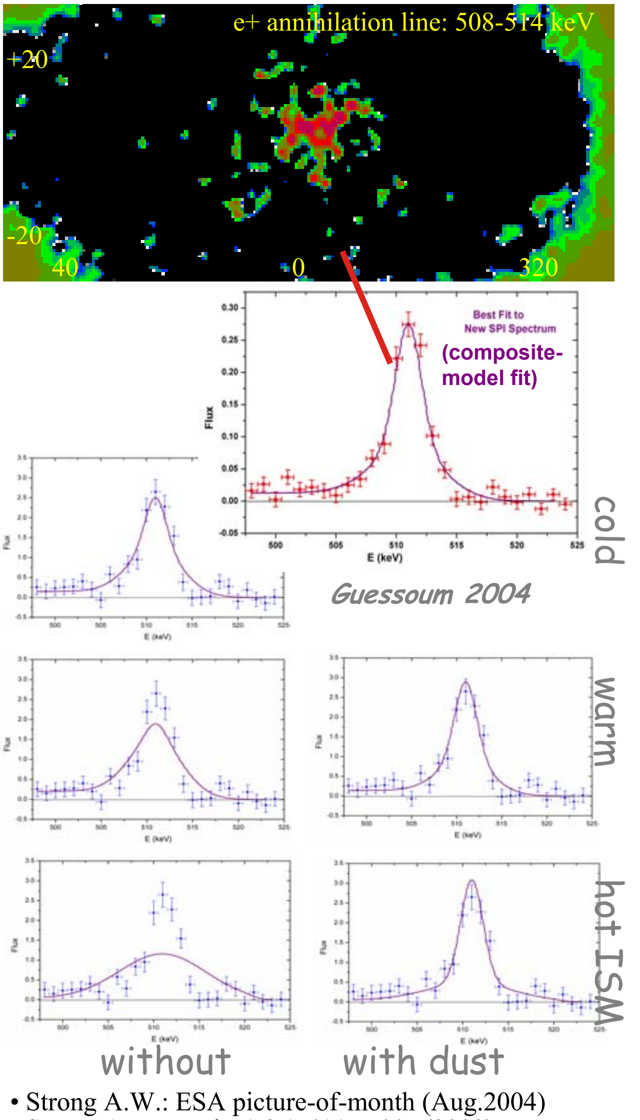


**References:**
- Lonjou V., et al.: ESA-SP552 (in press) (2004)
- Jean P., et al.: A&A 407, L55 (2003)
- Guessoum N., et al.: ESA-SP552 (in press) (2004)
- Strong A.W.: ESA picture-of-month (Aug.2004)
- Strong A.W., et al.: A&A 411, L447 (2003)
- Weidenspointner G., et al.: ESA-SP552 *(in press)*(2004)

*A.W. Strong, R. Diehl, H. Halloin, V. Schönfelder, et al.*

# Spectroscopy of the UMa association

We determine the properties of the UMa association and work on a clean member list. For that reason we have taken high-resolution spectra with high signal-to-noise ratio of a large sample of members and possible members in order to do stellar atmosphere analysis. We have shown that precise stellar atmosphere analysis is possible with the Coudé-Échelle spectrograph at the Thüringer Landessternwarte in Tautenburg.

The UMa open cluster and a large number of additional stars form the UMa association. This structure has an intermediate age between the Hyades and the Pleiades open clusters but is much closer so that we can study its evolutionary stage very well. However recent membership assignments (Montes et al., 2001; King et al., 2003) are in conflict for several stars. Additionally age determinations range widely from 100 Myrs (König et al., 2002) to 500 Myrs (King et al., 2003).

Spectra with high spectral resolution and high signal-to-noise ratio of a large sample of members and candidates of the UMa association will enable us to address those problems homogeneously and in detail. One major part of this work is the stellar atmosphere analysis of the late-F to early-K type stars following the method of Fuhrmann (2004). So far such an analysis has not been done homogeneously for a larger sample of the UMa association. We have observed most stars of our northern sample with the fibre-coupled Échelle spectrograph FOCES on Calar Alto (Spain) – like Fuhrmann (2004). The Coudé-Échelle spectrograph at the Thüringer Landessternwarte in Tautenburg (TLS) also allows stellar atmosphere analysis at a high level of precision as is illustrated in the following example with HD 217813, a member of the UMa association. The spectrum was obtained at TLS in July 2003. High signal-to-noise ratio and high spectral resolution allow the precise determination of e.g. effective temperature $T_{\rm eff}$ and surface gravity log***g*.**

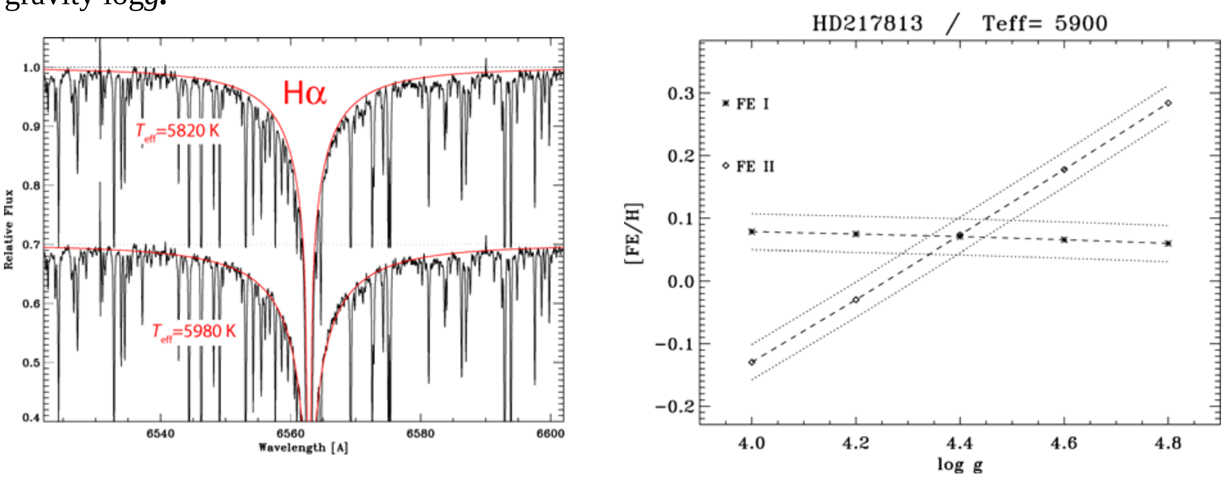


**Left:** Fitting synthetic spectra (red) to observed Balmer lines (black) – here Hα – allows to constrain $T_{\rm eff}$ to 5900±80K. **Right:** The surface gravity is determined by the iron ionisation equilibrium, i.e. FeI and FeII lines are required to yield the same Fe abundance. This results in: $\log g = 4.40^{+0.18}_{-0.10}$

**References:**

- Fuhrmann, K. 2004, AN, 325, 3
- König, B., Fuhrmann, K., Neuhäuser, R., Charbonneau, D., & Jayawardhana, R. 2002, A&A, 394, L43
- King, J., Villarreal, A., Soderblom, D., Gulliver, A., & Adelman, S. 2003, AJ, 125, 1980
- Montes, D., López-Santiago, J., Gálvez, M., et al. 2001, MNRAS, 328, 45

*M. Ammler, K. Fuhrmann, B. König, R. Neuhäuser*

# X-ray shadowing and the Local Interstellar Medium

We have observed the darkest regions in the soft X-ray sky with XMM-Newton. Among these are the Ophiuchus Molecular Cloud and the Bok globule Barnard 68.

Analysing these deep X-ray shadows we have found clear indications that a significant fraction of the diffuse emission below 650 eV originates in the foreground of the absorbers, closer than 120 pc.

Moreover, a detailed spectral analysis has shown that the X-ray emission towards the opaque objects cannot be reproduced by a plasma in collisional ionization equilibrium with $10^{6.0}$ K; further components to the X-ray background are needed to explain these spectra, and/or the emitting plasma is not in collisional ionization equilibrium. Thus the standard model for the Local Bubble (a region devoid of H I) has to be changed accordingly.

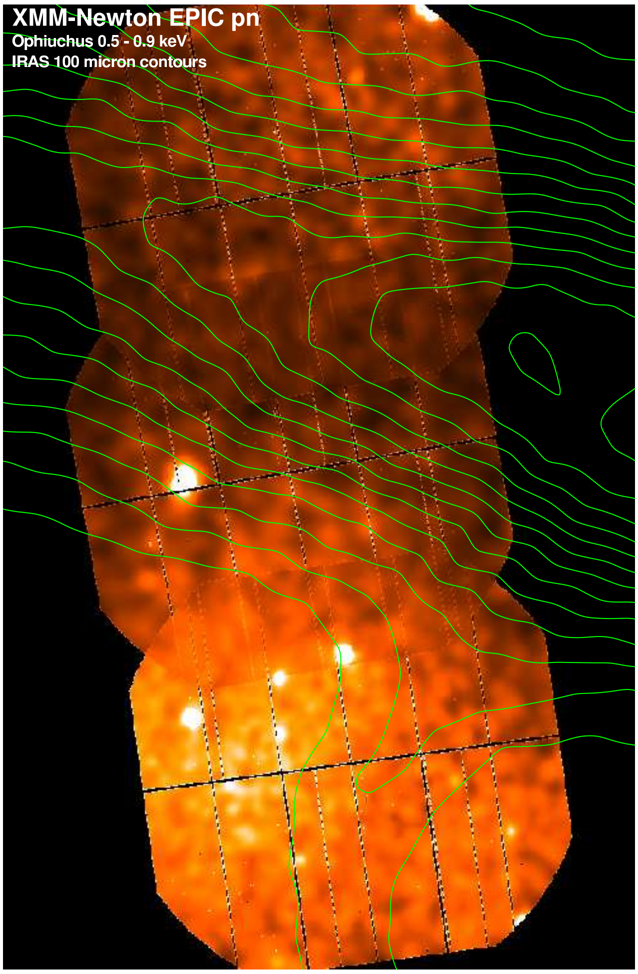


*Figure: XMM-Newton EPIC-pn intensity image of the Ophiuchus molecular cloud region in the energy band $0.5-0.9$ keV, green lines show the IRAS 100 $\mu$m contours.*

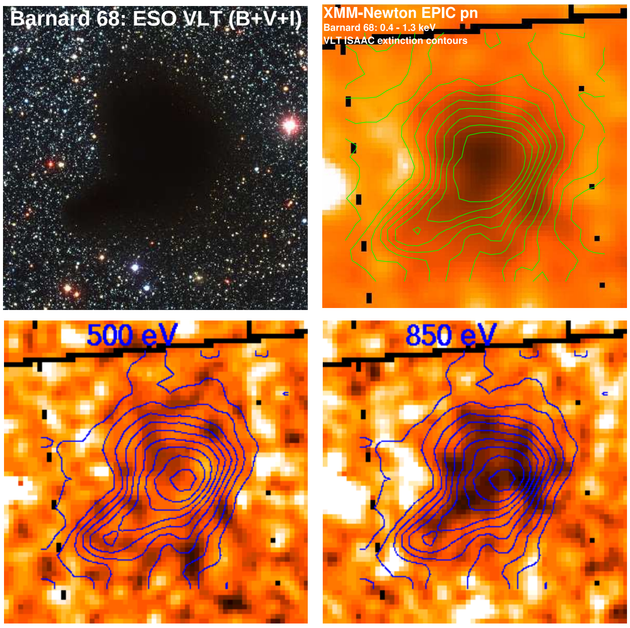


*Figures: Upper left: 3-colour image (B, V, I) of the Bok globule Barnard 68, obtained at ESO VLT. Upper right: EPIC-pn X-ray image (0.4 – 1.3 keV) with ISAAC extinction contours overlayed. Bottom Left: narrow-band image in 0.40 – 0.60 keV range. Bottom Right: narrow-band image in 0.75 – 0.95 keV range. The X-ray shadow is clearly evident in the 0.5 – 1.0 keV range. Most of the Fe-L emission at $\sim$ 850 eV originates in the background, and the shadow is much weaker at the oxygen line energies.*

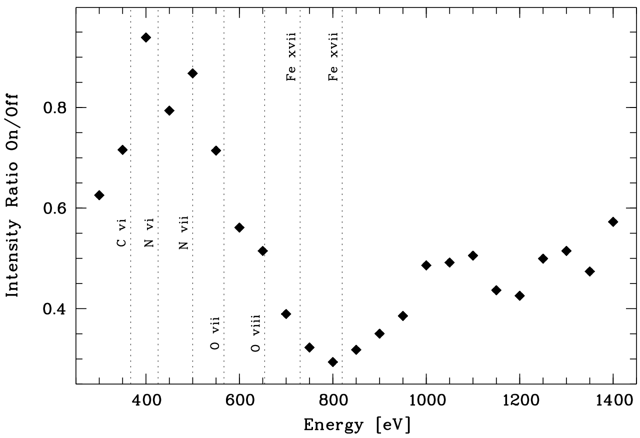


*Figure: Depth of the X-ray shadow (ratio of on-cloud to off-cloud intensities) for the Bok globule Barnard 68 as function of energy. This shows that a significant fraction of the emission below 600 eV originates in the foreground of the cloud.*

References:


M.J. Freyberg, D. Breitschwerdt & J. Alves, 2004, Mem.Soc.Ast.It. 75, 509

M.J. Freyberg, 2004, Ap&Sp.S. 289, 229



*M.J. Freyberg, P. Mendes, D. Breitschwerdt*

# Galactic GeV γ-ray excess and gradient

**The observed Galactic GeV γ – ray excess is shown to be probably a result of differences between the locally observed cosmic-ray spectrum and the interstellar spectrum. The cosmic-ray source distribution is compatible with the supernova remnant distribution as traced by recent deep pulsar surveys when variations in $H_2$ /CO are included. This has implications for the mass and distribution of molecular hydrogen in the Galaxy.**

The EGRET data are an important source of information on cosmic rays and Galactic structure. There are two puzzling aspects of the subject which have attracted attention: there is an excess around 1 GeV above the emission expected based on the locally-observed cosmic-ray spectrum, and the distribution of cosmic-rays deduced from γ-rays is flatter than that of supernova remnants in the Galaxy, although these are thought to be the cosmic-ray sources. We believe to have the solution to both these problems, thus improving our understanding of the diffuse emission.

**Gamma-ray spectrum**

We show that the GeV excess is present everywhere on the sky, so cannot be due to unresolved sources, which would be concentrated in the plane. Instead a moderate deviation of the cosmic-ray spectrum from that observed locally can explain the ubiquity of the excess. The main effect is a larger electron intensity, increasing the inverse Compton emission. Important and new is the inclusion of EGRET data above 10 GeV (beyond the standard EGRET data range) which is well fitted by our new model (figure on right), but not by alternative models.

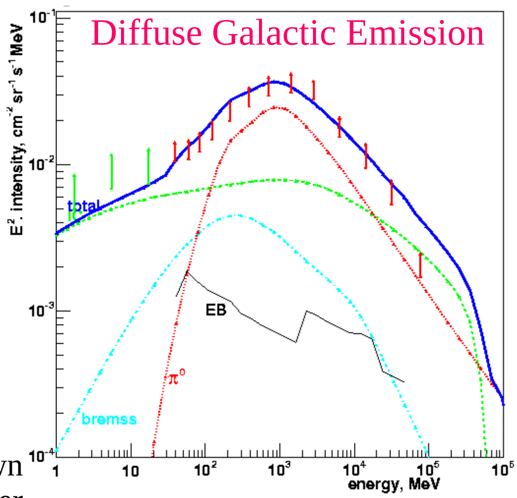


**Cosmic-ray sources and molecular gas**

Since the time of the COS-B satellite it has been known that the distribution of cosmic-ray sources appears flatter than that of supernova remnants; a new determination of the distribution of pulsars (Parkes Multi-Beam survey), which should have a radial distribution close to that of SNR, shows the discrepancy with gamma-rays is quite marked. We suggest a radial variation in the scaling factor of CO to $H_2$ column density, which is the basis for computing the gamma-rays associated with molecular hydrogen. The known Galactic metallicity gradient combined with the expected steep dependence of the $H_2$/CO factor with metallicity imply that this factor increases rapidly with radius. There is thus less $H_2$ in the inner Galaxy and this compensates the larger cosmic-ray gradient, giving a consistent picture.

As well as improving our understanding of the diffuse γ - ray emission, this will have important consequences for the mass and distribution of molecular gas in the Galaxy.

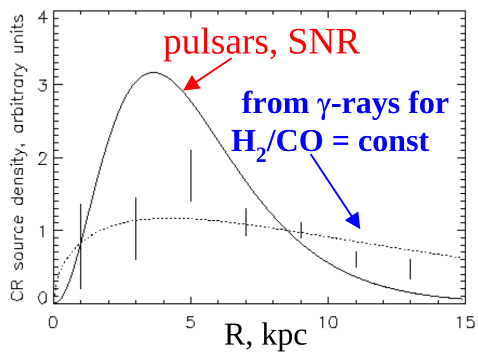


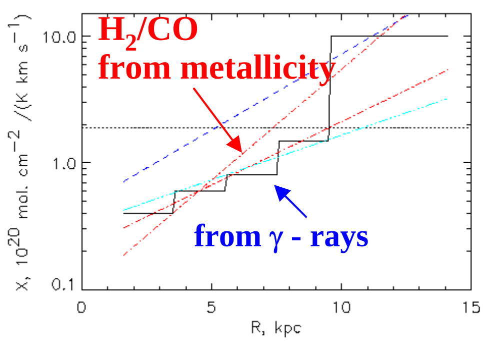



**References:**

- Strong, A.W., Moskalenko, I.V., Reimer, O. (2004) ApJ, 613, 962
- Strong, A.W., et al. (2004) A&A 422, L47


*A.W. Strong*

# Towards the 2. COMPTEL Source Catalog

**The 1. COMPTEL source catalog (Schönfelder et al. 2000), covering the first 4-5 years of the 9-year mission, lists 32 steady sources. We are currently working towards the 2. and final COMPTEL source catalog. At the current stage of the analyses, we expect this final catalog to contain at least 45 MeV point sources.**

The COMPTEL experiment aboard CGRO pioneered the MeV sky (0.75 – 30 MeV) between 1991 and 2000. To finalize the data analyse, we re-analysed consistently all COMPTEL data from the beginning to the end of the mission by carrying out all-sky point source analyses in different energy bands for different time periods (sum of all data as well as subintervals). The goal of the analyses is to derive 1) a consistent survey on MeV sources, and 2) the variability behavior for the brighter MeV sources. These results will be summarized in the 2. COMPTEL source catalog.

Up to now, we found evidence for about 15 new source detections. The majority are spatially coincident with EGRET γ-ray sources (identified as well as unidentified ones), whose MeV emission is probably detected. The rest are unknown MeV sources, for which no identification has been proposed yet. Some new sources are visible in the example maps below.

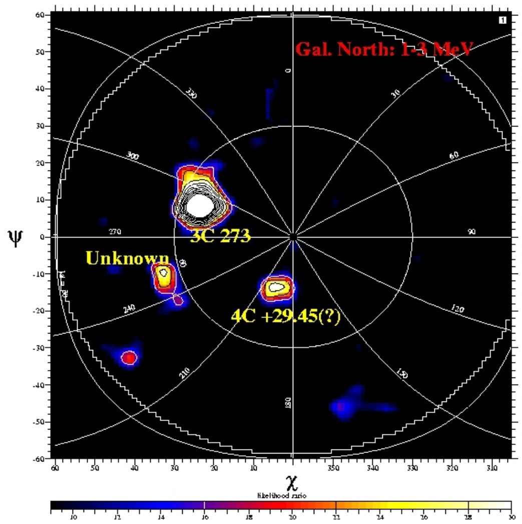


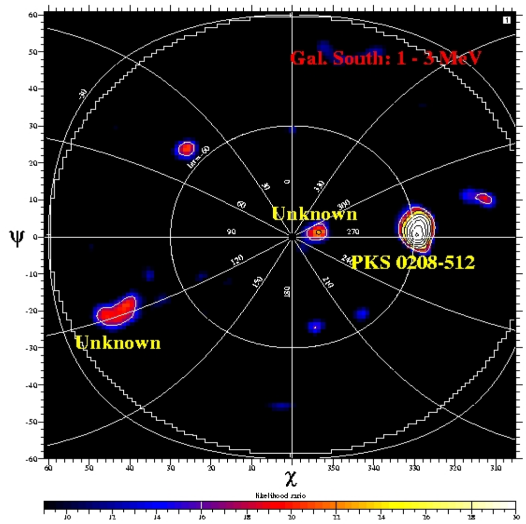


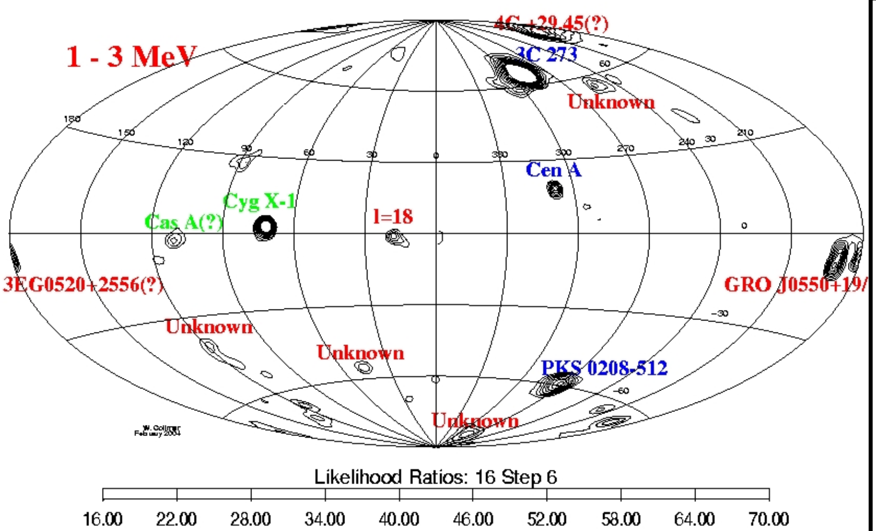


Left: COMPTEL *all-mission all-sky point source map* in galactic co-ordinates (1–3 MeV). The map shows, apart from the Crab (re-moved for display reasons), the strongest MeV sources on average. The upper two maps are from the same data, however centered on the galactic north (left) and south (right) poles. Some new MeV source candidates are visible, e.g. the blazar 4C 29.45 and 3EG 0520+2556, an identified and an unidentified EG-RET source. The most significant of several yet unknown source features are labeled.

*W. Collmar, V. Schönfelder, H. Steinle, A. Strong, S. Zhang*

# Differential Photometry with variable Reference Stars

We have developed a new algorithm for differential photometry. It solves the problem of identifying proper comparison stars without prior detailed study of the field of view. The variability of the comparison stars is determined in a self-consistent way and a weighted average of them is used as a reference level. A simple error model is applied to the data giving reliable error bars for all measurements. By comparing derived errors with observed variation of the comparison stars (CS), badly behaved comparison stars can be rejected.

## Differential Photometry Algorithm

After reading in the instrumental magnitudes and errors of all objects (science object and CS 1 through N), the instrumental errors are corrected according to the error model with two parameters (formula see fig. 1).
The algorithm proceeds by looping over the following two steps until convergence is reached:
1) calculate new weights for all CS
2) use weights to calculate differential magnitudes for the science object and all CS

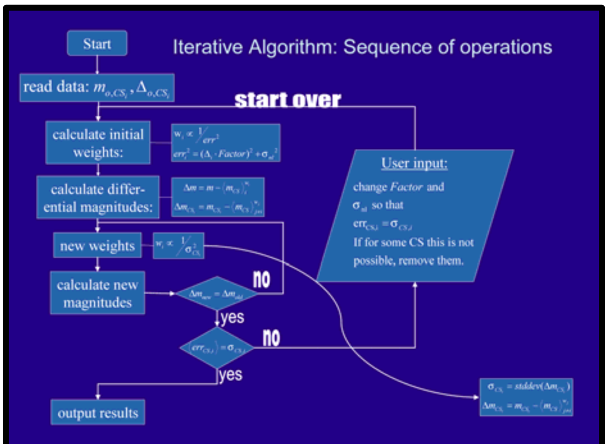


Fig. 1: Flow chart showing the structure of the differential photometry algorithm. Details see text.

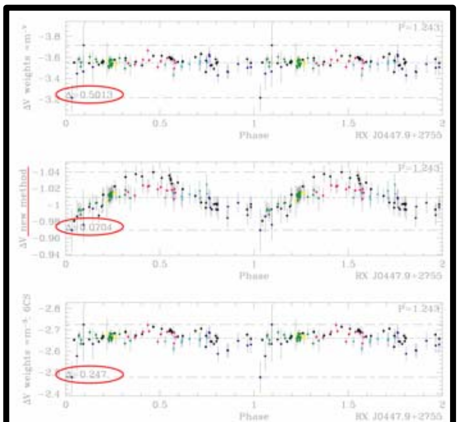

Fig.2: Comparison of phase folded lightcurves with and without the new algorithm. Please note the different scales.

Details of step 1):
• use estimator for the standard deviation s to calculate weights: w ~ 1/s²
1st run: s = arithmetic mean of modified instrumental errors
later: s = standard deviation of differential magnitudes of the CS
• weights are then: w ~ 1/s²
Details of step 2):
• the weighed mean magnitude of all CS is subtracted from the object to get the differential magnitude for each exposure
• for each CS the same is done ignoring itself. The remaining weights are rescaled to a sum of one

### Principle

➢The variability and thus quality of each CS is automatically determined statistically
➢This variability is used to calculate the best mean CS

### Results

➢automatic detection of good / bad CS
➢averaged CS has lowest possible variation
➢reliable error bars for all measurements

If statistical errors dominate, the algorithm is superior to all predefined weighting schemes. Phase-folded light curves of an example object are shown in figure 2: Using the new method, a variation can be clearly detected, whereas this is not possible for alternative weighting schemes that weight by brightness power-laws.

### Conclusion

The new algorithm leads to a significantly improved accuracy. This is especially so when the FOV is a priori unknown and all field stars are candidate comparison stars. When the precision gets high, all CS are subject to show small intrinsic variability. This is best taken into account using this algorithm (see broeg et. al submitted to AN 2004).

*C. Broeg, M. Fernández*

# Background and Sources: a joint estimation method

A probabilistic technique for the joint estimation of background and sources in high-energy astrophysics has been developed. Bayesian probability theory has been applied to gain insight into the coexistence of background and sources through a probabilistic two-component mixture model, which provides consistent uncertainties of background and sources. The analysis is applied to ROSAT PSPC data in Survey Mode with the aim of detecting faint and extended sources which have been missed so far by the Standard Analysis Software System (SASS).

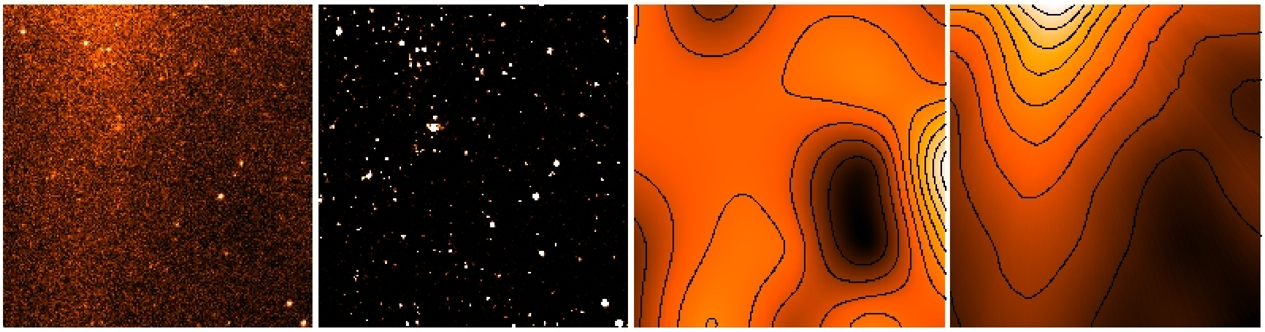

*Images are described from left to right. (1) RS930625n00 field from ROSAT PSPC in Survey Mode, broad energy band (0.1-2.4 keV), is located in the vicinity of the north ecliptic pole. The field of view corresponds to 6.4° × 6.4° in the sky. The observatory's exposure time ranges from 1.7 to 14 ksec. (2) Source probability map for the combined soft (0.1-0.4 keV) and hard (0.5-2.0 keV) energy bands. The map accounts for the width of the instrumental point spread function. (3) The thin-plate spline map, shown for the broad energy band, models the background rate. (4) The corresponding background map, which is the estimated background intensity, is obtained from the thin-plate spline multiplied by the observatory's exposure time (compare with image 1).*

The coexistence of background and sources is described with a probabilistic two-component mixture model where one component describes background contribution only and the other component describes background plus source contributions. A background map for the complete field size is inferred simultaneously to a probability map for having source intensity in addition to the background intensity in a pixel cell (or domain). For background estimation and source detection we assume that the background is smooth, e.g. spatially slowly varying compared to source dimensions. To allow for smoothness the background rate is modeled with a two-dimensional Thin-Plate spline. Each pixel cell (or domain) is characterized by the probability of belonging to one of the two mixture components. The mixture model technique allows to consider all pixels for the background spline estimation even those containing additional source contribution. The source probability is evaluated also by correlating information with neighbouring pixels in order to enhance the detection of weak and extended sources.

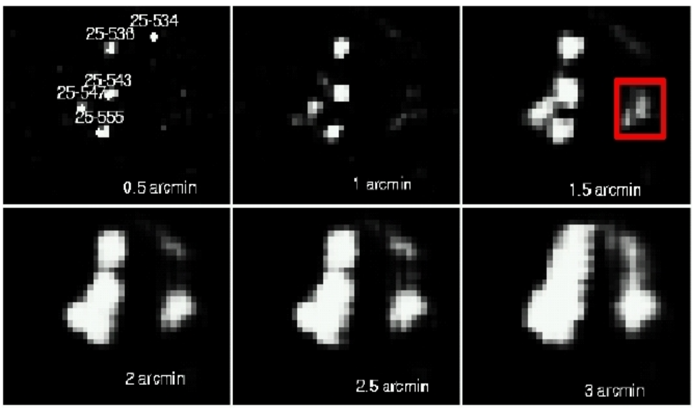


*Example of source detections at different correlation lengths (arcmin), covering a field of view of nearly 30´ at the side. On the first image, the SASS sources are overplotted to the source probability map. The SASS source indicated with 25-534 is recovered at a correlation length of 2'. The red box guides the eyes to a new source detection which has been missed by SASS. A search in the NASA/IPAC Extragalactic Database reveals several galaxies close to the position of this source, indicating that this emission is due to a group or a cluster of galaxies.*

*F. Guglielmetti, W. Voges, R. Fischer, G. Boese*

# Galaxies and Active Galactic Nuclei

# The Galactic Center

**The center of our Milky Way is a unique laboratory for studying the properties and evolution of a dense nuclear star cluster and for exploring the physics of accretion and the strong gravity regime around a massive black hole. Becoming available in 2002, we have begun a comprehensive study of the central parsec using diffraction limited imaging, spectroscopy and polarimetry with NACO on the VLT. This research has resulted in a number of results that constitute major breakthroughs in the field:**

- determinations of individual three dimensional, stellar orbits within a few light days of the central black hole. In particular, the data give a highly precise determination of the elliptical orbit of the star S2 around SgrA*. The orbital period is 15 years and the peri-bothron distance is 17 light hours. These measurements constrain the density of the central dark mass to exceed $10^{19}$ $Mpc^{-3}$ and exclude all stable non-black hole configurations, beyond any reasonable doubt (Schödel et al. 2002, 2003a,b)
- a direct geometric determination of the distance to the Galactic center from the orbital parallax method, that is, the simultaneous fitting of the sky and line of sight orbital data (7.94±0.42 kpc, Eisenhauer et al. 2003)
- first detection of quiescent emission and flares from the black hole, including the tantalizing detection of a 17 minute quasi-periodicity in several flares. The IR emission comes from energetic electrons or hot gas just outside the event horizon and the periodicity suggests that the black hole has about half the maximum possible spin (Genzel et al,. 2003b)
- discovery of a stellar cusp centered on the position of the black hole, as well as the finding that the massive young stars reside in two coeval but counter-rotating disks (Genzel et al., 2003a)

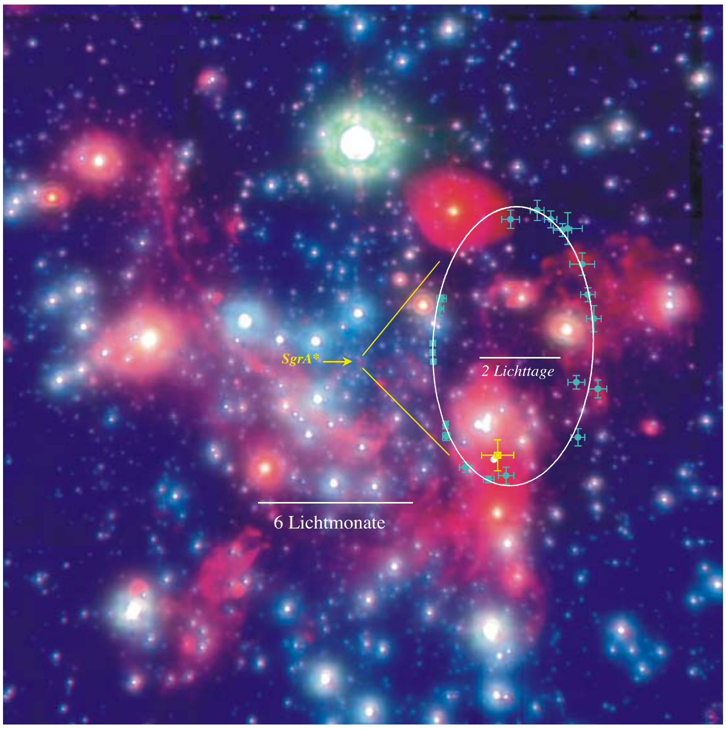


Orbit of the star S2 around the black hole Sgr A*, superposed on a 3-color image of the galactic center taken with NACO in the H, Ks, and L'-Bands.

*R. Genzel, T. Ott, F. Eisenhauer, T. Paumard, R. Abuter, S. Trippe*

# Discovery of a Binary Black Hole in NGC 6240

Imaging spectroscopy performed with the *Chandra* X-ray observatory let to the discovery of two active black holes in the nucleus of the luminous infrared galaxy NGC 6240. This is the first positive identification of an active binary black hole at the center of a galaxy. This discovery shows that massive black holes can grow through mergers in the centers of galaxies, and that these events may be detectable with future space-borne gravitational wave observatories.

The galaxy NGC 6240 is a prime example of a luminous infrared galaxy, a massive galaxy formed in the course of a recent collision and subsequent merger of two smaller galaxies. Because of the large amount of dust and gas in such galaxies, it is difficult to observe their innermost regions with optical telescopes. However, X-rays can penetrate the veil of gas and dust. Imaging spectroscopy performed with the *Chandra* X-ray observatory (Komossa et al. 2003) revealed that the nucleus of NGC 6240 contains not one, but two supermassive black holes, actively accreting material from their surroundings (Fig. 1). Both black holes reveal their presence by heavily absorbed but intrinsically luminous high-energy X-ray radiation and strong neutral fluorescent iron lines; the characteristic signatures of obscured active nuclei (Fig. 2).
The detection of a binary black hole supports the idea that black holes at the centers of galaxies can grow by merging with other black holes. Detection of binary black holes and analysis of their properties is important for our understanding of galaxy formation and evolution (see Komossa 2003 for a review). Over the course of the next few hundred million years, the two black holes in NGC 6240 will drift toward one another and finally merge. Toward the end of this process a burst of gravitational waves will be produced of the kind which will be detectable with the planned space-based gravitational wave interferometer *LISA*. A search for further binary black holes in luminous infrared galaxies using *Chandra* is presently ongoing.

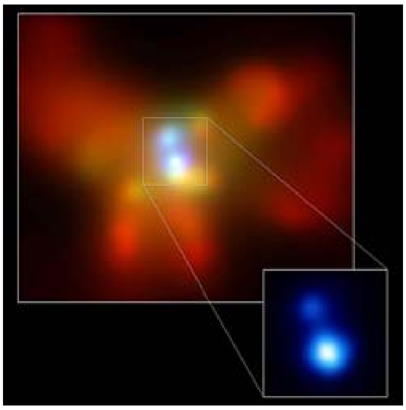

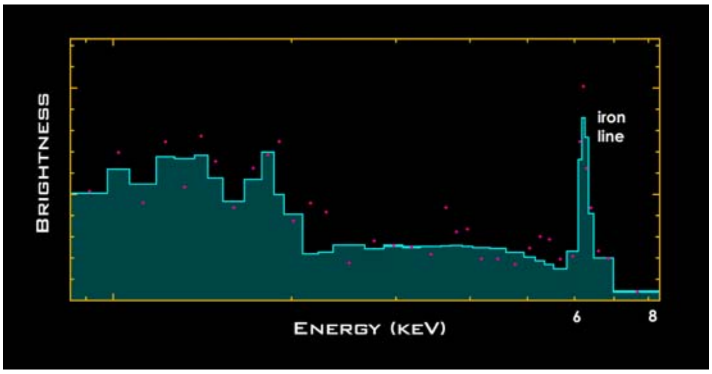


*Fig. 1*: *Chandra* X-ray energy image of NGC 6240 (red: low-energy X-rays, blue: high energy X-ray emission). The inset zooms onto the center of the galaxy and shows the hard X-ray emission from the environment of the two active black holes. *Fig. 2*: X-ray spectrum of the Southern nucleus of NGC 6240, showing strong iron line emission and hard absorbed, but intrinsically luminous, X-ray emission (the low-energy X-ray emission visible in the spectrum is due to extended starburst-related emission projected onto the nucleus). The spectrum of the Northern nucleus, intrinsically weaker, looks very similar thus revealing the presence of two active cores in NGC 6240.

**References:**

• Komossa S., Burwitz V., Hasinger G., Predehl P., Kaastra J., Ikebe Y., 2003, ApJ 582, L15
• Komossa S., 2003, in *The Astrophysics of Gravitational Wave Sources*, J. Centrella (ed.), AIP Conf. Proc. 686, 161

*S. Komossa, G. Hasinger, V. Burwitz, P. Predehl, et al.*

# Relativistic Fe lines in the mean X-ray spectra of AGN

**We derived average rest-frame X-ray spectra for type-1 and type-2 AGN using the 770 ksec XMM-Newton survey of the Lockman Hole field in combination with extensive optical identifications of the AGN population. In both types of AGN a clear relativistic line profile is revealed, which indicate that the average supermassive black hole has significant spin.**

We selected a sample of 94 spectroscopically identified AGN for which more than 200 counts were observed in the 0.5-10 keV band. The sample was divided into 53 type-1, 41 type-2 AGN, based on their optical spectra. Power law spectral fits were performed for all objects and the spectral residuals were transformed into the source frame and co-added for both types of AGN. The resulting mean X-ray spectra show a prominent fluorescent Fe line. In both type-1 and type-2 AGN, a clear relativistic line profile is revealed. A Laor line profile with an inner disk radius smaller than the last stable orbit of a Schwarzschild black hole is most consistent with the data, indicating that the average super-massive black hole has significant spin. Equivalent widths of the broad relativistic lines range between 400-600 eV. We use a disk reflection model to compare the observed strength of the line with the amplitude of the reflection component, concluding that to consistently describe the observations the average iron abundance should be about three times the solar value.

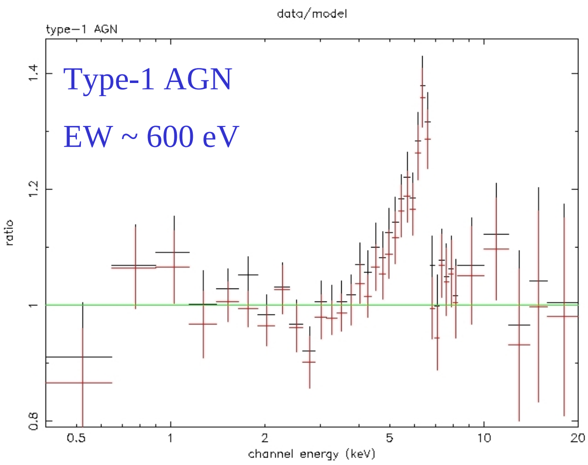


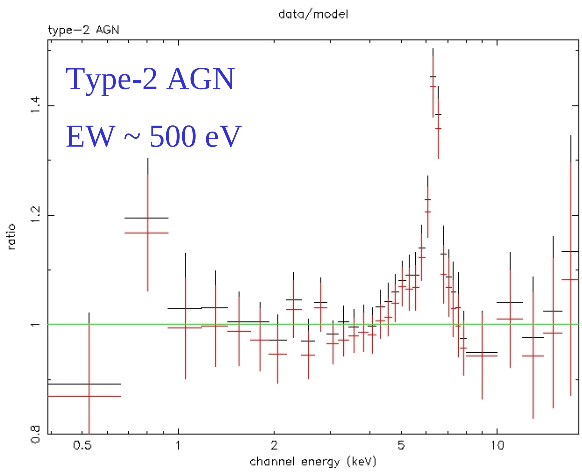


Mean EPIC-PN (black) and MOS (red) residual spectra for type-1 (left) and type-2 (right) AGN show a clear excess between 4 and 8 keV (rest-frame), most probably due to Fe $K_{\alpha}$ emission from iron in low to moderate ionization states with a mean energy near 6.4 keV (i.e., < FE XVI) The skewed shape of the line is best explained as being due to Doppler and gravitational redshifts of emission originating from the inner part of an accretion disk around a rotating (Kerr-metric) super-massive black hole. We observe a narrow Fe line near 6.4 keV (source-frame), in addition to the broad spectral feature in our type-2 AGN sub-sample. The high relative strength of the Fe line features in our sample is thought to be due to a high metallicity in the average source population of our relatively high redshift samples.

**Reference:**

A. Streblyanska, G. Hasinger, A. Finoguenov, X. Barcons, S. Mateos, and A.C. Fabian, 2004, XMM-Newton observations of the Lockman Hole III: A relativistic Fe line in the mean X-ray spectra of type-1 and type-2 AGN, submitted to A&A

*A. Streblyanska, G. Hasinger, A. Finoguenov*
*in collaboration with X. Barcons (Santander) and A. Fabian (Cambridge)*

# The Orbit of S2 in the Galactic Center

**By measuring the orbit of the star S2 around Sgr A* in the center of our galaxy, we could confidently rule out any non-black hole explanation for this source. The black hole has a mass of 3.4±1.5 million solar masses.**

Over the last decades, it has become a standard paradigm that massive black holes are located at the centers of most, if not all, galaxies. They are believed to be the central engines powering the enormous energy ouput and luminosity of active galactic nuclei and of quasars, the most distant and most luminous objects observed in our universe. Observations of other galactic nuclei have already provided strong evidence that these massive black holes exist. However, this evidence has always been indirect and did not exclude alternative explanations (such as the neutrino ball model). By showing in a direct and straightforward way that such a massive black hole does indeed exist in the heart of our own galaxy, the Milky Way, we provide a firm and compelling fundament for this key hypothesis of modern astronomy.
In 2002 we have observed 2/3 of a complete orbit of the star currently closest to the enigmatic radio source Sagittarius A*, which is thought to mark the location of our Milky Way's massive central black hole. This orbit provides overwhelming evidence that SgrA* is indeed a supermassive black hole of more than 2 million solar masses.
Previous measurements could not rule out some alternatives to the black hole model. Two such alternatives are a ball of massive, degenerate fermions, like neutrinos, or a cluster of dark astrophysical objects, such as stellar mass black holes or neutron stars. These two alternative explanations can now be excluded by analyzing the orbit of S2.

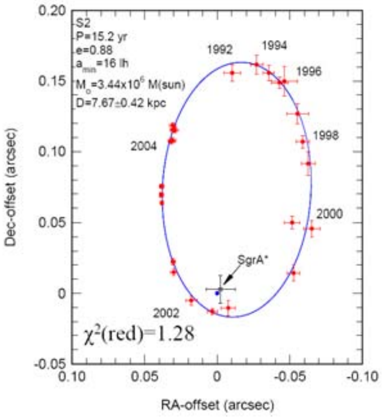


In spring 2002 S2 was passing with the extraordinary velocity of more than 5000 km/s at a mere 17 light hours distance through the *perinigricon*, the point of closest approach to the black hole. By combining all measurements of the position of S2 made between spring 1992 and summer 2002, we have obtained enough data in order to determine a unique keplerian orbit for this star. It has a period of 15.2 years. From Kepler's 3rd law we can determine the enclosed mass to be 3.4±1.5 million solar masses.

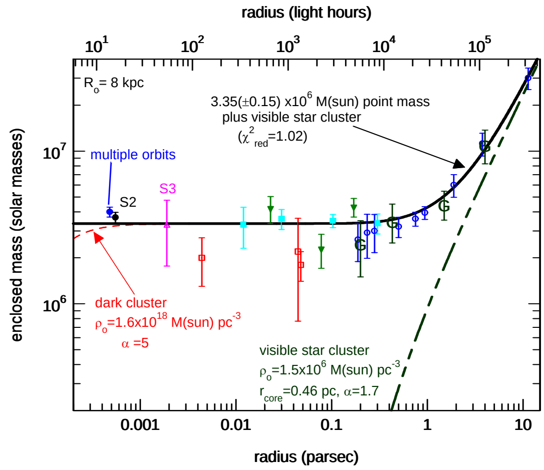


Enclosed mass derived from different studies of gas dynamics and stellar dynamics at various distances from the Galacic Center. The point at the shortest distance is the mass measurement added with the aid of the newly determined orbit. The fascinating feature of this plot is that the best fit curve for the enclosed mass is flat inside of about 0.2 parsecs. From this we draw the compelling conclusion that a massive black hole must be present at the center of the Milky Way.

published as: Schödel et al., Nature 419, 694 (2002)

*R. Schödel, T. Ott, R. Genzel, R. Hofmann, M. Lehnert, A. Eckart*

# Infrared Flares in the Galactic Center

**By recording variable infrared emission from Sgr A* in the center of our galaxy, we were, for the first time, able to measure the spin of a black hole.**

During observations of the Galactic Centre with the new Very Large Telescope adaptive optics (AO) imager NACO on 9 May 2003, we observed a powerful flaring by a factor of 5 in the H-band (1.65µm) emission towards SgrA*. The flare lasted for 30 min. Its rise and decay can be well fitted by an exponential of timescale 5 min. In a second observing run in June 2003, we observed two more flares on two consecutive days, this time in the Ks band (2.16µm). The K-band flares rose to a factor of 3 above the quiescent level, and each lasted for 85 min. Their characteristic rise/decay times were 2 to 5 min. Both flares exhibited significant and similar temporal substructure. The 16 June flare showed five major peaks spaced by 13 to 17 min, resembling a 15-40%, quasi-periodic modulation of the overall flare profile. The 15 June flare had three major peaks separated by 14 and 17 min, followed by a weaker peak 28 min later.

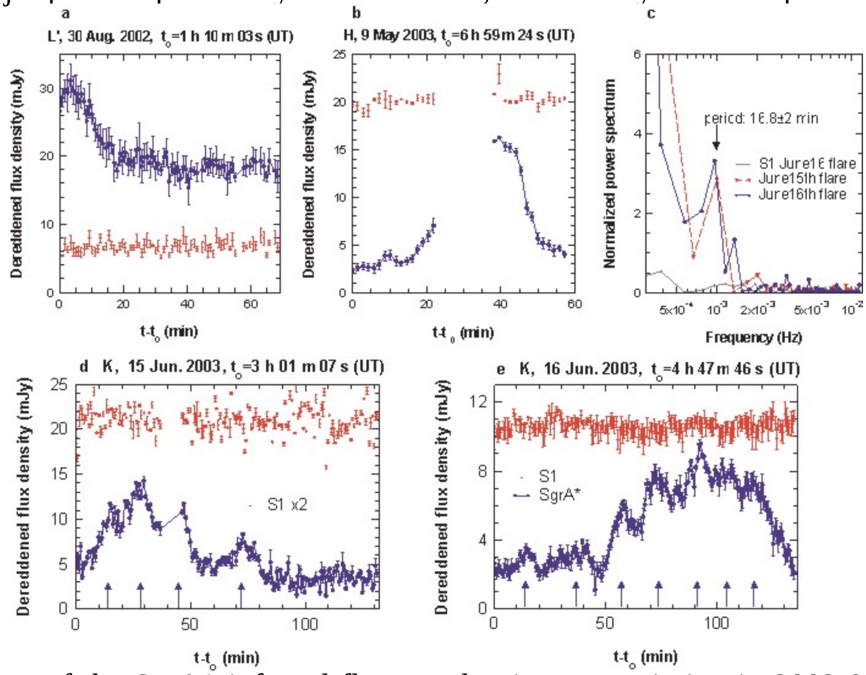


Light curves of the SgrA* infrared flares and quiescent emission in 2002-03. SgrA* data are shown as filled blue circles (connected with a solid curve). For comparison, the light curves of the nearby star S1 are shown as light red crosses.

The two K-band flares observed on the 15th and 16th of June 2003 are the flares that were completely covered by observations. Although they happened more than 24 hours apart and thus appear to be unrelated events, they both show a striking quasi-periodicity of the flare with a period of about 17 min. Of all possible periodic processes near a black hole (acoustic modes of a thin disk, Lense-Thirring precession, precession of orbital nodes, orbital motion), the period of matter circling the black hole near the last stable orbit is the shortest one. The observed period of 17 min is so short, however, that the only reasonable explanation is that the oscillations are produced by Doppler boosting of hot gas near the last stable orbit of a spinning (Kerr) black hole. The spin of the black hole will allow for a last stable orbit closer to the event horizon and thus with a shorter orbital frequency. From the observed 17 min period we estimate that the supermassive black hole Sgr A* has a spin that is half as big as the maximum possible spin of such an object.

published as: Genzel et al., Nature 425, 934 (2003)

*R. Genzel, T. Ott, R. Schödel, B. Aschenbach, A. Eckart, T. Alexander*

# The Stellar Population in the Galactic Center

**With the new integral field spectrograph SPIFFI, which was mounted to the VLT in 2003, the stellar population of the central cluster around the supermassive black hole Sgr A* could be determined with unprecedented accuracy and completeness.**

As the nearest galactic nucleus, the center of the Milky Way is a unique laboratory for study of the physical processes the operate in the vicinity of a supermassive black hole.
SPIFFI provides simultaneous spectra of all stars in the field of view, permitting spectroscopic classification of a huge number of bright blue and red stars. Combining proper motions and radial velocities for the blue stars reveals their surprising dynamics: they populate two rotating stellar discs that are at large angles to each other, and that rotate in the opposite sense to the rest of the Galaxy. The stars in these two discs have very similar stellar content and appear to have formed coevally about 5 Myr ago in a metal-rich starburst that lasted for several Myr. How did these massive stars come to exist so near to the central black hole? They are too young to have formed further away and migrated in, but strong tidal forces would prevent star formation by the usual mechanism of molecular cloud collapse. The presence of two coeval stellar discs suggests an origin in a sudden dissipative event, such as the collision of two infalling clouds that created debris gas discs that then formed the stars.

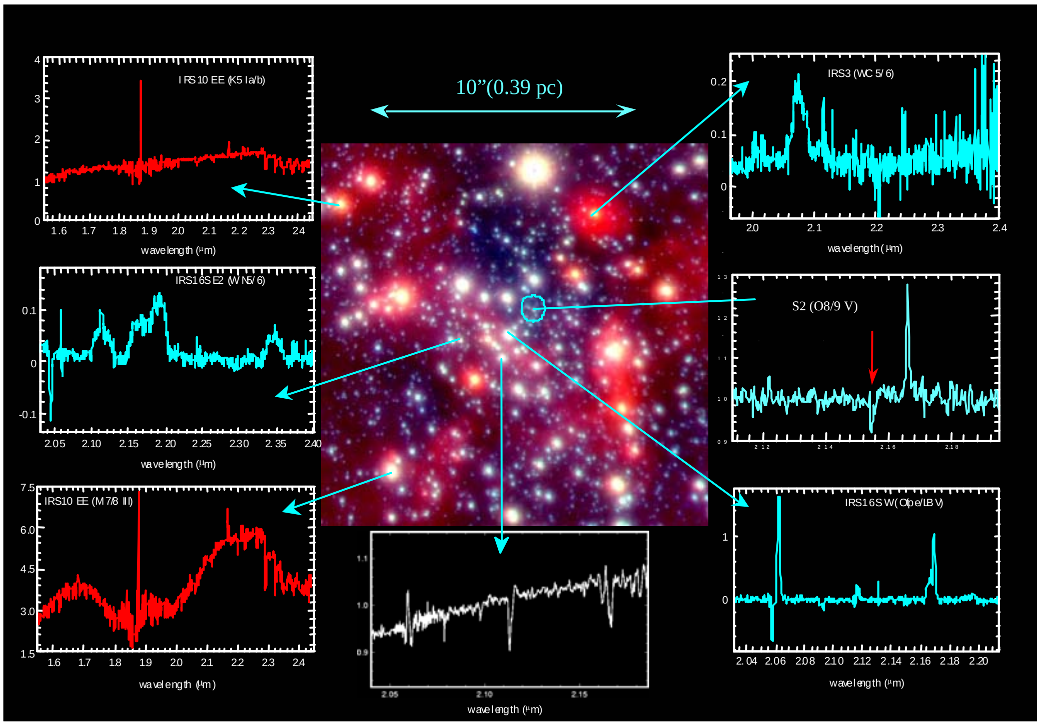


Selected SPIFFI spectra superposed on a NACO H/K/L’ color composite image of the central region. The spectra display the wide range of stellar types found in the cluster, ranging from late type main sequence O stars (the star S2 near SgrA*, oval in image), two luminous blue variables (IRS 16SW, lower right), early WN (middle left) and WC (top right) Wolf-Rayet stars, two red supergiants (the brightest star IRS 7 at the top/middle of the image), bright asymptotic giant branch stars (IRS 9, lower left) and normal red giants (top left). In addition to this, removal of the ionized ISM emission allowed us to identify the absorption lines of a group of at least nine He- and N-rich OB supergiants (bottom).

published as: Eisenhauer et al., The Messenger, Sept. 2003, p. 17i
and: Paumard et al., Proceedings of XXXIXth Rencontres de Moriond, astro-ph/0407189

*F. Eisenhauer, T. Paumard, R. Genzel, T. Ott, R. Abuter*

# The Distance to the Galactic Center

**The distance to the Galactic center ($R_0$) is a fundamental parameter for determining the structure of the Milky Way. We report here the first primary distance measurement to the Galactic center with an uncertainty of only 5%.**

Through its impact on the calibration of standard candles, such as RR Lyrae stars, Cepheids, and giants, the Galactic center distance holds an important role in establishing the extragalactic distance scale. This determination has become possible through the advent of precision measurements of proper motions and line-of-sight velocities of the star S2. This star is orbiting the massive black hole and compact radio source Sgr A* that is located precisely at the center of the Milky Way. The essence of the method is that the star's line-of-sight motion is measured via the Doppler shift of its spectral features in terms of an absolute velocity, whereas its proper motion is measured in terms of an angular velocity. The orbital solution ties the angular and absolute velocities, thereby yielding the distance to the binary.

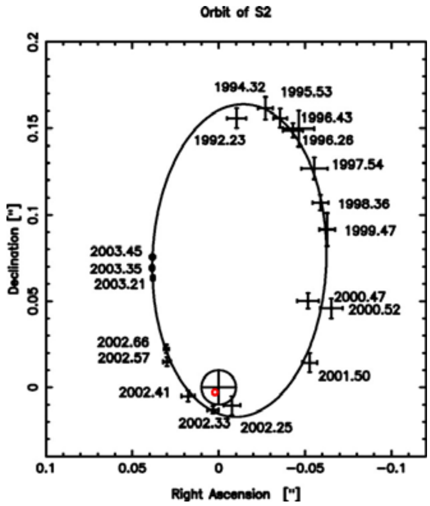


Position measurements of S2 in the infrared astrometric frame. Crosses (denoting 1 error bars) with dates mark the different position measurements of S2, taken with the MPE speckle camera SHARP on the NTT (between 1992 and 2001) and with NACO on the VLT (in 2002 and 2003). The continuous curve shows the best-fit Kepler orbit, whose focus is marked as a small error circle. The focus of the ellipse is within a few milliarcseconds at the position of the compact radio source, which is marked by a large circled cross. The size of the cross denotes the ±10 mas positional uncertainty of the infrared relative to the radio astrometric reference frame.

H I Br absorption spectra of S2, obtained on 2003 April 8/9 with SPIFFI (*upper two panels*), on May 8/9 (*lower left panel*), and on June 11/12 (*lower right panel*) with NACO at the VLT. The SPIFFI spectrum is sky-subtracted and in a 0 1 × 0 2 aperture; the NACO spectrum is slit-nodded and in a 0 086 × 0 1 aperture. These differences account for the fact that the minispiral emission features between -400 and +400 km s$^{-1}$ LSR are visible in the SPIFFI data but not in the NACO spectrum.

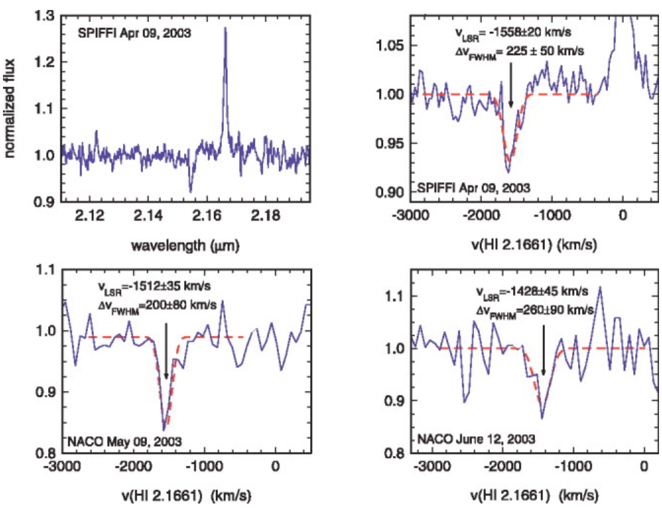


published as: Eisenhauer et al., ApJL 597, 191 (2003)

*F. Eisenhauer, T. Ott, R. Genzel, R. Schödel, R. Abuter*

The strongest X-ray flare from Sgr A*

**In October 3, 2002 *XMM-Newton* has observed the brightest X-ray flare from SgrA*, the supermassive black hole (3 x $10^6$ solar masses) at our Galactic center. This flare had a short duration of about one hour and a peak 2-10 keV luminosity of about 3.6 $10^{35}$ erg $s^{-1}$, i.e., a factor 160 higher than the SgrA* quiescent value *(Porquet et al. 2003, A&A, 407, L17)*.**

Sgr A* is the central supermassive black hole of a mass of about 3 x $10^6$ solar masses at the dynamical center of our Galaxy (e.g., *Schödel et al. 2002, Nature, 419, 694).* Surprisingly, this source is much fainter than expected from accretion onto a supermassive black hole. Sgr A* radiates in X-ray (2-10 keV luminosity ~ 2 $10^{33}$ erg s-1) at about 11 orders of magnitude less than its corresponding Eddington luminosity. The recent discovery of X-ray flares from Sgr A* has provided new exciting perspectives for the understanding of the processes at work in our Galactic nucleus. The first detection of such events was found with Chandra in October 2000 (*Baganoff et al. 2001, Nature, 413, 45*), with a duration of about 3 hours and a peak flare luminosity of about 45 times the quiescent state of Sgr A*.

In October 3, 2002, XMM has observed the brightest X-ray flare from SgrA*, detected so far:

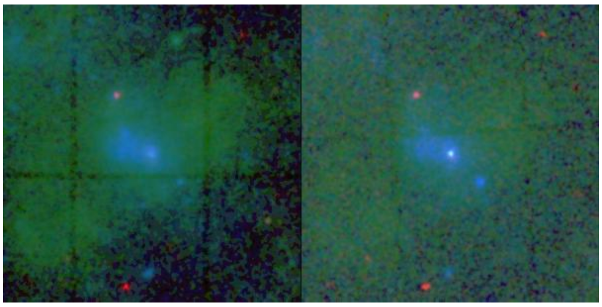

**Figure 1:** EPIC (MOS+PN) images (2-10 keV) center on Sgr A* from two XMM-Newton observations . Left: February 3, 2002. Right: October 3, 2002.

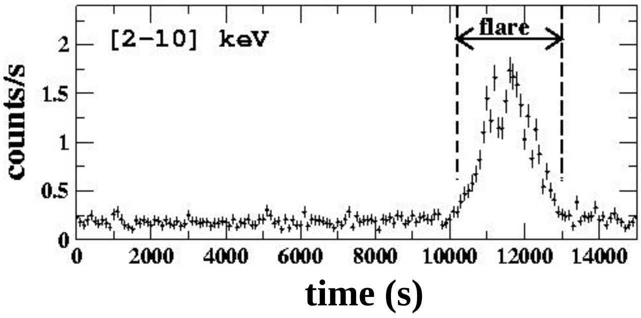


**Figure 2:** EPIC (MOS+PN) light curve within a radius of 10” around Sgr A* during the XMM-Newton observation on October 3, 2002.

## Main results:

✓ Flare duration of about one hour; peak 2-10 keV luminosity of ~ 3.6 $10^{35}$ erg $s^{-1}$, i.e., about 160 higher than the Sgr A* quiescent value.

✓ During the flare, a significant variation of the flux occurs on a time scale as short as 200s, which constrains the emitting size region to about 7 Schwarzschild radii.

✓ The overall flare spectrum is well represented by an absorbed power law with a soft photon spectral index of $\Gamma$=2.5±0.3: much softer than the weaker flares, i.e. $\Gamma$~1.3.

✓ No significant spectral change during the flare is observed.

⇒ **The present accurate determination of the flare characteristics challenges the current interpretation of the physical processes occurring inside the very close environment of Sgr A* by bringing new constraints for the theoretical flare models.**

*D. Porquet, P. Predehl, B. Aschenbach, N. Grosso*

# A new effect of General Relativity and the determination of mass and spin of black holes

The classical problem of a test particle orbiting a rotating black hole has long been solved. Stable circular orbits exist down to a minimal orbital radius *r*, the marginally stable circular orbit. As for Newtonian mechanics both the energy *E* and the angular momentum *L* of the particle are monotonic functions of *r* for the full range of the black hole spin parameter *a*. This means that there this is no preference for any specific value of *r* and *a*. The strictly monotonic behaviour with *r* has generally been assumed to hold for the orbital velocity $v^{(\Phi)}$ as well. But this is not the case. By a detailed analysis of the Boyer-Lindquist functions I have shown that the monotonic behaviour of $v^{(\Phi)}$ breaks down for $a > 0.9953$ at small, but stable *r* and $v^{(\Phi)}$ develops a minimum-maximum structure (c.f. Fig. 1). This can be taken as an indication that these orbits are no longer stable despite the fact that they satisfy the formal Bardeen stability criterion.

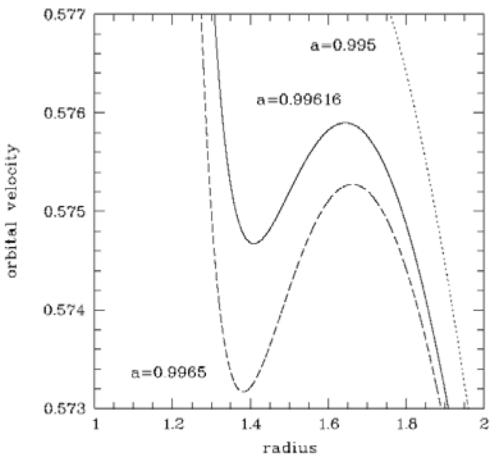


The min-max behaviour of $v^{(\Phi)}(r)$ suggests some oscillatory behaviour, which is supported by the finding that for *a=0.99616* the rate of change of $v^{(\Phi)}$ per unit length of *r* equals the radial epicyclic frequency at *r=1.546*. This resonance stabilizes the motion of the particle in an oscillating mode. Furthermore at exactly these *a* and *r* the vertical and the radial epicyclic frequencies are in a 3:1 resonance. Black holes with *a=0.99616* should show quasi-periodic oscillations with a 3:1 ratio, possibly a 3:2:1 structure, if harmonics or beat frequencies are effective.

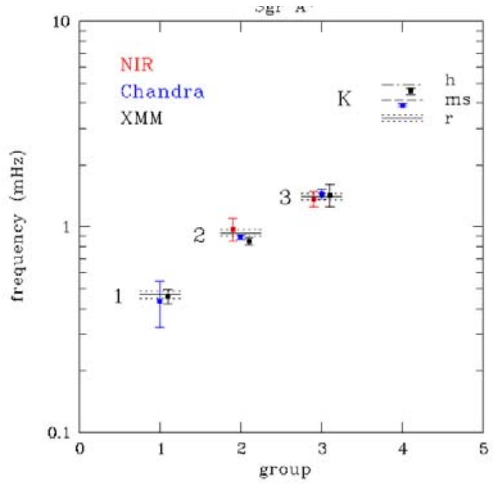


I have associated the quasi-periodic oscillations found so far in three bright, independent flares from the Galactic Center black hole Sgr\,A* (Genzel et al. 2003 in the NIR, Aschenbach et al. 2004 in *Chandra* and *XMM-Newton* data) with this effect. These flares show the 3:2:1 frequency ratio (c.f. Fig. 2). Since *a* and *r* are fixed in general relativity units by the theory the mass of the black hole is given by picking just one of the three frequencies. For Sgr A* the black hole mass is (3.28±0.13)×106 $M_O$, and of course, *a=0.99616*. Group #4 shows the expected Kepler frequencies (K) at *r=1.546* (r), the marginally stable orbit (ms) and at the event horizon (h). The measurements indicate the presence of quasi-periodic light-variations from below the marginally stable orbit close to the event horizon.

For *a=0.99616* and *r=1.546* commensurable orbits may exist which would change the mass-frequency-relation. The analysis shows that for *a=0.99616* just one additional orbit with a commensurable orbital period exists at *r=3.919*. The ratio of the Kepler frequencies is 3:1 and the ratio of the frequencies of the vertical and radial epicyclic modes is 3:2. In this case quasi-periodic oscillations would occur at two frequencies with a ratio of 3:2. Twin high-frequency 3:2 quasi-periodic oscillations have been found in galactic black hole binaries of stellar mass, which for three of them have been roughly determined dynamically. For all three systems known the agreement is very good, but the accuracy of the mass determination is significantly improved down to the few percent level given by the frequency measurements. A general discussion of the implications of this new effect are given by Aschenbach, 2004, A&A, in press.

*B. Aschenbach*

# ISM and star formation in the LMC N4 HII complex

**We present the analysis of ISOCAM-CVF spectro–imaging and J,H and K photometry data of the HII region complex N4 in the Large Magellanic Cloud (LMC). We apply a dust features – gas lines – continuum fitting technique on the whole ISOCAM-CVF data cube, which allows the production of images in each single emission and therefore a detailed analysis of dust (both continuum and bands), and ionized gas. The NIR photometry provides, for the first time, complementary information on the stellar content of N4.**

The MIR (5–17 $\mu$m) spectral characteristics of N4 are very similar to what has been observed in Galactic HII region complexes: strong PAH bands and significant continuum in its PDR; weak PAH bands, strong dust continuum and fine structure lines from the ionized gas, in the HII region; weak dust features with almost no continuum from the outskirt of the molecular cloud. The images in the single 7.7 $\mu$m band and SIV( 10.5 $\mu$m) (fig.1), obtained with our fitting technique, clearly shows that the HII region core is completely devoid of PAHs. On the other hand, the ionized gas arises almost completely in the dust cavity where the two main exciting stars (#2, #3 in fig. 2) of N4 are located. We find that what mostly affects dust is not the metallicity, but destruction by the hard and high Interstellar Radiation field. This mechanism is more efficient on smaller dust particles/molecules, thus affecting the dust size distribution.

The NIR analysis of the stellar content of N4 reveals 6 point sources (labeled in the NIR composite map). Objects #2, #3, #5 and #6 are reddened O MS stars. Stars #1 and #4 have large IR excess, colors not corresponding to reddened young MS stars and J band brightness corresponding to Class I and /or Herbig Ae/Be objects candidates. Star #1 is most probably a non resolved multiple compact young massive system. Star #4 has the largest IR excess of the sample. It has IR characteristics of a massive young stellar object (YSO's) similar to N122 in 30Dor.

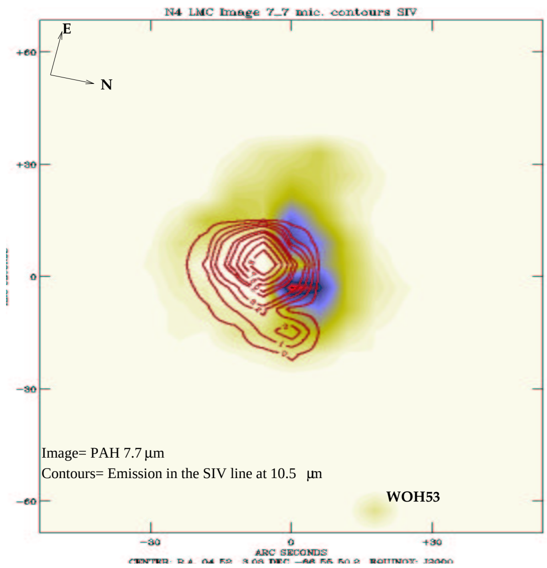


Map from Lorentzian fit of the 7.7 $\mu$m PAH band. Contours: image from Gaussian fit of the SIV (10.5 $\mu$m) line.

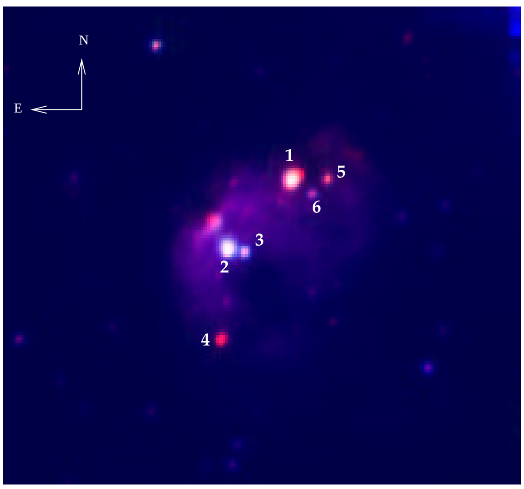


Figure2. NIR Composite map of N4: red is K, green is H and blue is J. Point sources identified as stars are numbered.

*A. Contursi (MPE), M.Sauvage, M. Rubio, D. Cesarsky and F. Boulanger*

# WeCAPP – Searching for Dark Matter in M31

**WeCAPP is a long term monitoring project searching for microlensing events towards M31. A search for very high $(S/N)$, short time scale events in a fraction of the data has resulted in two events WeCAPP-GL1 and GL2. Modelling the stellar content of bulge and disc and assuming a 100% MACHO halo fraction yields that halo lensing is more likely than self lensing, and that the most probable masses are in the range of the brown dwarf limit of hydrogen burning.**

## Motivation

Studying the lensing effect of foreground objects to background stars towards M31 allows to statistically separate between self-lensing and true MACHO events: the high inclination of M31 (77°) produces a near-far asymmetry of the hale event rate. The near side of the disk will show less halo events than the more distant one. In contrast Galactic halo-lensing as well as self-lensing events should not show this asymmetry after the effect of dust has been taken into account. As most of the sources for possible lensing events are not resolved at M31's distance of 770 kpc the difference imaging technique (Alard & Lupton 1998) has to be applied to identify these so called 'pixellensing' events (Gould 1996).

**Fig. 1** $V$-,$R$-, and $I$-band composite image of the observed field of the M31 bulge taken at Calar Alto Observatory with a field of view of 17.2 arcmin (3.75 kpc).

## WeCAPP-GL1 and GL2

In the data covering the years 2000/2001 we detected our first two high $(S/N)$, short timescale microlensing events. Both were filtered out from $4 \cdot 10^6$ pixel light curves using a variety of selection criteria which ensure that we did not confuse real microlensing with other variable sources like Mira stars. We therefore only considered well-sampled events with timescales of $1\,\mathrm{d} < \mathrm{t_{fwhm}} < 20\,\mathrm{d}$, high amplitude, and low $\chi^2$ of the microlensing fit.The two-color photometry $(R, I)$ shows that the events are achromatic and that giant stars with colors of $(R{-}I) \approx 1.1\,\mathrm{mag}$ in the bulge of M31 have been lensed. The most likely magnifications are 70 and 11, which are obtained for giant luminosities of $\mathcal{M}_I = -2.5\,\mathrm{mag}$.

Both lensing events lasted for only a few days ($t_{\mathrm{fwhm}}$ of 1.4 d and 5 d). The event GL1 is likely identical with PA-00-S3 reported by the POINT-AGAPE project.

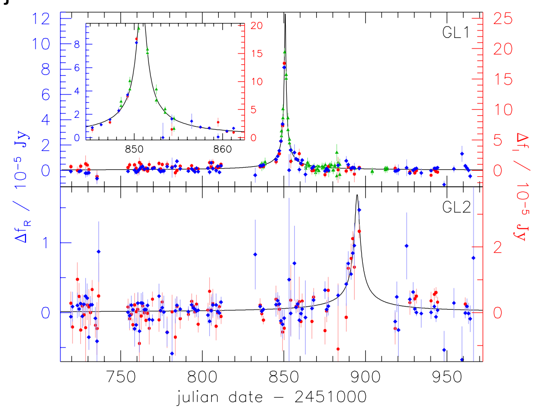


**Fig. 2** Light curves of GL1 (upper panel) and GL2 (lower panel). The $I$-band light curve (red symbols, right axis) is scaled to the $R$-band light curve (blue symbols, left axis).

## Mass estimates

Assuming the source to be a red giant with $\mathcal{M}_I = -2.5\,\mathrm{mag}$ we calculate the probability $p(M, t_{\mathrm{E}})$ that a microlensing event of observed timescale $t_{\mathrm{E}}$ can be produced by a lens of the mass $M$. The results are shown in Fig. 3. For M31 halo lenses the most probable masses are 0.08 $M_\odot$ for GL1 and 0.02 $M_\odot$ for GL2. Taking these most likely halo lens masses, the ratio of the probabilities that the lenses are in the halo (assuming a 100% MACHO fraction) relative to bulge and disk $p_{\mathrm{halo}}/(p_{\mathrm{bulge}}{+}p_{\mathrm{disk}})$ is 1.6 for GL1 and 3.3 for GL2. It is therefore likely that lenses residing in the halo of M31 caused the events in both cases.

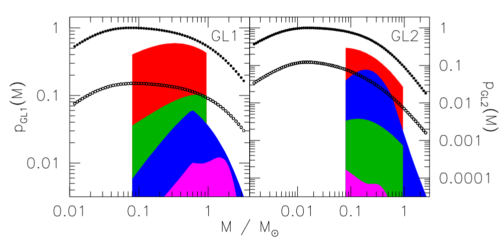


**Fig. 3** Mass probability for GL1 (left) and GL2 (right) for lens-source configurations: halo-bulge (filled), halo-disk (open circles), bulge-bulge (red), bulge-disk (green), disk-bulge (blue), disk-disk (magenta).The maximum of each curve is scaled to reflect the total probability of a respective lens-source event relative to the case of a halo-bulge lensing event with the most probable MACHO mass.

**References:**

Riffeser et. al. (2003) ApJ 599L, p. 17

Gössl, C. A., Riffeser, A. (2002) A&A 381, p. 1095

Riffeser et. al. (2001), A&A 379, p. 362

*A. Riffeser, F. Fliri, R. Bender, S. Seitz*

# XMM-Newton survey of M 31 and M 33

**We have homogeneously analyzed all archival XMM-Newton EPIC observations of the Local Group galaxies M 31 and M 33 and detected 856 and 408 sources, respectively. The sources are classified using X-ray hardness ratio and information from other wavelengths.**

In our analysis we used five energy bands (0.2-0.5, 0.5-1.0, 1-2, 2-4.5, 4.5-12 keV), defining four hardness ratios from adjacent energy bands, and all EPIC instruments to create images and do source detection. We identified or classified the sources in the galaxies (supersoft sources (SSSs), supernova remnants (SNRs), X-ray binaries (XRBs)), foreground stars and objects in the background (galaxies, cluster of galaxies, active galactic nuclei (AGN)) and more than doubled the number of sources known in the fields. (Pietsch, W., Freyberg, M., Haberl, F. 2004b, A&A, submitted; Pietsch, W., Misanovic, Z., Haberl, F., et al. 2004a, A&A, 426, 11)

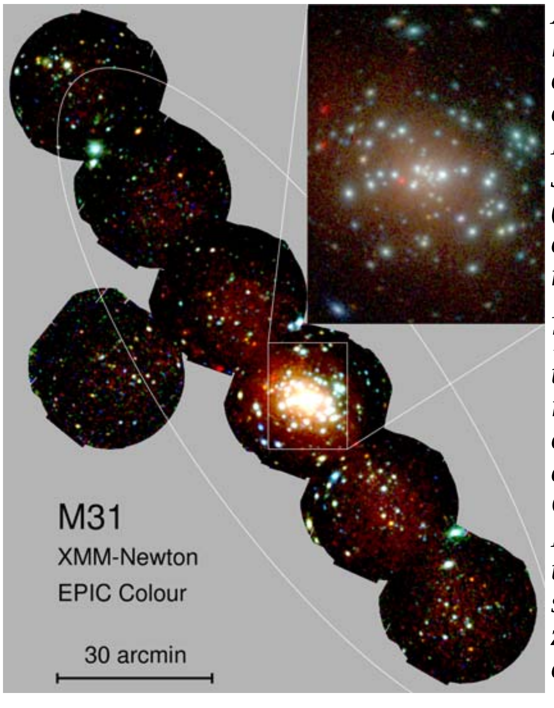


*XMM-Newton EPIC low background three colour images combin-ing PN and MOS cameras for M 31 (**left**) and M 33 (**right**). Red, green and blue show respectively (0.2-1, 1-2, 2-12) keV bands. The optical extent of the galaxies is indicated by $D_{25}$ ellipses. The images are smoothed with a Gaussian of 20" FWHM. The insert in the M 31 image shows a factor 3 zoom-in on the centre area (5" smoothing).*

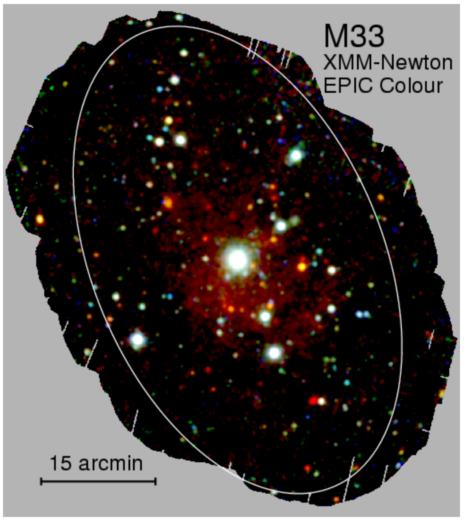


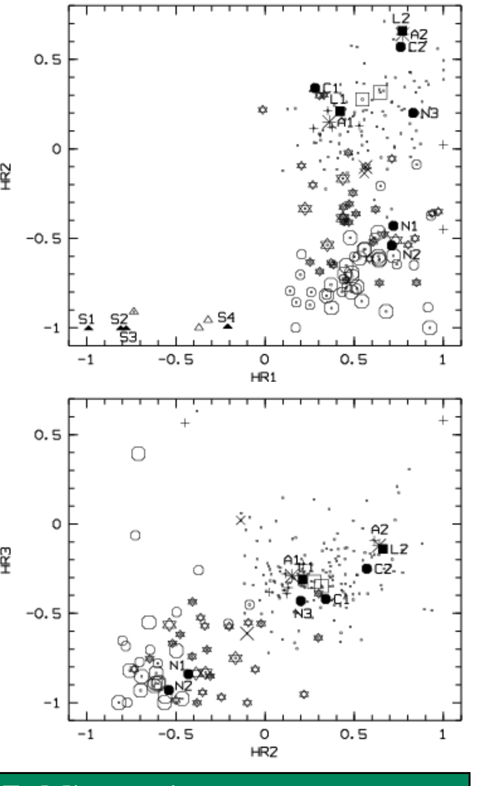


*Two Hardness ratio (HR) diagrams of M 33 (**right**) sources detected by XMM-Newton. Shown as dots are only sources with HR errors smaller than 0.2. Foreground stars and candidates are marked as big and small stars, AGN as crosses, SSS as triangles, SNRs as hexagons Globular cluster sources and XRBs as squares. In addition, HR from measured objects in the Galaxy or Magellanic Clouds or determined from model spectra for the source classes are shown by filled symbols.*
*SSS clearly separate by their HR1. Thermal SNRs and foreground stars cover the same area in the HR2-HR1 diagram and can by separated using optical information. XRBs, „plerionic“ type SNRs and AGN do not separate in the HR diagrams and all show „hard“ HRs.*
*In both galaxies, many new SSS, SNRs and foreground stars are detected or now identified by their X-ray properties.*

*W. Pietsch, M. Freyberg, F. Haberl, Z. Misanovic*

# ISO spectra of NGC6240: Strong starburst and AGN

The merging galaxy NGC 6240 is an object presenting many aspects of importance for the role of star formation and AGN activity in [ultra]luminous infrared galaxies and can be studied in great detail due to its proximity. We have analysed and combined all spectra of NGC 6240 obtained with the Infrared Space Observatory for an in-depth study. The mid-infrared spectrum shows starburst indicators in the form of low excitation fine-structure line emission and aromatic `PAH' features. An unusually strong high excitation [OIV] line is observed which most likely originates in the Narrow Line Region of the optically obscured AGN that is also seen in hard X-rays. NGC 6240 shows extremely powerful emission in the pure rotational lines of molecular hydrogen. We argue that this emission is mainly due to shocks in its turbulent central gas component and its starburst superwind. The total shock cooling in infrared emission lines accounts for ~0.6% of the bolometric luminosity, mainly through rotational $H_2$ emission and the [OI] 63µm line.

**We use NGC 6240 as an exemplary case to critically analyse several ways of estimating the total luminosities of the starburst and the AGN, and discuss their systematic and statistical uncertainties. We use several infrared-based estimates as well as the X-ray evidence. Based on a combination of all estimates, the contributions to the bolometric luminosity of NGC 6240 are most likely in the range 50-75% starburst and 25-50% AGN.**

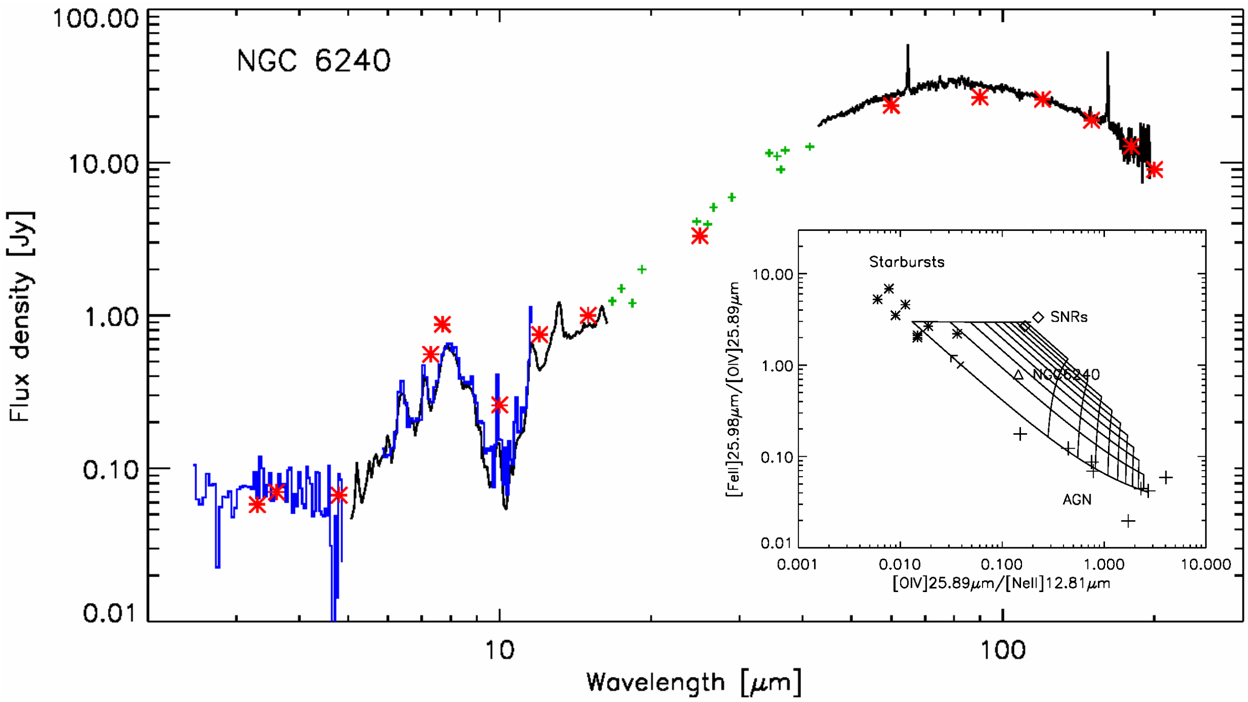


Spectral energy distribution of the merging luminous infrared galaxy NGC 6240, from the complete set of 2.5-200µm Infrared Space Observatory spectra that we have analysed. The insert shows a new diagnostic diagram based on mid-infrared fine structure line. The strength of [OIV] in NGC 6240 is due to the presence of the optically obscured AGN(s), already studied in X-rays, in addition to powerful starburst activity.

**References:**
• Lutz, D., Sturm, E., Genzel, R., Spoon, H.W.W., Moorwood, A.F.M., Netzer, H., Sternberg, A. 2003, A&A, 409, 867

*D. Lutz, E. Sturm, R. Genzel*

NGC 6240 is in many ways a prototype of the class of gas-rich, infrared luminous mergers. The system has two rapidly rotating, massive bulges/nuclei at a projected separation of 1.6“ (750pc), each of which contains a powerful starburst and a luminous, highly absorbed X-ray active AGN. NGC 6240 is also the most luminous local source of ro-vibrationally excited $H_2$ line emission. Most of the starburst activity (as traced by Brγ) occurs in the two nuclei on scales of 200pc, although there appears to be one extranuclear source in the gas bridge between the nuclei. The vibrationally excited $H_2$ emission is very different and follows a complex spatial and dynamical pattern. The $H_2$ kinematics are extremely complex and very different from the relatively simple counter-rotating pattern of the stars. The gas bridge is redshifted relative to the nuclei and exhibits a very steep velocity gradient as it curves around towards the southern nucleus, where it appears to crash into the nuclear regions. From the bright $H_2$ peak just NE of the southern nucleus two gas streamers emerge and envelop the southern galaxy. This pattern resembles the gas bridges found in situations of gas rich mergers after the first peri-approach – we may be observing the two galaxies after the first hang-out phase in the process of falling back. $H_2$ spatial distribution, kinematics, and level populations strongly favor a galactic shock model as the origin of the spectacular $H_2$ emission.

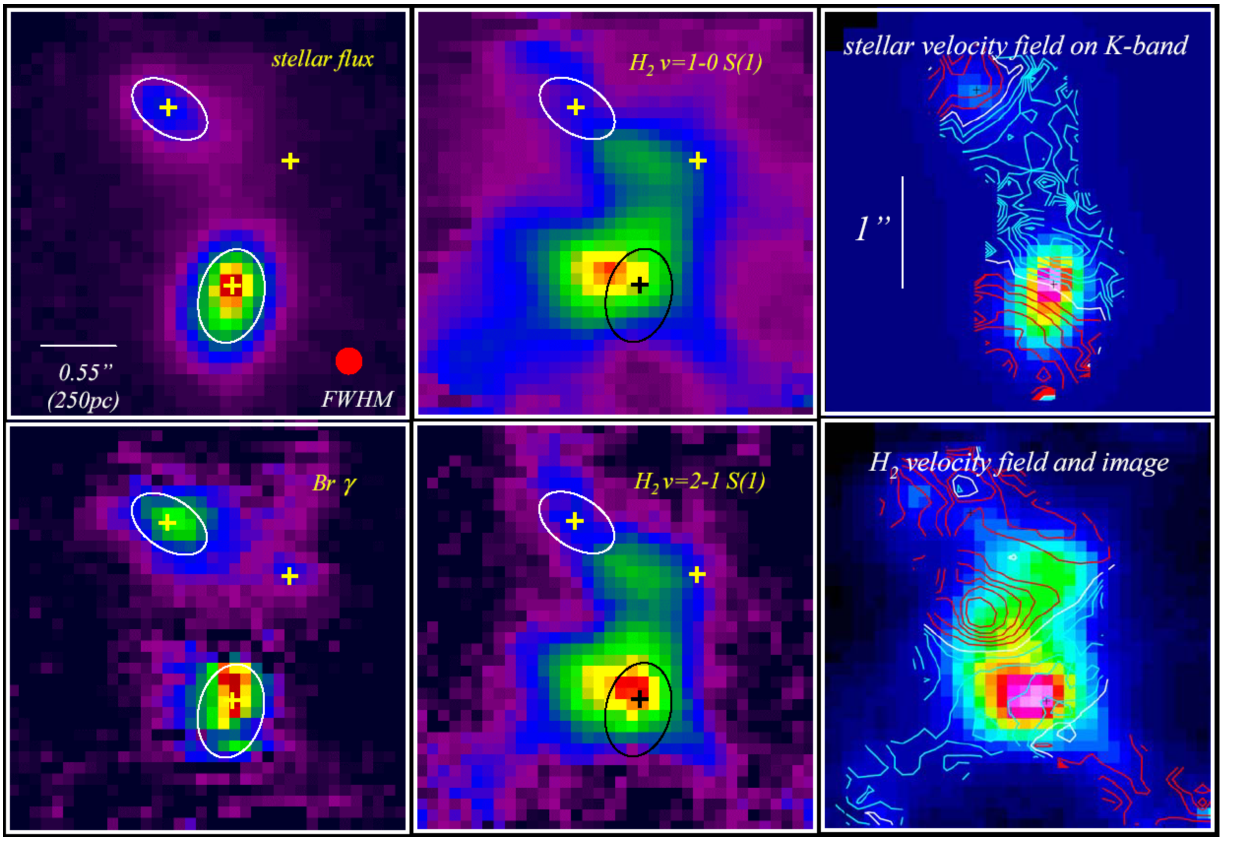


SPIFFI images, stellar and $H_2$ kinematics of the luminous merger galaxy NGC 6240, as observed with 0.1” pixels and 0.27” spatial resolution during SPIFFI guest instrument observations in spring 2003. In all images the positions of the two nuclei and an extra-nuclear Brγ source are marked.

**References:**
• Eisenhauer, F., et al. 2004, Astron. Nachrichten, 325, 120

*M. Tecza, R. Abuter, R. Davies, F. Eisenhauer, R. Genzel, A. Gilbert, M. Horrobin*

# Molecular Hydrogen Excitation in ULIRGs

A detailed analysis of the molecular hydrogen and ionised hydrogen/helium line fluxes in a sample of ULIRGs provides a consistent picture of young star clusters surrounded by dense photo-dissociation regions that are irradiated by intense far-ultraviolet radiation.

In ultraluminous galaxies (ULIRGs) the $H_2$ 1-0 S(1) line is often stronger than Brγ, but its excitation mechanism is not known even though it has the potential to distinguish between dynamical excitation in shock waves and radiatively driven processes. Using ISAAC on the VLT, we have found that there is little variation in the K-band $H_2$ ratios between ULIRGs. In all cases the ν=1-0 emission appears thermalised at about 1000 K, but the 2-1 and 3-2 transitions show evidence of being radiatively excited by far-ultraviolet (FUV) photons, indicating that the $H_2$ emission in ULIRGs arises in dense photon-dominated regions (PDRs). The line ratios in the nuclei are consistent with cloud densities between $10^4$ and $10^5$ cm$^{-3}$, exposed to FUV radiation fields at least $10^3$ times more intense than the ambient FUV field in the local interstellar medium. Starburst models for the ULIRGs based on the $H_2$ properties as well as the intensities of the He I and Brγ recombination lines provide a consistent picture of young 1-5 Myr star clusters surrounded by relatively dense PDRs that are irradiated by intense FUV fluxes.

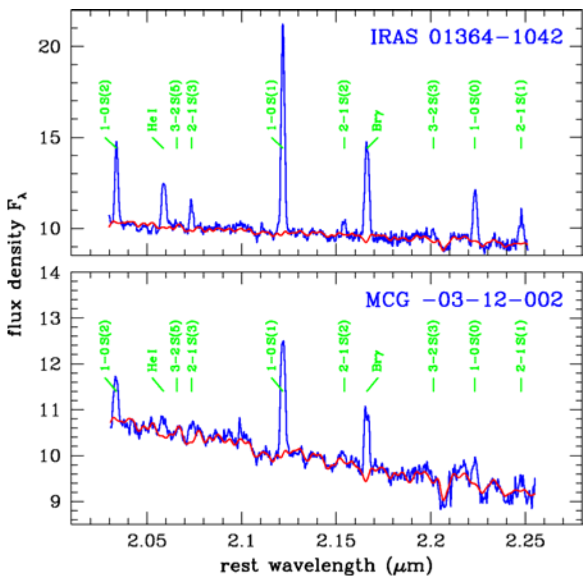


K-band spectra of 2 galaxies in the ULIRG sample, with the positions of the emission lines marked. Overplotted is the stellar continuum, derived in each case from a set of template spectra. This has been fitted and subtracted in order to facilitate measurement of the fluxes of weak lines.

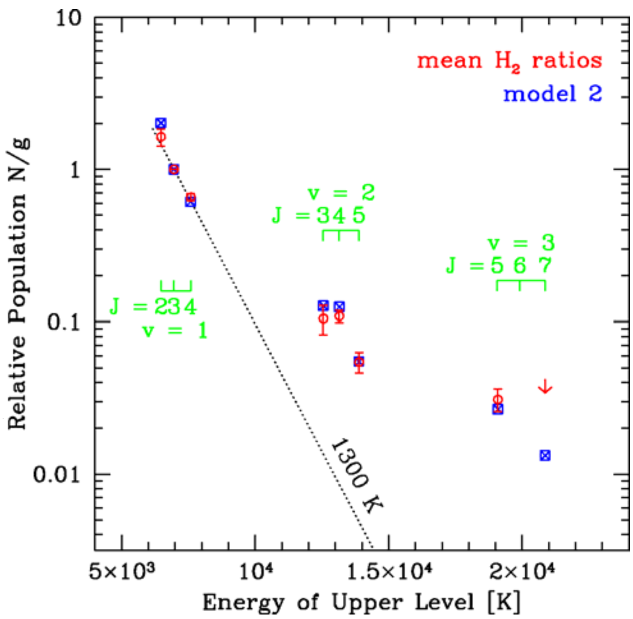


Excitation diagram showing the relative populations of the upper levels of the observed $H_2$ transitions. The data (red) shown are the mean ratios for all the ULIRGs in the sample, with the error bars indicating the standard deviation between the objects. The model (blue), which provides an excellent match to the data, is that described above.

published as: Davies, Sternberg, Lehnert, Tacconi-Garman, 2004; ApJ, 597, 907

*R. I. Davies, M. Lehnert*

# Gas & dust in the HyLIG BALQSO IRAS14026+4341

Hyperluminous infrared galaxies (HyLIGs) are the most extreme members of the infrared galaxy population ($L > 10^{13} L_\odot$) and have luminosities that are amongst the highest measured in the Universe, second only to powerful gamma-ray bursts. They show evidence of harbouring coeval AGN and starbursts and have disturbed morphologies. Yet, their evolutionary role, their connection to the well studied ultraluminous galaxies (ULIGs), to starbursts and AGN remain uncertain. I summarise the first results[9] from our IRAM 30m program to investigate the molecular gas content of an unbiased sample of HyLIGs for which little is currently known. We investigate the presence and quantity of molecular material and how this may relate to obscured star formation and an active nucleus.

**Gas in IRAS 14026+4341** IRAS 14026+4341 is a radio-quiet, low-ionisation broad-absorption line (BAL) QSO[1] harboured within an elliptical-like host which is interacting with a small companion[2]. The gure to the right shows the weak ($3\sigma$ detection) of the CO($1\rightarrow0$) transition very close to the optical redshift (z=0.323). After tting the line with a single Gaussian and applying the conversion factor between CO luminosity and mass of $H_2$[3] we derive a molecular gas mass of $9.74\times10^9 h_{65}^{-2} M_\odot$ similar to those determined for ULIGs[4].

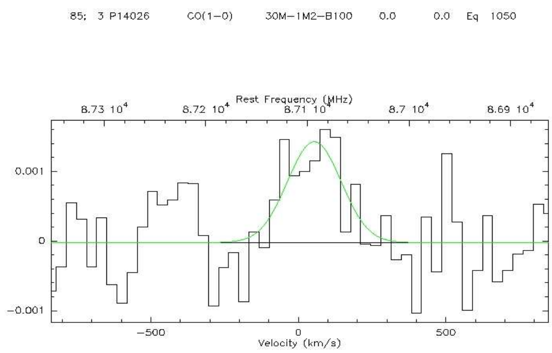


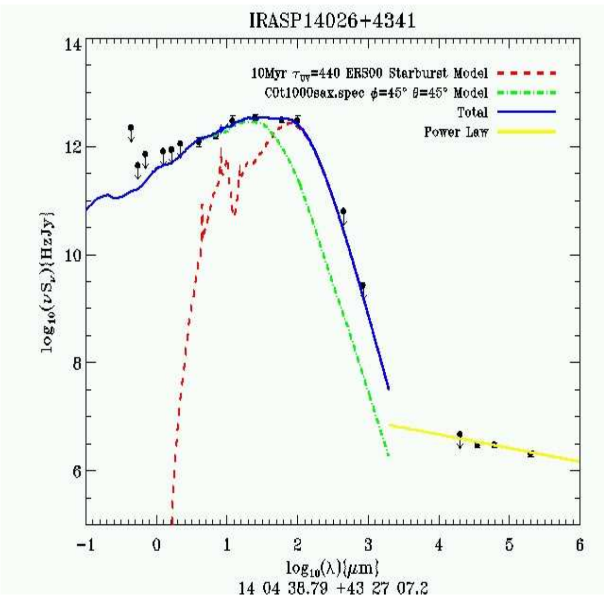


**Dust in IRAS 14026+4341** The gure to the left shows the compiled optical-mm SED for this galaxy modelled using detailed radiative transfer models of starbursts and dusty tori. We nd coeval starburst and AGN activity where the AGN dominates (64%) of the IR luminosity. Interestingly the best- t AGN model is inclined at to the line-of-sight by 45° with a 90° opening angle indicating the emission grazes the surface of the obscuring torus. This independently derived result, as well as being consistent with the steep radio spectral index ($\alpha$=0.8), is also consistent with the 'orientation' models proposed for BALQSOs[e.g.5,6,7]. The resulting gas-to-dust ratio, that is an evolutionary indicator of the mass of gas yet to be turned into stars, is $\sim 30$. The value is consistent with previous measurements of high-z QSOs[8] but lower than the canonically expected value.

**Summary** A multiwavelength comparison of optical, infrared, (sub-)mm, and radio data for IRAS 14026+4341 yields a consistent result of a strong AGN and coeval starburst activity with a modest amount of molecular gas. At the current star formation rate, our derived gas content will be depleted in ~10Myr. The low gas-to-dust mass ratio suggests that IRAS P14026+4341 is a complex QSO+starburst system where star-formation is at more advanced stage than gas-rich starbursts or ULIGs.

[1]Low et al. 1989; [2]Hutchings & Morris 1995; [3]Solomon et al. 1997; [4]Downes & Solomon 1998; [5]Schmidt & Hines 1999; [6]Reichard et al. 2003; [7]Hewett & Foltz 2003; [8]Cox, Omont et al.; [9]Verma et al. in prep.

*A. Verma et al.*

# The Nature of Starburst Activity in M82

Starburst galaxies are important constituents of the universe at all accessible redshifts. However, a detailed and quantitative understanding of the starburst phenomenon is still lacking. Progress has been hindered by the scarcity of spatially resolved data and by dust obscuration often hampering high-resolution studies in the optical/UV. In this context, we carried out a detailed investigation of the nearby (3.3 Mpc) archetypal starburst galaxy M82. We used mainly near-IR integral field spectroscopy from the MPE 3D instrument and mid-IR spectroscopy from the ISO SWS, covering the central actively star-forming regions.

**We derived a typical duration for individual burst sites of ~ $10^6$ yr. The data are consistent with the formation of very massive stars ($\gtrsim$ 50–100 $M_\odot$) and require a flattening of the IMF below a few $M_\odot$ assuming a Salpeter slope at higher masses. The global starburst activity in M82 occurred in two successive episodes each lasting a few $10^6$ yr, peaking ≈ 10 and $5\times10^6$ yr ago. The first episode took place throughout the central regions and was particularly intense at the nucleus while the second episode occurred predominantly in a circumnuclear ring and along the stellar bar. This sequence likely resulted from the gravitational interaction between M82 and its neighbour M81, and subsequent bar-driven evolution. The short burst duration on all spatial scales indicates strong negative feedback effects due to the collective mechanical energy released by massive stars, rapidly inhibiting star formation after the onset of each starburst episode.**

*MPE 3D:*

*K-band emission*

*Brγ line emission*

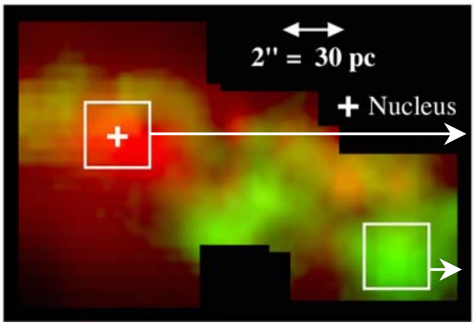


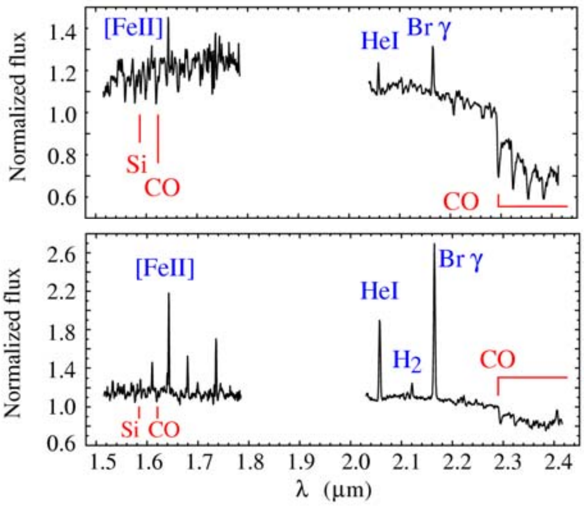


Composite map and representative spectra of the nuclear starburst regions of M82 from MPE 3D. The *K*-band continuum emission and the absorption features trace evolved red (super)giants while H (e.g. Brγ) and He recombination lines trace HII regions around young OB stars. The relative spatial distributions in strength of these features indicate important variations on scales ~ few tens of pc in the evolutionary stage of the starburst.

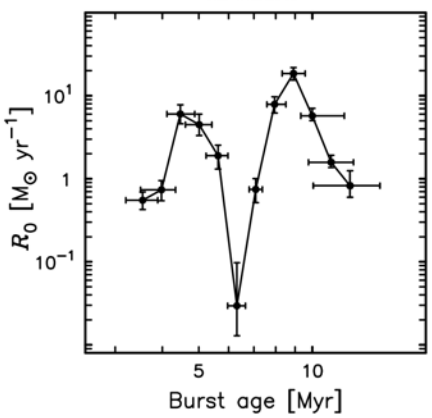


Global star formation history of the central regions of M82, reconstructed from the modeling of all individual pixels within the MPE 3D field of view. Two distinct starburst episodes are outlined, peaking ≈ 10 and 5 Myr ago and lasting each a few Myr only.


**References:**

• Förster Schreiber, N.M., Genzel, R., Lutz, D., & Sternberg, A. 2003, ApJ, 599, 193



*N.M. Förster Schreiber, R. Genzel, D. Lutz, A. Sternberg*

# Nuclear Dynamics and Star Formation in Mkn 231

Adaptive optics H- and K-band data of the ULIRG/QSO Mkn 231 from the Keck II telescope have allowed us, for the first time, to directly resolve the active star forming region close around its AGN.

The stellar luminosity profile, traced through the stellar absorption features, is well represented by an exponential function, implying the stars exist in a disk rather than a spheroid. Constraints from the dynamical mass and K-band stellar luminosity indicate that the stars in this region are young (10-100 Myr) and contribute 25-40% of the bolometric luminosity. The spatially resolved dynamics of the $H_2$ 1-0S(1) and [Fe II] lines, as well as the stellar dynamics, are also consistent with a nearly face-on disk, confirming the result from the luminosity profile. This result explains why Mkn231, the product of a major merger between gas rich spirals, does not resemble moderate mass ellipticals as other mergers do. The stars we are seeing are not those which have relaxed into a spheroid, but instead those which have formed very recently in gas that itself cooled into a molecular disk as a result of the merger.

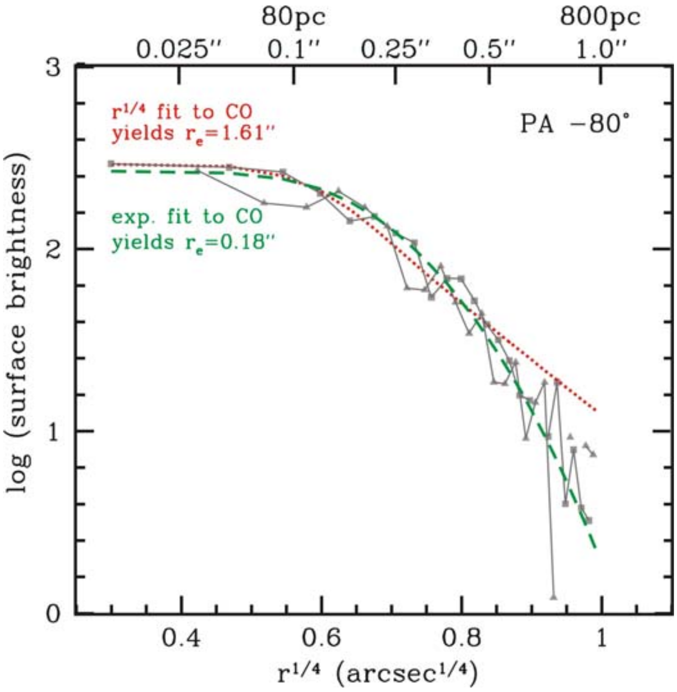


Spatial profiles of the CO absorption 'flux', plotted as logarithms against $r^{1/4}$, so that a de Vaucouleurs law appears as a straight line. Overplotted are exponential (dashed green) and $r^{1/4}$ (dotted red) profiles, convolved with the spatial beam. The former is clearly a better match to the data. Inset are the same profiles, together with the continuum (blue) on linear scales.

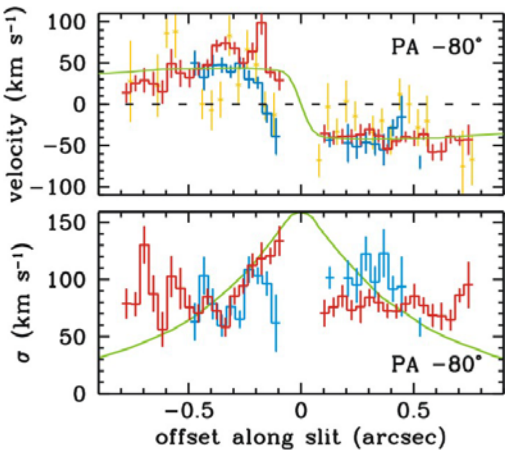


Rotation curve (upper panel) and velocity dispersion (lower panel) along one slit position angles. Data from the 2.12μm $H_2$ is red, from 1.64μm [Fe II] is blue, and from H-band stellar absorption features is orange. The dynamics for an axisymmetric planar mass model is overplotted in green.

published as: Davies, Tacconi, & Genzel 2004; to appear in ApJ, 1 October 2004,

*R. I. Davies, L. J. Tacconi, R. Genzel*

# Nuclear Dynamics and Star Formation in NGC 7469

The unique combination of mm interferometry and near infrared adaptive optics has enabled us to construct a dynamical model of the central kpc of NGC7469, revealing a sub-arcsec ring, inside which is a young compact star forming region with a luminosity 20% that of the AGN.

High-resolution mm data from the IRAM interferometer and near-infrared adaptive optics data from the Keck II telescope, has provided a tool to probe the distribution and dynamical structure of the stars and gas in NGC 7469 across 2 orders of magnitude in spatial scale. The kinematics of the mm CO 2-1 and K-band $H_2$ 1-0S(1) lines can be reproduced at their different resolutions by a single axisymmetric mass model comprising 3 components: a broad disk, a circumnuclear ring with radius 2-2.5", and a nuclear ring with a radius of 0.2" (65 pc). From the dynamical mass and estimates of the stellar mass, we find that the CO-to-$H_2$ conversion factor is 0.4-0.8 times that for the Milky Way, following the trend to small factors seen in intense star-forming environments. While the gas dominates the mass on scales of several arcsec, in the central 0.2" most of the mass is due to stars. This nuclear star cluster has a FWHM of 0.15-0.2" (50 pc) and lies inside the nuclear gas ring. Constraints from the dynamical mass and K-band stellar light indicate that its age is < 60 Myr and it contributes ~10% of the galaxy's bolometric luminosity.

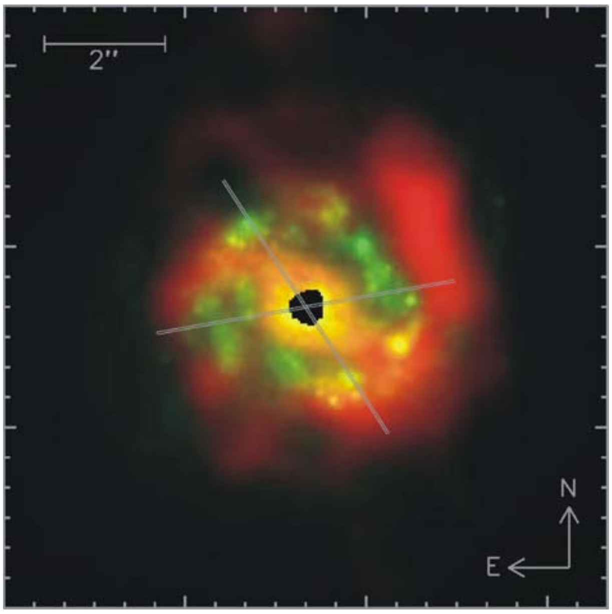


Image showing the molecular gas, as traced by our CO2-1 data (red) and the stellar continuum (J-band HST NICMOS data, green). Yellow regions indicate the presence of both. The nucleus has been masked out. The 37mas wide long slits we used for the adaptive optics spectroscopy are shown.

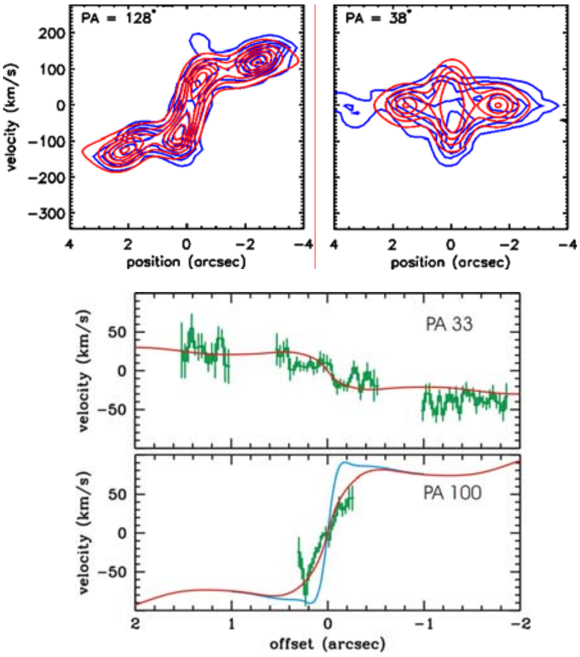


Top: position-velocity maps of the CO2-1 data for 2 position angles (blue) with our dynamical model (red) superimposed.
Bottom: the rotation curves for the 1-0S(1) line (green). The same dynamical model (but at the much higher spatial resolution; red) is superimposed. The blue curve in the lower panel indicates how the rotation curve would appear if there were a large unresolved mass.

published as: Davies, Tacconi, & Genzel 2004; ApJ, 602, 148

*R. I. Davies, L. J. Tacconi, R. Genzel*

# A MIR spectroscopic atlas of starburst galaxies

We have consolidated detailed mid-infrared (MIR) spectroscopic data on a sample of nearby starbursts observed by the *Infrared Space Observatory* (ISO) to provide a spectroscopic atlas of MIR emission features (2.4-45.2$\mu$m). The spectra are rich in fine structure (FSL) and hydrogen recombination lines and thus are excellent probes to investigate the nature of starbursts. We use FSL ratios of neon, argon and sulphur to construct diagnostic excitation diagrams and, in combination with H-recombination line data, we determine their elemental abundances. The derived Ne abundances span approximately an order of magnitude, up to values of ~3 times solar. The excitation ratios measured from the Ne and Ar lines correlate well with each other (positively) and with abundances (negatively) (see figure below). The FSL data have been combined with a similar study of active galaxies to construct diagnostic diagrams that discriminate the two types of activity based upon their MIR spectra (Sturm et al. 2002 A&A 393 821).

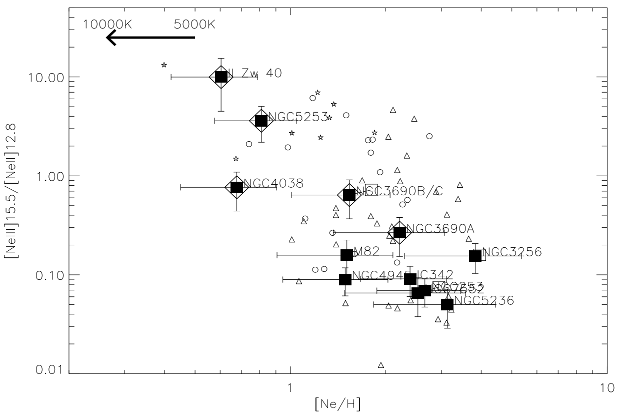


**Figure**: Abundance against excitation for the starbursts ( lled squares) showing a clear anti-correlation of the lower excitation of metal-rich galaxies than H II regions (small open circles, triangles and stars). Also, low metallicity and high excitation WR galaxies (squares enclosed by diamonds) are separated.

**Low excitation of starbursts** Ratios of FSLs of different ionisation states of the same species are a measure of the excitation of a galaxy's ISM. Our results show a clear dependence od excitation upon metallicity We con rm earlier results  nding that for a given abundance (Ne, Ar or S), the starbursts are of relatively lower excitation than a comparative sample of Galactic HII regions. The low excitation has been ascribed to low upper-mass cut-offs to the IMF or ageing of the stellar population. The presence of massive star in starburst systems is well known and thus ageing of the stellar population and dilution of the excitation ratio as a result are the preferred explantion. The excitation is hence governed by a combination of metallicity and other effects like ageing of the population, which should be accounted for in modelling starbursts as composite HII regions.

**Underabundance of Sulphur** We  nd sulphur abundances that are consistently lower than Ne or Ar by up to an order of magnitude in metal rich & dusty objects. While raising practical limitations on the use of S lines as tracers of star forming activity, we cannot determine the precise origin of this de cit although favour depletion onto dust grains as the most likely cause. Our results imply that (a) the FSL transitions of neon are favoured over FSL of sulphur as a star formation indicator for future spectroscopic surveys of faint galaxies and (b) sulphur is a unsuitable tracer of metallicity.

**Wolf-Rayet Galaxies** Both in excitation and abundance, a separation of objects with visible Wolf-Rayet (WR) features (high excitation, low abundance) is noted from those without (low excitation, high abundance). This is contrary to expectations of higher Wolf-Rayet fractions at higher metallicity from stellar evolutionary models. The most plausible reasons for this behaviour include obscuration coupled with a lack of convincing MIR Wolf-Rayet tracers, dilution by less obscured regions in the optical spectrum and changes in the spectral signatures of Wolf-Rayet stars at higher metallicity.

*A. Verma, D. Lutz, E. Sturm, R. Genzel, A. Sternberg, W. Vacca* (2003, A&A, 403, 829)

# PAHs in energetic extragalactic environments

The mid-infrared dust emission features at 3.3, 6.2, 7.7, 8.6, 11.3 and 12.7 µm, commonly ascribed to PAHs (polycyclic aromatic hydrocarbons), are a powerful diagnostic of the conditions in dusty external galaxies. In order to better characterise the usefulness of PAH emission as a tracer of star formation, we are undertaking a programme of 3 µm narrow band imaging of a sample of nearby template galaxies covering a wide range of metallicity, star formation activity, and nuclear activity. Here we show high spatial resolution images of PAH feature emission from the central regions of the nearby starburst galaxies NGC253 and NGC1808, taken with ISAAC at the VLT-UT1. Globally, the feature emission is seen to peak on the central starburst regions of both sources. On smaller scales, however, we see no general spatial correlation or anti-correlation between the PAH feature emission and the location of sites of recent star formation, suggesting that the degree to which PAH feature emission traces starburst activity is more complicated than previously hypothesized based on results from data with lower spatial resolution. We do find spatial correlations, though, when we consider the feature-to-continuum *ratio*, which is low at the positions of known super star clusters in NGC1808 as well as at the position of the IR peak in NGC253. We take this to imply a decrease in the efficiency of PAH emission induced by the star formation, caused either by mechanical energy input into the ISM, or photoionisation or photodissociation of the PAH molecules.

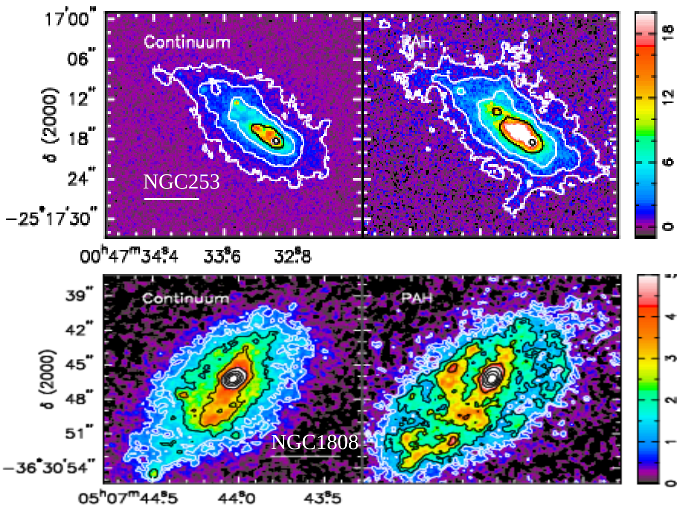


3.21 µm continuum emission (left) and 3.28 µm continuum-subtracted PAH feature emission (right) from NGC253 (top) and NGC1808 (bottom). The bars in the left panels indicate 100 pc. The images have not been scaled to a common peak level. PAH emission can be traced on the scales of the central star formation regions and super star clusters (see also the figure to the right). On larger scales the NGC253 image shows tails to the south and north, tracing the well known superwind, and providing strong support that winds can be heavily mass-loaded. This observation has important implications for enriching galaxy halos and possibly the intergalactic medium with small dust grains.

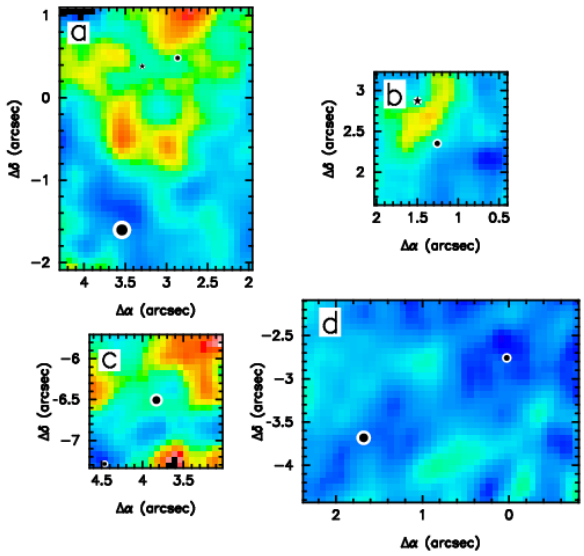


Blow-ups of regions in NGC1808. Shown as circles are the positions of young super star clusters, as observed in the K-band by Tacconi-Garman et al. (1996). In each case the K-band knot lies at a position of low feature-to-continuum ratio.

**References:**

• Tacconi-Garman, L. et al. 1996: AJ, 112, 918

*E. Sturm, L. Tacconi-Garman, M. Lehnert, D. Lutz, R. Davies, A. Moorwood*

# Dust attenuation in a galaxy like the Milky Way

The attenuation by internal dust of the stellar light produced either in the bulge or in the disk of a dusty, giant late-type galaxy like the Milky Way is investigated through Monte Carlo calculations of radiative transfer of stellar and scattered radiation made with the DIRTY code (Gordon et al. 2001). Model results for the total photometry of bulge and disk are presented.

*The extinction curve describes the combined absorption and out-of-the beam scattering properties of a mixture of dust grains of given size distribution and chemical composition in a screen geometry as a function of wavelength; the attenuation function is the combination of the extinction curve with the geometry of a dusty stellar system, in which a substantial fraction of the scattered light is returned to the line of sight.* The attenuation function ($A_\lambda$) gives the total fraction of light (in magnitudes) at the wavelength $\lambda$ escaping from the system, either directly or after (multiple) scattering by dust, in the direction to the outside observer.

For a cylindrically symmetric model of a late-type galaxy, where the dust is distributed in the exponential disk either in a homogeneous medium or in a two-phase clumpy one, $A_\lambda$ *depends on the inclination* ($i$)*, the opacity* (equal to $2 \times \tau_V$, where $\tau_V$ is the central face-on extinction optical-depth from the surface to the mid-plane of the disk in the V band)*, and the structure of the dusty interstellar medium* (ISM). Pierini et al. (2004a) investigate this through Monte Carlo calculation of radiative transfer, and show that:

- *the attenuation function is different for the bulge and disk components* (cf. Fig. 1 and 2);
- *the structure of the dusty ISM affects more the observed magnitude than the observed colour*;
- *the contribution of the scattered radiation to the total monochromatic light received by the outside observer is significant, particularly in the UV.*

Radiative transfer is fundamental to interpret the observed spectral energy distribution of a late-type galaxy at any redshift (Pierini, Gordon, & Witt 2003; Pierini et al. 2004b).

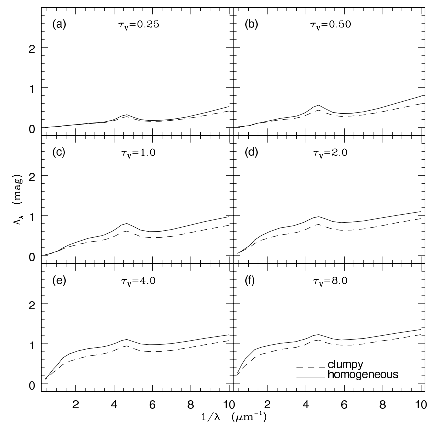


**Figure 1**: the attenuation function for the bulge of a late-type galaxy seen at $i = 0^o$ (i.e. face on).

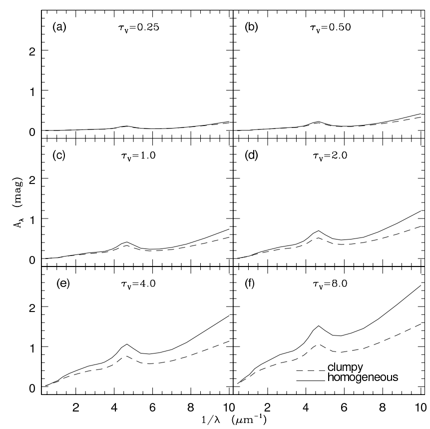


**Figure 2**: the attenuation function for the disk of a late-type galaxy seen at $i = 0^o$.


REFERENCES:

*Gordon K. D., Misselt K. A., Witt A. N., Clayton G. C., 2001, ApJ, 551, 269*

*Pierini D., Gordon K. D., Witt A. N., 2003, RMxAC, 17, 200*

*Pierini D., Gordon K. D., Witt A. N., Madsen G. J., 2004a, ApJ, in press (preprint: astro-ph/0409183)*

*Pierini D., Maraston C., Gordon K. D., Witt A. N., 2004b, MNRAS, submitted*



*D. Pierini, K. D. Gordon, A. N. Witt, G. J. Madsen*

# ERGs: dust attenuation and classification

**The extremely red galaxies (ERGs) at $1 \leq z \leq 2$ have a mixed nature. Their observed optical/near-IR colours may be reproduced by models of either old ($> 1$ Gyr), passively evolving stellar populations, or dusty starbursts with young/intermediate-age stellar populations, but also by models of the early (with a delay up to 1 Gyr), dusty, post-starburst phases of galaxy formation.**

Near-IR/optical colours like $\mathrm{I_c} - \mathrm{K} \geq 4$, significantly different from those of typical field objects, are used to select ERGs in existing deep surveys. The ERGs are held to witness either the full assembly of massive (with a stellar mass $\geq 10^{11}\ \mathrm{M_\odot}$) galaxies at high redshift ($z > 1$), or, conversely, a large amount of star-formation activity, largely enshrouded by dust. *A two-colour classification method for ERGs was proposed to distinguish between objects at $1 \leq z \leq 2$ that host either old, passively evolving stellar populations, or on-going star formation in a dusty interstellar medium* (ISM) (Pozzetti & Mannucci 2000 – PM00). Pierini et al. (2004) model old, passively evolving stellar populations (in a dusty ISM or not) plus dusty starburst and post-starburst galaxies (DSGs and DPSGs, respectively) by combining results from stellar population evolutionary synthesis models (Fioc & Rocca-Volmerange 1997; Maraston 1998) for extreme star-formation histories (young/intermediate-age stellar populations in DSGs) and from Monte Carlo computations of radiative transfer of the stellar and scattered light through different dusty media (Witt, Thronson, & Capuano 1992; Witt & Gordon 2000). As main results, Pierini et al. (2004) show that

- *the statistical significance of the PM00 method is confirmed, but this method breaks down if objects undergoing an early post-starburst phase and still retaining their dusty ISM exist at $1 \leq z \leq 2$;*
- *the interpretation of dusty ERGs is affected by potential observational biases and uncertainties on the properties of the ISM* (see Fig. 1 and 2).

REFERENCES:


*Fioc M., Rocca-Volmerange B., 1997, A&A, 326, 950*

*Maraston C., 1998, MNRAS, 300, 872*

*Pierini D., Maraston C., Bender R., Witt A. N., 2004, MNRAS, 347, 1*

*Pozzetti L., Mannucci F., 2000, MNRAS, 317, L17*

*Witt A. N., Gordon K. D., 2000, ApJ, 528, 799*

*Witt A. N., Thronson H. A., Capuano J. M., 1992, ApJ, 393, 611*


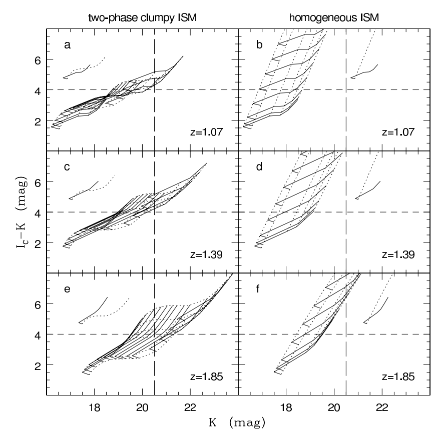


**Figure 1**: $\mathrm{I_c} - \mathrm{K}$ vs. $\mathrm{K}$ for model DSGs with a 100 Myr-burst and DPSGs, as a function of redshift, opacity ($\tau_V$), and structure of the dusty ISM. Solid or dotted lines connect models with constant $\tau_V$ or age. The behaviour with increasing age (solid line) or increasing $\tau_V$ (dotted line) is shown in each panel.

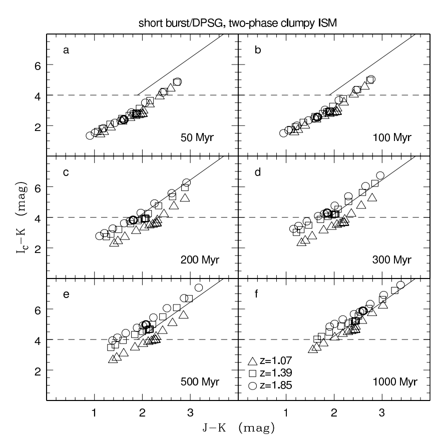


**Figure 2**: $\mathrm{I_c} - \mathrm{K}$ vs. $\mathrm{J} - \mathrm{K}$ for the models in the left column of Fig. 1. In each panel models of selected age are reproduced as triangles, squares or circles according to their redshifts, with $\tau_V$ increasing from 0.25 to 50 from the lower left to the upper right.


*D. Pierini, C. Maraston, R. Bender, A. N. Witt*

# Molecular Gas in Two Lyman Break Galaxies

With the IRAM Plateau de Bure Interferometer, we have performed sensitive searches for CO(3-2) emission from two Lyman break galaxies (LBGs). The lensed system MS 1512-cB58 (cB58) is detected at the 5.5σ level, and appears to be steadily forming stars following the Schmidt law for disk galaxies. The very dusty system Westphal-MD11 (WMD11) is not detected; its implied high LIR/L´CO ratio can be explained if its dust emission arises from a compact core radiating near its blackbody limit. The stark difference in the molecular gas content of two LBGs with comparable observed 850 μm flux densities underlines the diversity of star formation histories among objects satisfying the Lyman break selection criteria.

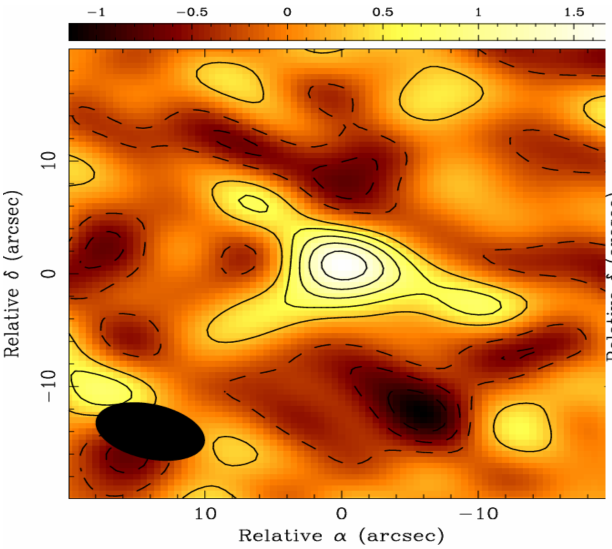


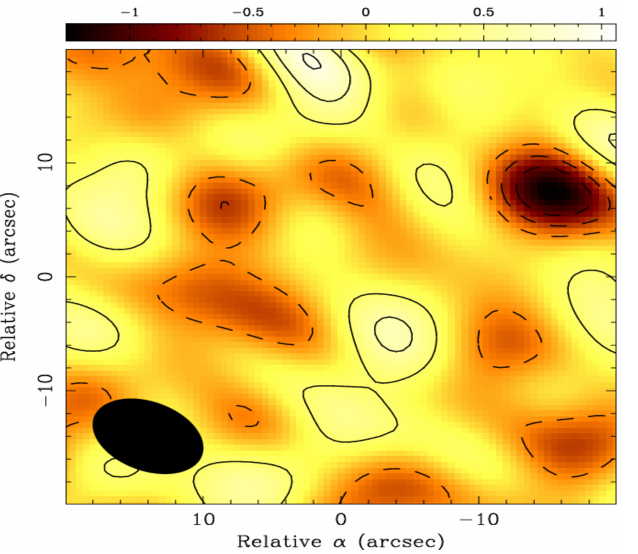


cB58 at z=2.73:

- lensed by factor ~30 (Seitz et al. 1998)
- $F_{CO(3\text{-}2)} = 0.37$ Jy km s$^{-1}$ $\Rightarrow M_{gas} \sim 6.6\times10^9\ M_\odot$
- $\Delta v_{CO} = 174$ km s$^{-1}$ $\Rightarrow M_{dyn} \sim 1.0\times10^{10}\ M_\odot$
- ~2/3 of baryons turned into stars matches enrichment to 0.4 $Z_\odot$ (Pettini et al. 2002)
- $\sigma_{SFR}$ and $\Sigma_{gas}$ follow local Schmidt law for disk galaxies

For details, see Baker et al. (2004, ApJ, 604, 125).

WMD at z=2.98:

- dusty SCUBA source (Chapman et al. 2000)
- $F_{CO(3\text{-}2)} \leq 0.11$ Jy km s$^{-1}$
- $\Rightarrow M_{gas} \leq 3.0\times10^9\ M_\odot$
- $L_{IR}/L'_{CO(3\text{-}2)}$ below blackbody limit (Solomon et al. 1997) only if $\tau_{dust}$>1 for $\lambda_{obs} \leq 850$ μm
- inferred blackbody R~300-600 pc matches sizes of local ULIRGs

For details, see Baker et al. (2004, ApJ, 613, L113).

*A.J. Baker, L.J. Tacconi, R. Genzel, D. Lutz, M.D. Lehnert*

# Detection of a compact dwarf galaxy at birth ?

We have measured the dynamical mass of the highly luminous star cluster W3 in the young merger remnant galaxy NGC 7252. The value of $8.2 \times 10^{7} M_{\odot}$ represents the highest mass being measured for an extra-galactic star cluster so far. We classify W3 with the *fundamental plane* of stellar systems. We find that W3 lies far from the most massive globular clusters and from dwarf ellipticals. Instead its structural properties are similar to compact dwarf galaxies (e.g. M32), possibly shedding light on the still mysterious nature of these objects. A previously deserted region of the fundamental plane starts to be populated.

Extreme star bursts involved in galaxy mergers produce star clusters with masses up to $10^{7} M_{\odot}$, that are suggested to evolve into globular clusters (GCs). However some objects seem to escape such prejudices, because their luminosity-estimated masses are much larger than those of the most massive GCs $\left(\approx 10^{6} M_{\odot}\right)$. **The most extreme case is W3 a star cluster in the young merger remnant NGC 7252** for which the luminous mass was estimated to be $\approx 10^{8} M_{\odot}$ (Maraston et al. 2001, **Fig. 1** for a K-band image). In order to check this value dynamically, we acquired a high-resolution spectrum with UVES mounted on the Very Large Telescope (Maraston et al. 2004, **Fig. 2**), on which we have measured the velocity dispersion and derived the stellar mass.

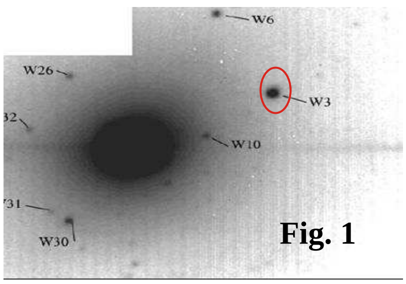


**Fig. 1**

Our result is the astonishingly high velocity dispersion of 45 km/s that, combined with the large cluster size (17.5 pc), translates into a dynamical virial mass of $8 \times 10^{7} M_{\odot}$, in perfect agreement with the luminous mass.

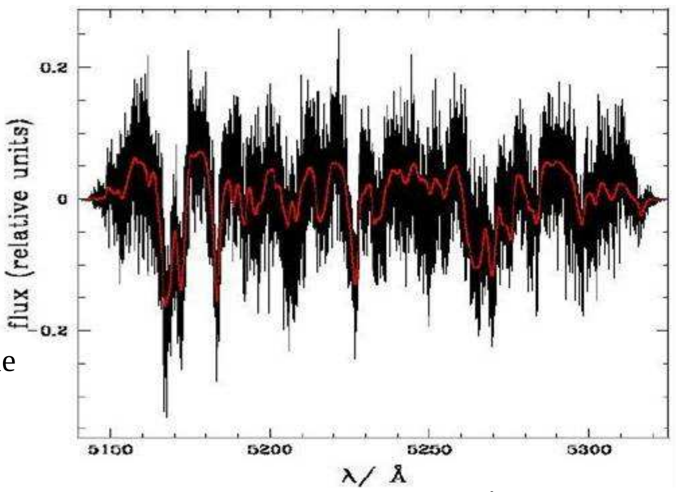


**Fig. 2**

In order to understand the nature of W3, we use the *fundamental plane* (Bender et al.1992), that connects the basic physical properties of stellar systems: the mass, the radius and the compactness (**Fig. 3**). B, E stand for bulges and ellipticals, dE for dwarf ellipticals, GC for globular clusters (G1 and wCen being the most massive GCs of the Local Group). W3 is shown as a red star, with the arrow indicating its position when aged to 10 Gyr. **W3 is too extended for its mass to be a GC, but is also too compact to be a dE. It seems more connected to the class of compact dwarf galaxies (UCDG, M32)** .

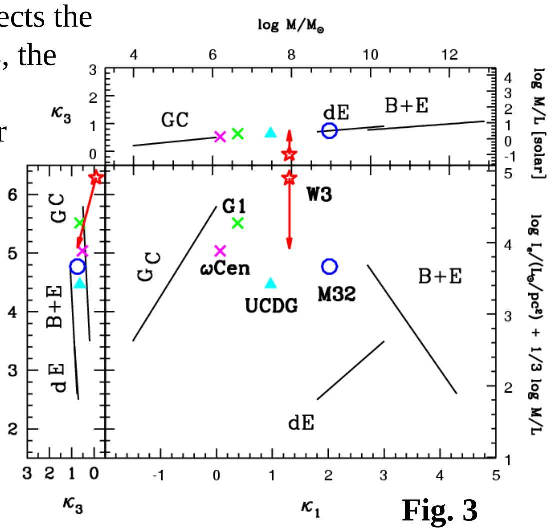


**Fig. 3**

**References:**

- Bender, R. et al. 1992, ApJ, 399, 462
- Maraston, C. et al. 2001, A&A, 300, 176
- Maraston, C. et al. 2004, A&A, 416, 467

*C. Maraston, N. Bastian, R.P. Saglia, M. Kissler-Patig, F. Schweizer, P. Goudfrooij*

# Orbital mapping of early-type galaxy dynamics

Refining Schwarzschild's (1979) orbit modelling, we construct highly accurate and fully general axisymmetric dynamical models of astrophysical bulges.

- **We extend the classical orbit sampling scheme** of the Schwarzschild code of Richstone & Tremaine (1988) and Gebhardt et al. (2000) involving now surfaces of section (SOSs) as rigorous tracers of orbital shape. Studying analytical test models we demonstrate the homogeneous representation of phase space in our orbit libraries (Thomas et al. 2004a). Figure 1 exemplifies the typical coverage of a SOS by orbits integrated for a library.
- **A newly implemented method to calculate precisely orbital phase-volumes** (Thomas et al. 2004a) allows the direct connection of orbit superpositions to distribution functions (DFs). Applications include:
- **Comprehensively comparing galaxy test models with orbit superpositions** (Thomas et al. 2004a,b) we prove the prospects of orbit libraries in the dynamical modelling of astrophysical bulges with previously unprecedented accuracy. Figure 2 illustrates how closely the predictions of orbit models match analytical calculations.
- **Our extended orbit models allow to recover the distribution functions of real galaxies**. Figure 3 presents an illustrative test calculation. See also the posters *Dark matter and stellar orbits in flattened ellipticals* and *Black Holes in Pseudobulges and Bulgeless galaxies*.

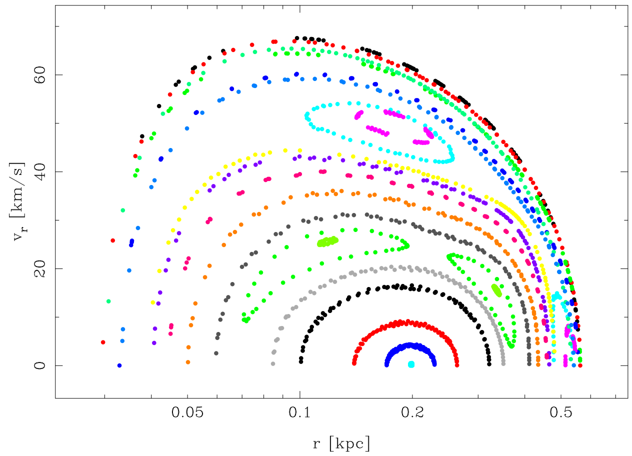


*Figure 1: A typical SOS, as included in a library: Orbital imprints of the same orbit are marked in one color. The SOS is homogeneously covered by orbits, implying an unbiased representation of phase-space by the library.*

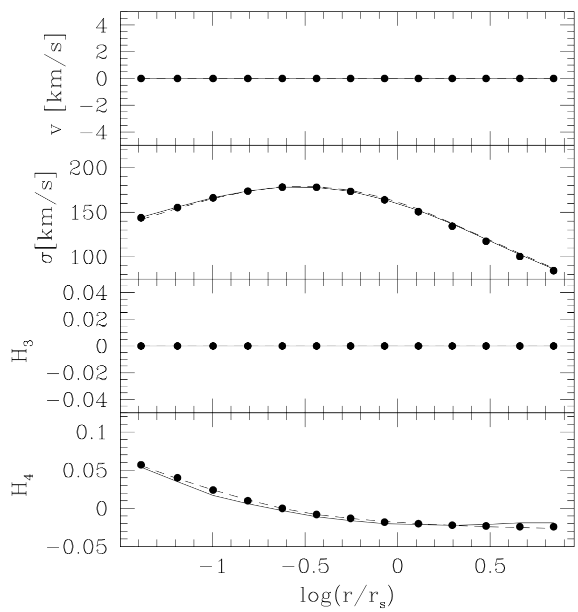


*Figure 2: Comparison of two methods to calculate projected kinematics of a spherical Hernquist model. Dots: directly from phase-space integration of the DF; lines: by an orbit library (solid/dashed: major/minor axis).*

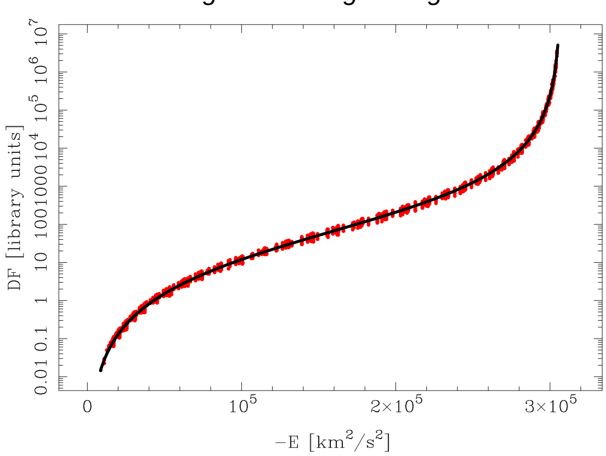


*Figure 3: Isotropic Hernquist DF (solid line) and orbital reconstruction from a fit to major and minor axes kinematic data (red dots). The fit matches with a rms of 13 % over a phase-space region covering 90% of the model's mass.*


*References:*

*J. Thomas, R. P. Saglia, R. Bender, D. Thomas, K. Gebhardt, J. Magorrian, D. Richstone, 2004a, MNRAS, 353, 391*

*J. Thomas, R. P. Saglia, R. Bender, D. Thomas, K. Gebhardt, J. Magorrian, E. M. Corsini, G. Wegner, 2004b, submitted to MNRAS*



*J. Thomas, R. P. Saglia, R. Bender, D. Thomas, N. Nowak and collaborators*

# Dark matter and stellar orbits in flattened ellipticals

We find outwardly rising mass-to-light ratios in regularized orbit models for Coma ellipticals. We achieve very good agreement between the stellar contribution to the total mass in dynamical models and in stellar population analysis of line indices, strengthening the need for dark matter to explain the remaining mass.

- **We construct regularized orbit models for a sample of flattened Coma early-type galaxies** and determine their mass composition and orbital structure. Figure 1 shows the match between orbit model and kinematic data for the E2 elliptical NGC 4807. We also plot the orbital structure of the galaxy, described by the anisotropy parameter $\beta_\vartheta$. A positive $\beta_\vartheta > 0$ in the outer parts of NGC 4807 indicates predominant radial orbits there.

- **By simulations of galaxy test models under realistic observational conditions we optimize regularization in the orbit models** (Thomas et al. 2004b). The bottom panel in Figure 1 demonstrates that a proper choice of the regularization parameter $\alpha \approx 0.02$ allows us to reconstruct internal velocity moments up to second order with an accuracy of about $\Delta = 15\%$ in the mean over 60 Monte-Carlo realizations of pseudo-data with realistic error bars.

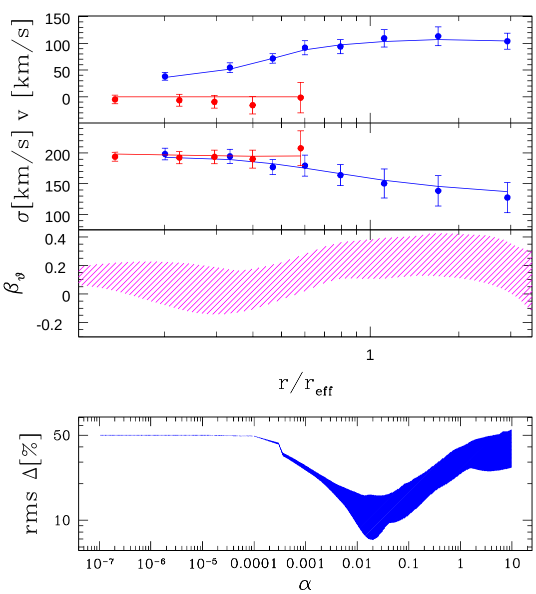


*Figure 1: Upper two panels: rotation $v$ and dispersion $\sigma$ of NGC 4807 (red/blue: major/minor axis; dots/lines: observations/best-fit model); magenta: 68 per cent confidence range of velocity anisotropy $\beta_\vartheta = 1-\sigma_\vartheta^2/\sigma_r^2$; bottom panel: accuracy of internal velocity moments as a function of regularization $\alpha$.*

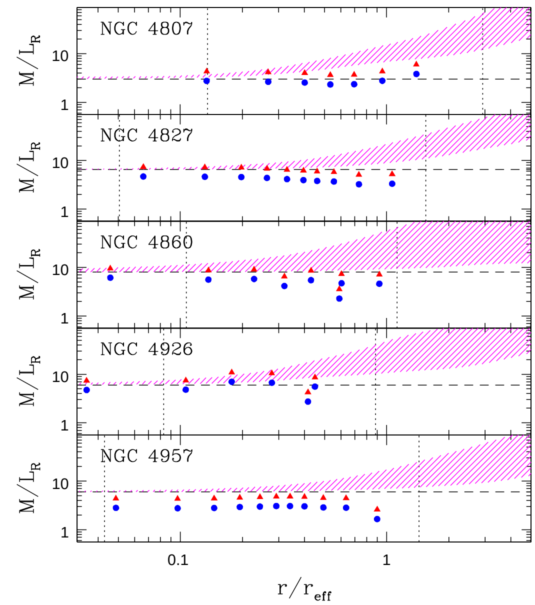


*Figure 2: Recovered mass-to-light ratios $M/L$ of 5 ellipticals in the Coma cluster. Dashed: best-fitting (projected) stellar $M/L$ in orbit models; magenta: 68 per cent confidence range of total $M/L$ in orbit models; triangles/dots: stellar $M/L$ from population analysis of line indices based on Salpeter/Kroupa initial-mass-functions. Vertical lines: spatial extent of kinematic data.*

- **We find evidence for dark matter in 5 Coma ellipticals.** As Figure 2 shows, the outwardly rising mass-to-light ratios $M/L$ exceed the stellar masses by far, indicating a dark matter halo.

- **Dynamically derived stellar masses agree well with stellar population analysis of line indices** (Maraston 1998; Thomas, Maraston & Bender 2003; see Figure 2).

*References:*

*C. Maraston, 1998, MNRAS, 310, 872*

*D. Thomas, C. Maraston, R. Bender, 2003, MNRAS, 339, 897*

*J. Thomas, R. P. Saglia, R. Bender, D. Thomas, K. Gebhardt, J. Magorrian, D. Richstone, 2004a, MNRAS, 353, 391*

*J. Thomas, R. P. Saglia, R. Bender, D. Thomas, K. Gebhardt, J. Magorrian, E. M. Corsini, G. Wegner, 2004b, submitted to MNRAS*

*J. Thomas, R. P. Saglia, R. Bender, D. Thomas, N. Nowak and collaborators*

# Large-scale ordered motion in a z=3.24 galaxy core

We present a study of the spatially resolved strong [OIII]$\lambda$5007 line emission from the z=3.24 gravitational arc behind the cluster 1E0657-56, based on 190 minutes of SPIFFI K band data. Detailed modelling of the lensing potential suggests that the galaxy center is seen in the arc core, whereas the arc consists of multiple images of peripheral regions of the same source (Mehlert et al. 2001).
Between the arc and the core, we find a velocity offset of $\sim$200 kms$^{-1}$, similar to rotation velocities of present-day massive galaxies. With a magnification factor $M$ $\sim$20, we estimate a mass of $\sim$10$^9$ M$_\odot$ within the inner kiloparsec. **This provides one of the most robust observations of small-scale ordered gravitational motion in the core of a high redshift galaxy and suggests that at least some galactic cores were already assembled by z$\sim$3.**

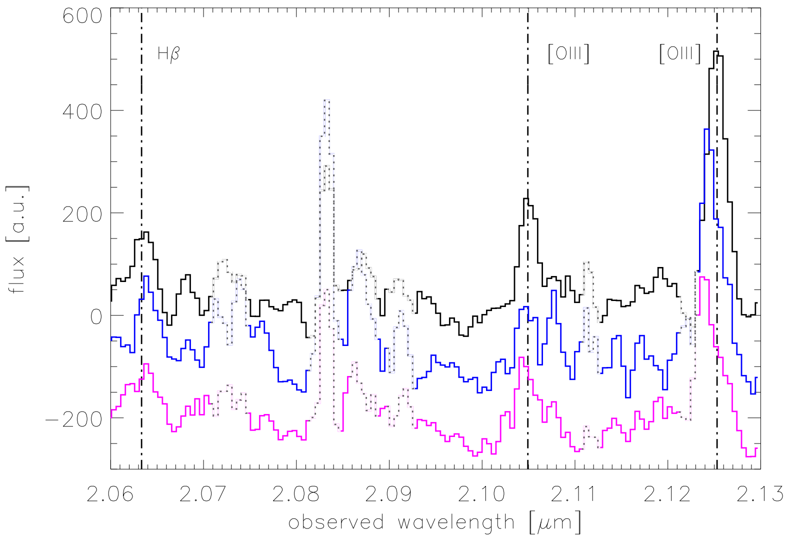


**Fig. 1:** Integrated spectra of the boxes in Fig. 2. Spectra of the arc core, box 'arc 1' and the sum of boxes 'arc 2' to 'arc 4' are shown in black, blue, and purple, respectively. The arc spectra were shifted and scaled by arbitrary amounts. Dotted gray lines indicate strong night sky line residuals.
The large [OIII]/H$\beta$ ratio indicates a low metallicity, similar to those of z$\sim$3 Lyman Break Galaxies (Pettini et al., 2001). Narrow widths and uniform line ratios in distinct regions disfavor strong AGN contribution. Velocities relative to the core are 117$\pm$19 kms$^{-1}$ (arc 1) and 213$\pm$18 kms$^{-1}$ (arc 2-4). In the arc, [OIII] is blueshifted relative to H$\beta$ by $\sim$250 kms$^{-1}$, hinting star-formation triggered outflows.

**Fig. 2:** Continuum-subtracted, combined [OIII]$\lambda$4959,5007 line image of the strongly lensed galaxy in the FORS deep field. The boxes indicate the areas from which the spectra in Fig. 1 were extracted. Contours show the rest-frame UV flux measured with FORS 1.
The inset shows the relative velocities in North-South direction, obtained from the integrated arc core emission in each slitlet. They indicate ordered motion extending over $\sim$3 seeing disks. The location (in pixels) is given on the abscissa. The vertical axis to the right of the arc core shows the origin of each data point in the image. Velocities are given in kms$^{-1}$, the reference velocity is chosen arbitrarily.

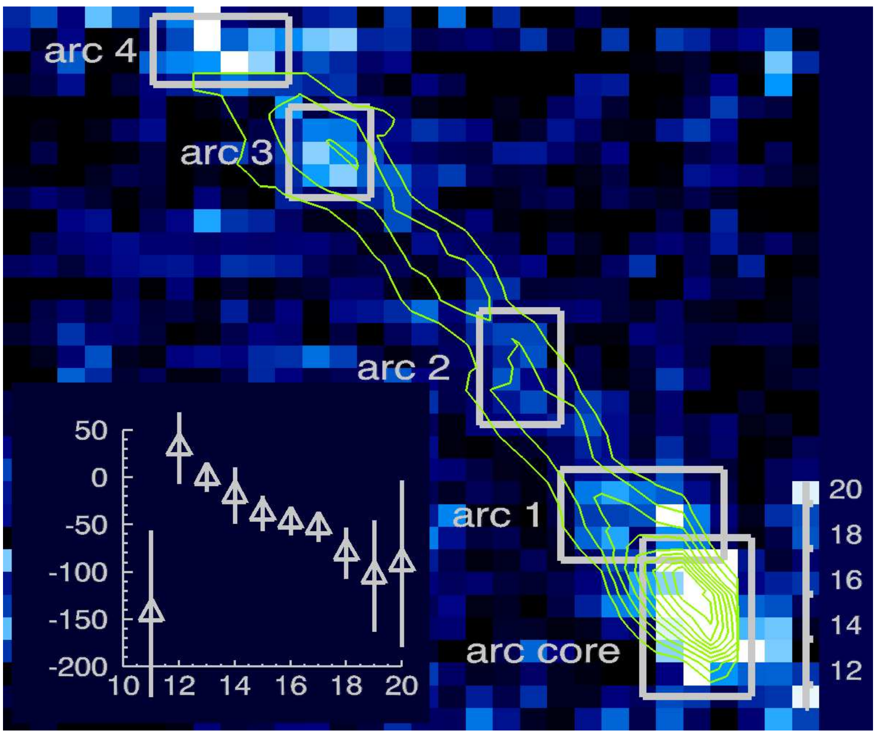


*N.Nesvadba, M.Lehnert, S.Seitz, R.Davies, F.Eisenhauer, D.Lutz, R.Genzel*

# Black Holes in Pseudobulges and Bulgeless Galaxies

**Using the newly available SINFONI instrument at the VLT, we will measure the central kinematics of pseudobulges and bulgeless galaxies, to study the properties of their supermassive black holes.**

Studies of the dynamics of stars and gas in the nuclei of nearby galaxies during the last few years have established that all galaxies with a massive (classical) bulge component contain a central supermassive black hole (SMBH) [1]. The mass $M_\bullet$ of SMBHs is closely correlated with their bulge luminosity/mass and with the bulge velocity dispersion $\sigma$ [2], which indicates a close link between bulge evolution and BH growth. Do these relations remain valid when galaxies with pseudobulges—grown via secular evolution and not via mergers as classical bulges—are considered? The few BH masses determined in pseudobulges seem to follow the $M_\bullet - \sigma$ relation, but much better statistics is required to draw any robust conclusions. Furthermore the knowledge about central black holes in bulgeless galaxies is still scarce. Do they contain black holes at all, and if, what is their mass? Bulgeless galaxies have not experienced major merger episodes and secular evolution processes have not yet become significant, so these galaxies might be the hosts of seed black holes in their earliest evolutionary stage.

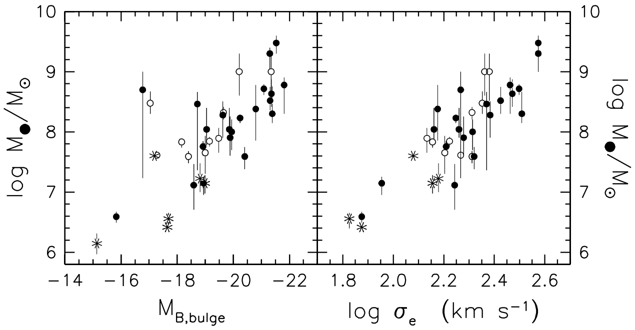


*Fig. 1: The $M_\bullet - M_{B,\mathrm{bulge}}$ (left) and $M_\bullet - \sigma_e$ (right) correlations for elliptical galaxies (filled circles), bulges (open circles) and pseudobulges (stars) (from [3])*

*Fig. 2: NGC 4826 is a galaxy with a pseudobulge. Pseudobulges are mostly found in late-type galaxies and are physically unrelated to ellipticals. The pseudobulge of NGC 4826 shows a rapid rotation $V$. $V/\sigma$ is well above the oblate line describing rotationally flattened isotropic spheroids in the $V/\sigma - \epsilon$ diagram (see [6] for a review).*

*Fig. 3: NGC 300 is a bulgeless Sd galaxy located in the Sculptor group. In the center there is a bright nucleus, i.e. a compact star cluster.*

We will observe the central regions of a number of bulgeless and pseudobulge galaxies using SINFONI (**SIN**gle **F**aint **O**bject **N**ear-IR **I**nvestigation) at ESO VLT. This recently commissioned instrument consists of the NIR ($1 - 2.5\ \mu$m) integral field spectrograph SPIFFI [4], the adaptive optics (AO) module MACAO, and the laser guidestar PARSEC and provides ideal means to measure stellar kinematics and therewith the BH mass in galaxy centers. Compared to STIS this new spectrograph has a larger collecting power, a higher resolution ($R \leq 4500$) and is able to penetrate dust, which makes it particularly suitable to observe late-type spiral galaxies. The preoptics of SINFONI allows to choose a field of view of $8'' \times 8''$, $3'' \times 3''$ or $0.8'' \times 0.8''$, which is sliced into $32$ slitlets of $64$ pixels each, resulting in $32 \times 64$ spectra.

We will derive the line-of-sight velocity distributions with the FCQ program [5] and perform the dynamical modelling based on the Schwarzschild orbit superposition method (see the poster "Orbital mapping of early-type galaxy dynamics").

**References**


[1] Richstone et al. 1998, Nature, 395, A14.
[2] Gebhardt et al. 2000, ApJ, 539, L13.
[3] Kormendy&Gebhardt 2001, AIPC, 586, 363.
[4] `http://www.mpe.mpg.de/SPIFFI/`.
[5] Bender 1990, A&A, 229, 441.
[6] Kormendy&Kennicutt 2004, ARA&A, 42, in press.


*N. Nowak, R. P. Saglia, R. Bender, J. Thomas, R. Genzel and the MPE IR group*

# Growing Black Holes: Tidal Disruption of Stars

Giant-amplitude X-ray flares from the centers of optically *non-active* galaxies were discovered and followed-up with the observatories *ROSAT*, *XMM*, *Chandra* and *HST*. These events, representing the highest amplitudes of variability ever recorded among galaxies, are interpreted in terms of flares of stars tidally disrupted by supermassive black holes at the centers of these galaxies; a process long predicted by theory (e.g., Rees, 1988, Nature 333, 523).

Three major feeding mechanisms have been studied in the context of black hole growth: accretion, black hole - black hole mergers, and tidal capture/disruption of stars. While there is ample evidence that accretion is ongoing in active galaxies, observational evidence for the two other processes remained elusive for many years. Given the intense theoretical work on, and importance of, these latter two processes, it is of great interest to see whether such events do occur in nature, how frequent they are, and which properties they show (on black hole mergers, see accompanying poster on NGC 6240).

With *ROSAT* several X-ray flares (e.g., Komossa & Bade 1999) from the directions of *optically inactive* galaxies (e.g., Gezari et al. 2003) were discovered, reaching quasar-like X-ray luminosities. Follow-up observations of RXJ1242-1119, the galaxy which flared most recently, revealed an amplitude of variability of a factor 1500 and we detected an \`afterglow´ of the flare located at the *center* of the galaxy (Komossa et al. 2004, Komossa et al., in prep.). With *XMM*, we could measure for the first time a post-flare high-energy spectrum in form of an unabsorbed powerlaw. Further flaring galaxies followed up with *Chandra* (Halpern et al. 2004) varied similarly strongly, by factors of 1000 (NGC 5905) and 6000 (RXJ1624+75). Such dramatic variability has never been observed before from galaxies. With the wealth of new data we now have excellent evidence that these events represent flares from stars tidally disrupted by supermassive black holes at the centers of the flaring galaxies.

These observations, and the presently ongoing search for new flares, are of great relevance in the context of black hole growth and galaxy evolution. In the future, flare studies may also open up a new window to study the general relativistic effects of precession of the stellar debris in the Kerr metric. They may also provide us with a new diagnostic of the circum-nuclear medium of these galaxies, since the bright flares will excite line-emission in surrounding gas .

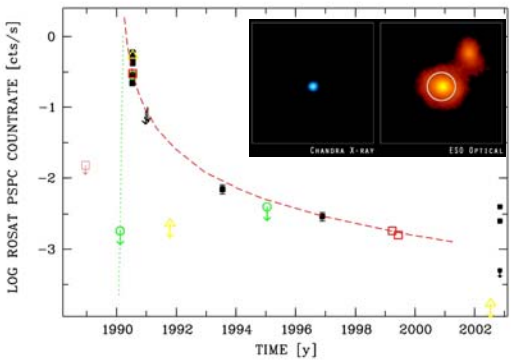


*Fig. 1*: Artist‘s sketch of the disruption and subsequent accretion of a star by a supermassive black hole. The accretion of the stellar debris causes a luminous flare of electromagnetic radiation. *Fig. 2*: Joint X-ray lightcurve of all flare events (shifted to the same $t_{max}$). The inset shows the optical image of RXJ1242-1119 which is in a pair (right) and *Chandra* detection of the ´afterglow´ emission of the once bright flare (left).


**References:**
- Gezari S., Halpern J., Komossa S., et al. 2003, ApJ 592, 42
- Komossa S., Halpern J., Hasinger G., et al. 2004, ApJ 603, L17
- Komossa S., Bade N., 1999, A&A 343, 775
- Halpern J., Gezari S., Komossa S., 2004, ApJ 604, 572



*S. Komossa, G. Hasinger, P. Predehl, et al.*

# Infrared vs. hard X-rays: A test of AGN unification

**Comparing the mid-infrared continuum of AGN to the absorption corrected X-ray emission, we do not see the strongly anisotropic mid-infrared emission predicted by ‚torus‘ models.**

Tests of this prediction have been hindered by the often large host contamination of IRAS data and by the scarcity of high resolution mid-IR imaging. As a new approach, we have used spectral decomposition to separate the 6μm AGN continuum from the host emission in the ISO low resolution spectra of 71 active galaxies and compare the results to observed and intrinsic 2-10keV hard X-ray fluxes. We find a correlation between mid-infrared luminosity and absorption corrected hard X-ray luminosity, but the scatter is significantly larger than previously found with smaller statistics. Main contributors are likely variations in the dust geometry, and AGN variability in combination with non-simultaneous observations. There is no significant difference between Type 1 and Type 2 objects in the average ratio of mid-infrared and hard X-ray emission. This is inconsistent with the most simple version of a unified scheme in which an optically and geometrically thick torus dominates the mid-infrared AGN continuum. Most probably, significant non-torus contributions to the AGN mid-IR continuum, for example from dust inside the Narrow Line Region, are masking the expected difference between the two types of AGN. Alternatively, radial density profile modifications to the clumpy torus models of Nenkova et al. (2002) may suggest that the anisotropy of the torus emission proper is smaller than commonly assumed.

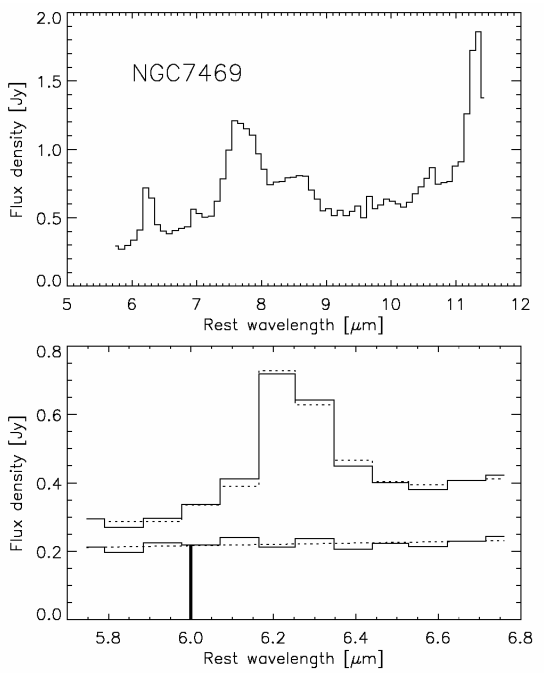


Spectral decomposition used to separate the AGN mid-infrared continuum from the host galaxy's aromatic emission features, shown here as an example for the Seyfert 1 galaxy NGC 7469 with its well-known circumnuclear starburst. We have applied this method to many AGN spectra in the ISO database.

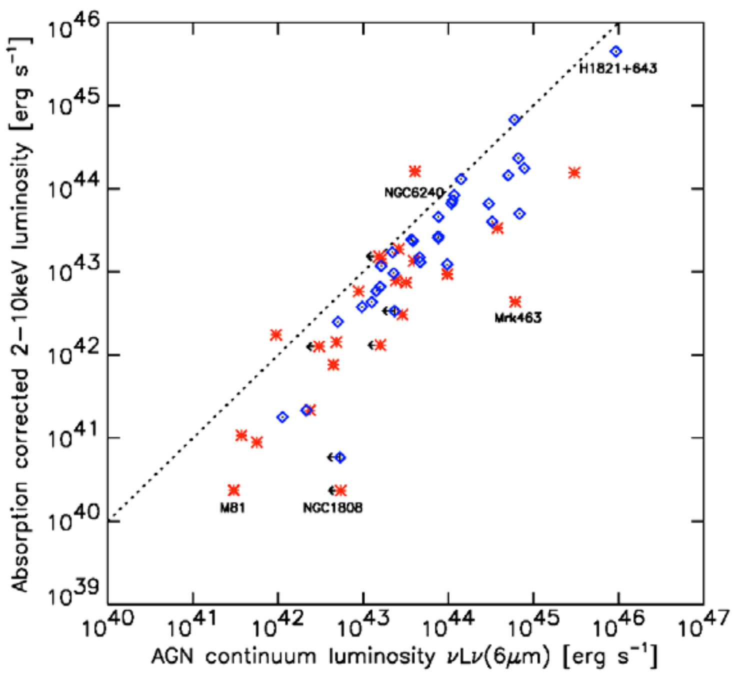


Comparison of absorption corrected hard X-ray luminosity and mid-infrared AGN continuum luminosity for a sample of Type 1 (blue diamonds) and Type 2 (red asterisks) AGN. The two quantities correlate well over a large range of luminoisities, and there is no evidence for a systematic difference in their ratio between Type 1 and Type 2 objects. The dotted line indicates slope 1, it is not a fit.

**References:**
- Lutz, D., Maiolino, R., Spoon, H.W.W., Moorwood, A.F.M. 2004, A&A, 418, 465
- Nenkova, M., Ivezic, Z., Elitzur, M. 2002, ApJ, 570, L9

*D. Lutz*

# Search for the 4.7μm CO band: AGN tori vs. shells?

In order to constrain the properties of dense and warm gas around active galactic nuclei, we have searched Infrared Space Observatory spectra of local active galactic nuclei (AGN) for the signature of the 4.7μm fundamental ro-vibrational band of carbon monoxide. Low resolution ISOPHOT-S spectra of 31 AGN put upper limits on the presence of wide absorption bands corresponding to absorption by large columns of warm and dense gas against the nuclear dust continuum. High resolution (R~2500) ISO-SWS spectra of NGC 1068 detect no significant absorption or emission in individual lines, to a 3σ limit of 7% of the continuum.

The limits set on CO absorption in local AGN are much lower than the recent Spitzer Space Telescope detection (Spoon et al. 2004) of strong CO absorption by dense and warm gas in the obscured ultraluminous infrared galaxy IRAS F00183-7111, despite evidence for dense material on parsec scales near an AGN in both types of objects. This suggests that such deep absorptions are not intimately related to the obscuring `torus' material invoked in local AGN, but rather are a signature of the peculiar conditions in the circumnuclear region of highly obscured infrared galaxies like IRAS F00183-7111. They may reflect fully covered rather than torus geometries.

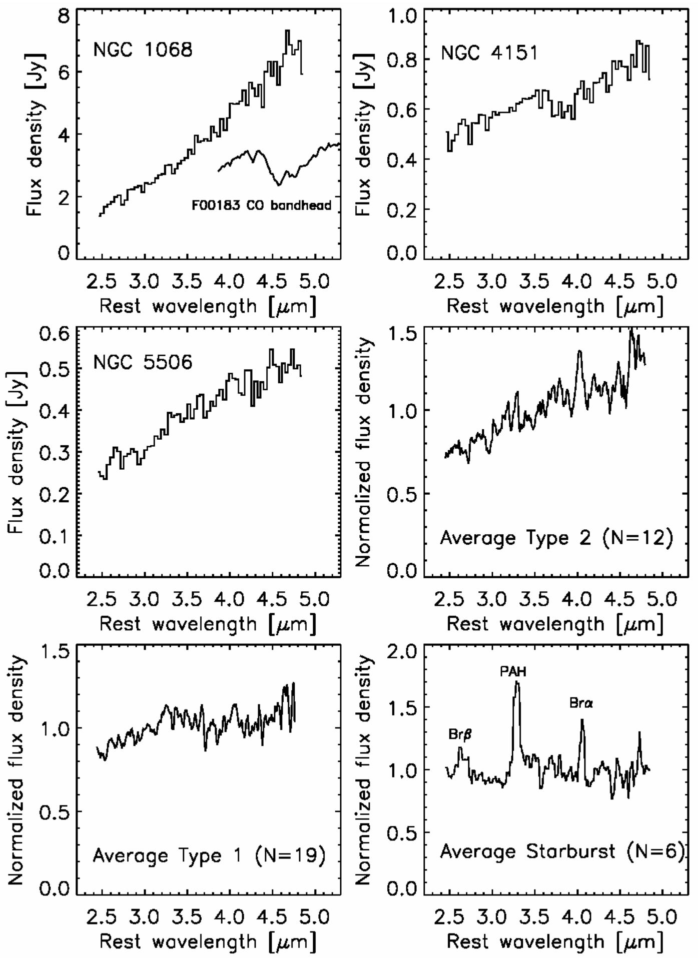


2.5-5μm Infrared Space Observatory spectra of several bright local AGN, together with average spectra of Type 2 AGN, Type 1 AGN, and starbursts.
The insert in the top left panel shows the detection of a strong absorption due to a large column of warm CO in the obscured ULIRG IRAS F00183-7111 (Spoon et al. 2004).
The spectra of local AGN do not show this feature, despite evidence for dense material on pc scales in both cases.


**References:**
- Lutz, D., Sturm, E., Genzel, R., Spoon, H.W.W., Stacey, G.J., 2004, A&A Letters, in press
- Spoon, H.W.W., Armus, L., et al. 2004, ApJS, in press (Spitzer Special Issue)



*D. Lutz, E. Sturm, R. Genzel*

# Exploring the central kpc in Seyfert galaxies

Studying a complete, local ($z<0.1$), X-ray flux limited (ROSAT PSPC countrate $>$0.3 cts/sec) sample of 93 AGN (Seyfert 1), we find relations between radio, optical, X-ray NUCLEAR emission and mass of the black hole (BH) (Fig. 1 and 2: see also Salvato, Greiner & Kuhlbrodt, 2004).

The X-ray nuclear luminosity has been computed using the flux measured by ROSAT in the 0.5-2 keV range (Schwope et al. 2000). Radio data are obtained from FIRST public catalogue at 1.4 Ghz while optical luminosity of the accretion disk is obtained fitting a 2 dimensional model of a point source and a bulge + disk component to R band images of the galaxies. Bulge luminosities are transformed in BH masses as in McLure & Dunlop 2002.

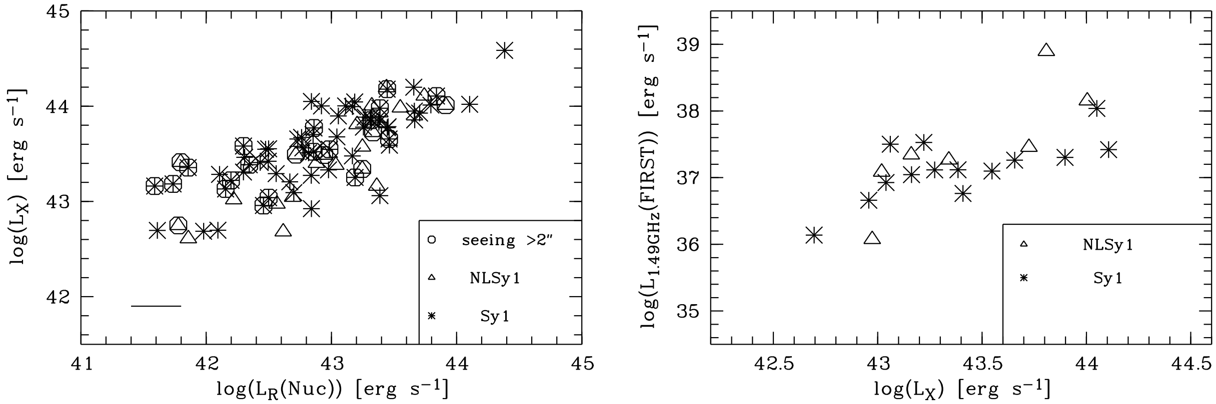


**Fig. 1** *Left:Relation between optical and X-ray nuclear luminosity with expected error bar for optical measurement at bottom-left. Right: relation between X-ray and radio continuum emission (right). For details see Salvato et al. 2004.*

The correlations between the nuclear radio, X-ray and optical luminosity may have their origin in the electron corona surrounding the accretion disk. The electron temperature depends primarily on the accretion rate and disk temperature. Moreover, the temperature and density of the corona determine the efficiency of the Compton scattering, and thus directly the slope and power of the X-ray spectrum. A change in the accretion rate would not only lead to a varying optical emission, but via the corona also to a varying X-ray and possibly radio emission.

In microquasars, Rau & Greiner (2003) have found a similar correlation between the strength of the radio emission and the X-ray power law slope. Adopting this similarity, one could argue that the core radio emission in Seyfert galaxies traces matter outflow from the central black hole. Objects with higher activity at X-ray wavelengths, i.e. higher accretion rate, therefore exhibit higher mass outflow from their central engine, thus implying a larger radio flux. Support to this idea also come from BH binaries studies (Gallo et al. 2003) and supermassive BHs (Merloni et al. 2003).

The optical luminosity of the accretion disk is also correlating with the BH mass (Figure to the right). The solid line indicates the predicted relationship for an optically thick accretion disk around a non rotating BH (Shakura & Sunyaev 1973) where, for a given BH mass, the R-band flux depends on the temperature (and thus on the accretion rate) of the objects $\dot{M} = 0.1\dot{M}_{Edd}$ . The curvature of the line is a measure of the differing bolometric correction for the different BH mass (and thus temperature).

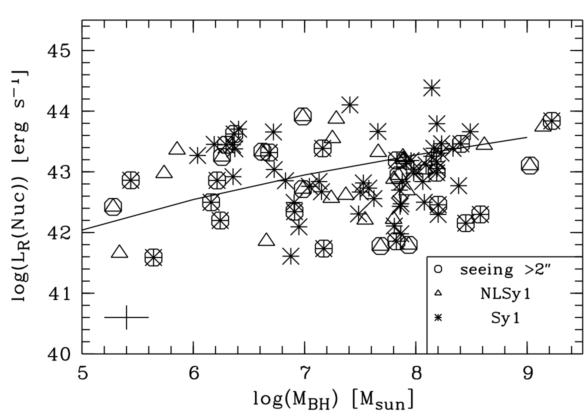



**References:** Gallo et al. 2003, MNRAS, 344,60; McLure & Dunlop, MNRAS, 331, 795; Merloni et al. 2003, MNRAS, 345, 1057; Salvato et al. 2004, ApJL, 600, L31; Schwope et al. 2000, Astron. Nach., 321, 1; Shakura & Sunyaev, 1973, A&A, 24, 337; Rau & Greiner, 2003, A&A, 397,711



*M. Salvato, J. Greiner, B. Kuhlbrodt*

# *XMM-Newton* observations of NLS1

Narrow-line Seyfert 1 galaxies (NLS1) offer an extreme view of AGN behaviour, and understanding these enigmatic objects will lead to an enhanced awareness of the AGN phenomenon in general. **Detailed analyses of *XMM-Newton* observations of NLS1 demonstrate that NLS1 may be the best sources to study relativistic effects close to the supermassive black hole.**

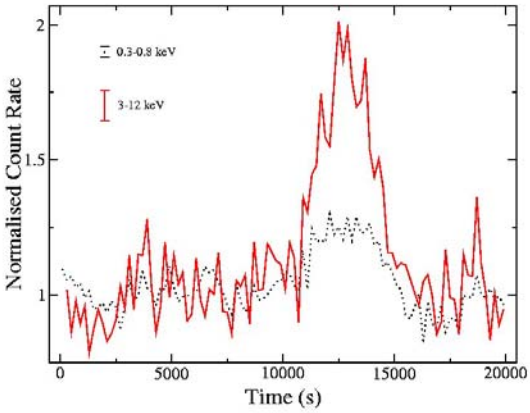


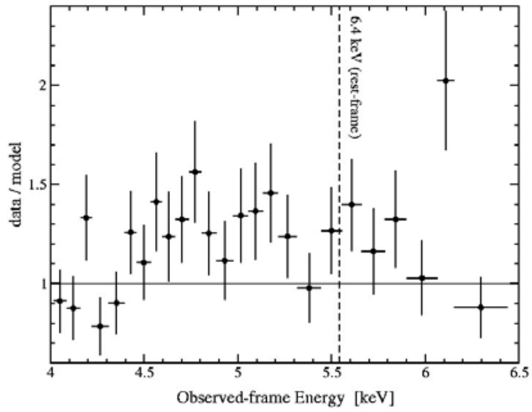


I Zw 1 displayed a significant *hard* X-ray flare (upper left panel). A similar hard flare was also observed in another NLS1, NAB 0205+024. Interestingly, the spectrum of NAB 0205+024 showed excess emission significanly redward of the expected 6.4 keV iron emission line (upper right panel). The combination of timing and spectral properties suggest illumination of a narrow annulus of the disc by a X-ray flare located close to the black hole (2004, A&A, 417, 29; astroph/0408507).

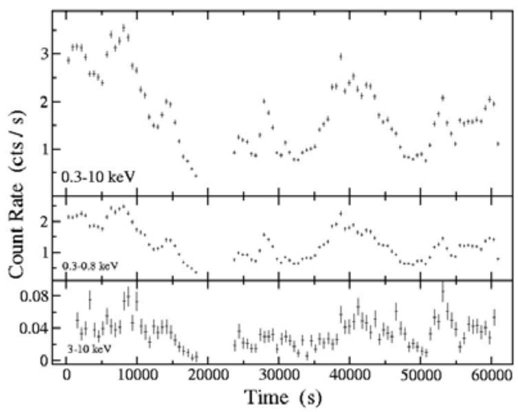


IRAS 13224-3809 presented a dramatic X-ray light curve (left panel), with persistent and rapid variability in all energy bands and on all time scales > 60s. In addition, alternating lags were detected between the high and low-energy bands, as well as evidence for flux-induced spectral variability (2004, MNRAS, 347, 269).

The very luminous quasar, PHL1092, exhibited the extreme variabilty that was observed previously with *ROSAT*. In addition, this most sensitive broad-band observation revealed spectral curvature in the 2-10 keV band (right panel), indicating partial covering or light bending effects (2004, MNRAS, 352, 744).

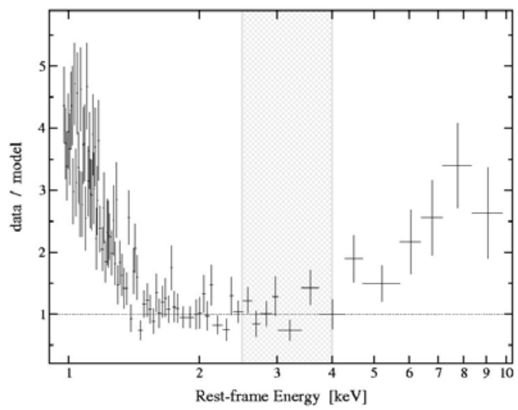


*L. C. Gallo, Th. Boller, A. C. Fabian, W. N. Brandt*

# Sub-mm detection of a high-z Type 2 QSO

- **We report on the first SCUBA detection of a Type 2 QSO at z=3.660 in the Chandra Deep Field South.**
- **The overall photometry (from the radio to the X-ray band) of this source is well reproduced by the SED of NGC6240.**
- **Its sub-mm (850 $\mu$m) to X-ray (2 keV) spectral slope ($\alpha_{\rm SX}$) is close to the predicted value for a Compton-thick AGN in which only $1\%$ of the nuclear emission emerges through scattering.**
- **We derive a SFR=550–680 M$_\odot$/yr and an estimate of the dust mass, M$_{\rm dust}$ $= 4.2 \times 10^8$ M$_\odot$.**

### Spectral energy distribution

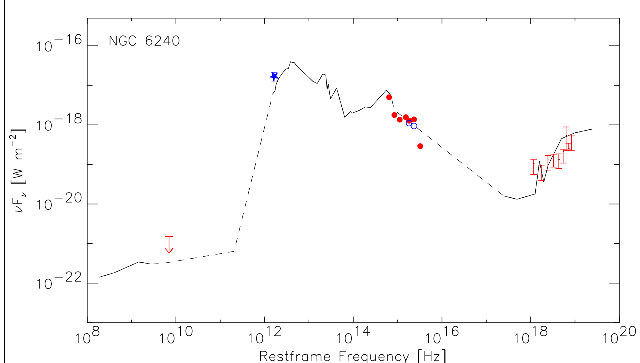


Detections and upper limits for CDFS-263 plotted over the SED of NGC 6240. The solid line shows where the photometry is available while the dashed line is where the template is extrapolated. The CDFS-263 data have been shifted to the rest frame. The star symbol shows the measured SCUBA ux.

CDFS-263 is a strong candidate for an AGN in the initial phase (before the X-ray absorbed phase ) described by Page et al. (2004) that corresponds to the main growth period of the host galaxy spheroid. It is a luminous X-ray source (L$_{\rm X}$ $> 10^{44}$ erg s$^{-1}$) with high X-ray absorption (N$_{\rm H}$ $> 10^{23}$ cm$^{-2}$) and detected in the sub-mm, S$_{850}$ $= 4.8 \pm 1.1$ mJy.

### Sub-mm to X-ray spectral flux

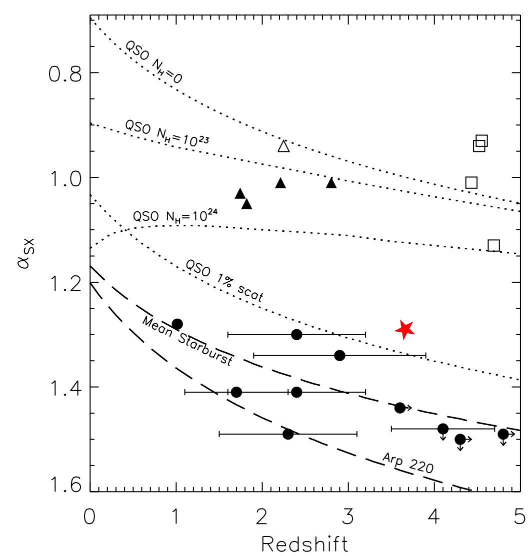


CDFS-263 yields a value of $\alpha_{\rm SX} = 1.29$ (star symbol). This value is incompatible with an unabsorbed AGN. One way to obtain this value of $\alpha_{\rm SX}$ is a sub-mm ux due to starburst activity plus an absorbed AGN in the center of the host galaxy that accounts for the X-ray emission, which is higher than what expected for a starburst galaxy alone.

For comparison we report in the gure other X-ray selected sources with sub-mm data measurements from the literature: Alexander et al. (2003) (circles); Page et al. (2001) ( lles triangles); Page et al. (2004) (empty triangles).

*V. Mainieri, I. Lehmann, I. Matute, G. Hasinger*

# A large sample of quasars observed with XMM-Newton

**The X-ray spectral analysis of 21 low redshift quasars (narrow line, radio-quiet and radio-loud) observed with XMM-Newton EPIC are reported *(Porquet et al. 2004, A&A, 422, 85)*. All sources are Palomar Green quasars with redshift between 0.05 and 0.4 and have low Galactic absorption along the line-of-sight.**

In Active Galactic Nuclei (AGN), the analysis of spectral X-ray features help us to probe the central regions of these powerful objects:

- The so-called soft excess seen below 2-3 keV is thought to be the high energy part of the optical-UV "big blue bump" extending down to 1 μm, which contains a large fraction of the bolometric luminosity. Soft X-ray excesses were detected for most AGN with ROSAT (e.g., Brinkmann 1992, MPE report 235, 143). Current interpretations of the soft excess range from direct thermal emission from the accretion disk to reprocessing of harder radiation absorbed in the thin disk.
- Emission and/or absorption features (mainly in the soft X-ray range, i.e. 0.1-2 keV) are observed. They are attributed to the warm absorbing-emitting medium (Warm Absorber) supposed to be located between the Broad Line Region and the Narrow Line Region (e.g., Porquet et al. 1999, A&A, 341, 58).
- The Fe Kα emission line observed in the 6-7 keV energy range is also an important spectral diagnostic tool to probe dense matter from the inner disk (e.g., Tanaka et al. 1995, Nature, 375, 659) to the Broad Line Region and the molecular torus (e.g., Reeves et al. 2001 A&A, 365, L134).

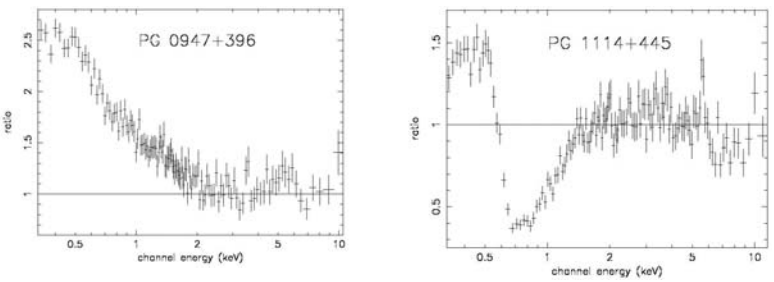


Figure 1: Data/model ratios of an absorbed power law in the 2-5 keV (observer frame)

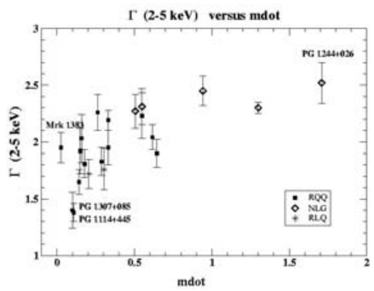


Figure 2: Correlation between $\Gamma_{2\text{-}5\ \mathrm{keV}}$ and the accretion rate.

## Main results:

- A significant majority of these quasars (90%, 19/21) exhibit a significant soft excess below ~ 1-1.5 keV (e.g., PG 0947+396; figure 1, *left*), except two objects showing a strong deficit due to the presence of a warm absorber: Izw1, PG 1114+445 (figure 1, *right*).
- Contrary to previous studies with ASCA and ROSAT (lack of soft response and limited spectral resolution, respectively) , the presence of absorption features near 0.6-1 keV is common in this sample (~50%).
- Significant detections of Fe Kα emission lines in at least twelve objects. Highly ionized lines tend to be found in the quasars with the steepest X-ray spectra.
- A strong correlation exists between the soft and hard X-ray continuum power law and the optical Hβ width, as well as with the accretion rate (Fig. 2). Soft and hard X-ray photon indices are strongly correlated as well, i.e. the steepest soft X-ray spectra correspond to the steepest hard X-ray spectra. We propose that a high accretion rate and a smaller black hole mass is likely to be the physical driver responsible for these trends.

*D. Porquet, J.N. Reeves, W. Brinkmann, P. O'Brien*

# Fe Kα lines in AGN observed with XMM-Newton

**Fe Kα fluorescent lines detected in X-rays near 6-7 keV are powerful diagnostics to probe the central region of Active Galactic Nuclei (AGN) which harbors a supermassive black hole ($10^6$-$10^9$ solar masses). Thanks to XMM-Newton and its unprecedented high sensitivity up to 12 keV, detailed and various line characteristics (e.g., energy, profile, intensity, shift) are detected.**

Here are reported the XMM-Newton observations and analysis of the Fe Kα fluorescent lines in three AGN: A radio-quiet quasar Q0056-363 *(Porquet & Reeves 2003, A&A, 408,119)*, a Narrow-line Seyfert 1 PG 1402+261 (*Reeves, Porquet & Turner 2004, ApJ, in press*) and an intermediate Seyfert 1.8 ESO 113-G010 (*Porquet et al. 2004, A&A, in press*).

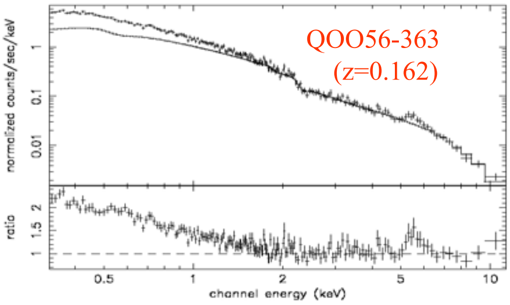


Figure 1: PN spectrum of Q0056-363 (observer frame). A power-law has been fitted to the 2.5-5 keV data and extrapolated to lower and higher energies.

Figure 1 shows the PN spectrum of Q0056-363. A broad, strong soft X-ray excess is seen below about 2 keV, and more interestingly a strong Fe Kα line at 6.4 keV (quasar frame). This line, formed in a plasma where iron is moderately ionized, has an equivalent width of ~ 250 eV, and a velocity width of ~ 25,000 km $s^{-1}$. Q0056-363 is presently the most luminous AGN known to exhibit such a broad and intense line profile from near neutral iron.

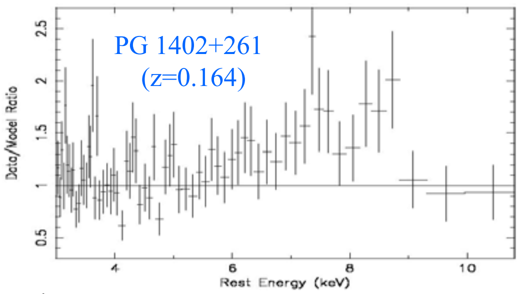


Figure 2: The iron line profile of PG1402+261 showing the ratio of the PN data to a broken power law continuum fit (quasar rest-frame).

Figure 2 shows the PN spectrum of PG 1402+261. The feature can be modeled by an unusually strong equivalent width (~2 keV) and a very broad (FWHM velocity of 110,000 km $s^{-1}$) iron Kα emission line. The line centroid energy at 7.3 keV appears blue-shifted with respect to the iron Kα emission band between 6.4-6.97 keV, whilst the blue-wing of the line extends to 9 keV.

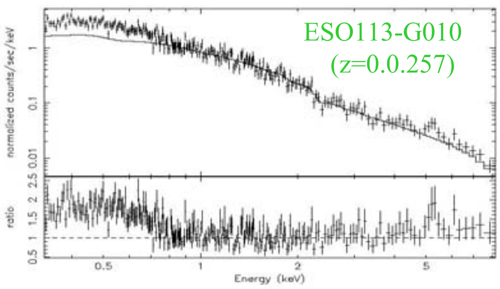


Figure 3: PN spectrum of ESO 113-G010 (z=0.0257, observer frame). A power law has been fitted to the 1-4 keV data and extrapolated to lower and higher energies.

Figure 3 shows the PN spectrum of ESO 113-G010. It shows a soft excess below 0.7 keV and more interestingly a narrow emission Gaussian line at 5.4 keV (quasar rest-frame), most probably originating from a red-shifted lines, ruling out a strong blue-wing to the line profile. The line is detected at 99% confidence from performing Monte Carlo simulations.

The line energy could indicate either emission from relativistic (0.17-0.23 c) ejected matter moving away from the observer, or by the emission from a small, localized hot-spot on the disk, occurring within a fraction of a complete disk orbit.

*D. Porquet, J.N. Reeves, T.J. Turner*

# Multifrequency Observations of the Gamma-Ray Blazar 3C 279 in Low State

**We detected the blazar 3C 279 with INTEGRAL/IBIS at hard X-ray energies (20 to 80 keV) at a time when it showed the lowest optical flux during the last 10 years. This observation provides new constraints for the modeling of 3C 279.**

The prominent Gamma-Ray blazar 3C 279 was observed by INTEGRAL for 300 ksec between June 1 and 5, 2003. The INTEGRAL observation was organized as a multifrequency campaign and therefore was supplemented by simultaneous observations in radio and mm bands, in near-IR and optical bands, and in X-rays by a 5 ksec Chandra observation.
The measured optical flux shows that 3C 279 was measured in the lowest activity state of the last decade (Fig. 1). IBIS/ISGRI detected the blazar at hard X-rays at the 6σ level (Fig. 2). The derived multifrequency spectrum shows the typical two-hump shape, i.e. synchrotron emission at low – and inverse-Compton emission at high energies. The comparison to a high-state spectrum (Fig. 3) reveals a new result: despite the large differences in the optical flux, the hard X-ray flux is close to the high-state measurement. This provides new constraints for the modeling of 3C 279.

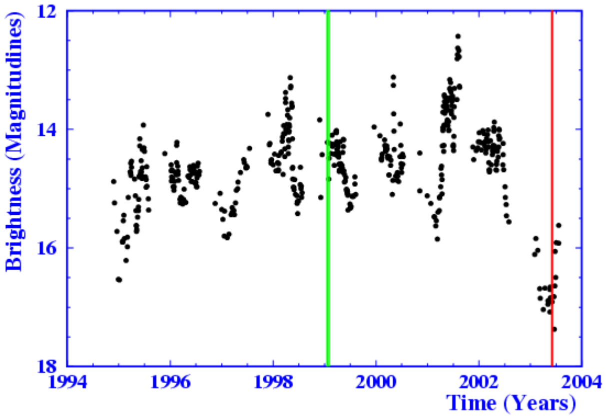


Fig. 1: Longterm R-band light curve of 3C 279 during the last decade. The red line is the observation time of INTEGRAL in 2003, and the green line corresponds to a Gamma-ray high state observation in 1999.

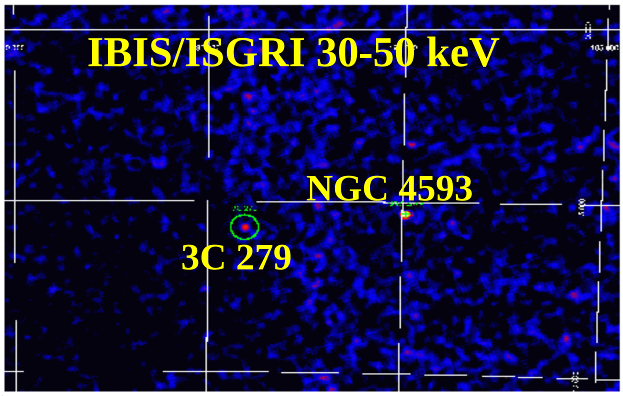


Fig. 2: The IBIS/ISGRI experiment detected 3C 279 between 20 and 80 keV with a significance of 6.6 σ., and the Seyfert galaxy NGC 4593 at 11.6σ. The spectrum shows a power-law shape (α: 1.9 ± 0.4).

Fig. 3: The multifrequency spectrum of 3C 279 in 2003 during optical low-state (red) is compared to a high-state measurement in 1999 (green). The new observational fact is, that despite the large difference in optical flux, the hard X-ray flux is close to the high-state measurement. The optical synchrotron flux is suppressed, but the SSC flux at hard X-rays is weakly affected. This provides a new constraint for the modeling of 3C 279.

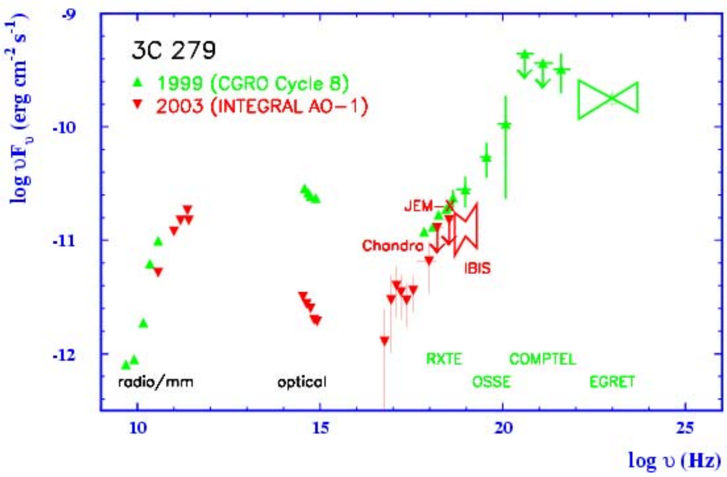


**References:**
• T. Balonek, 2004, priv. comm.
• W. Collmar, M. Böttcher, V. Burwitz, et al., 2004, ESA SP-552, in press

*W. Collmar, V. Burwitz, S. Komossa, P. Kretschmar, K. Pottschmidt, et al.*

# Acceleration in Relativistic Pair-Reconnection

Three-dimensional numerical simulations of reconnection under suppression of Hall effects have been performed under the assumption of thin current layers and for large systems. It is found that reconnection sets on independent of the existence of Hall effects. The onset is very fast with many x-points developing along the current layer and very strong particle acceleration up to substantially relativistic energies $\gamma \sim 100$ at the end of the simulation in our case which can be scaled to astrophysical conditions.

Collisionless reconnection generates a chain of magnetic X-points (Figure 1 top) moving to both sides and colliding with each other. The reconnection electric field of the main X-point is shown in different sections in the 4 colour graphs, in the same plane as the whole structure above (upper left), in the central plane perpendicular to it (along the current, upper right) and in an aboveward slightly displaced plane (lower left) where also the density is taken (lower right). The electric field is mainly inductive, given by the temporal change of the magnetic field in collisionless reconnection, and it is extended into the third dimension (along the current) over a finite length only. Outside the

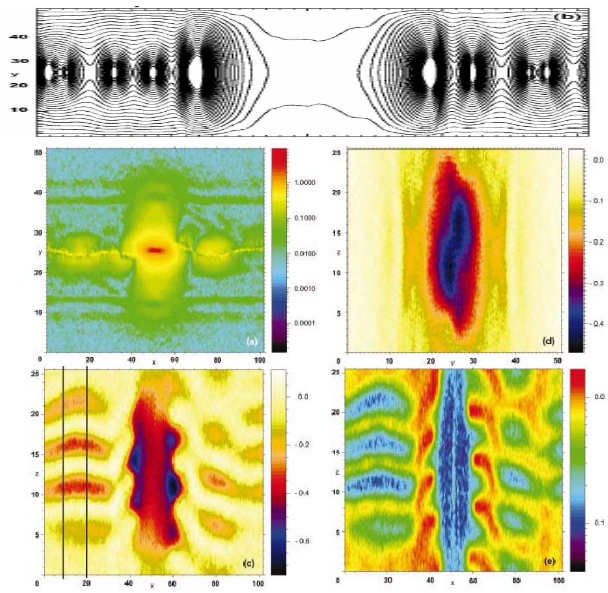

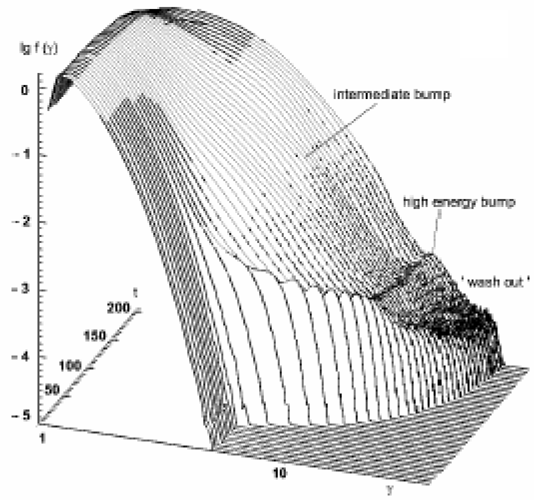


**Figure 1**. *Left*: Magnetic (left top) and electric field in different sections, and density ripples (left, lower right) in early state of relativistic pair reconnection.

symmetry plane density ripples evolve indicating evolution of a two-stream instability also seen in the electric field. These ripples contribute resistance, while the inductive field act accelerating. Particles encountering the reconnection sites become accelerated. An initial equilibrium distribution evolves with time into a top-flattened distribution exhibiting a long power law tail of slope approximately -3. Large $\gamma$ factors can be reached in this process which is shown in Figure 2 below which gives two shapshots of the acceleration of one positron initially in cyclotron rotation. After catching up the main X-point it experiences the inductive electric field, is accelerated, assumes a large gyroradius, overruns the moving X-point and catches up the next one where it again accelerates until having gained so much energy that it escapes the current sheet along the moving magnetic field. This mechanism very efficiently generates energetic particles.

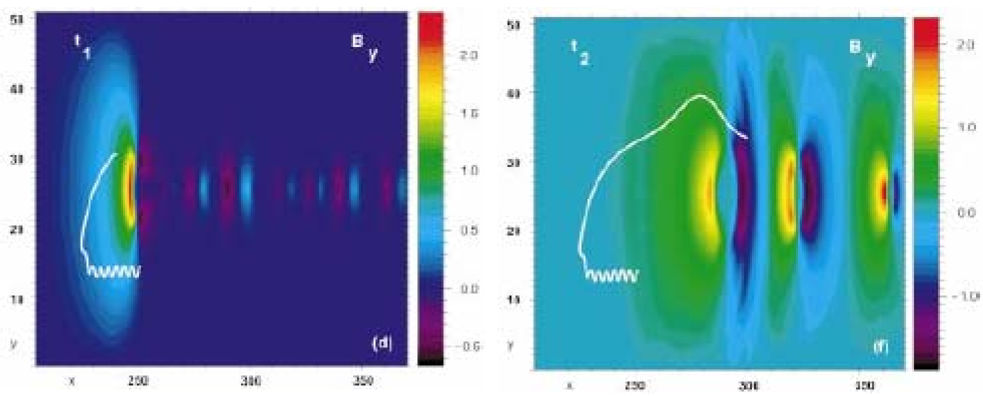

Figure 2. Two phases of a gyrating positron that is accelerated encountering an X-line.

Jaroschek,C.H. et al., Phys. Plasmas **11**(3), 1-13(2004).

*C. H. Jaroschek, R. A. Treumann, and M. Scholer*

# Synchrotron Radiation in Pair Reconnection

Numerical simulation of relativistic magnetic reconnection in pair plasmas and the resulting particle acceleration is used for the estimation of the synchrotron emissivity from pair plasmas generated for instance in the vicinity of AGNs. It is found that considerable synchrotron radiation can be emitted from those structures in magnetic reconnection activity.

Generation of intense synchrotron emission from reconnection in strong magnetic fields is of great interest in astrophysical problems. It requires the presence of energetic electrons which can have been accelerated in the process of reconnection, and it requires strong enough reconnecting fields or at least strong enough fields at the sites where the fast presumably relativistic particles are injected from the reconnecting accelerator. This is of interest in proton-electron plasmas as long as one restricts oneself to the solar system or magnetized stars, it is of interest as well for pair plasmas when considering AGNs, black hole environments, and the interior of pulsar magnetospheres. We performed PIC simulations on the latter problem as treating proton-electron plasmas is technically very difficult with present computing facilities. The simulation has been fully relativistic in particles and of course in the fields.

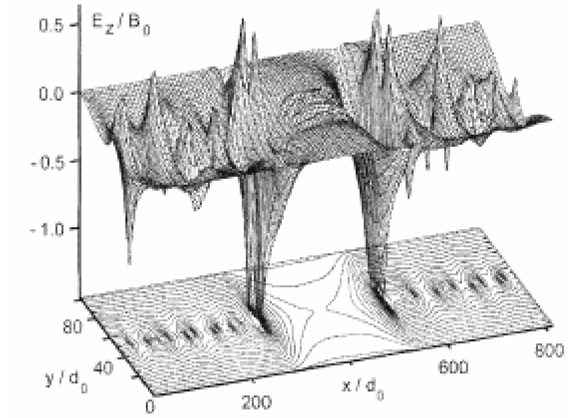


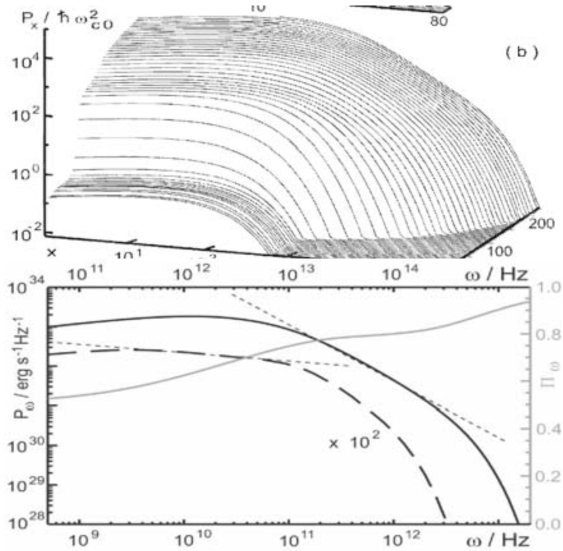


**Figure 1**. *Left*: Accelerating reconnection-electric field. *Right*: Time evolution of synchrotron power emissivity (*top*) and total power spectrum (*bottom*) for the corresponding pair plasma.

Figure 1 shows the locally evolving electric fields in reconnection which accelerate the particles into a power law distribution with high energies. These, in gyrating in the local magnetic fields emit a synchrotron spectrum which is shown integrated over the entire simulation box. Considerable synchrotron power is found being emitted from the box which results from the particle acceleration. This power is generated mainly locally in the reconnection sites and thus is the minimum power available from such processes. When the particle distribution would be collimated into a strong field close to a star or elsewhere the emission would be even higher. Since in application to astrophysical problems the reconnection sites are microscopically small, the size of the particle (in this case pairs) inertial length, one must rescale it to the accessible (observable) spatial volume. We have chosen as such a region the presumable source location of light-jets generated in AGNs. Since the system is absolutely collisionless for the simulation time and synchrotron cooling times exceed it by a factor the order of $10^8$, it is sufficient to estimate the filling factor of the volume to achieve at measured synchrotron emission levels of ~$10^{47}$ ergs/s in certain luminous intraday variable quasars showing extremely hard flat-spectrum radio spectra comparable to our simulation findings of spectral index about -0.2 up to a cut-off frequency of ~100 GHz. Roughly $10^5$ reconnection emission events can be superposed in 1 ks of observation time which guarantees spatial coherence on this scale. Plasma thermalization and synchrotron self-absorption play no role on the individual reconnection scale which lasts only $10^{-7}$ s. Strong polarization at high frequencies > 10 THz is due to the contribution of individual reconnection zones as found in our simulation study.


Jaroschek, C.H., H.Lesch and R.A.Treumann, *Ap.J.* **605**, L9-L12 (2004).



*C. H. Jaroschek and R. A. Treumann*

# Large Scale Structure and Cosmology

# SPIFFI Observes an Old, Fat, and Rich Starburst

**The SPectrometer for Infrared Faint Field Imaging (SPIFFI) has been used to obtain J, H, and K band integral field spectroscopy of the z = 2.565 luminous sub-millimeter galaxy SMM J14011+0252. The brighter of this system's two components proves to be an intense starburst remarkably old, massive, and metal-rich for the early epoch at which it is observed.**

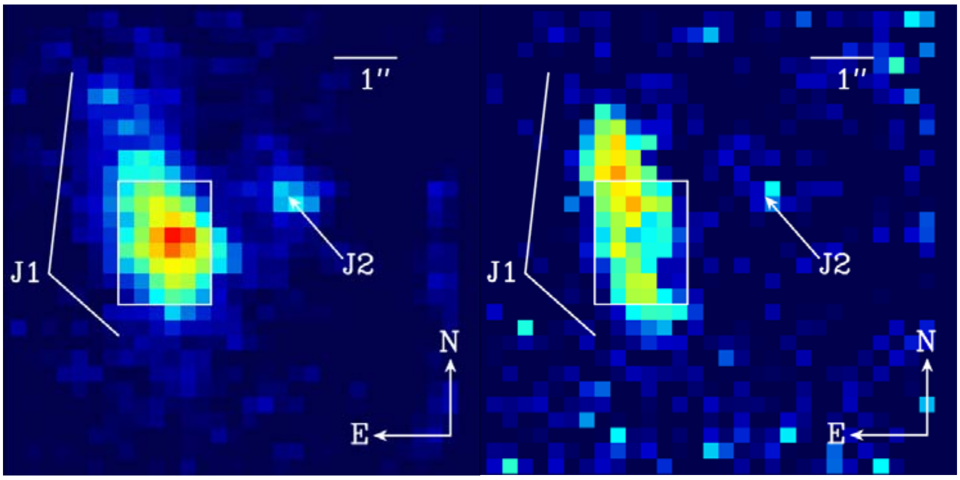


8”x8”images of line-free K-band continuum (left) and continuum-subtracted $H_\alpha$ line emission (right). Molecular gas and dust emission peak between components J1 and J2 (Ivison et al. 2001; Downes & Solomon 2003). The box indicates the aperture used to extract the spectrum shown below. For details, see Tecza et al. (2004, ApJ, 605, L109).

SMM J14011+0252 was one of the first submillimeter galaxies (SMGs) to have an optical counterpart identification (Barger et al. 1999) validated by CO interferometry (Frayer et al. 1999). Because it lies behind the z = 0.25 cluster Abell 1835, it is gravitationally lensed; however, spatially resolved maps of its CO emission have led to quite different conclusions about whether it is a weakly magnified large source (Ivison et al. 2001) or a strongly-magnified small source (Downes & Solomon 2003). Our SPIFFI observations have for the first time separated the system's line and continuum emission, revealing quite different morphologies (above). A global spectrum of component J1 (below) shows a strong continuum break between J and H bands, which can best be explained as the Balmer break of a z~2.5 stellar population that has been forming for ≥100 Myr. The line fluxes imply (via the locally calibrated $R_{23}$ estimator) an oxygen abundance that is supersolar by ~0.3 dex. This abundance, the ~$1.6\times10^{10}$ $M_\odot$ of gas still remaining, and a closed-box enrichment model imply a total baryonic mass ~$7.9\times10^{10}$ $M_\odot$, consistent with the local mass--metallicity relation (Tremonti et al. 2004). This result offers independent confirmation of the proposition that SMGs have much larger baryonic masses than typical UV-selected galaxies at the same epoch (Genzel et al. 2003).

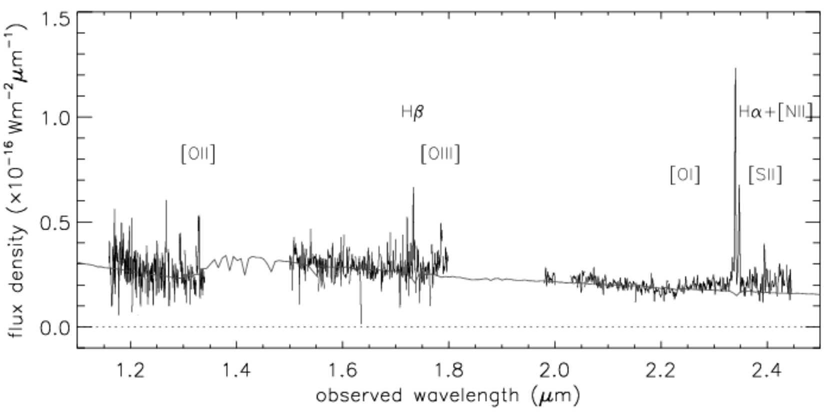


**Estimated global parameters:**
- **magnification ~ 5**
- **gas mass ~ $1.3\times10^{10}$ $M_\odot$**
- **stellar mass ~ $6.6\times10^{10}$ $M_\odot$**
- **stellar age ~ 220 Myr**
- **star formation ~380 $M_\odot$ $yr^{-1}$**
- **metallicity ~ 1.9 $Z_\odot$**

*M. Tecza, A. Baker, R. Davies, R. Genzel, M. Lehnert, D. Lutz, N. Nesvadba, S. Seitz, L. Tacconi, N. Thatte, R. Abuter, R. Bender*

# The Star Formation history in FDF & GOODS fields

We measure the star formation rate (SFR) as a function of redshift up to $z \approx 5$ based on B, I and (I+B) selected galaxy catalogs from the FORS Deep Field (FDF; [2]) and the K-selected catalog from the GOODS-South field [3].

Distances are computed from spectroscopically calibrated photometric redshifts (based on multicolor photometry from UV to NIR) accurate to $\Delta z/(z_{spec}+1) \leq 0.03$ for the FDF and $\leq 0.056$ for the GOODS-South field. The SFRs are derived from the observed luminosities at 1500 Å [1].

- We find that the total SFR estimates derived from B, I and I+B catalogs agree very well while the SFR from the K catalog is lower by $\approx 0.2$ dex (Fig. 1, upper 4 plots and lower left plot).
- We show that the latter is solely due to the lower star-forming activity of K-selected intermediate and low luminosity ($L < L_*$) galaxies (Fig. 1, lower right plot).
- There is no evidence for significant cosmic variance between the SFRs in both fields.
- At all redshifts, luminous galaxies ($L > L_*$) contribute only $\sim \frac{1}{3}$ to the total SFR, i.e. the integrated SFR of $L < L_*$ galaxies is a factor of $\sim 2$ higher than the one of $L > L_*$ galaxies.
- The SFRs derived here are in excellent agreement with previous measurements provided we assume the same faint-end slope of the luminosity function as previous works ($\alpha \sim -1.6$). However, our deep FDF data indicate a shallower slope of $\alpha = -1.07$ ([4]), implying a SFR lower by $\approx 0.3$ dex.
- We find the SFR to be roughly constant up to $z \approx 4$ and then to decline slowly beyond, if dust extinction is assumed to be constant with redshift.

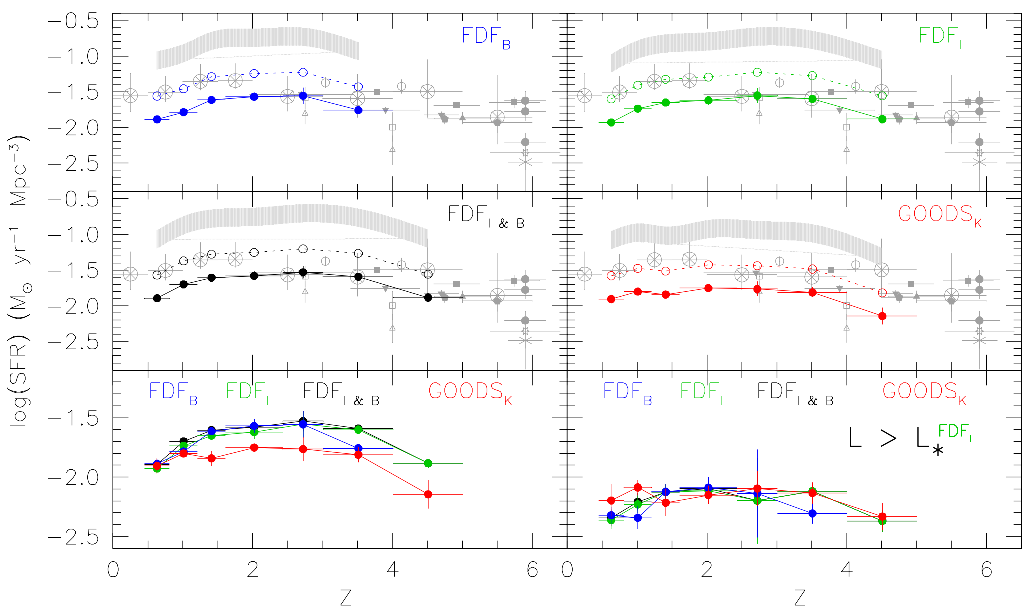


**Fig. 1** *The four plots at the top show the SFR as a function of redshift computed from the B-selected (blue), I (green) and I+B-selected (black) FDF, and K-selected (red) GOODS-South field. The points are connected by the thick lines for clarity. The grey-shaded region shows the effect of dust corrections with correction factors between 5 and 9, following [5]. The dotted lines show the effect of assuming a faint-end slope $\alpha$ of the luminosity function of -1.6 for a better comparison with the literature (grey symbols; see [1] for details). The SFRs are based on $\alpha = -1.07$ as derived from the FDF and GOODS data. The plots at the bottom show the SFRs of the four catalogs together (left) and the SFRs derived considering the contributions of the galaxies brighter than $L_*^I$ only (right).*

# References


[1] A. Gabasch, M. Salvato, R.P. Saglia, et al. *ApJL in press*, 2004.
[2] J. Heidt, I. Appenzeller, A. Gabasch, et al., *A&A*, 398:49–61, January 2003.
[3] M. Salvato et al. *in preparation*, 2004.
[4] A. Gabasch, R. Bender, S. Seitz, et al., *A&A*, 421:41–58, July 2004.
[5] K. L. Adelberger and C. C. Steidel. *ApJ*, 544:218–241, November 2000.



*A. Gabasch, M. Salvato, R.P. Saglia, R. Bender, U. Hopp, S. Seitz, N. Drory, G. Feulner, M. Pannella*

# Stellar Masses of Galaxies from MUNICS and FDF

The stellar mass assembly history of field galaxies is a powerful test of galaxy evolution models. Stellar masses can be derived by fitting composite stellar population (CSP) models (e.g. [2]) of varying age, star-formation history, metallicity and dust attenuation to the galaxies' optical and near-infrared broad-band photometry [1].

- We have tested this procedure by comparing stellar masses derived in this manner to masses from spectral features for SDSS galaxies [11]. The result is presented in Fig. 1 and shows good agreement between the two methods [7].
- Applying this to the near-infrared optical galaxy survey MUNICS [3, 5, 9, 13] and FDF [10, 12], we can derive the evolution of the stellar mass function of field galaxies with redshift, see Fig. 2 [4, 6], as well as the evolution of the total stellar mass density of the universe, see Fig. 3 [8].

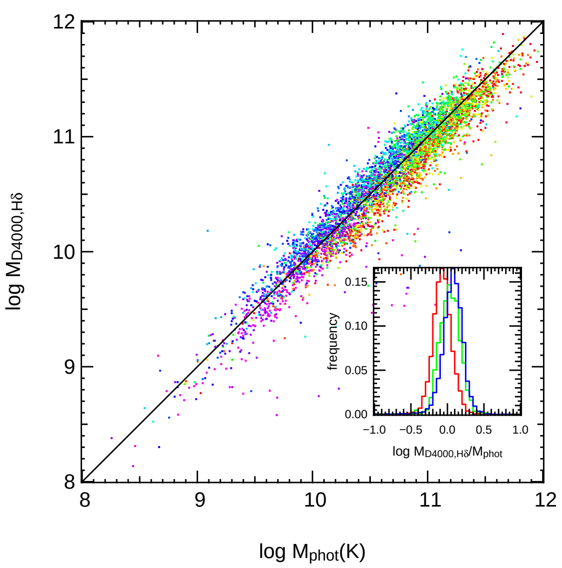


**Fig. 1** *Comparison of stellar masses for SDSS galaxies derived from spectroscopic indices and from fitting CSP models to the broad-band photometry and then converting the $K$-band luminosity to stellar mass using $M/L_K$. The colours denote H$\alpha$ equivalent width (a measure for the star-formation rate) from no emission (red) to strong emission (purple). The small panel shows a histogram of the residuals as a function of H$\alpha$ equivalent width.*

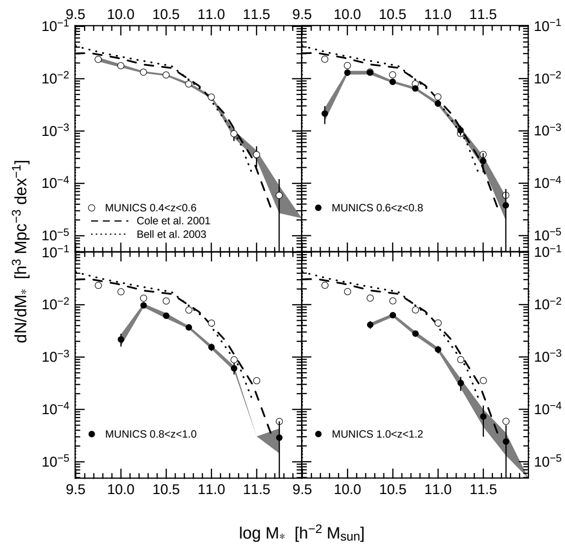


**Fig. 2** *The evolution of the stellar mass function with redshift. The open and closed symbols are the MUNICS values at $0.4 < z < 0.6$ and at higher redshifts, respectively. The lowest $z$ values are shown in all panels for comparison. Error bars denote the uncertainty due to Poisson statistics. The shaded areas show the 1 $\sigma$ range of variation in the mass function given the total systematic uncertainty in $M/L_K$. The dotted and dashed lines show the $z = 0$ stellar mass function derived similarly to our methods using SDSS, 2dF, and 2MASS data.*

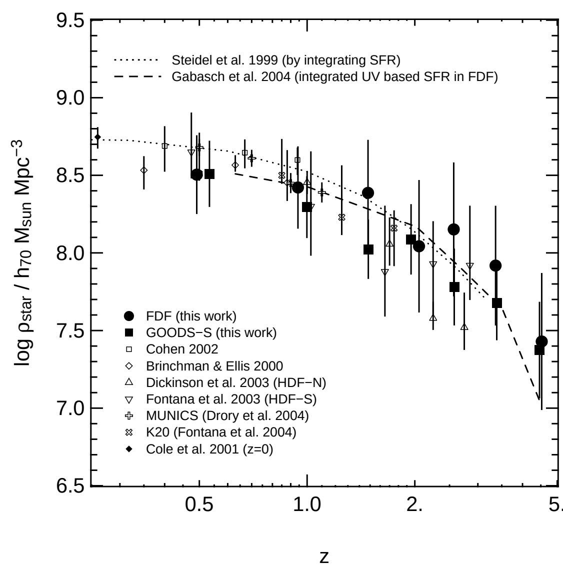


**Fig. 3** *The evolution of the total stellar mass density in the universe. The closed circles are the MUNICS and FDF values, open symbols are values from the literature. The integrated star formation rate (derived from the UV luminosity, dotted and dashed curves) is shown for comparison.*

References:

[1] Brinchmann, Ellis, 2000, ApJL, 536, 77
[2] Bruzual, Charlot, 2003, MNRAS, 344, 1000
[3] Drory, Feulner, Bender et al., 2001a, MNRAS, 325, 550
[4] Drory, Bender, Snigula et al., 2001b, ApJL, 562, 111
[5] Drory, Bender, Feulner et al., 2003, ApJ, 595, 698
[6] Drory, Bender, Feulner et al., 2004, ApJ, 608, 742
[7] Drory, Bender, Hopp, 2004, ApJL, in press
[8] Drory, Salvato, Gabasch et al., 2004, ApJL, submitted
[9] Feulner, Bender, Drory et al., 2003, MNRAS, 342, 605
[10] Heidt, Appenzeller, Gabasch et al., 2003, A&A, 398, 49
[11] Kauffmann et al., 2003, MNRAS, 341, 33
[12] Noll, Mehlert, Appenzeller et al., 2004, A&A, 418, 885
[13] Snigula, Drory, Bender et al., 2002, MNRAS, 336, 1329

*R. Bender, N. Drory, G. Feulner, Yu. Goranova, U. Hopp, C. Maraston, J. Snigula*

# Probing Turbulence in the Coma Galaxy Cluster

Spatially-resolved gas pressure maps of the Coma galaxy cluster are obtained from a mosaic of XMM-Newton observations in the scale range between a resolution of 20 kpc and an extent of 2.8 Mpc. A Fourier analysis of the data reveals (for the first time) the presence of a scale-invariant pressure fluctuation spectrum in the range between 40 and 90 kpc and is found to be well described by a projected Kolmogorov/Oboukhov (KO) -type turbulence spectrum. Deprojection and integration of the spectrum yields the lower limit of $\sim 10$ percent of the total intracluster medium pressure in turbulent form. The results also provide observational constraints on the viscosity of the gas. Projected pressure maps (upper left) are used for the analyses to minimize the effects of contact discontinuities and strong shocks. The Gaussianity of the normalized residual pressure fluctuations (upper right) and the correlations between relative density and temperature gradients close to the adiabatic value (lower left) give further evidence for a turbulent intracluster medium in the center of Coma. The power spectrum is well fit by projected KO spectra with reasonable slopes (lower right). Simulations show that a 100 ks pointing with the XRS instrument onboard the Astro-E2 satellite (to be launched Feb. 2005) will enable us to confirm the presence of a turbulent plasma ($\sigma_v \geq 100$ km/s) as a significant kinetic Doppler broadening of the line widths of the Fe K-line complex in excess to thermal broadening.

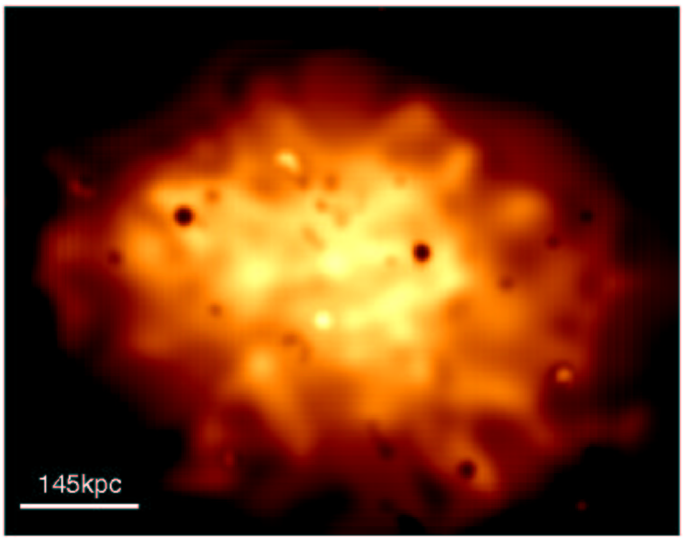


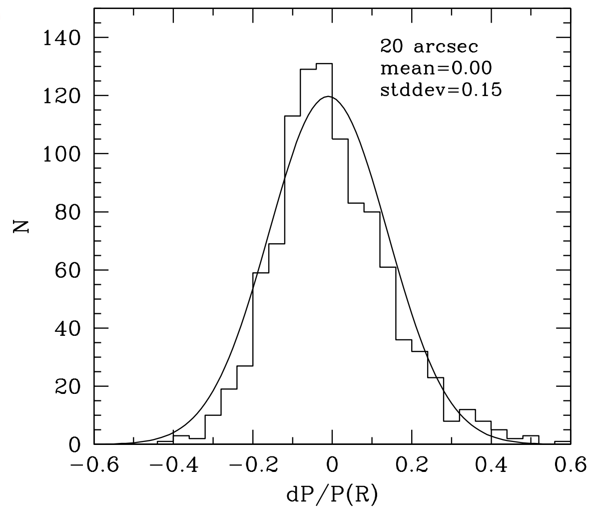


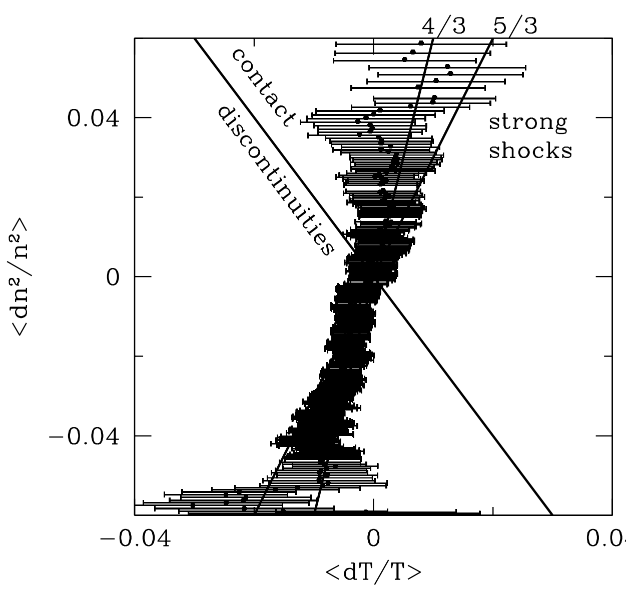


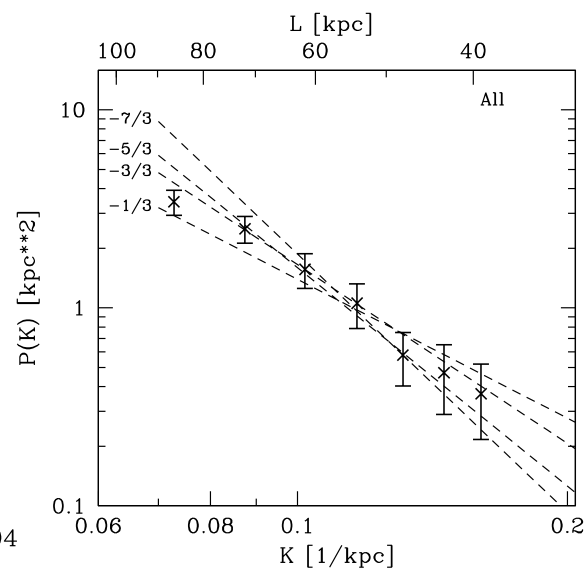


**P. Schuecker, A. Finoguenov, F. Miniati, H. Böhringer & U.G. Briel**

# Evolution of the Luminosity Function in the FDF

We use the very deep and homogeneous dataset of the VLT FORS Deep Field [1] (a UBgRIzJKs survey to $I_{AB} \sim 26.8$ over 40□') to investigate the redshift evolution of the restframe galaxy luminosity functions [2] from the UV (see Fig. 1) to the g'-band up to redshift of $z \sim 5.0$. The catalog contains about 5600 galaxies with accurate photometric redshifts ($\Delta z/(z_{spec}+1) \leq 0.03$) and only $\sim 1$% outliers making it possible to derive precise restframe absolute magnitudes. We obtain the following results:

- The characteristic luminosity $M^*$ increases from $\langle z\rangle \sim 0.5$ to $\langle z\rangle \sim 5$ by $\sim$ 3.1 magnitudes in the UV, by $\sim$ 2.6 magnitudes in the u' and by $\sim$ 1.6 magnitudes in the g' and B bands (Fig. 3).
- Simultaneously the characteristic density $\phi^*$ decreases by about 80 % – 90 % in all analyzed wavebands (Fig. 2).
- The slopes of the luminosity functions in the UV and u' bands are very similar ($\alpha = -1.07 \pm 0.04$) but differ from the slopes in the g' and B bands ($\alpha = -1.25 \pm 0.03$).
- A UV slope of $\alpha \leq -1.6$, as assumed in other studies for $\langle z\rangle \sim 3.0$ and $\langle z\rangle \sim 4.0$, can be excluded on at least a $2\sigma$ level.

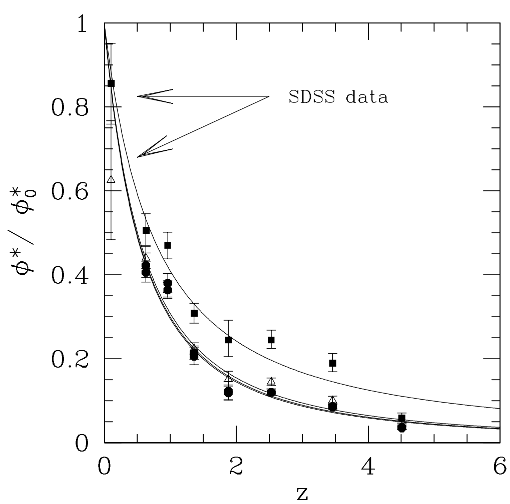


**Fig. 2** *Redshift evolution of $\phi^*$ for the filters g' (filled squares), u' (open triangles) and the two UV bands at 2800 Å and 1500 Å (filled circles). The arrows mark the values for $\phi^*$ as derived in the Sloan Digital Sky Survey.*

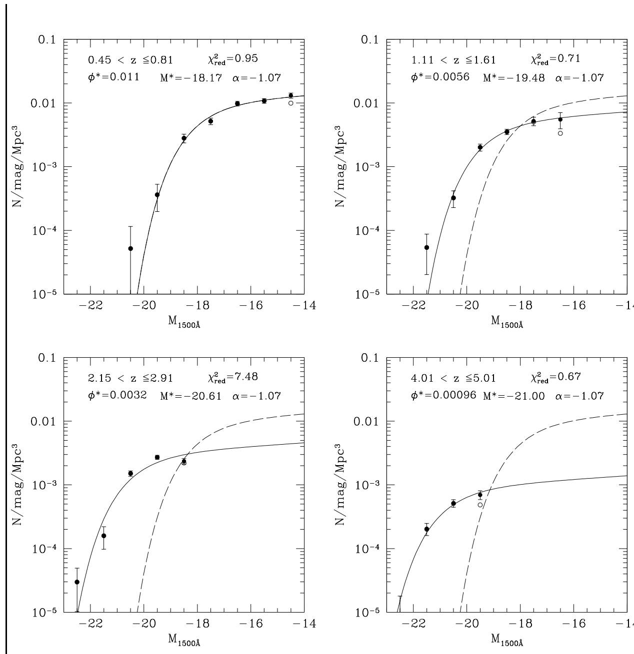


**Fig. 1** *Luminosity functions (filled symbols) at 1500 Å for different redshifts. The fitted Schechter functions are shown as solid lines. The Schechter fit for redshift $\langle z\rangle = 0.6$ is indicated by a dashed line.*

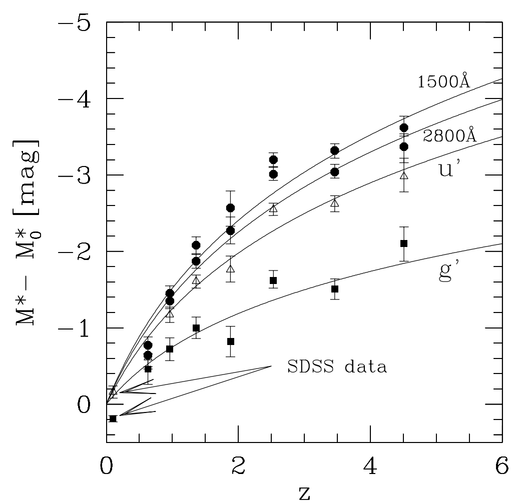


**Fig. 3** *Redshift evolution of M* for the filters g' (filled squares), u' (open triangles) and the two UV bands at 2800 Å and 1500 Å (filled circles). The arrows mark the values for M* as derived in the Sloan Digital Sky Survey.*

## References


[1] J. Heidt, I. Appenzeller, A. Gabasch, et al. *A&A*, 398:49–61, January 2003.

[2] A. Gabasch, R. Bender, S. Seitz, et al *A&A*, 421:41–58, July 2004.



*A. Gabasch, R. Bender, S. Seitz, U. Hopp, R.P. Saglia, G. Feulner, J. Snigula, S. Noll and the FDF team*

# XMM-Newton observations of the Lockman Hole

**We studied the X-ray source population of the Lockman Hole field, the celestial area of lowest Galactic X-ray absorption in the longest and most sensitive X-ray exposure performed by XMM-Newton. Extensive optical follow-up spectroscopy of the AGN content of the field was obtained using the Keck DEIMOS multi-slit spectrograph.**

The field was observed by XMM-Newton in 18 individual pointings for a total of 770 ksec, corresponding to 20 days of XMM-Newton observing time. The 34´ x 30´ colour composite image of the combined data set, shown below (the energy bands 0.5-2, 2-4.5, and 4.5-10 keV are displayed in red, green, and blue, respectively), contains more than 500 X-ray sources corresponding to ~2000 sources per sq. deg. at the survey limit of 2 x $10^{-16}$ erg/$cm^2$ s in the 0.5-2 keV band (see the log N–log S diagram, below). The different X-ray colours represent a multitude of spectral shapes, including unabsorbed (type–I AGN/QSOs) and absorbed (type-II AGN/QSOs)) power law as well as complex multi-component spectra. Follow-up optical spectroscopy with the Keck DEIMOS multi-slit spectrograph in two observing runs in 2003 and 2004 resulted in a cumulative total of 116 identifications (54 type-I AGN/QSOs, 43 type-II AGN/QSOs, 10 normal galaxies, 3 groups/clusters, 6 stars), equivalent to 41 % of the core X-ray sample within 10´ around the field center. Additional optical spectroscopy is planed for 2005. The field also was covered with deep multi-band optical and IR imaging using various 4m and 8m class telescopes. In addition to hundreds of active galactic cores, the field contains a substantial number of X-ray emitting clusters of galaxies. A wavelet analysis identified 20 candidates for which follow-up spectroscopy is intended (see X-ray contours plotted on R band image for two exampes) .

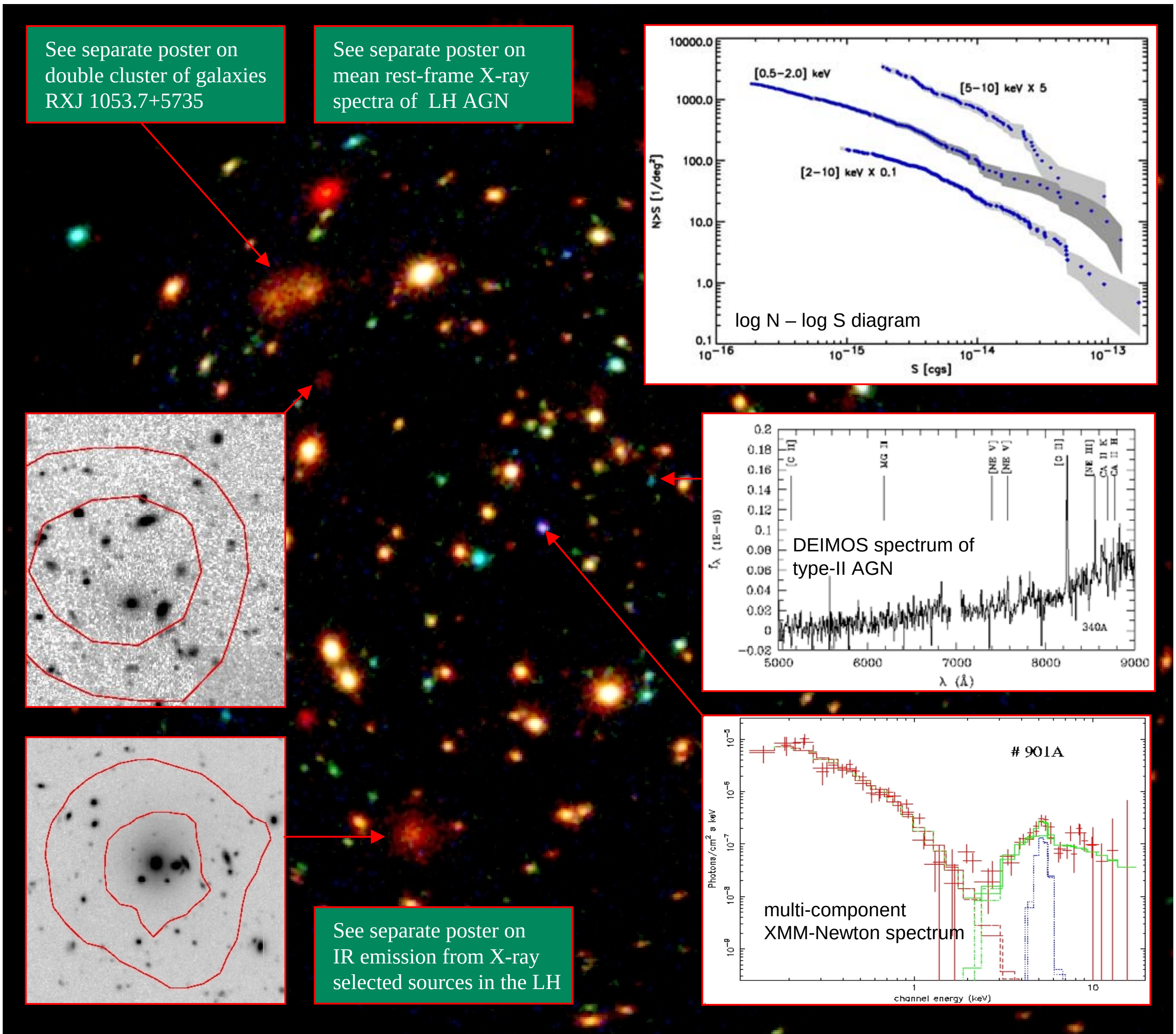


*H. Brunner, A. Finoguenov, Y. Hashimoto, G. Hasinger, I. Lehmann, V. Mainieri, I. Matute, A. Streblyanska, G. Szokoly*

*in collaboration with X. Barcons (Santander), A. Fabian (Cambridge), Pat Henry (Hawaii), and M. Schmidt (Caltech)*

# Mid-IR emission from X-ray sources in the Lockman Hole

**The Lockman Hole has become a selected window in the sky due to its deep coverage both in the X-rays with *XMM* and mid-IR with *ISO* and the extensive multiwavelength coverage available. We had derived spectral energy distributions for the mid-IR emitting X–ray population and constrained the contribution of accretion power to the IR cosmic background.**

In the framework of the unified scenario for AGN, an important infrared (IR) emission is expected from reprocessed energy of the central black hole by dust and gas. The Lockman Hole (LH) represents one of the largest area covered with both deep X-rays ($f_{[0.5-2.0]}$=2x$10^{-16}$ cgs) and mid-IR observations ($S_{15}$=0.2 mJy at 15$\mu$m). The analysis of this datasets has provided 58 common (X–ray–IR) emitters with low probabilities of random association (<0.1%). This sample doubles the amount of previously known X-ray–mid-IR emitters in this field and gives a direct measure of the accretion power importance in the Cosmic Infrared Background

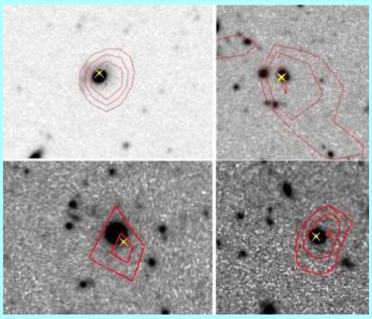

R-band images of *XMM-ISO* sources. Red countours come from the ISO data ($3\sigma$, $4\sigma$, $6\sigma$). 'Crosses' symbols indicate the center of the X-ray sources.

The spectroscopy is ongoing and presently complete at 40% level with a mean redshift of 0.95.

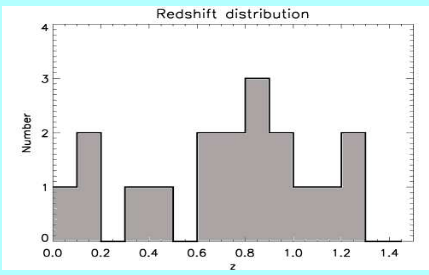


Redshift distribution of the already identified fraction of X–ray–IR emitters in the LH ($< z >\sim 0.95$).

The physical nature of the sources and their evolution with cosmic time can only be understood by comparing the overall source SEDs with well known local templates (e.g. Circinus, NGC 6240, etc). Thanks to the extensive multiwavelength coverage available in the LH, the spectral energy distribution reconstruction has been possible for a large fraction of our population probing population changes for different classes of objects (type-I & II AGN, starburst, etc).

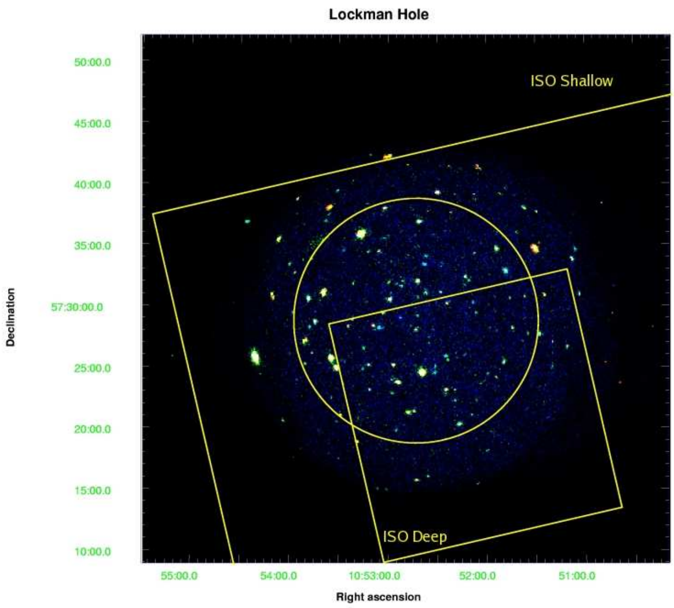


X-rays 'real-color' image of the combined PN and MOS images (~800 ksec) in the Lockman Hole. Overlaid squares represent the area covered by the shallow and deep *ISO* surveys at 15$\mu$m. Circle corresponds to the highest X-ray exposure region of 10 arcmin.

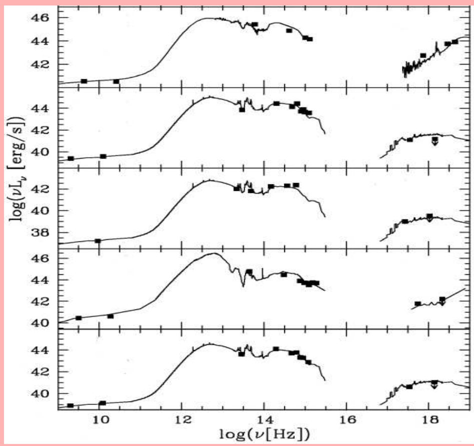


*I. Matute, G. Hasinger, I. Lehmann, G. Rodighiero, D. Fadda, C. Cesarsky*

# The Extended *Chandra* Deep Field South

ABSTRACT: While the recent *Chandra* and *XMM–Newton* surveys have generated plentiful AGN samples, they do not detect signi cant numbers of moderate-luminosity AGN at high redshift ($z > 3$).**To pin down the cosmic evolution (i.e., luminosity function) of X-ray emitting AGN up to $z \sim 5$, the region surrounding the CDF-S is being observed by *Chandra* to reach comparable depths over an area 4× larger**. The expanded areal coverage is crucial to measure the full extent of the large scale structures evident in the CDF-S and study the AGN clustering properties. We are beginning an optical spectroscopic identi cation program of the X-ray sources detected in the Extended Chandra Deep Field-South (E-CDF-S) using VLT/VIMOS. **With extensive observations of this region in various wavebands (e.g. COMBO-17, GEMS *Spitzer*/HST, ESO Deep Public Survey), we are carrying out one of the deepest multi-wavelength campaigns to date**.

## Evolution of X-ray emitting AGN

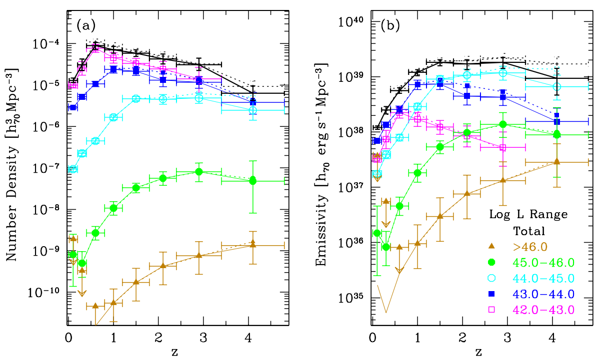


Co-moving space and luminosity density versus redshift for ve different luminosity classes (Hasinger et al. in prep) show that luminous AGN ($log\ L_X > 44$; 0.5-2 keV) evolve in a different manner than lower luminosity ($log\ L_X < 44$) AGN. **It is apparent that a larger sample at $z > 3$ is needed.**

## Chandra Deep Fields

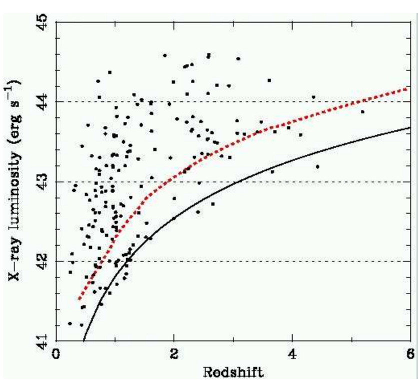


Luminosity/redshift distribution of X-ray sources in the CDF-N+S. With most AGN at $z < 1.5$, a wider area survey is needed to have signi cant statistics at $z > 3$. The E-CDF-S (solid line; detection limit) will be 3× more sensitive than the 100 ksec *XMM–Newton* observation of the Lockman Hole (dotted line; Hasinger et al. 2001).

## E-CDF-S sky coverage

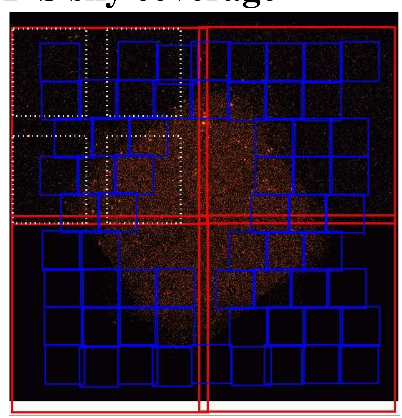

E-CDF-S *Chandra* pointings shown as red squares (17′ × 17′ each) overlaying the 1 Msec CDF-S and **two new observations to the north**. The two southern *Chandra* observations are scheduled this fall. The blue squares mark the GEMS HST/ACS coverage. The dashed regions mark the footprint of the VLT/VIMOS multi-slit spectrograph.

## Optical magnitude distribution

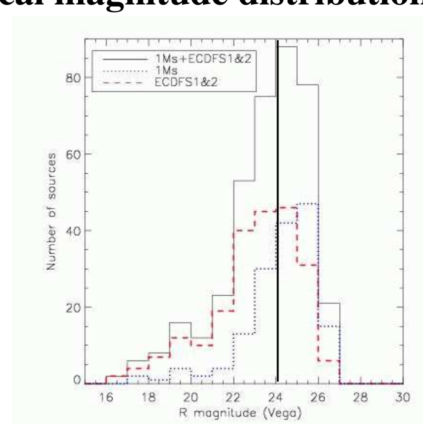


Optical magnitude of the counterparts to X-ray sources in the 1 Ms CDF-S (dotted), **E-CDF-S (dashed)** and combined (solid). **The optical limit ($R = 24$) of our survey will enable us to identify a high fraction ($\sim 70\%$) of the X-ray sources.**

*J. Silverman, G. Hasinger, I. Lehmann, V. Mainieri, G. Szokoly & the E-CDF-S team*

# Resolving the X-ray background with Chandra

Optical spectroscopy results of the 1 Msec CDFS Chandra exposure are published. 137 of the 251 X-ray sources are identified, 122 of the 161 in the R<24 sample. 124 identified field objects are also published. An X-ray based AGN classification scheme is presented based on X-ray fluxes and redshift (which can be photometric) that is an order of magnitude more efficient that pure optical classification for deep X-ray surveys.

### X-ray background is (nearly) resolved

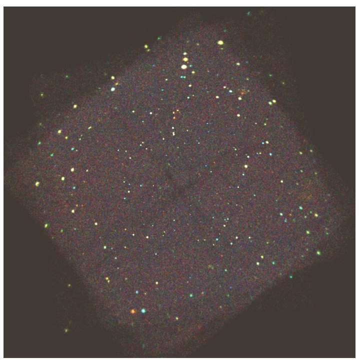

The 1Msec Chandra image (color composite of different energy bands). Depending on the absolute background ux level accepted, 70 100% is resolved into discrete sources 50-70% in the hard band.

### Optical followup in the CDFS field

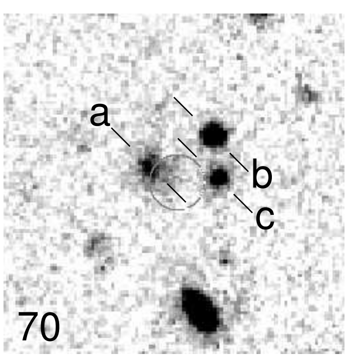


The VLT/FORS optical image (R-band) of the CDFS with X-ray error circle and possible counterparts drawn. In most cases there is only one counterpart.

### Optical spectroscopy

11 nights of VLT/FORS observations (low resolution multi object spectroscopy): 288 counterparts for 251 X-ray sources were observed, 137 X-ray sources are reliably identi ed. **Data is (really) public.** Field objects with good spectra are also published (124 objects).

### Classification

Classical Seyfert classi cation is problematic for these faint surveys. A new classi cation scheme based on X-ray data and redshift is proposed, motivated by the uni ed AGN model. It is objective, simple ($f_s$, $f_h$ and $z$), effective, a natural extension of Seyferts and can use photometric redshifts.

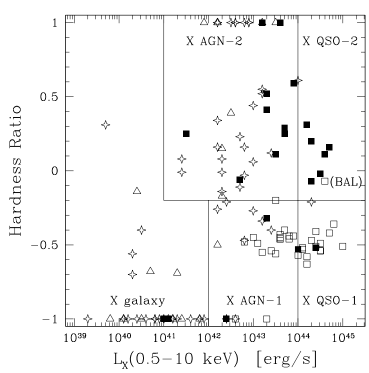


Our X-ray diagnostic applied to the CDFS X-ray objects. Only objects marked with open squares (BLAGNs) and solid squares (high excitation lines) can be identi ed optically as AGNs.

### Type-II QSOs

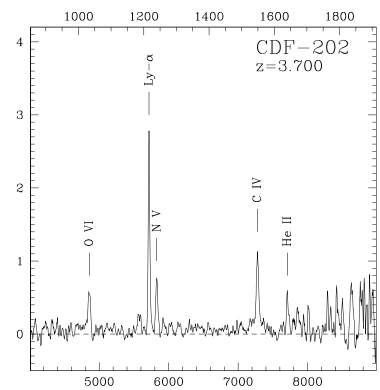


8 high luminosity X-ray sources with signi cant absorption found. These type-2 QSOs are at high redshift and are optically faint.

### Large scale structures

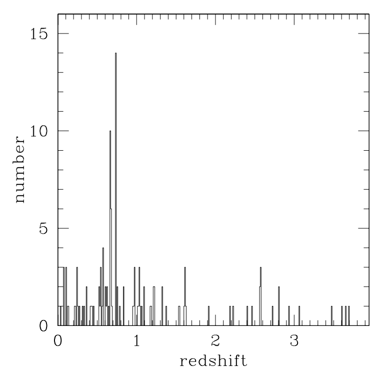


Two large scale structures were found in the sample at redshifts of 0.674 and 0.734. These are dominantly populated by type-2 AGNs.

### Data release

*http://www.mpe.mpg.de/CDFS/*

*G.P. Szokoly, G. Hasinger, I. Lehmann, et.al.*

# Evolution of AGN in the Cosmic web

**The Deep XMM-Newton/Cosmos survey will homogeneously cover the 2 deg$^2$ contiguous area of the Cosmos field to a sensitivity level similar to that of the deepest ROSAT surveys. We will obtain about 2000 obscured and un-obscured AGN, which are crutial to study the formation and evolution of super-massive black holes, the evolution of the spatial distribution and the correlation with galaxy morphology and evolution.**

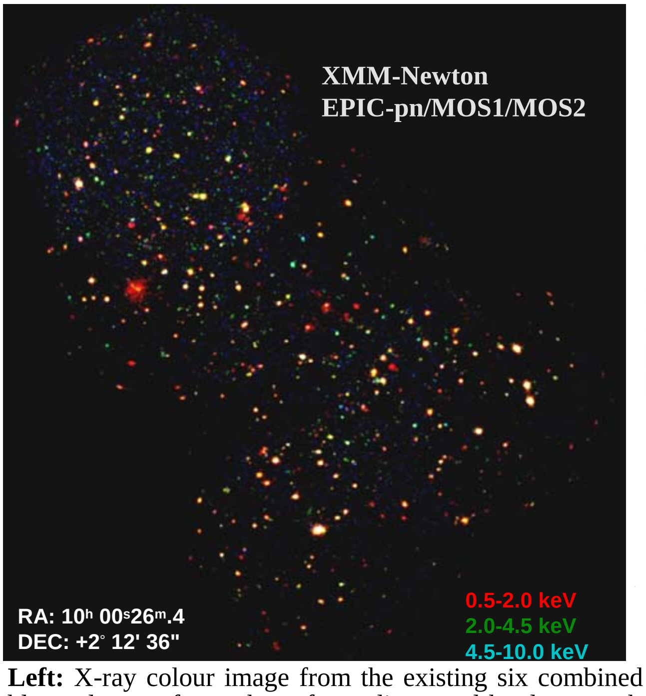


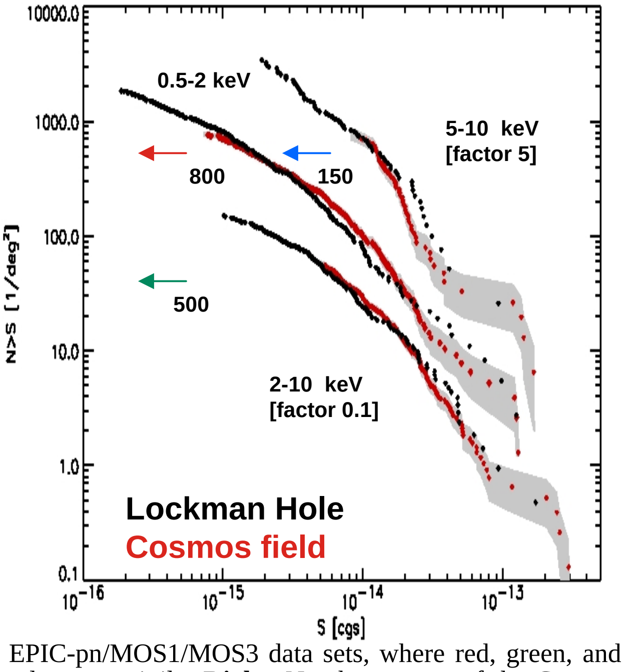


**Left:** X-ray colour image from the existing six combined EPIC-pn/MOS1/MOS3 data sets, where red, green, and blue colours refer to the soft, medium, and hard energy bands, respectivily. **Right:** Number counts of the Cosmos field in different energy bands compared with those from the 1Msec Deep XMM-Newton Lockman Hole survey.

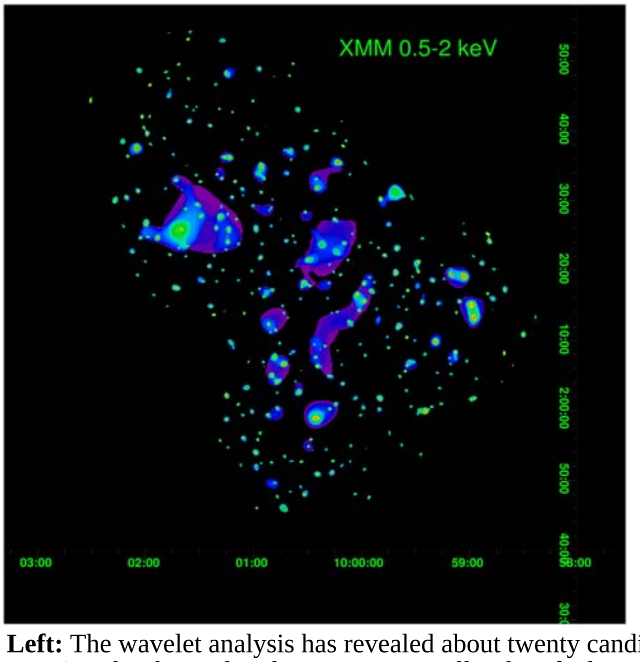


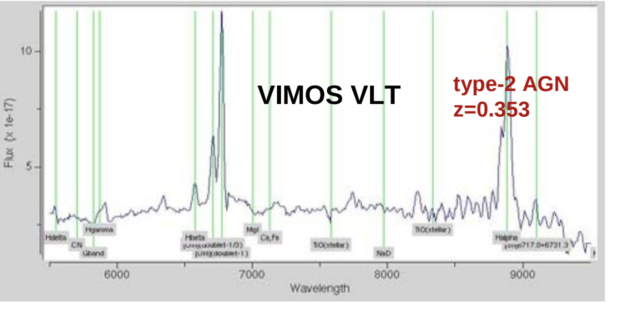


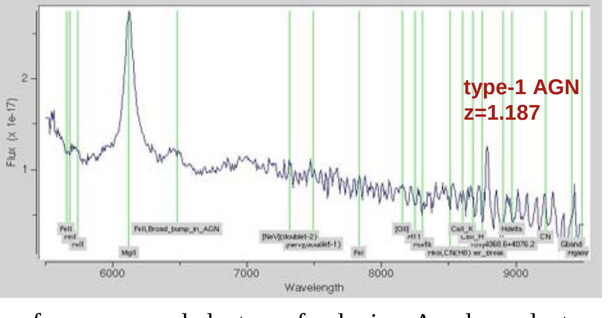


**Left:** The wavelet analysis has revealed about twenty candidates for groups and clusters of galaxies. A galaxy cluster at z=0.73 has been already spectroscopically identified using VLT FORS2 spectra. **Right:** First VIMOS VLT spectra of two X-ray sources taken in May 2004 reveal an obscured and un-obscured AGN.

*I. Lehmann, G.Hasinger, A. Finoguenov, I. Matute, V. Mainieri, H.Brunner, M.Brusa*

# Anti-hierarchical Evolution of AGN

**The evolution of AGN shows a strong dependence on X-ray luminosity. The space density of high-luminosity AGN reaches a peak around z~2, similar to that of optically selected QSO, while the space density of low-luminosity AGNs peaks at redshifts below z<1. New ingredients in structure formation models are necessary to understand this anti-hierarchical behaviour.**

Using ~1000 AGN from ROSAT, XMM-Newton and Chandra surveys (Figure 1) we are able to derive reliable space densities for low-luminosity (Seyfert-type) X-ray sources at cosmological redshifts for the first time. The evolution of the luminosity function (Figure 2) can only be described by luminosity-dependent density evolution and is much less at low X-ray luminosities.

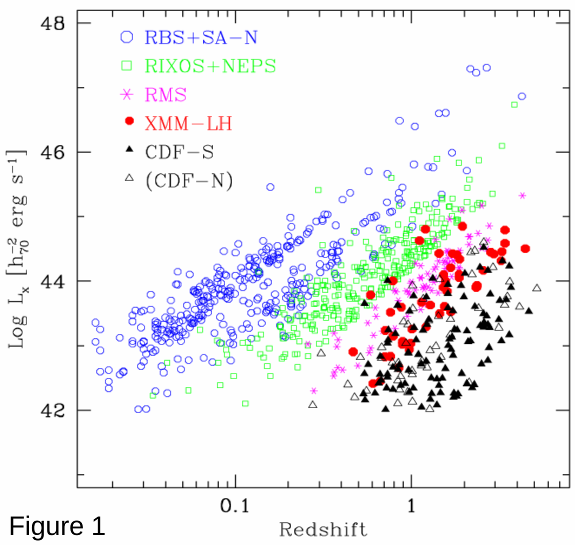


Figure 1

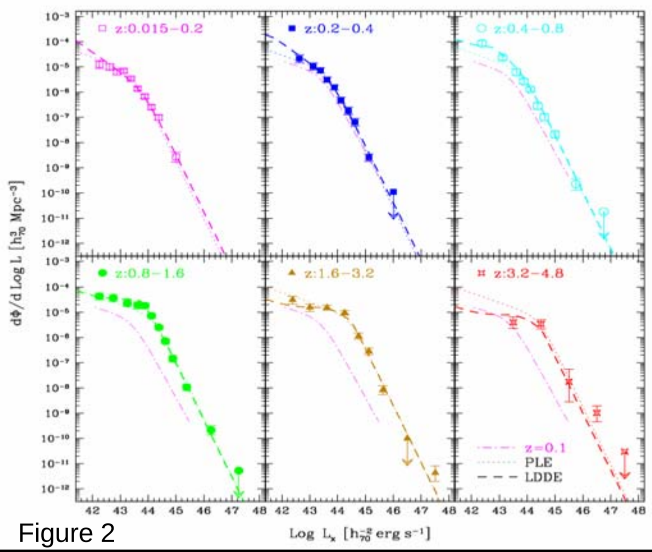


Figure 2

The space density plotted as a function of redshift (Figure 3) peaks at much lower redshifts for lower-luminosity sources, implying an anti-hierarchical black hole growth. Using a rigorous treatment of the optical identification completeness we can show that the space density of AGN with X-ray luminosities $L_X<10^{45}$ erg s$^{-1}$ declines significantly towards high redshifts. For $L_X=10^{44-45}$ erg s$^{-1}$ the high-redshift decline is consistent with that of the optical QSO samples (Figure 4).

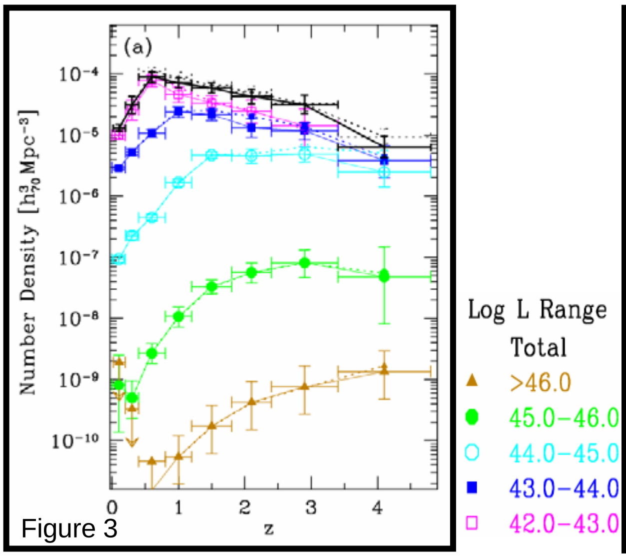


Figure 3

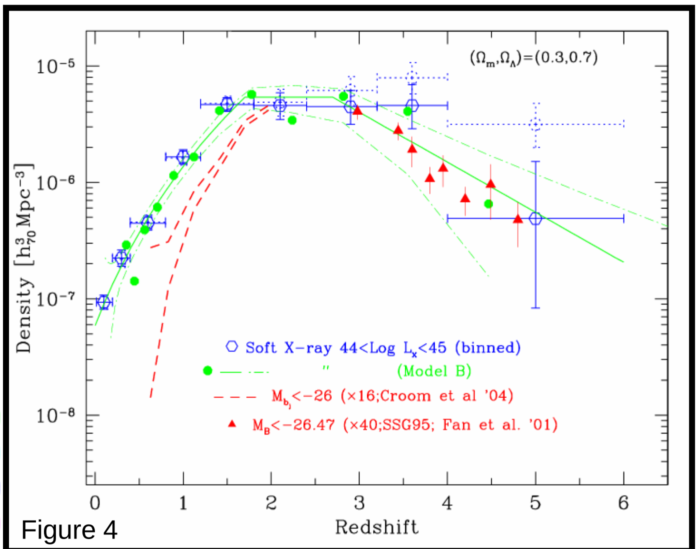


Figure 4

*G. Hasinger (in collaboration with M. Schmidt, Caltech and T. Miyaji, CMU)*

# CO Detections of Luminous Submm Galaxies

**Together with researchers from the IRAM community, the US and the UK we have initiated a survey of CO emission of high redshift submm galaxies using the IRAM Plateau de Bure interferometer, which brings to 12 the number of submillimeter galaxies with CO detections.** These CO line observations confirm the optical redshifts, which lie in the range z=1 to 3.5, and indicate very large molecular gas (few x$10^{10}M_{\odot}$) and dynamical (>$10^{11}M_{\odot}$) masses. The derived total gas and stellar masses imply that the SMGs are very massive systems, dominated by baryons in their inner R<10 kpc. This is similar to what is observed for local giant ellipticals and consistent with numerical simulations of the formation of the most massive ellipticals. We derive a lower limit to the comoving number density of such massive objects at high redshift that is well above the number density of massive objects predicted from recent semi-analytical models of galaxy formation. This discrepancy highlights the critical open questions concerning the detailed cooling and feedback processes governing the formation of a massive galaxy in the framework of hierarchical structure formation.

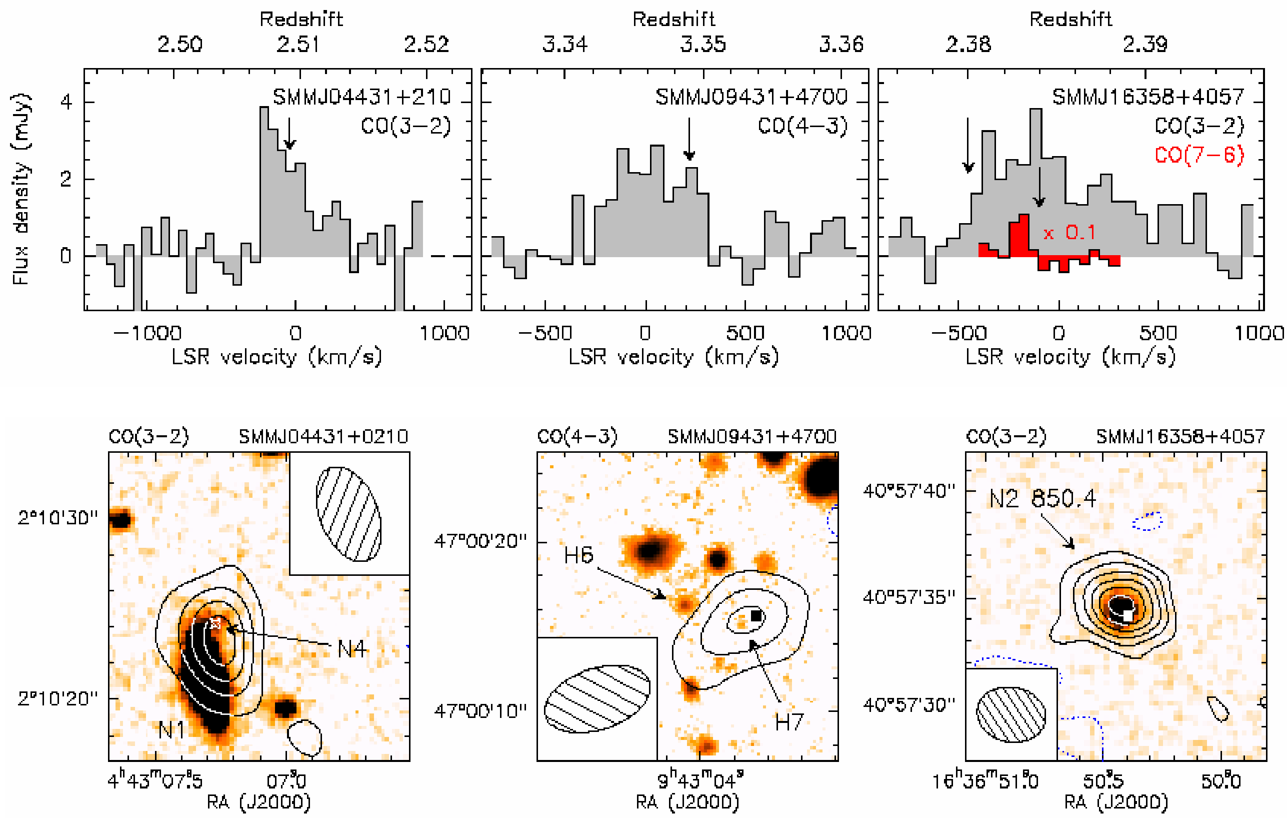


Top: CO spectra of three of the submillimeter galaxies observed with the IRAM PdBI. Bottom: Velocity integrated CO maps, overlayed on K band (left and right) or I-band (center) images. The beam size is indicated.

**Publications from this work:**


• Neri, R., Genzel, R., Ivison, R.J., Bertoldi, F., Blain, A.W., Chapman, S.C., Cox, P., Greve, T.R., Omont, A., Frayer, D.T. 2003, ApJ, 597, L113

• Greve, T., Bertoldi, F., Smail, I., Neri, R., Blain, A.W., Ivison, R.J., Chapman, S.C., Genzel, R., Omont, A., Cox, P., Tacconi, L.J., Kneib, J.-P. 2004, MNRAS, submitted


**In collaboration with: F. Bertoldi, A. Blain, S. Chapman, P. Cox, T. Greve, R. Ivison, R. Neri, A. Omont, I. Smail**


*R. Genzel, L.Tacconi*

# Sub-arcsecond mm imaging of submm galaxies

**Together with researchers from the IRAM community, the US and the UK we have obtained ~0.6″ resolution, IRAM interferometry of the 1.3mm continuum and line emission of four submillimeter galaxies at redshifts between 2.3 and 3.4.** The CO 3-2 or 4-3 line profiles in at least two of the sources are double-peaked, indicative of ordered orbital motion in a rotating disk or galactic merger. The FWHM intrinsic source sizes of all four sources are less than 0.5″. Including the previously resolved SMMJ02399-0136 (Genzel et al. 2003) the median FWHM corresponds to about 3 kpc. The compactness of the sources excludes that the far-infrared/submillimeter emission comes from a cold (T<30K), extended dust distribution. Our measurements show that the submillimeter galaxies we have observed resemble scaled up version of the local Universe, ultra-luminous infrared galaxies (ULIRG) population. Their central densities and potential well depths are comparable to those of elliptical galaxies or massive bulges. The submm galaxy properties properties fulfill the criteria of ‚maximal‘ starbursts in which most of the initial gas reservoir of $\sim 10^{11} M_\odot$ is converted to stars on a time scale $\sim 10 t_{dyn} < 10^8$ years.

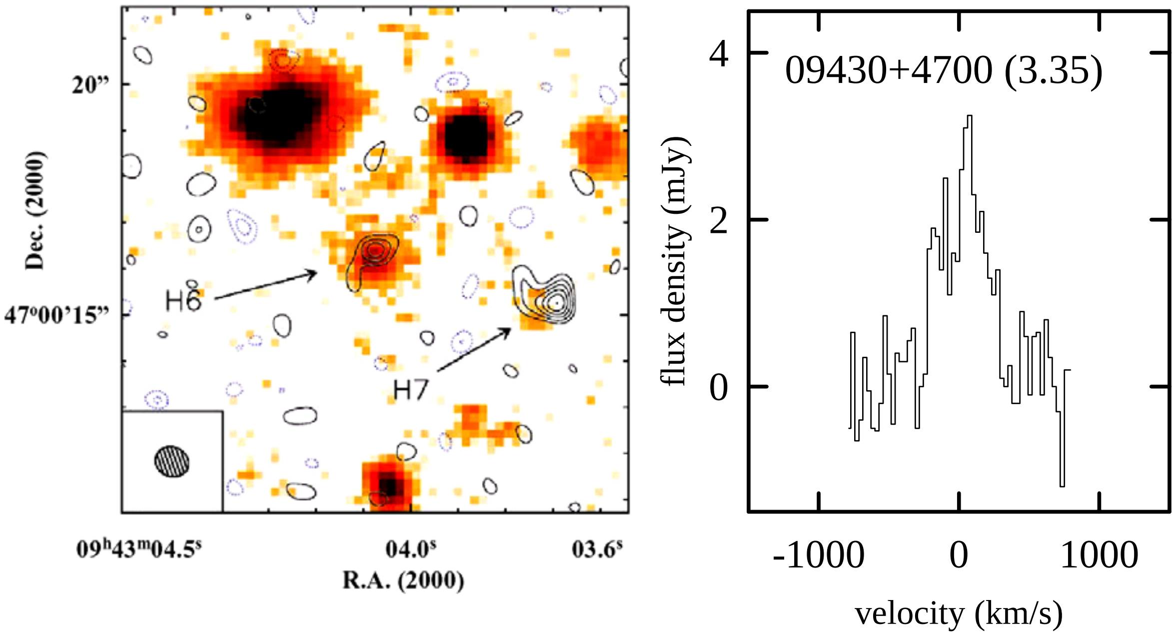


Left: Contour map of the 1.26mm continuum emission of SMMJ0431+4700, superposed on an I-band image from Ledlow et al. (2003). The synthesized beam has a FWHM of 0.74”x0.63”. Contours are in steps of 2,3,4…7 times the rms noise level in the map. CO 9-8 at 238.6 GHz contributes no more than about 1σ to the peak source flux. H6 and H7 are two radio sources in the field. The Lyα redshift of H6 is 3.349, our CO redshift of H7 is 3.346, showing that H6 and H7 are located in the same physical structure with a projected separation of ~25 kpc and a velocity diference of ~200 km/s. Right: CO 4-3 integrated emission from H7. The velocity scale is relative to z=3.346.

**Publications from this work:**

•Genzel, R., Baker, A.J., Tacconi, L.J., Lutz, D., Cox, P., Guilloteau, S., Omont, A. 2003, ApJ, 584, 633

• Tacconi, L.J., Neri, R., Genzel, R., Ivison, R.J., Bertoldi, F., Blain, A., Chapman, S.C., Cox, P., Greve, T., Omont, A., Smail, I. 2004, ApJ, submitted

**In collaboration with: F. Bertoldi, A. Blain, S. Chapman, P. Cox, T. Greve, R. Ivison, R. Neri, A. Omont, I. Smail**

*L.Tacconi, R. Genzel, A. Baker, D. Lutz*

# The faint counterparts of MAMBO mm galaxies

We have pursued identifications for 18 sources from our MAMBO 1.2mm survey of the region surrounding the NTT Deep Field, using accurate positions from VLA 1.4 GHz interferometry and in a few cases IRAM mm interferometry, and deep BVRIzJK imaging at ESO. We find thirteen 1.2mm sources associated with optical/near-infrared objects in the magnitude range K=19.0 to 22.5, while five are blank fields at K>22. Two of the thirteen optical/near-infrared objects are likely foreground objects distinct from the dust sources, one of them possibly lensing the mm source. **Compared to published identifications of objects from 850μm surveys of equivalent depth, the median K and I magnitudes of our counterparts are roughly two magnitudes fainter and the dispersion of I-K colours is less.** Real differences in the median redshifts, residual misidentifications with bright objects, and small number statistics are likely to contribute to this significant difference, which also affects redshift measurement strategies. Some of the counterparts are red in J-K, but the contribution of such mm objects to the recently studied population of near-infrared selected ($J_s$-$K_s$>2.3) high redshift galaxies is only of the order a few percent. The recovery rate of MAMBO sources by pre-selection of optically faint radio sources is relatively low (~24%), in contrast to some claims of a higher rate for SCUBA sources. From a comparison with submm objects with CO-confirmed spectroscopic redshifts roughly two thirds of the (sub)mm galaxies are likely at z>~2.5. This fraction is probably larger when including sources without radio counterpart.

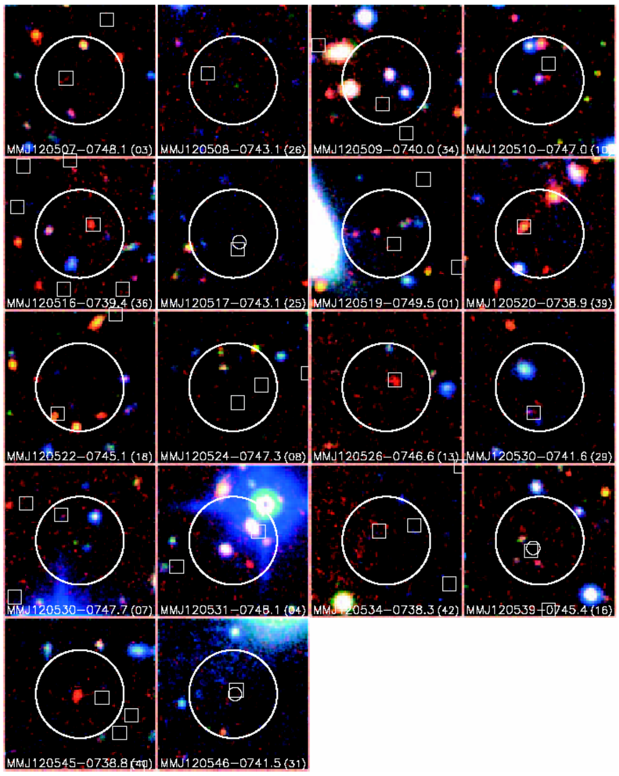


Deep BzK 'true' color identification images, overlayed with the original MAMBO beams (large circles) and the accurate interferometric locations using the VLA (small squares) or IRAM Plateau de Bure interferometer (small circles).
Optical identifications of the MAMBO sources range from extremely red but well detected objects to fields that are blank at K>22.

The counterparts of the NDF MAMBO mm sources (left panel below) are typically two magnitudes fainter than those of identifications from the SCUBA 8mJy survey at 850μm survey (Ivison et al. 2002, right panel below)

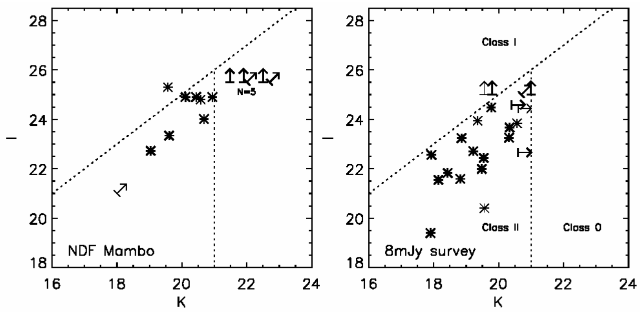


**References:**
• Dannerbauer, H., Lehnert, M.D., Lutz, D., Tacconi, L., Bertoldi, F., Carilli, C., Genzel, R., Menten, K.M. 2002, ApJ, 573, 473
• Dannerbauer, H., Lehnert, M.D., Lutz, D., Tacconi, L., Bertoldi, F., Carilli, C., Genzel, R., Menten, K.M. 2004, ApJ, 606, 664

*H. Dannerbauer, R. Genzel, M. Lehnert, D. Lutz, L. Tacconi*

# The High Redshift Galaxy Spectroscopic Imaging Survey in the Near-Infrared with SINFONI (SINS)

It is becoming increasingly clear that most of the baryonic mass in galaxies was put in place between z≈1 3. However, the real test of our understanding of galaxy formation and evolution is not just when the mass accumulated, but rather: How did it accumulate? Was the mass accumulation rate mass-dependent so that more massive galaxies formed earlier in the history of the Universe? Why do some galaxies have large amounts of angular momentum, while others do not?
We have developed an ambitious program to determine the spatially resolved dynamics, ionization, and metallicity of a large sample of high redshift galaxies with SINFONI at the VLT. This survey constitutes a majority (60% or ~50 nights) of our entire GTO program. Our sample is chosen to be a representative subsample of several samples with well-de ned selection criteria such as the BM/BX of Steidel, Shapley, et al. (see below), LBGs at z~3, bright K-band selected (e.g., K20), (sub)mm, infrared, narrow-band H-alpha and Ly-alpha, and other optical/near-IR color (R-K/J-K) selected galaxies in the redshift range of 1-3.5. Through this imaging spectroscopy study, we will determine: the growth/merger rate of galaxies, metallicities, frequency of superwinds, and the relationship between various classes of high redshift objects e.g., what are the relative masses, metallicities, and evolutionary state/star-formation history of objects across all of these selection criteria? Below are two examples of what we can learn through SINFONI observations.

SINFONI images of the galaxy pair BX404/405 constructed by combining all the K-band spectral elements and inset spectra of the reion near H$\alpha$ at z=2.03 of each component. The relative velocity of BX 404 and 405 is ~150 km s$^{-1}$ and a projected separation of 30 kpc. The emission line object to the south and west of BX404/405 has a velocity of 150 and 300 km s$^{-1}$ relative to BX405 and BX404 respectively. The two components of BX405 have velocities that differ by about 70 km s$^{-1}$ over about 6 kpc. The velocity and size allow a roughly dynamical mass estimate of ~$10^{10}$ M$_\odot$ for BX405. If BX 404/405 are part of a larger gravitationally bound structure, their relative velocities and projected distances suggest M$_{dyn}\approx 10^{11}$ M$_\odot$. The ratio of [NII]/H$\alpha$ crudely implies that BX 404 has roughly solar metallicity,

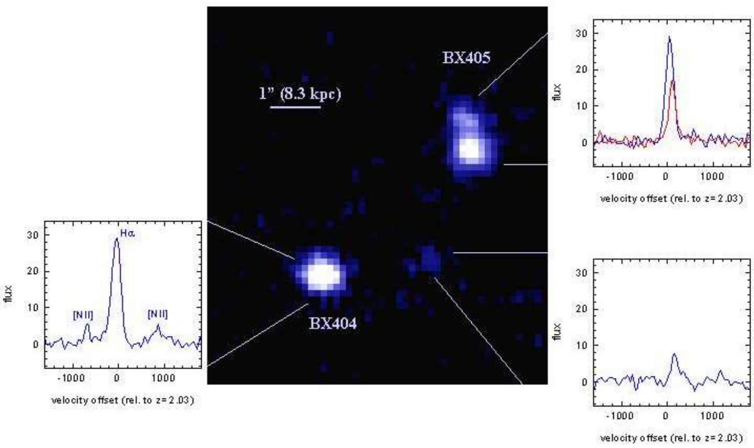


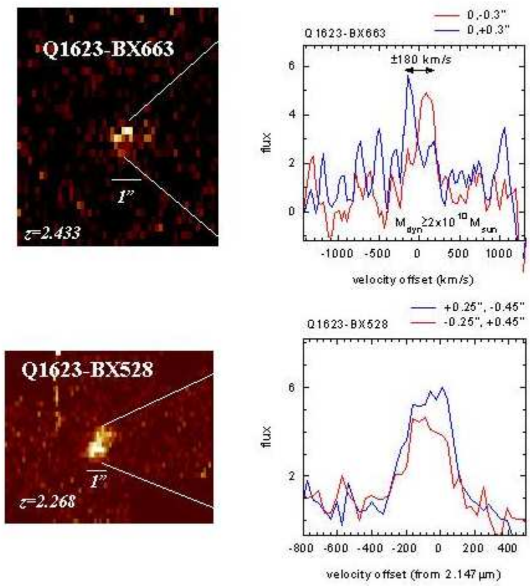


SINFONI K-band images of two galaxies Q1623-BX663 and BX528 and inset 1D-spectra of the region around H$\alpha$ at z=2.433 and 2.268 for each galaxy. The SINFONI data of BX663 reveals a velocity shear of 180km s$^{-1}$. With a projected separation of about 0.6 arc seconds or about 5 kpc, the velocity offset suggests M$_{dyn}$>2 $\times 10^{10}$ M$_\odot$. The SINFONI data of BX528 reveals only a small velocity offset across the galaxy (≈50km s$^{-1}$). The 2 components have FWHMs of ≈350 and ≈250 km s$^{-1}$ with each component separated by about 8 kpc in projection. The relatively broad lines of the individual regions compared to the small shear suggests that these are two interacting/merging galaxies. Assuming the line widths are due to virialized motions in each galaxies we can crudely estimate 1 and 3$\times 10^{11}$ M$_\odot$ each component respectively.

*M. Lehnert, F. Eisenhauer, R. Genzel, D. Lutz, N. Nesvadba, A. Gilbert, L. Tacconi*

# High Redshift Galaxies and the Sources of Reionization

Two of the most outstanding issues in modern astrophysics are what reionized the Universe and how did the rst objects form? We are attempting to address these questions in a series of VLT observations using the Lyman Break selection technique. To probe galaxies at the highest redshifts, we have obtained deep R-,I, and z-band exposures using FORS2 on the VLT. These images have 3$\sigma$ detection limits in a 2 arcsec aperture of $R_{AB}$=27.6, $I_{AB}$=26.3, and $z_{AB}$=26.7. The galaxies are selected through their red colors in R-I and I-z. Our primary interest are galaxies with large R-I colors which probe redshifts between 4.8 and 5.8. With last semesters observations, we have now observed about 160 arcmin$^2$ or a completeness corrected co-moving volume of $\approx 4\times10^5$ Mpc$^3$. Follow-up observations using the FORS2 multi-object spectrometer have yielded a spectroscopic redshift determinations of about half the total sample of about 50 galaxies. The galaxies have star-formation rates of a few tenths to about 20 $M_\odot$ yr$^{-1}$ as estimated from the strength of their UV continuum. The I-z colors of galaxies with 4.8<z<5.8 are consistent with very young ages (<100 Myrs) and low extinction ($A_V$<0.5). The rest-frame UV spectra and sensitive X-ray ux upper-limits on similarly selected sources in the CDFS indicate that these sources are not generally AGN.
Overall, our results indicate that the Universe was reionized by stars and not AGN, with most of the ionizing photons arising in relatively faint low mass galaxies.

Lehnert, M. D., & Bremer, M. N. 2003, ApJ, 593, 630
Bremer, M. N., Lehnert, M. D. et al. 2004, MNRAS, 347, 7
Lehnert, M. D., & Bremer, M. N. 2004, ESO Messenger, 115, 27

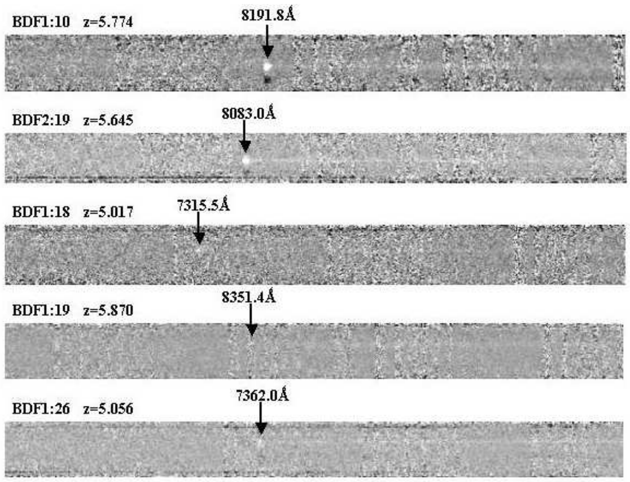


Two dimensional spectra of sources of break galaxies. The name and redshift are indicated above and to the left (blue) end of each spectrum and the wavelength Ly-alpha emission is indicated by the downward arrow. Continuum emission and then a break is visible in each. The lines show obvious redward asymmetries consistent with the line being Ly-alpha. These asymmetries are obvious even in the rendition for the top two spectra shown of the right.

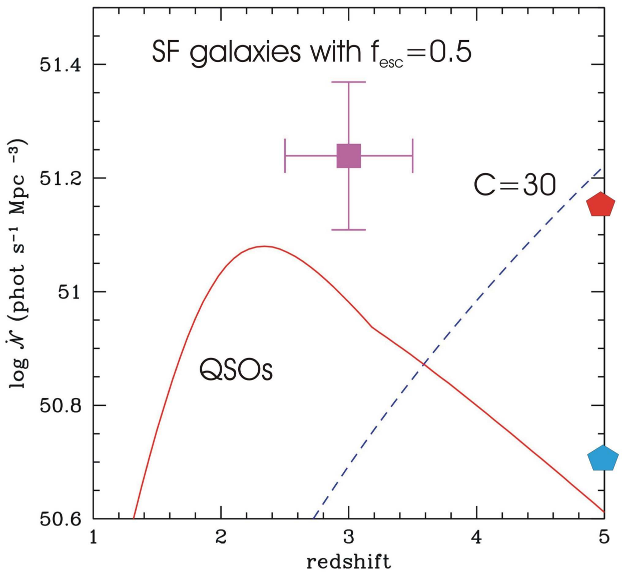


A reproduction of a gure from Madau et al. (1999) which shows the number of ionizing photons per unit volume versus redshift. The solid red line shows the contribution from optically selected QSOs while the dotted blue curve shows the number of photons needed assuming a clumpy distribution of Hydrogen. The large solid purple square represents star-forming galaxies at z$\sim$3 assuming an escape fraction of 50%. The cyan hexagon represents the UV ionizing photon density we have observed at z$\sim$5.3, while the red hexagon is the UV ionizing photon density based an extrapolation of our best t luminosity function to 0.2 L$^*$. In both cases, the we assume escape fraction is 100%. This implies that for these sources to reionize even their local volume, they must have a high escape fraction and the Universe needs to have a relatively smooth distribution of Hydrogen.

*M. D. Lehnert*

# AGB stars to date high-z galaxies with Spitzer

We present new stellar population models that include the contribution of the Thermally-Pulsing Asymptotic Giant Branch (TP-AGB). The TP-AGB phase marks the spectrum with peculiar spectro-photometric features in the near-IR ($\lambda > 0.6$ μm) for a very short period ($0.4 < t/\mathrm{Gyr} < 2$). Now that the Spitzer Space Telescope has access to the rest-frame near-IR at high redshifts, these models allow the use of the TP-AGB phase as age indicator also for primeval galaxies.

The determination of galaxy ages, that is accomplished by comparing observed spectra with stellar population models, is crucial to constrain galaxy formation models. However this task is very complicated since the stellar light is degenerate with respect to age and chemical composition. An exception are ages around 1 Gyr, when Thermally Pulsing Asymptotic Giant Branch (TP-AGB) stars are the dominant source of energy in the bolometric and near-infrared. In fact TP-AGB stars develop only in the narrow age range 0.4 to 2 Gyr and distinguish themselves by peculiar spectrophotometric features, like red colours (e.g. V-K~3.2) and molecular absorption bands. If detected, these stars are a robust age indicator for the underlying stellar population. However they are usually not included in stellar population models.
**Here we present stellar population models that include the TP-AGB phase.**

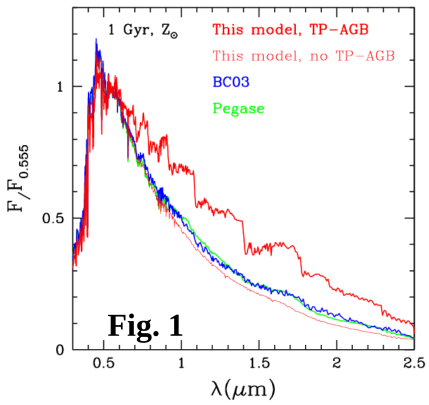


**Fig. 1**. Model SED of a 1 Gyr stellar population including the TP-AGB phase (thick red). Note the same model in which the phase was subtracted (thin red). Other models in the literature (blue, green) do not show the features of TP-AGB stars (Maraston 2004).

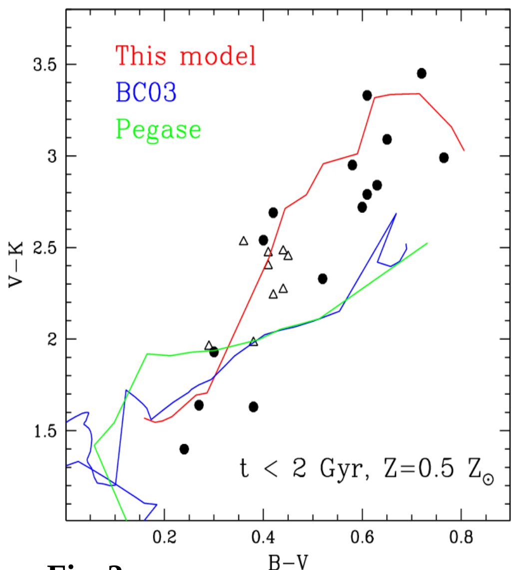


**Fig. 2**

**Fig. 2**. Model calibration with ~ 1 Gyr old globular clusters (GCs) . Only our models can reproduce the GC data.(Maraston 2004).

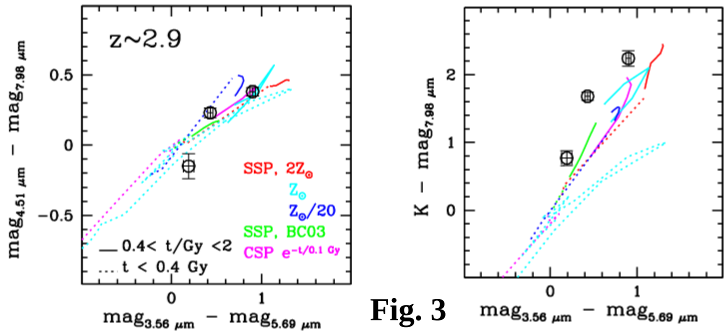


**Fig. 3**. Galaxy observed-frame colours at redshift ~3. The Spitzer data by Yan et al. 2004 (symbols) are compared with several stellar population models. AGB-ages between 0.4 and 2 Gyr are the thick lines, ages < 0.4 Gyr the dotted lines. One galaxy sticks out for having colours so red to require the inclusion of TP-AGB stars, **therefore is very likely ~1 Gyr old**. The galaxies have been dated to be 2.5 Gyr old by Yan et al. 2004 on the basis of models not containing the TP-AGB phase (green lines). Howerer, this age is **larger than the age of the Universe at this redshift** (Maraston 2004)


**References:**
•Yan et al. 2004, ApJ, *in press*, astro-ph 0408070
•Maraston, C. 2004, MNRAS, *submitted*



*C. Maraston*

# Age indicators for galaxies up to z~1

**We have computed the higher-order Balmer absorption line indices Hγ and Hδ for stellar population models with variable element ratios (Thomas, Maraston, & Korn 2004). The response of these indices to abundance ratio variations is taken from detailed line formation and model atmosphere calculations by Korn, Maraston, & Thomas (2005). We find that Hγ and Hδ, unlike Hβ, are very sensitive to α/Fe ratio changes at super-solar metallicities. With our new models we can now obtain consistent age estimates from Hβ, Hγ and Hδ.**

Both Hγ and Hδ line indices increase significantly with increasing α/Fe. This effect cannot be neglected when these line indices are used to derive the ages of metal-rich, unresolved stellar populations like early-type galaxies. We re-analyze the local elliptical galaxy sample of Kuntschner & Davies (1998), and show that consistent age estimates from Hβ and Hγ are obtained, only if the effect of α/Fe enhancement on Hγ is taken into account in the models. This result rectifiesa problem currently present in the literature, namely that Hγ and Hδ have up to now led to significantly younger ages for early-type galaxies than Hß. Our work particularly impacts on the interpretation of intermediate to high-redshift data, for which only the higher-order Balmer lines are accessible observationally.

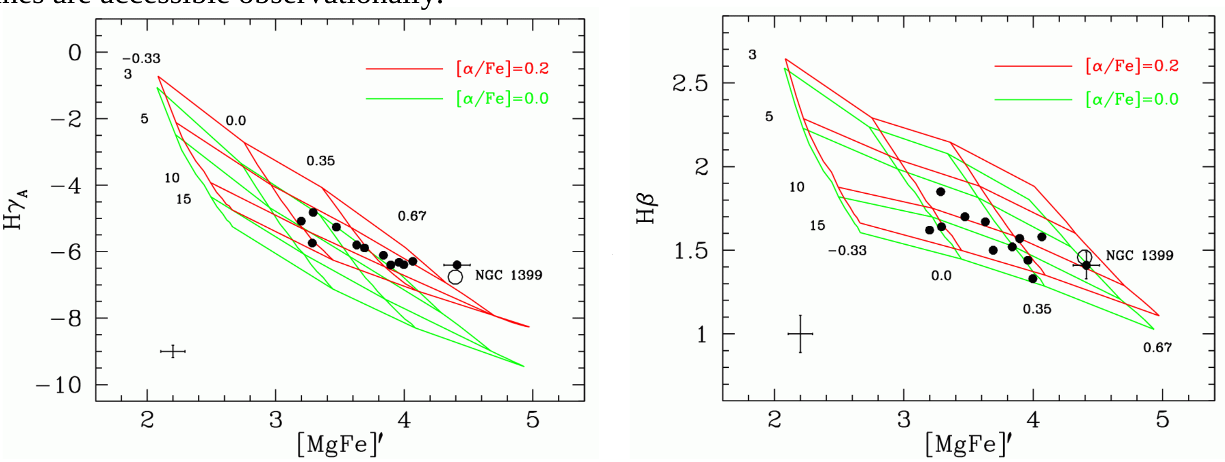


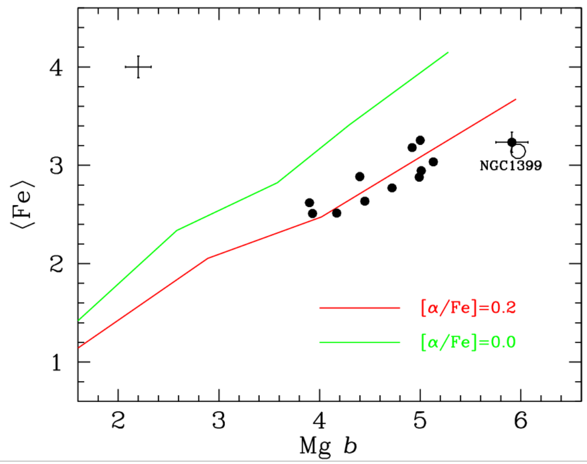


Balmer line indices HγA (top left-hand panel), Hβ (top right-hand panel) as functions of the α/Fe-independent index [MgFe]'. The bottom right-hand panel shows Mg *b* vs. <Fe>. Red and green lines are the α/Fe-enhanced and the solar-scaled models, respectively. Models for the ages 3, 5, 10, and 15 Gyr (only 10 Gyr in the bottom right-hand panel), and the metallicities [Z/H] = -0.33, 0.0, 0.35, 0.67 are shown (see labels). Filled circles are elliptical galaxy data from Kuntschner & Davies (1998).

The stellar population models are computed as explained in Thomas, Maraston, & Bender (2003) using new model atmosphere calculations of Korn, Maraston, & Thomas (2005).


**References:**

- Korn, A., Maraston, C., Thomas, D., 2005, A&A, submitted
- Kuntschner, H., Davies, R., 1998, MNRAS, 295, L29
- Thomas, D., Maraston, C., Bender, R., 2003, MNRAS, 339, 897
- Thomas, D., Maraston, C., Korn, A., 2004, MNRAS,



*D. Thomas, C. Maraston, A. Korn*

# The ESO Distant Cluster Survey (EDisCS)

The EDisCS project (White et al., submitted) is an ongoing programme to study cluster galaxies at high redshift. The sample consists of 19 clusters at z = 0.4–0.8, see Fig. 1 for an example. The first main result is the detection of a deficit of faint red sequence galaxies in the high redshift EDisCS clusters (Fig. 2). This excludes a synchronous formation of all red sequence galaxies, implying that a large fraction of the faint red sequence galaxies in current clusters moved there relatively recently.

The data taking has just finished, and a total of 36+22 VLT+NNT nights have been invested on deep optical imaging in 3 bands, deep NIR imaging in 1–2 bands, and deep optical spectroscopy giving spectra of ∼2000 galaxies (∼ half cluster, half field). In addition, HST/ACS imaging of the 10 highest redshift clusters has been obtained. Science goals:

- Obtain a uniform photometric and spectroscopic database for a large and representative sample of galaxy clusters covering the last half of the Hubble time
- Characterise the sizes, luminosities, morphologies, internal kinematics, star formation properties and stellar populations of cluster galaxies
- Compare cluster samples at z = 0.8, 0.5 and 0.1 (Sloan) to establish trends as a function of redshift and cluster properties
- Compare with high-resolution simulations of galaxy and galaxy cluster formation in a CDM universe to determine the role of various physical processes (e.g. harassment, stripping, strangulation, cannibalism, merging, induced star-formation, SN/AGN feedback) in establishing the properties of galaxies

Other results include:

- The first EDisCS clusters show a large range in velocity dispersion (Fig. 3). This is true for the sample as a whole, and it probably stems from the optical rather than X-ray selection. This allows us to study the influence of the cluster properties on the cluster galaxies.
- A weak lensing analysis has provided mass maps for the clusters (Clowe et al., submitted).

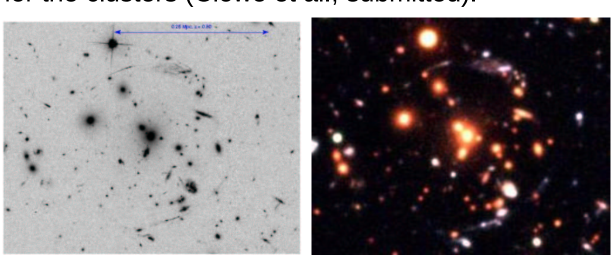

Figure 1. The central part of EDisCS cluster cl1216 at z = 0.80. Left: HST/ACS, right: VLT/FORS2.

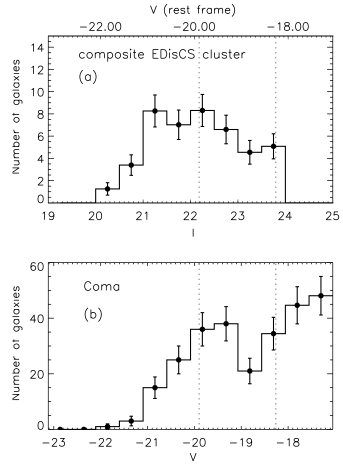


Figure 2. Number of galaxies on the red sequence for four z = 0.7–0.8 EDisCS clusters and for Coma. The EDisCS clusters have a deficit of faint galaxies on the red sequence (those between the dotted lines). From De Lucia et al. (2004, ApJ, 610, L77).

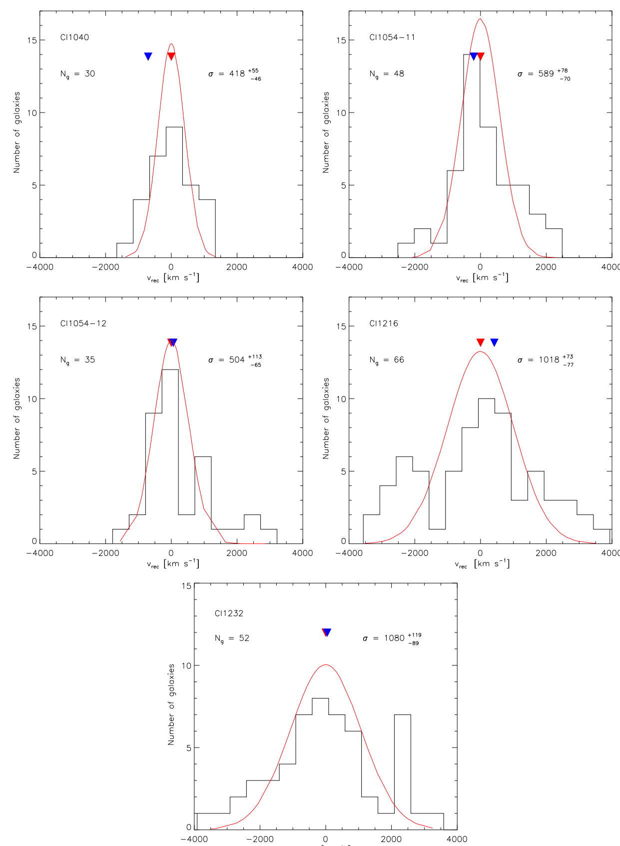


Figure 3. Velocity histograms for the first 5 EDisCS clusters. The velocity dispersion $\sigma$ is given and illustrated by the red gaussian. The blue arrow indicates the velocity of the BCG. The two $\sigma \approx 1000$ km/s clusters show significant substructure. From Halliday et al. (2004, A&A, in press, astro-ph/0408071).

*B. Milvang-Jensen, R. P. Saglia & R. Bender for the EDisCS collaboration*

# EPIC-XMM-Newton Observations of two nearby Galaxy Clusters

**We observed the two nearby galaxy clusters A3667 and A754 with the XMM-Newton. To cover the large angular extent of the clusters, mosaics involving 4 to 6 observing fields have been performed. Images were produced in the energy bands from 0.5 to 2.0 keV and 2.0 to 7.0 keV. We used a wavelet-filtering method to show variations in the surface brightness distribution down to a 5-sigma significance. With those images we produced hardness ratio maps. Using the soft surface brightness maps and the hardness ratio maps, we produced pressure and entropy maps.**

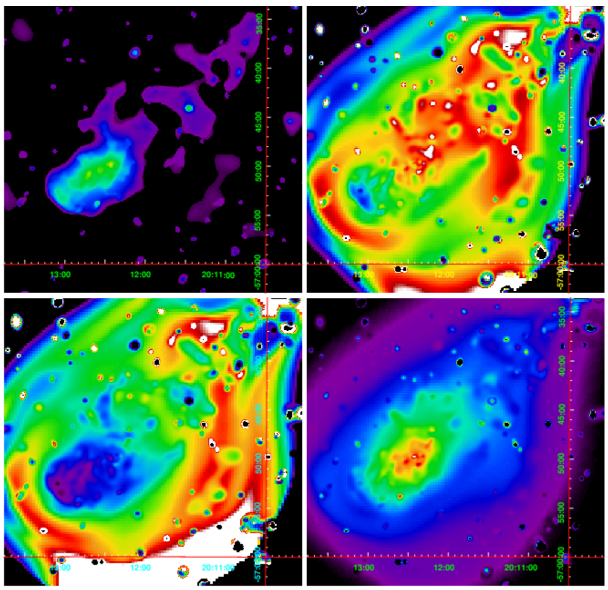

**A3667:** In the cluster A3667, Chandra detected a cold front with a very steep discontinuity in the X-ray surface brightness across it (Vikhlinin et al. 2001 and Mazzotta et al. 2002). With the EPIC data we clearly detect the very irregular shape of the cluster's surface brightness distribution and also the very steep drop around the cold front (see top-left figure, in which we show only the smallest wavelet scales). In addition to the three peaks in the center of the cluster we find striking evidence of turbulence down-stream of the cold front especially towards the north (confirming the findings of Chandra) and also towards the NW. This turbulence is even more evident in the hardness-ratio map (see top-right figure). This map shows hot gas flowing around the cold front probably developing Kelvin-Helmholtz instabilities. We observe structure in the cold front, resembling a mushroom head and stem. Such structure was found in simulations of cluster merger by Heinz et al. (2003). The intensity maximum is coincident with the lowest entropy (see bottom-left figure). We observe tails of low-entropy gas coming off the concave surface of the cold front. The pressure map (bottom-right figure) confirms that the cold front is not a shock front, there is no factor 4 increase of pressure accross the front. The pressure peak is not coincident with the cold front, rather with the brightest cluster galaxy. There is elongation in the pressure and in the entropy towards the north-west from the A3667 center.

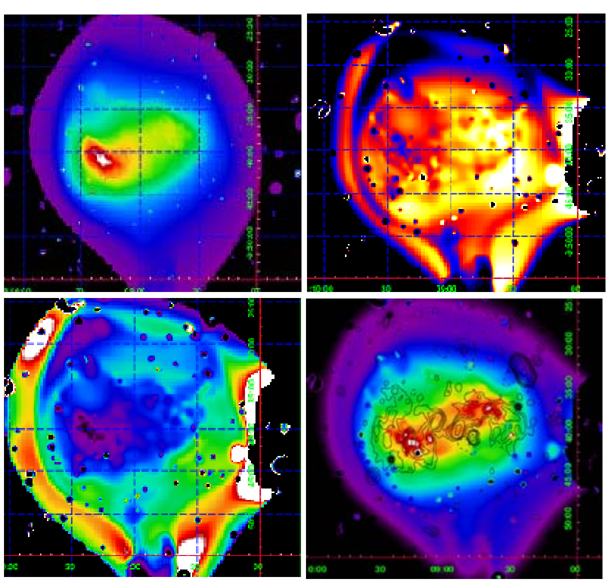

**A754:** The Abell cluster A754 is an example of a cluster experiencing a major merger. This was found in the observations made with ROSAT, which resulted in the first temperature map of A754 (Henry & Briel 1995) and also in ASCA data (Henriksen & Markevitch 1996). In the EPIC image, we clearly detect the very irregular shape of the cluster's surface brightness distribution, especially the bright elongated bar with the maximum in the brightness (see top-left figure). Moreover, the surface brightness west of the bar also shows turbulent-like substructure. The hardness ratio map (see top-right figure) confirms the hotter region west of the bar (also seen in the ROSAT and ASCA maps) and it shows additional temperature variations across the face of the cluster. It shows that only the northern part of the bar is at a low temperature, found also recently by Chandra (Markevitch et al. 2000). In addition, we find a hot outer rim seen in spectroscopic fits of the outer region. Different from earlier findings, we interpret our new observations as indicating the merging subcluster came from the north-west and has passed through the main cluster core. As expected, the peak of the pressure (bottom-right figure) is coincident with the peak of the surface brightness. We also find enhanced pressure in the NW region away from the highest X-ray intensity. These two high pressure regions seem to be associated with the diffuse radio emission, seen in observations at 20cm (Bacchi et al. 2003, contour lines in pressure map, bottom-right figure).

*U. G. Briel, A. Finoguenov, and J. P. Henry*

# High Redshift Double Cluster of Galaxies:

## XMM-Newton observations of RX J1053.7+5735 at $z \sim 1.1$ in the Lockman Hole

**The cluster RXJ1053.7+5735 in the Lockman Hole shows an unusual double-lobed X-ray morphology, indicative of a possible equal-mass cluster merger. We combined all XMM Lockman Hole EPIC observations to date (PV, AO-1 & AO-2 phases), totaling effective exposure times $\sim$ 648 ks, 738 ks, and 758 ks for pn, MOS1, and MOS2, respectively. With this 'deep' dataset, we could detect the Fe K line and obtain a strong constraint on cluster metallicity, which is difficult to achieve for clusters at z $>$ 1. The Fe line also allows us to directly estimate the redshift of diffuse emission, with a value z = 1.14 $^{+0.01}_{-0.01}$. This is one of the first clusters whose X-ray redshift is directly measured prior to the secure knowledge of cluster redshift by optical/NIR spectroscopy.**

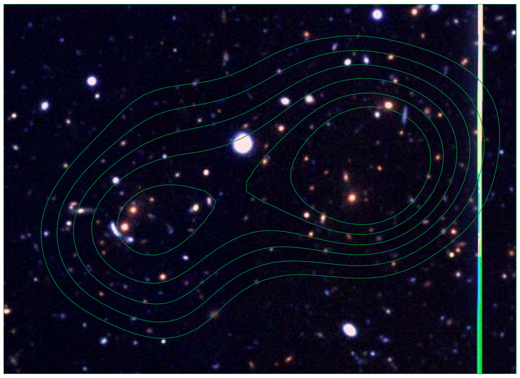

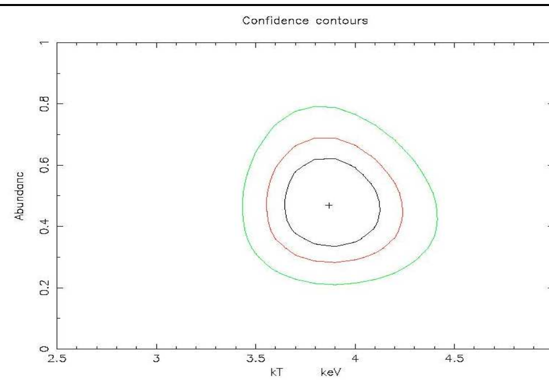


**Left:** XMM contour on top of a Subaru color image made from $R$, $I$, & $Z$ band. The image is 2 x 1.5 arcmin. North is up and East is left. **Right:** Two-dimensional $\chi^2$ contours at 68.3, 90, and 99% confidence levels for the temperature $kT$ and the abundance $Z/Z_\odot$ of the cluster.

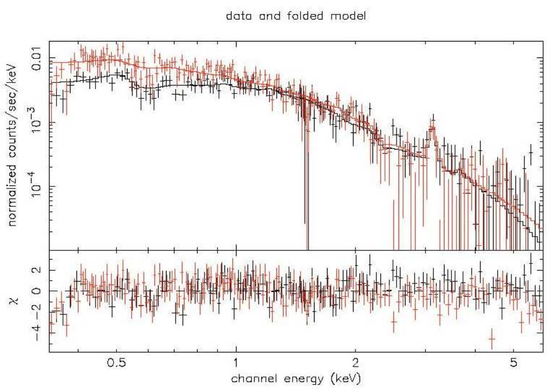


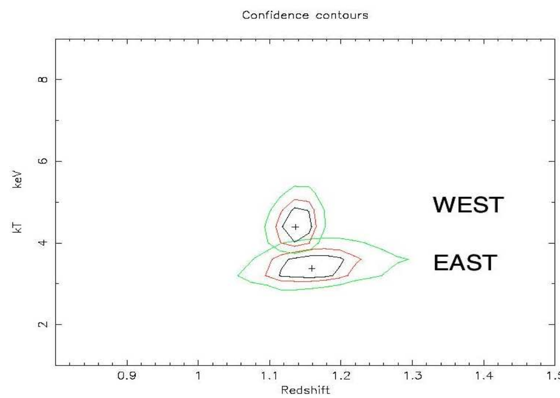


**Left:** Rebinned spectra, residuals, and best-fit models for the cluster with MOS1+2 (lower spectrum) , and pn (upper spectrum). **Right:** Two-D. $\chi^2$ contours at 68.3, 90, and 99% confidence levels for the temperature $kT$ and the redshift of the eastern and western lobes of the cluster.

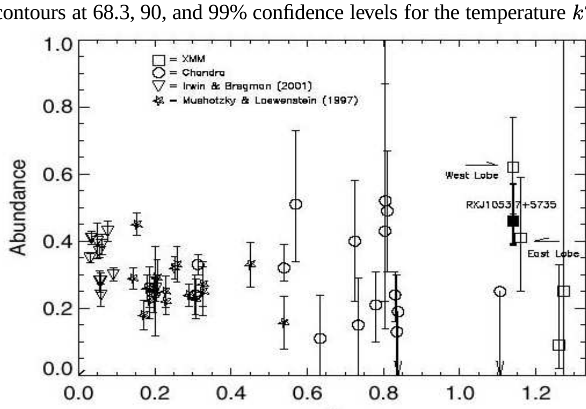


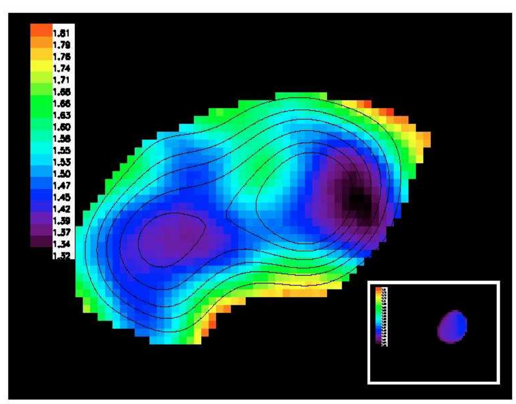

**Left:** New XMM abundance and its 1$\sigma$ error for the cluster plotted with high-z clusters from Tozzi et al. (2003). For comparison, the low-z samples from Mushotzky & Loewenstein (1997), and Irwin & Bregman (2001) are also plotted. **Right:** The X-ray hardness ratio map (1-8 keV)/(0.2-1 keV). The full-band (0.2-8 keV) contours are overlaid on the hardness ratio map.

*Y. Hashimoto, G. Hasinger, H. Böhringer, H. Brunner, V. Mainieri in collaboration with X. Barcons, X., A.C. Fabian*

# Dark matter and gas entropy in poor clusters

We present an XMM-Newton analysis of the total mass and entropy profiles of a small sample of poor galaxy clusters, and compare to those of one hot cluster. The scaled mass profiles are found to be remarkably similar, and the dispersion in their NFW parameterisations are found to be consistent with the results from numerical simulations. The entropy profiles are similar beyond ~0.1 r200, but require non-standard scaling with temperature, indicating the strong effect of non-gravitational gas physics on the X-ray properites.

The distribution of mass M(r) and the entropy S(r) reflect respectively the physics of the gravitational collapse and the thermodynamic history of the gas. We calculate mass profiles from the spatially resolved gas temperature and density information assuming spherical symmetry and hydrostatic equilibrium. We then fit these profiles with the NFW mass model. We calculate the entropy from the same density and temperature profiles using the equation S = kT ne-2/3. The key characteristics of the clusters under consideration are summarised in Table 1. Note that four of these clusters have very similar temperatures.

Table 1. Cluster sample.

| Name | z | kT |
|---|---|---|
| A1983 | 0.044 | 2.20 |
| A2717 | 0.050 | 2.53 |
| MKW9 | 0.038 | 2.58 |
| A1991 | 0.056 | 2.65 |
| A1413 | 0.141 | 6.51 |

Results

Thescaled  mass profiles show ~20 per cent scatter. The concentration parameters are consistent with the expected dpendence with mass. The scatter in the entropy profiles is reducd by ~40 per cent, to ~22 per cent, if they are scaled as $S \propto T^{0.65}$. Note the remarkable difference in entropy  properties at small radius.

The dark matter collapse seems well understood, but non-gravitational processes have a marked effect on  the gas physics. More details in Pratt & Arnaud (2004).

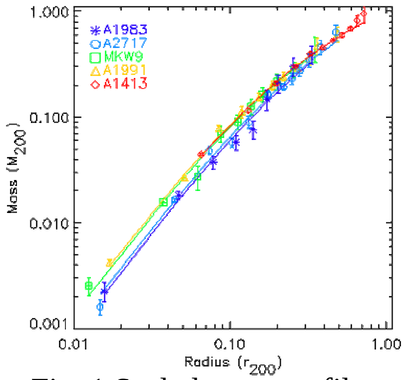


Fig. 1 Scaled mass profiles.

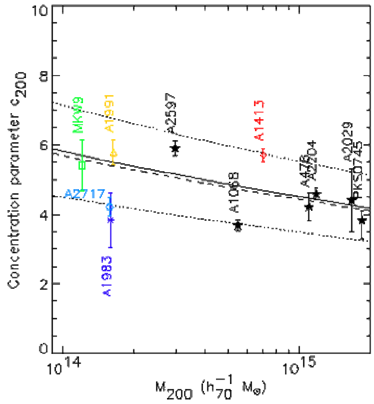


Fig. 2 NFW concentration parameter vs mass

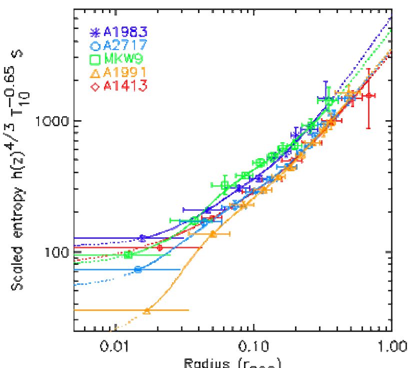


Fig. 3 Entropy profiles with $S \propto T^{0.65}$ scaling

**References:**
• Pratt & Arnaud, 2004, astroph/0406366

*G.W. Pratt & M. Arnaud*

# The Velocity Dispersion of Poor Groups of Galaxies

Poor groups of galaxies constitute the most common galaxy associations. We test with the $L_x$ - $\sigma$ relation if groups resemble scaled down versions of clusters. We find with proper measurements of the velocity dispersion, $\sigma$, that the groups and clusters are characterized by a similar power law in the $L_x$ - $\sigma$ relation, with a shift steepening for the groups.

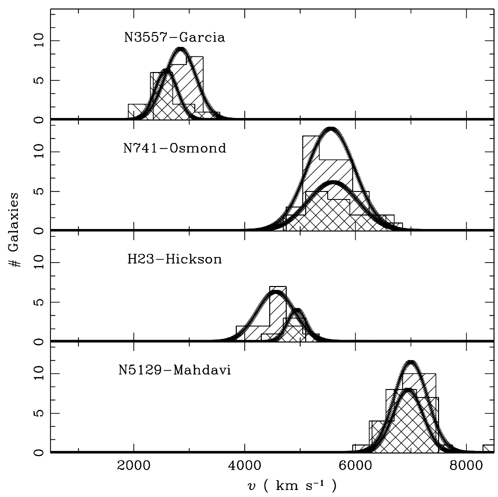


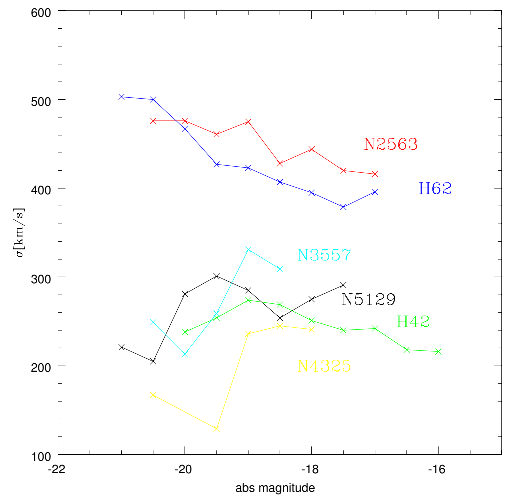


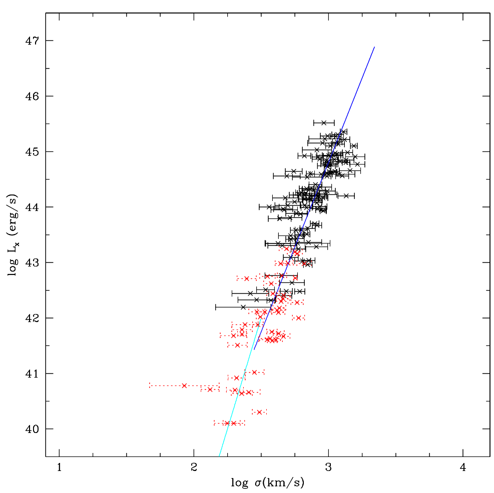


Upper left: Comparison of sparse and complete sampled velocity distributions for four groups.
Upper right: Velocity Dispersion as a function of limiting magnitude for six groups.
Lower left: The corrected $L_x$ -$\sigma$ relation, black data points being the clusters and red data points being the groups.

Based on the sample of poor groups by Mulchaey et al. (2003), we revisit the scaling relations of the properties of poor groups. One reason of the partly conflicting results in the literature is the low number statistics of galaxy velocities for poor groups (Figure1). We find that $\sigma$ changes with the number of measured velocities and that robust velocity dispersions can only be derived with a complete galaxy velocity survey down to an absolute magnitude of -19 in R (Figure2). By selecting only the groups with robust velocity dispersions we also find a similar relation for groups and clusters down to log $L_x \sim 42.5$ and that for fainter X-ray groups only spiral rich systems (like HCG16) are breaking the similarity between groups and clusters of galaxies (Figure3).

*M. Zimer, H. Böhringer, J. Mulchaey*

# Exploring the Structure of Galaxy Clusters at $z \sim 0.3$

**Precise determination of global properties of galaxy clusters and their scaling relations with cluster mass is a task of prime importance for the use of clusters as cosmological probes. In a detailed XMM-Newton study of thirteen X-ray luminous REFLEX Survey clusters at $z \sim 0.3$ we found that the clusters show in many properties a closely self-similar behavior. This helps to establish tighter scaling relations and to get good estimates of physical cluster properties from these global parameters which are easy to observe.**

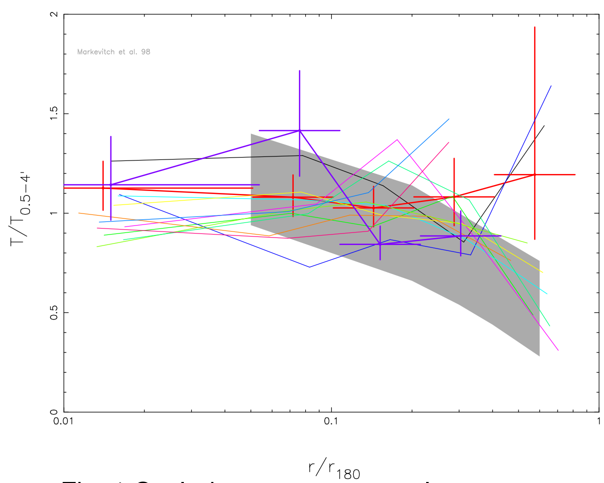


Fig. 1 Scaled temperature pro les.

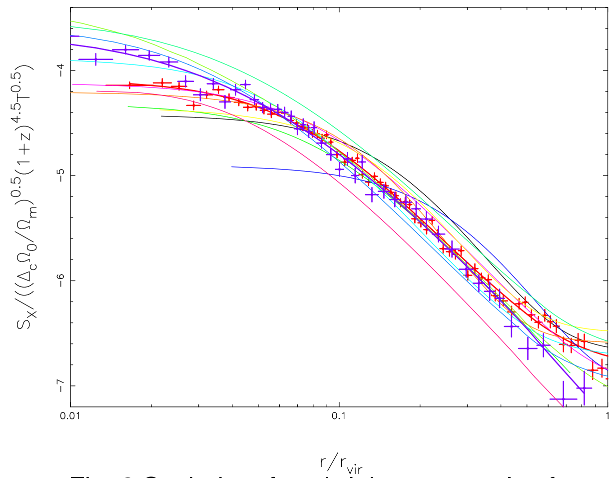


Fig. 2 Scaled surface brightness pro les for pn.

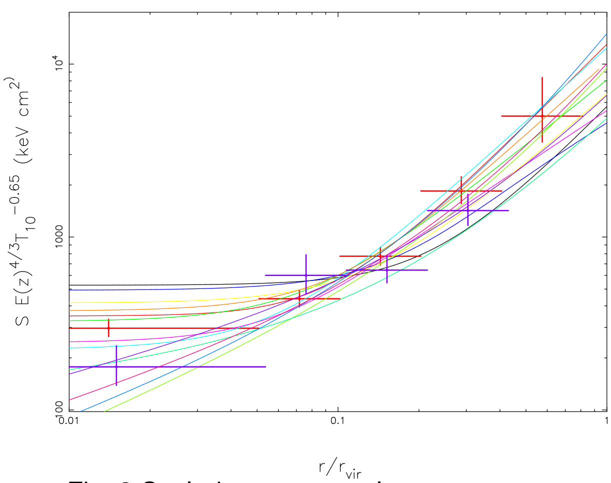


Fig. 3 Scaled entropy pro les.

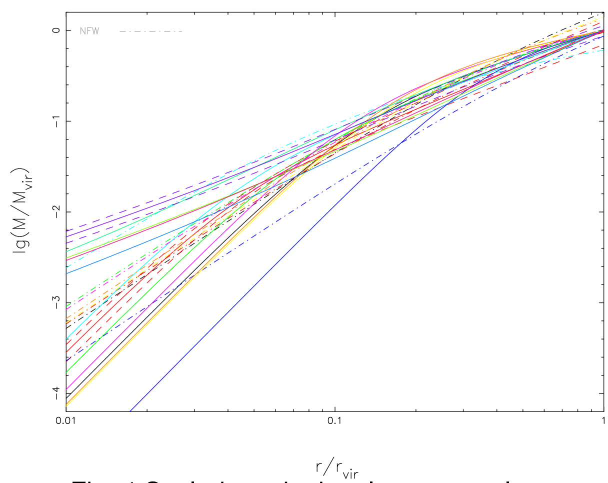


Fig. 4 Scaled gravitational mass pro les.

For our study we scale the properties to the cluster global parameters, e.g. radii scaled to the virial radii derived from the mass modeling using the ICM temperature and density pro les. We use $r_{180}$ for the temperature pro le scaling as shown in Markevitch et al (1998). We nd: (1) very similar scaled temperature pro les with a broad maximum at $0.1 r_{\rm vir}$, (2) self-similar surface brightness scaled according to the standard self-similar model (e.g. Arnaud et al. 2002) in which ve cooling ow clusters (eight non-cooling ow clusters) are well tted by an extended NFW (beta) model, (3) self-similar behavior of the entropy using the empirical temperature scaling of Ponman et al. (2003), and (4) gravitational mass pro les scaled by the virial mass in which the NFW model provides a satisfactory t for the non-cooling ow clusters in the $r > 0.1 r_{\rm vir}$ region and the cooling ow clusters show higher mass distributions in the cores. We adopt a at Universe of $\Omega_{\rm m} = 0.3$, $\Omega_\Lambda = 0.7$, and $H_0 = 70$ km s$^{-1}$ Mpc$^{-1}$. Error bars (con dence intervals as dashed curves) correspond to the 68% con dence level shown only for two typical examples: an example of a non-cooling ow (cooling ow) cluster is shown in red (blue).

*Y.-Y. Zhang, H. Böhringer, A. Finoguenov, Y. Ikebe, K. Matsushita, P. Schuecker, L. Guzzo, C. A. Collins*

# The All-Sky ROSAT X-ray Cluster Survey

**We are in the process of completing our survey of X-ray galaxy clusters in the ROSAT All-Sky Survey down to nominal X-ray flux limits of $2 \times 10^{-12}\,\mathrm{erg\,s^{-1}\,cm^{-2}}$ in the ROSAT energy band $(0.1 - 2.5)$ keV. The sample excludes the galactic plane below $|b_{II}| < 20$ deg and other crowded regions. It results from the combination of the published NORAS and REFLEX catalogues as well as their extensions to lower flux and contains about 1 500 clusters with redshifts $z \leq 0.6$. It will be used in combination with improved cluster scaling relations for precise cosmological tests, with particular regard to the the shape and amplitude (biasing) of the matter power spectrum up to $1.0\,h^{-1}\,\mathrm{Gpc}$, its normalization $\sigma_8$, and the equation of state of the dark energy $w$. The survey also provides insights into cosmography and the potential to find interesting and rare objects.**

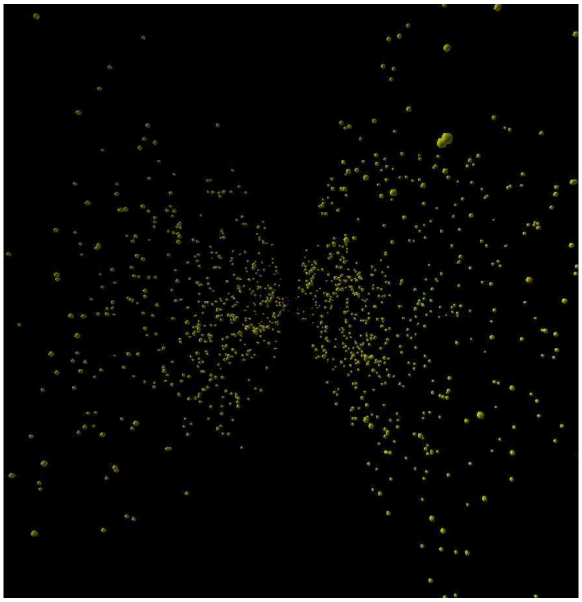

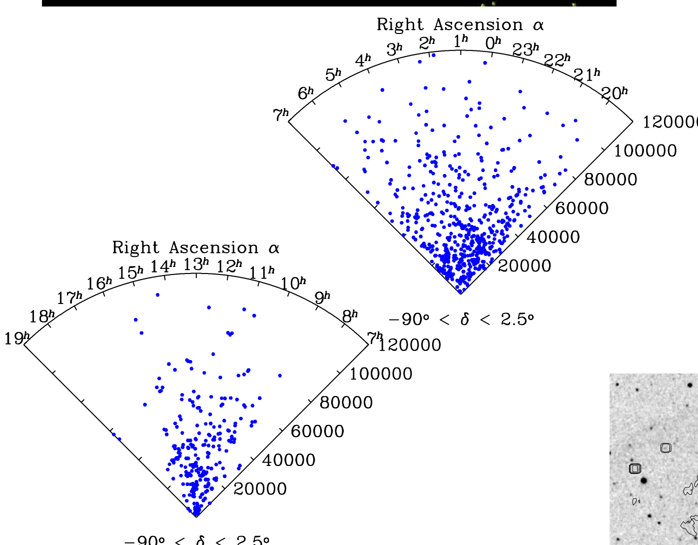


3-dimensional representation of the complete survey and cone diagrams of the redshift distribution of X-ray clusters in the southern hemisphere. The radial axis $cz$ in units of km/s. Superclustering on 100 Mpc scales (10,000 km/s) is clearly seen. Sample dilution towards larger distances is introduced by the X-ray ux limit.

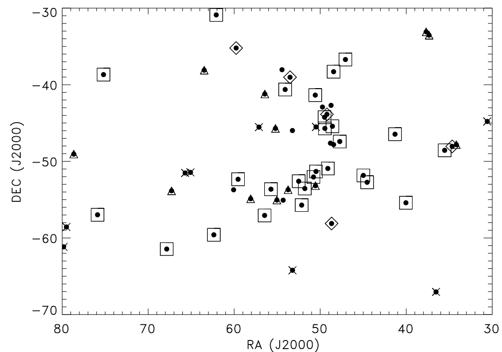


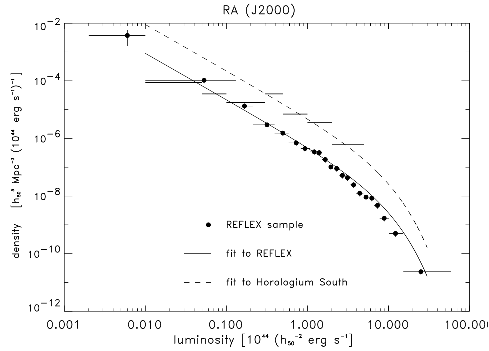


Abell (dots only) and X-ray cluster distribution in the Horologium-Reticulum supercluster. The lower panel shows the X-ray luminosity function of the southern concentration of the superclusters compared to that of REFLEX. The density of X-ray luminous clusters is about 10 times and the underlaying dark matter density about 3 times higher than the cosmic mean, indicating that the southern and northern concentration in the supercluster are close to collapse.

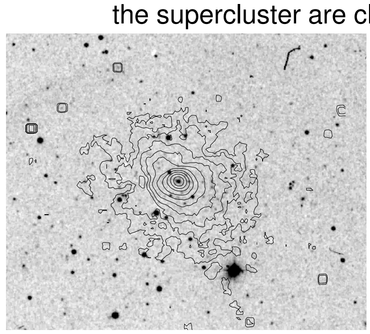

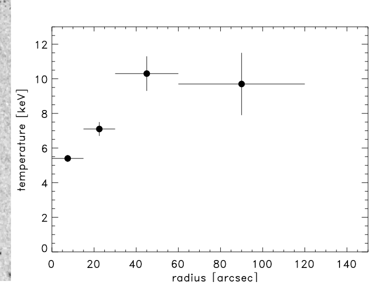


RXCJ1504-0248, the most prominent cooling core cluster at $z < 0.4$ discovered in the REFLEX survey. The CHANDRA image (right) shows an extremely compact cluster and the temperature pro le (left) shows the cooling core structure.

**Hans Böhringer & Peter Schuecker**

# Cosmology with X-ray Clusters

With REFLEX as the largest homogeneously selected sample of X-ray clusters of galaxies, we measured on very large scales the average cluster number density and its spatial fluctuations. These measurements yield direct observational constraints on the Gaussianity of the cosmic matter field, the average matter density $\Omega_{\rm m}$, and the normalization of the matter fluctuations $\sigma_8$. The combination of the cluster counts with recent type-Ia supernovae distances yields tight constraints on the equation of state of the dark energy $w$ and thus on the validity of the strong and the null energy condition of General Relativity.

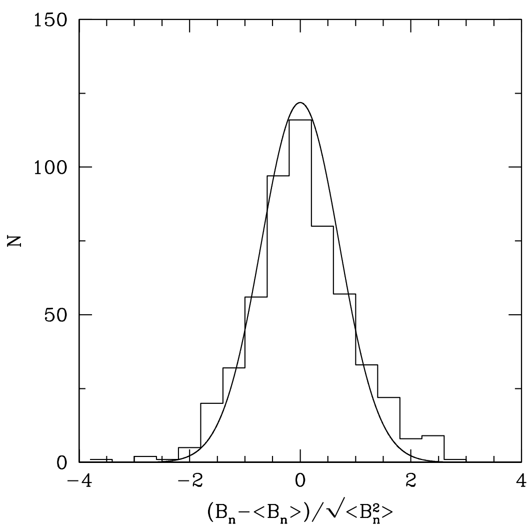


The eigenvalues of the REFLEX correlation matrix test the Gaussianity of the spatial fluctuations of the REFLEX clusters up to Gpc scales. Their 93%-KS probability for Gaussianity provides a well-defined starting point for precise cosmological tests using REFLEX cluster counts.

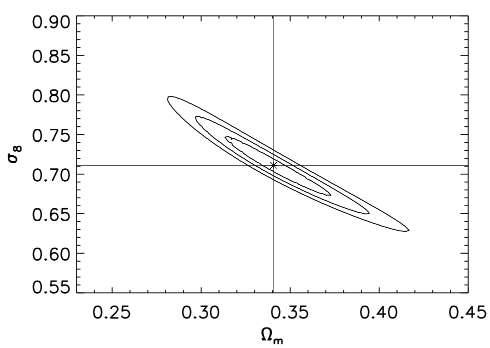


The eigenvectors of the REFLEX correlation matrix provide a natural way to combine average cluster counts and their spatial fluctuations for cosmological tests which break the degeneracy between $\sigma_8$ and $\Omega_{\rm m}$ in likelihood maps.

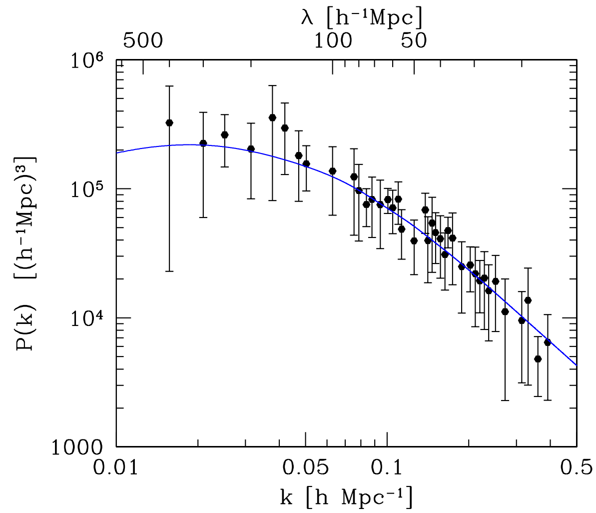


The amplitudes of the Fourier modes of the REFLEX number counts constitute the cluster power spectrum. It is well fit by a $\Lambda$Cold Dark Matter model with a low matter content.

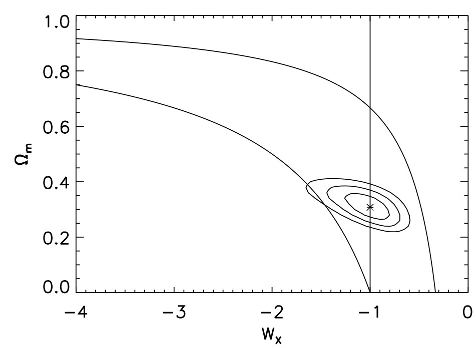


The combination of REFLEX cluster counts and type-Ia SNe luminosity distances are found to be consistent with the cosmological constant ($w = -1$). The likelihood contours fall within a region where the null energy condition is valid (lower curve) and the strong energy condition violated (upper curve), suggesting a Universe in a phase of accelerated cosmic expansion, and leaving not much room for exotic types of dark energy.

**P. Schuecker & H. Böhringer**

# Probing Dark Energy with OmegaCAM

**A first step towards a better understanding of the dark energy is the measurement of its equation of state $w$. Our design studies of a kilo square degree multicolour imaging survey to be performed with the OmegaCAM imager at the VLT Survey Telescope show that $w$ can be measured with errors on the 10-20% level. Photometric redshifts allow a very precise determination of the location of the baryonic acoustic oscillations in the angular power spectrum of galaxy density fluctuations within independent redshift shells between $z = 0.5 - 1.4$. Further cosmological constraints are provided by three-dimensional galaxy power and bi-spectra which can be measured with the OmegaCAM survey on scales up to $1.2\,h^{-1}\,\mathrm{Gpc}$. Of central importance for the proposed survey are also measurements of weak lensing of faint galaxies for studies of a scale-dependent biasing, and $w$.**

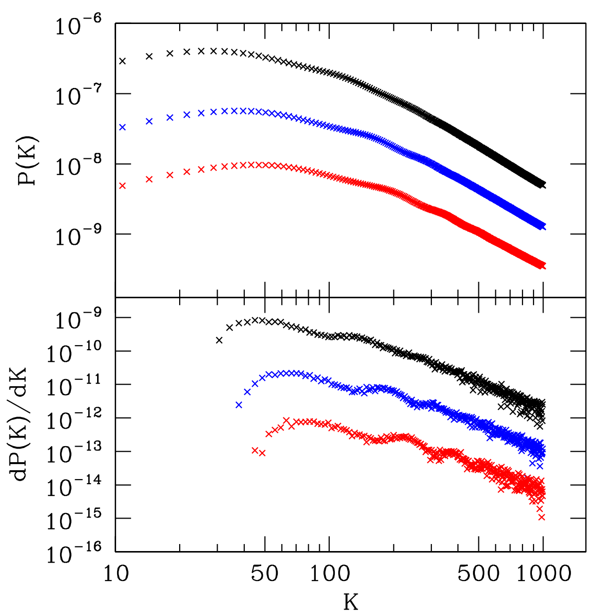


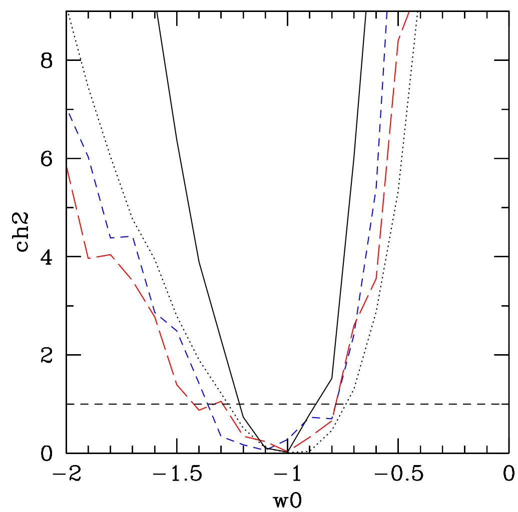


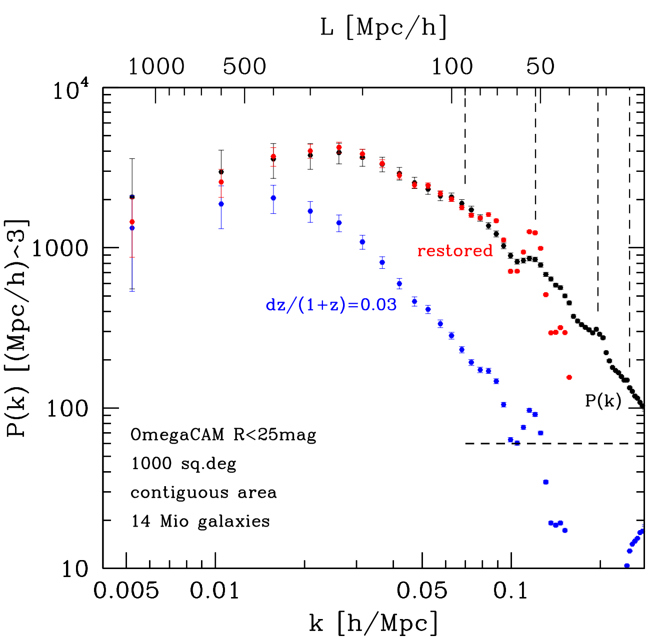


**Upper left:** Simulated angular power spectra $P(K)$ measured in three redshift shells $\Delta z = 0.3$ centered at $z = 0.65$ (black), 0.95 (blue), 1.25 (red), and their derivatives $dP/dK$. They clearly show the baryonic acoustic oscillations used for our proposed cosmological tests. **Lower left:** Simulated three-dimensional power spectra obtained without photometric redshift errors (black), with redshift errors of $\sigma_z = 0.03/(1+z)$ (blue), and after correction for redshift errors (red). Between $80\,h^{-1}\,\mathrm{Mpc}$ and $1.2\,h^{-1}\,\mathrm{Gpc}$, power spectral densities can be clearly measured. These data thus nicely supplement the measurements of the angular power spectrum on small scales. **Upper right:** $\chi^2(w)$ distribution obtained in different redshift shells (dashed, dotted lines) and after combination of all 3 redshift shells (continuous line) based on $dP/dK$ as expected for the proposed survey. Further tests are in progress to measure also a possible change of $w$ with $z$ expected to be the cleanest discrimination of dark energy models from a cosmological constant.

**P. Schuecker, R. Bender, U. Hopp, R. Saglia & S. Seitz**

# Extragalactic Gamma-Ray Background

**A re-evaluation of the extragalactic gamma-ray background has been made using a new model of the Galactic emission. The background spectrum deviates from the power-law of earlier analyses, and shows a positive curvature as expected for an origin in a population of blazars.**

The determination of the extragalactic gamma-ray background (EGRB) depends critically on the correct accounting for the Galactic emission. A new model (see separate poster) provides a more satisfactory prediction of the EGRET data than ever before, all over the sky and over the full EGRET energy range. This has been used as the basis for a re-evaluation of the EGRB.
The technique is to fit the model to the data at latitudes |b| > 10°, with the intercept yielding the EGRB. This means that errors in the absolute Galactic intensity are eliminated, and only the modelled angular distribution is used.

An important difference from previous analyses is the large contribution from inverse-Compton emission at high latitudes. This has the effect of reducing the EGRB by a factor of up to 2 . While previous work gave a power-law spectrum, we find a positive curvature.
The origin of the EGRB is generally believed to be the sum of undetected blazars, based on extrapolating the log N-log S from EGRET- detected blazars. Such a sum of sources with a range indices naturally produces the positive curvature which we observe.

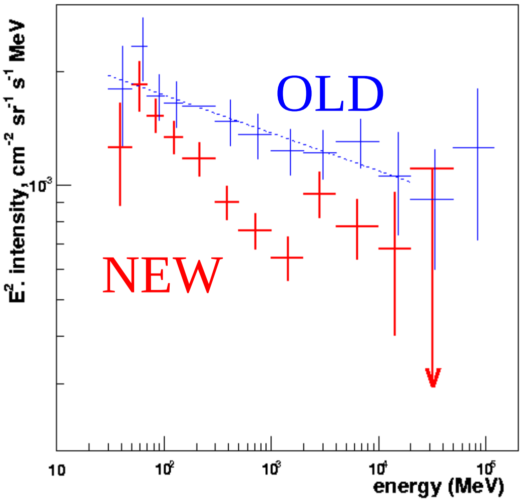


Extragalactic Gamma-Ray Background from EGRET data:
OLD is `standard' background (Sreekumar et al. 1998)
NEW is this work.

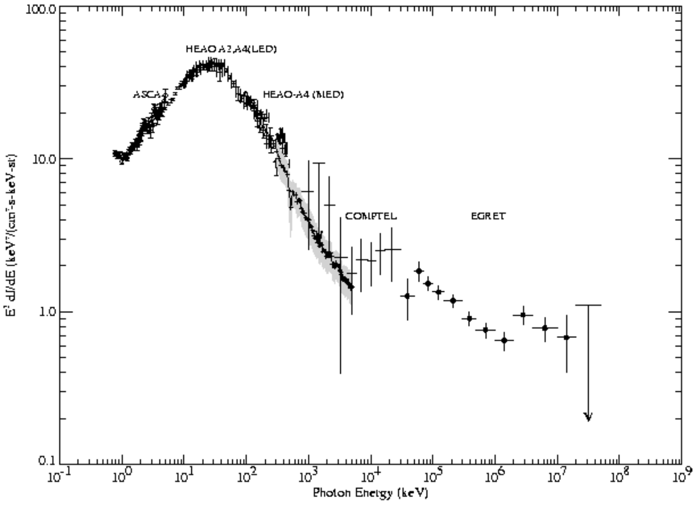


Broad-band extragalactic background including new EGRET result.

**References:**
• Strong, A.W., Moskalenko, I.V., Reimer, O. (2004) ApJ 613, 956
• Sreekumar, P., et al. (1998) ApJ , 494, 523

*A. W. Strong*

# Complex Plasmas

# Highly Resolved Fluid Flows - "Liquid Plasmas" at the Kinetic Level

Fluid flow around an obstacle was observed at the kinetic (individual particle) level using "complex (dusty) plasmas" in their liquid state. These "liquid plasmas" have bulk properties similar to water (e.g., viscosity), and a comparison in terms of similarity parameters suggests that they can provide a unique tool to model classical fluids. This allows us to study "nanofluidics" at the most elementary – the particle – level, including the transition from fluid behaviour to purely kinetic transport.

The experiments were carried out in a radio-frequency (rf) plasma chamber. A temperature gradient was used to compensate for gravity. The microparticles (diameter  3.7µm) develop a steady axially symmetric flow pattern with an upward flow at the perimeter and a homogeneous uniform downward flow of diameter 2 cm along the chamber axis (Fig. 1,2). The mean separation between the particles is 90 µm.

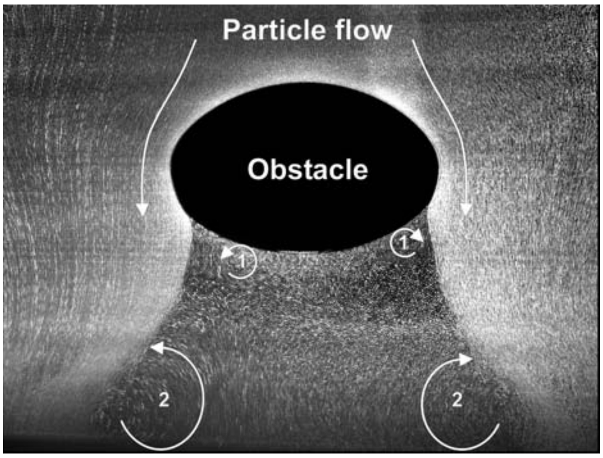


*Fig. 1: Topology of the particle flow around the "void".*

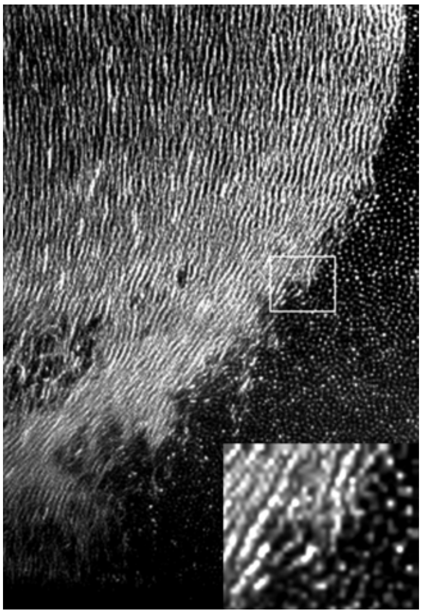

*Fig.2: An example of the mixing layer – an enlargement of the left side of the flow regime shown in Fig. 1*

The "obstacle" is a lentil shaped "void" – a region in which plasma processes prevent particle penetration. Surrounding the void upstream, a laminar boundary layer is formed. Behind the obstacle a "wake" is formed, which is separated from the laminar flow region by a mixing layer. Some momentum has to be transferred into the wake region, since adjacent to its boundary a vortex flow is established, with a rotation direction suggesting that the energy source is in the flow. Further downstream there is a second vortex (torus) in the wake, which rotates in the same way, also suggesting the flow as the energy source.

The mixing layer between the flow and wake exhibits instability growth on scales much smaller than the hydrodynamic scale, if we identify this as the density or shear velocity gradient along the flow lines. The solution to this puzzle is probably due to the curved flow driving a collisional instability, which has been observed for the first time at the kinetic level.

**References:**

Morfill, G. E., M. Rubin-Zuzic, H. Rothermel, A. V. Ivlev, B. A. Klumov, H. M. Thomas, and U. Konopka, Highly Resolved Fluid Flows - "Liquid Plasmas" at the Kinetic Level, Phys. Rev. Lett., **92** (2003)

*G. E. Morfill, M. Rubin-Zuzic, H. Rothermel, A. V. Ivlev, B. A. Klumov, H. M. Thomas, U. Konopka*

# MOMENTUM TRANSFER IN COMPLEX PLASMAS

**Momentum transfer in complex plasmas is investigated assuming an interaction potential between the charged species of the screened Coulomb (Yukawa) type. Momentum transfer cross sections and rates are derived. The obtained results have a wide range of applications including calculations of different kind of drag forces, classification of possible complex plasma states and transport properties.**

Momentum transfer between different charged components in complex plasmas is investigated. A detailed model analysis of grain-electron, grain-ion, and grain-grain collisions is performed (electron-ion collisions are well described within standard plasma theory). Assuming the screened Coulomb (Debye-Hückel or Yukawa) interaction potential (attractive or repulsive) the momentum-transfer cross sections are calculated numerically. In Fig. 1 these cross sections are shown as functions of the so called *scattering parameter* $\beta$, which is the ratio of the Coulomb radius to the screening length. It can be shown to be the unique parameter describing scattering of pointlike particles interacting via the Yukawa potential. For typical complex plasma parameters the characteristic value of $\beta$ for different types of collisions are: For electron-grain $\beta \ll 1$, for ion-grain $1 < \beta < 30$, and for grain-grain $\beta \gg 1$. The standard Coulomb scattering theory is applicable only for electron-grain collisions, but for ion-grain and grain-grain collisions different approaches should be used. Based on our numerical calculations the required approaches are developed, the role of the finite grain size is investigated, and analytical approximations for the momentum transfer cross sections are proposed. The latter are used to estimate the characteristic momentum-transfer rates in complex plasmas. The obtained results have a number of applications, e.g., calculation of the ion drag [1-3] and electron drag [4] forces, development of criteria to classify the possible states of complex plasmas in terms of the momentum transfer [5-7], investigation of the hierarchy of the momentum transfer in grain-grain and grain-neutral collisions[7].

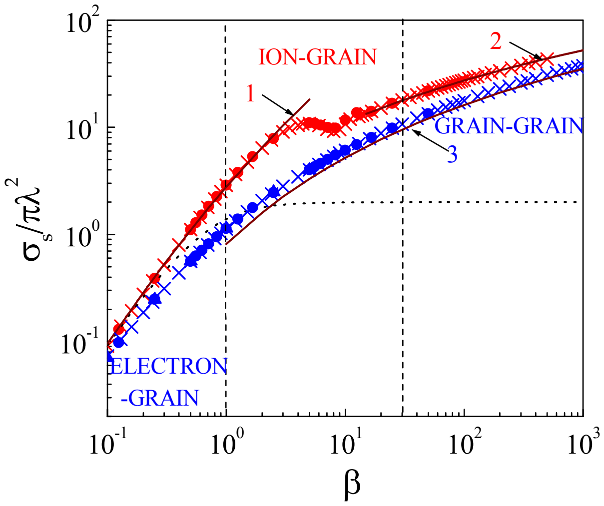


**Fig. 1** Momentum-transfer cross section, $\sigma_s$, normalized to $\pi\lambda^2$ (where $\lambda$ is the plasma screening length), versus the scattering parameter $\beta$. The upper (red) data are for attractive and the bottom (blue) data are for repulsive screened Coulomb potentials. Crosses correspond to our numerical calculation, circles and (blue) triangles are earlier numerical results by Hahn *et al.* and Lane and Everhart, respectively. Solid curves correspond to our analytical approximations. The dotted line corresponds to the Coulomb scattering theory. The later underestimates considerably the cross sections above $\beta \sim 1$. Vertical dashed lines conditionally divide $\beta$-axis into three regions: $\beta \ll 1$ is typical of electron-grain collisions; $1 < \beta < 30$ is typical of ion-grain collisions; $\beta \gg 1$ is typical of grain-grain collisions.

[1] S. A. Khrapak, A. V. Ivlev, G. E. Morfill, and H. M. Thomas, Phys. Rev. E **66**, 046414 (2002).
[2] S. A. Khrapak, A. V. Ivlev, S. K. Zhdanov, and G. E. Morfill, Phys. Rev. Lett. **90**, 225002 (2003).
[3] S. A. Khrapak *et al.*, IEEE Trans. on Plasma Sci. **32**, 555 (2004).
[4] S. A. Khrapak and G. E. Morfill, Phys. Rev. E **69**, 066411 (2004).
[5] G. E. Morfill *et al.*, Phys. Scripta **T107**, 59 (2004).
[6] G. E. Morfill *et al.*, Contrib. Plasma Phys. **44**, 450 (2004).
[7] S. Khrapak, A. Ivlev, and G. Morfill, Phys. Rev. E (in press, 2004).

*S. Khrapak, A. Ivlev, S. Zhdanov, G. Morfill, and H. Thomas*

# Kinetics of non-Hamiltonian ensembles

**Kinetics of particle ensembles with variable charges is investigated. It is shown that the energy of such non-Hamiltonian systems is not conserved in the interparticle collisions. The case when the equilibrium charge depends on the particle coordinate is studied, and the collision integral describing the momentum and energy transfer in collisions is derived. The mean thermal energy exhibits explosion-like growth, diverging at a finite time.**

One of the remarkable features distinguishing complex (dusty) plasmas from usual plasmas is that charges on the grains are not constant, but fluctuate in time around some equilibrium value which, in turn, is some function of spatial coordinates[1]. Ensembles of particles with variable charges are non-Hamiltonian systems, because the mutual collisions do no conserve the energy. Therefore, the use of thermodynamic potentials to describe such systems is not really valid. An appropriate way to investigate their evolution is to use the kinetic approach. We studied the case when the equilibrium charge depends on the particle coordinate and derived the collision integral describing the momentum and energy transfer in collisions[2]. From the solution of the corresponding kinetic equation we obtain that the mean particle energy grows in time.

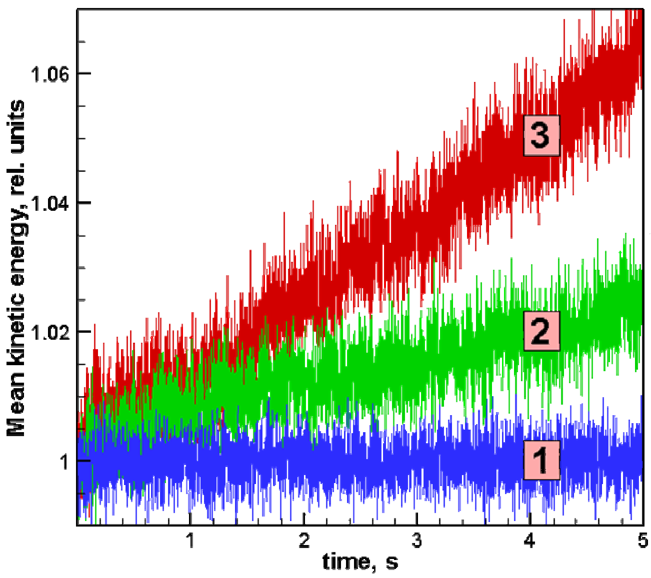


Collisions of particles with neutral gas cause the dissipation which may inhibit the instability. For the particles interacting via the Yukawa potential with the screening length, $\lambda$, and weakly inhomogeneous charges, $Q$ (the inhomogeneity spatial scale is $L_Q=|Q/Q'|>>\lambda$), the condition for the energy growth is that the product of the neutral friction rate $\gamma_{\rm fr}$ and the interparticle collision time $\tau_{\rm coll}$ obeys the inequality:

$$\gamma_{\rm fr}\tau_{\rm coll} \leq (\lambda/L_Q)^2.$$

When the inequality is satisfied, the energy changes as $\propto (t_{\rm cr}- t)^{-2}$, with $t_{\rm cr} \sim (L_Q/\lambda)^2\tau_{\rm coll}$, exhibiting the explosion-like growth. The figure shows the initial stage of the mean energy grows, as obtained from the molecular dynamics simulations. The particle energy (normalized to the initial temperature) is plotted as function of time for different values of the charge gradient: $\lambda/L_Q = 0$ (1), $10^{-2}$ (2), and $1.5\times10^{-2}$ (3). Of course, the mean energy remains constant without the gradient. For finite $L_Q$, the energy scales initially as $\propto (\lambda/L_Q)^2 t$, in agreement with the theory. The drift part of the kinetic energy rapidly decreases in the simulations after a few interparticle collisions (at $t < 10^{-1}$ s for this example) and is negligible at later stages. Therefore, the plotted curves actually show the thermal part of the mean energy.

The obtained solutions can be of significant importance for laboratory dusty plasmas as well as for space plasma environments, where inhomogeneous charge distributions are often present. For instance, the instability can cause the dust heating in low-pressure complex plasma experiments and be responsible, e.g., for the melting of plasma crystals, or might operate in protoplanetary disks and, thus, affect kinetics of the planet formation, etc.

**References:**
[1] V. N. Tsytovich, Phys. Usp. **40**, 53 (1997).
[2] A. V. Ivlev *et al*., Phys. Rev. E (2004, to be published in November issue)

*A. V. Ivlev, S. K. Zhdanov, B. A. Klumov, V. N. Tsytovich, and G. E. Morfill*

# PHASE STATES OF COMPLEX PLASMAS

**Possible states of complex plasmas are classified in terms of the momentum transfer in binary grain-grain collisions.**

Momentum transfer in binary grain-grain collisions is investigated assuming the repulsive screening Coulomb (Debye-Hückel or Yukawa) potential of interaction between the grains. The momentum transfer cross sections and rates are obtained. This allows us to obtain further insight into the possible states of complex plasmas. Figure 1 represents different "phase states" of complex plasmas as functions of the electrostatic coupling parameter $\Gamma_{\rm ES} = U(\Delta)/T$ [where $U(r)$ is the potential energy of interaction] and the mean grain separation $\Delta$, normalized either to the grain size $a$ or the screening length $\lambda$. The vertical dashed line at $\kappa = 1$ conditionally divides the system into Coulomb and Yukawa parts.

The following states can be identified [1,2]:

(i) Above the red solid line we have Coulomb or Yukawa crytals, the crystallization condition is $\Gamma_{\rm ES} > 106(1+\kappa+\kappa^2/2)^{-1}$ [3]. (ii) Above the blue solid line we have Coulomb or Yukawa non-ideal plasmas – the characteristic range of grain-grain interaction (in terms of the momentum transfer) is larger than the intergrain distance (in terms of the Wigner-Seitz radius), $(\sigma/\pi)^{1/2} > (4\pi/3)^{-1/3}\Delta$, which implies that the interaction is essentially multiparticle. (iii) Regions below blue solid line correspond to Coulomb or Yukawa ideal plasmas – the range of grain-grain interaction is smaller than the intergrain distance and only pair collisions are important. (iv) Below the lower dotted line the electrostatic interaction is not important and the system is like a usual granular medium. (v) In the region between the upper dotted line and the solid blue line the pair Yukawa interaction asimptotically reduces to the hard sphere limit and complex plasma forms a "Yukawa granular medium".

Next we investigate complex plasma properties in terms of competition between the momentum transfer rate in mutual grain-grain collisions $\nu_{dd}$ and the interaction with surrounding medium (neutral gas), characterized by $\nu_{nd}$. Figure 2 shows that there is a broad range of parameters where complex plasmas have the properties of one-phase fluids ($\nu_{dd}/\nu_{nd} \gg 1$), and those of two-phase fluids $\nu_{dd}/\nu_{nd} \sim 1$. In the extreme limit of very small $\nu_{dd}/\nu_{nd}$ we can also have "tracer particles" in the background medium.

The broad range of states that is accessible for complex plasmas and the possibility to study a variety of processes at the kinetic level makes these systems extremely attractive for further research. The reported results can be important for "engineering" experiments which aim to make use of special properties of complex plasmas.

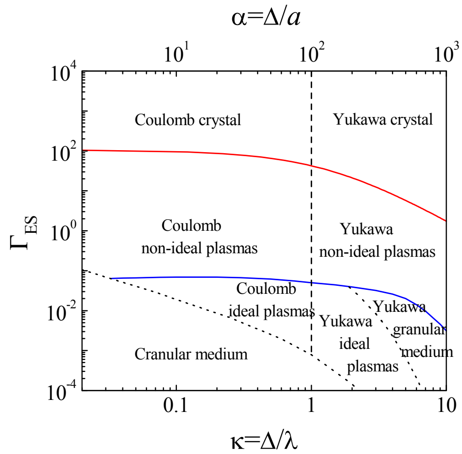


**Fig. 1** Possible "phase states" of complex plasmas.

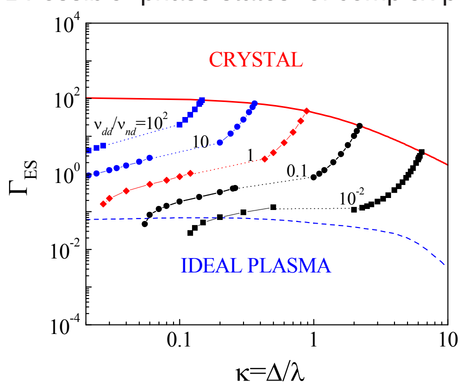


**Fig. 2** Typical contours of constant ratios of the momentum transfer rates in grain-grain collisions relative to grain-background (neutral gas) collisions in $(\Gamma,\kappa)$ parameter space. Also shown in the figure are the melting line and the boundary between ideal and non-ideal plasmas. The calculations are performed for a set of typical complex plasma parameters [2].


[1] G. E. Morfill *et al.*, Phys. Scripta **T107**, 59 (2004).
[2] S. Khrapak, A. Ivlev, and G. Morfill, Phys. Rev. E (in press, 2004).
[3] O. Vaulina and S. Khrapak, JETP **90**, 287 (2000).



*S. Khrapak, A. Ivlev, and G. Morfill*

# The adaptive electrode in electronegative plasma

Electronegative discharges are often used in plasma processing of materials because they are highly chemically reactive and show peculiar plasma characteristics, such as transport and plasma boundaries, useful for etching and deposition. The electronegative sheath presents several physical effects, which have been unraveled by a new diagnostic; we have injected small particles in the sheath and record their equilibrium positions. The segmented, adaptive electrode is used as a powerful tool for introducing local modifications of the sheath and allows us to do fine control of the particle behavior.

Particles levitate in the sheath region, gravity being compensated mainly by the upward electrostatic force. The equilibrium position depends on the presence of negative ions in two ways: the electric field of the sheath can be a non monotonic function of the electronegativity and the particle charge is strongly affected by the modified Bohm flux of positive ions.

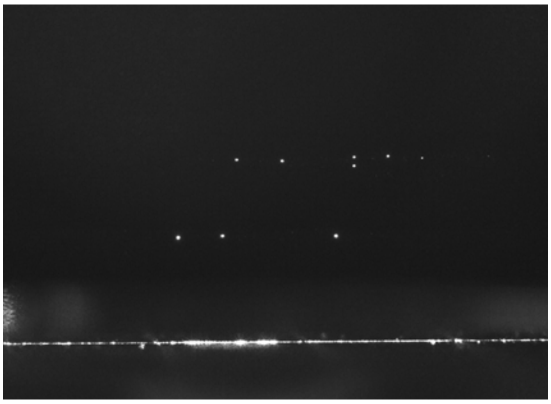

The particles, 3.42 μm size, injected in the plasma settle in two layers. The picture shows 17X13mm.

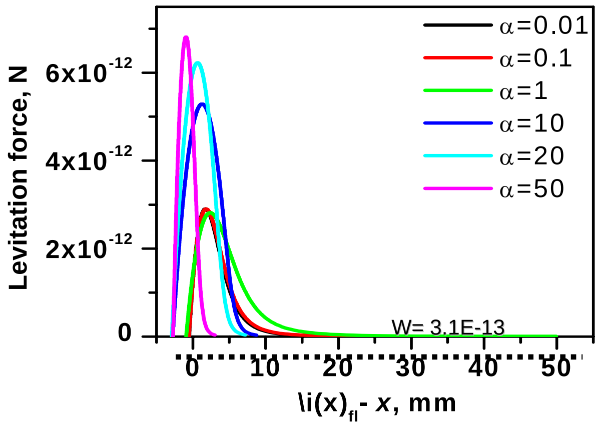


The levitation force for $r_{part}=1.7\cdot 10^{-6}$(m) and $n=10^{15}$ and Te=3eV.The dashed line shows the weight of particles.

Solving Poisson equation for the sheath and the equation of flux continuity we have modeled the levitation force, which matches with good accuracy the position of the upper particles layer. The distribution of heavy particles (3.4μm, 6.8μm in diameter) in two layers is due to the modification of the Bohm criterion in electronegative discharges. The behavior of the fine particles (1.29μm) is explained by 2-energy distribution of negative ions.

The experiments presented are, to the authors knowledge, the first experimental proof of a structured electronegative plasma sheath, a possibility so far only mathematically and numerically investigated. Languir probe measurements provided experimental values for the electronegativity to make a link between theory and experiments. The range of instability is narrow so that the purity of the gas was essential. The effect of the RF voltage drop on the electrode sheath, not taken into account in the calculation of the levitation force, has been estimated to affect both, the charge of the particle and the electric field. The dependence on energy of the collision coefficients was not always available in literature. However, using the most probable reactions we have demonstrated the existence of three negative species in RF Oxygen plasma. The experimental data are consistent with our deduction.

**References:**


• "Diagnostics of the electronegative plasma-sheath at low pressures using micro-particles" B.M. Annaratone, T. Antonova, H.M. Thomas, G.E. Morfill, 2004, Phys. Rev. Letters, 93, 185001



*B. Annaratone, T. Antonova, H. Thomas, G. Morfill*

# The adaptive electrode: complex-plasma manipulation
## (how to move particles using RF)

This project is an experimental study on the nature, the dimensions and the time scale of the perturbation introduced by RF biasing of areas adjacent the plasma. The theoretical analysis of the RF sheath, and of the charging of particles in it, has disclosed a levitation force on particles, which is substantially different from the DC one often used in complex plasmas modeling. Experimentally the RF heavily-loaded sheath presents characteristics completely different from the normal case $V_{RF}=V_{DC}$. Regions of extra ionisation and complex electrostatic structures arise in which it is possible to find uniform gravity compensation in 3-D. This allows for the first time the formation of 3-D clusters under gravity condition.

This work presents a new plasma configuration with localised RF on the boundary, useful for particle manipulation. The electrostatic structure have been visualised by nano-particles grown in the plasma and by injected microparticles.

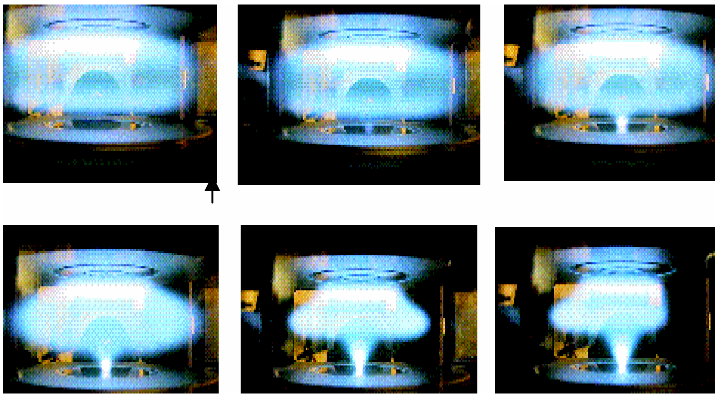

The glow emitted above a pixel kept at $V_{DC}$=0V and RF driven ($V_{RFpp}$=0, 47, 47, 60, 100, 140V respectively). Upper electrode voltage $V_{RFpp}$=250V P=81Pa. PKE chamber.

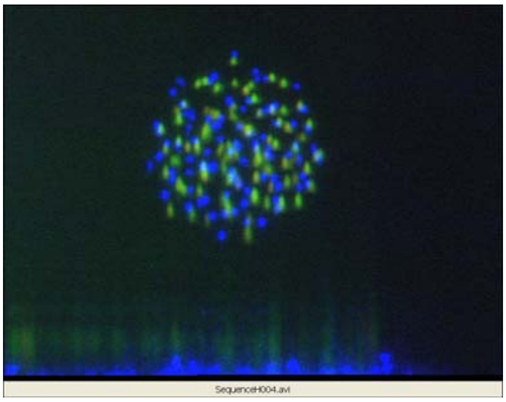

A cluster of 70 particles. The green-red picture shows 2.3x1.7mm$^2$. The same cluster, observed at 90$^0$, is shown by the blue dots.

We have theoretically proved, and experimentally demonstrated, that, without applied DC, particles of a large range of diameters, can be collected, transported and stored in a flexible and reversible manner. Although anode-like effects are clearly visible the particles do not fall on the electrode. An obvious application is the cleaning of the plasma. The effects here described are independent of the plasma chemistry, they have been achieved in electropositive and electronegative plasmas. They are also independent of the nature of the return pattern of the RF current as they were observed in experiments with metal and floating electrodes/chambers.

The particle can find equilibrium positions in volumes where three dimensional clusters form. By a fine adjustment of the RF applied to a DC-grounded pixel we were able to control the number of particles in the cluster and also its shape. At low pressure a poloidal motion sets up. A three-dimensional simultaneous visualization technique has been used for recording vibrations and structure transitions.

In the equilibrium positions the vertical confinement is provided by the electric field of double layers/striations combined with the suitable conditions for the charging. The analysis of the structures will clarify whether the horizontal confinement is due to plasma pressure or by internal forces among the cluster component (Leonard-Jones like potential) or by ion drag.

**References:** 'Complex-plasma manipulation by radiofrequency' B. M. Annaratone, T. Antonova, D. D. Goldbeck, H. M. Thomas and G. E. Morfill, Plasma Physics and Controlled Fusion, EPS invited papers 2004

*B. Annaratone, T. Antonova, D. Goldbeck, H. Thomas, G. Morfill*

# Study of the Crystallisation Process of Complex Plasmas

We present new laboratory experiments with complex plasmas consisting of small particles of 1.28 µm in diameter, where we studied the dynamics of the crystallisation process in detail.

The experiments were performed in a plasma chamber similar to PKE-Nefedov. We first created a large cylindrically shaped plasma crystal (r×h=4×2.5 cm, 80 µm particle distance) and then melted the system by a short variation in the radio frequency amplitude. Already after a few seconds the complex plasma started to recrystallise. An upward moving crystal wave front was observed. The vertical extension of the front was 2-3 particle distances broad. Within this interface the particles were quickly cooled - the mean particle velocity was 2.5 times in the disturbed zone. The crystal front decreased with height from 0.25 mm/sec at bottom and stopped after approx. 45 sec. Different structural domains were build up, with transitional interfaces in between with considerably higher disorder.

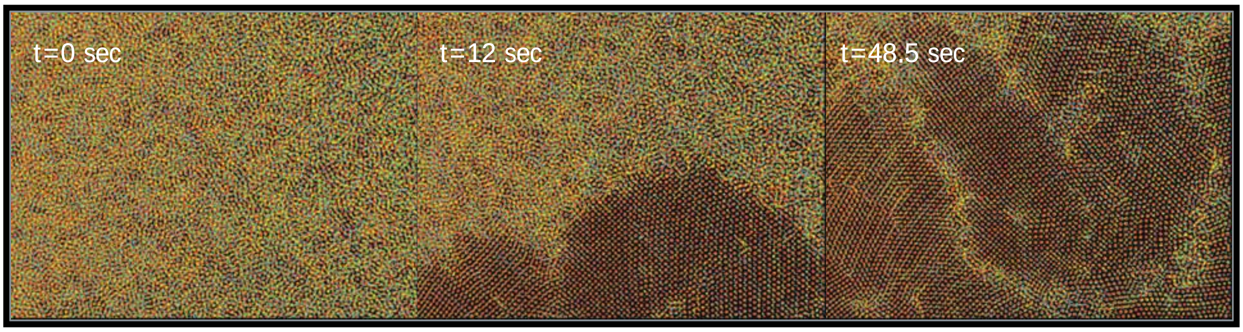


*Each of the images displays a superposition of all particles at ten subsequent time steps (1 sec in total). This colour-coding provides a direct qualitative view of the kinetic energy of the particles.*

Detailed investigations showed that the randomly vibrating particles from the disturbed phase loose their kinetic energy through Coulomb collisions. Numerical simulations predict that this dissipated energy is transferred out of the crystal via shock waves or compressional waves. During the crystallisation process the complex plasma became vertically compressed. In simulations we find in the beginning of the sedimentation many metastable crystalline states (hcp) together with fcc. The particles rearrange to the state with lowest potential energy which is a very slow process (comparable to the observations) and is driven by thermal motion.

Additional experiments showed that beside such nonequilibrium crystallisation processes also a crystallisation close to the local thermal equilibrium can occur. The crystal formation starts mostly from bottom, because there the compression is higher (due to gravity) than on top. The growth velocity decreased with height (max. 0.25 mm/sec at bottom), since at smaller compression it is easier to melt the crystal and to slow down the process. The crystal is build up with particles from the liquid-like state located above. During crystallisation the particles in the "liquid" state lose energy through collisions with neighbours. The energy is dissipated by waves, which are propagating through the crystal medium (numerical results).

In future experiments we will repeate the measurement with CCD cameras of higher temporal and spatial resolution. In addition fast 3D scans will be performed during crystallisation to identify structure changes during the crystal growth.

*M. Rubin-Zuzic, G. Morfill, H. Thomas, A. Ivlev, B. Klumov, H. Rothermel, W. Bunk, R. Pompl*

# Crystallization waves in complex plasma: numerical simulations

**We present molecular dynamics (MD) simulations in Yukawa system of the formation and evolution of a crystallization wave. We have found the coexistance of various lattice types (including metastable ones) behind crystallization wave front. Local order analysis shows the presence of fcc, bcc and hcp phases - it is a clear manifestation of a non-equilibrium phase transition in the system.**

Kinetic observations of crystal growth in real time are possible by using complex plasmas. A plasma crystal is first melted into a disordered liquid-like phase (e.g., by a short increase of the plasma discharge power). Afterwards, the system starts to recrystallize. Often this occurs in the form of a crystallization wave (CW) propagating in the direction of the decreasing particle density, against gravity. We provided MD simulations of the crystallization process, revealing the qualitative features observed in experiments. The temperature field in the system is shown on the top figure. It is color-coded (temperature rises from black to yellow). The front has a well developed fractal structure, with an abrupt temperature drop within the transition layer (blue) from the liquid/gaseous (green-yellow) to the crystalline (black) phase. After the CW front passed, (right figure shows particle density behind CW front, the spatial dependence of mean energy of the layers is depicted on the inner figure ) the crystalline structures formed behind the front revealing a sequence of transitions from one lattice configuration to another. Bottom figures demonstrate some results of the local order analysis of the crystallized region. Left figure shows the spatial distribution of bcc, fcc, hcp and liquid domains in the region. The right figure presents local analysis of the coupling parameter, showing how the crystallization process evolves versus time.

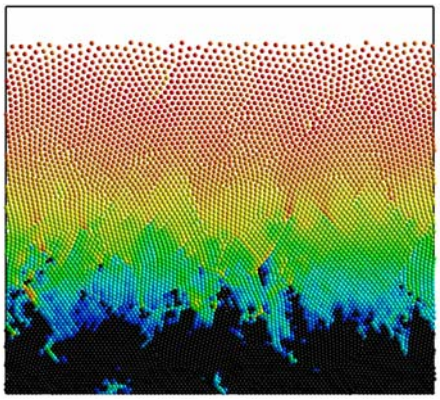

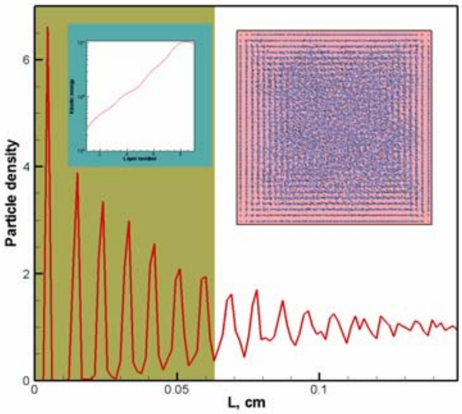


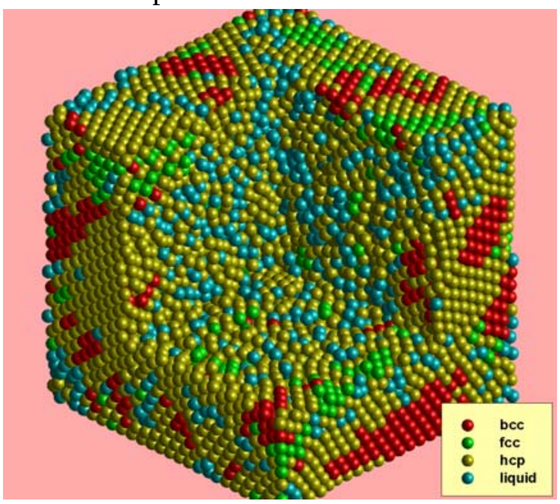


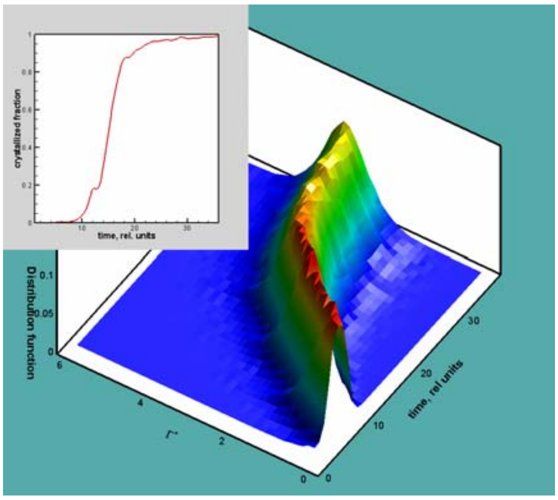


*B. A. Klumov and G. E. Morfill*

# Electrostatic Modes in Collisional Complex Plasmas under Microgravity Conditions

**A linear dispersion relation, which allows for a highly collisional complex plasma and includes an ion drift was revised in the light of the recent PKE-Nefedov wave experiments performed under microgravity conditions on board of the International Space Station.**

We have revised a dispersion relation, describing dust density perturbations in a highly collisional complex plasma with an ion drift, thus adapting this for realistic conditions in recent complex plasma experiments performed under microgravity conditions on board of the International Space Station.

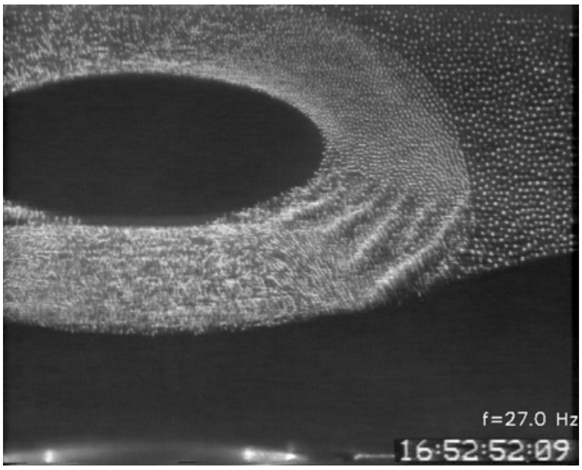


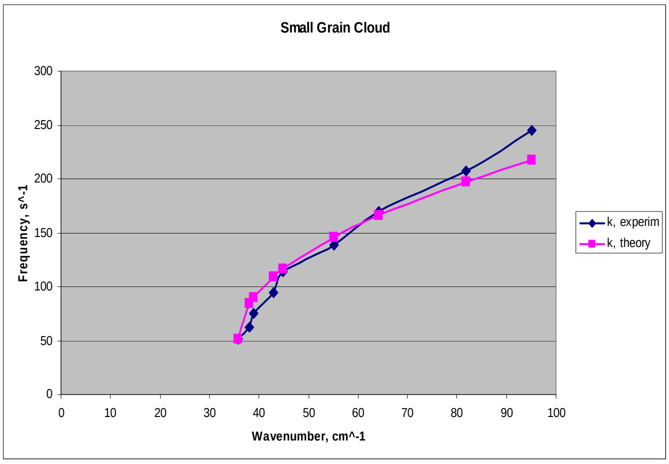


The dust density perturbations have been studied for the wave frequencies larger than the dust-neutral momentum transfer frequency.

Taking into account a relation between plasma parameters in an equilibrium state, two unstable modifications of the dust-acoustic modes have been obtained. The relevance of these perturbations to space observations of dust density waves in a specific wave channel (Fig.1) has been analyzed. It is shown that a new mode characterized by a square-root dependence of the wave frequency on the wavenumber can satisfy the propagation conditions in the given range of wavenumbers and thus can explain the peculiarities of the measured dispersion relation.

The comparison of theory and observations was made separately for two different complex plasma domains formed by small and large microparticles (SGC and LGC, respectively). Good qualitative agreement is found between the measured dispersion relations and the theoretically predicted square-root dependence of the wave frequency on the wavenumber in both complex plasma regions (Fig.2 relates to the SGC). This allows a determination of the basic complex plasma parameters. The theory predicts that the grain charges in SGC and LGC are smaller than estimations of the OML theory, and the complex plasma formed by two different grain species is nonuniform: the plasma density is lower, while the electric field is higher in the part of the complex plasma formed by larger microparticles.

*V.V. Yaroshenko B. M . Annaratone, S.A. Khrapak, H.M. Thomas, G.E. Morfill*
*V.E. Fortov, A. Lipaev, V.I. Molotkov, O.F.Petrov and M. Turin*

# Vertical wave packets in a 2D complex plasma

**Vertical wave packets which propagated keeping their width constant were observed in a monolayer plasma crystal. The explanation of their unusual behavior is based on three-dimensional equations of motion and uses a long-wavelength weak dispersion weak inhomogeneity approximation. A new plasma diagnostic method was developed that is based on the ratio between vertical and dust-lattice wave speeds. The method works well for plasmas with the screening parameter less than 2.**

## Experimental setup

- Particles form a monolayer
- Wire is below the particles
- Negative pulse is applied
- Vertical pulses propagate

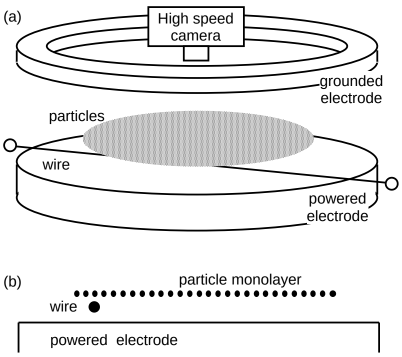


## Conditions of experiment

- argon, 1.0 Pa, 0.5 sccm
- 4 W ccrf-discharge
- 8.9 $\mu$m spherical plastic particles
- 740 - 820 $\mu$m particle separation
- 25 V, 10 ms pulse excitation

## Diagnostics

- 200-300 $\mu$m thick laser sheet
- 200 mW, 532 nm Nd:YAG laser
- 230.75 fps, high-speed video
- 4.42 × 2.21 cm (1024 × 512 pixels) field of view

## Visualisation

- scattered light intensity
- is binned along the wire
- plotted *vs* distance and time
- wave packets are identified
- angle shows the wave speed

## Plasma crystal

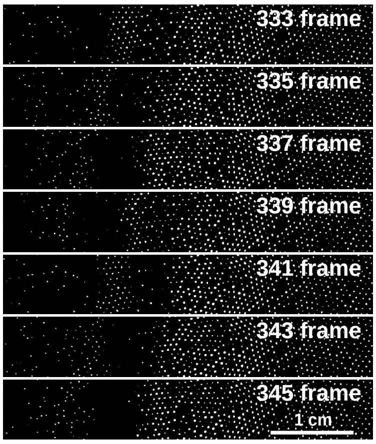


## Wave packet

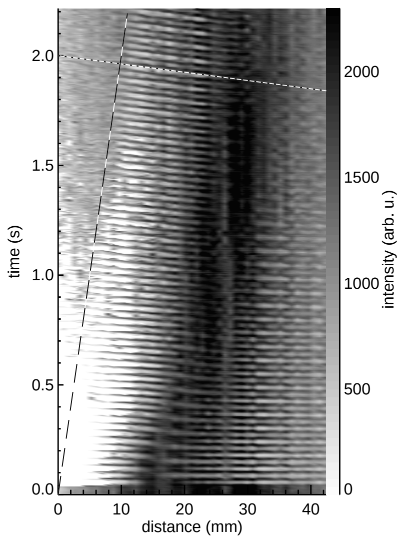


- phase speed: $V_{ph} = -290 \pm 20$ mm/s
- group speed: $V_{gr} = 4.5 \pm 0.5$ mm/s

## Theory

- monolayer hexagonal lattice
- constant charge
- 3D equations of motion
- strong vertical confinement
- weak horizontal confinemet
- Yukawa interaction
- damping due to neutral gas
- dispersion relations
- vertical transverse wave mode

## Plasma diagnostics

- ratio vertical/compressional characteristic speeds

$$R = \frac{c_v}{c_{DL}} = \frac{(V_{gr}V_{ph})^{1/2}}{c_{DL}}$$

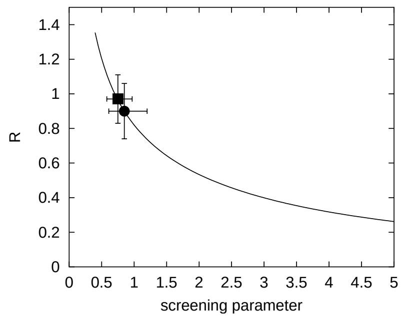


- $R(\kappa) = 0.97$ is measured
- screening parameter $\kappa = 0.75$ is calculated

## Summary

- waves packets do not spread due to dispersion and inhomogeneity
- inverse optical dispersion
- phase speed is 65 times higher than the group speed
- ratio $R(\kappa)$ can be used for plasma diagnostics

*D. Samsonov, S. Zhdanov, and G. Morfill*

# Wave modes in a 2D complex (dusty) plasma


**The waves in a 2D Yukawa lattice were studied in this work experimentally and theoretically. The wave spectra were studied for various directions of propagation with respect to the main crystal axes. It was found that there are two wave modes with a polarization alternating between the longitudinal and transverse. In the short-wavelength regime the spectra strongly depended on the wavelength and the direction of propagation. The results obtained from the experiment, theory, and simulation well agree with each other.**


## Experimental setup

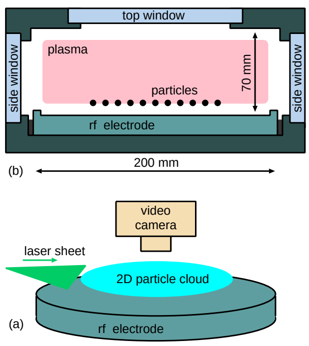


## Experimental conditions

- argon, pressure 1.0 Pa
- argon flow rate 1.8 sccm
- 2W cc-rf discharge at 13.56MHz
- 8.9 $\mu$m plastic microspheres
- Optical access: top window, four side windows

## Experimental procedure

- Particles injected into the plasma, charged negatively, and levitated at a height of 9 mm above the lower electrode
- Radial bowl-shaped confinement
- Hexagonal 2D lattice is formed
- Particle separation $a = 780\ \mu$m
- Cluster diameter 7 cm
- Illumination with a laser sheet
- DVC-recording at 33 frames/s
- Particle identification and tracing yields velocities
- 2D Fourier-transform of the particle velocity field yields wave spectra

## Theoretical model

$$m\ddot{\mathbf{r}}_s = \mathbf{f}_s^{fr} + \mathbf{f}_s^{conf} + \mathbf{f}_s^{int} + \mathbf{f}_s^{exc}$$
$$\mathbf{f}_s^{fr} = -m\nu\dot{\mathbf{r}}_s$$
$$\mathbf{f}_s^{conf} = -m\Omega_{conf}^2\mathbf{r}_s$$
$$\mathbf{f}^{int} = -\nabla U_s$$
$$U_s = Q^2 \sum_{j\neq s} r_{sj}^{-1} \exp\left(-r_{sj}/\lambda_D\right)$$

- Without excitation, the lattice relaxed to an equilibrium state
- Weak stochastic excitation caused small displacements of the particles
- Naturally occurring waves enhanced resonantly

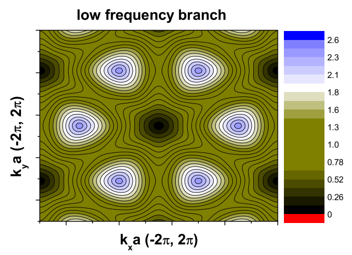


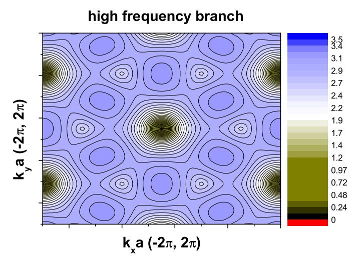


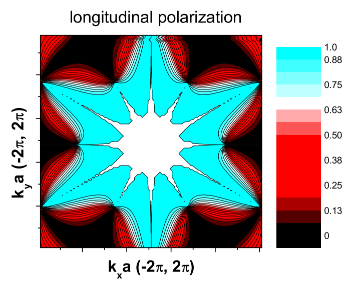


## Observations

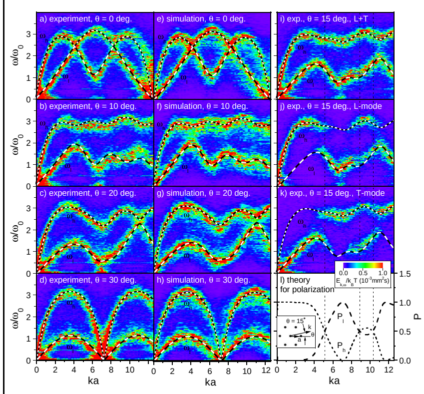


- Two Brillouin zones were studied
- High and low frequency wave branches were observed
- Spectra were strongly dependent on a wave number and on an angle of the wave propagation

## Summary

- Long wavelength spectra are isotropic
- Short wavelength spectra are highly anisotropic
- The eigen-vectors of the dynamic matrix form anisotropic family, and at an arbitrary wave number the wave modes have mixed polarization
- Dynamics matrix approach was proved as being optimal to describe the waves
- Phonon spectra can be modelled by MD


*S. Zhdanov, S. Nunomura, D. Samsonov, and G. Morfill*

# Origin of the curved nature of Mach cone wings in complex plasmas

**In this work the shape of DMC (dynamic Mach cones) formed by nondispersive linear sound waves in a nonuniform complex plasma is calculated analytically using the method of wave rays. The cases of transversely and longitudinally inhomogeneous media are considered. The theory is compared with experimental observations of Mach cones with curved wings in a two-dimensional complex plasma with a good qualitative agreement. A novel plasma diagnostic method is proposed.**

## Experimental setup

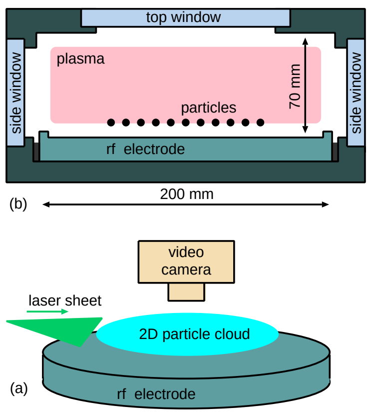


## Experimental conditions

- Ar, pressure 1.2 Pa
- argon flow rate 0.5-6 sccm
- 50 W capacitively coupled rf discharge at 13.56 MHz
- 8.9 $\mu$m plastic microspheres $\rho$= 1.51 g/cm$^3$
- Optical access: top view, side view

## Experimental procedure

- Particles injected into the plasma, charged negatively (Q = 17000 e), and levitated at a height of 9 mm above the lower electrode
- Radial bowl-shaped confinement
- Hexagonal 2D lattice is formed
- Particle separation $a = 590$ $\mu$m
- Cluster diameter 7 cm
- Illumination with a laser sheet
- video recording at 25 frames/s
- Particle identification and tracing yields velocities

## Max cone images

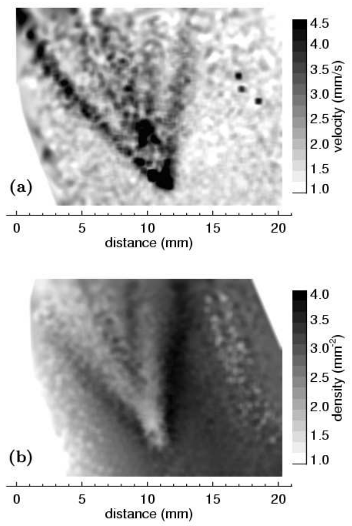


- V-shaped disturbances travelling through the hexagonal lattice
- Created by fast particles, moving under the layer

## Interpretation

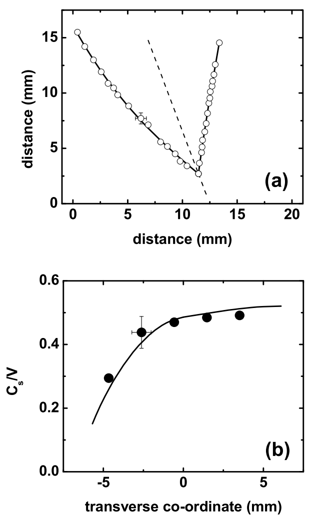


## Theory of waverays

- Simple basic equations:

$$\dot{\mathbf{r}} = \mathbf{v}_g, \quad \dot{\mathbf{k}} = -\partial_{\mathbf{r}}\omega$$

$$\omega = kC_s(\mathbf{r}, \mathrm{t}), \quad \mathbf{v}_{\mathrm{g}} = \mathbf{k}\mathrm{C}_{\mathrm{s}}/\mathrm{k}$$

- Optimal way to solve analytically direct (find a cone) and inverse problem (restore a medium property)
- Observed bending of Mach cone wing agreed qualitatively with the theoretical predictions
- Comparison to theory allowed to reconstruct the acoustic speed profile across the cone trajectory
- The speed of the perturbing body was determined to be $V = 35 \pm 7$ mm/s
- Cone wing curved towards the crystal center, where the lattice was denser ($n_{max} = 3.3$ mm$^{-2}$)

## Summary

- The DMC contains information on either the time history of changes in the medium or of gradients in the medium
- Dynamic Mach cones can be used for diagnostics of inhomogeneous or time-dependent complex plasmas
- Different dusty plasma inhomogeneities can affect the Max cone shape in different ways
- Theory based on linear nondispersive waves provides a good approximation even at the kinetic level and for strong gradients

*S. Zhdanov, G. Morfill, D. Samsonov, M. Zuzic, O. Havnes*

# Wave dispersion relation of two-dimensional plasma crystals in a magnetic fiel

**The wave dispersion relation in a two-dimensional strongly-coupled plasma crystal is studied by theoretical analysis and molecular dynamics simulation taking into account a constant magnetic field parallel to the crystal normal. The expression for the wave dispersion relation clearly shows that high- and low-frequency branches exist as a result of the coupling of longitudinal and transverse modes due to the Lorenz force acting on the dust particles.**

Micro particles that are introduced into a plasma environment charge up to a high negative value due to ion and electron bombardment. As a result of the strong Coulomb interaction between the particles often so-called "plasma crystals" are built up. The inter-particle potential is considered to be of the Yukawa type. There have been many theoretical and experimental studies on wave phenomena in "plasma crystals". In these studies two wave modes, named "longitudinal dust lattice waves" and "transverse dust lattice waves", have been identified and extensively analyzed. However, the influence of an external magnetic field on the wave dispersion has been considered barely, although magnetic fields play an important role for many common complex plasma environments. In this study, we analytically derive the wave dispersion relation in a two-dimensional plasma crystal under magnetic field influence, where the wave propagation and particle displacement are perpendicular to the magnetic field $\mathbf{B}$ [1]. The dispersion relation can be expressed by

$$\left[\omega^2 - 2\sum_{m=1,m\neq i}^{N} K_{x\,m}^{\ i}\sin^2\left(\frac{k_x x_0^m}{2}\right)\right]\left[\omega^2 - 2\sum_{m=1,m\neq i}^{N} K_{y\,m}^{\ i}\sin^2\left(\frac{k_x x_0^m}{2}\right)\right] - \omega_c^2\omega^2 = 0, \tag{1}$$

where $\omega_c = |QB_z/m_d|$ is the cyclotron frequency of the dust particles.
In the limit of a vanishing magnetic field, $\omega_c$ = 0, we get the two well known, independent longitudinal and transverse wave modes from Eq.(1). When we apply a magnetic field though, the longitudinal and transverse modes in the plasma crystal are coupled due to the Lorentz force. Then, the dispersion relation has a cut-off at $\omega_c$ in the limit of long wave lengths where $k_x \to$ 0.
Fig.1 show the wave spectrum due to thermal motion of the dust particles in a simulated plasma crystal under magnetic field, where dash lines are from Eq.(1). We can see a high-frequency $\omega_H$ and low-frequency branch $\omega_L$. The profile of the dispersion relations that we obtained from the thermal particle motion are in good agreement with our theoretical predictions given in Eq.(1).

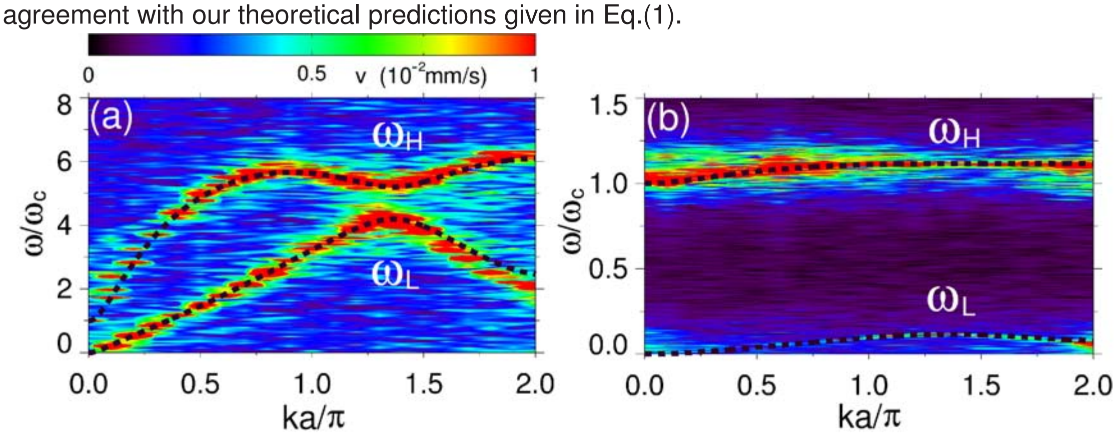


Figure. 1 ; Dependence of the dispersion relation on the magnetic field strength which is represented by the parameter $\omega_c/\omega_0$, where $\omega_c$ is the dust cyclotron frequency and $\omega_0$ the dust plasma frequency defined as $\omega_0 = \sqrt{Q^2/4\pi\varepsilon_0 m_d a^3}$, where $a$ is the mean inter-particle distance. Figure (a) and (b) are for $\omega_c/\omega_0 = 0.52$ ($\omega_c/\omega_0 < 1$ ; a weakly-magnetized plasma crystal), and for $\omega_c/\omega_0 = 6.85$ ($\omega_c^2/\omega_0^2 >> 1$ ; a strongly-magnetized plasma crystal), where a screening parameter $\kappa = a/\lambda_D$ is 1.0.

[1] G. Uchida, U. Konopka, and G. Morfill, Phys. Rev. Lett. **93**, 155002 (2004).

*G. Uchida, U. Konopka, and G. Morfill*

# Agglomerations of Magnetized Particles in Complex Plasmas

Dust-dust interactions in complex plasmas are studied when effects of an external magnetic field become important. It is shown that the forces from particle magnetization may result in mutual repulsion as well as attraction. It was found that magnetized grains can coalesce, forming field-aligned chains. A model was developed to determine the length of these structures. These findings were then applied to recent complex plasma experiments with paramagnetic particles.

Recently, multilayer complex plasma structures field have been observed in an external magnetic field [1]. In these experiments, spherical micrometer sized paramagnetic particles were levitated in the sheath region. The levitation increased with the strength of the magnetic field. Moreover, some particles attracted each other and formed elongated structures—grain chains, oriented vertically, parallel to the field lines of the external magnetic field (Fig.1).

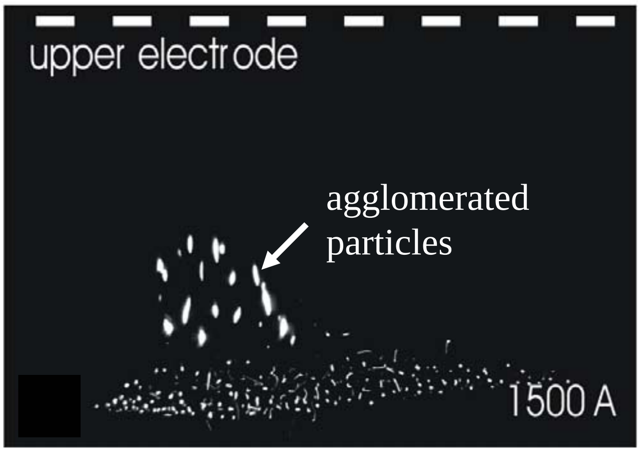


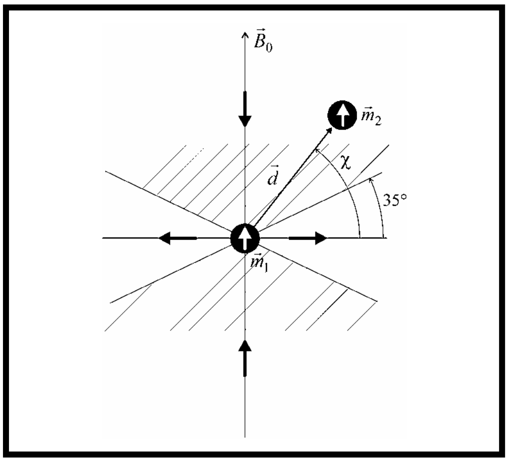


These features cannot be explained on the basis of pure electrostatic forces. Short-range dipole interactions between magnetized grains have to be invoked.

Various mutual dust–dust interactions, including the forces due to induced magnetic and electric moments of the grains were considered. It turns out that the electromagnetic forces from particle magnetization and polarization may result in mutual repulsion as well as attraction (in Fig.2. the interactions between two identical magnetized particles is shown schematically. The domain of angles corresponding to the attractive force is hatched).

The further analysis was mainly focused on particle coagulation. It was found that magnetized grains can coalesce, forming field-aligned chains. Since the “disruptive” electrostatic forces increase with the distance from the centre of a chain, whereas the “cohesion” magnetostatic forces decrease, there is an intrinsic length scale for these particle chains. A model was developed to determine the length of these structures. These findings were then applied to recent complex plasma experiments with paramagnetic particles. The theoretical estimations have revealed good agreement with experimentally observed data.

Our results are of direct interest to laboratory studies of magnetized complex plasmas, indicating several new effects. In particular, the model predicts that the chain length will increase when the magnetic field is increased, when the permeability of the particle material is higher and the grain size is larger. In addition, our results could be of importance when studying dust particle agglomeration in astrophysical environments and for aerosol removal, cleaning and purification devices.

**References:**
1. D. Samsonov, S. K. Zhdanov, V.Steinberg and G.Morfill, New J. Phys, **5**, 24, (2003)

*V. Yaroshenko, G. Morfill, and D. Samsonov*

# Vertical oscillations of paramagnetic particles in complex plasmas

**Vertical vibrations of paramagnetic particles in discharge plasmas are treated taking into account the magnetic force associated with gradients of an external magnetic field. For a single particle a novel type of oscillation associated with these gradients is found. In a one-dimensional particle string the magnetic force causes a new low-frequency oscillatory mode. The study of vertical vibrations of magnetized grains provides a tool for determining complex plasma parameters.**

Up to now, oscillatory modes of magnetized grains in a discharge plasma were considered only in homogeneous magnetic fields [1], which implies that a magnetic levitation was not discussed as well as the role of inhomogeneous magnetic field in the particle dynamics. At the same time, recent complex plasma experiments with paramagnetic particles immersed in a magnetic field demonstrated that levitation heights could be controlled by the magnetic force [2]. In this work

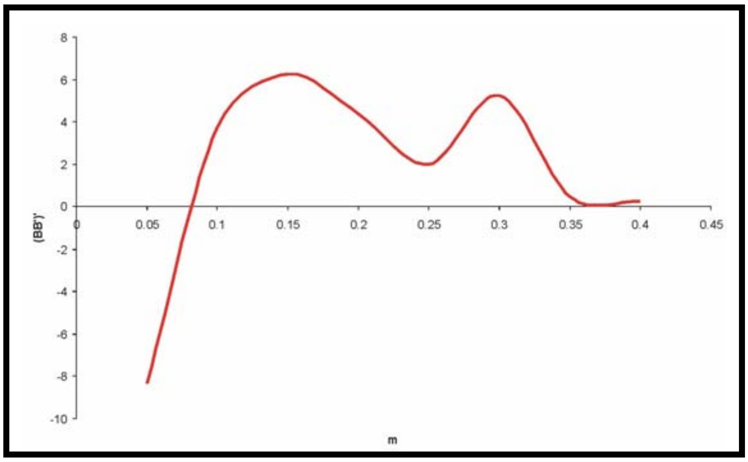


we therefore treat the grain levitation in an external magnetic field and consider vertical vibrations of the magnetized particles around an equilibrium taking into account magnetic field gradients.

For a single magnetized particle a novel type of vertical vibrations in discharge plasmas is found. These vibrations can be stable or unstable depending on the distribution of the magnetic field inside the particle cloud. The normalized magnetic frequency as a function of the distance between the magnetic coils and levitating particles is shown in Fig. 1. The vertical resonance frequency is independent on particle mass, but is completely specified by the magnetic field profile inside the complex plasma and magnetic properties of the grain material. A numerical estimate of the resonance frequency for the typical complex plasma parameters in the magnetic experiments [2], gives magnitudes ~50-70 $s^{-1}$. Such values can be easily measured in experiments and the latter can provide a tool for determining the complex plasma parameters.

In a one-dimensional particle string the magnetic force causes a new low-frequency oscillatory mode, which is characterized by inverse optic-mode-like dispersion when the wavelength far exceeds the intergrain distance. The characteristics of the mode are specified by the gradients of the external magnetic field and thus can be effectively controlled in experimental conditions. This opens new opportunities for the investigation of the particle behavior at the kinetic level as well as for stimulating phase transitions in the system, and for the study of self-organized structures in the experiments.

**References:**
1. S. V. Vladimirov, G. E. Morfill, V. V. Yaroshenko, and N.F. Cramer, Phys. Plasmas, **10**, p. 2659, 9 (2003).
2.D.Samsonov, S.K. Zhdanov, V.Steinberg and G.Morfill, New J. Phys, **5**, 24, (2003)

*V. V. Yaroshenko, G. E. Morfill, and D. Samsonov*

# Measurement of the micro particle charge in a weakly ionized plasma of a dc discharge

**Investigation of charging of micro particles in the quasineutral plasma of a DC discharge (PK-4 facility) has been carried out and confirmed the effect of ion-neutral collision.**

The particle charge is one of the most important characteristics of dusty (complex) plasmas, which determines, to name but a few, the interaction of a particle with the plasma electrons and ions, electromagnetic fields, interaction between the particles themselves, etc. Recently, experiments of particle charges have been performed in the PK-4 facility.

**FIG. 1:** The particle charge obtained from experiments [force balance for low number of injected particles (open circles); force balance for pressures above the threshold (open squares), solution of dispersion relation (solid squares)] and from MD simulations (red diamonds). The area between the two dotted lines corresponds to the charge given by the OML model for Havnes parameters between P=0.2 (upper line) and P=3 (lower line).

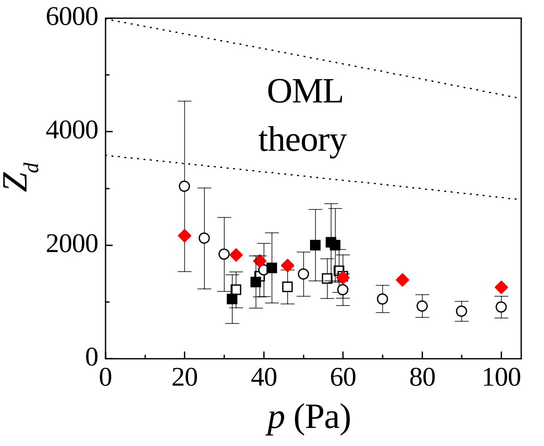


The charge of particles was determined experimentally in a bulk dc discharge plasma in the pressure range from ~20 up to ~150 Pa. The charge was obtained by two independent methods: One based on analysis of the particle motion in a stable particle flow and another on transition to unstable flow. The experiments with relatively small dust particles (0.6 µm) were performed in ground based conditions. Some experiments with larger particles (1.7 and 3.4 mm) were also performed in microgravity conditions during ESA 36$^{th}$ parabolic flight campaign (March, 2004). The experimental charges agreed well with results of molecular dynamics simulations of the particle charging carried out for conditions similar to those of the experiment (see Fig. 1). The charges obtained are considerably smaller than those predicted by the standard orbit motion limited theory (especially, at higher pressures). This provides a first experimental confirmation that ion-neutral collisions significantly affect particle charging. The results have been published in Refs. [1-2].

References:


[1]. S. Ratynskaia, M. Kretschmer, S. Khrapak, R. A. Quinn, M. H. Thoma, G. E. Morfill, A. Zobnin, A. Usachev, O. Petrov, and V. Fortov, Dust mode in collisionally dominated complex plasmas with particle drift, IEEE Trans. Plasma Sci., **32** ( 2), 2004

[2]. S. Ratynskaia, S. Khrapak, A. Zobnin, M. H. Thoma, M. Kretschmer, A. Usachev, V. Yaroshenko, R. A. Quinn, G. E. Morfill, O. Petrov, and V. Fortov, Experimental determination of dust particle charge at elevated pressures, Phys. Rev. Let., **93** (8) 2004, 085001.



S. Khrapak, S. Ratynskaia, M.H. Thoma, M. Kretschmer, G.E. Morfill and PK-4 Team

# Particle Growth Experiments (PAGE)

Particle growth and the behavior of particle clouds in hydrogen-methane capacitively-coupled rf plasmas are investigated. We determine the evolution of the particle number for several temperatures and gas compositions. Most of these particles are due to flakes of layers delaminated from electrode surfaces. If we introduce diamond seed particles in the apparatus, we observe nucleation of small new grains on the surfaces of the diamond particles.

The behavior of particle clouds and particle growth in reactive plasmas is studied in a capacitively coupled rf discharge. We use a three electrode assembly with the electrodes, 10 cm in diameter, being oriented horizontally. The rf power is applied to the upper electrode. To change the plasma conditions in the levitation region, a grided electrode is put between two rf electrodes. The particles are levitated between this grided and the lower electrode. To collect the particles directly from the particle clouds, we use a NFP (negatively charged fine particle) collector [1].

Particles generated in the plasma without introducing seed particles are mainly amorphous carbon. Most of the particles levitated are flakes, delaminated from the surface of the upper two electrodes. However we also find a few nano-diamond particles for the following growth condition, $CH_4$: 1sccm, $H_2$: 20sccm, temperature of electrodes: 800K. If we pour diamond seed particles (average size ~2.8 micron) into the apparatus, we observe nucleation of new particles on their surface as shown in Fig. 1 (size up to 100 nm after 8 hours plasma exposure at 800K). In order to increase the growth rate of diamonds and improve the quality, we have installed a tungsten hot filament between the gridded electrode and the lower electrode. To insert the W hot filament, three effects are expected. The first is to heat the particles more efficiently. The second is to produce more atomic hydrogen efficiently. The third is the decrease of the electron temperature [2]. The energetic electrons in plasma are absorbed to the filament instead of the electrons emitted from the filament because the hot filament system is electrically floating. The low electron-temperature electrons replace the high electron-temperature electrons in plasma. Figure 2 shows a picture of particles and the filament. In this case the temperature of the filament is 2300 K and the temperature of the particle levitation region is 1000K.

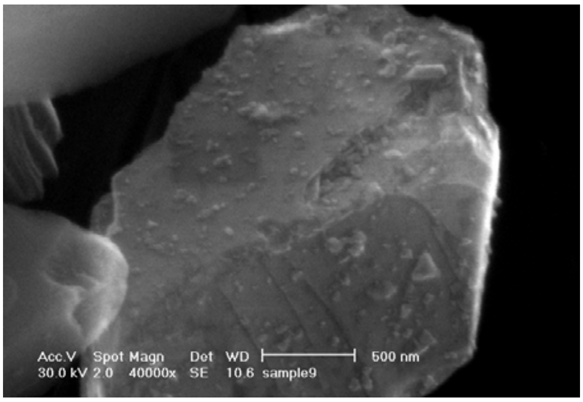


Fig.1: SEM image of diamond particle.

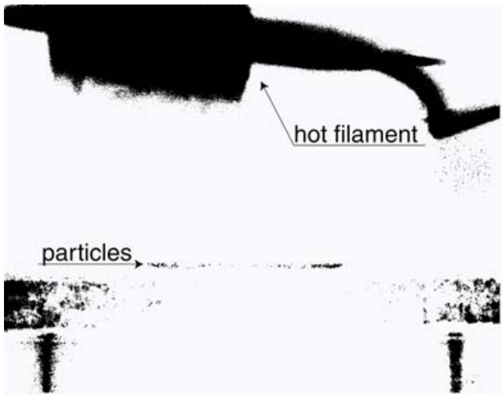


Fig.2: Particle-confinement with hot filament.

**References:**
• [1] G. Uchida, S. Iizuka, and N. Sato, *Proceedings of the 17$^{th}$ symposium on plasma processing*, 617(2000).
• [2] I. Alexeff and W. D. Jones, Appl. Phys. Lett., **9** (1966) 77.

*T. Shimizu, W. Jacob, H. Thomas, G. Morfill, Y. Watanabe, and N. Sato*

# Technology Transfer

# Non-linear Dynamics of the Atomic Force Microscope

**The atomic force microscope can be considered as a non-linear mechanical system which exhibits non-linear interactions and chaotic modes of motion. We have computed the Correlation Dimension, the Bifurcation Diagram and a Poincaré Map for experimental data obtained by dynamic atomic force microscope. From the analysis we infer a period doubling mode and chaotic modes of the system.**

Atomic-force microscopy (AFM) is a nowadays widely used tool for surface analysis. Dynamic AFM methods like tapping mode$^{TM}$ or non-contact mode are commonly used for imaging although a thorough understanding of the data can be difficult due to the nonlinear tip–sample interaction. In the tapping-mode the micro cantilever is resonantly forced to oscillations with an amplitude of about ten to one hundred nanometers. Close to the specimen the tip periodically interacts with the surface which reduces the oscillation amplitude.

From theoretical investigations it is known that the nonlinear interaction with the specimen can lead to chaotic dynamics although the system behaves regularly for a large set of parameters. The nonlinear tip–sample interaction also leads to the generation of higher harmonics. These harmonic signals allow one to reconstruct the transient tip–sample interaction forces.

In this contribution we analyze the non linear dynamics of amplitude modulation AFM. While changing the most important control parameter, the tip-sample distance, one observes a wide range of states – some of them in particular known from chaotic systems.

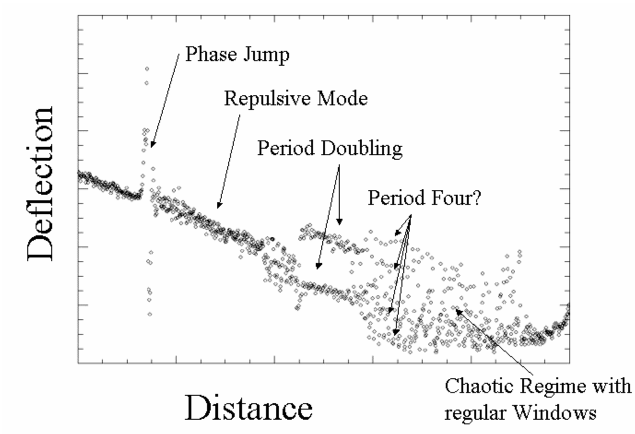


Fig. 1. Bifurcation Diagram for the experimentally recorded AFM data. The large panel shows a close-up for the transition from regular to chaotic behavior. After a transition from the attractive to the repulsive mode the system undergoes a period-doubling and finally a ends in a chaotic regime.

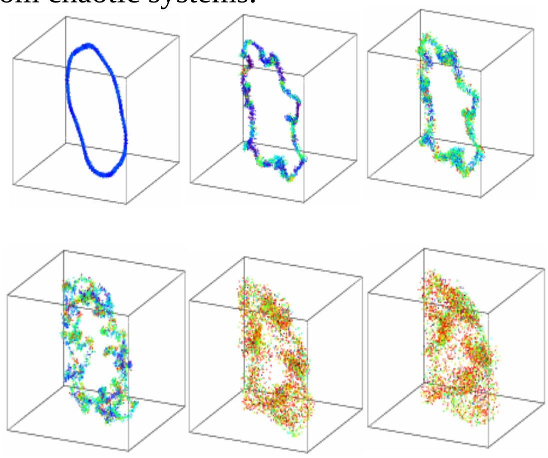

Fig. 2. 3-D phase space embeddings for six different epochs. The first panel shows the return plot in the regular region. The second panel is located at the phase jump from the attractive to the repulsive mode. The fourth panel represents the period doubled mode. The fifth panel shows a period four mode and the last panel coincides with the chaotic regime.

The system under consideration shows features that are typical for a dynamical system with a low number of degrees of freedom in the regular and chaotic regime. Far away from the surface the system is in a regular regime, while during the approach a phase jump, a period-doubling regime and a chaotic regime develop. System characteristics of this type have been observed for the Duffing-oscillator which can serve as a model system for an AFM.

**References:**

• F. Jamitzky, M. Stark, W. Bunk, W. M. Heckl, R. W. Stark , “Nonlinear dynamics of a micro-cantilever in close proximity to a surface”,  Proceedings of the IEEE NANO 2004

collaboration with M. Stark, R.W. Stark and W. M. Heckl

*F. Jamitzky, W. Bunk*

# Unveiling non-linearities via the Structure Analysis of Fourier Phase Maps

We present a method to detect non-linearities based on the characterization of the structural features of the Fourier phase maps. A Fourier phase map is a 2*D* set of points $M = \{\phi_{\vec{k}}, \phi_{\vec{k}+\vec{\Delta}}\}$ where $\phi_{\boldsymbol{k}}$ is the phase of the ***k***-mode of the Fourier transform and **Δ** a phase shift. The phase maps are analyzed using the spectrum of weighted scaling indices to detect phase coupling. We propose a test of significance based on the comparison of properties of phase maps created from the original data and surrogate realizations. We show that the method reveals new features and assess the performance of surrogate data generating algorithms.

The Fourier phases are powerful indicators of the structure of a data set. Studies of phase coupling are found in astrophysics where the aim is to test for non-Gaussian signatures in the Cosmic Microwave Radiation Background[1] (CMB). We propose a method to detect non-linearities which uses the method of surrogates[2] to generate an ensemble of data sets which mimic the linear properties of the original data however wiping out higher-order correlations. Then, we create for both the original and the surrogate data phase maps which are subsequently characterized by means of the spectrum of weighted scaling indices[3]. The scaling index $\alpha_i$ is a local quantity that characterizes the scaling behavior of a point distribution in the neighborhood around $x_i$. For instance, for almost uniform 2*D* point distributions all α-values will be around 2. We apply our method to two different time series, namely the *z*-component of the Lorenz system in a chaotic regime and the logarithmic daily returns of the Dow-Jones for the period 1930-2003. The surrogate method destroys higher-order properties using of a phase randomization procedure. Thus, the phase maps of surrogate data should be more uniform. We propose a test of non-linearities based on the frequency distribution of α values $P(\alpha)$. We generate 20 surrogate data sets and create for the original

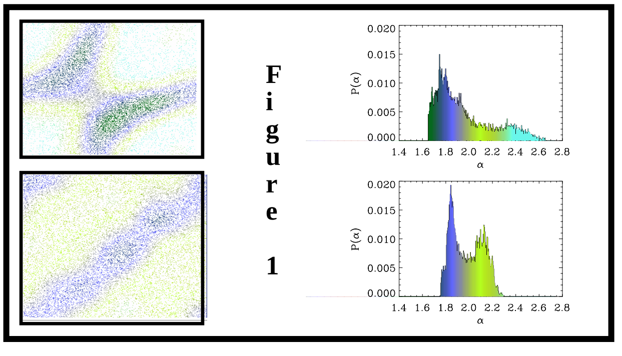


**Figure 1**

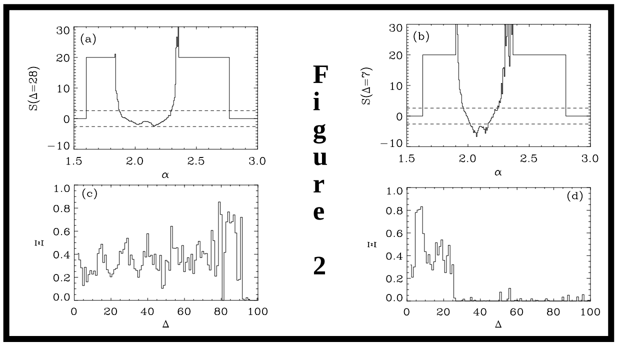


**Figure 2**

and the surrogate data phase maps for phase shifts $\Delta=\{\Delta_1,\ldots,\Delta_m\}$ where $\Delta_m$ is the maximum phase shift considered. The significance is defined through the following expression $S = \left(P_o(\alpha,\vec{\Delta}_l) - \left\langle P_s(\alpha,\vec{\Delta}_l)\right\rangle\right) / \sigma\left(P_s(\alpha,\vec{\Delta}_l)\right)$ where <> and σ are the mean value and standard deviation over the surrogate ensemble. The test result is positive if $S < -2.6$ for $1.9 < \alpha < 2.1$ or $S > 2.6$ for α elsewhere. This condition determines the region of the phase map where significant differences between the original and surrogate phase maps exist. If this region is tiny, we can not state that the original and the surrogate phase maps are different. Then, we define a new quantity Ξ through $\Xi = \sum_i P_o(\alpha_i,\Delta)$ where $\alpha_i$ are the values which fulfill the condition. Ξ is then the probability to significantly distinguish between the original and the surrogate phase maps. Upper row (lower row) of Fig.1 show color-coded α–images of the phase map for the Lorenz system (Dow Jones) and the $P(\alpha)$ distribution. It is possible to locate on the images the different α values. Note that $P(\alpha)$ indicates that the surrogate phase map is more uniform. Upper row of Fig. 2 show examples of *S* for the Lorenz system (left) and Dow Jones (right). The dashed lines at ± 2.6 indicate the confidence interval. In both cases, there is a wide range of α-values with high *S* values. Lower row of Fig. 2 show Ξ for the Lorenz system (left) and Dow Jones (right). For the Lorenz series Ξ ~ 0.4 while for the Dow Jones only Δ values lower than 25 lead to positive test results. In summary, the Lorenz system showed signatures of non-linear behavior at all Δ scales. However, for the Lorenz system surrogates are not always free from phase coupling. Then, our method can assess the quality of surrogate data. Our results indicate that a typical scale of non-linearities $\Delta_c$ exists for the Dow Jones. This may help to understand the financial-price dynamics. For weak non-linearities as in the CMB of radiation, the use of surrogate data sets and local structure measures to assess phase maps may be more appropriate than the use of global measures.

**References:**

1. L. Chiang et al., Astrophys. J. **590**, L65 (2003)
2. T. Schreiber, Phys. Rev. Lett. **80**, 2105 (1998)

*R. Monetti, W. Bunk, F. Jamitzky, C. Räth, and G. Morfill*

# Image Enhancement Using Information Measures

An image can be represented as a point distribution in a state space that is made up by the pixel and colour coordinates. In order to characterise the structural or textural content of an image the calculation of the local scaling properties in this state space is often very helpful. However, this approach implies a relation between the spatial scale and colour scales, which is usually not given a priori. We developed a procedure, which objectifies and optimises the partitioning and scaling of the state space by means of the structural information content. This remapping yields in many cases images of enhanced significance and improve the quantitative results by the use of scaling property techniques with respect to the structural content.

Structural or textural elements of an image are recognised by its locally increased correlation function. One way to assess these correlations is the investigation of the local structural information content. The surrounding of each pixel is scanned by applying a two-dimensional shift operator. As a result of this procedure one obtains a two-dimensional distribution of colour-colour transitions associated with structural elements of the image. This two-dimensional distribution is evaluated using mutual information which results in a specific averaged information content of each colour value. In this way the specific contribution to the total information content of the image can be assigned to each colour value. Finally a non-linear rescaling of the colour values is achieved by an homogenous partitioning of the respective information space. This technique gives enhanced images with a better visual impression but is used in particular as a preprocessing step to the calculation of local scaling properties.

The following examples show applications of this method for a classification problem and image enhancement. Fig.1a displays three different Brodatz textures (A, B, C) with equal mean and standard deviation. The classification relies primarily on the different structural properties. After rescaling of the colour scale, local scaling properties are computed using the scaling index method. The classification performance as a function of the size of the texture probe is plotted for three different cases: The black curve denotes a simple gray value-based thresholding procedure. The two other curves represent the classification based on the scaling index method: The texture classification using the information-optimized images (red curve) is superior to the original images (blue curve) as input.

In Fig.1b the effect of this method on an image of a skin lesion is demonstrated: The structure of the lesion is enhanced (lower image) compared to the original image.

*a)*

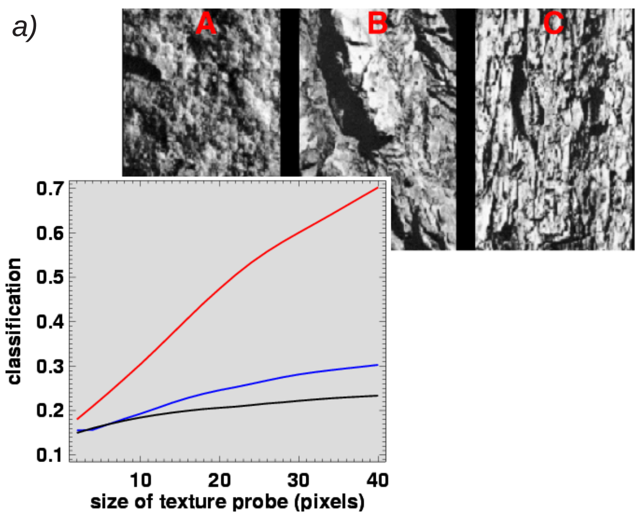


*b)*

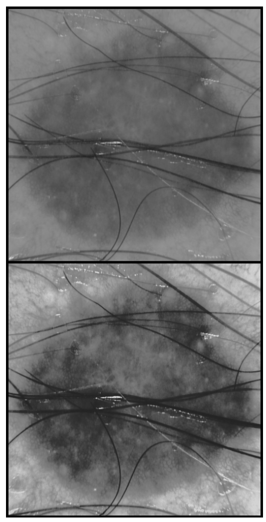

*Fig.1a: The curves show the classification performance as a function of texture probe size for a simple gray value thresholding procedure (black curve) and for an analysis based on the scaling index method (red and blue curve). The scaling indices applied to the enhanced images (red curve) yields better classification results compared to the scaling index method executed on the original images (blue curve). Fig.1b: Image enhancement applied to an image of a skin lesion (upper image: original, lower image: structure enhanced version)*

This technique will be extended to multi-parameter problems, where a “natural” relation of the different scales of the state space axes is missing.

*Th. Aschenbrenner, W. Bunk, F. Jamitzky*

# Particle Tracking Using an Evolutionary Approach

The investigation of the dynamics of the plasma crystal requires an efficient tracking of the particles. In our approach the matching of the particles in subsequent images may be considered as optimising some smoothness condition. Biologically motivated techniques like genetic algorithms or evolutionary strategies are an interesting alternative for solving such complex problems. In this study, the suitability of these techniques for particle tracking is examined.

The analysis of many features of the plasma crystal dynamics requires the knowledge of the particle trajectories. Their determination is difficult in the presence of hundreds of particles which may flow in and out of the focus of the camera and particle trajectories may cross in the visible plane. In the turbulent or chaotic regime this task becomes even more difficult. Such problems can be approached by applying a heuristic method that optimises several properties.

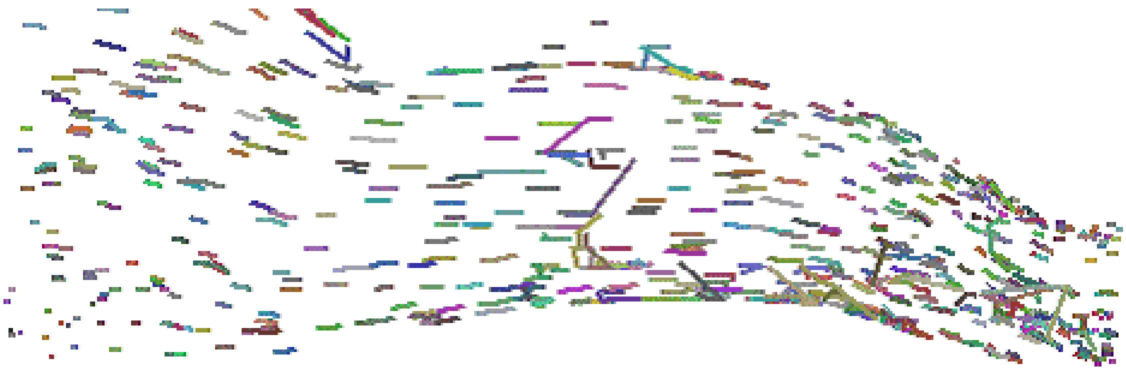

*Displayed are the trajectories of particles as they were determined by an evolutionary approach. Starting point of the analysis are the particle positions in five consecutive time steps. The algorithm joins this unordered set of particles to trajectories, which were colour marked for better distinction here. The errors in the result can be corrected by suitable post-processing.*

Genetic algorithms or evolutionary strategies mimic biological phenomena like mutation, genetic recombination and selection in order to solve multi-objective optimisation problems. For that purpose a pool of “individuals” is generated, of which each represents a possible solution. In each iteration step, descendents are created based on this parent generation by recombination and mutation. The quality of a solution by an individual is evaluated with a fitness function. A selection mechanism guarantees that only the “fittest individuals” (i.e. the best solutions of the problem) attain the next generation. These methods, which are motivated by nature, are an interesting alternative to other optimisation procedures as for example simulated annealing.

Applied to particle tracking, an individual consists of a set of paths. Recombination can be implemented e.g. by mixing two different paths and mutation is imitated by randomly changing an element of a path. The fitness of each individual is assessed with respect to the properties of the single trajectories: the length of the path is evaluated as well as the constancy in direction and speed.

In numeric experiments good results could be obtained. However the multiplicity of free parameters appears problematic because of the high computation time needed. In order to reduce the dimensionality of the problem, a more compact description of the individuals is necessary. The computational effort can substantially be reduced by parallelisation of the algorithm. However, this technique seems to be a promising approach for analysing the plasma crystal experiments.

*R. Pompl, W. Bunk*

# Molecular Simulations of the Dynamics of Grain Boundaries in Two-Dimensional Networks

**The temporal evolution of domain boundaries of hydrogen-bound molecular monolayers at the liquid solid interface is evaluated from a recorded series of subsequent Scanning Tunneling Microscopy (STM) images. To explain the different experimentally observed time scales of the dynamics occurring at grain boundaries, molecular mechanics simulations were applied to calculate the binding energy of edge molecules of finite islands of both trimesic (TMA) and terephthalic (TPA) acid on a graphite substrate.**

Many technologically relevant materials are brought to application in a polycrystalline state, i.e. the active area consists of grains with a more or less broad size, shape, and orientation distribution. Nucleation – i.e. the density and spatial distribution of the nuclei – as the first step of crystal growth determines the average size and distribution of the crystallites. If the available thermal energy allows, a reorganisation of the microstructure still can take place. STM has already proven it's value for the investigation of organic and inorganic grain boundaries. For two-dimensional molecular layers on atomically clean substrates, generally homo-nucleation – i.e. the nuclei are comprised of at least a critical number of the crystallizing species – occurs and the monolayer growth is terminated when the grains touch one another. The grains are separated by grain boundaries which perturb the translational symmetry of the otherwise crystalline material. Hence, this kind of defect has a high impact on important physical properties in particular transport properties like the electrical conductivity.

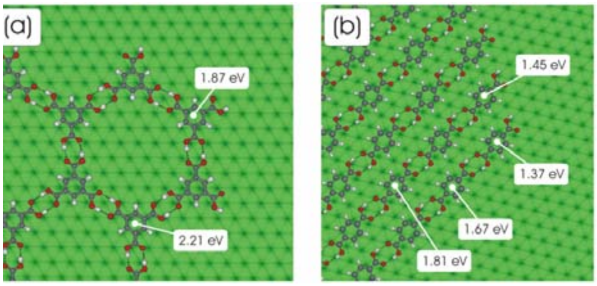


**Figure 1** Molecular mechanics simulations of finite islands of **(a)** TMA and **(b)** TPA were utilized to obtain a estimate for the binding energy of edge molecules. Two adjacent carboxylic groups form two H-bonds, symbolyzed by black dotted lines. The corresponding binding energies of non-equivalent edge-molecules are indicated within the models. TPA islands show two substantially different facets where the molecules being bound by either two or four H-bonds, which results in a significant difference in binding energy of 0.22 eV.

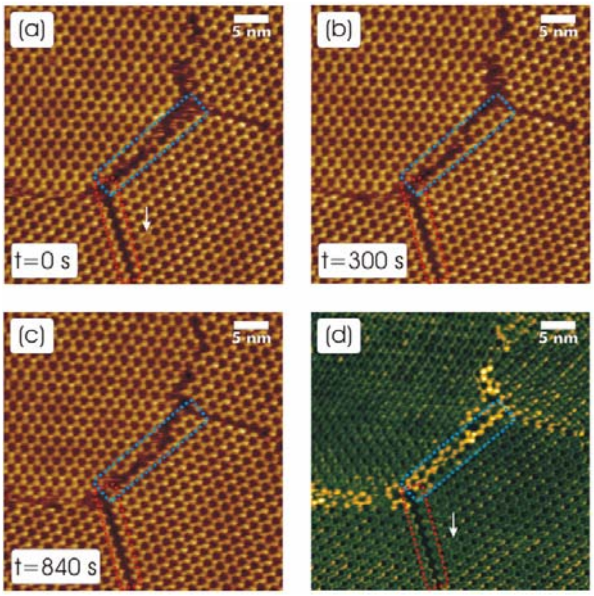


**Figure 2** **(a) – (c)** selected snapshots of a series of STM images of TMA domain boundaries (40x40 nm²). Only slight changes happen directly at the domain edge and the domain size and shape is mainly preserved **(d)** standard deviation of all 47 images of the series. Bright colours indicate larger values of the standard deviation, therefore represent regions, which evince enhanced molecular dynamics.

collaboration with M. Lackinger, S. Griessl and W. M. Heckl

**References:**

- Lackinger, M.; Griessl, S. J. H.; Markert, T.; Jamitzky, F.; Heckl, W. M. *J. Phys. Chem. B* **2004**, in press.
- Griessl, S. J. H.; Lackinger, M.; Jamitzky, F.; Markert, T.; Hietschold, M.; Heckl, W. M. *Langmuir* **2004**, in press.
- Griessl, S. J. H.; Lackinger, M.; Jamitzky, F.; Markert, T.; Hietschold, M.; Heckl, W. M. *J. Phys. Chem. B* **2004**, *108*.

*F. Jamitzky*

# Sand Grains as Indicator for Water on Mars

**In the search for aqueous habitats on Mars direct proof for (ancient) flowing water is still lacking although remote sensing has provided indications for young fluvial systems. To demonstrate that such proof can be given we examined surface marks on recent terrestrial sand grains with the atomic force microscope (AFM) and applied quantitative 3d-analysis that can numerically distinguish between aeolian and aquatic transport in sedimentary deposits on Earth.**

The surfaces of natural quartz grains as well as olivine, feldspar pyroxene and monazite sands of known origin have been imaged, each image providing a 3d map of the mineral surface. A fully automated analysis of distribution patterns of the structural elements that build up the grain surfaces shows that wind transported quartz grains have linear elements that are short and distributed irregularly on the surface whereas the linear elements on water transported grains are longer with orientations that reflect the mineral symmetry.

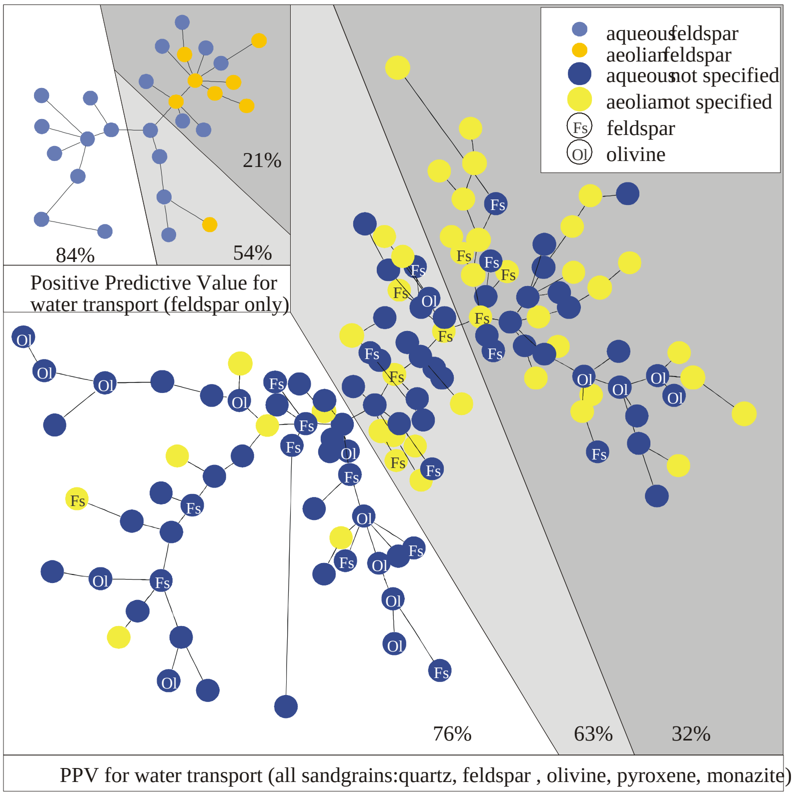


Because the surface patterns found on aqueous grains are due to anisotropic etching, they can be used as diagnostic fingerprints for the existence of aqueous transport systems in present or past. We use a cluster analysis of the cross-correlation-distance of distribution patterns in the structures of aeolian and aquatic sand grains to build a minimal spanning tree (see Figure), that provides a map for the relationship of the various sediments found on earth. The analysis shows that the method is highly significant and that water and wind transport can clearly be differentiated.

Feldspar and olivine sands which are typically for Mars contribute an even higher Positive Predictive Value to the discrimination than quartz grains. Simple AFM experiments on a possible Mars lander are capable of proving the existence of flowing water in active runoff systems and to analyse the paleo environments of Mars.

collaboration with A. Kempe, R. Stark and W. M. Heckl.

**References:**
• Discrimination of Aqueous and Aeolian Paleoenvironments by Atomic Force Microscopy - A Database for the Characterization of Martian sediments. Kempe, A., Jamitzky, F., Altermann, W., Baisch, B., Markert, T. & Heckl, M.W., 2004. Astrobiology 4 (1), 51-64.

*F. Jamitzky, W. Bunk, T. Aschenbrenner, R. Pompl*

# Spatio-Temporal Analysis of Brain Activity *

New methods, that combine non-linear data analysis techniques with elements from graph theory are applied to standard EEG recordings in the context of epilepsy. The correlation between these synchronously obtained time series is quantified by means of measures derived from information theory. The resulting quantities form the basis of a hierarchical clustering analysis that characterises the spatio-temporal ordering and the degree of synchronisation of brain activity.

A precise localisation of the origin of epileptic seizures based on surface electroencephalograms (EEGs) is still a challenge. In interictal periods (time between epileptic attacks) visual inspection of EEGs often shows no epileptic signs. Therefore it is desired to find characteristics that allow the recognition of an epileptic disease in interictal EEG-recordings even if typical pathological patterns are missing. The non-invasive scalp-electrodes are placed according to the standardised 10-20-International System of Electrode Placements. So every single EEG-recording consists of 21 synchronous channels. We apply several correlation measures to pairs of time series. For every time step ($t_{step} \approx 1-2\,s$) we end up with a correlation matrix. We observe that the use of non-linear distance measures based on e.g. mutual information is most appropriate to distinguish between normal and pathological brain activity. For clustering purposes these correlation measures have to be transformed to dissimilarity metric measures ("distances"). To assess the spatio-temporal dynamics of brain activity a hierarchical tree is generated based on this metric.
Fig. 1 shows the development of the derived parameter (mean mutual information) for patient A suffering a frontal lobe epilepsy (red symbols) and a reference case B. An effective therapy in patient A yields values which are comparable to the reference patient. The observed distinctive feature could be confirmed in a small study with more than 30 EEGs from eight patients.

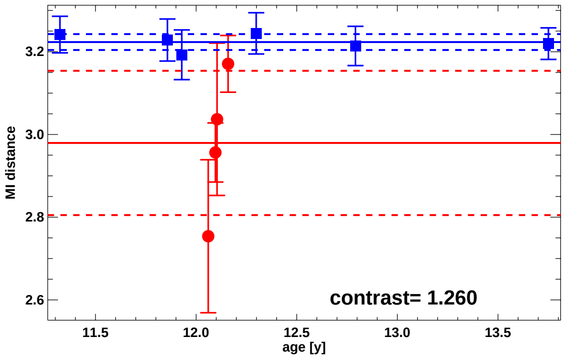


*Fig.1: Mean mutual information for patient A (red) and B (blue). The filled circles denote the mean mutual information, the vertical lines indicate the standard deviation of the single EEG-recordings. The horizontal lines label the mean mutual information for patient A and patient B, the dashed lines mark the respective standard deviations. As a consequence of medication patient A "approaches" the region where patient B resides during a longer time of observations.*

Comparison of the panels in Fig. 2 reveals significant differences in the spatial structuring of both patients: The aggregation levels of the hierarchical trees indicate the much stronger coupling of the EEG-channels in patient A. Also the different spatial distributions of dependencies between the time series are striking.

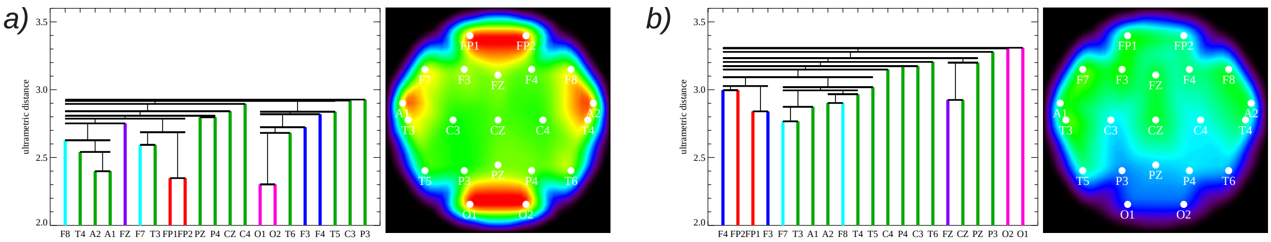


*Fig.2: Characterisation of Clustering behavior of patient A during an epileptic seizure (a) and patient B as a reference (b). In the left part of each panel the exact hierarchical tree is shown, while at the right side a two dimensional approximation of the cluster behaviour is displayed. High synchronisation is colour coded in red, low in blue.*

Even though some indications for the location of the epileptic focus could be found with this methods, it is so far not possible to define this area exactly. In future work we hope to narrow down the search area by optimising this technique.

* Collaboration with S. Springer, Heckscher Klinik für Kinder- und Jugendpsychiatrie, München

*W. Bunk, Th. Aschenbrenner, S. Springer *, R. Pompl*

# Structure Analysis of Proximal Femur HRMRI's using a 3D Anisotropic Method for the Prediction of Mechanical Strength

We introduce the scaling vector method (SVM): a technique to obtain local non-linear structural information from data sets suitable in cases where anisotropy plays an important role. We apply the SVM to High Resolution Magnetic Resonance Images (HRMRI) of human proximal femur specimens IN VITRO. By means of the SVM, we extract a 3*D* non-linear local anisotropic texture measure which we use to compare with similar isotropic texture measures, bone mineral density (BMD) and standard isotropic 2*D* (linear) morphometric parameters in the prediction of the biomechanical properties of the trabecular bone.

Proximal femur fractures are the most severe complications of osteoporosis. The structure characterization methods must account for the textural properties of proximal femur images which contain a large portion of bone tissue forming a mineralized trabecular network oriented along the major stress lines. 15 human proximal femur specimens were analyzed. Coronal HRMRI's were obtained using a 1.5 *T* scanner using a 3D-spin-echo sequence. A matrix of 384 x 512 was applied with a field of view of 75 x 100 *mm*, yielding a pixel size of 0.195 × 0.195 $mm^2$. Nineteen 0.9 *mm* thick sections were acquired. BMD ($g/cm^2$) of the femoral neck was determined using DXA. Bone strength was determined in compression. The maximum compressive strength (*Sm*) ranged from 3.20 to 16.95 *kN*. Only one of the fractures was a pertrochanteric fracture and the remaining 14 were neck fractures. For all specimens, central coronal femur images were selected where a rectangular ROI was chosen to evaluate the morphological parameters bone volume/total volume (*BV/TV*), trabecular separation (*Tb.Sp*), trabecular thickness (*Tb.Th*), and trabecular number (*Tb.N*). Consider a grey scale tomographic image $g=G(x,y,z)$. Each pixel contains space and gray value information that can be encompassed in a four dimensional vector $\mathbf{p}=[x,y,z,G(x,y,z)]$ which defines a 4*D* point distribution. The SVM characterizes the structural information of the images via the estimation

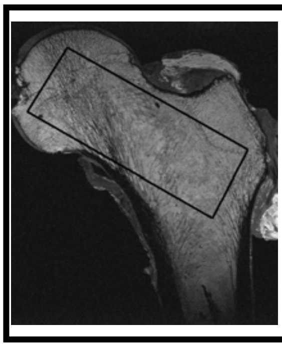

**Figure 1**

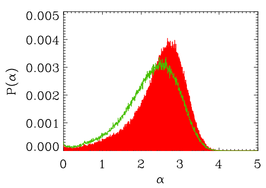


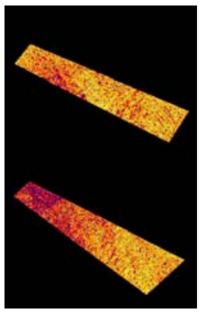

**Figure 2**

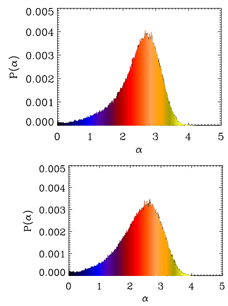


of local scaling properties of the above mentioned point distribution. We define a local weighted cumulative point distribution ρ: $\rho(p_i, L) = \sum_j e^{-(d_{ij}/L)^2}$ where *L* is the scaling range and $d_{ij}$ a generalized quadratic distance

$$d_{ij}^2 = \lambda_x (x\cos\theta + y\sin\theta)^2 + \lambda_y (x\sin\theta - y\cos\theta)^2 + \lambda_z z^2 + \lambda_g g^2$$

where $\lambda_i$ are the weighting factors of the different directions and θ is the rotation angle. Note that $\lambda_x = \lambda_y$ corresponds to the isotropic case. The weighted scaling vectors $\alpha_i$ are obtained by calculating the logarithmic derivative of ρ with respect to *L*. The frequency distribution of scaling vectors $P(\alpha)$ characterizes the bone structure. We perform a correlation analysis based on a filtering procedure applied to the $P(\alpha)$ spectrum which considers two sliding windows of variable width. We call α-fraction to the fraction of pixels $\Delta P(\alpha)$ with scaling-vector values within the sliding window. We use the following structure measure $m^d = \Delta_{w_1} P(\alpha) / \Delta_{w2} P(\alpha)$ The window position and width were chosen to achieve optimal correlation between $m^d$ and *Sm*. Figure 1 shows a HRMRI of the proximal femur where the black square limits a section of the 3*D* ROI. On the right, the $P(\alpha)$ spectra for two femur specimens (Red: *Sm* = 4.25 *kN* Green: *Sm*=13.6 *kN*). Note that weaker bones lead to spectra shifted to higher α-values. Figure 2 shows two different color-coded femur α–images and the corresponding spectra. Different α-values can be located on the images.

| | $m_{ani}^d$ vs Sm | $m_{iso}^d$ vs Sm | BMD vs Sm | BV/TV vs Sm | Tb.N vs Sm |
|---|---|---|---|---|---|
| **Correl. Coeff.** | 0.91 | 0.85 | 0.72 | 0.6 | 0.52 |

**Conclusions**: The results suggest that 3D local non-linear anisotropic structural parameters has a superior performance in the prediction of biomechanical strength in cases where directional properties play a relevant role.

**References:**

1. R. Monetti et al., Proc. SPIE: Medical Imaging **5032**, 1777 (2003)
2. R. Monetti, et al., Proc. SPIE: Medical Imaging **5370**, 1777 (2004)
3. H. Boehm, et al., Invest. Radiol **38**, 269 (2003)

*R. Monetti, H. Boehm, D. Mueller, E. Rummeny, T. Link and C. Raeth*

# Using 3-dim Scaling Properties in Magnetic Resonance Images for the Prediction of Osteoporotic Fractures

MAX-PLANCK-GESELLSCHAFT

MPE

Bone structure, in addition to bone mineral density, is an important component in determining bone strength and risk of fracture. High resolution magnetic resonance imaging (HR-MRI) has recently been introduced to assess bone structure. In this project we are using a newly developed 3D-based scaling index method in comparison with standard 2D-techniques based on bone histomorphometry to analyze HR-MR images of the distal radius to investigate the trabecular structure in patients with and without osteoporotic spine fractures. These structure analysis techniques were compared with BMD in their diagnostic performance to differentiate patients with and without fractures.

## Methods and Materials:

Axial HR-MR images of the distal radius were obtained at 1.5 T in 66 women (28 postmenopausal women with osteoporotic spine fractures and 38 postmenopausal controls). A three-dimensional gradient-echo sequence was used with a voxel size of 500x195x195 µm. Trabecular structure analysis was performed using algorithms based on our new local 3D scaling index method as well as standard morphological 2D parameters. In addition BMD measurements of the spine using quantitative CT (QCT) and dual energy X-ray absorptiometry (DXA) were obtained in all patients. Receiver operating characteristics (ROC) analyses were used to determine the diagnostic performance in differentiating patients with and without fractures. The results were statistically validated using bootstrapping and jackknifing techniques.

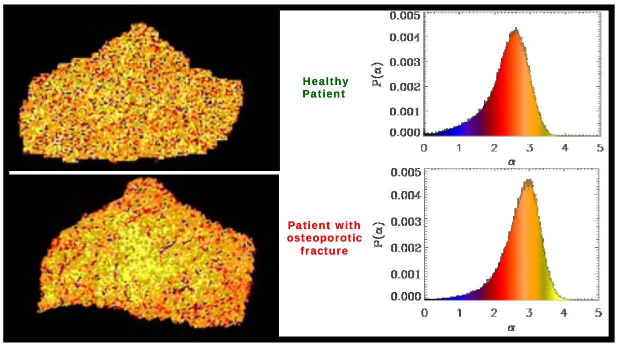


*Figure 1: Color coded images of the segmented part of axial HR MR images of the distal radius. The colour coding corresponds to the α-value of each pixel The different filter response to different structural elements is obvious.*

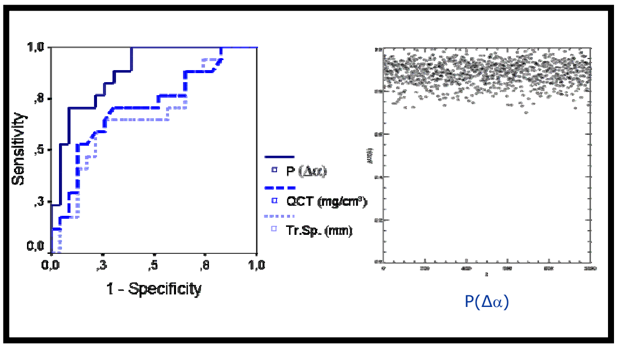


*Figure 2: Left: ROC-curves comparing P(Δ α ) (Az=0,88), BMD (Az=0,71) and apparent trabecular separation as the best 2D-Parameter (Az=0,69). Right: The diagram represent the Az-(AUC)-results of the bootstrap method for P(Δα).*

## Results:

Significant differences between both patient groups were obtained using structure analysis and spine BMD ($p<0.01$). In comparison with BMD of the spine (Area under curve (AUC)= 0.72) and the 2D based structure parameters (AUC up to 0.69) the best results were found for the local 3D scaling index method (AUC=0.87). For the bootstrapping technique the AUC-values calculated for the scaling index method (mean value: 0.862, standard deviation: ± 0.009) were significantly better ($p<0.001$) than those measured with BMD (0.721, ± 0.016) or the standard 2 D parameters (0.693, ± 0.015).

## Conclusion:

The results of our study show that trabecular structure measures derived from HR-MRI of the radius using a newly developed algorithm based on a local 3D scaling index method can improve the diagnostic performance in differentiating postmenopausal women with and without osteoporotic spine fractures.

**References:**
•1.Boehm HF et al., Local 3D Scaling Properties for the Analysis of Trabecular Bone Extracted from High-Resolution Magnetic Resonance Imaging of Human Trabecular Bone: Comparison with Bone Mineral Density in the Prediction of Biomechanical Strength In Vitro. Invest Radiol. 2003
•2.Rath, C et al., Analysing large-scale structure - I. Weighted scaling indices and constrained randomization. Mon Not R Astron Soc 2002

*D. Mueller, R. Monetti, H. Boehm, C. Raeth, T.M. Link, E.J. Rummeny, G.E. Morfill*

# Topological Analysis of Bone Structures Based on Minkowski Functionals

Topological texture measures based on the Minkowski Functionals[1] (MF) in 2D and 3D have successfully been employed to predict the mechanical competence of trabecular bone *in-vitro*[2]. In this *in-vivo* study, the MF in 2D and 3D are used to characterize the micro-structure of the distal radius in post-menopausal women as depicted by high-resolution magnetic resonance imaging (HRMRI) for identification of patients with vertebral fractures. Results are compared with bone mineral density (BMD) and standard texture measures in 2D, i.e. apparent trabecular separation (app.Tb.Sp) and apparent trabecular bone volume fraction (app.BV/TV).

HRMRI of the distal radius in 36 age-matched post-menopausal women (age 66 +/- 6 yrs) were obtained at 1.5 T using a 3D gradient-echo sequence with a spatial resolution of 195 x 195 x 500 µm. 13 of the women had vertebral fractures as diagnosed on lateral radiographs of the spine (Fig. 1). BMD was measured by quantitative computed tomography in the lumbar spine.

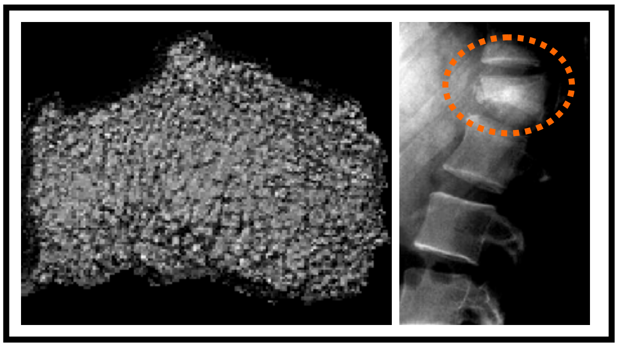

Fig. 1: HRMRI of the distal radius (left) and lateral x-ray of the spine with fractured vertebra (circle).

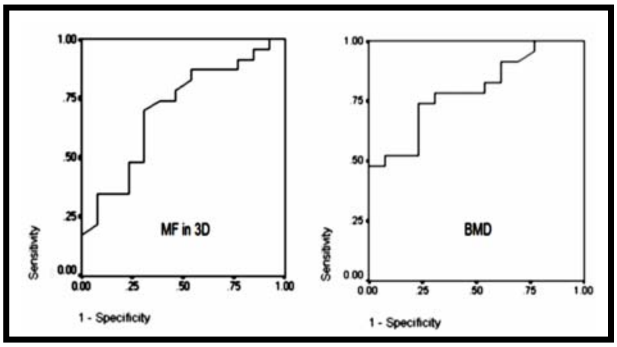


Fig. 2: ROC-analysis for correct identification of individuals with vertebral fractures using the MF in 3D (left) and BMD (right).

From the image data, the MF in 2D {3D} corresponding to area, perimeter, and Euler-Number {volume, surface, mean integral curvature, and the Euler Number} were obtained as a function of gray-level threshold. In order to assign a scalar quantity to each image set, an optimised filtering procedure using two independently sliding windows of variable width was employed. As a standard of reference, standard texture measures in 2D were extracted from the image data[3]. The predictive potential of BMD, the linear and the topological texture measures was expressed using the receiver operator characteristic (ROC), validation of results was achieved by leave-one-out (LOO) analysis.

Mean values of BMD, linear and topological measures significantly differed for the fracture group and the controls ($p < .05$). When employing ROC-analysis for identification of fracture patients, an area-under-the-curve (AUC) of .73 was found for BMD, AUC for the linear measures ranged from .60 (app.BV/TV) to .65 (app.Tb.Sp), whereas the topological measures resulted in an AUC of .78 (2D) and .79 (3D) (Fig. 2).

In conclusion, topological descriptors are well suited to identify patients with vertebral fractures by texture analysis of HRMRI of the distal radius. Texture measures based on the MF in 2D and 3D are equally reliable. The diagnostic performance of topological analysis is superior to bone densitometry and linear texture measures.

**References:**

1. K. Michielsen, H. De Raedt, and T. Kawakatsu, *Phys Rep* **347**, pp. 461-538 (2001)
2. H.F. Boehm, C. Raeth, R.A. Monetti, et al., *Proc of the SPIE: Medical Imaging*, pp. 470-79 (2003)
3. S. Majumdar, H. K. Genant, S. Grampp, et al., *J Bone Miner Res* **12**, pp. 1-9 (1996)

*H. F. Boehm, T. M. Link, R. A. Monetti, D. Mueller, E. J. Rummeny, G. Morfill, C. W. Raeth*

# Discrimination of Biological Cell Components using Minkowski Functionals

A major challenge in tomographic imaging of sub-cellular structures is the segmentation of the image data with respect to identification macro-molecular structures such as the actin-cytoskeleton or cell organelles. The Minkowski Functionals [1] in 3D - a set of global topological descriptors corresponding to volume, surface, mean integral curvature, and Euler-Poincaré characteristic - have been introduced to medical image processing in the context of structural analysis of bone architecture [2, 3].
In this work we provide a morphological filtering algorithm based on the Minkowski Functionals in 3D for the segmentation of macro-molecular structures in intact eukaryotic cells depicted by cryo-electron tomography.

We analyse 3D image data of an ice-embedded *Dictyostelium* amoeba directly grown on an electron microscopy grid (Figure 1) [4]. The specimen is scanned by low dose transmission electron microscopy employing a CM 300 FEG TEM with a single axis tilt series of -50° to +41.5° at an increment of 1.5°. The reconstructed 3D representation of the dataset contains 128 x 255 x 255 voxels. Image pre-processing involves binarization and noise reduction by removal of objects with less than 50 connected voxels.

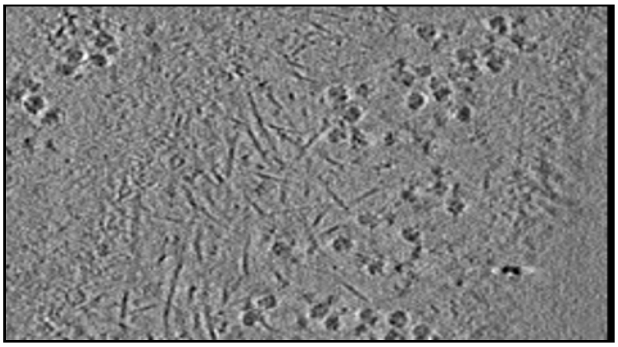

***Figure 1***: Microscopic image slice reconstructed from cryo-electron tomography of the *Dictyostelium* amoeba.

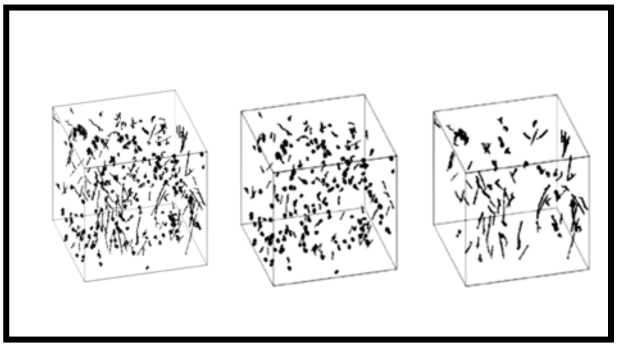

***Figure 2:*** The binarized image data comprises 201 convex image components (*left*), which are then separated by Minkowski-based thresholding into spherical (*middle*) and filamentary (*right*) objects.

The resulting sub-population of 201 image components have volumes of 50 to 1338 voxels, surface areas of 90 to 2616, mean integral curvatures of 11 to 207 and Euler-Numbers of 1 to 3.
By inspection, 86 of these are classified as filamentary structures, 78 as spherical and the remaining 37 as complex objects (Figure 2). Significant MF-based segmentation results are achieved when considering the 3rd functional (mean integral curvature). Filamentary image components tend to be characterized by high curvatures whereas spherical objects have lower values. When choosing a cut-off value for mean integral curvature at 30, the group of 111 objects with curvature ≤ 30 consist of 61 spherical, 28 filamentary and 22 complex structures. The set of image components with curvature >30 comprises 58 filamentary, 17 spherical and 15 complex objects. The area-under the-curve for mean integral curvature was 0.77 for correct detection of spherical image components and 0.78 for filamentary structures.

In conclusion, the morphological properties of binarized tomographic image data expressed in terms of the Minkowski Functionals in 3D can successfully be employed for segmentation of filamentary and spherical image components. This new approach may serve as a tool for reducing the time-consuming process of segmenting macro-molecular structures as depicted by cryo-electron tomography of intact eukaryotic cells which today still involves a substantial amount of human interaction. In future, considerable effort will be put into finding an automatic binarization procedure. We also hope to improve segmentation / classification results further by consideration of additional morphological properties.

**References:**


1. K. Michielsen, H. De Raedt, T. Kawakatsu. *Phys Rep* **347**, pp. 461-538, 2001.
2. C.W. Raeth, R.A. Monetti, D. Mueller, et al.. Proc. of the SPIE: Medical Imaging: Image Processing, 5370-142, 2004.
3. H.F. Boehm, T.M. Link, R.A. Monetti, et al. Proc. of the SPIE: Medical Imaging: Image Processing, 5370-23, 2004.
4. O. Medalia, G. Gerisch, W. Baumeister. *Microsc Microanal* **9** (suppl. 3), pp. 380-81, 2003.



*H.F. Boehm, F. Jamitzki, R.A. Monetti, D. Mueller, A. Linaroudis, R. Hegerl, C.W. Raeth*

# Experimental/Hardware Projects

Organisation at MPE

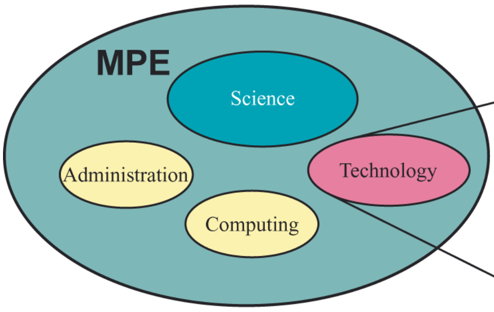


Organisation of technical groups at MPE

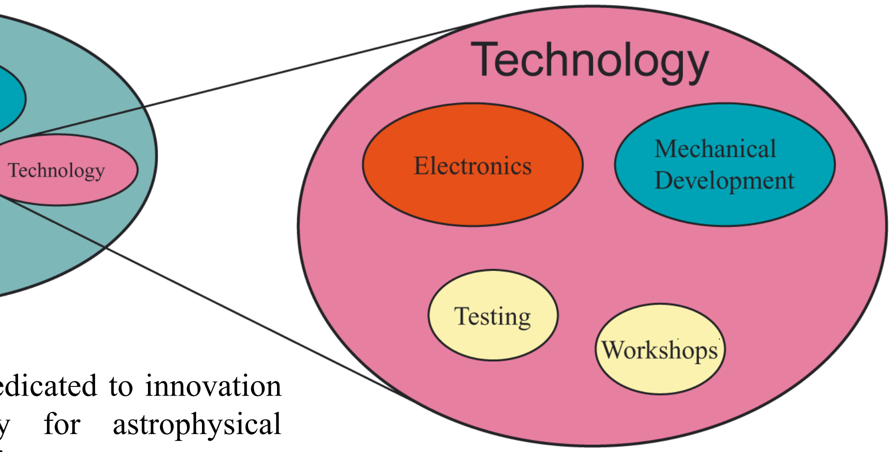


The technical groups are dedicated to innovation excellence and reliability for astrophysical experiments on ground and in space.

Science at the institute depends on instruments developed built and tested mostly by the technical groups of the institute, who are involved in big space borne projects like EPIC on XMM, PACS on Herschel, FIFI-LS on SOFIA, DUO-Camera on the NASA-SMEX-Mission DUO, PK 3+ and PK 4 for the ISS, GBM on GLAST and MEGA on a balloon and also in instruments for ground use like SPIFFI/SINFONI and PARSEC for the ESO VLT, LUCIFER for the LBT, the GROND Gamma-Ray-Burst experiment for La Silla f rom ESO and CAST at CERN.

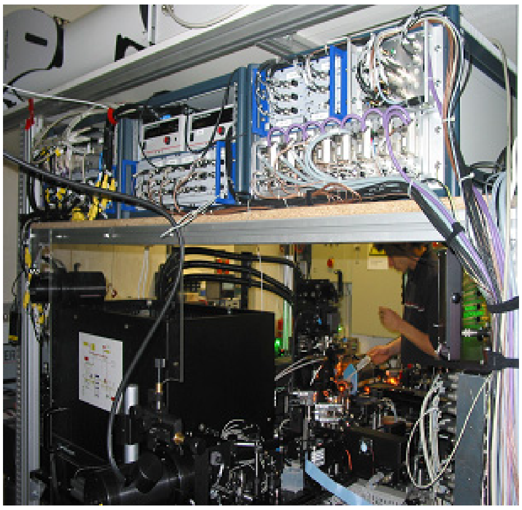

*PARSEC Electronics*

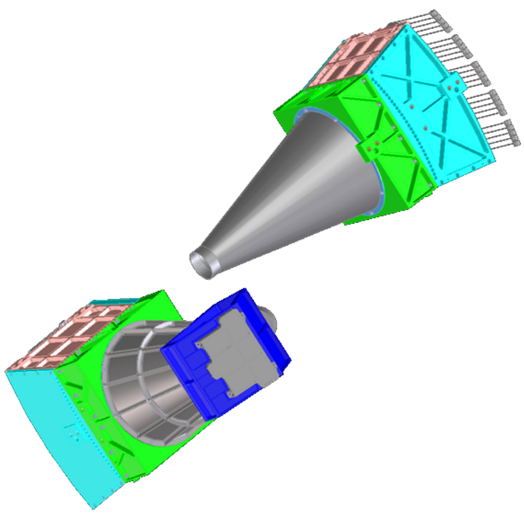

*PACS Detectors*

# Mechanical Engineering

**Mechanical Department**

**Tasks: Development of Instruments for the experimental Astrophysics**

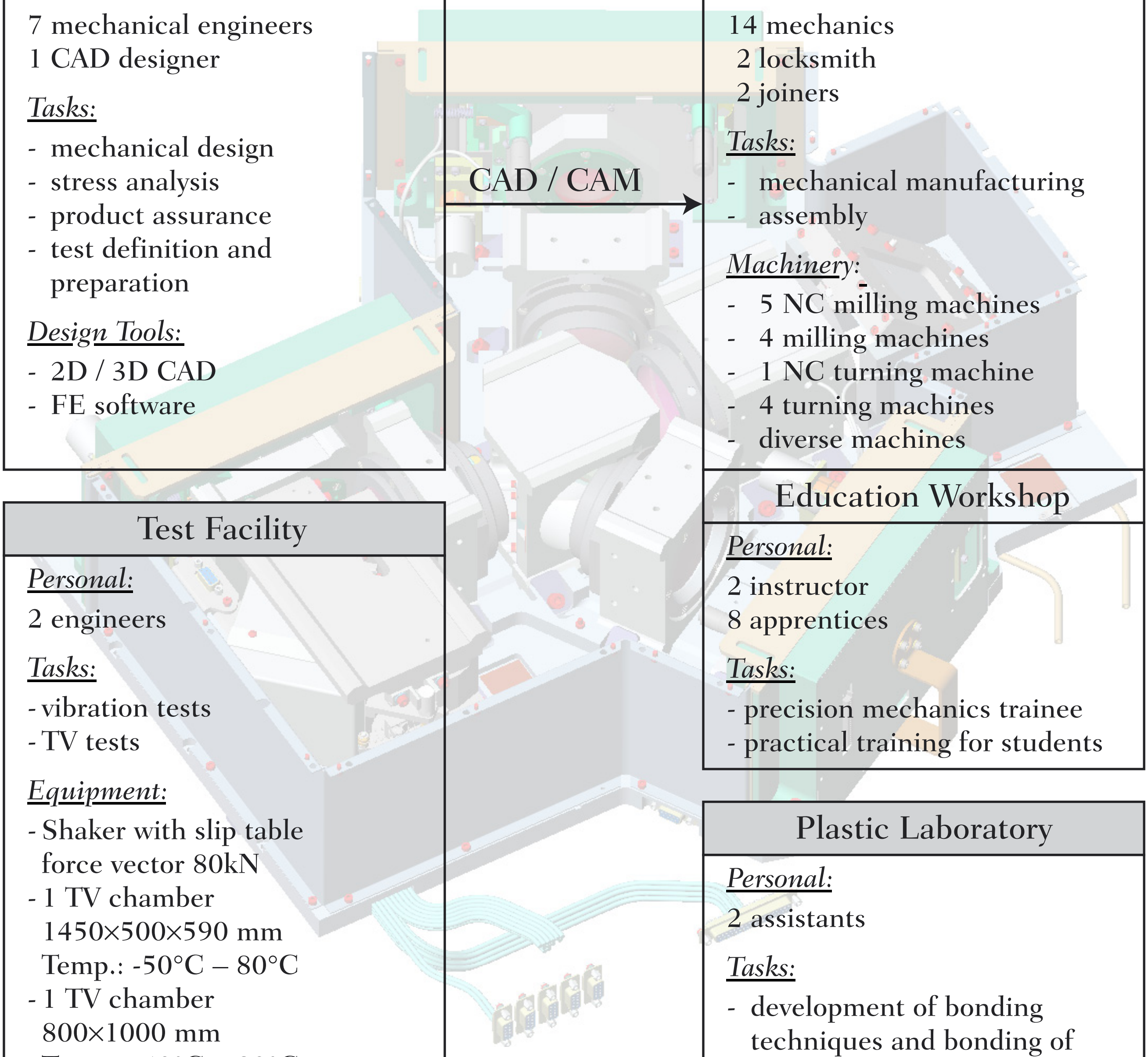

## Mechanical Development

*Personal:*

7 mechanical engineers
1 CAD designer

*Tasks:*

- mechanical design
- stress analysis
- product assurance
- test definition and preparation

*Design Tools:*

- 2D / 3D CAD
- FE software

CAD / CAM →

## Machine Shops

*Personal:*

14 mechanics
2 locksmith
2 joiners

*Tasks:*

- mechanical manufacturing
- assembly

*Machinery:*

- 5 NC milling machines
- 4 milling machines
- 1 NC turning machine
- 4 turning machines
- diverse machines

## Test Facility

*Personal:*

2 engineers

*Tasks:*

- vibration tests
- TV tests

*Equipment:*

- Shaker with slip table
  force vector 80kN
- 1 TV chamber
  1450×500×590 mm
  Temp.: -50°C – 80°C
- 1 TV chamber
  800×1000 mm
  Temp.: -40°C – 80°C
- Climatic Chamber
  770×1020×745 mm
  Climate Area: 10 - 95% r.H.
  -75°C – 180°C

## Education Workshop

*Personal:*

2 instructor
8 apprentices

*Tasks:*

- precision mechanics trainee
- practical training for students

## Plastic Laboratory

*Personal:*

2 assistants

*Tasks:*

- development of bonding techniques and bonding of plastics and metallic materials
- optical couplings
- fabrication of:
  · composites
  · MLI blankets

# ELECTRONICS

**Engineering:**

25 engineers and technicians

- Support for experiment development and proposals
- Design of experiment elctronics
- Design of experiment software
- Tests
- Instrument operation

**Electrical Workshop:**

5 technicians

- Qualified manufacturing
- Soldering
- Cabling
- Bonding
- Integration support

**Housekeeping:**

4 technicians

- Operation and supervision of technical equipment in the different buildings (Power, Air-conditioning, Water, Heating)

Collaboration with NASA, ESA, ESO, DLR, Industry and other scientific Institutes.

Background: Layout of DUO Test electronics

# MPI Halbleiterlabor

The MPI Halbleiterlabor (semiconductor laboratory) is a joint research facility of the Max-Planck institutes for physics and for extraterrestrial physics. In a 1000 $m^2$ large clean room, silicon detectors are produced and tested for research activities. The XMM-Newton PN-CCD detector and the Silicon Drift Detectors used on the Mars Rovers ‘Spirit’ and ‘Opportunity’ have been fabricated there. Presently, detectors for the future DUO and XEUS mission are developed.

The Halbleiterlabor has a highly flexible production line, which can process ultra-pure silicon wafers on both sides. The devices can be produced (Fig. 1), mounted (Fig. 2) and tested without even leaving the cleanroom area.

The technology is continuously being optimized and extended. These optimizations are aimed towards low noise performance (by minimizing leakage current and integrating electronics on-chip), low-energy response (by ultra-thin entrance windows), and large area devices (by tight process control).

The Laboratory routinely produces several detector types which have been invented by its members:

Fig 1: The part of the production area, shown here, contains an 8-tube furnace (back left), inspection (front) and wet etching equipment (back right).

•**Silicon strip detectors** are used in high energy physics experiments like the HERA-B experiment at DESY or the future ATLAS detector at CERN.

•**Fully depleted charge coupled devices** with parallel readout are used onboard the X-ray satellite XMM-Newton. New flight CCDs with frame store are currently produced for the DUO mission .

•**Silicon drift detectors** are used for high-resolution, high-rate spectroscopy at synchrotron light sources like ESRF or DESY, for X-ray microscopy at BESSY and for the hadron physics experiment SIDDHARTA. They also work in the NASA Mars rovers and are foreseen for the ESA mission XEUS.

•**Active pixel devices** with **DEPFET** amplifiers are developed for XEUS and TESLA (Fig. 3). High position resolution, thinned material and fast readout are key items for this next detector generation.

The activities of the MPI Halbleiterlabor also find interest in industry. In particular, products based on silicon drift diodes originally designed and fabricated for scientific experiments have been successfully introduced as X-ray detectors in scanning electron microscopes.

Fig. 2: The mounting area includes a water-guided laser dicer (back left) and an automatic bonder.

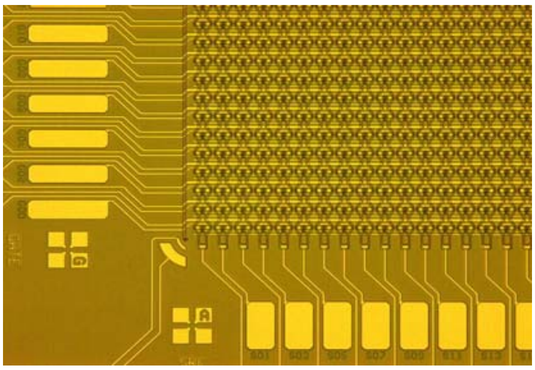

Fig. 3: Recently processed active pixel matrix with DEPFET amplifiers for the ESA mission XEUS.

*MPI Halbleiterlabor • Otto-Hahn-Ring 6 • 81739 München • www.hll.mpg.de*

# Photodetector Array Camera & Spectrometer (PACS) for the ESA Herschel Space Observatory

The Herschel Space Observatory, an ESA cornerstone mission to be launched in summer 2007, will explore the formation and evolution of galaxies and stars through photometric and spectroscopic observations in the far-infrared and submillimeter wavelength range. With a 3.5 m telescope, passively cooled to ~80 K, it will step into a new regime of angular resolution and sensitivity at these wavelengths and, for the first time, allow observations of luminous objects in the distant universe at the expected peak of their emission.

MPE as the PI-institute in a European consortium of 15 institutes from 6 countries is leading the construction and operation of one of the three focal plane instruments, the Photodetector Array Camera & Spectrometer (PACS). PACS will be a combined imaging photo/spectrometer for the wavelength range 57–210 μm. In its photometric mode it will image two bands simultaneously (60-85 or 85-130 μm and 130-210 μm) with point a source detection limit of ~3 mJy (5σ, 1h), enabling e.g. deep surveys of the extragalactic FIR background down to the confusion limit. In spectroscopy mode PACS will image a field of ~ 50" x 50", resolved into 5 x 5 pixels, with an instantaneous spectral coverage of ~ 1500 km/s at a spectral resolution of ~ 75–300 km/s and with a point source detection limit of 3–10 x $10^{-18}$ W/m$^2$ (5σ, 1h).

Focal Plane Footprint

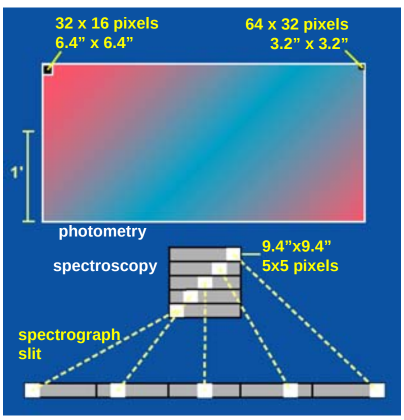


Focal Plane Unit Layout

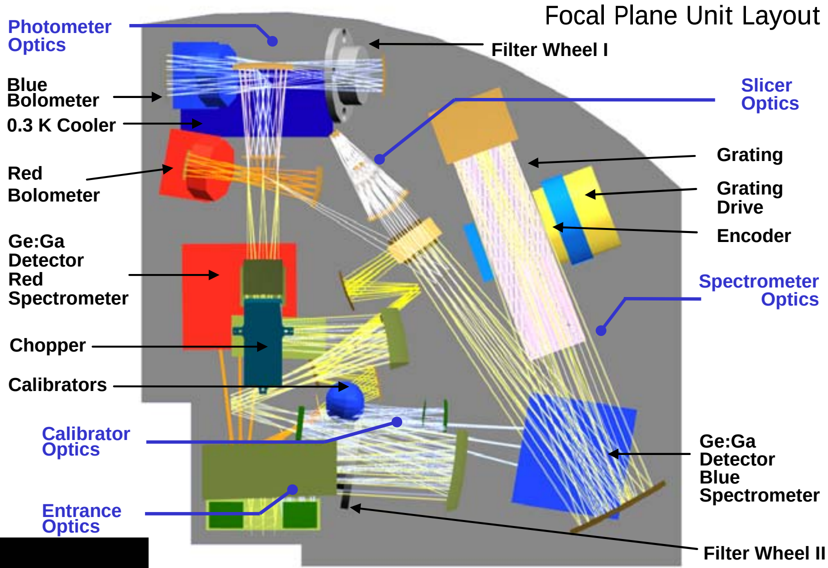


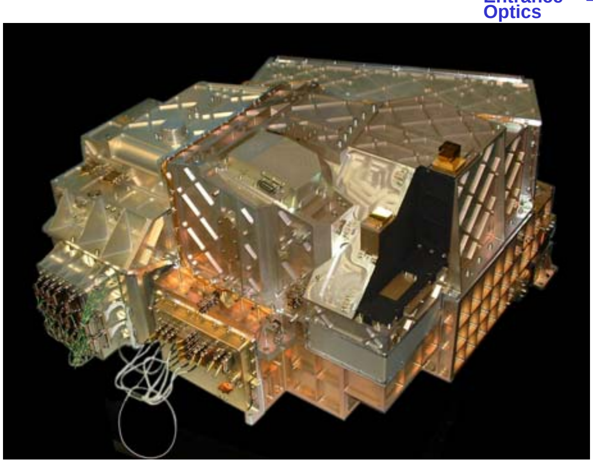

The PACS Focal Plane Unit involves complex optics (image slicer, anamorphic collimation and imaging), precision cryomechanisms (chopper and grating drive), and advanced far-infrared detectors (16x25 pixels stressed Ge:Ga photoconductor arrays and 64x32/ 32x16 pixels filled Si bolometer arrays). The entire unit is kept at ~5 K; the photoconductor arrays are operated at 1.8 K while the bolometers are cooled to 0.3 K through a dedicated $^3$He sorption refrigerator. The Focal Plane Unit is controlled by several warm electronics units. Tests and calibration of the complete system (Qualification Model) including cryogenic telescope simulator optics are ongoing at MPE.


Poglitsch, A., Waelkens, C., Geis, N., Proceedings of the SPIE, Volume 4850, pp. 662-673 (2003)



*A. Poglitsch, O.H. Bauer, M. v. Berg, D. Cesarsky, A. Contursi, H. Feuchtgruber, N. Geis, R. Katterloher, D. Lutz, T. Müller, J. Schubert, E. Sturm, E. Wieprecht*

# Herschel - PACS On-Ground Calibration

A **cryogenic test facility** for on-ground calibration and characterization will be used for the qualification model (CQM), flight model (PFM) and flight spare model (FS) of the Herschel PACS instrument. The test set-up comprises a test cryostat providing the satellite temperature levels 1.75 Kelvin for operation of all PACS detectors and 3 to 5 K for instrument focal plane structure cooling, as well as a cryogenic test optics with a Herschel telescope simulator operated at about 5 K. The test optics is designed to provide a realistic IR background (expected Herschel telescope temperatures 70-90K). The set-up is mounted on the same optical bench of the test cryostat that carries the PACS focal plane unit. The instrument characterization program includes alignment checks, optimization of detector operating parameters, spectral response function measurement, spectral and spatial instrumental profiles, detector flat fielding, wavelength calibration and point source simulation.

Two cryogenic blackbody sources were developed for absolute flux calibration. Several IR sources can be selected via different optical paths using cryogenic mechanisms, based on newly developed miniature cryo-torquer motors in combination with gear-boxes, which actuate flip-mirror mechanisms and a chopper wheel. A satellite representative cryogenic and ambient test harness (1600 wires!) is included to approximate on-board signal paths and EMC conditions during the instrument performance tests. Design and hardware status of the test facility are shown on the right and below.

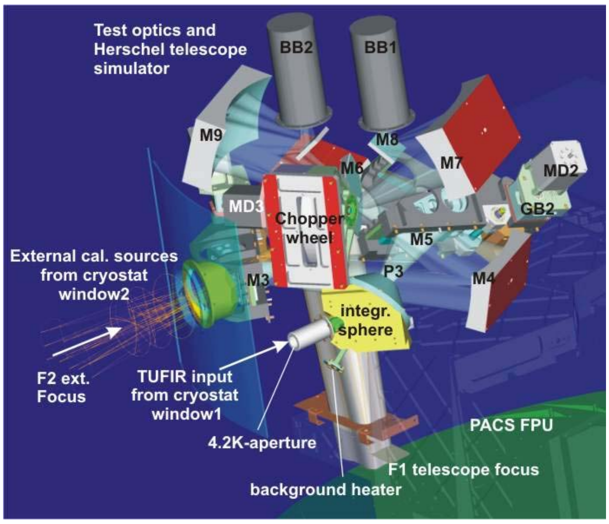


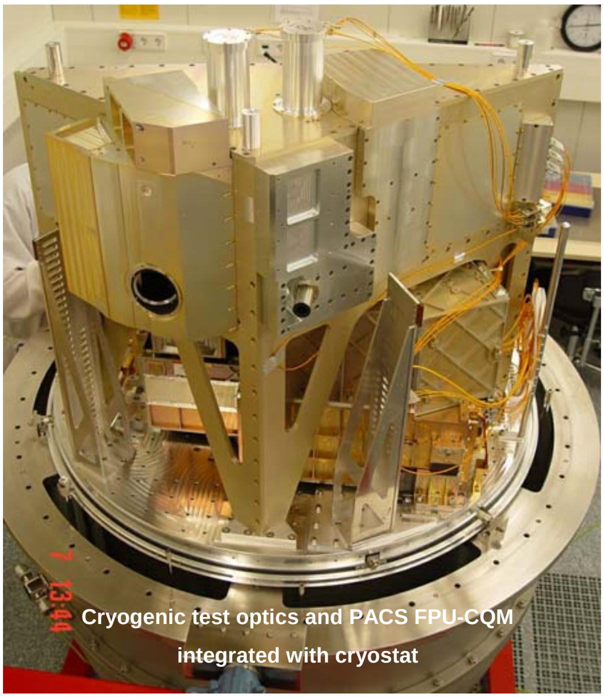

Cryogenic test optics and PACS FPU-CQM integrated with cryostat

**The cryogenic test facility consists of**

- Optics comprising 10 gold coated spherical and flat aluminum mirrors
- Herschel telescope simulator producing a focus outside the cryostat window, accessible for external sources
- Optics internal alignment accuracy is 1 arcmin
- Two cryogenic blackbody sources for absolute flux calibration (10 – 80K, 1 mK stability)
- Two flip mirror mechanisms driven by newly developed cryogenic torquer motors
- One chopper wheel to switch between the BBs
- Integrating sphere to feed in calibration sources operated outside the cryostat, e.g., FIR lasers
- External X-Y stage with a point source mask
- Water vapor absorption cell

**Reference:**
Jakob G., Geis N., Katterloher R., Thiel M., SPIE Vol 5487, 2004

*G. Jakob, N. Geis, R. Katterloher, M. Thiel*

# The PACS Electrical Ground Support System at MPE

MPE is hosting the PACS Instrument Control Center, responsible for software development, calibrations, and operations of the PACS instrument for ESA's Herschel mission. As a first step, the PACS Electrical Ground Support System (EGSE) consists of those electrical systems and related software, which provide the functionality required to test and operate the PACS instrument at various stages of its development. Here we give an overview of the major EGSE units to support Instrument Level Tests (ILT) and its setup at MPE. To minimize costs and the resource requirements for the development and operation of the HERSCHEL satellite, a common approach to instrument testing and in-flight operations has been taken, with the maximum reuse of equipment of software in all phases of the mission.

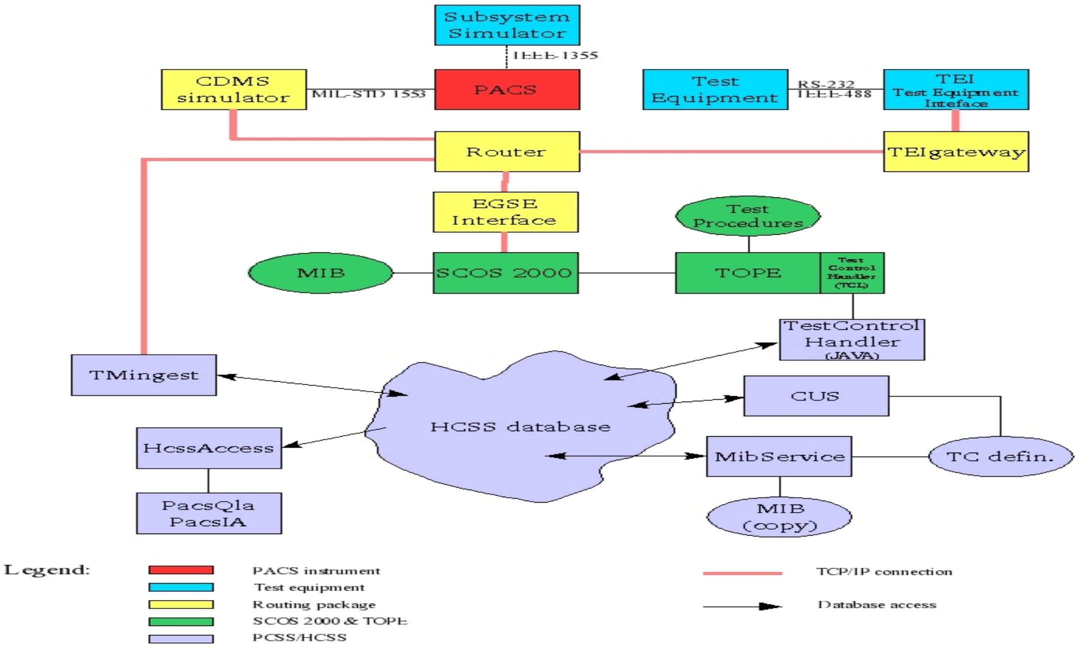


- The **CDMS** (Central Data Management Subsystem) Simulator simulates the CDMS subunit of the HERSCHEL satellite.
- The **Router** is the main application to distribute Telemetry.
- The **TEIgateway** (Test Equipment Interface) and **TEI** are the interface to **Test Equipment** like external calibration sources.
- **SCOS2000** is the HERSCHEL real time monitoring and commanding system used by all three instruments and ESA mission control.
- The mission specific behavior of **SCOS2000** is controlled by a set of files named **MIB** (Mission Implementation Base). It contains Mnemonics of Telemetry commands and definitions.
- **SCOS 2000** is extended by **TOPE** (Test and Operations Procedure Environment) which allows to execute Test Procedures.
- **TestControl** is the Interface between **TOPE** and **HCSS**. Using the **TestControlHandler** observations are commanded which were defined within **CUS** and stored in **HCSS**.
- **HCSS** (Herschel Common Science System) is the common software environment of the HERSCHEL software. The backbone of **HCSS** is an Object Oriented Database.
- **CUS** (Common Uplink System) is used to define Observations and Test Procedures. It use Telecommand definitions provided by the **Mibservice**, which is the interface to the **MIB** (copy)
- **TmIngestion** is responsible to inject data to the Database of HCSS.
- **PacsQla** displays PACS detector data in near real time
- **PacsIA** is the interactive analysis system of PACS data for all phases of the mission

*E. Wieprecht, E. Wiezorrek*

# Stressed Ge:Ga Far Infrared Detector Arrays for Herschel/PACS and SOFIA/FIFI LS

The spectrometer of the Photodetector Array Camera and Spectrometer (PACS) on board the Herschel satellite and the Field Imaging Far Infrared Line Spectrometer (FIFI LS) on board the Stratospheric Observatory for Infrared Astronomy (SOFIA) will use Gallium doped germanium arrays in a 16x25 pixel configuration. The arrays of slightly stressed Ge:Ga detectors cover a wavelength range from 55 to 105 µm (PACS) or 42 to 110 µm (FIFI LS), whereas the highly stressed detectors will cover a range from 105 to 210 µm.

The detector pixels are located within integrating cavities with area filling light cones. The arrays are operated with cryogenic multiplexed integrating amplifier readout electronics located close to the detector modules.

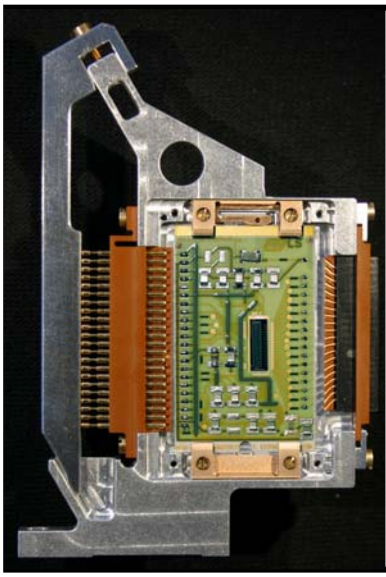

Cryogenic Readout Electronics (CRE) for FIFI LS. It will be connected directly to the detector module and operate at liquid helium temperature.

PACS QM fully assembled high stressed Ge:Ga detector array with its light cones in front. Baffle- and filter system of the FIR camera is dismounted in this picture.

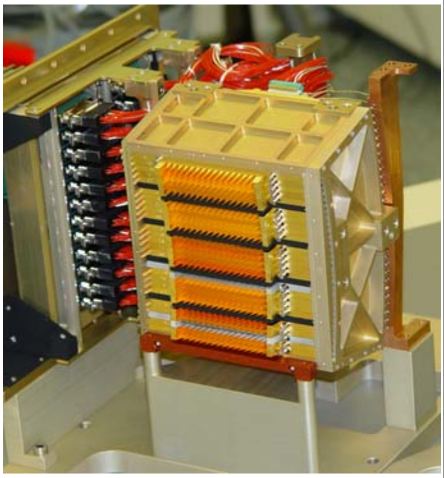

Detector signals of a single pixel (highly stressed Ge:Ga photoconductor) during space environmental radiation testing (protons 16.5 MeV) with two identified glitch events. In general, glitch events in the integration ramps are not very prominent, but the increase of detector responsivity after irradiation is considerably high.

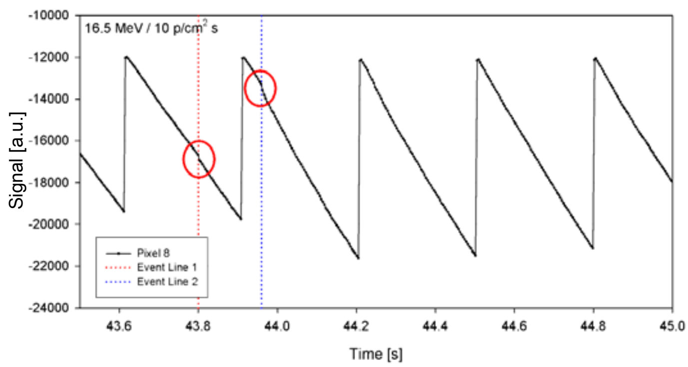


**References:**
• "Photoconductor array development for PACS and FIFI LS," in Millimeter and Submillimeter Detectors for Astronomy II, Proceedings of SPIE 5498, 2004, A. Poglitsch et al.
•"Characterization of high- and low-stressed Ge:Ga array cameras for Herschel's PACS instrument", in Millimeter and Submillimeter Detectors for Astronomy II, Proceedings of SPIE 5498, 2004, Stephan M. Birkmann et al.

*R. Hönle, J. Schubert, J.W. Beeman (LBNL), N. Geis, U. Grözinger (MPIA), R. Katterloher, A. Poglitsch, W. Raab, H. Richter (ASTEQ)*

# FIFI LS

## A Far-Infrared Field-Imaging Line Spectrometer for SOFIA

We are building FIFI LS, the Field-Imaging Far-Infrared Line Spectrometer, which will utilize the unprecedented high angular resolution and sensitivity of the joint NASA/DLR airborne observatory SOFIA. FIFI LS will be able to efficiently map spectral lines in two FIR bands simultaneously (Red 42-110 µm, Blue 110-220 µm) with its integral field concept. The scientific aim of FIFI LS is the interstellar medium of galaxies and galactic HII regions to investigate star formation, active galactic nuclei, and baryonic dark matter.

SOFIA is a Boeing 747SP equipped with a 2.5m telescope operated by NASA & DLR to carry out infrared observations in an altitude up to 14km. Several institutes in the US and two in Germany are building instruments for SOFIA. FIFI LS is one of them, getting ready for the first science flights of SOFIA end of 2005.


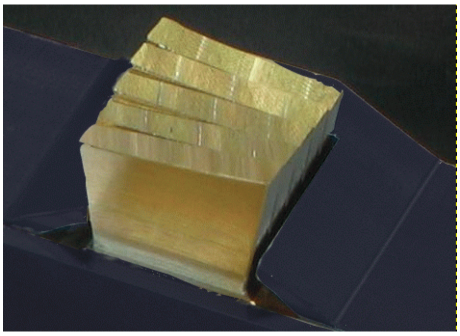

On the left, you see one of the two image slicers, that enable FIFI LS to do spectroscopy of its 5x5 pixel field of view at once. The image slicer rearranges the field of view onto the 25x1 pixel pseudo-slit of the grating spectrometer. The grating disperses the light of each of the 25 spatial pixels onto 16 spectral pixels. Thus, the detector of each channel consists of 25x16 Ge:Ga detector pixels (cf. Ge:Ga Detector development).

The vacuum vessel of FIFI LS has a volume of about 1m$^3$. As shown on the right, it uses three cryogen vessels ($LN_2$, LHe, superfluid He) for cooling the optics and detectors. The entrance optics features a K-mirror for image de-rotation, at $LN_2$ temperature. The gratings with their drives and position sensors (green) are mounted on the LHe working surface. The two detectors block require temperatures about 2K provided by the superfluid He. Below the cryostat, there is an additional visible light camera for guiding.

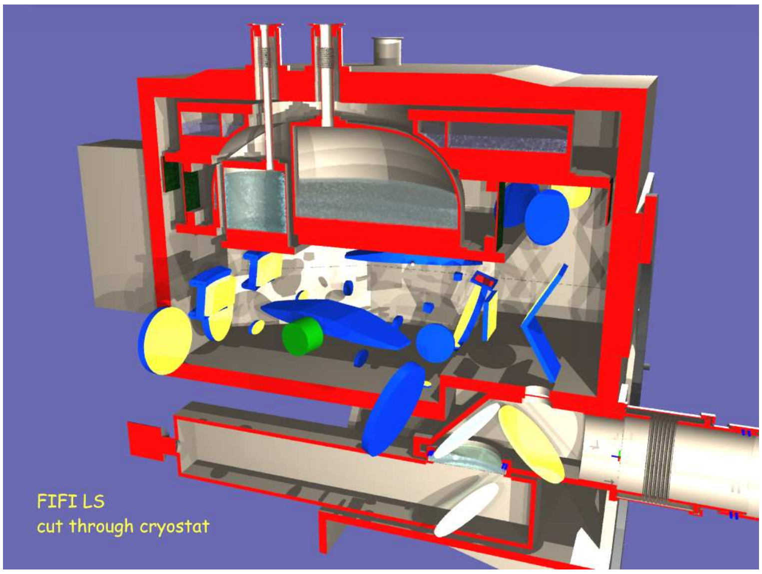


**References:**
**Realizing Integral Field Spectroscopy in the Far-Infrared,** Looney et al. (2003), ApJ 597, 628
**FIFI LS: the far-infrared integral field spectrometer for SOFIA,** Raab et al. (2004), Proc. of SPIE

| ***FIFI LS Basic Data*** | Detector | Pixels | Pixel size | Field of view | Velocity resolution | Line sensitivity | |
|---|---|---|---|---|---|---|---|
| Blue 42-110 µm | Ge:Ga | 25x16 | 6" | 30'x30' | 50-150 km/s | 50 µm: 5.5 $10^{-17}$ W/m$^2$ | 100 µm: 3.5 $10^{-17}$ W/m$^2$ |
| Red 110-210 µm | stressed Ge:Ga | 25x16 | 12" | 60'x60' | 100-250km/s | 150 µm: 2.2 $10^{-17}$ W/m$^2$ | 200 µm: 1.4 $10^{-17}$ W/m$^2$ |

*R. Klein, A. Poglitsch, F. Fumi, N. Geis, R. Hönle, W. Raab, M. Schweitzer, W. Viehhauser*

# GaAs BIB detector development

A **GaAs BIB detector development program for far infrared astronomy** was started three years ago as a common effort of four institutions: MPE (Germany), UC Berkeley, LBNL and NPS Monterey (USA). Our actual research program is supported by a NASA grant # NNG04GB82G.

**Rationale for a n-GaAs BIB** (Blocked Impurity Conduction Band) Detector Array:

•GaAs has the shallowest stable dopant (e.g., Te: 5.7 meV) of any well-explored semiconductor.

•Extension of the photoconductive cut-off wavelength to 330 µm (30 $cm^{-1}$) with GaAs BIB devices is expected (cut-off wavelength limit of stressed Ge:Ga photoconductors is 210µm)

•Manufacture of planar structured detector arrays at an affordable price seems feasible.

•Complexity advantage of photoconductors over bolometers: Operation at 1.6 K avoids the more demanding $^3$He cooling technique required for 0.3K or $^3$He/$^4$He for 0.1K bolometers.

•GaAs BIB detectors should get rid of g-r noise characteristic of bulk GaAs photoconductors.

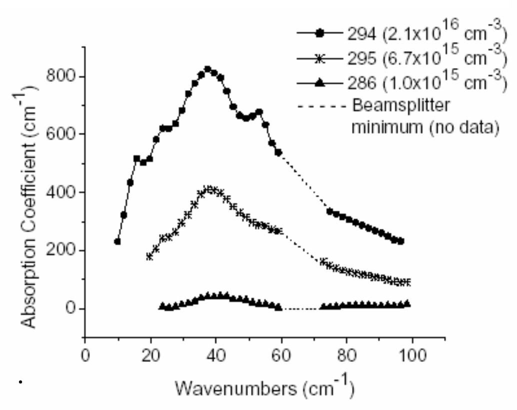


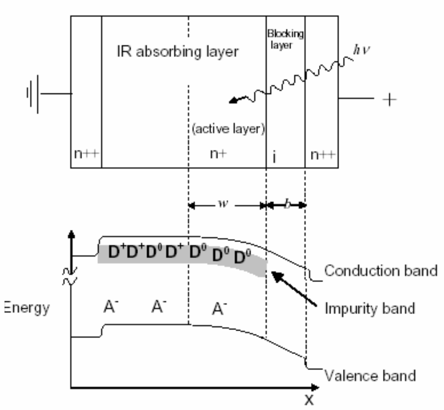


Experimental work is assisted by theoretical modeling. GaAs BIB modeling predicts that $4x10^{15}$ $cm^{-3}$ majority doping improves the FIR absorption by a factor 100 w.r.t. bulk devices even for a 10 µm thick layer.

**Experiment status:**

GaAs layers are grown using the Liquid Phase Epitaxy process. A centrifuge system with magnetic bearings was set up at UCB and is operational for 3 years. Growth parameters could be optimized meanwhile and replacement of the graphite crucible with a small sapphire crucible leads to a significant reduction of unwanted donors (impurity concentration is now few $10^{12}$ $cm^{-3}$). Controlled doping of n-GaAs (e.g. with Te) is proven. The reproducibility of the growth processes will be the next goal. Then, manufacture of a BIB detector pilot sample is within reach.

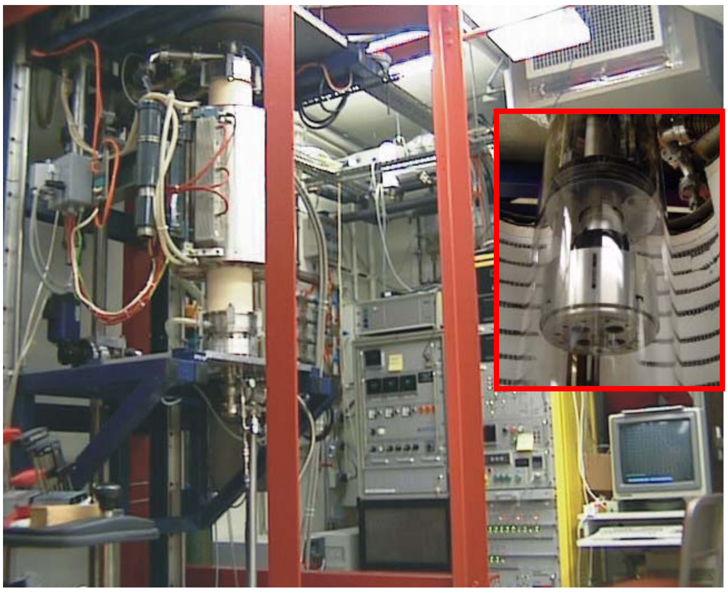

**Reference:**


Reichertz L.A., Beeman J.W., Cardozo B.L., Haegel N.M., Haller E.E., Jakob G., Katterloher R., SPIE Vol 5543



*R. Katterloher, L. Reichertz, N. Haegel, B. Cardozo*

# SPIFFI / SINFONI: First Light at the VLT

SPIFFI is the Near Infrared Integral Field Spectrometer for the VLT. Here report on the first light of the SPIFFI visitor instrument at the ESO VLT in March 2003, and the successful installation as part of the adaptive optics assisted SINFONI facility in July 2004. Amongst others, the highlights of the two observing periods in 2003 and 2004 include the first geometric distance measurement of the Galactic Center, the first infrared spectrum of its flaring black hole, the unprecedented spatially resolved spectroscopy of the Circinus galaxy and NGC 6240, and spatially resolved kinematics and abundance estimates of high-redshift submillimeter and UV selected galaxies.

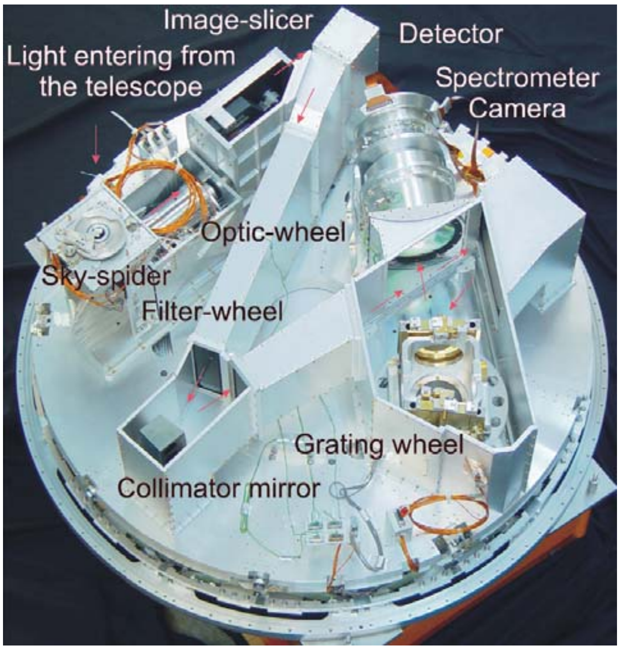


SPIFFI provides imaging spectroscopy of a contiguous, two-dimensional field of 64 x 32 spatial pixels in the wavelength range from 1.1 – 2.45 µm at a resolving power of 2000 to 4000. As a result, the instrument delivers a simultaneous, three-dimensional data-cube with two spatial dimensions and one spectral dimension. The left picture shows an inside view of SPIFFI: The telescope focal plane is re-imaged and magnified onto the so-called image slicer which rearranges the two-dimensional field into a pseudo-long slit for subsequent dispersion in the spectrometer equipped with the most recent Rockwell HAWAII 2kx2x array. The right picture shows the SINFONI facility installed at the ESO VLT. The blue cylinder hosts the ESO built adaptive optics module MACAO, the Aluminium cylinder is the SPIFFI cryostat. Scientific highlights of the commissioning and observing runs in 2003 and 2004 are presented separately in dedicated poster abstracts of this booklet: The first geometric distance measurement of the Galactic centre and spectroscopic classification of the early type stellar population in the immediate vicinity of the Galactic Center, the first infrared spectrum of its flaring black hole, unprecedented spatially resolved spectroscopy of NGC 6240 and the Circinus galaxy, and spatially resolved kinematics and abundance estimates of high-redshift submillimeter and UV selected galaxies.

**References:**


• Eisenhauer et al. 2003, SPIE, 4841,1548
• Eisenhauer et al. 2003, ESO Messenger, 113, 17
• Bonnet et al. 2004, ESO Messenger, 117


*F. Eisenhauer R. Abuter A. Gilbert R. Genzel M. Horrobin, M. Tecza, N. Thatte*

# PARSEC – the laser for the VLT

PARSEC is a sodium line laser which produces a stable single high quality 10 W continuous wave output beam. In Spring 2004 it had its European Acceptance Test and is currently undergoing joint testing as part of the Laser Guide Star Facility. In 2005 the LGSF will be commissioned with the adaptive optics instruments NACO and SINFONI for which, with Strehl ratios expected to reach 40% in the K-band, it will greatly increase the useful sky coverage.

The PARSEC system is based on dye laser technology, with many innovations. Commercial 532nm lasers excite a dye solution which is pumped through sapphire nozzles at a pressure of nearly 30 bar. In the master laser, a low power single frequency and single mode beam is produced, and used to feed a power amplifier which is phase-locked to the seed beam and, in typical conditions, can boost the output power to 15 W. Steerable mirrors keep the beam aligned with an accuracy of a few microns, and considerable automation allows the laser to be started from a remote site.

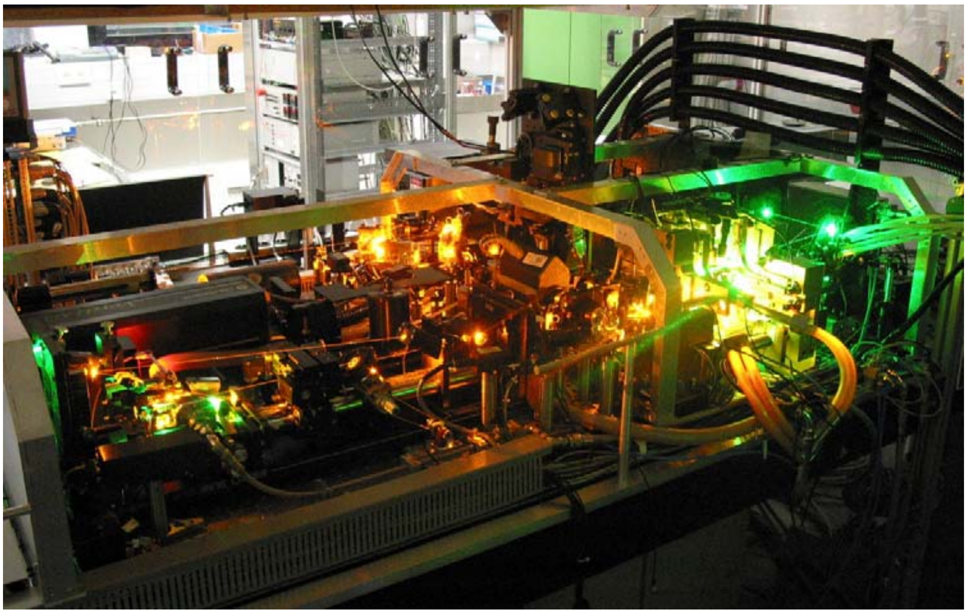

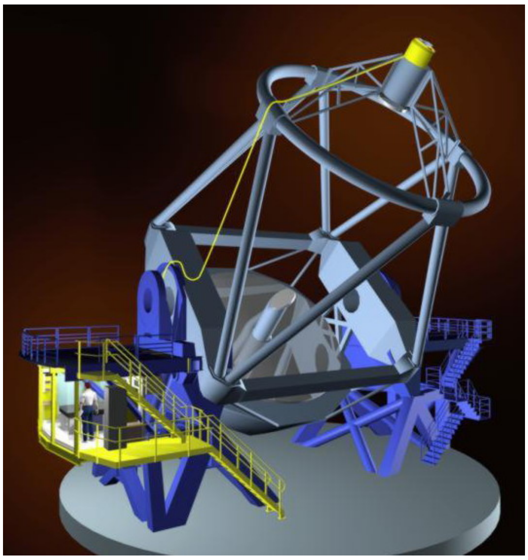

Above: the PARSEC laser bench in the lab at MPE, without the cover. The master laser is front left; the amplifier on the far right. The highest output power achieved to date is 23.9 W.

Left: a drawing of the how the laser system will be installed on the VLT UT4. The laser itself will sit on the bench in the clean room under the Nasmyth platform. The output beam will be taken to the launch telescope above the secondary mirror by a single mode photonic crystal fibre.

*R. I. Davies, S. Rabien, T. Ott*

# KMOS – a NIR multi IFU spectrograph for the VLT

• KMOS is a 2nd generation instrument for the ESO Very Large Telescope that will offer ~24 deployable integral-field units for cryogenic near-infrared multi-object spectroscopy at R~3500.

• Main science drivers for KMOS are: mass assembly of galaxies from moderate to high redshifts, extremely high redshift galaxies and re-ionisation, the connection between galaxy formation and black hole growth, stellar populations and star formation in nearby galaxies.

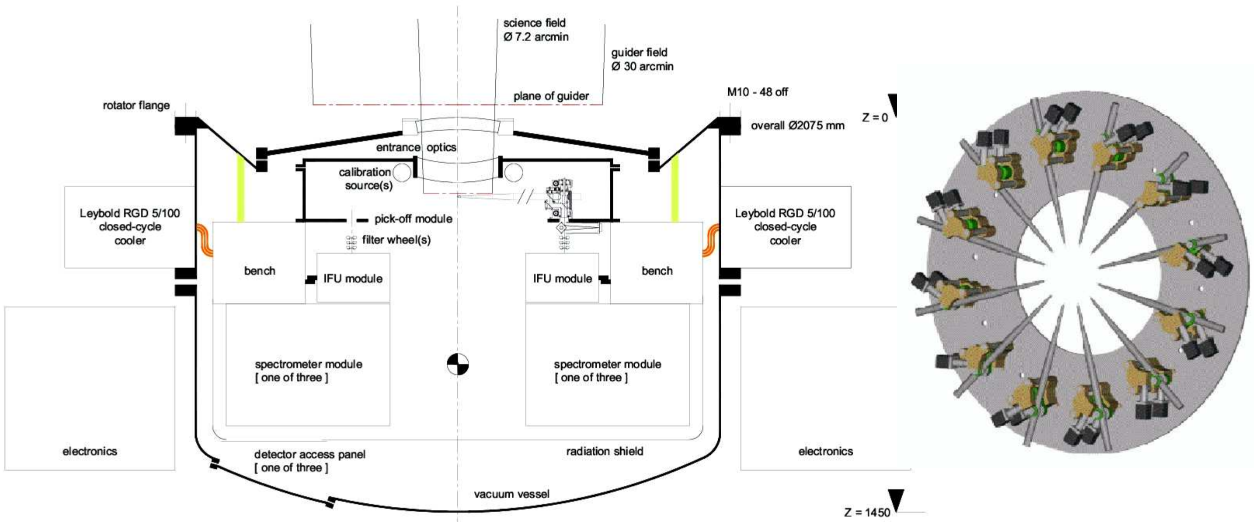


**Left:** KMOS baseline design: 2x12 configurable arms (in two layers) position fold prisms at user-specified locations in the Nasmyth plane of the VLT. The 24 sub-fields are then fed to image slicer IFUs that partition each sub-field into 14 identical slices, with 14 pixels along each slice. The 14x14 elements of 8 arms are combined and dispersed in one of three cryogenic spectrometers. Each of the spectrometers employs a 2kx2k HgCdTe detector and provides 1000 Nyquist-sampled spectral resolution elements corresponding to a spectral resolution of ~3500.
**Right:** Layout of one layer of pick-off arms.

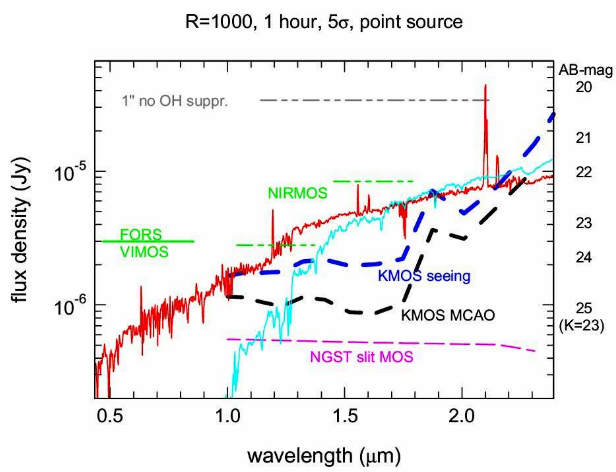


Expected sensitivity of KMOS

| Requirement | Baseline Design |
|---|---|
| Throughput | J=30%, H=40%, K=40% |
| Sensitivity (5σ,8h) | J=22.0, H=21.0, K=20.5 |
| λ coverage | 1.0 μm to 2.45 μm |
| Spectral resolution | R=3380,3800,3750 (JHK) |
| Number of IFUs | 24 |
| IFU size | 2.8”x2.8” |
| Sampling | 0.2” |
| Patrol field | 7.2’ diameter |
| Close packing | >3 within 1 sq.arcmin. |

Baseline capabilities of KMOS

KMOS is being built by a consortium of the following institutions: Max-Planck-Institute for Extraterrestrial Physics, University Observatory Munich, Astronomy Technology Center Edinburgh, University of Durham, University of Oxford, and European Southern Observatory.


**Reference:** Sharples, R.M., Bender, R., Lehnert, M., Ramsay Howat, S.K., Bremer, M., Davies, R.L., Genzel, R., Hofmann, R., Ivison, R.J., Saglia, R.P., Thatte, N.A.: 2005, SPIE, in press; 2003, SPIE 4841, 1562



*R. Bender, R. Genzel, R. Hofmann, M. Lehnert, B. Muschielok, R.P. Saglia and the KMOS consortium*

# Image Selection and Image Slicing for KMOS

**ABSTRACT: For KMOS, an imaging multi-object spectrograph for the VLT, a fiber integral-field-unit (IFU) has been studied, and the prototype of a pickoff arm carrying a fiber-IFU and a steering mirror have been built.**

KMOS is a second generation near-infrared imaging multi-object spectrograph for the VLT. The instrument is presently in the concept phase, first light is planned for 2009. KMOS will be built by a British and German consortium. During the concept phase, MPE has worked on fiber-IFUs, positioners for these IFUs, and steering mirrors. All these components have been designed for operation at LN2 temperature.

**Fiber IFUs**: A 2-dimensional array of micro-lenses positioned on a source image feeds a fiber bundle. The fiber outputs are arranged along the spectrograph input slit. A 1-dimensional array of micro-lenses adapts the fiber output f-number to that of the spectrograph. We have measured fiber transmissions in J and H-band, and have procured micro-lens arrays. An open problem is the connection between fibers and micro-lens arrays with a position accuracy of a few micrometers and stability over a wide temperature range.

**IFU positioner**: A pickoff arm for cryogenic environment has been built to position a fiber-IFU anywhere in a sector covering about 30% of the patrol field. Cryogenic tests have been postboned because a higher priority has been given to steering mirrors.

**Steering mirror**: A completely different concept for field selection employs an array of field optics covering the telescope image plane in combination with an array of steering mirrors placed in the pupil images. By tilting a steering mirror about two axis, it images one small subfield (typically $2''$x$2''$) within the area coverd by its field optics element (typically $1'$x$1'$) on the IFU entrance port. Advantages of this solution are small mirror tilts of less than 1 mm at the edge of a 20 mm diameter steering mirror as compared to 20 cm excursions of an IFU positioner. The main disadvantage is the reduced flexibility in source selection. We have built and tested a steering mirror unit carrying a 20 mm diameter mirror for use with a field lens of $1'$ width (34 mm at the VLT). The unit is driven by two linear drives specified for operation at 4 K. The stroke is measured by linear variable differential transducers (LVDTs, also specified for operation at 4 K) with a resolution of 0.2 $\mu m$. The mirror is suspended in a gimbaled mount with joints made from 100 $\mu m$ thick steel sheets. Joints between the motors and the mount are 100 $\mu m$ thick steel wires with 1 mm free length.

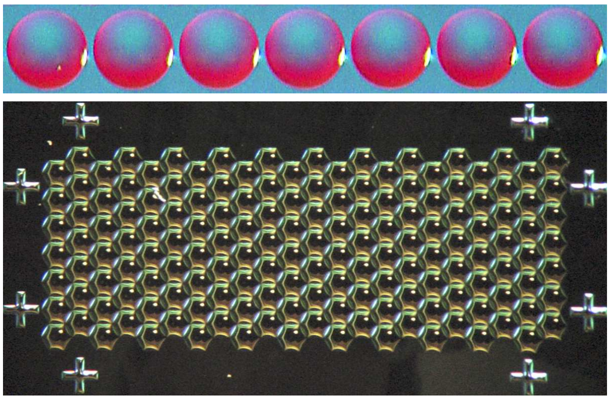

Pictures of the prototype 1d (top) and 2d (bottom) microlens arrays. Center to center separation of the lenses in the 1d-array: 150 $\mu m$, width of the hexagonal lenses in the 2d-array: 300 $\mu m$.

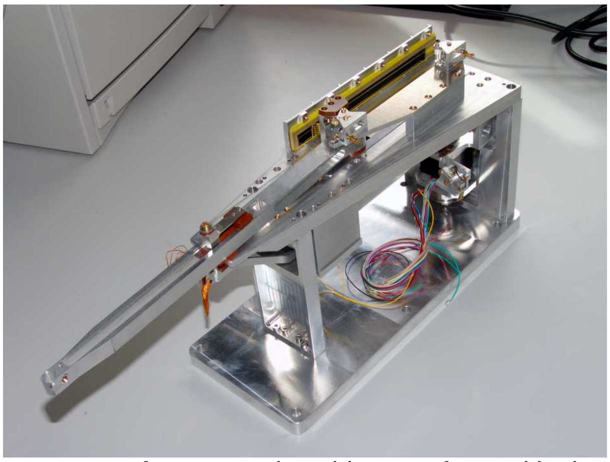

Prototype of a cryogenic spider arm for positioning a fiber-IFU. Length of the unit: about 40 cm.

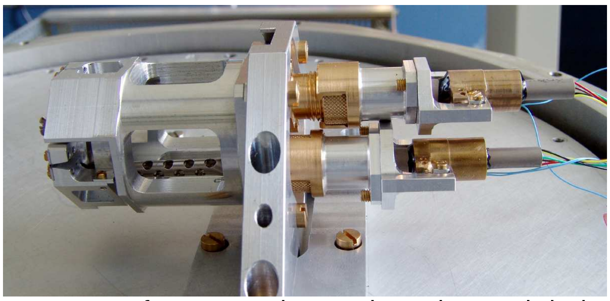

Prototype of a cryogenic steering mirror unit in its test mount. The motors are hidden inside their brass mounts on the right side. The grey tubes on the far right are the position sensors. The gimbaled mirror mount is located to the far left.

*R. Hofmann*

# Participation in and Status of the LBT

LBT, twin 8.4 meter telescopes being built on Mount Graham, Arizona, is an international collaboration, with partners from the United States, Italy, and Germany. The LBT Beteiligungsgesellschaft (LBTB) or German consortium contributes 25% of the total cost of the project, with MPE contributing 33.6% of this total. The LBTB consists additionally of MPIA, MFIfR, AIP, and the Landessternwarte Heidelberg. Besides supporting the overall infrastructure of the telescope, MPE is providing instrumentation (e.g., mask exchange unit of LUCIFER) and telescope components (e.g., twelve hardpoints – six are used to control the position of each of the LBT primaries).
The LBT is expected to have first light with Mirror #1 in October of this year. An early science demonstration program with the Large Binocular Camera-Blue will be executed in the first few months of 2005. The LBC is a pair of wide field (FOV≈30') imaging cameras, one optimized for the blue (LBC-B;3200–6000A) which is currently being integrated and commissioned, and one optimized for the red (LBC-R;5000A–1$\mu$m). The LBCs are facility instruments developed by the Observatories of Roma, Arcetri, Padova and Trieste.
At MPE, we are primarily interested as using the LBT to deploy innovative instrumentation to conduct unique scientific programs. We are especially interested in taking advantage of the combined focus which is a unique feature of the LBT and by addressing problems that require significant allocations of 8m time. One of the early science goals of ours with the LBT will be to investigate the rest-frame optical emission and absorption line properties and gas phase metal abundances of a large sample of high redshift ($z>2$) galaxies with LUCIFER MOS.

The hot dry weather and late summer monsoon season often leads to favorable conditions for forest fires in Arizona. The hot weather provides the fuel of dry timber and monsoon provides frequent lightning ground strokes. This year Mt. Graham experienced an almost catastrophic fire season. The "Nuttall and Gibson fires", ingnited by lightning, burned almost 30,000 acres, cost approximately 10 M$, and 28 injuries to extinquish. The picture on the left taken on July $6^{th}$ shows how close the fire came to the observatory – within several hundred meters.


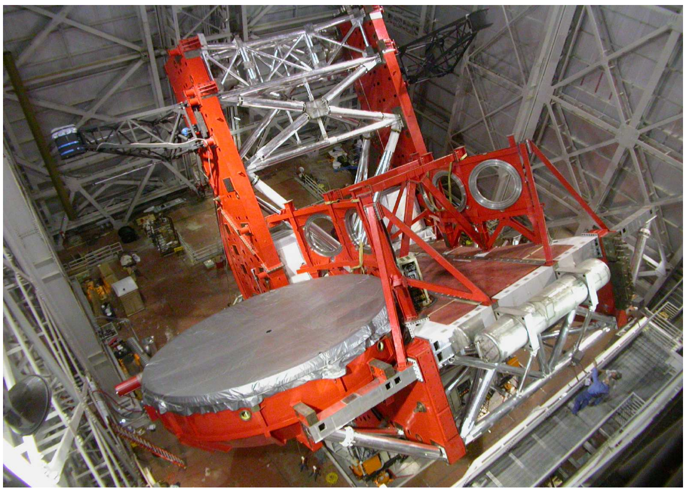

The status of the telescope as viewed from the walkway along the back side of the enclosure in late July. As can be seen in the picture, the first primary is in its mirror cell, but not yet aluminized, and the LBC-Blue is mounted on the prime focus swing arm. The LBC-Blue is currently undergoing testing and commissioning. The aluminizing bell jar has arrived in Arizona from Ohio and aluminization of mirror #1 is scheduled for October. First light for mirror 1 is expected in mid-October and first light for mirror 2 ("second light") is expected mid-2005. The LBT will also have two adaptive secondaries with several hundred actuators each. These are scheduled for integration and commissioning at the end of this year for the first and the end of 2005 for the second.

*M. Lehnert, R. Hofmann, R. Genzel, D. Lutz*

# The LUCIFER Multi-Object-Spectroscopy Unit

**ABSTRACT: A cryogenic multi-object spectroscopy (MOS) unit for LUCIFER has been developed and is presently being tested. This MOS unit exchanges slit masks between a clamp mechanism in the focal plane area and two storage cabinets inside the LUCIFER cryostat. The unit also permits the exchange of a cold mask cabinet between LUCIFER and an auxiliary cryostat.**

LUCIFER, the near-infrared camera and spectrograph for seeing- and diffraction limited observations at the LBT, is being built by a German consortium led by the Landessternwarte Heidelberg (LSW). The project started in 1999, first light is planned for 2006.

The most powerful observing mode of LUCIFER is seeing limited multi-object spectroscopy with multi-slit masks. The cryogenic MOS unit developed at MPE handles 10 longslit and field limiting masks in a stationary storage cabinet and 23 multi-slit masks in an exchangeable cabinet. A robot picks up a mask from its slot in the storage cabinet, carries it over a distance of up to 50 cm to the focal plane area, and deposits the mask in a focal plane unit where it is positioned with an accuracy of $\pm 10\,\mu m$ and fixed by a clamping mechanism. The unit works in arbitrary orientations of the rotating instrument, which is mounted at a bent Gregorian focus of the LBT.
The multi-slit masks have to be custom made for each field to be observed, and after observing 23 fields, the whole lot has to be replaced. Warming up the cryostat and breaking the vacuum for mask exchange is not feasible, because the thermal cycle time of LUCIFER is comparable to the observing time for the 23 masks. Therefore, the MOS unit has been designed to permit mask cabinet exchange without warmup of the instrument. For this procedure, an auxiliary cryostat is connected to LUCIFER, the interface between the two cryostats is evacuated, the 32 cm diameter gate valves at both cryostats are opened, and the mask cabinet is transferred between the two cryostats on rails. Actually, two auxiliary cryostats are available, one accepts the used masks, the other one houses the pre-cooled new masks.

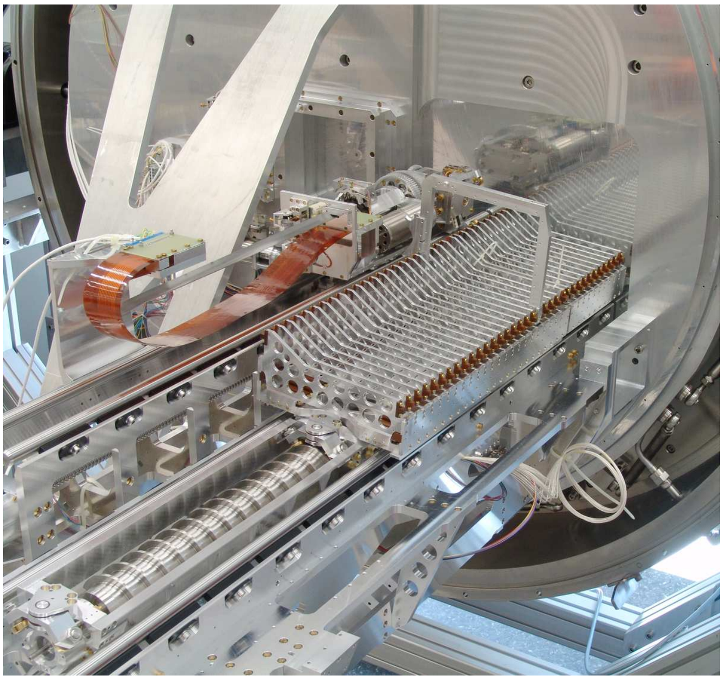

The LUCIFER MOS unit mounted in the test cryostat. From front to back: Mask cabinets on rails with drive screw, one mask inserted; mask handling robot with flexible board power lines; cryostat base plate and focal plane clamp mechanism (partially hidden behind the bright support strut.)

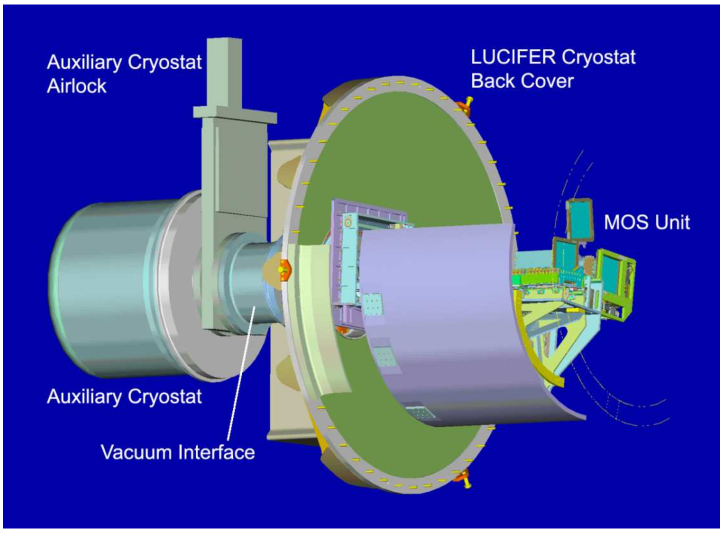


3d-model of the setup for mask cabinet exchange.

*R. Hofmann and H. Gemperlein*

# OmegaCAM

Omegacam is a 1□°wide-field, optical camera that will be the sole instrument for the 2.6 m VLT Survey Telescope (VST) in Chile. Specifically designed for wide-field imaging and excellent image quality, it is being built by a consortium of institutes from Germany, the Netherlands, Italy and ESO, and will become operational at ESO's Paranal observatory during the summer of 2005.

**OmegaCAM and the Wide-field Imaging of the Sky**

OmegaCAM and the VST will act as a pure survey instrument. During its 10 year mission OmegaCAM will map a large fraction (about 30,000 square degrees) of the sky visible in Chile. To achieve this extraordinary area, OmegaCAM combines 32 CCD detectors to create a 16,384 x 16,384 pixel array. This implies an unprecedented field-of-view of one square degree (equivalent to 4 full moons), at a scale of 0.21 arcsec per pixel. Expressed in standard computer monitor resolution, a single OmegaCAM exposure would result in a picture measuring more than 20 square meters, whereas the size of the total proposed surveys would be almost one square kilometer.

OmegaCAM will be instrumental in providing statistics on large samples of objects, as well as finding unusual rare objects. Aside from its role in providing large area public surveys, a large number of individual science programmes have been proposed. These include searches for supernovae, Kuiper belt and Oort cloud objects, gamma ray bursts, and high proper motion objects, as well as mapping large scale structures, Galactic halo populations, and high redshift galaxies and quasars. Clearly, the VST and OmegaCAM will provide a veritable flood of objects for follow-up observations with the VLT telescopes. Currently, the final instrument housing has been machined and delivered to the Universitaets-Sternwarte Muenchen, where mechanical and electronic integration has been completed. Tests of the camera shutter performance, the filter exchange and positioning mechanism, safety measures, and the controlling software modules were conducted in all camera orientations and fulfilled all specifications.

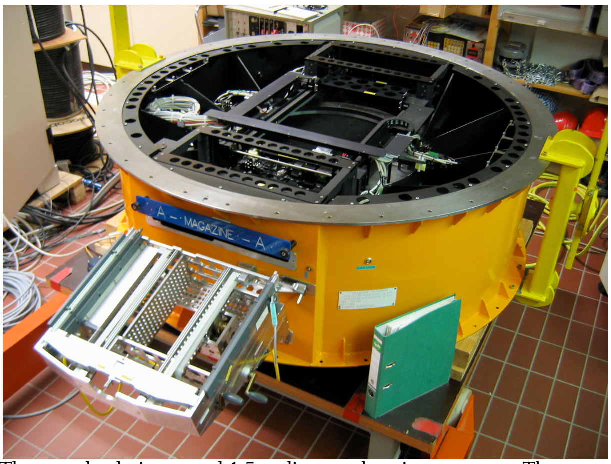


The completely integrated 1.5 m diameter housing structure. The camera shutter has been removed to reveal the filter positioning unit (at center), and the filter magazines at the top and bottom (each of which holds up to 6 filters). Fully loaded with 12 filters, OmegaCAM will contain more that 40 kg of filter glass. The filter loading platform is attached to the outside of the housing and a *Leitz* binder is shown for scale.

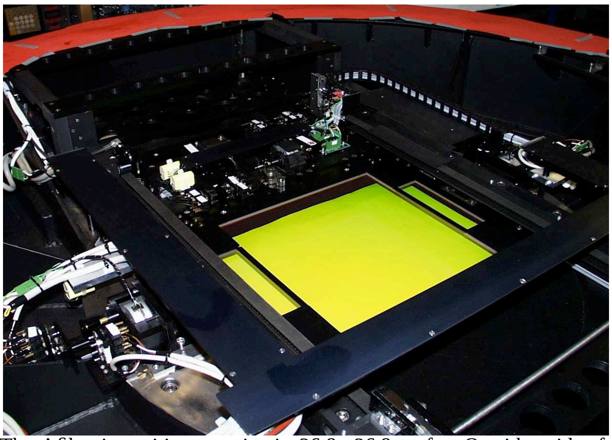

The r' filter in position covering its $26.8\times26.8$ cm fov. On either side of the main filter are the auxiliary filters for the two CCD's for autoguiding and the two CCD's for image analysis. OmegaCAM's primary filter set will be the Sloan u',g',r',i', and z' filters. In addition, there will be Johnson $B$ and $V$ and Strömgren $v$ filters for stellar projects, a 4-segment H$\alpha$ filter for redshifts $<13\,000\,\mathrm{kms}^{-1}$, a night sky emission line gap filter near 860 nm for deep extragalactic projects, and a ugri segmented filter for photometric monitoring.

The final acceptance test of the integrated instrument (without the detectors) is being completed, and the detector system is nearing its final configuration. Once tested, it will then be integrated into the instrument for final overall testing. When completed, OmegaCAM can then be shipped to Paranal in February, 2005. The first four filters intended for OmegaCAM have been delivered (see fig. 2), with the remaining 7 filters expected by the summer of 2005.

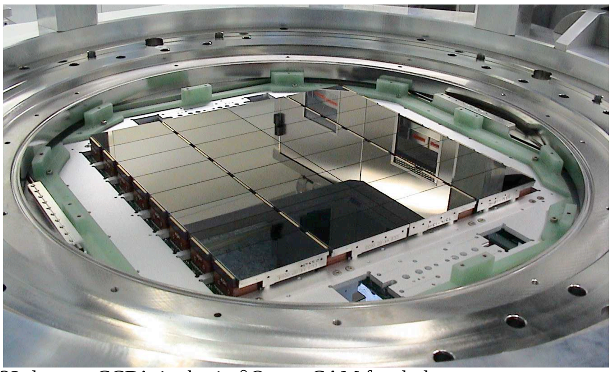

32 dummy CCD's in the 1□° OmegaCAM focal plane.

*R. Bender, U. Hopp, B. Muschielok, M. Neeser, R. Saglia, and the Ω-CAM Team*

# Astro-WISE

The **ASTRO-WISE** (**A**stronomical **W**ide-field **I**maging **S**ystem for **E**urope) programme will provide an astronomical survey system by creating the tools necessary to reduce and mine the data produced by the new generation of wide-field sky survey cameras. The programme consolidates the common expertise of the partners and co-ordinates the development of software tools including an exchangeable computing infrastructure with which users can calibrate, analyse, and extract sources from wide-field images. Astro-wise has ambitious goals in terms of on-the-fly-reprocessing, parallel processing, data-basing of very large data volumes (several 10's of Tbytes), designing and creating dynamic archives, and federating data volumes over the various national data centers involved. Astro-wise will become one of the first operational Virtual Observatory systems.

**Wide-field Imaging of the Sky**

The recent, rapid development of large digital CCD detector devices allows deep and ultra-sharp imaging on previously unheard of scales, in a multitude of different filters. At ESO's Paranal (Chile) site a new telescope is nearing completion which will be entirely dedicated to the wide-field imaging of the sky—the VLT Survey Telescope (VST). Its dedicated wide-field instrument OmegaCAM will, in a single image, map an area of the sky as large as 4 times that of the full moon (1□°) in an array of 16k×16k pixels (256 million pixels) with an unprecedented combination of field size and image quality.

The enormous data volumes produced by this wide-field imager brings astronomical research to the edge of modern information technology. For OmegaCAM, an annual rate of about 30 TB of raw science image data is expected, which after reduction will deliver about 10 TB/year of image data ready for scientific research. **Each** OmegaCAM image will contain about $10^5$ astronomical objects and the estimated yearly production of source-list tables describing the properties of these objects (position, brightness, shape descriptors, colour, etc.) will be of the order of 1 TB/year. This new branch of observational astronomy is now well on its way: the VST and OmegaCAM will be operational in the summer of 2005, while its counterpart camera in the Northern hemisphere, MegaCAM, has already begun observing. By late 2007, VISTA, a wide-field telescope optimized for near infrared wavelengths, will also be operating on Paranal.

**Astronomical Wide-field Imaging System for Europe**

In the context of Astro-wise, national data centers in Germany (München), Italy (Napoli), France (Paris), and the Netherlands (Groningen), will support their users' community and provide the infrastructure for the processing, storage, and distribution of these enormous data volumes. The centers will operate high performance, multi-node computer clusters and provide many TB's of direct access storage.

The specific objectives of Astro-wise are:

- to develop, maintain, and provide access to a computational environment to process wide-field imaging data; the EU-wide shared environment will house both up-to-date calibration data and pipeline software.
- to develop and disseminate software tools needed to access the wide-field image data (e.g. TB regime search and visualisation tools).
- to provide infrastructure for the production and dissemination of survey data to be accessed by virtual observatories.

The implementations of these objectives in the TB regime differ from the current approach in which raw data is processed with a standard pipeline to deliver a static catalogue. Instead, with Astro-wise's dynamical approach a given user can query this system, re-derive the results, and optimize them to his particular scientific goals. The system would provide a first step towards the building of a Virtual Observatory.

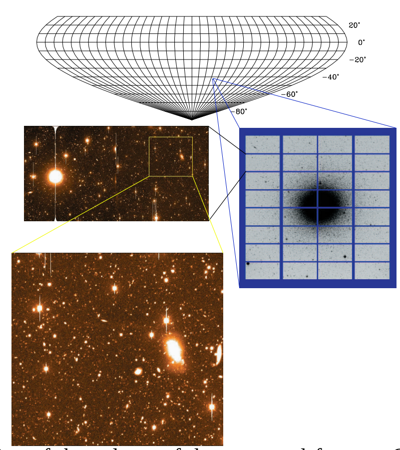


An Illustration of the volume of data expected from an OmegaCAM sky survey. Top: The Southern sky with a 10×10 degree raster (a public surveys will be about 1000□°). A single OmegaCAM exposure is shown as a small square. Right: A Simulated OmegaCAM exposure, with the 32-CCD mosaic clearly visible. Left: An actual CCD image, covering the same amount of sky as each OmegaCAM CCD to a similar depth. The lower image is a sub-section at the resolution of this poster.

Web page: `http://www.astro-wise.org/`

*R. Bender, M. Neeser, R. Saglia, J. Snigula*

# GROND – GRB Optical/NIR Detector

The GROND instrument is being developed at MPE for installation at the MPI/ESO 2.2m telescope on La Silla (Chile) in 2005. The main scientific goal is the rapid identification of high-redshift (z>5) gamma-ray bursts to allow VLT follow-up observations in the same night.

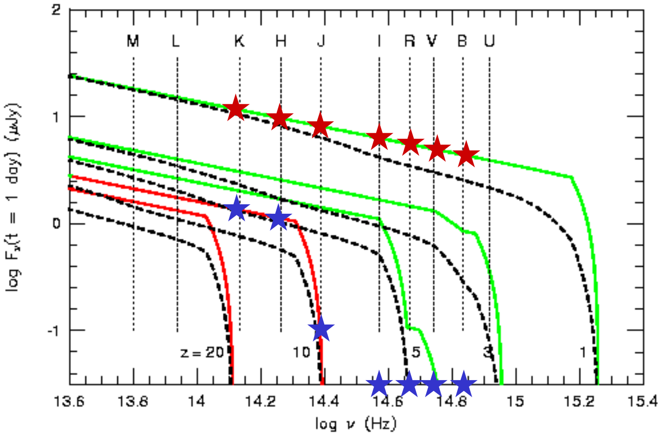


GROND will image the GRB afterglow in 7 colous simultaneously. The GRB distance will be estimated by the photometric redshift algorithm using the Ly-α break.

The optical bench of GROND with its other components: the guiding camera (blue) next to the entrance window (lower right), the closed-cycle cooler and the vacuum connectors on the back side.

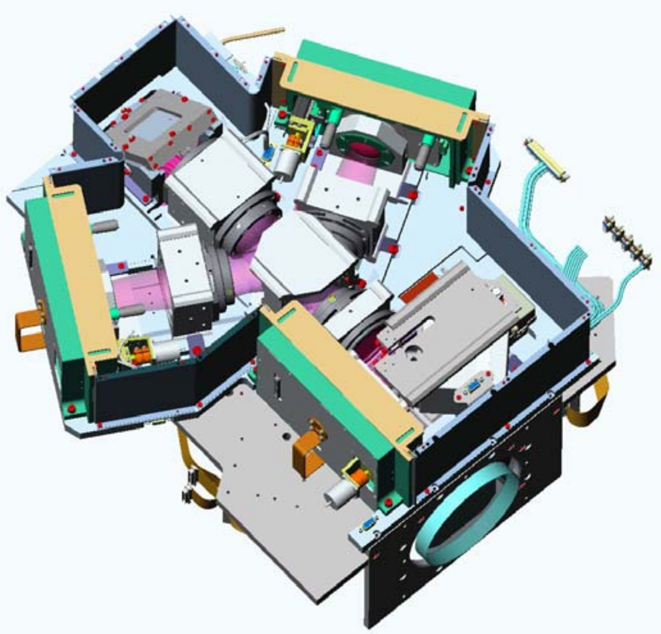

Near-infrared side of GROND. The entrance window is shown in the lower right, and the visual light is first split off by dichroics on the hidden side of the figure. Light is then deflected in a U-shape up to the infrared side (upper left), and then split into the JHK bands wik each having one HAWAII1 detector (green boxes).

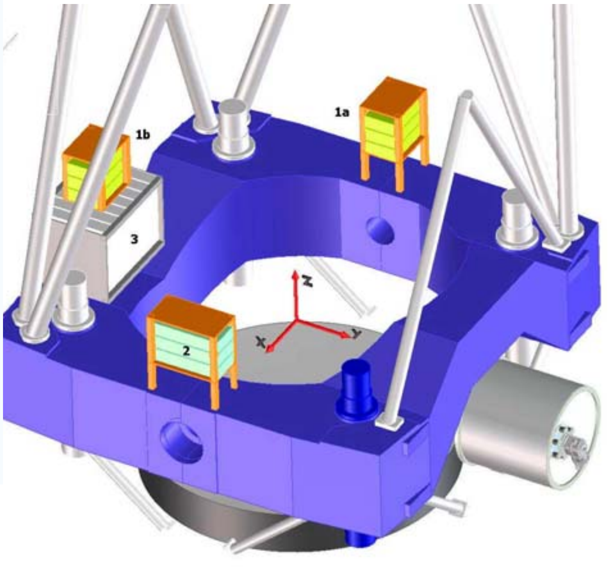


GROND vessel (grey cylinder at the right) at the 2.2m telescope. Other pieces to be placed onto the center piece are the FIERA (1a/1b) and IRACE (2) detector electronic boxes and the GROND electronics box (3).

*W. Bornemann, C. Clemens, J. Greiner, H. Huber, S. Huber, H. Mayer-Haßelwander,F. Schrey, I. Steiner, G. Szokoly, C. Thöne, A. Küpcü Yoldas, W. Zaglauer, MPE workshop*

# pnCCD for Low Light Level Optical Photons

CCDs fabricated in pn-technology, originally designed as X-ray detectors, can find their niche in optical applications as well. They offer a wide range of pixel sizes (36µm – 150µm), high quantum efficiency (close to 100% from 300nm – 1000nm), a uniform fill factor and massive parallel fast readout. The present limitation for light detection is dominated by readout noise while the contribution of the detector leakage current is negligible. Optimizing the readout may even allow single photon detection.

Different to many other CCD concepts, the pnCCD is depleted from both sides of the silicon substrate. By increasing the voltage at the rear contact, the potential minimum is shifted towards the registers at the front side of the device, thus forming spatially well defined potential wells for charge collection. The readout anode of each channel is connected on-chip with a first stage of amplification.

Different approaches for an on-chip amplifier were realized respectively are under study at the semiconductor laboratory:

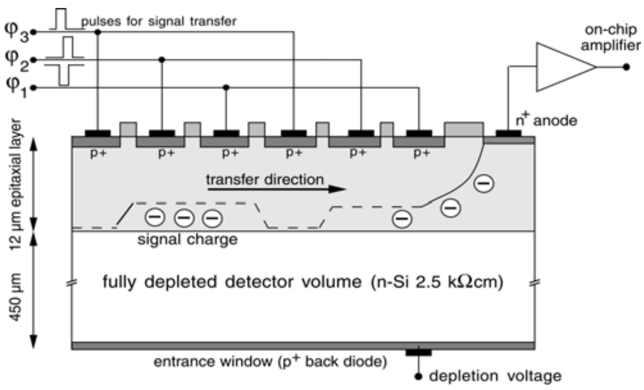


**Fig. 1:** Schematic cross section of a pn-CCD

• **JFET** amplifier, operating in a source follower mode, gives a high dynamic range of $2*10^5$ and a low readout noise, summing up in combination with following amplification stages to less than 3 electron (rms) total noise contribution.

• A multiple non-destructive readout through a double **DEPFET** arrangement (DEPleted Field Effect Transistor). In such a device, the signal charges are swapped several times between the two internal gates. Each time the signal is amplified and read out. After $N$ cycles the theoretical noise reduction limit is given by $\sqrt{N}$. Although readout time is increased by the same factor $N$, high frame rates (typically 500 per second) are still possible since the multiple signal reading is done in parallel for all columns of a CCD. As compared to existing devices, this concept, apart from the superior readout speed, maintains output linearity down to signals from very few or single photons.

• An **avalanche** structure, being operated in either proportional or Geiger mode, for a direct amplification of signal electrons after their transfer to the readout anode. Not reducing electronic noise of signal amplification stages, it increases the signal to noise ratio by a factor of 100 e.g., allowing a detection of single optical photons. When operated in a proportional mode, information about the number of signal electrons per pixel will be obtained. Technology and device simulations as well as design studies are currently in progress at the semiconductor laboratory.

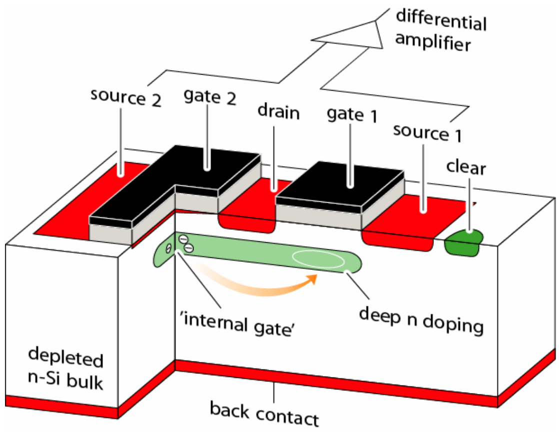


**Fig. 2:** Double DEPFET arrangement for multiple, non-destructive readout


**References:**
• L. Strüder et al., Astron. Astrophys. 365 (2001) L18
• L. Strüder, Nucl. Instr. And Meth. A454 (2000) 73-113

# High-Speed CCDs for optical and NIR astronomy

Fully depleted silicon pnCCDs, developed for the XMM-NEWTON and DUO missions, exhibit high quantum efficiencies from the near infrared to the vacuum UV region. The multiparallel readout allows for frame rates higher than 1 kHz for a device having a format of 264 * 264 pixel and a pixel size of 50µm. An electronic noise contribution of less than 3 electrons (rms) was achieved. The high speed, low noise and high quantum efficiency make these devices especially suited for the use as wavefront sensors in adaptive optics systems.

Back-illuminated pn-CCDs have been developed at the semiconductor laboratory of the Max-Planck-Institut für extraterrestrische Physik over the past years as X-ray sensitive imaging detectors.

Many outstanding characteristics of these X-ray devices, as their high intrinsic quantum efficiency of more than 90% within the entire energy range between 300eV and 10keV and their exceptionally low readout noise of less than 3 electrons (rms), make them ideal detectors in the optical region as well. Measurements of the internal quantum efficiency from the vacuum UV (VUV) to near infrared (NIR) region have revealed nearly 100% within the entire range.

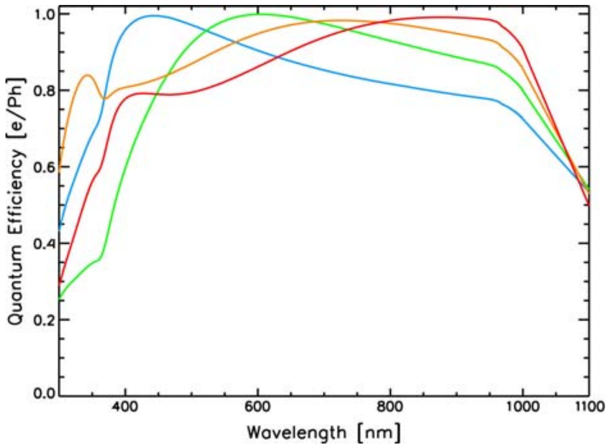


**Fig. 1:** Quantum efficiency for different anti-reflective coatings.

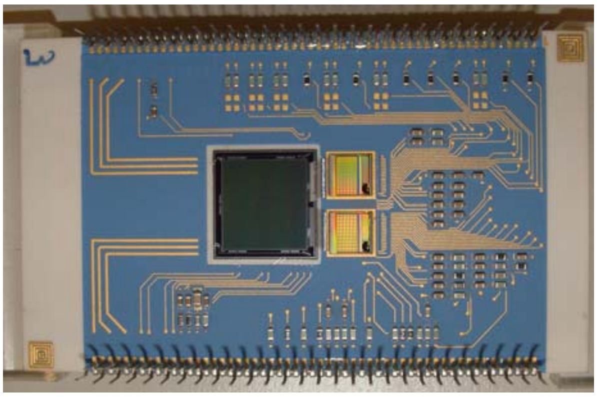

**Fig. 2:** 50µm pixel size CCD with two CAMEX readout chips.

Parallel to developments in order to improve the detector performance are developments in readout and data acquisition electronics. Operating a 264*264 CCD at 1000 frames per second generates a constant data flow of 140 MByte/s. Electronic subcomponents with integrated data correction and data reduction routines are also currently under development.

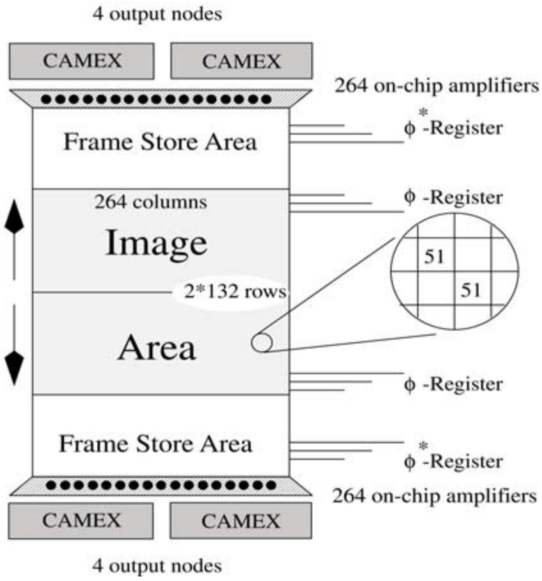


**Fig. 3:** Design of a future double-sided readout CCD.

**References:**
- R. Hartmann, K.-H. Stefan and L. Strüder, Nucl. Instr. And Meth. A439 (2000) 216-220
- N. Meidinger et al., Nucl. Instr. And Meth. A512 (2003) 341-349

*MPI Semiconductor Laboratory, PNSensor and FZ Jülich*

# The PANTER X-ray Test Facility

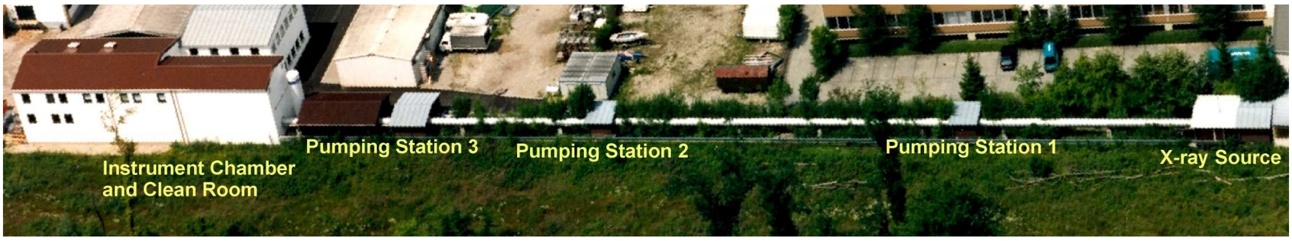


The PANTER facility is located in Neuried in the southwest outskirts of Munich. With its 130 m long vacuum tube (1 m diameter) and the X-ray source system and the main test chamber (3.5 m ∅, 12 m long) it has mostly been used for the characterization of X-ray telescopes as well as tests of detectors, focal plane instruments, reflection gratings, filters, etc.

Recent activities are e.g. accompanying and supplementary calibrations and tests for the EPIC-pn camera onboard of XMM-Newton, measurements for the proposed DUO and ROSITA missions, tests of mirrors for the Astro-E2 mission, and tests of multi-layer mirrors for future projects.

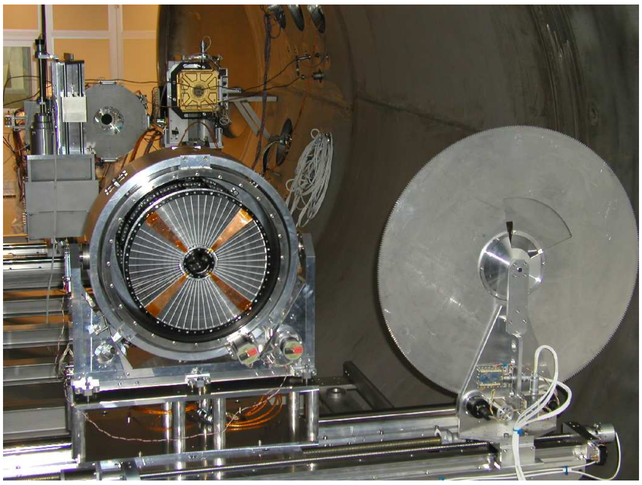

Astro-E2 mirror module (left) with PSPC and EPIC-pn focal plane instruments (back) and mask for selected illumination (right)

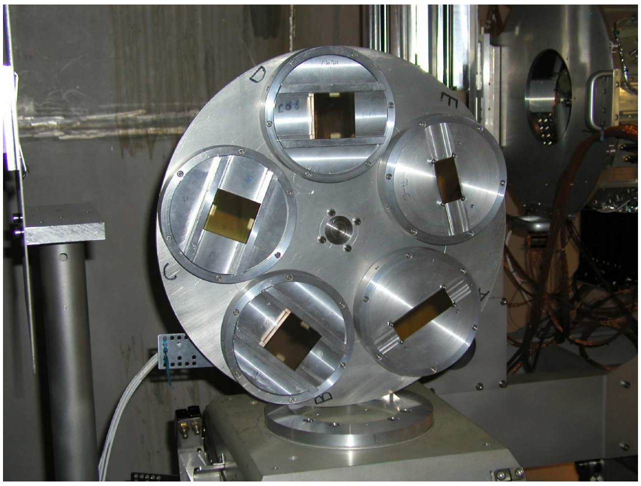

Two contamination probes from the International Space Station for the ROSITA project (right) and three plane mirror probes for DUO (left)

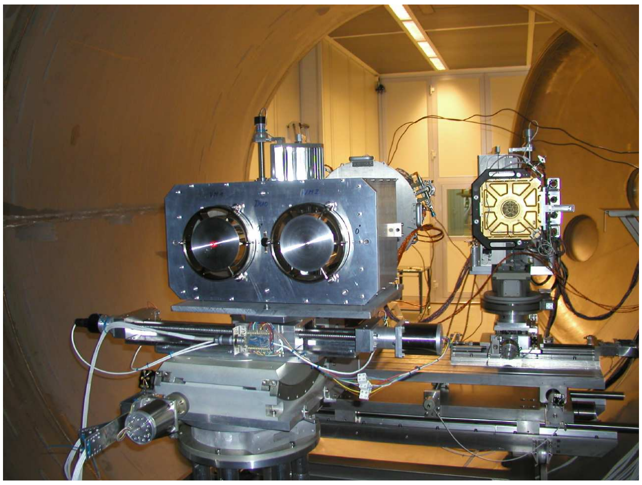

DUO dual mirror box (left) with single shell mounted in each box, with ROSAT PSPC (right)

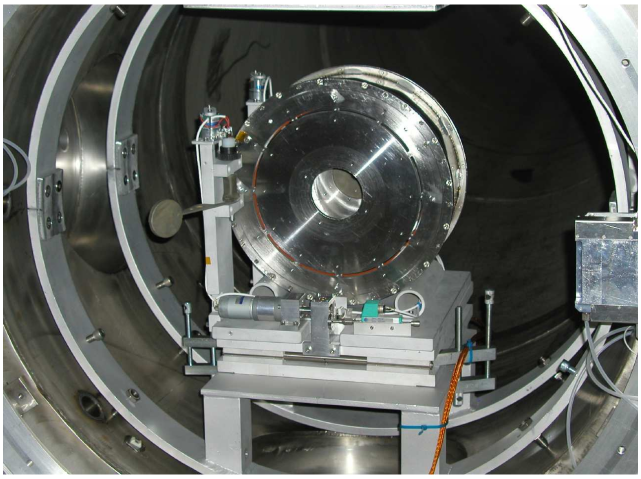

Multi-layer mirrors with 16 m focal length mounted inside vacuum tube

*The PANTER team*

# X-Ray Evolving Universe Spectrometer (XEUS)

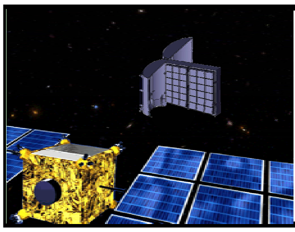

**There are two big science themes for a for a new large X-ray telescope XEUS (also addressed as "NGXT") which is going to be part of the ESA cosmic vision programme (2015-2025): the quest for the first massive Black Holes and the evolution of the cosmic web in connection with the life cycle of matter.**

**The first Black Hole:**

Before the first star can form, the Universe has to cool down to ~100 K to allow molecular hydrogen cooling.

The first star is expected to be massive (~300 $M_\odot$), shines for ~1 Million years, sterilizes its cosmic environment, explodes in a GRB hypernova, pollutes its environment with heavy elements and leaves a seed Black Hole.

While the galaxy forms, the BH continues to grow exponentially, quickly producing a powerful quasar, if enough fuel can be provided.

Sensitive X-ray observations can study the first GRB explosions and can detect mini-QSOs with $10^4$ $M_\odot$

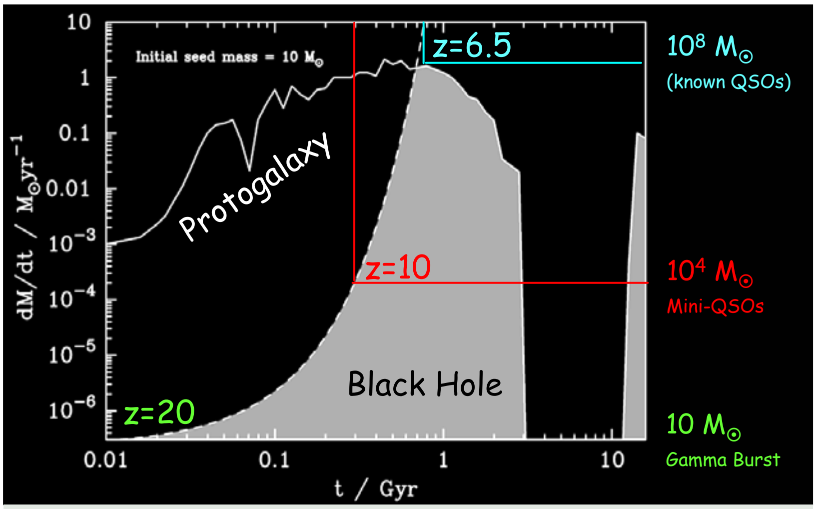


Need **N**ew **G**eneration **X**-ray **T**elescope to detect and study BH in conjunction with forming galaxy ($S_{min}$ ~ $10^{-18}$ erg $cm^{-2}$ $s^{-1}$).
$10^4$ $M_\odot$ @ redshift 10 detectable.

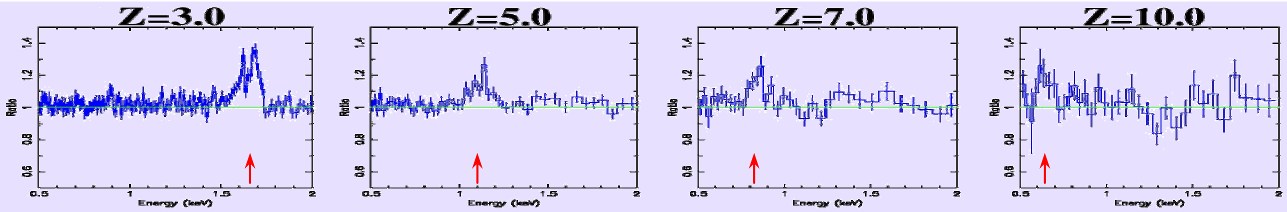


**XEUS view of relativistic Fe line:** We get this or better quality for many objects in each field

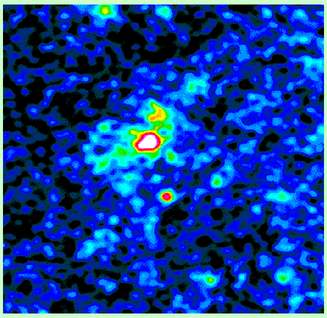

**Enrichment of elements in early clusters XEUS:**

Simulation of a 5 keV cluster at z=2

Element abundances of O, Ne, Mg, S, Si, Fe, …

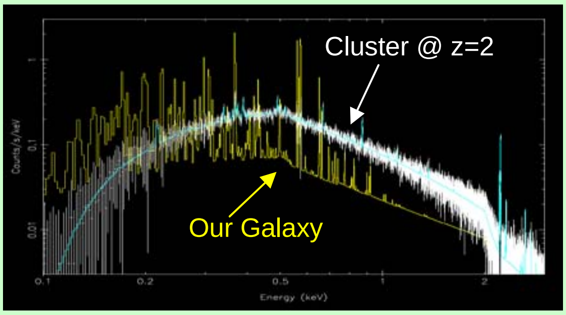


**Scientific Requirements:**

| | |
|---|---|
| Sensitivity: | 10-18 erg $cm^{-2}$ $s^{-1}$ |
| | → > 10 $m^2$ area @1 keV |
| Energy band: | 0.1 to ~100 keV |
| Angular resolution: | 2-5 arcsec |
| Spectral resolution: | 1-2 eV |

**Technology development required:**

- Factor ~10 lighter mirrors, high precision optics
- Formation flying, 1 $mm^3$ accuracy over ~50 m
- Imaging calorimeter, better than 2 eV
- Large, fast active pixel detector with μs timing

*G. Hasinger, T. Boller, P. Friedrich*

# The Wide Field Imager for XEUS

A new type of Active Pixel Sensor (APS) is capable to meet the unprecedented requirements for the central Wide Field Imager (WFI) instrument of ESA's future XEUS mission: simultaneous energy and position resolved detection of X-rays with high quantum efficiency at high count rate on a large format sensor. First prototypes of the APS have been produced and tested in the MPI Semiconductor Laboratory.

The X-ray Evolving-Universe Spectroscopy (XEUS) mission is under study by the European Space Agency ESA as follow-up to the XMM-Newton satellite. XEUS consists of a Mirror Spacecraft (MSC) with an aperture of several m² and a Detector Spacecraft (DSC) aligned to a focal length of 50 m. The DSC carries two high-resolution cryogenic Narrow Field Imagers (NFIs) and a Wide Field Imager (WFI). The WFI will perform deep surveys, positioning sources for the NFIs and measuring their broad band spectra. The WFI requirements are high efficiency with moderate energy resolution and large field of view (FOV). They are achieved by the combination of three complementary imaging spectrometers:

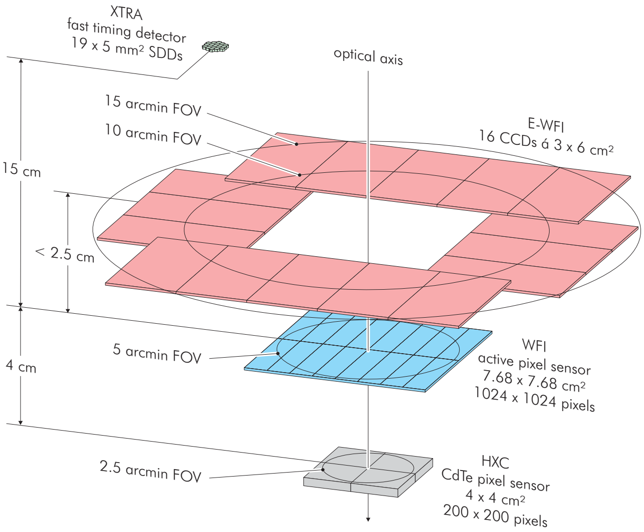


Fig. 1: Layout of the XEUS WFI focal plane. Vertical distances are not to scale.

Because of the high photon throughput, the central region, where pointing targets will be located, requires the use of a fast **Active Pixel Sensor** (APS). The size of the APS is such as to cover a 5 arcmin section of the FOV. As the XEUS mirror will have a good off-axis performance the FOV is extended to a diameter of almost 15 arcmin by a frame of CCDs around the central APS. This **Extended Wide Field Imager** (E-WFI) area significantly increases the number of scientific objects per deep field observation. The **Hard X-ray Camera** (HXC) consisting of a pixelated CdTe array is placed behind the APS and will detect the high-energy X-rays that penetrate the APS without interaction.

In addition to the imaging spectrometers the WFI includes the **Fast Counting Spectrometer XTRA** to perform studies of time-variable point sources. Figure 1 shows the arrangement of the XEUS WFI instruments.

Two of these systems are under development at the MPI Semiconductor Laboratory:

The central **WFI instrument** is an **Active Pixel Sensor** (APS) based on the integrated amplifier DEPFET. The APS has a format of 1024 x 1024 pixels with a pixel size of 75 x 75 µm². It is made monolithically on 450 µm thick, fully depleted silicon and backside illuminated with a 100% fill factor. The DEPFET principle allows for random accessible pixels with flexible readout modes (full frame, windowing, fast timing). Due to parallel readout the full frame readout time is in the order of few msec. At present 64 x 64 APS prototypes of the first production batch are under test. The measured electronic noise of 5 electrons ENC at an operation temperature of -60°C is already close to the XEUS specifications.

Next to the XEUS primary scientific goals the telescope's large aperture will be used to collect X-rays from time-variable objects with a periodicity in the msec range. To perform timing studies the dedicated **instrument XTRA** (XEUS Timing for Relativistic Astronomy) is integrated in the WFI. As the time-variable objects are among the brightest sources the detection system must be able to handle count rates up to $10^7$ per sec with a timing resolution of 10 µsec and a simultaneous energy resolution in the order of 300 eV (FWHM at 6 keV). The detector for XTRA is a monolithic array of 19 **Silicon Drift Detectors** (SDDs), each 5 mm² large. Each SDD cell in combination with high-rate readout electronics is able to operate at an incoming rate of 1 million photons per sec with an energy resolution of 250 eV (FWHM at 6 keV).

**Reference:** X-ray Evolving-Universe Spectroscopy – The XEUS Instruments, ESA-Report SP-1273, Nov. 2003

*MPI Semiconductor Laboratory, The XEUS Instrument Working Group, PNSensor*

# DEPMOSFET sensor matrix prototypes for the XEUS Wide Field Imager

Active Pixel Sensors based on the DEPMOSFET (DEpleted P channel MOSFET) are a promising candidate for the APS section for the XEUS Wide Field Imager. They combine excellent energy resolution, high readout speed in combination with random accessible pixels and low power consumption with a 100% fill factor and high quantum efficiency. DEPMOSFET matrix design variants from the first prototype production are currently under study at the MPI HLL and show very good performance.

The DEPMOSFET is a P-channel MOSFET integrated onto a fully depleted, high-resistivity n-type silicon bulk (fig. 1). Using the principle of sideward depletion, a potential minimum is generated underneath the surface of the silicon, which can be enhanced and localized by the help of an additional deep-n implantation directly below the transistor channel. Electrons released in the silicon bulk will drift to this so-called “internal gate” and stay there, modulating the transistor current by inducing additional charge carriers in the channel. Thus, the transistor current is a function of the charge stored in the internal gate. The charge can be removed by applying a positive voltage pulse to an adjacent n+-doped “clear”-contact. The charge information can be retrieved by comparing the transistor current values before and after the clear pulse.

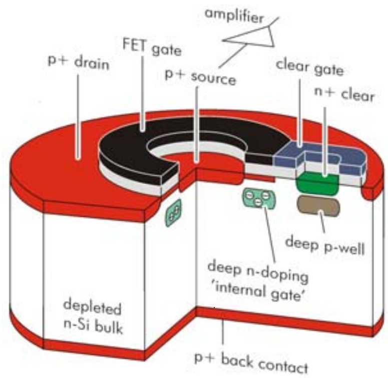


***Fig. 1:*** *Cross section of a circular DEPMOSFET pixel cell. Charges collected in the ‘internal gate’ modulate the transistor current.*

Within the matrix, the pixels’ gate and clear contact are connected row wise, while the sources are connected column wise and the drain contact is global. The pixels are biased using a column-individual current source and are thus operated in source follower mode. By applying appropriate voltages to the external gate contacts, all except for one pixel rows can be turned off. As the internal gate persists, independent from the state of the external gate, the pixels are sensitive all the time. Thus, the matrix can be read out row by row in a 64 column parallel mode. The devices require additional control circuitry, which provides the clear and gate pulses, and an analog read out IC. A variant of the CAMEX IC providing 64 channels with an 8-fold CDS filtering stage each is used for that purpose.

The test of the different designs included in the recent production is in progress. The devices have 64 x 64 pixels of 75 x 75 μm² size, the total sensor area is 4.8 x 4.8 mm². Several readout hybrids have been built (fig. 2) and tested (fig. 3, fig. 4). The devices show excellent homogeneity and energy resolution values as good as 6.1 electrons have been measured for the first prototypes for a temperature of -40° C. The next prototyping production, including larger sensor prototypes, will start in 2005.

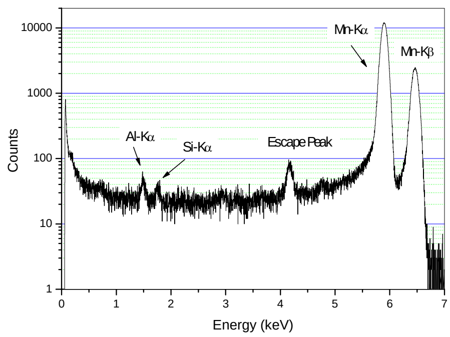


***Fig. 3*** *Example for $^{55}$Fe spectrum measured with DEPMOSFET pixel sensor hybrid at -40 °C. The FWHM of the Mn-Kα is 131 eV, corresponding to 6.1 electrons ENC.*

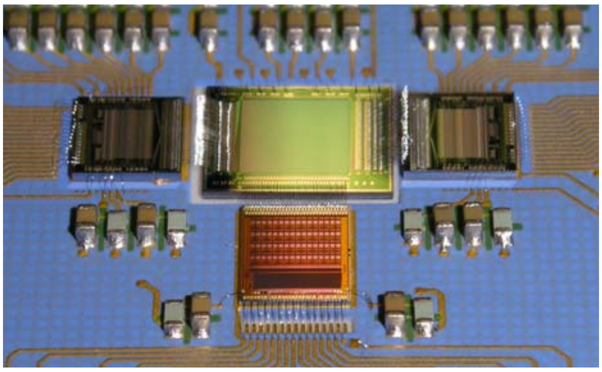

***Fig. 2:*** *Photo of a fully assembled DEPMOSFET pixel hybrid. The sensor IC sits in the middle. The ICs on the left and the right control the external gates and the clear. The IC below is the analog front end CAMEX 64G.*

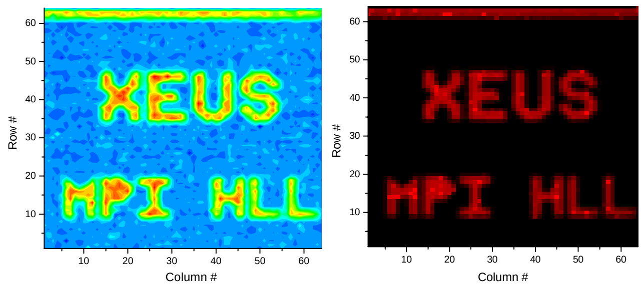


***Fig. 4:*** *Imaging measurement with DEPMOSFET pixel sensor with an 300 μm thick silicon baffle, illumination with an $^{55}$Fe source. Minimum structure size was 150 μm. Shown: sum of X-ray energy per pixel (left), number of photons per pixel (right).*

**References:**


- *J. Treis et al*. First results of DEPFET based Active Pixel Sensor prototypes for the XEUS Wide Field Imager, *submitted to Proceedings of SPIE Astronomical Telescopes and Instrumentation, 2004*
- *L.Strueder et al.* Xeus wide field imager: first experimental results with the x-ray active pixel sensor DEPFET, *SPIE Proceedings 5165, 2003.*


*DEPMOSFET Team, MPI Halbleiterlabor and PNSensor*

# XTRA – XEUS Timing for Relativistic Astronomy

The XTRA (XEUS Timing for Relativistic Astronomy) instrument aboard ESA's projected XEUS mission is designed to measure count rates up to 10 million X–ray photons per sec with a time resolution of 10 µsec and an energy resolution in the order of 300 eV FWHM for a 6 keV line. This detector, an array of Silicon Drift Detectors, is developed at the MPI Semiconductor Laboratory.

The X-rays generated in the inner accretion flows around black holes and neutron stars carry information about regions of the strongly curved space-time in the vicinity of these objects. This is a regime in which important predictions of the theory of general relativity are still to be tested. Both high resolution X-ray spectroscopy and fast timing studies can be used to diagnose the orbital motion of the accreting matter in the immediate vicinity of the collapsed star, where the effects of strong gravity become important.

Due to its unprecedented collecting area in the order of 10 m², the XEUS telescope will enable timing studies with extremely good photon statistics. The detector for the XTRA instrument is a monolithic array of 19 Silicon Drift Detectors (SDDs) developed at the MPI Semiconductor Laboratory (figure 1). Each detector cell has a sensitive area of 5 mm² and the front-end transistor of the amplifying electronics is integrated on the detector. A single SDD cell in combination with high-rate readout electronics is able to provide an energy resolution of 250 eV (FWHM at 6 keV) at an incoming rate of $10^6$ photons per sec (figure 2). SDDs have demonstrated to be radiation hard with respect to hard X-rays up to an integrated dose of $10^{13}$ absorbed photons (18 keV), corresponding to 3 years of continuous operation with a constant rate of $10^5$ per sec. SDD arrays of this type exist and are used in various X- and γ-ray spectroscopy systems.

The enormous flux of photons will be distributed over the full detector area by placing the detector 15 cm out of the focal plane, either by mechanical construction or by displacement of the detector spacecraft. To extend the XEUS fast timing capability to higher energies it is considered to place a high-Z semiconductor detector, e.g. CdTe or CZT, underneath the SDD array.

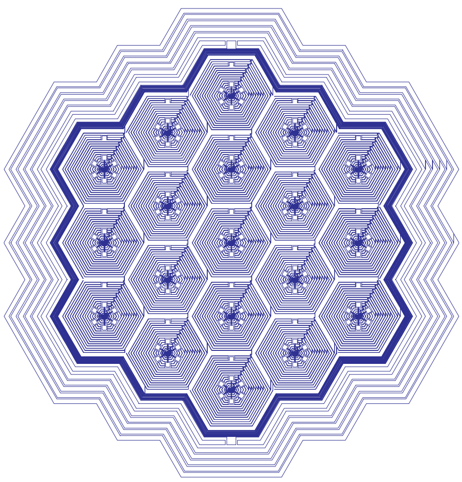

Fig. 1: Layout plot of a 19 cell SDD. Each detector cell has a sensitive area of 5 mm². The first stage of the amplifying electronics is integrated in the hexogonal cells' centers.

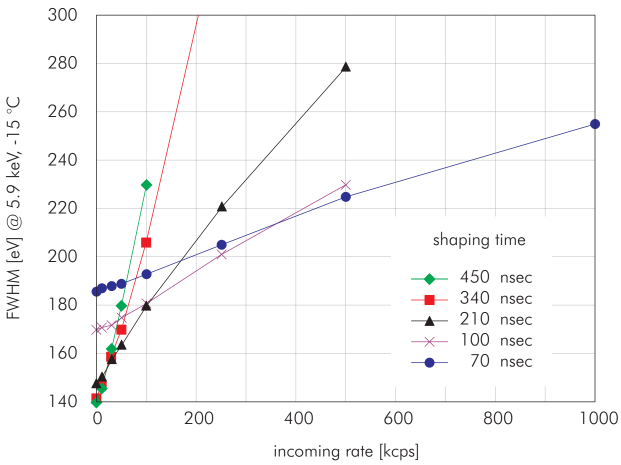


Fig. 2: Measured count rate capability of a SDD. For the extremely short pulse shaping time of 70 nsec the energy resolution is still 250 eV (FWHM @ 5.9 keV) at an incoming photon rate of $10^6$ per sec.


References:

- X-ray Evolving-Universe Spectroscopy – The XEUS Instruments, ESA-Bulletin SP-1273, Nov. 2003
- L. Strüder, D. Barret, C. Fiorini, E. Kendziorra, P. Lechner, Fast Timing on XEUS, Proc. of the SPIE vol. 5165 no. 1 (2004), pp. 19-25



*MPI Semiconductor Laboratory, D. Barret (CESR, Toulouse) and PNSensor*

# From XMM-Newton to XEUS

One of the new discoveries with XMM-Newton is the detection of sharp spectral drops above about 7 keV. After 3 years of intensive investigations, the physical nature is still unclear. We show that XMM-Newton observations require long exposure times to solve this outstanding physical problem. XEUS does have the capabilities to reveal the physical nature of these high-energy features detected in some NLS1s with moderate exposure times.

One of the open questions which still requires further investigations is the detection of dramatic spectral drops above 7 keV in Narrow-Line Seyfert 1 Galaxies. Presently two models provide an acceptable fit to the data, the partial covering model (Holt et al. 1980) and the light bending model (Fabian et al. 2002). With XMM-Newton both models give an acceptable fit to the data (c.f. Fig. 1) within moderate 40 ks observations.

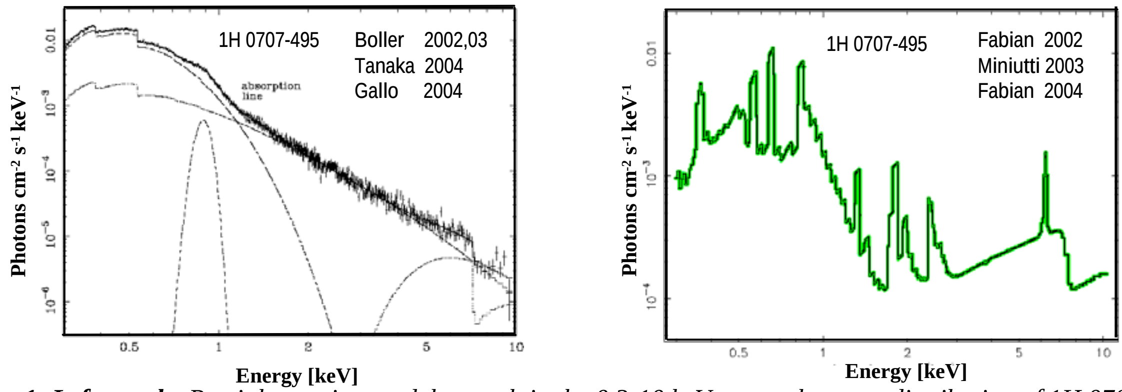


***Fig. 1, Left panel:*** *Partial covering model to explain the 0.3-10 keV spectral energy distribution of 1H 0707-495. A patchy high density absorber associated with the accretion disc causes the photoelectric absorption edge above 7 keV and the strong soft X-ray excess emission from the accretion disc which reaches the observer nearly unabsorbed.*

***Right panel:*** *Reflection dominated model for 1H 0707-495 in its low state. The sharp spectral drop is explained by the blue horn of an high equivalent width Fe K $\alpha$ emission line. Strong light bending effects play an important role in this scenario. Both, partial covering and light bending model explain the dramatic spectral drops above 7 keV. XEUS will allow us to discriminate between both models (c.f. Fig. 2).*

In Fig. 2 we show that with XEUS we will be able to discriminate between both models. The simulations show that a partial covering model cannot be fitted with a reflection model and opposite. XEUS observation will be able to discriminate between absorption dominated- and light bending dominated models.

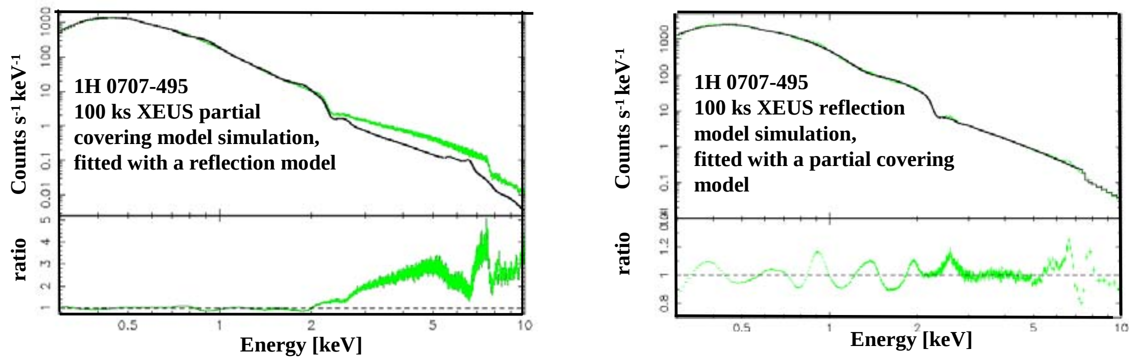


***Fig. 2:*** *XEUS simulation for 1H 0707-495 based on the XMM-Newton observation. The simulated partial covering model was fitted with a reflection model (left panel) and a reflection model was fitted with a partical covering model (right panel). Significant residua indicate that XEUS can discriminate between the two models.*

**References:**

Boller Th., Fabian, A.C., Sunyaev R., et al., MNRAS 329, 1,2002
Boller Th., Tanaka Y., Fabian A.C., et al., MNRAS 343, 89, 2003
Fabian A.C., Ballantyne D., Merloni A., et al., MNRAS 331, 35,2002
Fabian A.C., Miniuttti G., Gallo, L. et al., MNRAS in press, 2004
Gallo L., Tanaka Y., Boller Th., et al., MNRAS 369, 2004
Holt S., Mushotzky R.F., Boldt E., et al., ApJ 241, 13 1981
Tanaka Y., Boller Th., Gallo L., PASJ 56, 9, 2004

*Th. Boller, L. Gallo, Y. Tanaka*

# Dark Universe Observatory (DUO)

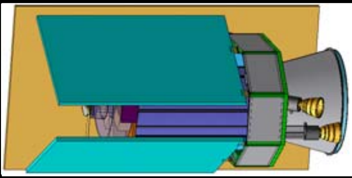

DUO is a candidate for the US Small Explorer (SMEX) program with strong contribution from MPE; Phase A is already finished. Scientific goal is the precise measure of cosmolocical parameters through the 3d-distribution of a large sample of (X-ray detected) clusters of galaxies.

**Standard Cosmology (WMAP *et al.*):**

- Flat, accelerating universe
- Early, rapid expansion (inflation)
- 73% Dark Energy, 23% Dark Matter, 4% gas, stars

**Dark Energy:**

- is smoothly distributed – needs whole Universe to study it
- Conspires with Dark Matter to make Universe 'flat'
- 'Deceleration parameter' is an acceleration, because Dark Energy dominates the universe
- Equation of state parameter: pressure vs. density $P = w\rho$
  If $w = -1$, DE = Einstein's 'Cosmological constant'
  If $w$ is more negative, Universe will rip apart (the 'Big Rip')

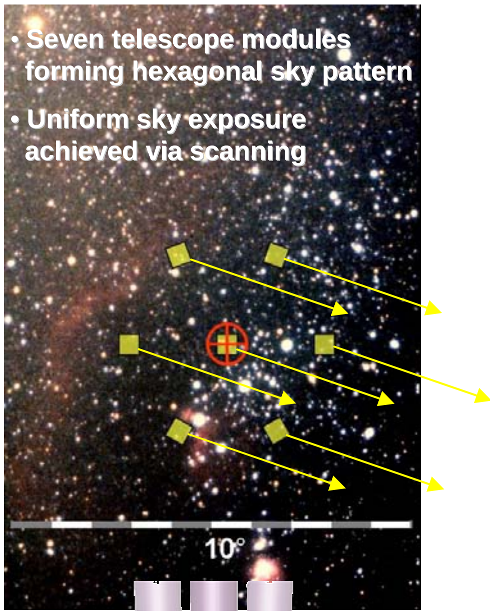


**Mission:**

- DUO will perform an X-ray sky survey for clusters of galaxies
- X-ray data distinguishes clusters of galaxies from Active Galactic Nuclei or stars because clusters are spatially extended
- Optical identifications and redshifts will come from the Sloan Digital Sky Survey (Wide Field: 8,000 clusters) and DUO follow-up program (Deep Survey: 1,800 clusters)


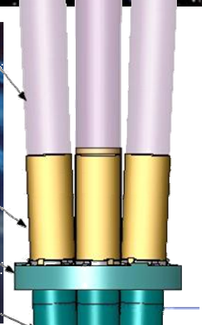

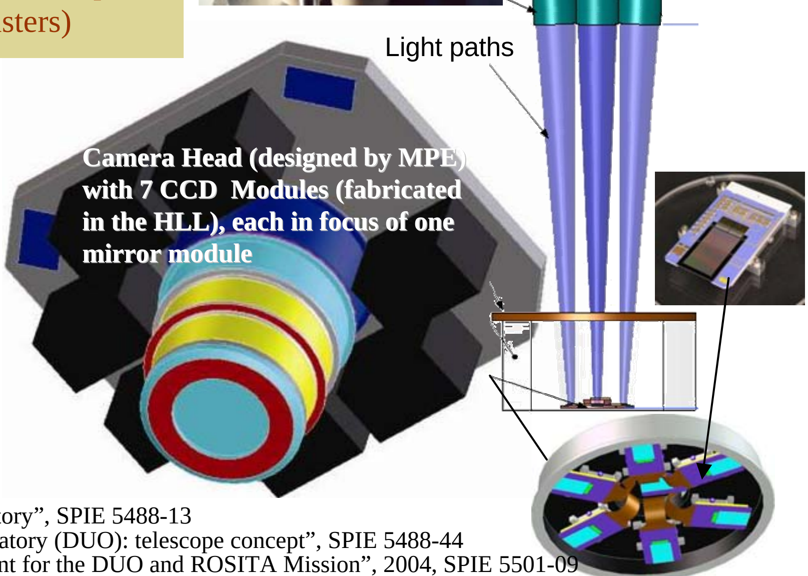


**Instrument Performance:**
Camera and telescope will be tested and calibrated in the PANTER X-ray facility

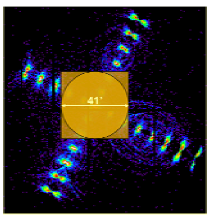


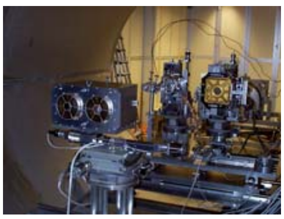

**References:**
• Griffith et al. 2004, "The Dark Universe Observatory", SPIE 5488-13
• Friedrich et al. 2004, "The Dark Universe Observatory (DUO): telescope concept", SPIE 5488-44
• Meidinger et al. 2004, "CCD-detector development for the DUO and ROSITA Mission", 2004, SPIE 5501-09
• Pfeffermann et al. 2004, "Shielding of cosmic ray induced background in CCD detectors for X-ray astronomy", SPIE 5501-39

*The DUO team*

# The DUO X-ray Camera

DUO (**D**ark **U**niverse **O**bservatory) requires an X-ray camera permitting a large FOV, high quantum efficiency over the 0.3–10 keV band, low background, ~75 µm spatial resolution (corresponding to less than 10 arcsec angular resolution), and adequate spectral resolution (~140 eV FWHM at 6 keV). The pn-CCDs developed in MPE's semiconductor laboratory over the past 16 years and which are flying on ESA's X-ray Observatory XMM-Newton meet these requirements . The DUO concept of individual telescopes requires a modular layout of the camera assembly. The camera includes 7 "CCD-modules" mounted in a single "camera housing" which, together with all the necessary electronics, forms the camera assembly.

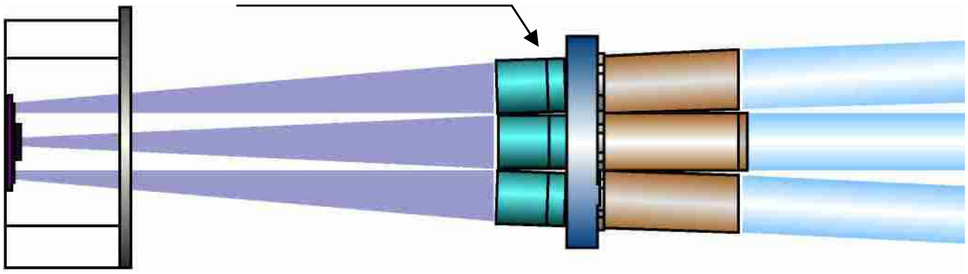


**Schematic drawing of the DUO instrumentation**

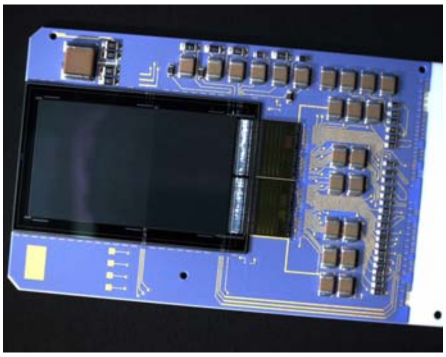

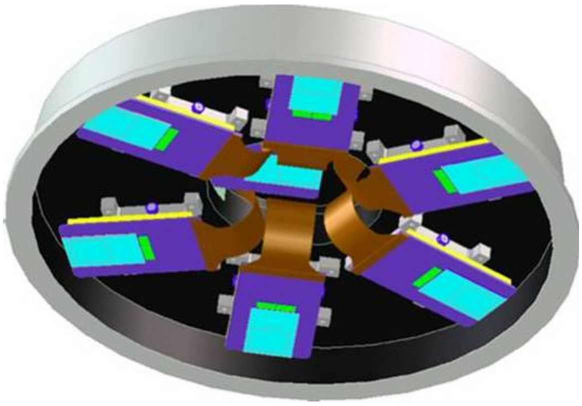

**CCD-Module:** Each frame-store CCD together with two CAMEX readout chips and passive front end electronics are mounted on a newly developed ceramic ($Al_2O_3$) carrier which demonstrates excellent mechanical and thermal properties. The operating temperature of the CCD is at -80 °C, provided by a thermoelectric cooler. Flex leads connect the CCD-modules with the supply and readout electronics

**Camera Head:** Seven CCD-modules are placed in a hexagonal arrangement corresponding to the foci of the seven mirror modules. The rigid mechanical structure also provides a proton shield against cosmic particles. This adaptation of the XMM-Newton camera design is optimized for reduced thermal conductivity. An additional graded shield of all near-CCD surfaces prevents the detection of induced fluorescence X-rays.

**References:**
- Strüder et al., "The European Photon Imaging Camera on XMM-Newton: The pn-CCD Camera", A&A, 365, L18-L26
- Griffith et al. 2004, "The Dark Universe Observatory", SPIE 5488-13
- Friedrich et al. 2004, "The Dark Universe Observatory (DUO): telescope concept", SPIE 5488-44
- Meidinger et al. 2004, "CCD-detector development for the DUO and ROSITA Mission", 2004, SPIE 5501-09
- Pfeffermann et al. 2004, "Shielding of cosmic ray induced background in CCD detectors for X-ray astronomy", SPIE 5501-39

*The DUO team*

# Frame store PN-CCD for the DUO mission

The PN-CCD detector is meanwhile operating for nearly 5 years very successfully on board of the XMM-Newton satellite as focal plane detector. The continuous development of the devices resulted in a ‘frame store PN-CCD’. This advanced charge coupled device will be provided for the DUO mission to investigate the questions related to the ‘dark energy’ problem in astrophysics. The seven flight detectors for DUO are currently produced in the MPI Semiconductor Laboratory, Munich. Pixel sizes, energy bandwidth, frame rates and device formats have been adapted to the scientific requirements of the DUO mission.

The frame store PN-CCD has been developed for single X-ray photon spectroscopy in the energy band from 0.3 keV to 10 keV with high quantum efficiency (≥ 90%), position and unprecedented time resolution. The addition of a frame store to the XMM-Newton PN-CCD allows X-ray photon accumulation in the image area independent of the simultaneous readout of the previous image from the frame store. Tests with the advanced PN-CCD type showed further improved performance with an energy resolution close to the theoretical limits.

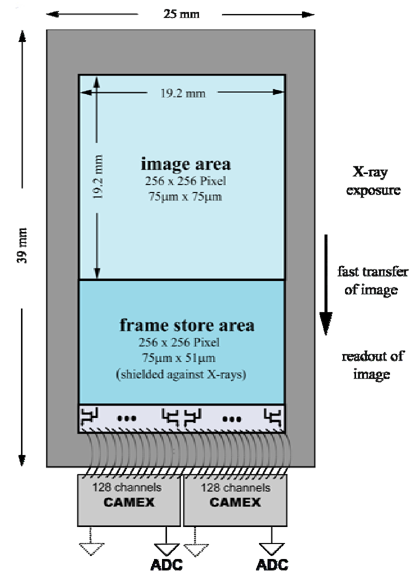


**Figure 1**: Schematic drawing of the frame store PN-CCD detector for DUO.

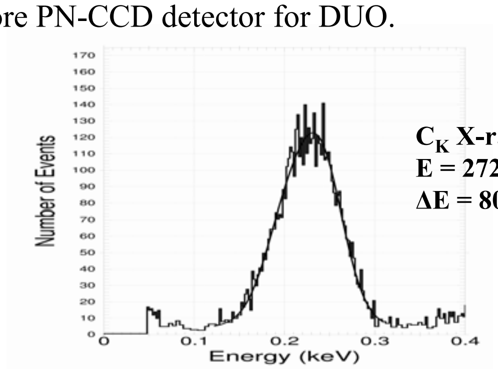


**Figure 2**: Spectrum showing the excellent low energy response of the frame store PN-CCD.

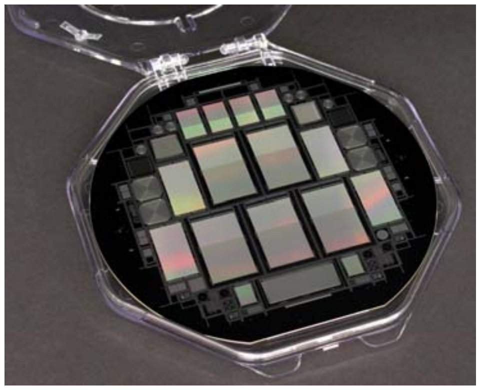

**Figure 3**: Frame store PN-CCD wafer of 6 inch diameter fabricated for DUO.

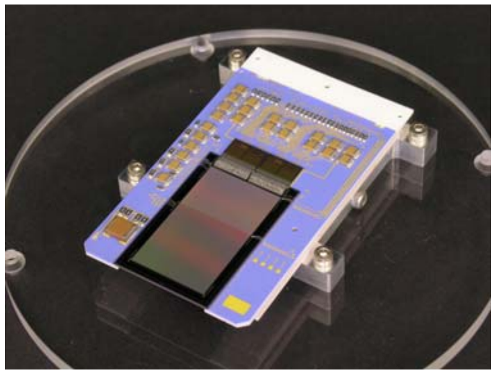

**Figure 4**: CCD detector module for DUO. The board carries the frame store PN-CCD and two 128-channel CAMEX analog signal processors for the parallel readout of the 256 CCD channels.

**References:**
- N. Meidinger et al., *CCD Detector Development for the DUO and the ROSITA Mission,* Proc. SPIE 5501, 2004.
- R.E. Griffiths et al., *DUO – The Dark Universe Observatory*, Proc. SPIE 5488, 2004.

# Characterization of silicon detectors using the Mesh method

The Mesh method is an excellent tool for the determination of the spatial properties of X-ray imaging detectors with high accuracy. The method has been adapted for testing the fully depleted pn-CCDs for the DUO / ROSITA missions and the DEPMOSFET device prototypes for the XEUS wide field imager and is now available at the MPI HLL. It is about to become a standard analysis tool for the purpose of device analysis.

The Mesh method is useful to address the following topics:

- Examination of charge splitting between pixels
- Measurement of diffusion and drift of signal electrons in the sensor material
- Scanning of the pixel structure in depth by repetitive measurements with different X-ray energies
- Analysis of insensitive regions of the sensor surface
- Combined topological examination and chemical analysis of the structured sensor surface by illumination with X-ray energies near the oxygen, aluminum, nitrogen and silicon absorption edges.
- Optimization of device operating conditions

The results of the Mesh measurements are used to determine the properties of the devices under test with high accuracy. Additionally, they can be used to test, verify and improve simulation tools and models, which, in effect, leads to better detectors.

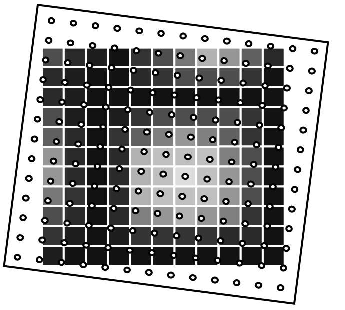

*Fig. 1: Principle of the Mesh method. The relative position of the holes with respect to the pixel borders causes different fractions of events with charge splitting (grey coded). The result is a Moire pattern.*

For the measurements, a “mesh” is placed in front of the sensor. The mesh consists of a carrier material intransparent for X-rays of the selected energy equipped with an evenly spaced grid of pinholes with a grid constant equal to or larger than the pixel size. The mesh is slightly tilted and shifted with respect to the pixel array (fig. 1). The mesh devices used consist of a gold foil of 3 $\mu$m to 10 $\mu$m thickness with a typical hole diameter of 5 $\mu$m. For convenience, the mesh grid constant is often chosen equal to the pixel pitch.

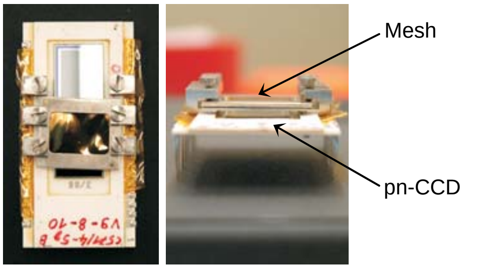


*Fig. 2: Experimental setup. The mesh is mounted in front of the sensor entrance window in a distace of about 1 mm. The sensor area not covered by the mesh is shielded with a copper baffle during measurement.*

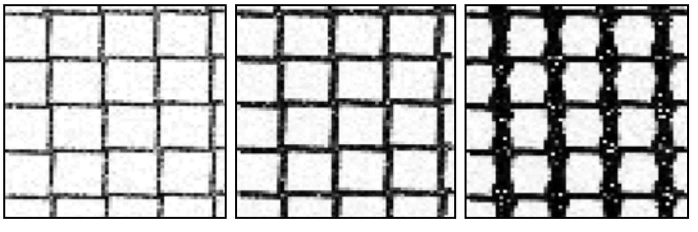

*Fig. 3: Example for Moire-patterns measured with the Mesh-Method on an XMM-type CCD. From left to right: Cu-K$\alpha$ (0.93 keV), Ti-K$\alpha$ (4.51 keV) with charge storage under two CCD registers, Ti-K$\alpha$ with charge storage under one register. From pattern angle and periodicity, the relative alignment of Mesh and detector can be calculated.*

Considering the spatial distribution of the ratio of charge splitting events (fig. 1), Moire-patterns can be observed. From the Moire-patterns, some effect of e.g. photon energy or operation mode of the device can be seen (fig. 3), but more significant information about the device properties can be obtained if the relative alignment of Mesh and pixel grid is used. This information can be calculated from periodicity and shape of the measured Moire-pattern. Then, the relative position with respect to the pixel borders can be determined for every hole, so any kind of data from the respective pixel can be correlated with the position of the incident photon. In effect, the entire pixel area is scanned with high spatial accuracy. Fig. 4, for instance, shows the difference in charge splitting behaviour for different charge storage modes within an XMM type CCD. The increased fraction of charge splitting events is already indicated by fig. 3. Only if the charge is stored under 2 shift registers, an unambiguous minimum for electrons is expressed, leading to sharp and well defined locations for the storage and transfer of electrons

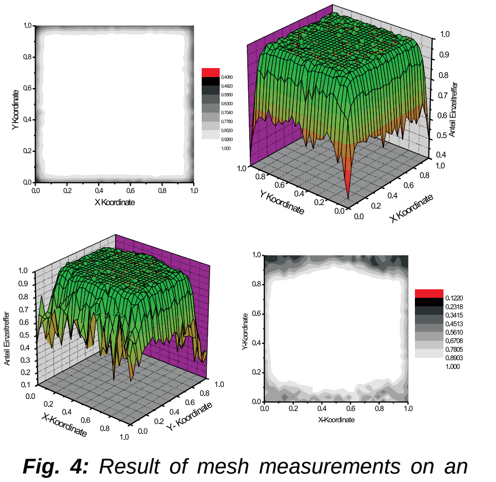


*Fig. 4: Result of mesh measurements on an XMM type CCD. Shown: Charge splitting ratio vs. position in pixel for charge storage under two registers (upper row) and under one register (lower row). The effect of increased charge splitting due to weakly defined potential minima for electrons can be clearly seen at the edges of the pixel.*

**References:**
- H. Tsunemi et al., NIM A 421 (1999), 90-98
- H. Tsunemi et al., NIM A 436 (1999), 32-39

*N.Kimmel, the MPI Halbleiterlabor team and PNSensor*

# DEPFET Macro Pixel Detectors

**Large cell pixel detectors have been developed for applications in X-ray astronomy. The devices have new features: (a) each cell consists of a small area drift chamber with a DEPFET readout structure in its centre; (b) a new type of DEPFET has been introduced which can be operated with lower voltages than was possible before. In the design the cell size can be adjusted to match the resolution of the image anywhere from about 50x50 µm to several millimetres.**

Matching the focal detector to the spatial resolution of the optical system of x-ray telescopes is important for reasons of data volume readout speed and power consumption. Pixel sizes of the order of millimetres are required for example for the proposed SIMBOL-X[1] and ECLAIR[2] missions. Such large pixel sizes are not reachable with CCDs or other „standard“ detectors. The concept chosen here combines the good charge collecting properties of Silicon drift diodes (SDD) [4] with the charge storage and delayed readout capabilities of DEPFETs[3]. A new type of DEPFET is placed in the centre of a drift diode (Fig. 1), forming the unit cell of a pixel detector. Signal charge generated anywhere in the bulk is collected in the internal gate of the DEPFET. It is measured by comparing the drain current before and after clearing the internal gate.

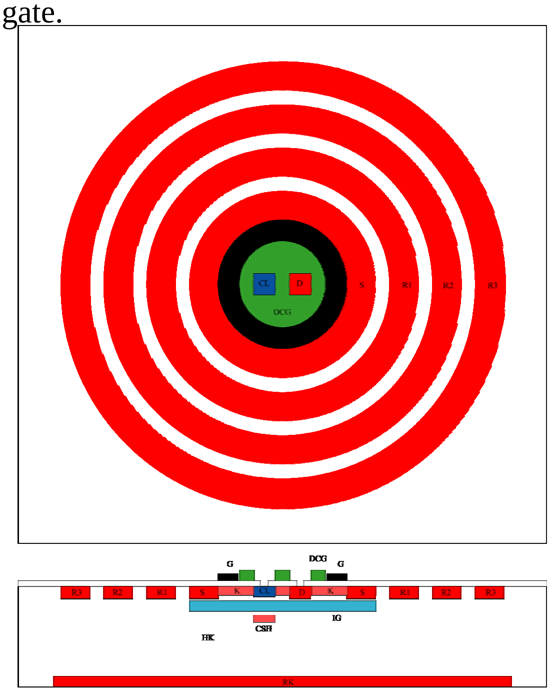

*Fig. 1: Macro-Pixel principle: top view and cross section.*

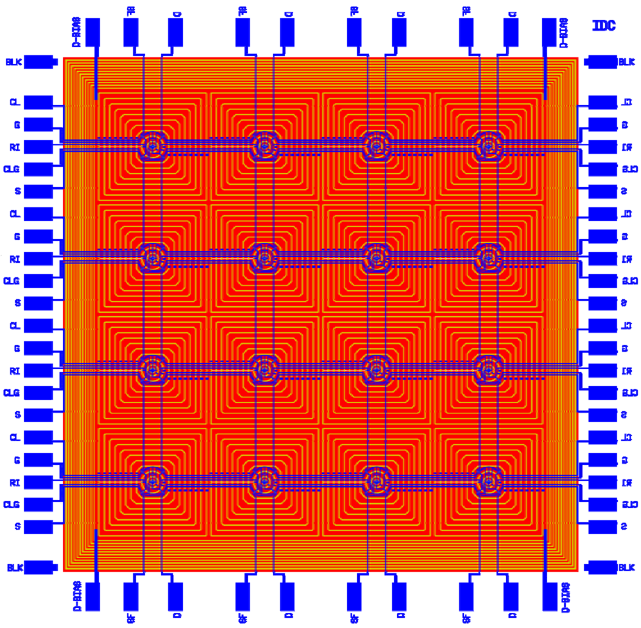

*Fig.2. Layout of a 4x4 1mm$^2$ cell size macro pixel detector.*

A 4x4 pixel matrix prototype with 1mm$^2$ pixel size (Fig.2) has been produced. Proper functioning has been verified with single pixel test structures. An energy resolution of 250eV at 5.9keV was reached at room temperature with the devices produced in our laboratory.

**References:**


1) **P. Ferrando et al.: "SIMBOL-X", , Proc. SPIE conf. 5168, San Diego, Aug. 2003**

2) **D. Barret: "**ECLAIRs **", AIP Conference Proceedings Volume 662 (2003), pp. 481-487**

3) **J. Kemmer and G. Lutz: ''New semiconductor detector concepts'', NIM. A 253 (1987) 365-377**

4) **J.Kemmer, G. Lutz et al.: "Low capacitive drift diode", NIM A253 (1987) 378-381**


*G. Lutz, R. Eckhard,P. Lechner, M. Porro, R.H. Richter, H. Soltau , L. Strüder*
*MPI Halbleiterlabor und PNSensor*

# Silicon Drift Detectors - in Heaven and on Earth

Silicon Drift Detectors (SDDs) have been proposed in 1984 by Gatti and Rehak. Since then a large variety of detectors for room temperature X-ray spectroscopy have been used in many different fields of science. In addition to their implementation in complex scientific instruments, they are used today in thousands of industrial applications in the field of quality asssurance & control and material characterization. Their main advantage is its operation close to room temperature, the high spectral resolution and the high count rate capability.

The basic physical reason of the above properties is the very small readout node capacitance and the special fabrication procedures, leading to very low thermal leakage currents. Fig. 1 (top left) shows the basic design of a circular SDD, including the on-chip electronics, Fig. 2 (top right) depicts the electrical potential of a SDD under typical operating conditions. The on-chip JFET in the center prepares the signals for further shaping and amplification. The achieved energy resolution is around 130 eV (FWHM) at 6 keV and 10.000 counts per second.

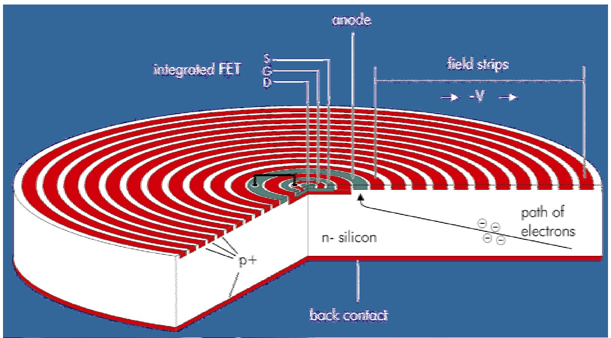


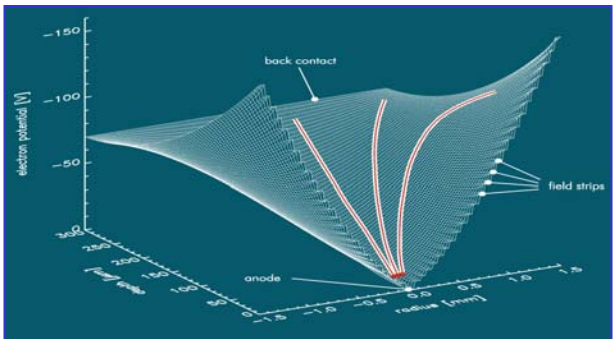


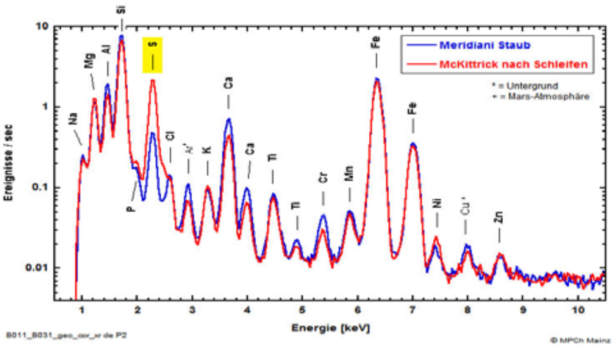


**Top left:** Basic design of a circular silicon drift detector with an integrated single sided JFET inside. The backside of the SDD has a homogeneous $p^+$ contact, negatively biased under normal operating conditions. The most positive area is the readout anode for electron collection.

**Top right:** The electrical potential inside the SDD. All electrons generated by ionizing radiation have to end after 100 ns at most at the positively biased anode contact.

**Bottom left:** A scanning SDD system analyzes the original manuscript of J.W. von Goethes Faust I and Faust II. The analysis of the ink has shown, that some parts of Faust I have been rewritten after Faust II was completed (Measurement made by O. Hahn, BAM, Berlin).

**Bottom right:** X-ray fluorescence measurements with Martian soil from different locations. A Cu source was used for the excitation of the atoms on Spirit and Opportunity aboard NASA´s MER mission. (PI of the APXS instrument: R. Rieder, MPI für Chemie, Mainz).

**References:**
- E. Gatti, P. Rehak, NIMA, 225, page 608 – 621, 1984
- L. Strüder, SPIE, Vol. 4141, page 29 – 48, 2000

*MPI Semiconductor Laboratory and PNSensor*

# Glass segmented mirrors for large X-Ray Optics

Extrapolation of the electroforming replication technique as it has been successfully applied to the XMM-Newton mirror systems is not feasible for mirror systems with diameters of 5-10 m because of constraints on the mirror mass. Realistic launch masses of up to 10 tons require a ratio of mass to geometric aperture being a factor of more than 20 below Chandra and a factor of about 5 below XMM-Newton. Combining high angular resolution and mass requirement is a challenge.

## Segmented Mirrors:

X-ray mirrors with diameters of several meters cannot easily be manufactured as closed shells. Instead, the mirror shells should be azimuthally divided in segments. The question of how many segments and how many nested shells are the optimum is closely related to the dynamical stability (eigenfrequencies) of the mounted mirror system; thinner mirrors must therefore be generally smaller in their azimuthal extension.

## Technical approach (“glass slumping”):

Although replicated electroformed nickel mirrors are too heavy with respect to their stiffness the replication technique itself is very attractive for large segmented mirror systems for the number of equal and similar mirror pieces is large and calls for series production.

Our approach is based on industrially manufactured float glass or display glass, respectively. Its advantage is low surface micro-roughness which is already sufficient for X-ray optics, high flexural rigidity compared e.g. to nickel and that it comes from mass production. Flat glass sheets can easily be deformed by thermal treatment (slumping) to get the desired shape of the optical element.

## Current Experiments:

At temperatures between the annealing point and the softening point the viscosity of the glass is such that it slumps into (or onto) a given mould. How the many process parameters have to be adjusted to optimize the accuracy of the reproduction of the mould’s shape is an essential part of our investigations. Some of these parameters are closely connected with each other.

Together with our industry partners we have experimentally investigated the slumping parameters and confined the interesting part of the parameter space. We are now planning for a small demonstration model of a Wolter mirror segment.



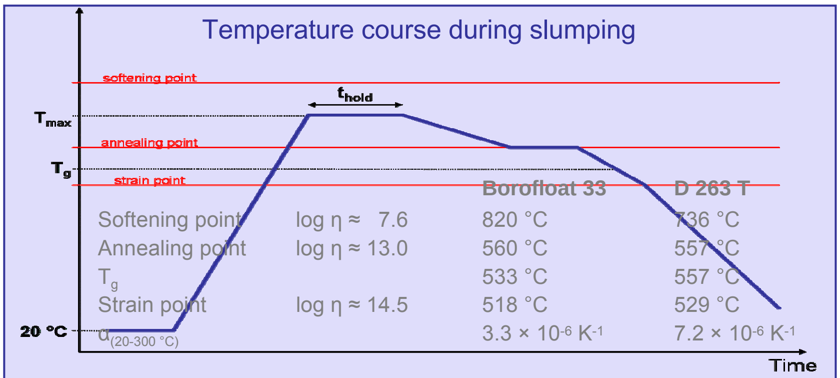


**Essential slumping parameters:**

- Glass type
- Mould material
- Slumping temperature $T_{max}$
- Holding time at $T_{max}$
- Cooling rate
- …

**References:**

- Citterio et al. 2004, “The manufacturing of XEUS X-ray glass segmented mirrors: status of investigation and last results”, Proc. SPIE v. 5168, p. 180
- Parmar et al. 2004, “Science with XEUS – the X-ray Evolving Universe Spectroscopy Mission”, SPIE 5488-24

*P. Friedrich, H. Bräuninger*

# X-ray optics with ultra high angular resolution

Schemes for future diffraction-limited x-ray telescopes are investigated. Based on transmission-based diffractive lenses, an angular resolution of about $10^{-3}$ arcsec will be achieved. For sake of efficiency, phase shifting Fresnel lenses are most likely preferred over simple zone plates. Using higher diffraction orders, Fresnel lenses may provide high focal intensities over several keV. Their chromatic error may be eliminated within a limited energy range by means of an additional refractive component, also enhancing the total focused power.

Thin transmissive X-ray lenses have the potential to overcome the era of low-resolution but high-mass Wolter telescopes, as they allow diffraction-limited imaging even in presence of relatively large manufacturing tolerances. For example, at an energy of 1 keV, an aperture diameter $Ø_A \cong 25$ cm would comply with $10^{-3}$ arcsec, generally to be considered as a „frontier“ with respect to scientific requirements. Unfortunately, high angular resolution comes along with long focal distance $F$. Sensible detector pixel sizes in the µm range lead to $F \sim 1$ km, far too much for single spacecraft design. Focal lengths would even be elongated for large-scale objectives with diameters of several meters necessary due to sufficient effective area. In this case, segmentation to small panels is inevitable as well as good support structure. The latter diminishes transmission – however, depending on chosen lens profile (fig. 1), residual effective areas of a few m² up to some 10 m² are attainable.

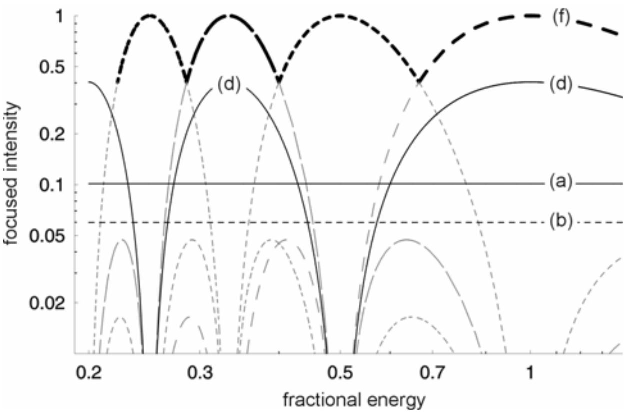


**Figure 1.** Focusing efficiencies of various diffractive lenses as a function of the fractional energy $E/E_0$. Amplitude modulated profiles like binary zone plates (a) exhibit energy-independent but modest intensity in the focal plane. „Photon Sieves“ (b), made of large numbers of tiny holes, perform even worse, but with the advantage of higher flexibility. Phase zone plates (d) show oscillating efficiencies up to 40% only at certain energies in 1st order. Neglecting absorption, up to 100% may be nevertheless theoretically achieved with Fresnel lenses at distinct energies $E = m^{-1} E_0$, when used in higher orders (f). In-between, efficiency decreases to ≥ 40%.

Unfortunately, diffractive lenses suffer from severe dispersion $F \propto E$, which requires fine spectral selection in focal plane in order to maintain angular resolution but at cost of low efficiency. Chromatic correction can be done in first order with the help of a refractive device of proper shape, leading to a so called „hybride“ lens. Despite severe absorption by thick refractive lens profiles, the enhanced bandwidth usually results in a net gain with respect to the sole diffractive analogue. This gain depends both on material properties at selected energy and the diffractive lens‘ zone number $N$ as well. For low-$Z$ solid-state materials like Be and Li, focused power may be enhanced by roughly a factor of 10 - 20 at 4 keV. Fig. 2 gives design limitations for such achromatic lenses partially based on this fact.

**Figure 2.** Approximate lower bounds on $f$-ratios and related zone numbers $N$ for solid-state hybride achromatic lenses. Dashed lines refer to a minimum gain of 4 compared to the corresponding single diffractive component. Solid borderlines originate from restrictions on lens curvature radii and forbid usage for more or less hard X-rays. Obviously, sensible application of plastics like polycarbonate ($C_{16}H_{14}O_6$) is limited to high energies. In contrast, Li, Be and their hydrides better perform for soft and medium X-rays.

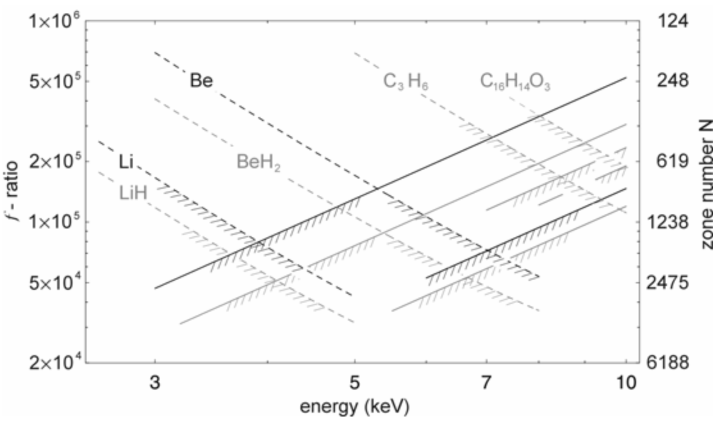


**References:**
• C. Braig and P. Predehl, "X-ray astronomy with ultra-high angular resolution", *Proc. SPIE,* to be published (2004).
• G. Skinner et al., "Fresnel lenses for X-ray and gamma-ray astronomy", *Proc. SPIE* **5168**, 459 (2004).

*C. Braig and P. Predehl*

# SPI Gamma-Ray Spectrometer on INTEGRAL

**Since Oct 2002, a high-resolution gamma-ray spectrometer operates in space, aboard the ESA INTEGRAL observatory. Satellite and instrument performances are excellent, so that the planned 2-year mission has been extended up to Dec 2008.**

INTEGRAL's main two instruments are coded-mask telescopes, an imager IBIS and a spectrometer SPI. One of the main science goals of ESA's INTEGRAL mission is to provide a new window into spectroscopy with gamma-ray lines, yet with imaging capability.

Previous experiments did not have the energy resolution to measure line broadenings, which are typically in the 0.1 to 50 keV range. Solid state detectors based on high-purity Ge can provide the needed resolution. Therefore the SPI instrument on INTEGRAL features a 19-element Ge camera with a total area of 500 $cm^2$, and uses a coded mask made from tungsten to allow imaging and signal-from-background discrimination. Stirling cryocoolers maintain the Ge operational temperature at ~90K. Limited by instrumental-background lines, narrow-line sources down to fluxes of 2 $10^{-5}$ ph $cm^{-2}s^{-1}$ can be studied.

With its coded-mask and a field-of-view of ~16x16°, diffuse emission and sources can be studied in its energy range of 15-8000 keV, and a timing resolution of 52µs also allows the study of pulsars and accreting source phenomerna.

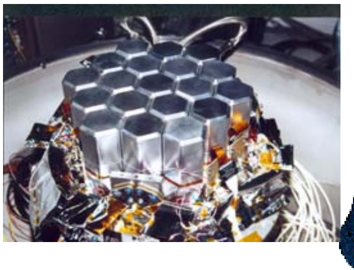

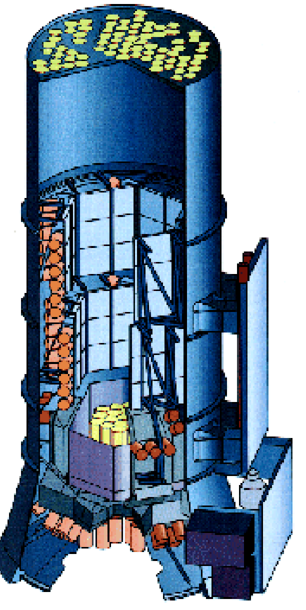

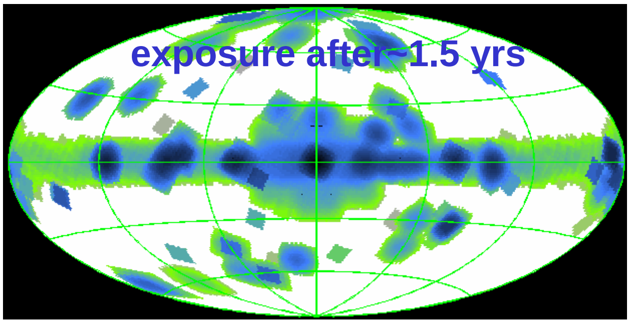



The spectrometer performance is excellent, although two detector elements have stopped functioning, within the first two mission years. Spectral resolution degrades during the mission, due to cosmic-ray bombardement of the Ge detectors, damaging the charge collection properties within the crystal. Every ~6 months, after ~20% degradation of resolution, "annealings" are conducted, where the Ge camera is heated to 105°C for ~2 days. This re-establishes the spectral resolution to typical values of 3 keV @ 1800 keV, adequate for measuring kinematics of radioactive isotopes through Doppler shifts, for isotopes such as $^{44}$Ti, $^{26}$Al, $^{60}$Fe, $^{56}$Ni.

**References:**

- Vedrenne G., J.P. Roques, V. Schönfelder, et al., A&A 411, L63 (2003)
- Roques J.-P., Schanne S., von Kienlin A., et al., A&A 411, L93 (2003)
- Winkler C., Courvoisier T. J.-L., Di Cocco G., et al., A&A 411, L1 (2003)

see several other posters on science results

*V. Schönfelder, R. Diehl, G. Lichti, A.W. Strong, A. von Kienlin, et al.*

# Swift at MPE

Swift is a dedicated GRB afterglow satellite mission to be launched in October 2004 by NASA. Contributions from MPE include (1) the calibration of the X-ray telescope at PANTER, (2) the development of software for analysing the Burst-Array-Telescope all-sky survey data, and (3) the participation in the decision about Swift‘s non-autonomous response to individual GRBs.

## XRT Calibration at PANTER

The X-ray telescope of Swift has been tested at PANTER twice: in July 2000 for the performance of the X-ray mirror, and in September 2002 for the end-to-end test.

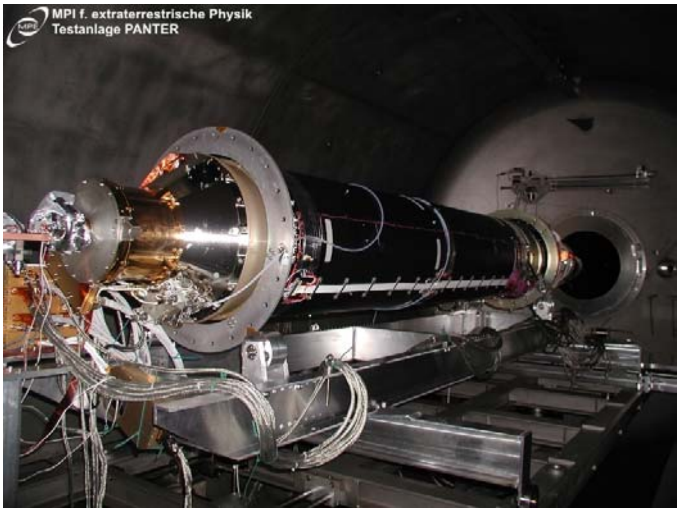


The Swift XRT pointing to the 1m aperture of PANTER‘s 130m long X-ray tube (right back).

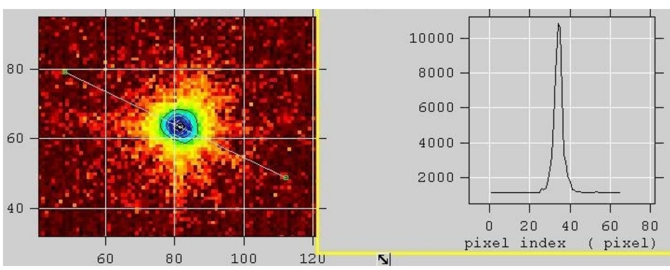


Swift-XRTs first light at PANTER on 23 Sep 2002: left the central part of the X-ray image (in pixel units), right the profile of the point spread function (18‘‘ HPD at 1.5 keV). Subsequent end-to-end calibrations have concentrated on measuring the PSF, the effective area, and the focus. Furthermore, the various operating modes of the detector have been tested and verified.

## Software development for BAT

MPE is providing 2 programs to be used in the analysis software of the Burst-Array-Telescope (BAT): (1) For each 5-min integration of BAT the shadow cast by the brightest X-ray sources outside the field of view of BAT through various structural and detector units of SWIFT onto the BAT detector is computed. (2) A sum of many BAT exposures with different pointing directions and roll angles under various background conditions will be computed by unfolding all the available data at once.

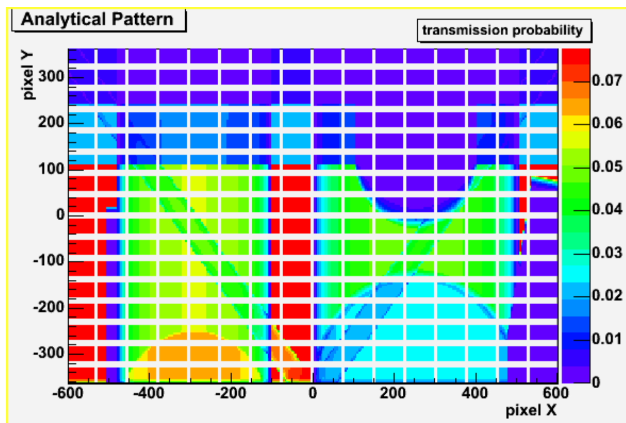


Computed shadows of the Swift X-ray and UV/optical telescopes onto the BAT detector plane at 100 keV.

## Participation as Burst Advocate

There will be one Burst Advocate for each GRB who is responsible for the data integrity, quick-look results, archiving, the organization of ground-based follow-up observations and the non-autonomous pointings of Swift to that GRB. MPE is providing BAs to work within the Leicester BA-group.

*M. Ajello, W. Burkert, M. Freyberg, J. Greiner, G. Hartner, G. Kanbach, A. Strong, W. Voges*

# GBM – a Burst Monitor for GLAST

GLAST is scheduled for launch in 2007. It is one goal of the main GLAST instrument, the LAT, to study the high-energy (~20 Mev - ~300 GeV) emission of GRBs. A second instrument, the GLAST burst monitor (GBM), will extend the energy measurements towards lower energies (~10 keV - ~25MeV) and will allow the exploration of the relation between the keV and the MeV-GeV emission from GRBs over 6 energy decades. This will give new insights into the unknown aspects of the high-energy emission of GRBs and its relation to the well-studied low-energy emission and after glow properties.

The GBM will be realised by a collaboration between MSFC and MPE. The MPE is responsible for the manufacturing of the detectors and the power supply, while MSFC is responsible for the digital processing unit. The calibration, the operation and the analysis of the data will be shared equally between both groups. The GBM consists of 12 NaI crystals (~10 keV - ~1 MeV) and 2 BGO crystals (~150 keV - ~25 MeV). The NaI crystals are aligned such that each is viewing the sky in a different direction. From the measured relative counting rates the arrival direction of a GRB can be determined. The mounting configuration and a NaI detector is shown in the two figures below.

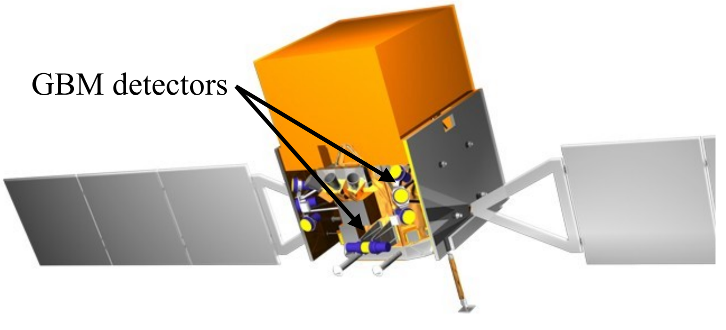


The emission characteristics of GRBs below ~1 MeV are known from BATSE. However, the knowledge at larger energies is sparse. From EGRET observations it is known that GRBs show delayed high-energy γ-ray emission. But what processes cause this emission is unknown. With the two GLAST instruments the energy spectrum of a GRB can be measured over 6 energy decades and insights into the production processes can be obtained. Especially it may help to disentangle the problem how these high-energy γ-rays can escape their source region without being absorbed via γ-γ interactions with low-energy photons. This requires the precise measurement of the γ-ray spectrum up to the highest energies. A simulated example of such a spectrum is shown in the figure below. The measurement of such spectra allows the determination of the relation between the low-energy and high-energy emission and the investigation of the evolution of the spectral parameters. Especially the hardness-intensity correlation can be better investigated. If the gamma-photometric redshift determination (Bagoly et al. 2003) or the luminosity-variability relation (Reichart et al. 2001) turn out to be correct then even the evolution of these parameters as a function of z can be explored.

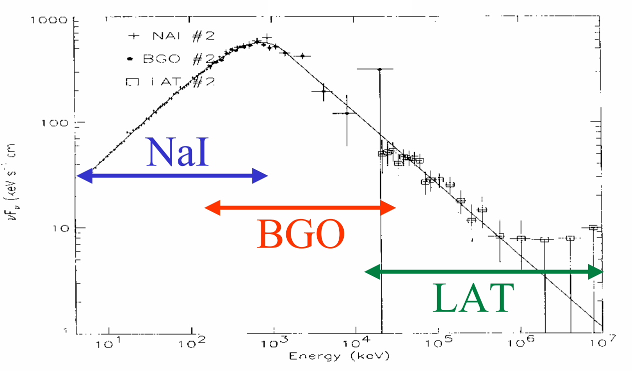


**References:**
- Bagoly, Z., I. et al.: A&A **398**, 919-925, 2003
- Kienlin, A. von, et al., SPIE , 2004
- Lichti, G. et al. SPIE **4851**, 1180, 2002
- Reichart et al.: Ap. J. **552**,57, 2001

*G. G. Lichti, R. Diehl, J. Greiner, V. Schönfelder, H. Steinle, A. von Kienlin*

# The MEGA Project

MEGA, short for **M**edium **E**nergy **G**amma-ray **A**stronomy, is the development of a new technology telescope in the energy band 0.4-50 MeV. As a successor to COMPTEL and EGRET, MEGA aims to improve the sensitivity for astronomical sources by at least an order of magnitude in a severely under-sensitive range between hard-X and high-energy γ-ray missions. MEGA would thus open the way for a future Advanced Compton Telescope (ACT). The wide energy range of MEGA, which spans nuclear γ-ray lines and energetic continuum spectra, the large field of view, and the capability for polarimetry will enable unique investigations into cosmic nucleosynthesis, particle accelerators around compact objects, and explosive high-energy events. We describe the design, prototyping, and calibration work achieved at MPE, and after the project has been discontinued at MPE, the outlook for a balloon test and a MidEx satellite mission proposal within a US led collaboration.

The ‚retarded‘ status of MeV astronomy: Detection of highly penetrating photons and strong systematic backgrounds make the development of a sensitive γ-ray telescope very challenging. Advanced detector technologies now allow a new start in this field.

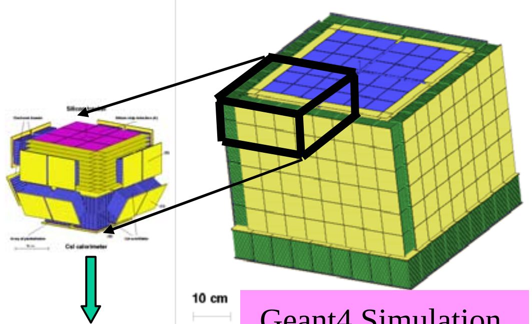


Prototype

Geant4 Simulation (satellite telescope)

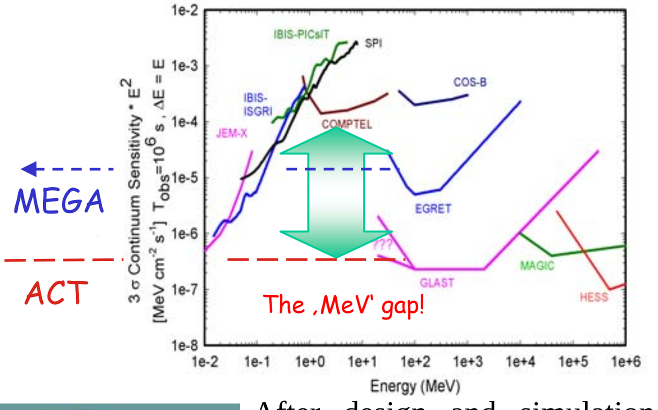


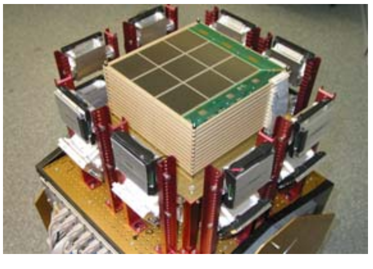

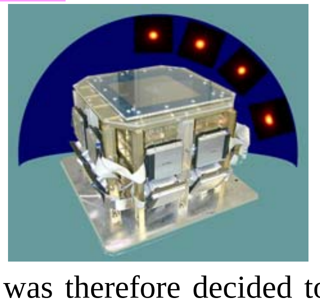

After design and simulation work (since 1996) a scaled prototype was built and calibrated with radioactive sources and a beam test. In Nov. 2003 the MPE directorate decided to discontinue further hardware development on MEGA.

It was therefore decided to transfer the existing MPE hardware (detectors, anticoincidence shield, balloon gondola) to the Univ. of New Hampshire (J. Ryan, PI) to prepare a NASA approved balloon flight in 2005. The US led **MEGA collaboration** (UNH, NRL, GSFC, UoA, LANL, UCR & MPE, IASF Bologna, U. Valencia, CESR Toulouse) plans to compete in the upcoming NASA MidEx round for a mission based on the MEGA development.

MEGABALL balloon payload

A possible MEGA satellite

*G. Kanbach, R. Andritschke, A. Zoglauer*, V. Schönfelder, F. Schopper et al.*

# Calibration of the MEGA Prototype

MAX-PLANCK-GESELLSCHAFT

The MEGA prototype telescope, which detects γ-rays in the range of 0.4 - 50 MeV, was completed in February 2003. Extensive lab calibrations (energies < 1.8 MeV) and a beam test (0.7 - 49 MeV) at the High Intensity Gamma Ray Source HIGS at Duke University, Durham, NC were conducted from February to May 2003. Spectroscopy and imaging in the complete energy range and over a wide field of view (>160°) were successfully demonstrated and the capability to detect polarization was verified. MEGA is presently the most advanced, calibrated, wide angle γ-ray camera for a broad spectral band. It is ready for a balloon flight to test for the sensitivity to a natural, near space background radiation environment.

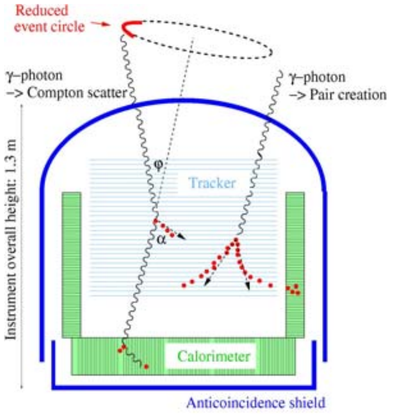


**Principle** of detection of low- to medium energy γ's

The MEGA prototype consists of 11 layers of double-sided silicon strip detectors and 20 calorimeter blocks (120 CsI(Tl) crystals each). ‚Good' events (i.e. γ-rays interacting in Compton scatters and pair creations) are selected from the background in a custom-made trigger and data acquisition system which reads out a total of 11328 channels. Combined Compton scattering and pair creation telescopes like MEGA measure a large amount of parameters for each recorded interaction. A list-mode likelihood algorithm (LM-MLEM) in combination with the basic detector response, is needed to process these data efficiently and to accurately image sources. We showed also that extended sources and sources on high background as expected in a space environment can be resolved.

**Calibration Measurements:** During April/May 2003 calibrations with a monochromatic, 100% polarized beam, tunable from 0.7 to 50 MeV, were performed at the HIGS facility of Duke University. A total of 15.5 Mio. events was recorded and analyzed.

**Point source images:** calibration beams from 2 to 49 MeV; event types range from untracked Compton interactions to pair creation events.

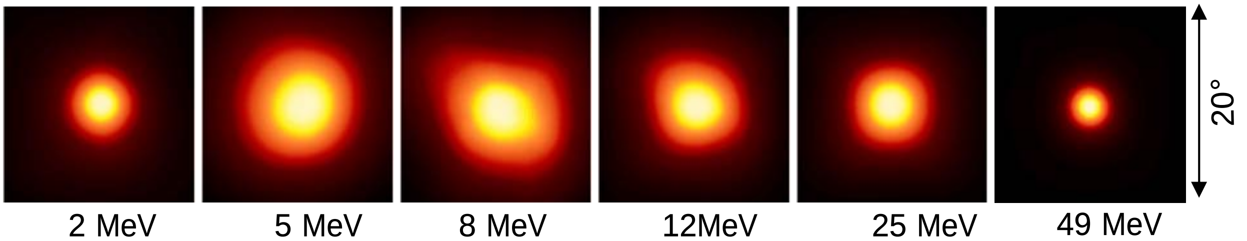


2 MeV 5 MeV 8 MeV 12MeV 25 MeV 49 MeV

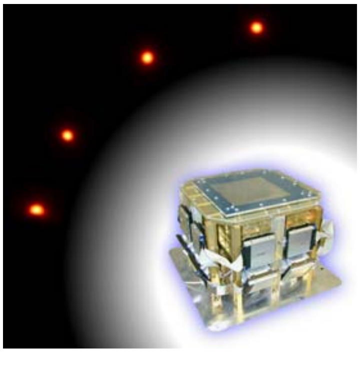

**Field of view:** beams at 49 MeV incident out to zenith angles of 80° were imaged successfully (left).

**Extended source:** a "radioactive" ring ($^{88}$Y at ~0.9 MeV on a rotating propeller) was imaged with the list-mode algorithm (right).

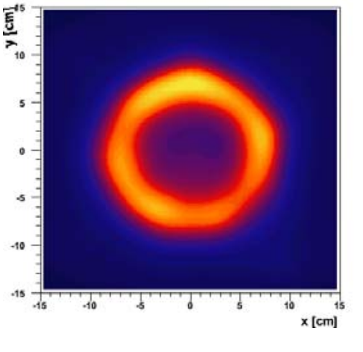


**References:** Andritschke, et al., New Astr. Rev. **48** (2004) 281 / Zoglauer A. et al., 5th Integral WS, 2004

* now at Univ. of California, Berkeley, USA

*R. Andritschke, A. Zoglauer*, G. Kanbach, & the MEGA collaboration*

# MEGA: measuring polarization in γ-rays

The prototype instrument MEGA, a combined Compton scattering and pair creation telescope, was calibrated with monoenergetic and 100% polarized photons in beams generated at Duke University's FELL HIγS facility. Polarization signatures are detected from 710 keV up to 5 MeV in agreement with expectations from Geant4 simulations. These properties demonstrate that Compton telescopes suitable for recording large angle scattering events, like MEGA, are ideal instruments to measure polarization in low energy γ-rays from astronomical objects. We know from tantalizing first observations (*RHESSI*) that gamma-ray bursts and solar flares are strongly polarized at MeV energies. It is to be expected that polarization in other sources like pulsars, binaries, and AGNs, where radiation processes of relativistic particles in strong magnetic fields or beamed geometries play an important role, will also provide decisive new insights into the physics of cosmic high-energy sources.

Most processes in high-energy astrophysics, such as synchrotron radiation, bremsstrahlung, Compton scattering, etc. generate polarized gamma-rays. Therefore, polarization measurements are of great value to understand the emission mechanisms of gamma-rays.

$$\frac{\partial\sigma}{\partial\Omega} = \frac{r_e^2}{2}\left(\frac{E_g}{E_i}\right)^2\left(\frac{E_g}{E_i} + \frac{E_i}{E_g} - 2\sin^2\varphi\cos^2\chi\right)$$

The polarization preserving properties of the Compton cross-section (right) result in a cosine shaped modulation of the azimuthal scatter angle of the Compton process. The maximum of the modulation is perpendicular to the original polarization vector.

**MEGA calibration:** Azimuthal scatter angle distributions (geometry and efficiency corrected) for measurements at 0.71, 2.0 and 5.0 MeV. As expected, the maxima of the modulation are found at ~0° and ~180°, perpendicular to the horizontal polarization vector of the incident beam. The amplitudes of the detected modulations are in agreement with Geant4 simulations.

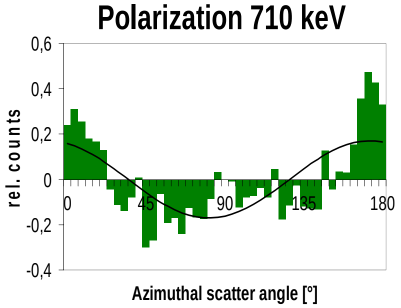


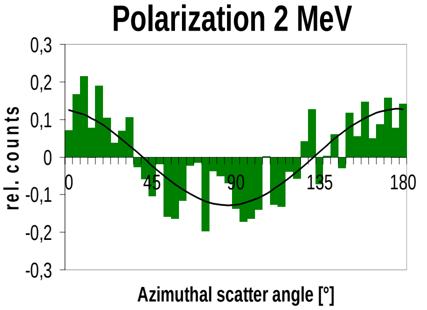


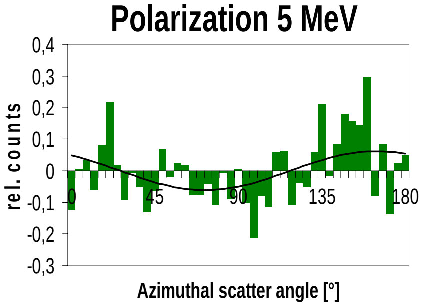


## Simulation of a gamma-ray burst with a MEGA satellite telescope:

The high-energy burst GRB910814, the second brightest GRB in the first year of COMPTEL, was used as a template for a simulated observation with a MEGA satellite configuration. Imaging to a sub-degree accuracy and a minimum detectable polarization (MDP) of 8% are found for this average GRB. MEGA with its wide field-of-view should register many such events.

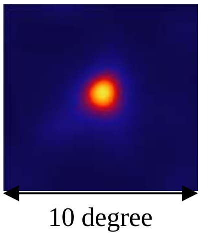
10 degree

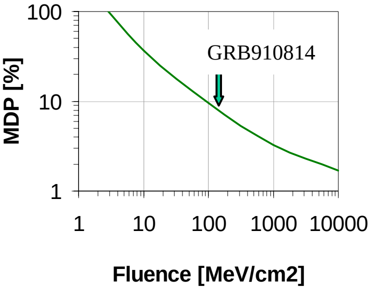


Reference: Zoglauer A. et al., poster 5th Integral Workshop, München, 2004

* now at Univ. of California, Berkeley, USA

*A. Zoglauer*, R. Andritschke, and G. Kanbach*

# The Compton Camera Imager

Compton camera systems offer the option to trace back the direction of the incident hard X – and Gamma rays by measuring all kinematic parameters of a Compton scattering process. A first step towards the goal of a full size instrument for medical research is the development of a Compton Camera Imager (CCI) for small animals for pharmaceutical research. With e.g. 830 keV ($Se^{72}$) incident Gamma rays a position resolution of 200 µm – 300 µm can be reached. The efficiency of the colimatorless system is about a factor of $10^3$ higher as compared to existing SPECT systems. Its spatial resolution is superior to that of PET systems.

Compton Camera Imagers (CCI) for medical diagnosis are under investigation since many years. A new approach was proposed in 2003 since new scatter detectors became available with adequate specifications, among those: position resolution of 150 µm in all directions, good energy resolution at room temperature, fast trigger signal of Δt better than 5 ns, high count rate capability. We have designed, fabricated and tested a controlled silicon drift detector which fulfills the above requirements to be implemented as scatter detector in a CCI system.

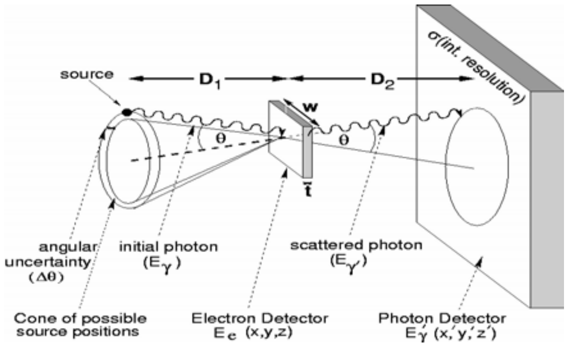


**Fig.1:** Basic geometry of a CCI. The incident photon hits the scatter detector. The position of the scatter process, the deposited energy of the electron and the time is measured precisely. The electron is stopped in the scatter (electron) detector, while the scattered photon is detected in the absorption (photon) detector.

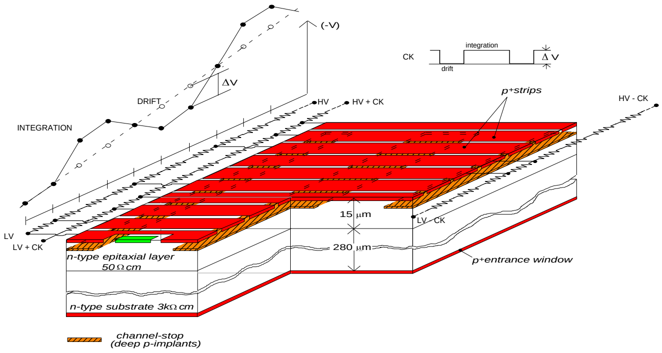


**Fig.2:** The controlled silicon drift detector as a scatter detector. The electrons of the signal charge cloud drift to the front side in the channel guide structure of the CDD, the holes are detected at the rear side for the fast timing signal.

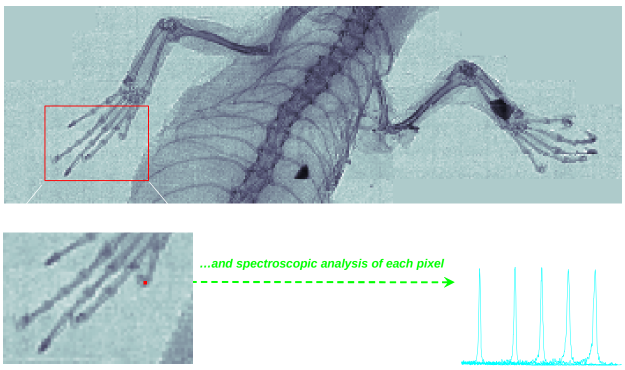


**Fig.3:** Image recorded at 100.000 frames per second with a CDD in a single photon counting mode. The energy resolution at room temperature was better than 250 eV FWHM. (The measurements were made at the synchrotron in Trieste by A. Castoldi, C. Guazzoni, Politecnico di Milano.

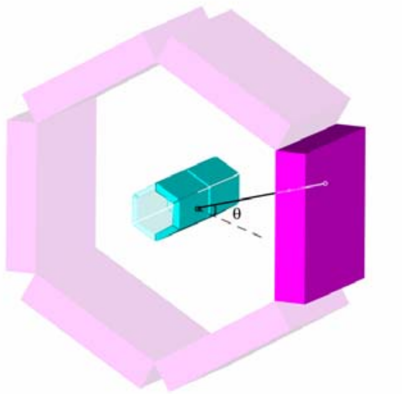


**Fig.4:** The inner (green/blue) detector must be as close as possible to the ``patient´´. The outer detector ring is the absorption detector for the detection of the position, time and energy measurement of the scattered photon from the Compton process.

The following institutions are part of the collaboration: Universität Siegen, Politecnico di Milano, Universität Bonn, Universität Essen, Forschungszentrum Jülich, University College London, SIEMENS medical Chicago, Vanderbilt University, University of Rome.

**References:**

• Castoldi, A. et al., NIMA 512, pp 250 - 256, 2003
• Conka-Nurdan, T. et al., IEEE, TNS, Vol. 51, No. 3, 2003

# X and Gamma Ray Detection with SDDs

Silicon Drift Detectors (SDDs) have been coupled to scintillators to simultaneously measure position energy and time of the incident radiation. High photon quantum efficiency and low noise amplification make silicon drift detectors suitable for the light detection of scintillators like CsI(Tl) or LSO etc. The segmentation of the SDDs allows for a precise reconstruction of the light centroid of the incident X-rays and hence a space point measurement of the position of the interaction within the scintillating crystal.

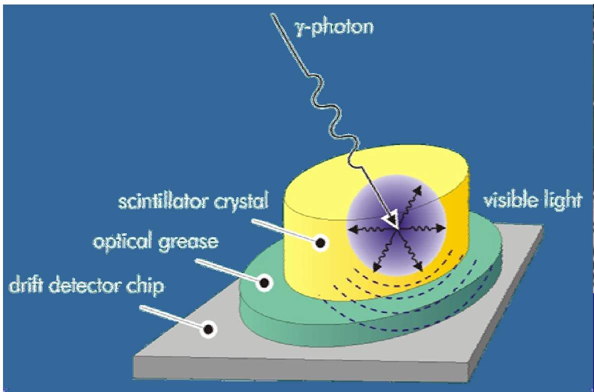


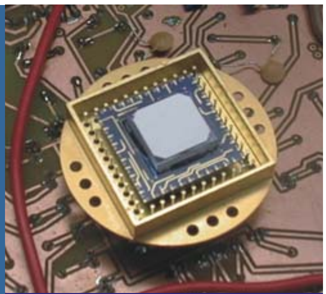

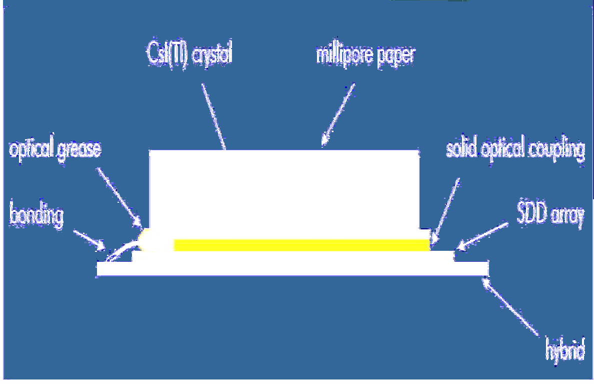


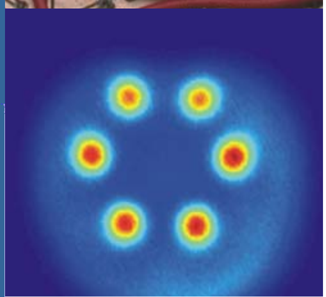

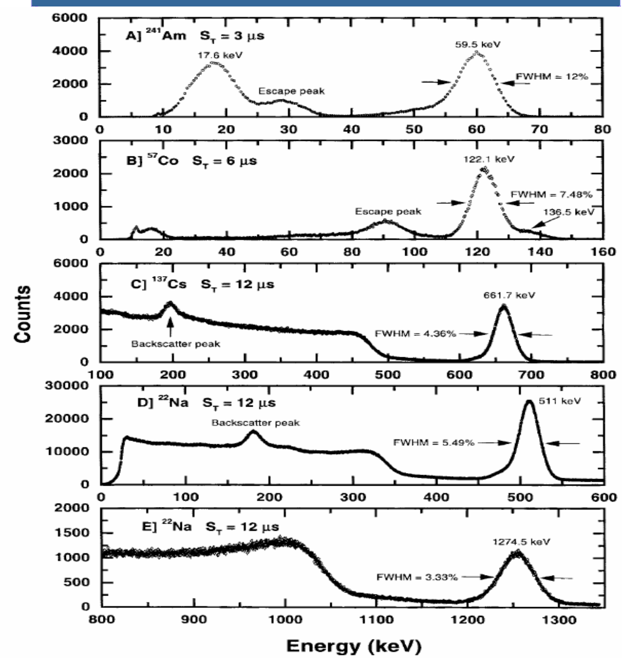


**Top left:** A scintillator is coupled to a light sensitive silicon drift detector with the help of optical grease.

**Center left:** The scintillator is covered with millipore paper for the diffuse reflection of the generated optical photons. Typically 20 electrons are produced for every keV of deposited X-ray energy in the scintillating crystal (here: CsI(Tl)).

**Top right:** photograph of a 19-cell SDD coupled to a CsI(Tl) crystal with a total area of approx. 1 cm$^2$. The detectors were operated at room temperature.

**Bottom left:** X- and Gamma ray spectra recorded with the above described set-up. From top to bottom: 59.5 KeV (FWHM = 12%), through 122,1 keV (FWHM = 7.5 %), 511 keV (FWHM = 5.5%), 661.7 keV (FWHM = 4.3 %) and 1274.5 keV with a FWHM = 3.3 % only. This result is superior than the actual best value taken with a photomultiplier readout of CsI(Tl) light.

**Bottom right:** A pinhole grid with 6 holes around a circle with a diameter of 3 mm and a hole diameter of 200 µm was illuminated with X-rays of 144 keV energy. The light distribution of all 19 cells were used to find the centroid of the scintillator light. As can be seen in the figure, this was done with unprecedended success. The position of the holes was measured with a spatial resolution of better than 200 µm (FWHM).

The described techniques are equally useful for applications in basic science, medicine, life science and material research. Actual projects are related to astrophysics and medicine. SIEMENS medical is studying the concept for the replacement of photomultiplier tubes in Anger cameras.The experimental work was done by C. Fiorini, A. Longoni from Politecnico di Milano, Italy, funded by INFN.

**References:** C.Fiorini et al., NIMA 512, pp 265 - 272, 2003

# CAST – CERN Axion Solar Telescope

With the CERN Axion Solar Telescope – CAST – we use a prototype LHC superconducting dipole magnet to search for a hypothetical pseudoscalar particle, the axion. The axion is with the neutralino one of the leading dark matter candidates. Based on data acquired in 2003 we set a new upper limit on the axion to photon coupling constant.

A possible axion source is the innermost core of the Sun where axions can be produced via Primakoff effect. With the CAST experiment at CERN (European Organization for Nuclear Research), we search for such solar axions, using a $L = 9.3$ m long and $B = 9.0$ T strong superconducting LHC prototype magnet providing a homogeneous transversal magnetic field to convert axions to observable X-ray photons via inverse Primakoff effect. The resulting photons are expected to be thermally distributed in the energy range of $1$–$7$ keV with a mean energy of 4.2 keV and can be observed with conventional X-ray detectors. The tracking system of CAST allows us to follow the Sun with the magnet for 1.5 h during sunrise and sunset. Due to the higher sensitivity of the CAST experiment compared to earlier experiments, we were already able to improve existing upper limits on the axion photon coupling constant $g_{a\gamma\gamma} \propto (BL)^{-1/2}\, t^{-1/8}\, b^{1/8}$ by a factor of $\approx 5$ for axion masses $10^{-2}$ eV$<$ $m_{\mathrm{a}} < 0.2$ eV based on data acquired in 2003. In the second phase of CAST planned for 2005–2007, we will expand the sensitivity of CAST to higher axion masses $m_{\mathrm{a}} > 0.2$ eV by filling the magnet tubes with a buffer gas. This will allow us to scan the parameter space favored by theoretical axion models for the first time.

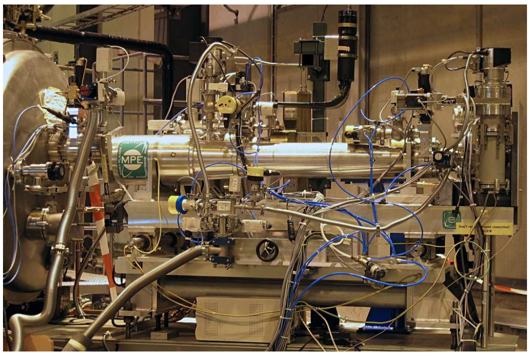

Left: The X-ray telescope and the pn-CCD detector in operation at the superconducting magnet at CERN.

Right: The pn-CCD detector located in the focal plane of the X-ray telescope.

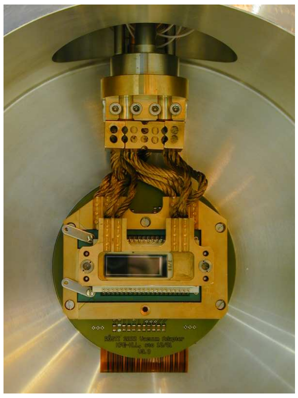

As the most sensitive detector system of CAST, we developed a Wolter I type grazing incidence X-ray mirror optics which was originally designed as a prototype for the German X-ray satellite ABRIXAS. The pn-CCD detector located in the focal plane of the X-ray telescope is a prototype of the fully depleted EPIC pn-CCD on-board of ESA's XMM-Newton mission which was developed at the MPI Halbleiterlabor. The detector is optimized for low background application by passive shielding and improved software rejection techniques. The combination of a focusing optics and a detector with high spatial and spectral resolution, improves the signal to background ratio of the CAST experiment by a factor of $\approx 200$ compared to a detector system without optics.

*The MPE/MPI CAST Team*

# PKE-Nefedov: Complex Plasmas on the ISS

MAX-PLANCK-GESELLSCHAFT

The PKE-Nefedov experiment is one of the first natural science experiments performed on the International Space Station ISS. It covers a new field of research under microgravity conditions – the complex plasmas. A complex plasma is a new form of matter with interesting properties that allow observations of its physics at the most fundamental – the kinetic – level. Interesting behaviours of complex plasmas under microgravity conditions have been observed (e.g. the 3-D crystalline structures observed in real space, collisions of complex plasma drops, shocks, instabilities etc.) in the 3 ½ years of operation.

Under microgravity conditions the typical static and dynamic behaviour of complex plasmas is illustrated in Figure 1 a). This figure shows a 3 second trajectory fragment of the microparticles, colour coded from red to blue. The dominant features which can be investigated here are:

- a microparticle free "void" in the centre of the system for most experimental parameters.
- a sharp boundary between the void and the complex plasma.
- demixing of complex plasma clouds formed by microparticles of different sizes.
- crystalline structures along the central axis.
- vortices in different areas away from the central axis.

All of the above mentioned features have been investigated in detail over the last years. These and other effects are published in a series of papers [1-7].

Fig. 1a

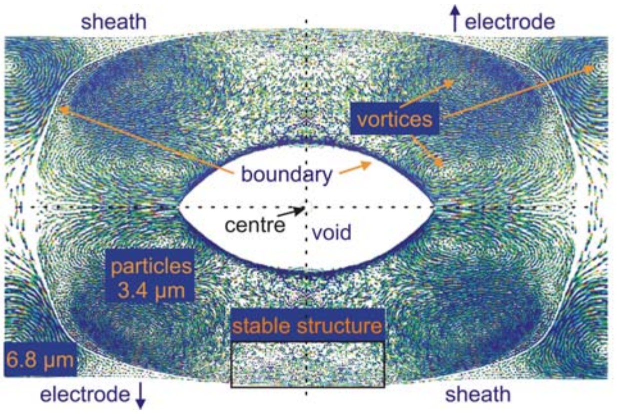


Fig. 1b

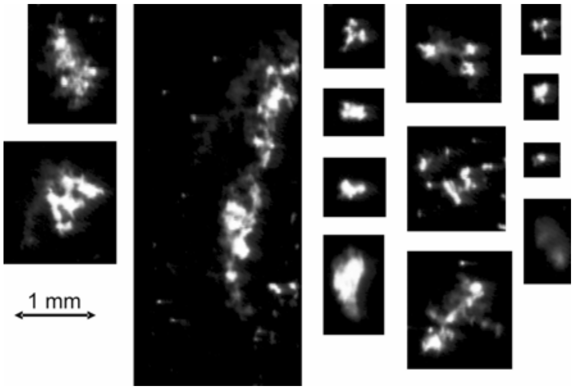


Beside the above described features of complex plasmas under microgravity conditions we observed interesting new phenomena not foreseen before. Just to mention two of those, this is the decharging [6] of the microparticles after the plasma source was switched off and the agglomeration of the microparticles after the injection into a neutral gas due to a new phase transition – the so-called gelation transition [7]. A zoo of grown agglomerates caused through this transition is shown in Fig. 1b.

**References:**

1. A. P. Nefedov, et al., New Journal of Physics **5,** 33.1–33.10 (2003)
2. V.E. Fortov, et al., Physical Review Letters. 90, 5005 (2003)
3. D. Samsonov et al., Phys. Rev. E **67**, 036404 (2003)
4. S. Khrapak et al., Physics of Plasmas **10**, pp. 1-4 (2003)
5. B. M. Annaratone, et al., Phys. Rev. E **66**, 056411 (2002)
6. A. V. Ivlev et al., Phys. Rev. Lett. **90**, 055003 (2003)
7. A. V. Ivlev et al., Phys. Rev. Lett. **89,** 195502 (2002)

*G.E. Morfill, H. M. Thomas and the PKE-Nefedov-team*

# PK-3 Plus – Future experiments on the ISS

PK-3 Plus is the follow-up experiment of PKE-Nefedov and is planned to be launched in December 2005. It will continue the very successful work on the ISS with a significantly improved hard- and software. The hardware, designed and manufactured at the Institute with the help of space industry, was tested in two parabolic flight campaigns. These first low-gravity experiments delivered first scientific results and showed the advanced possibilities of this new laboratory.

The research of complex plasmas under microgravity conditions is very important for the understanding of this new field of research and it complements the experiments in the laboratory. Gravity introduces the major force under laboratory conditions. Weaker forces are not measurable due to its strength. Therefore long-term experiments under µg conditions are very important. PKE-Nefedov, as the first long-term experiment of this kind of research performed on the ISS, showed insights into the physics of complex plasmas that made interest on more and better experiments. Therefore, PK-3 Plus, as the direct follow-up experiment was designed and built at the Institute. This facility allows much more detailed investigations due to its advanced hard- and software. The major changes were carried out 1) on the design of the plasma chamber (see Fig. 1a) for a better symmetry, homogeneity and reproducibility of experimental runs and 2) on the diagnostics. This allow much deeper investigations of the microgravity behaviour of complex plasmas.

a

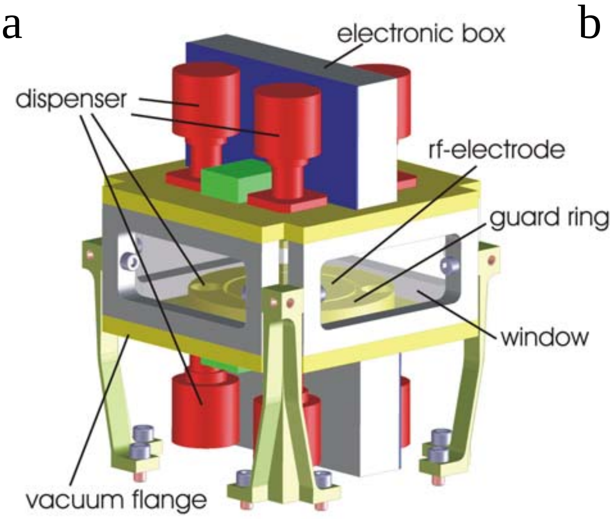


b

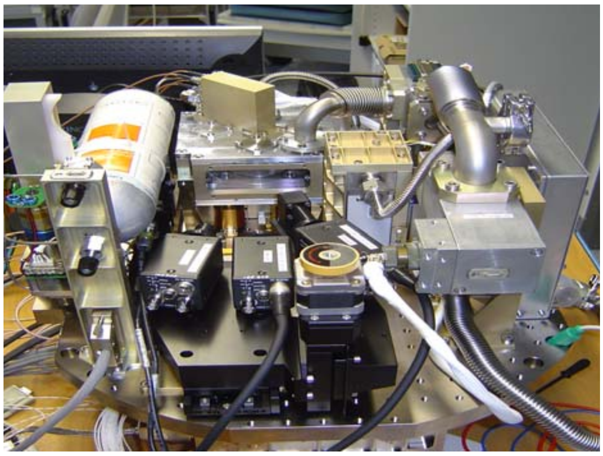

In two parabolic flight campaigns we tested the facility on its µg properties and received the first scientific results. The symmetry and homogeneity of the distribution of the microparticle cloud could only be tested under microgravity conditions and show the expected behaviour. Long experimental runs in the laboratory with additional diagnostics, like mass spectrometer, show the long term stability of the system resulting from the continuous gas flow through the plasma chamber.
The flight hardware is now in the manufacturing phase and will be delivered to Russia middle of next year for the launch to the International Space Station.

*G. Morfill, H. Thomas, H. Rohtermel, U. Konopka, M. Zuzic-Rubin, A. Ivlev and the PK-3 Plus Team*

# The Complex Plasma Experiment PK-4

PK-4 is a complex plasma experiment in a combined dc/rf discharge. As plasma chamber a glass tube with dc electrodes is used. This set-up is in particular suited to investigate the liquid phase of complex plasmas. PK-4 shall be operated on board of the International Space Station from 2007 on to study complex dc plasmas under microgravity.

Complex plasmas are low-temperature plasmas containing microparticles with a diameter of a few microns. Due to the high electron mobility in the plasma the microparticles collect up to 100.000 electron charges on their surface. Therefore they interact strongly with each other, leading to liquid and even crystal phases [1]. So far, complex plasmas are mostly studied in rf plasma chambers. PK-4 uses a dc or combined dc/rf discharge produced in a glass tube of 40 cm length and 3 cm diameter (see Fig.1 and 2). In this way, the microparticles streaming through the glass tube can be observed, allowing in particular to study the fluid phase of a complex plasma.

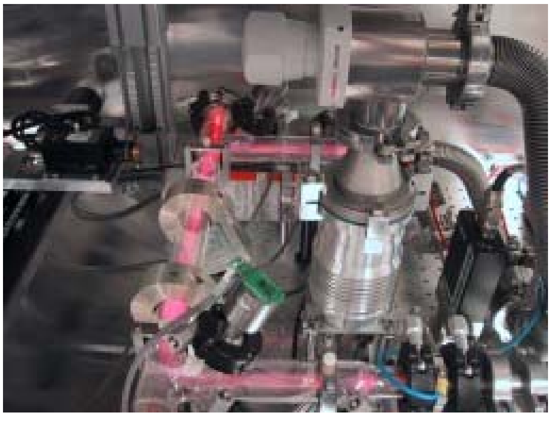

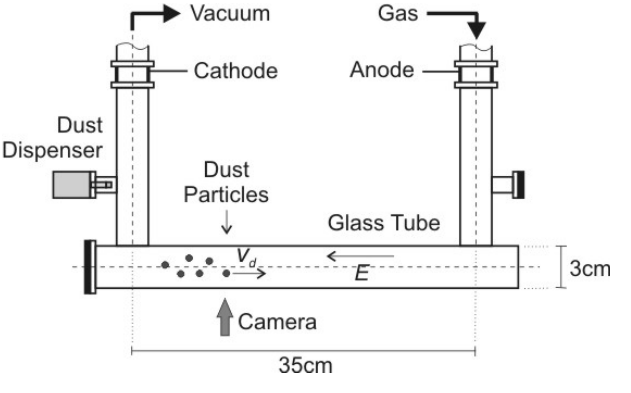


Since 2002 we perform experiments with PK-4 within a laboratory predevelopment phase, funded by DLR, in collaboration between MPE and IHED (Moscow). So far we have investigated dust waves and charging of the microparticles [2], the ion drag force acting on the microparticles, microparticle cloud collisions, and the simulation of a Lavalle nozzle. In addition measurements of the plasma conditions in the PK-4 plasma chamber were performed. These experiments were conducted in the laboratories at MPE and IHED as well as in two ESA parabolic flight campaigns. The final aim of PK-4 is the investigation of a complex dc plasma under microgravity on board of the International Space Station following the successful complex rf plasma experiments PKE-Nefedov and its successor PK3-Plus. The preparations of the space experiment PK-4, scheduled for 2007, will start with the next phase in 2005.

**References:**

[1] H.M. Thomas et. al, Phys. Rev. Lett. 73 (1994) 652
[2] S. Ratynskaia et al., Phys. Rev. Lett. 93 (2004) 085001

*MPE: M. Fink, H. Höfner, S. Khrapak, M. Kretschmer, G.E. Morfill, R. A. Quinn, S. Ratynskaia, K. Tarantik, M.H. Thoma*
*IHED: V. Fortov, Y. Gerasimov, O. Petrov, A. Usachev, A. Zobnin*